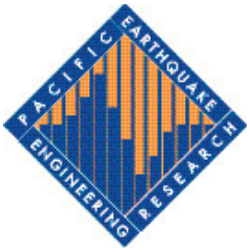

PACIFIC EARTHQUAKE ENGINEERING
RESEARCH CENTER

Global Collapse of Frame Structures under Seismic Excitations

Luis F. Ibarra

and

Helmut Krawinkler

Stanford University

PEER 2005/06
SEPT. 2005

Global Collapse of Frame Structures under Seismic Excitations

Luis F. Ibarra

and

Helmut Krawinkler

John A. Blume Earthquake Engineering Center
Department of Civil & Environmental Engineering
Stanford University

PEER Report 2005/06
Pacific Earthquake Engineering Research Center
College of Engineering
University of California, Berkeley

September 2005

ABSTRACT

Global collapse in earthquake engineering refers to the inability of a structural system to sustain gravity loads when subjected to seismic excitation. The research described in this report proposes a methodology for evaluating global incremental (side-sway) collapse based on a *relative intensity measure* instead of an engineering demand parameter (EDP). The relative intensity is the ratio of ground motion intensity to a structural strength parameter, which is increased until the response of the system becomes unstable. At this stage the relative intensity – EDP curve becomes flat (zero slope). The largest relative intensity is referred to as "collapse capacity."

In order to implement the methodology, deteriorating hysteretic models are developed to represent the monotonic and cyclic behavior of structural components. Parameter studies that utilize these deteriorating models are performed to obtain collapse capacities and quantify the effects of system parameters that most influence collapse for SDOF and MDOF systems. The dispersion of the collapse capacity due to record to record variability and uncertainty in the system parameters is evaluated. The latter source of dispersion is quantified by means of the first-order second-moment method. The studies reveal that softening of the post-yield stiffness in the backbone curve (post-capping stiffness) and the displacement at which this softening commences (defined by the ductility capacity) are the two system parameters that most influence the collapse capacity of a system. Cyclic deterioration is an important but not dominant issue for collapse evaluation. P-delta effects greatly accelerate the collapse of deteriorating systems and may be the primary source of collapse for flexible but very ductile structural systems.

The report presents applications of the proposed collapse methodology to the development of collapse fragility curves and the evaluation of the mean annual frequency of collapse.

An important contribution is the development of a transparent methodology for the evaluation of incremental collapse in which the assessment of collapse is closely related to the physical phenomena that lead to this limit state. The methodology addresses the fact that collapse is caused by deterioration in complex assemblies of structural components that should be modeled explicitly.

ACKNOWLEDGMENTS

This work was supported in part by the Pacific Earthquake Engineering Research Center through the Earthquake Engineering Research Centers Program of the National Science Foundation under award number EEC-9701568. The work reported herein is part of the PEER mission to develop and disseminate technologies to support performance-based earthquake engineering.

Any opinions, findings, and conclusions or recommendations expressed in this material are those of the author(s) and do not necessarily reflect those of the National Science Foundation.

This report was originally published as the Ph.D. dissertation of the first author. The financial support provided by PEER is gratefully acknowledged. The authors would like to thank Professors C. A. Cornell, Gregory G. Deierlein, and Eduardo Miranda, who provided constructive feedback on the manuscript. Several graduate students, present and former, at the Stanford University John A. Blume Earthquake Engineering Center have provided assistance and valuable input. In particular, the help provided by Ricardo Medina, Ashraf Ayoub, Curtis Haselton, Francisco Parisi, Fatheme Jalayer, Dimitrios Vamvatsikos, Jack Baker, Jorge Ruiz-Garcia, Christoph Adam, Farzin Zareian, and Rohit Kaul is much appreciated.

CONTENTS

LIST OF FIGURES

[1] Section 6.2.4 contains the definitions of contributions to variance of collapse capacity such as $\sigma^2_{\ln S_{a,c}(\alpha)}$

LIST OF TABLES

1 Introduction

1.1 MOTIVATION FOR THIS STUDY

Protection against collapse has always been a major objective of seismic design. In earthquake engineering, collapse refers to a structural system's loss of capacity to resist gravity loads when subjected to seismic excitation. Global collapse may imply dynamic instability in a side-sway mode, usually triggered by large story drifts, which are amplified by P-Δ effects and deterioration in strength and stiffness of the components of the system.

Assessment of collapse safety necessitates the capability to predict the dynamic response of deteriorating systems, particularly for existing older construction in which deterioration commences at relatively small deformations. Because of the lack of hysteretic models capable of simulating deteriorating behavior, global collapse is usually assumed to be associated with an "acceptable" story drift or the attainment of a limit value of deformation in individual components of the structure. This approach does not permit a "redistribution" of damage and does not account for the capacity of the system before collapse to sustain deformations that are significantly larger than those associated with loss in the resistance of individual elements.

Thus, a systematic approach to integrate all the sources of global collapse needs to be developed. The approach should include the effect of backbone strength deterioration, cyclic deterioration, (CD), and P-Δ effects on the global collapse of structural systems. In the context of this report, global collapse implies incremental "side-sway" collapse of at least one story of the structure.

1.2 OBJECTIVE

The main objective of the study is to develop a methodology for evaluating global (side-sway) collapse for deteriorating structural systems. The evaluation of collapse is based on a measure called the "relative intensity," which is defined as the ratio of the ground motion intensity to a

structural strength parameter. The relative intensity at collapse is called "collapse capacity." The components of this methodology are:

- Development of hysteresis models that incorporate all important phenomena contributing to global collapse;
- Computation of the collapse capacity for representative sets of frame structures and ground motions;
- Evaluation of statistical measures of the collapse capacity, and of the effect of uncertainties in ground motions and in structural parameters on these statistical measures;
- Development of collapse fragility curves; and
- Evaluation of the mean annual frequency of collapse.

1.3 OUTLINE

The general methodology for assessing side-sway collapse is described in Chapter 2, where the main concepts used in this investigation are introduced and advantages and limitations of the procedure are illustrated. A literature review of the most salient findings in the evaluation of structural collapse is also included.

Chapter 3 focuses on the development of deteriorating component hysteretic models, including strength deterioration of the backbone curve and cyclic deterioration of strength and stiffness. The calibration of the hysteretic models with experimental results is illustrated. The models are implemented in an in-house single-degree-of-freedom (SDOF) program that carries out dynamic and quasi-static inelastic analysis, and in a dynamic nonlinear analysis program for multi-degree-of-freedom (MDOF) systems.

Collapse evaluation of SDOF systems is the topic of Chapter 4. A parametric study is carried out to determine the main parameters that influence collapse, such as type of hysteretic model, ductility capacity, and post-capping stiffness. Statistics for collapse capacity are computed considering record-to-record (RTR) variability.

Chapter 5 deals with global collapse of generic frames whose inelastic behavior is modeled by springs at the ends of structural members. Initially, collapse capacity is obtained for strong column–weak beam frames, considering columns with infinite strength. Later, the "strong column–weak beam" concept is tested by adjusting the strength of the columns to specific strong

column factors. A procedure for obtaining equivalent SDOF systems for deteriorating MDOF systems including P-Δ effects is also presented.

In Chapter 6 the sensitivity of collapse capacity to uncertainty in the system parameters is investigated by using the first-order second-moment method (FOSM). Different alternatives for applying the FOSM method to the evaluation of collapse capacity are investigated. Monte Carlo simulation is used for verifying the accuracy of FOSM results. The additional variance of collapse capacity due to uncertainty in the system parameters is computed for representative SDOF systems and a baseline MDOF generic frame.

Collapse fragility curves are presented in Chapter 7, and are based on collapse capacity information of SDOF and MDOF systems. These fragility curves are combined with hazard curves for a specific site to show how the collapse methodology may be employed to obtain the mean annual frequency of collapse for a given system.

The main conclusions, as well as future research directions, are presented in Chapter 8. Four appendices are included. Appendix A presents the methods used for computing statistical values. Appendix B describes the main characteristics of the generic frames used in the study. Appendix C demonstrates quantitatively that a lognormal distribution can be fitted to the distribution of collapse capacity due to RTR variability. Appendix D presents a comparison of computations of additional variance of collapse capacity in the linear and log domain of the data.

2 Collapse Methodology

2.1 INTRODUCTION

In earthquake engineering, "collapse" refers to the incapacity of a structural system, or a part of it, to maintain gravity load-carrying capacity under seismic excitation. Collapse may be local or global; the former may occur, for instance, if a vertical load-carrying component fails in compression or if shear transfer is lost between horizontal and vertical components (e.g., shear failure between a flat slab and a column). Global collapse may have several causes. The spread of an initial local failure from element to element may result in cascading or progressive collapse (Liu et al., 2003; Kaewkulchai and Willamson, 2003). Incremental collapse occurs if the displacement of an individual story is very large, and second-order (P-Δ) effects fully offset the first-order story shear resistance. In either case, replication of collapse necessitates modeling of deterioration characteristics of structural components subjected to cyclic loading, and the inclusion of P-Δ effects.

In this study a global collapse assessment approach is proposed considering deteriorating hysteretic models. This approach permits a redistribution of damage and takes into account the ability of the system to maintain stability until structure P-Δ effects overcome the deteriorated story shear resistance.

2.2 PREVIOUS RESEARCH ON GLOBAL COLLAPSE

Improvements on collapse assessment approaches have been developed on several fronts. Researchers have worked independently in understanding and quantifying P-Δ effects and in developing deteriorating nonlinear component models that can reproduce experimental results. In addition, some efforts have been carried out to integrate all the factors that influence collapse in a unified methodology. The following is a summary of salient studies.

P-Δ Effects. The study of global collapse started by including P-Δ effects in seismic response. Even though hysteretic models considered a positive post-yielding stiffness, the structure tangent stiffness became negative under large P-Δ effects, eventually leading to collapse of the system. For instance, Jennings and Husid (1968) utilized a one-story frame with springs at the ends of the columns utilizing bilinear hysteretic models. They concluded that the most important parameters in collapse are the height of the structure, the ratio of the earthquake intensity to the yield level of the structure, and the second slope of the bilinear hysteretic model. They stated that the intensity of motion needed for collapse depends strongly on the duration of ground motion. This conclusion was drawn without consideration of cyclic deterioration behavior, and simply because the likelihood of collapse increases when the loading path stays for a longer time on a backbone curve with a negative slope.

Sun et al. (1973) studied the gravity effect on the dynamic behavior of an SDOF system and its effect on the change of the period of the system. They showed that the maximum displacement that a system may undergo without collapse is directly related to the stability coefficient and the yield displacement of the system. In 1986, Bernal studied this coefficient in depth and proposed amplification factors based on the ratio of spectral acceleration generated with and without P-Δ effects. He considered elastic-plastic SDOF systems and used the same stability coefficient for all the period range of interest. Under these assumptions, no significant correlation between amplification factors and natural period was found. McRae (1994) extended the results of Bernal's study to address structures with more complex hysteretic response while considering the P-Δ effect.

Bernal (1992, 1998) analyzed two-dimensional moment-resisting frames, concluding that the minimum strength (base shear capacity) needed to withstand a given ground motion without collapse is strongly dependent on the shape of the controlling mechanism. Dynamic instability was evaluated from an equivalent elastic-plastic SDOF system that included P-Δ effects. A salient feature of his model is the applicability to buildings that may have different failure mechanisms. The importance of the failure mode had been recognized elsewhere (Takizawa, 1980), but prior studies had been limited to single-story structures or had been restricted to buildings with global failure mechanisms.

Degrading Hysteretic Models. Bilinear elastic-plastic hysteresis models were the first to be used because of their simplicity, and the first model with softening of the reloading stiffness was proposed by Clough and Johnston (1965). In this model, the degradation of the reloading

stiffness is based on the maximum displacement that has taken place in the direction of the loading path. Because of this characteristic, this model is often referred to as the peak-oriented model. The original version was slightly modified by Mahin and Bertero in 1975 (see Section 3.3.2). In 1970, Takeda (Takeda, 1970) developed a model with a trilinear backbone that degrades the unloading stiffness based on the maximum displacement of the system. His model is designed for reinforced concrete (RC) components, and the envelope is trilinear because it includes a segment for uncracked concrete. In addition to models with piecewise linear behavior, smooth hysteretic models have been developed that include a continuous change of stiffness due to yielding and sharp changes due to unloading, i.e., the Wen-Bouc model (Wen, 1976).

Experimental studies have shown that the hysteretic behavior is dependent upon numerous structural parameters that greatly affect the deformation and energy-dissipation characteristics. This has led to the development of more versatile models, such as the smooth hysteretic degrading model developed by Sivaselvan and Reinhorn (2000), which includes rules for stiffness and strength deterioration, as well as pinching. However, the model does not include a negative stiffness. The model of Song and Pincheira (2000) is also capable of representing cyclic strength and stiffness deterioration based on dissipated hysteretic energy. The model is essentially a peak-oriented one that considers pinching based on deterioration parameters. The backbone curve includes a post-capping negative stiffness and a residual strength branch. Because the original backbone curve does not deteriorate, unloading and accelerated cyclic deterioration are the only modes included, and prior to reaching the peak strength, the model is incapable of reproducing strength deterioration.

In this investigation, deteriorating models are developed for basic bilinear, peak-oriented, and pinched hysteretic models. These models include a backbone curve with negative post-capping branch and a branch of residual strength, which is optional. Deterioration is based on energy dissipation according to the rules proposed by Rahnama and Krawinkler (1993) (see Chapter 3). Relevant works by others regarding the effect of deteriorating hysteretic models on the response are presented in Chapters 4 and 5.

Analytical Collapse Investigations. Takizawa and Jennings (1980) examined the ultimate capacity of an RC frame under seismic excitations. The structural model employed was an equivalent SDOF system characterized by degrading trilinear and quadrilinear (strength-degrading) hysteretic curves. This is one of the first attempts to consider P-Δ effects and material deterioration in the evaluation of collapse. More recently Aschheim and Black (1999) carried out

a systematic study to assess the effects of prior earthquake damage on the peak displacement response of SDOF systems. Prior damage was modeled as a reduction in initial stiffness under the assumption that residual displacements are negligible. They used modified Takeda models to show that SDOF systems with negative post-yield stiffness were prone to collapse, whether or not they had experienced prior damage.

Mehanny and Deierlein (2000) investigated collapse for composite structures consisting of RC columns and steel or composite beams. For a given structure and intensity of the ground motion (GM) record, they carried out a second-order inelastic time history analysis (THA) of the undamaged structure and calculated cumulative damage indices, which were used to degrade stiffness and strength of the damaged sections. The damaged structure was reanalyzed through a second-order inelastic static analysis considering residual displacements and including only gravity loads. Global collapse was assumed to occur when the maximum vertical load the damaged structure could sustain was less than the applied gravity loads ($\lambda_u < 1$). If collapse did not take place the record was subsequently scaled up to determine the ground motion intensity at which collapse occurs.

Lee and Foutch (2001) evaluated the performance of new steel moment-resisting frames as a part of the FEMA/SAC project. Their analytical models included a fracturing element implemented by Shi (1997) in the Drain-2DX program. For evaluating the global drift capacity of the SAC buildings, they utilized the "IDA" approach (Vamvatsikos and Cornell, 2002). The onset of global dynamic instability was defined as the point where the local slope of the IDA curve decreased to less than 20% of the initial slope of the IDA curve in the elastic region. The frames were subjected to sets of 20 SAC GMs. Jalayer (2003) also employed the IDA concept for estimating the global dynamic instability capacity of a regular RC structure. She included strength deterioration caused by shear failure of the columns based on the model developed by Pincheira et al. (1999).

Williamson (2003) studied the response of SDOF systems subjected to several ground motion records including P-Δ effects and material deterioration based on a modified Park and Ang damage model. He detected large sensitivity to both the properties of the structure and the characterization of the ground motion.

Miranda and Akkar (2003) evaluated the lateral strengths required to avoid collapse in bilinear SDOF systems with negative post-yield stiffness. They detected a significant influence of the period of vibration for short-period systems with small negative post-yield stiffness. They

reported that the dispersion of the aforementioned lateral strengths increases as the negative post-yield stiffness decreases and as the period of vibration increases.

Adam and Krawinkler (2003) investigated the difference in the response of highly nonlinear systems under different analytical formulations. They concluded that large displacements formulation produces about the same responses as conventional (small displacement) formulations, even in cases where collapse is close.

Experimental Collapse Investigations. A large number of experiments have been carried out to relate collapse with shear failure and ultimately with axial failure in columns. For instance, Yoshimura and Yamanaka (2000) tested several reinforced concrete columns subjected to low axial load. They detected that lateral and axial deformation, as well as input energy at collapse vary depending on the loading protocol imposed on each specimen. On the other hand, the ratio of vertical deformation increment to lateral deformation increment at collapse does not vary with the loading path. They concluded that collapse occurs when lateral load decreases to about 10% of the maximum load. Nakamura and Yoshimura (2002) evaluated columns experiencing shear failure prior to flexural yielding and others failing in shear after flexural yielding. They concluded that axial failure occurs when the shear capacity is reduced to approximately zero.

Sezen (2002) tested full-scale shear-critical reinforced concrete building columns under cyclic lateral loads until the column could no longer sustain the applied axial load. The tests demonstrated that the loss of axial load not necessarily follows immediately after loss of lateral load capacity. Elwood and Moehle (2002) concluded that shear failure in columns does not necessarily lead to collapse of the system. Shear failure usually is accompanied by a reduction of axial capacity that depends on several factors. They found that in columns having lower axial loads, axial load failure occurs at relatively large drifts, regardless of whether shear failure had just occurred or whether shear failure had occurred at much smaller drift ratios. For columns with larger axial loads, axial load failure tends to occur at smaller drift ratios, and might occur almost immediately after loss of lateral load capacity. They also collected data for developing an empirical model to estimate shear strength deterioration.

Vian and Bruneau (2001) carried out a series of shake table tests of a SDOF steel frame system subjected to earthquakes of progressively increasing intensity up to collapse due to geometric nonlinearities (P-Δ effect). They concluded that the stability coefficient has the most significant effect on the behavior of the structure. As this coefficient increases, there is a

decrease in the maximum sustainable drift and spectral acceleration that can be resisted before collapse. Kanvinde (2003) extended the work of Vian and Bruneau by testing additional SDOF systems. He detected that current methods of nonlinear dynamic analysis such as the OpenSees platform (OpenSees, 2002) are very accurate for predicting collapse for systems in which the P-Δ effect dominates the onset of collapse.

In conclusion, despite the large number of research studies on the topic, the response of structural systems under the combination of geometric nonlinearities and material deterioration has not been investigated in detail. Thus, a need exists for carrying out systematic research on global collapse considering all the sources that lead to this limit state.

2.3 DESCRIPTION OF GLOBAL COLLAPSE ASSESSMENT APPROACH

In this investigation, global collapse refers to the inability of a system to support gravity loads because of excessive lateral displacement, which significantly reduces the story shear resistance and produces instability in the system. Traditionally, the collapse potential has been estimated by using non-deteriorating systems to predict engineering demand parameters[2] (EDPs) and assigning judgmental limits to these parameters. In recent years, deteriorating systems have been used to estimate collapse but still based on pre-established EDPs limits. However, EDPs become very sensitive when the system is close to collapse, and small perturbations in the input produce large variations in the response (Fig. 2.1). For this reason, in the proposed methodology global collapse is described by a *relative intensity measure* instead of an EDP. The relative intensity measure is the ratio of ground motion intensity to a structural strength parameter. In this study, the ground motion intensity measure is the spectral acceleration at the fundamental period of the structure normalized by the acceleration of gravity (g), and the strength parameter is the yield strength of the structure normalized by its seismic weight (see Section 2.3.4). For a given structure and ground motion, collapse evaluation consists of a series of dynamic analysis starting with a relative intensity that produces an elastic response of the system. Then the relative intensity is increased until collapse takes place. The relative intensity at collapse is called the "collapse capacity" (see Section 2.3.4).

[2] EDPs are the output of response prediction; some of the most relevant ones are story drift, ductility, hysteretic energy, etc.

This process requires analytical replication of collapse and necessitates modeling of deterioration characteristics of structural components. The use of deteriorating models permits a redistribution of damage and takes into account the ability of the system to sustain significantly larger deformations than those associated with reaching the ductility "capacity" in one component. In this study deteriorating hysteretic models have been developed that are relatively simple but sufficiently versatile to model all basic deterioration modes in components of different materials (Chapter 3).

Dynamic analysis requires the specification of system properties and input ground motions, but variations in these quantities may produce large dispersion in the resulting response. Therefore, collapse needs to be evaluated in a probabilistic framework that includes uncertainties in the frequency content of the ground motions (Chapter 4 for SDOF systems and Chapter 5 for MDOF structures) and in the input parameters of the system (Chapter 6). A final product of collapse assessment could be the mean annual frequency of collapse, which is obtained by combining fragility curves with the hazard information at a given site (Chapter 7). Fragility curves are developed directly from the collapse capacities of the system.

The following is a description of the steps involved in the methodology proposed to assess global collapse.

2.3.1 Selection of Ground Motions

The global collapse approach is based on time history analysis. Thus, a set of ground motions must be carefully selected according to specific objectives. The set must be sufficiently large to provide reliable statistical results. In this study, the intensity measure (IM) of GMs is the 5% linear elastic spectral acceleration at the fundamental period of vibration of the structural system, $S_a(T_1)$. Section 4.2.4 describes a set of 40 "ordinary" GMs, LMSR-N, which is extensively used in this investigation. Additional sets for near-fault and long-duration GMs are also included in Chapter 4.

2.3.2 Deterioration Models

Collapse evaluation is based on hysteretic models that account for history-dependent strength and stiffness deterioration. Deteriorating models have been developed for bilinear, peak-oriented, and pinching hysteretic models (described in Chapter 3). The monotonic backbone curve of these

systems consists of an elastic branch, a strain-hardening branch, a negative tangent stiffness branch, and in some cases a residual strength branch of zero slope (Fig. 3.2). In addition, cyclic deterioration is accounted for by using energy dissipation as a deterioration criterion. The following four modes of deterioration are included: basic strength, post-capping strength, unloading stiffness, and accelerated reloading stiffness deterioration. Figure 2.2 shows the response of an SDOF system represented by a peak-oriented model with rapid cyclic deterioration. Basic strength and post-capping deterioration move the strain-hardening and post-capping branches toward the origin, respectively. Unloading stiffness deterioration flattens the unloading stiffness after each reversal, whereas accelerated reloading stiffness deterioration increases the target maximum displacement.

In this research the term "deteriorating models" is used for hysteretic models that possess a post-capping stiffness branch in the backbone curve and/or are subjected to cyclic deterioration. The term "non-deteriorating" or "happy" is used for models without a post-capping branch (infinite ductility capacity) that are not subjected to cyclic deterioration, although geometric nonlinearities (P-Δ effects) could be present.

2.3.3 Structural Systems

In general, the collapse assessment methodology is the same for SDOF and MDOF systems. A large variety of SDOF systems are used in Chapter 4 to determine the parameters that most affect global collapse. The information synthesized from SDOF systems is used to narrow the number of parameters to be studied in MDOF structures. The MDOF structures to be studied are generic frames that include nonlinear behavior by means of concentrated plasticity (Chapter 5). The generic frames are single-bay frames of 3, 6, 9, 12, 15, and 18 stories, with a flexible and stiff version for each number of stories.

2.3.4 Collapse Capacity

To obtain the collapse capacity associated with a particular ground motion, the structural system is analyzed under increasing relative intensity values, expressed as $(S_a/g)/\eta$ for SDOF systems. The intensity of the ground motion (S_a) is the 5% damped spectral acceleration at the elastic period of the SDOF system (without P-Δ effects), whereas $\eta = F_y/W$ is the base shear strength of

the SDOF system normalized by its seismic weight. The relative intensity can be plotted against the EDP of interest, resulting in $(S_a/g)/\eta$ - EDP curves.

For MDOF structures, the relative intensity is expressed as $[S_a(T_1)/g]/\gamma$, where $S_a(T_1)/g$ is the normalized spectral acceleration at the fundamental period of the structure without P-Δ effects, and the parameter γ is the base shear coefficient V_y/W, which is equivalent to η. These relative intensity definitions permit a dual interpretation:

(1) If the ground motion intensity is increased and the strength of the system is kept constant, the resulting $(S_a/g)/\eta$ - EDP (or $[S_a(T_1)/g]/\gamma$– EDP) curves represent incremental dynamic analyses (IDAs) (Vamvatsikos and Cornell, 2002).

(2) If the ground motion intensity is kept constant (given hazard) and the strength of the system is decreased, the resulting $(S_a/g)/\eta$ – EDP or ($[S_a(T_1)/g]/\gamma$– EDP) curves represent EDP demands for various strength levels and are referred to as "strength variation curves." In this case, $(S_a/g)/\eta$ is equivalent to the conventional strength reduction factor, *R,* for structures without overstrength. Note that when the strength is decreased the entire backbone curve scales down (Fig. 2.3). This is a simplification of real behavior that must be cautiously interpreted because in many common structures, a reduction in the strength parameter is not necessarily accompanied by a similar reduction in the deformation capacity of the structure. An investigation developed in parallel with this work (Krawinkler et al., 2003) recognizes that structural systems have a bracketed range of deformation characteristics and that the strength of the system can be modified without significantly altering the deformation characteristics.

For SDOF systems both interpretations provide the same normalized EDPs, whereas for MDOF structures the normalized EDPs should be very similar (see Section 5.2).

An illustration of typical relative intensity–normalized displacement curves [$(S_a/g)/\eta$ – EDP] [3] is shown in Figure 2.4. Most of the figures of this report contain information in the heading that defines the ground motions and the properties of the structural system used to derive the results. The following information is contained in the heading of Figure 2.4:

- Type of basic hysteresis model: peak-oriented model (see Section 3.2)
- Set of ground motions: LMSR-N (see Section 4.2.3)

[3] The nomenclature and representative results discussed in the rest of this chapter correspond to SDOF systems.

- Percentage of critical damping of the system: $\xi = 5\%$
- P-Δ effect considered: P-Δ = "0.1*N*," (see Section 4.3.6)
- Strain-hardening ratio: $\alpha_s = 0.03$ (Section 3.2.1 and Fig. 3.2)
- Post-capping stiffness coefficient: $\alpha_c = -0.10$ (Section 3.2.1 and Fig. 3.2). This parameter defines the slope of the branch of the backbone curve after the peak strength is reached
- Ductility capacity: $\delta_c/\delta_y = 4$ (Section 3.2.1 and Fig. 3.2). It refers to the ratio of the displacement at which peak strength is attained (δ_c) over the yield displacement (δ_y)
- Cyclic deterioration parameters: $\gamma_{s,c,k,a} = 100$ (Section 3.3).

The most common EDPs in this investigation are the maximum displacement normalized by the spectral displacement, δ_{max}/S_d, and the maximum displacement normalized by the yield displacement, δ_{max}/δ_y. Occasionally, the normalized hysteretic energy, NHE, is also utilized.

In the particular case of Figure 2.4, the EDPs correspond to normalized displacements and the curves represent $[(S_a/g)/\eta - \delta_{max}/S_d]$ for an intermediate ductile SDOF system and a set of 40 ground motions The deteriorating characteristics of the system cause the individual curves to eventually approach a zero slope as $(S_a/g)/\eta$ increases, implying the proximity of collapse because the relative intensity can no longer be increased. The last point of each individual curve represents the relative intensity value at which the system collapses for a particular ground motion. This point is denoted as "collapse capacity" or $(S_{a,c}/g)/\eta$ [4] and is equivalent to the *R*-factor at collapse. To obtain $(S_{a,c}/g)/\eta$ for a given record, the relative intensity is increased in small steps until numerical instability is detected; then the algorithm utilizes the bisection method to determine the collapse capacity within a specified tolerance. Occasionally numerical instability occurs at several relative intensity levels, i.e., the system experiences global collapse at some relative intensity level only to reappear as a non-collapsed system at a higher relative intensity level. Vamvatsikos and Cornell (2002) refer to this phenomenon as "structural resurrection." However, this behavior has a marginal effect on statistical results because it occurs in very rare occasions. Therefore, in this work only the first collapse is taken into account, at least the first one to be detected by the proposed algorithm.

[4] Collapse capacity is expressed in this form for the sake of simplicity. Rigorously, its nomenclature should be $[(S_a/g)/\eta]_c$ for SDOF systems and $\{[S_a(T_1)/g)/\gamma]\}_c$ for MDOF systems. Collapse is produced by an increment of the ground motion intensity, then the collapse capacity is represented as $S_{a,c}/g$ for a given η. On the other hand, if collapse is due to a decrease in the strength of the system, collapse capacity should be expressed as $1/\eta_c$ for a given S_a/g.

The dynamic analyses for different relative intensities can be carried out for a number of ground motions sufficiently large to perform statistical evaluation of the results. As illustrated in Figure 2.4, the median collapse capacity is obtained by carrying out "vertical statistics" on the individual collapse capacities (see Section 2.3.8). Note that the median $(S_a/g)/\eta$ curve is based on "horizontal statistics" of the EDP at different intensity levels and terminates when 50% of the records have led to collapse of the system. Therefore, the last point of the median curve does not represent exactly the median collapse capacity, which must be obtained from "vertical" statistics. The terms "horizontal" and "vertical" are relative; hence, the use of these terms presupposes that EDPs are plotted on the horizontal axis and the relative intensity on the vertical axis.

An example of the dependence of $(S_{a,c}/g)/\eta$ on ground motions and the system period is shown in Figure 2.5, which presents collapse capacities for individual records as well as median and 16th percentile values. The results are obtained by performing collapse analysis for structural systems whose period is varied in closely spaced intervals. For instance, the individual collapse points of Figure 2.4 are used in Figure 2.5 to obtain collapse statistics at T = 0.5 s. For this case, the statistical values for the collapse capacity are almost constant with period, except in the short-period range. The $(S_{a,c}/g)/\eta$ - T curves are called "collapse capacity spectra" and are extensively used in the rest of this work to evaluate collapse capacity, to determine the influence of various parameters on collapse, and to generate fragility curves.

This example also illustrates the large dispersion in collapse capacity that can be obtained due to differences in the frequency content of the ground motions. This points toward the need to find more effective IMs in order to reduce the variability in the structural demands.

2.3.5 Effect of Deterioration Prior to Collapse

Although this investigation focuses on collapse evaluation, useful information has been generated on the response prior to collapse. Relative intensity versus EDP curves for deteriorating systems permit an assessment of the effect of deterioration when compared to equivalent curves for non-deteriorating systems. For instance, Figure 2.6 presents median $(S_a/g)/\eta$ - δ_{max}/δ_y curves for identical systems, except for the ductility capacity parameter (δ_c/δ_y). The uppermost curve is for a non-deteriorating (infinitely ductile) system (δ_c/δ_y = infinite), in which case collapse will never occur unless the P-Δ effect is large. The other three curves are for systems with specific ductility capacities. Due to cyclic deterioration effects, the median curve

for the system with δ_c/δ_y = 6 starts to deviate from that of the infinitely ductile system at a ductility (δ_{max}/δ_y) smaller than the ductility capacity of the system. Section 4.3.1 presents salient findings of the response of deteriorating systems prior to collapse.

2.3.6 Effects of Uncertainty in System Parameters

In the first part of the study, collapse capacity is evaluated considering record to record variability (RTR) as the only uncertainty in the computation of collapse capacity. However, as illustrated in Figure 2.7, system parameters like ductility capacity and post-capping stiffness can also be considered in a probabilistic framework, even though experimental information that can be used to define statistical properties of the parameters of the hysteresis model is rather limited.

In Chapter 6, the first-order second-moment (FOSM) method is used to compute the additional variance of collapse capacity due to uncertainty in the system parameters, whereas Monte Carlo simulation is used to verify some results. The FOSM method approximates the collapse capacity variance based on a Taylor's series expansion of a performance function (g) about the expected values of the random variables. One of the main advantages of the method is that the first and second moments are estimated without knowing the distribution of the function "g." For instance, Figure 2.8 presents the contributions to the variance of collapse capacity from several sources, including RTR variability, uncertainty in post-capping stiffness, ductility capacity, and cyclic deterioration, assuming a standard deviation of the log of the data of 0.60. The example does not include correlation among the different parameters. Depending on the characteristics of the system, the contributions of uncertainty in the system parameters to the total variance may be small or comparable to the contribution due to RTR variability.

2.3.7 Collapse Fragility Curves and Mean Annual Frequency of Collapse

A direct application of collapse capacity evaluation is the computation of the mean annual frequency of collapse, which is obtained by integrating the collapse fragility curve for a given η value over a S_a hazard curve pertaining to a specific site.

Fragility curves can be developed from collapse capacities for a set of ground motions as those shown in Figure 2.4. The collapse capacity distribution is assumed to be lognormal (see Appendix C) and the first and second moments are computed from individual collapse points.

This information is used to generate the cumulative distribution function (CDF), which corresponds to a fragility curve and describes the probability of collapse given the value of $(S_a/g)/\eta$. Typical results are presented in Figure 2.9 for several of the studied SDOF systems with the same period but with variations in system parameters. As observed, the probability of collapse may be very sensitive to the hysteretic properties of the system. For computing the mean annual frequency of exceedance, these fragility curves need to be de-normalized by a specific η value that defines the strength of the structural system.

Once a fragility curve is computed and hazard information for the site is available, the mean annual frequency of collapse can be computed as follows (Medina, 2002; Jalayer, 2002):

$$\lambda_c = \int_0^\infty F_{C,S_{a,c}}(x) \mid d\lambda_{S_a}(x) \mid \tag{2.1}$$

where $F_{C,S_{a,c}}(x)$ represents the probability of S_a capacity, $S_{a,c}$, exceeding x, and $\lambda_{Sa}(x)$ is the mean annual frequency of S_a exceeding x (ground motion hazard). $F_{C_{Sa}}(x)$ corresponds to the fragility curve obtained from individual collapse capacities. The process of integrating Equation (2.1) is illustrated in Figure 2.10. In this context, the structural strength parameter (γor η) is kept constant and the individual curves of 2.10 represent IDAs.

Mean annual frequencies of collapse for a specific site and ductile SDOF systems are shown in Figure 2.11 for selected η values. As observed, the mean annual frequency of collapse strongly depends on the lateral strength and period of the system (see Chapter 7). These results are obtained by numerical integration of collapse fragility curves with hazard curves for selected periods pertaining to the specific site. The hazard curves used in this case were generated from the equal-hazard response spectra values calculated for a Van Nuys, California, site (Somerville and Collins, 2002) (see Chapter 7).

2.3.8 Statistical Considerations

The central value and a measure of dispersion can be evaluated by means of "computed" or "counted" statistics (Appendix A). Both methods have pros and cons; thus, their use is dictated by the types of analyzed data. For instance, for given $(S_a/g)/\eta$ values, EDP data can be evaluated by using counted statistics, in which the median and percentiles of interest are directly obtained from the sorted data. Counted statistics are used because increments in $(S_a/g)/\eta$ eventually lead

to collapse of a deteriorating system under one or more ground motions. Once the first collapse takes place, the data for higher relative intensity levels are incomplete and the counted process appears to be the most appropriate[5].

On the other hand, the first and second moments of collapse capacities are obtained from computed statistics of the individual $(S_{a,c}/g)/\eta$ values. This procedure can be used because deteriorating systems always collapse if the relative intensity is large enough. Computed statistics are preferred because they permit the formulation of closed-form solutions to calculate the mean annual frequency of collapse, and because the ratio of computed medians is the median of the ratios (see Appendix A). The latter feature adds flexibility to the parametric study because median collapse capacities of two systems can be compared without having to compute the individual collapse capacity ratios among them. Counted statistics are still needed for systems in which collapse does not occur for all the ground motions or occurs at very large relative intensities.

2.3.9 Normalization

In this study most of the data are presented in a normalized format to provide flexibility; see the $(S_a/g)/\eta$ - δ_{max}/S_d curves of Figure 2.4. This information can be de-normalized to fulfill specific needs, e.g., the generation of IDAs used to compute mean annual frequencies of collapse. In Figure 2.4, the horizontal axis shows δ_{max}/S_d, which corresponds to the maximum displacement normalized by the spectral displacement, S_d,:

$$S_d \approx \frac{T_1^2}{4\pi^2} S_a \tag{2.2}$$

Equation 2.2 is an identity only when S_a corresponds to the pseudo-spectral acceleration. In the case of the vertical axis, the $(S_a/g)/\eta$ parameter can be de-normalized to produce IDAs or strength-variation curves. For instance, if η is given, curves of Figure 2.4 become IDAs, as the ones shown in Figure 2.12. This graph indicates that for a given $\eta = 0.1$, the median collapse capacity for this SDOF system is associated with a ground motion intensity of about $S_a = 0.5g$. On the other hand, if S_a/g is kept constant, strength-variation curves are produced. As an

[5] A regression analysis of binary data is proposed by Shome and Cornell (1999) to carry out statistics on EDPs when some of the systems have collapsed.

example, Figure 2.13 presents $1/\eta - \delta_{max}$ curves when the curves of Figure 2.4 are de-normalized for $S_a = 0.5g$. According to this graph, the median $1/\eta$ at collapse is about 10, i.e., $\eta_c \approx 0.1$.

In the case of collapse capacity spectra [$(S_{a,c}/g)/\eta - T$ curves], a meaningful de-normalization can be achieved by considering different spectral accelerations for each period according to available seismic hazard information. For instance, the median collapse capacity spectrum of Figure 2.5 can be de-normalized by using the design spectrum of Figure 2.14, which corresponds to a Los Angeles soil type D site for a probability of exceedance of 10% in 50 years. If the median collapse capacities of Figure 2.5 are modified at each period according to the corresponding spectral acceleration of this spectrum, the median strength associated with collapse for different periods shown in Figure 2.15 is obtained. As can be seen, the median strength the system needs to avoid collapse decreases rapidly with an increase in period (except for very short periods).

This investigation deals almost exclusively with normalized data because of the generality provided by this format. However, it is important to keep in mind that this information may provide a different perspective in other formats. For instance, the normalized collapse capacities of Figure 2.5 remain essentially constant for periods longer than 0.6 s. However, the median strength associated with collapse of Figure 2.15 decreases continuously with an increase in period.

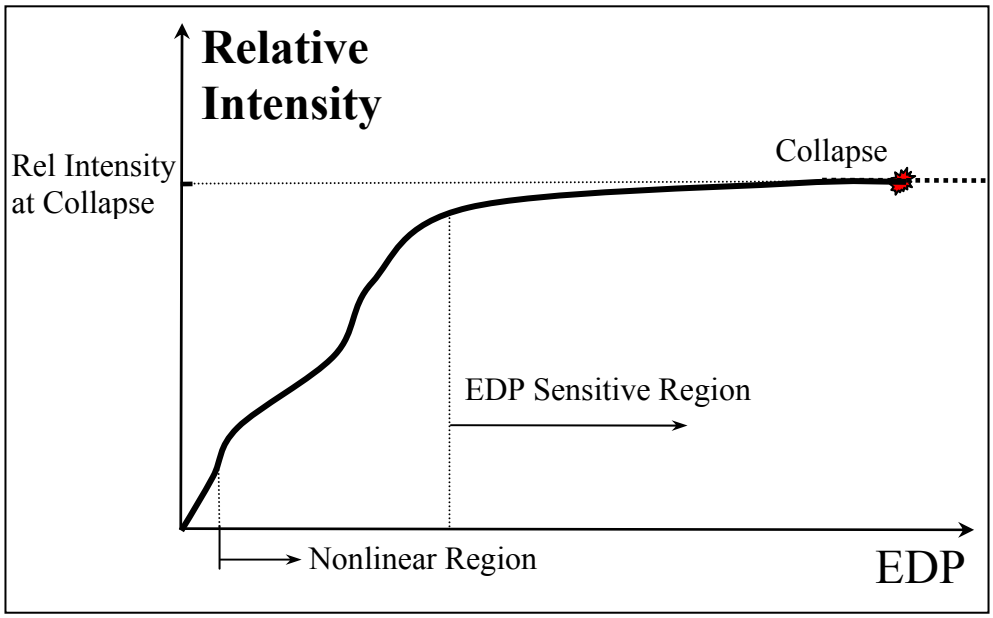

Fig. 2.1 Relative intensity–EDP curve

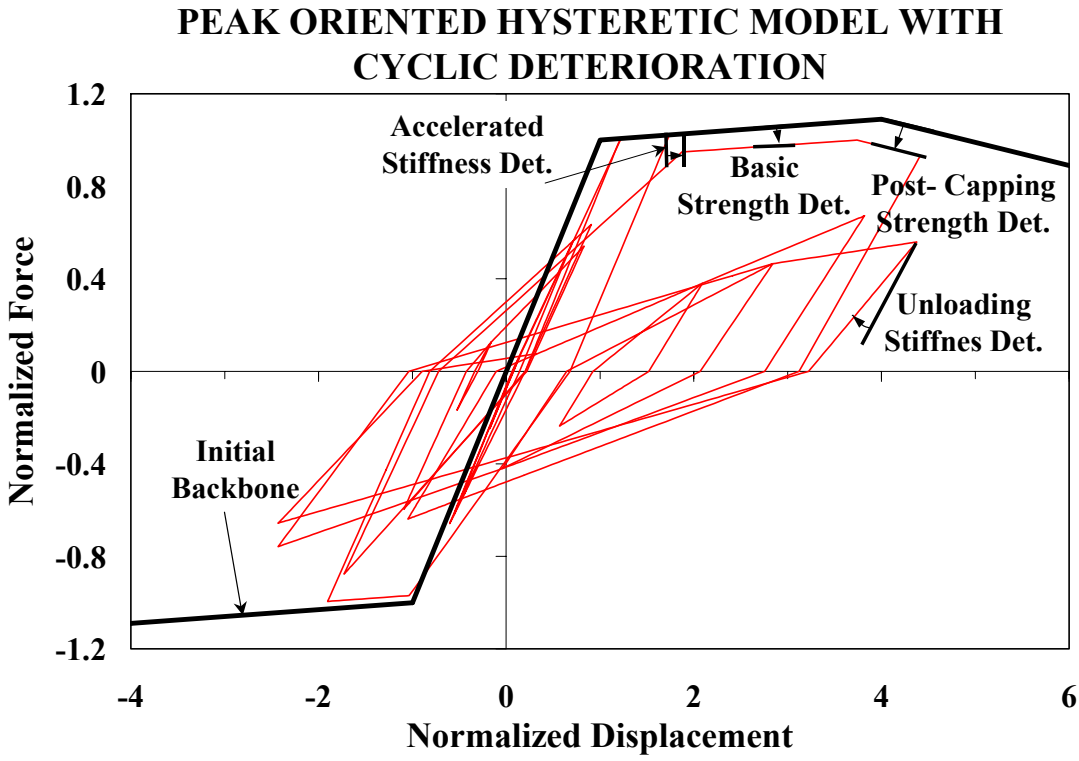

Fig. 2.2 SDOF response of a peak oriented model with rapid cyclic deterioration

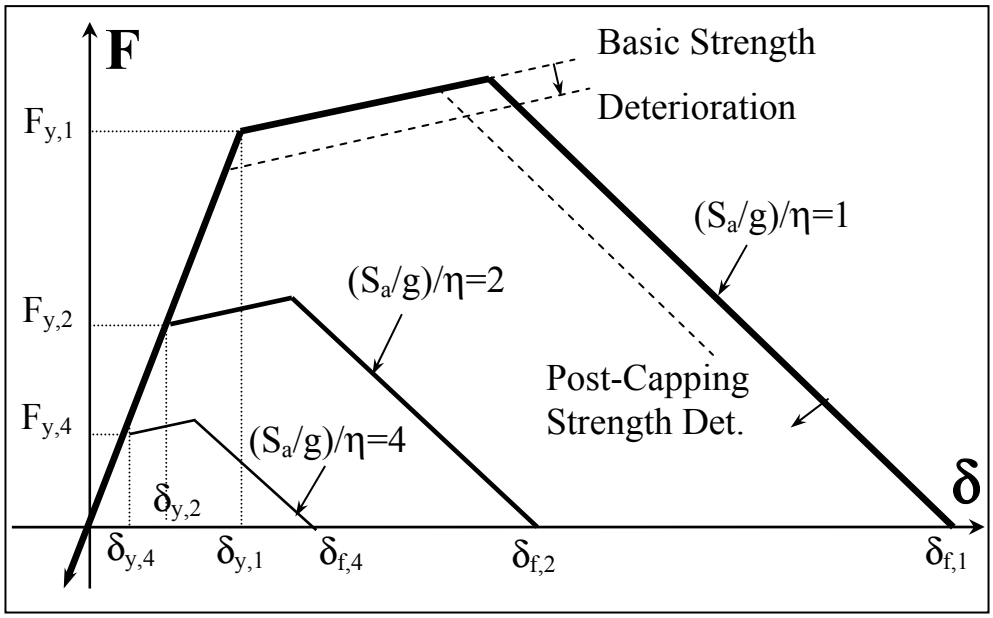

Fig. 2.3 Backbone curves for different η values (constant S_a/g)

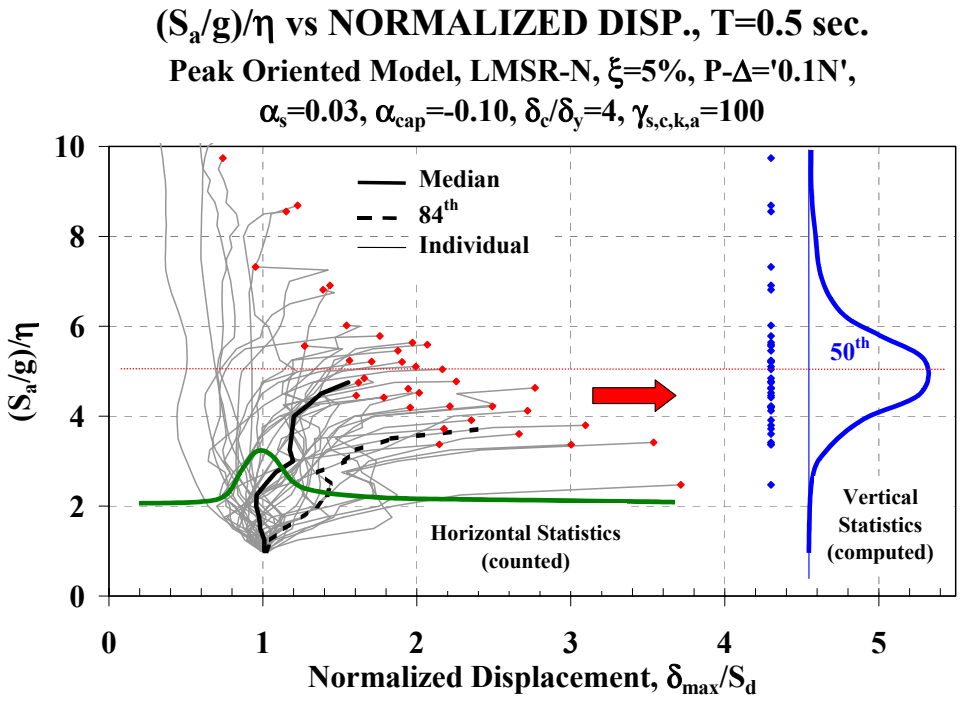

Fig. 2.4 $(S_a/g)/\eta$ - δ_{max}/S_d curves

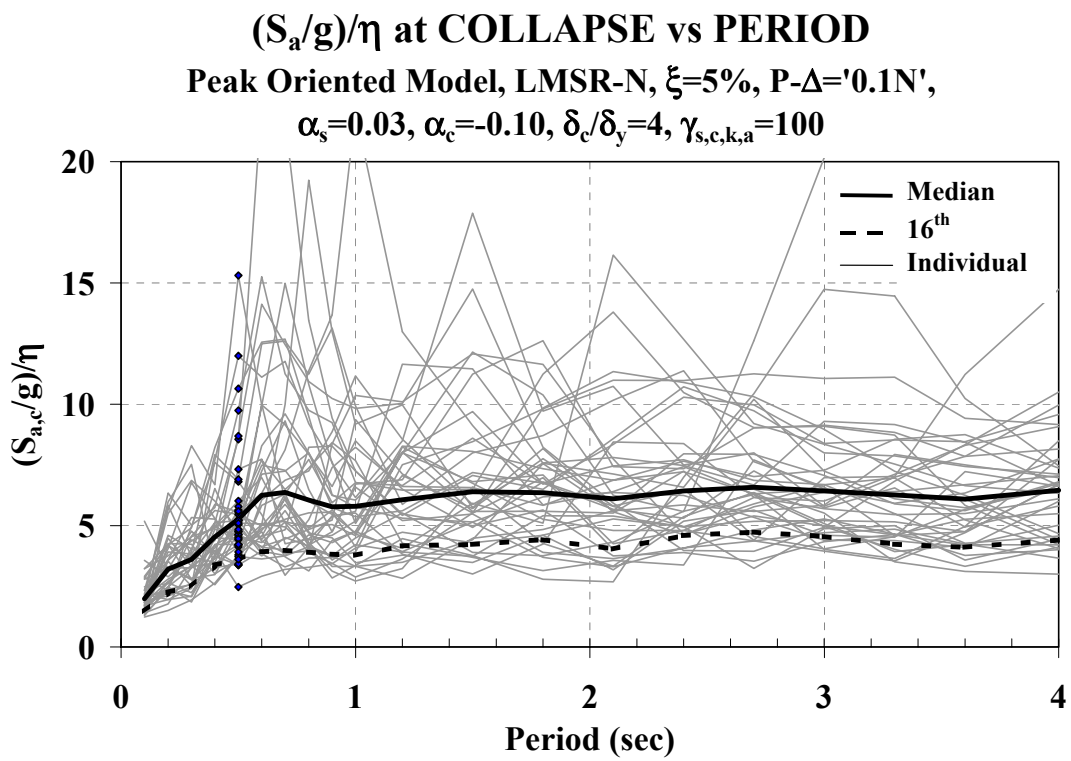

Fig. 2.5 Variation of collapse capacity with period

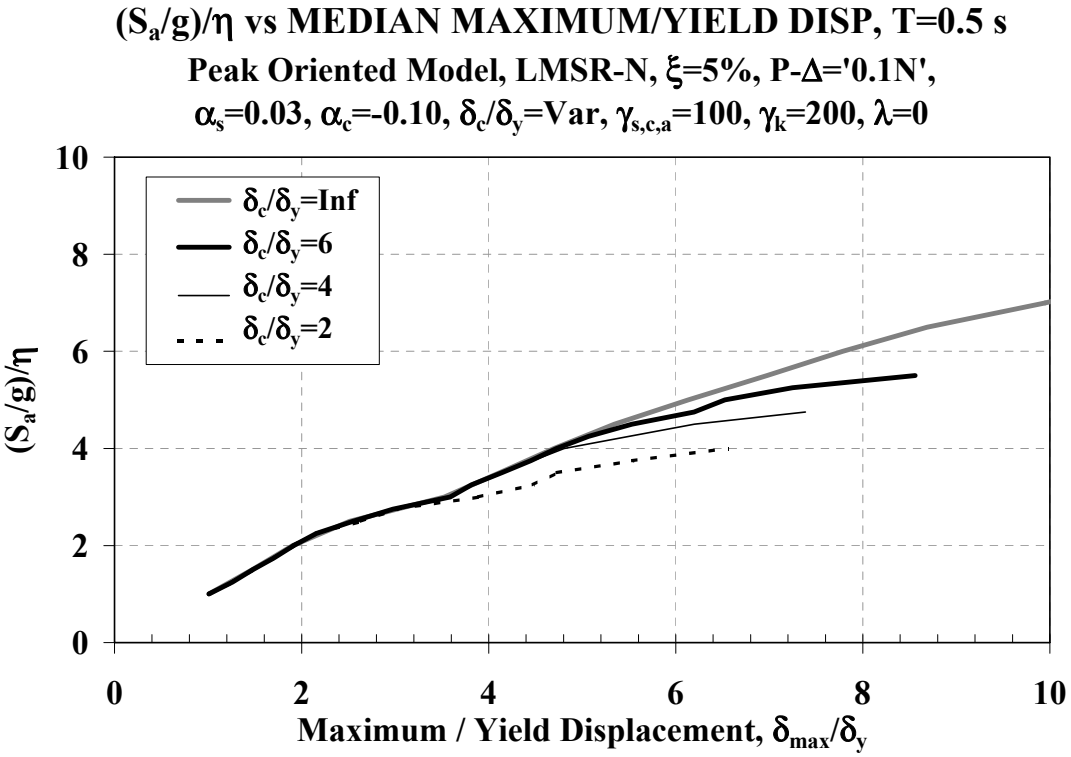

Fig. 2.6 Median $(S_a/g)/\eta$ - δ_{max}/δ_y curves, different δ_c/δ_y values

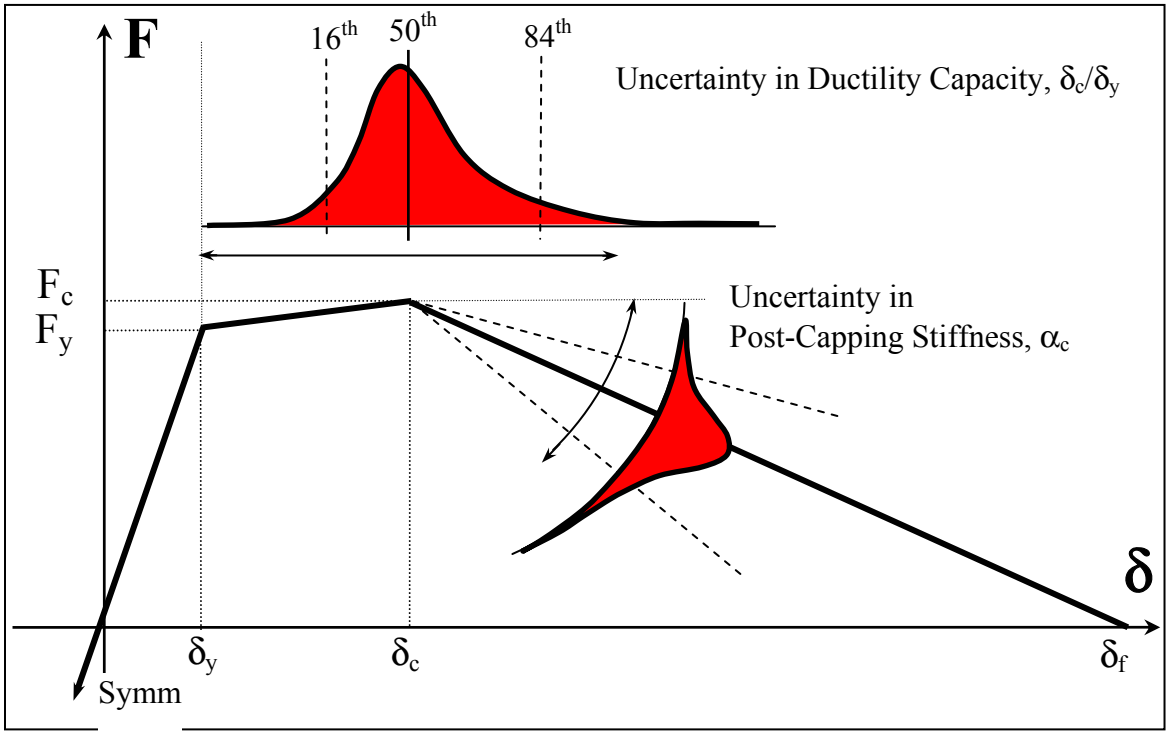

Fig. 2.7 Representation of uncertainty in system parameters

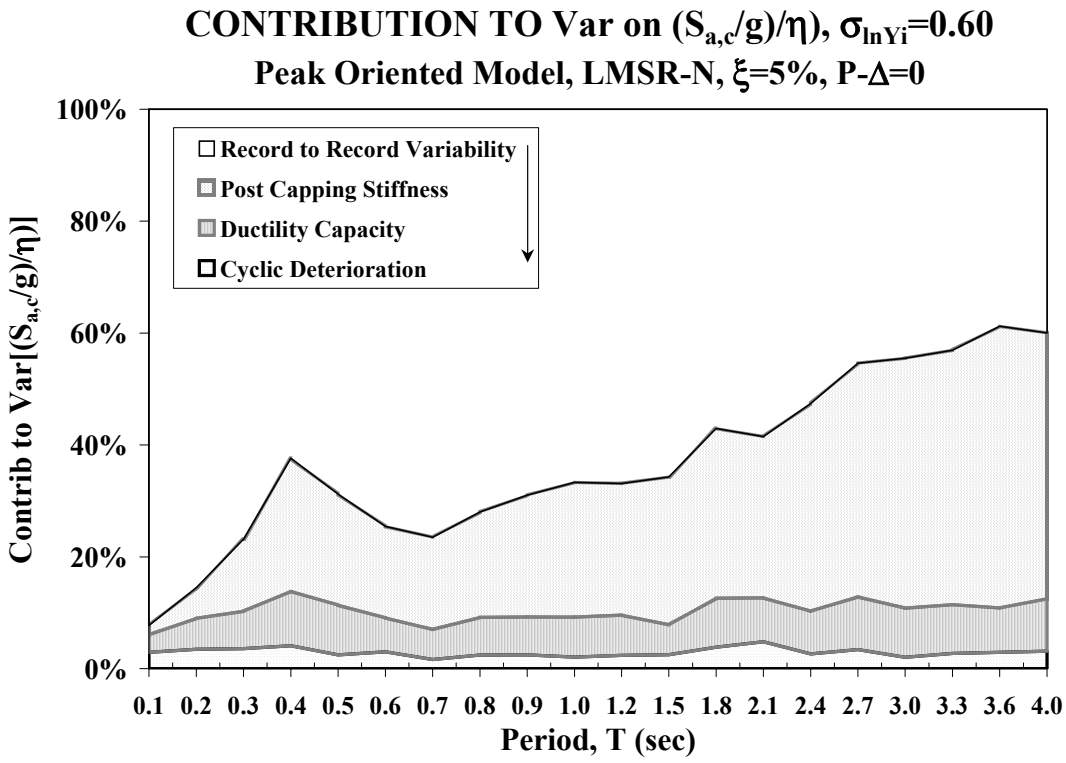

Fig. 2.8 Contribution of uncertainty in system parameters to variance of $(S_{a,c}/g)/\eta$

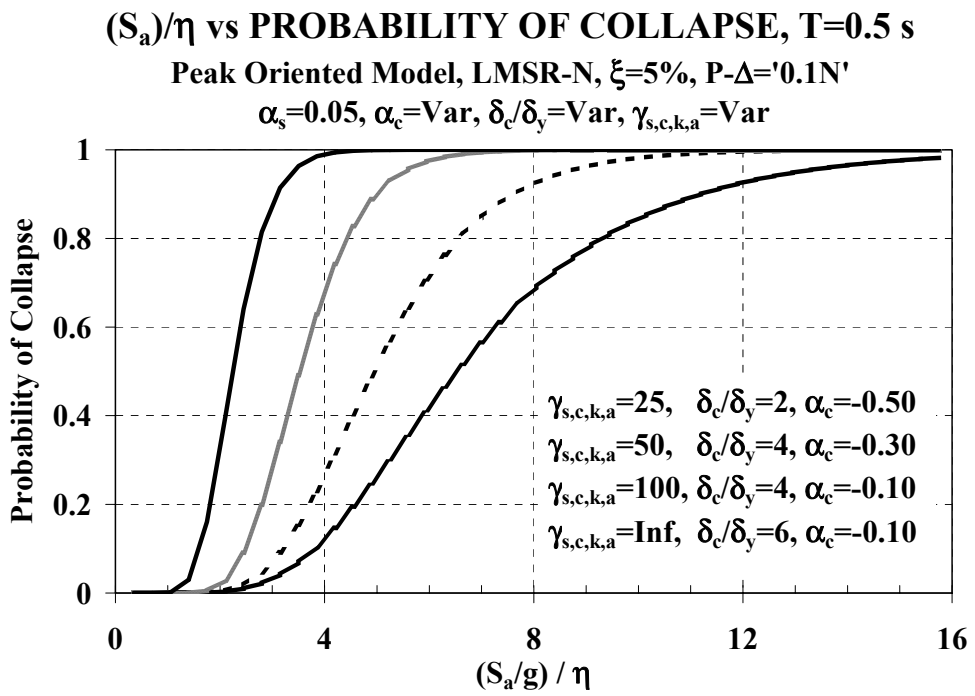

Fig. 2.9 Examples of fragility curves for SDOF systems with T = 0.5 s

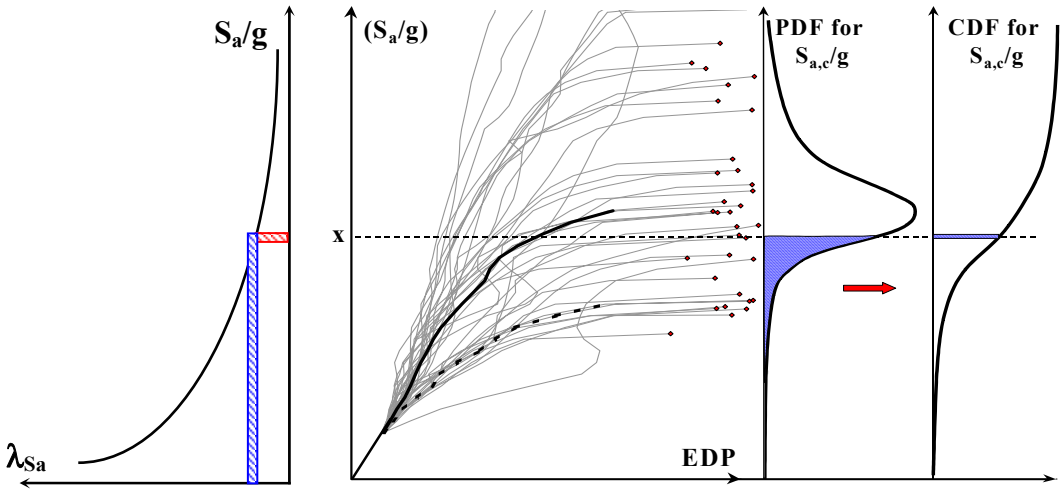

Hazard Curve
$\lambda_{Sa}(x)$

Probability of $S_{a,c}/g$ exceeding "x"
given $S_a/g \Rightarrow F_{C,Sa}(x)$

Fig. 2.10 Assessment of mean annual frequency of collapse

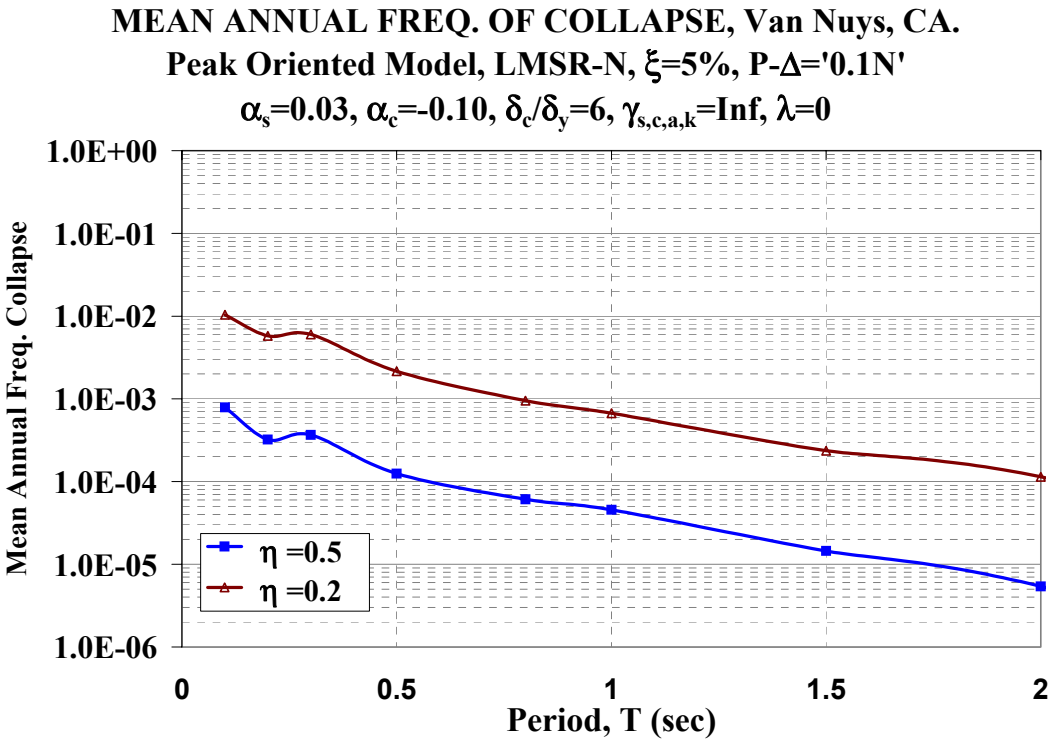

Fig. 2.11 Period and strength dependence of mean annual frequency of collapse for ductile SDOF systems (Van Nuys location)

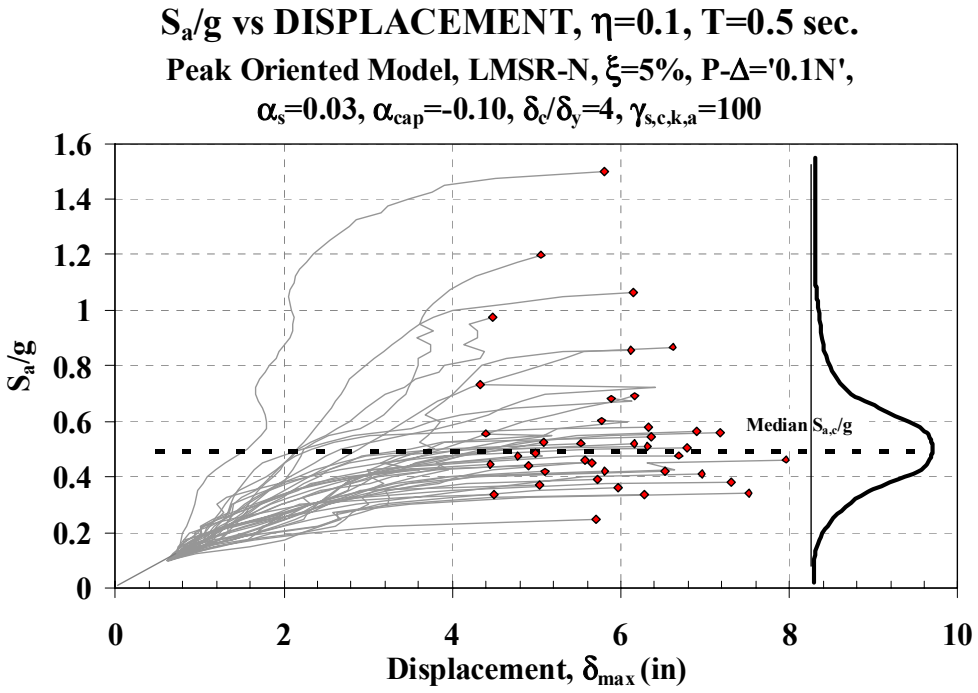

Fig. 2.12 IDA curves for an intermediate ductile SDOF system, $\eta = 0.1$

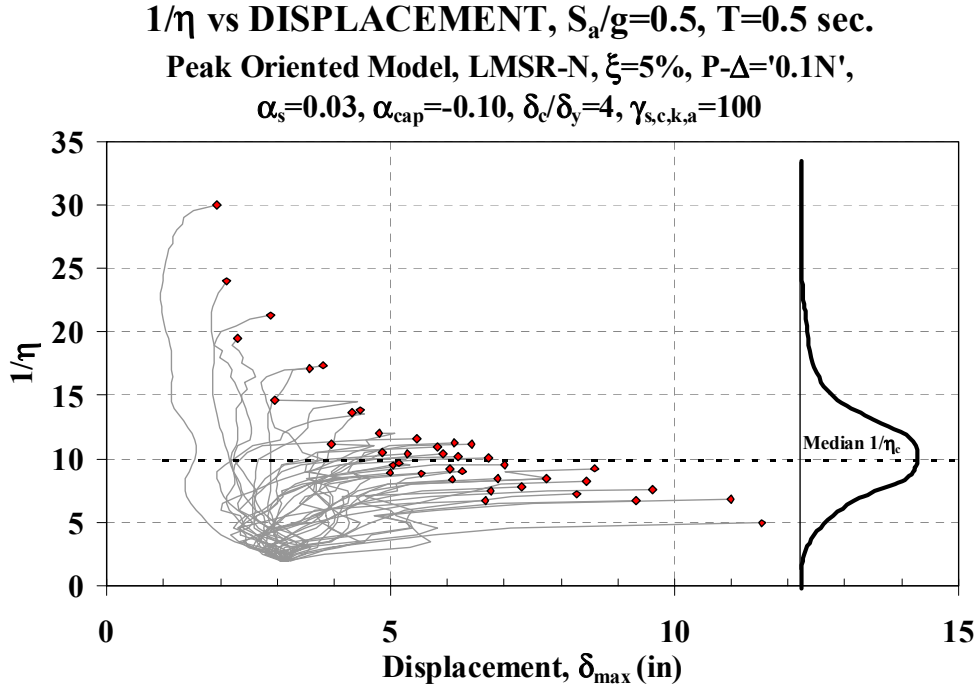

Fig. 2.13 Strength variation curves for an intermediate ductile SDOF system, $S_a/g = 0.5$

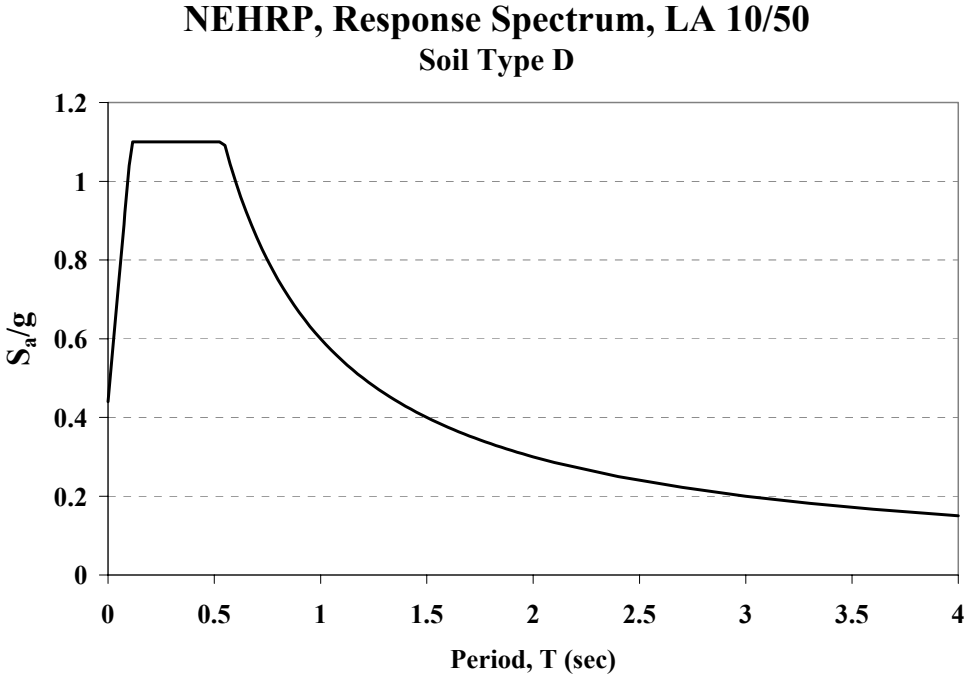

Fig. 2.14 NEHRP design spectrum for soil type D, L.A. site

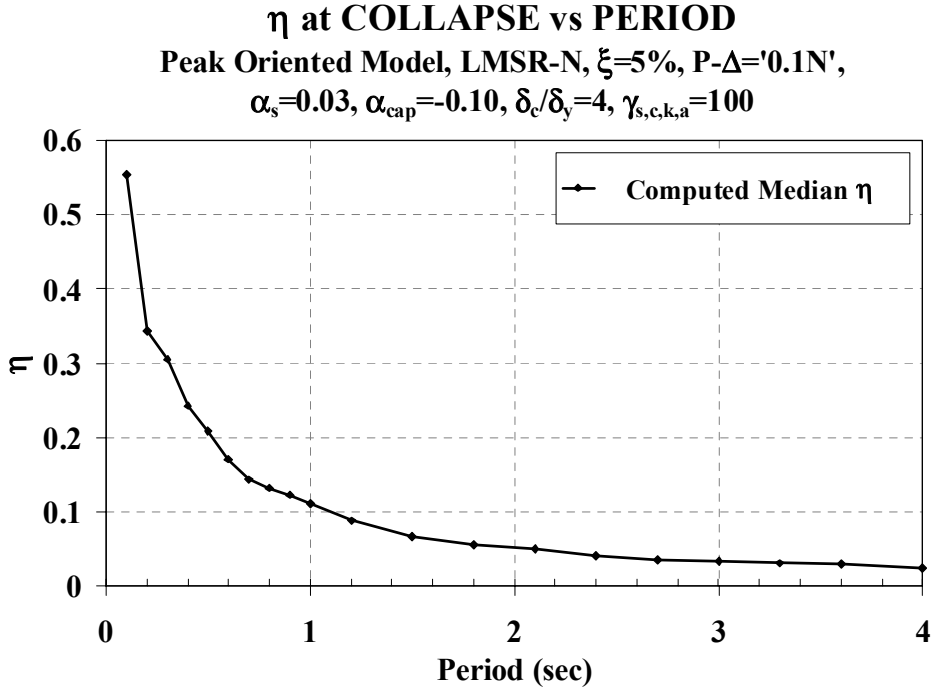

Fig. 2.15 Median strength associated with collapse for an intermediate ductile system, $S_a(T)/g$ according to NEHRP design spectrum

3 Hysteretic Models

3.1 INTRODUCTION

Collapse assessment requires hysteretic models capable of representing all the important modes of deterioration that are observed in experimental studies. Figure 3.1 illustrates a monotonic load-displacement response and a superimposed quasi-static cyclic response of "identical" plywood shear wall panels (Gatto and Uang, 2002). The monotonic test result shows that strength is "capped" and is followed by a negative tangent stiffness. The cyclic hysteretic response indicates that the strength in large cycles deteriorates with the number and amplitude of cycles, even if the displacement associated with the strength cap has not been reached (1). It also indicates that strength deterioration occurs in the post-capping range (2), and that the unloading stiffness may also deteriorate (3). Furthermore, it is observed that the reloading stiffness may deteriorate at an accelerated rate (4).

Several hysteretic models have been developed to represent the behavior of components that exhibit characteristics of the type illustrated in Figure 3.1 (Kunnath et al., 1991, Sivaselvan and Reinhorn, 2000; Song and Pincheira, 2000). However, few models integrate all the important deterioration sources such as strength deterioration in the backbone curve (post-capping stiffness branch) and cyclic deterioration of strength and stiffness. For this reason, deteriorating models were developed in this study for bilinear, peak-oriented, and pinched hysteretic systems. The models are implemented in an in-house computer program called SNAP that carries out dynamic and quasi-static inelastic analysis for SDOF systems[6]. The component deterioration models are also implemented in a computer program for MDOF systems that carries out dynamic nonlinear analyses, DRAIN-2DX (1993). The models incorporate a backbone curve that represents the monotonic response. Under cyclic behavior, several system parameters may deteriorate after

[6] SNAP is based on the program NLDYNA developed by Rahnama (Rahnama and Krawinkler, 1993).

each excursion. The sources of cyclic deterioration are basic strength, post-capping strength, unloading stiffness, and accelerated reloading stiffness deterioration.

3.2 BASIC HYSTERETIC MODELS

The following is a description of the three hysteretic models used in this study and the modifications introduced when post-capping strength deterioration is included in the backbone curve.

3.2.1 Description of Backbone Curve

The backbone curve defines the monotonic response and is the same for all hysteretic models (Fig. 3.2). This also defines the boundaries for the load-displacement relationship. The backbone curve is defined by the following parameters:

Initial Stiffness (K_e). It defines the elastic branch of the curve and is located between the origin (0, 0) and the yielding point (δ_y, F_y).

Hardening Stiffness (K_s). This stiffness is defined by connecting the yield point to the peak point (δ_c, F_c). The hardening stiffness is defined as a fraction of the initial stiffness:

$$K_s = \alpha_s K_e \tag{3.1}$$

The cap displacement (δ_c) is the point where the post-capping branch begins. If δ_c is normalized by the yielding displacement, the ratio is called ductility capacity, δ_c/δ_y. The peak strength (F_c) is attained at the end of the hardening branch:

$$F_c = F_y + K_s(\delta_c - \delta_y) \tag{3.2}$$

Post-Capping Stiffness (K_c). This stiffness is defined by connecting the peak point to the beginning of the residual strength branch (δ_r, F_r). The post-capping stiffness is also defined as a fraction of the initial stiffness:

$$K_c = \alpha_c K_e \tag{3.3}$$

Residual Strength Branch. The residual strength is a fraction of the initial yield strength:

$$F_r = \lambda F_y \tag{3.4}$$

Residual strength is not modified when cyclic deterioration shrinks the backbone curve. The displacement at which the residual strength branch starts, δ_r, is calculated as:

$$\delta_r = \delta_c + (F_c - F_r)/K_c \tag{3.5}$$

The parameters α_s, δ_c/δ_y, α_c and λ are obtained from calibration of the hysteretic models with load-deformation data obtained from experiments (see Section 3.5).

3.2.2 Bilinear Model

This model is based on the standard bilinear hysteretic rules with kinematic strain hardening. These basic rules are preserved once post-capping and residual strength branches are included. However, it is necessary to introduce the "strength limit" shown in Figure 3.3 when the backbone curve includes a branch with negative slope. The limit for strength corresponds to the smallest strength reported on the post-capping branch in previous excursions. In Figure 3.3, the loading curve starting at 5 should continue up to intersect 6′, according to kinematic rules. However, this loading segment ends when it intersects the "strength limit" at point 6. The limit corresponds to the strength of point 3, which is the smallest strength in the nonlinear range of the backbone curve in earlier cycles. If this condition were not established, the strength in the loading path could increase in later stages of deterioration.

3.2.3 Peak-Oriented Model

This model keeps the basic hysteretic rules proposed by Clough and Johnston in 1965, but the backbone curve is modified to include strength capping and residual strength. The presence of a negative post-capping stiffness does not modify any basic rules of the model. Figure 3.4a shows the deterioration of the reloading stiffness for a peak-oriented model once the horizontal axis is reached (points 3 and 7). The reloading path targets the previous maximum displacement.

Mahin and Bertero (1975) proposed that the reloading path be directed to the maximum displacement of the last cycle instead of the maximum displacement of all former cycles if the former path results in a larger reloading stiffness. This is exemplified in Figure 3.4b, where the reloading from point 10 is directed to point 7 (maximum displacement of last cycle) instead of point 2 (maximum displacement of all earlier cycles), as in the original peak-oriented model. Once point 7 is reached, the path is redirected to point 2.

3.2.4 Pinching Model

The pinching model is similar to the peak-oriented one, except that reloading consists of two parts. Initially the reloading path is directed toward a point denoted as "break point," which is a function of the maximum permanent deformation and the maximum load experienced in the direction of loading. The break point is defined by the parameter κ_f, which modifies the maximum "pinched" strength (points 4 and 8 of Fig. 3.5a), and κ_d, which defines the displacement of the break point (points 4′ and 8′). The first part of the reloading branch is defined by $K_{rel,a}$ and once the break point is reached (points 4′ and 8′), the reloading path is directed toward the maximum deformation of earlier cycles in the direction of loading ($K_{rel,b}$)

Reloading without $K_{rel,a}$. If the absolute deformation at reloading (point 13, Fig. 3.5b) is larger than the absolute value of $(1-\kappa_d)\delta_{per}$, the reloading path consists of a single branch that is directed toward the previous maximum deformation in the direction of loading.

3.3 CYCLIC DETERIORATION

3.3.1 Deterioration Based on Hysteretic Energy Dissipation

Four cyclic deterioration modes may be activated once the yielding point is surpassed in at least one direction: basic strength, post-capping strength, unloading stiffness, and reloading stiffness deterioration. The basic cyclic deterioration rules are the same for all the hysteretic models with the exception of the accelerated stiffness deterioration, which does not exist in the bilinear model. The peak-oriented model will be used to illustrate the effect of cyclic deterioration.

The cyclic deterioration rates are controlled by the rule developed by Rahnama and Krawinkler (1993), which is based on the hysteretic energy dissipated when the component is subjected to cyclic loading. It is assumed that the hysteretic energy-dissipation capacity is a known quantity that is independent of the loading history.

The cyclic deterioration in excursion i is defined by the parameter β_i, which is given by the following expression:

$$\beta_i = \left(\frac{E_i}{E_t - \sum_{j=1}^{i} E_j} \right)^C \tag{3.6}$$

where

E_i = hysteretic energy dissipated in excursion *i*

ΣE_j = hysteretic energy dissipated in all previous excursions (both positive and negative)

E_t = hysteretic energy-dissipation capacity, $E_t = \gamma F_y \delta_y$

γ expresses the hysteretic energy-dissipation capacity as a function of twice the elastic strain energy at yielding ($F_y\delta_y$). It is calibrated from experimental results and can be different for each deterioration parameter.

c = exponent defining the rate of deterioration of the evaluated hysteretic parameter (strength or stiffness). Rahnama and Krawinkler (1983) suggested that a reasonable range for *c* is between 1.0 and 2.0. If the displacement history consists of constant amplitude cycles, a unit value for *c* implies an almost constant rate of deterioration of the hysteretic parameter. For the same displacement history, a value *c* = 2 slows down the rate of deterioration in early cycles and accelerates the rate of deterioration in later cycles.

Throughout the time history analysis, β_i must be within the limits $0 < \beta_i \leq 1$. If this inequality does not hold ($\beta_i \leq 0$ or $\beta_i > 1$), the hysteretic energy capacity is exhausted and collapse takes place. Mathematically:

$$\gamma F_y \delta_y - \sum_{j=1}^{i} E_j < E_i \tag{3.7}$$

3.3.2 Basic Strength Deterioration

It is defined by translating the strain-hardening branch toward the origin by an amount equivalent to reducing the yield strength to:

$$F_i^+ = (1 - \beta_{s,i}) F_{i-1}^+ \quad \text{and} \quad F_i^- = (1 - \beta_{s,i}) F_{i-1}^- \tag{3.8}$$

in which

$F_i^{+/-}$ = deteriorated yield strength after excursion *i.*

$F_{i-1}^{+/-}$ = deteriorated yield strength before excursion i.

There is a positive and a negative value for each deterioration parameter because the algorithm deteriorates the strength independently in both directions. That is to say, F_i^- is updated after every positive inelastic excursion, and F_i^+ is updated after every negative inelastic excursion.

The parameter $\beta_{s,i}$ is calculated with Equation 3.6 each time the inelastic path crosses the horizontal axis and is associated with the appropriate γ value to model basic strength deterioration (γ_s).

The basic strength deterioration mode also includes the deterioration of the strain-hardening slope, which is rotated in accordance with the following equation:

$$K_{s,i}^+ = (1-\beta_{s,i})K_{s,i-1}^+ \quad \text{and} \quad K_{s,i}^- = (1-\beta_{s,i})K_{s,i-1}^- \tag{3.9}$$

The strain-hardening slope is also deteriorated independently in both directions. The slope of the strain-hardening branch is equal to zero when the yield strength has deteriorated to zero. If a residual branch is included in the backbone curve, the analytical model deteriorates the strain-hardening stiffness to zero ($K_{s,i}^{+/-} = 0$) when the yield strength deteriorates to λF_{yo} (F_{yo} is the initial yield strength).

A peak-oriented model is used in Figure 3.6a to illustrate the basic strength deterioration mode. At point 3, β_s is calculated for first time and the maximum strength that can be reached on the negative side is reduced from F_y^- to F_1^-. The slope of the hardening branch decreases from $K_{s,0}^-$ to $K_{s,1}^-$. At point 7, β_s is calculated again and the positive yield strength is modified from F_y^+ to F_1^+. Observe that the current β_s value does not modify the yield strength based on F_1^-, but deteriorates the positive yield strength for the first time. A similar deterioration occurs with the positive hardening slope.

3.3.3 Post-Capping Strength Deterioration

This deterioration mode translates the post-capping stiffness branch toward the origin and, unlike basic strength deterioration, the slope of the post-capping branch is kept constant. The post-capping branch is moved inward by an amount equivalent to reducing the reference strength according to the following equation:

$$F^{+/-}_{ref,i} = (1-\beta_{c,i})F^{+/-}_{ref,i-1} \tag{3.10}$$

$F^{+/-}_{ref}$ is the intersection of the vertical axis with the projection of the post-capping branch (Fig. 3.6b). There is a positive and negative reference strength parameter for independently deteriorating the positive and negative post-capping strength. β_c is associated with an appropriate γ value to model post-capping strength deterioration (γ_c).

The deterioration of post-capping strength is computed each time the horizontal axis is crossed, but the deterioration parameter may not affect the loading path in the early stages of nonlinearity. In Figure 3.6b, the first post-capping deterioration is calculated at point 3 and the negative reference point moves to $F^{-}_{ref,1}$. This backbone modification does not affect the loading path due to the small magnitude of the negative displacement. At point 6, the deterioration of the post-cap strength is computed again and this time the loading path is modified because the updated cap displacement (δ^{+}_{c1}) is exceeded in this excursion.

3.3.4 Unloading Stiffness Deterioration

The unloading stiffness (K_u) is deteriorated in accordance with the following equation:

$$K_{u,i} = (1-\beta_{k,i})K_{u,i-1} \tag{3.11}$$

where

$K_{u,i}$ = deteriorated unloading stiffness after excursion i

$K_{u,i-1}$ = deteriorated unloading stiffness before excursion i

$\beta_{k,i}$ is associated with an appropriated cyclic deterioration parameter γ_k.

The parameter β_k is the only one that is calculated when a load reversal takes place in the inelastic range. Furthermore, this is the only deterioration mode in which the deterioration parameter in one direction is also used to update the deterioration parameter in the other direction. Consequently, the unloading stiffness is updated up to twice as much as the other deterioration parameters. Thus, if the same energy-dissipation capacity is expected for the four deterioration modes, it is recommended to assign a larger value to γ_k than to γ_s, γ_c and γ_a. If the same energy is dissipated in the positive and negative directions, then γ_k should be about twice as large as the other γ values, i.e., $\gamma_k = 2\gamma_{s,c,a}$.

Figure 3.6c shows a peak-oriented model that includes unloading stiffness deterioration. At point 2 the first reversal in the inelastic range occurs and the unloading stiffness deteriorates from K_e to a deteriorated value $K_{u,1}$. At point 5 the first reversal on the negative side takes place and $K_{u,2}$ is calculated based on the updated β_u and $K_{u,1}$. Unlike other deterioration modes, $K_{u,2}$ is updated based on the value of the unloading stiffness on the other side of the loop.

The deterioration of unloading stiffness takes place each time that a reversal occurs and the updated unloading stiffness is used for subsequent updates of this parameter. However, the unloading stiffness update is disregarded if the reversal is considered an interruption in the direction of loading. In peak-oriented and pinching models, an interruption occurs when the path is on the unloading stiffness and a reversal takes place before the path targets the maximum displacement on the opposite side (Fig. 3.6c). In bilinear models, an interruption occurs when the path is on the unloading stiffness and has a reversal before reaching the backbone curve on the opposite side.

3.3.5 Accelerated Reloading Stiffness Deterioration

This deterioration mode increases the absolute value of the target displacement, defined as the maximum positive or negative displacement of past cycles, according to the direction of loading. Accelerated reloading stiffness deterioration is defined only for peak-oriented and pinching models and is governed by the following equation:

$$\delta_{t,i}^{+/-} = (1 + \beta_{a,i})\delta_{t,i-1}^{+/-} \tag{3.12}$$

There is a target displacement (δ_t) for each loading direction, and the reloading stiffness deterioration is calculated each time the horizontal axis is crossed (Fig. 3.6d). Equation 3.6 is employed to compute β_a based on the corresponding parameter γ_a.

3.4 CALIBRATION OF HYSTERETIC MODELS WITH COMPONENT TESTS

The proposed hysteretic models have been calibrated with load-deformation data obtained from experiments on steel, reinforced concrete, and wood components. The best way of defining the backbone curve parameters (ductility capacity and post-capping stiffness) is with a monotonic test because cyclic deterioration effects are not present. The parameter γ is estimated from

experiments in which the specimen is subjected to cyclic loading. The following are examples of some calibrations for different materials.

3.4.1 Steel Specimens

Figures 3.7–3.8 illustrate the calibration of the bilinear model on beam load-displacement relationships for steel beam-column subassemblies (Uang et al., 2000). Because monotonic tests were not available to obtain the backbone curve for the simulations, the parameters of the backbone curve (F_y, δ_y, δ_c, α_s, and α_c) were estimated from the load-displacement relationship of the second excursion of the near-fault tests. This second excursion is considered to be equivalent to a monotonic load-displacement relationship because only small structural damage occurred during the first excursion in the opposite direction. Based on this approach, the following properties are utilized for all four simulations: F_y = 103 kips, δ_y = 1.03 in., α_s = 0.03, α_c = -0.03, δ_c / δ_y = 2.75, and no residual strength (λ = 0). The cyclic deterioration parameters are: c = 1.0 and $\gamma_s = \gamma_c = \gamma_k = \gamma_a$ = 130. The use of different γ values for each deterioration mode could have resulted in a better calibration. However, γ's are set at the same value because the objective is to find representative parameters that can be used when no experimental results are available.

Specimens LS1 and LS4 were tested using the standard SAC loading protocol (Fig. 3.7). The main difference between them is that the beam in specimen LS4 is braced to help it achieve its full plastic moment capacity. The analytical model provides a good correlation with the experimental loops. However, the response at early cycles cannot be fully reproduced because steel components develop cyclic strain hardening, a feature that is not included in the analytical model.

Specimens LS2 and LS3 were tested using the SAC near-fault loading protocol. The specimens were loaded in opposite directions. As in the former case, the absence of cyclic strain hardening in the analytical model can be observed in the early cycles of the history where the load-deformation response of the model underestimates that of the experiment. In general, good correlation is observed between experimental and analytical loops for the four tests, although the same hysteretic properties are utilized for different loading protocols.

Figures 3.9–3.10 show plots of negative and positive normalized hysteretic energy (NHE = total hysteretic energy dissipated / $F_y\delta_y$) as a function of the number of cycles for all four specimens. In all cases the history of NHE is similar for both the analytical model and the

experimental results. Thus, the bilinear hysteretic model is able to replicate the cumulative energy dissipated under the action of various loading protocols. Note that the sum of positive and negative NHE is smaller than the analytical input parameter $\gamma_{s,c,k}$ = 130. The reason is that although γ's were directly calibrated from experimental results, complete loss of restoring force is not reached in any case. According to the hysteretic loops, specimen LS-2 is the closest to lose all its restoring force. Consequently, this is the case where the sum of positive and negative NHE is closest to the input parameter $\gamma_{s,c,k}$ = 130 because the hysteretic energy capacity is almost exhausted.

3.4.2 Wood Specimens

Figure 3.11 illustrates the calibration of the pinching model on plywood shear wall load-displacement relationships (Gatto and Uang, 2002). Four different loading protocols are used in the calibrations: ISO, SPD, CUREE standard, and CUREE-near-fault. The CUREE loading protocols were developed by Krawinkler et al. (2001) for wood-frame testing. The following properties for the backbone curve were obtained from a monotonic test and were utilized in the simulations: F_y = 7 kips, δ_y = 1.0 in., α_s = 0.10, α_c = -0.13, δ_c/δ_y = 4, λ = 0, and $\kappa_f = \kappa_d$ = 0.25. The cyclic deterioration parameters used were: c = 1.0, $\gamma_s = \gamma_c = \gamma_a$ = 50, and $\gamma_k = \infty$ (no unloading stiffness deterioration). The graphs show that the pinching hysteretic model is able to simulate cyclic deterioration observed in the plywood shear wall panel tests for the four loading protocols.

Figure 3.12 shows plots of positive and negative NHE as a function of the number of cycles. In all cases, the history of the NHE of the analytical model is below the one corresponding to the experimental results because the model remains elastic until δ_y is achieved. That is to say, the models do not dissipate energy below this threshold, whereas the experimental results exhibit energy dissipation at displacement levels well below the estimated value of δ_y. Although the trends in the history of NHE between the model and test results are slightly offset by this difference, the pinching model is able to replicate the cumulative energy dissipated, especially at relatively large deformation levels.

3.4.3 Reinforced Concrete Specimens

The calibration of reinforced concrete (RC) specimens utilizes the experiments carried out by Moehle and Sezen (Sezen, 2000). They tested four columns with deficient transverse reinforcement, which were connected to very rigid top and base beams to produce double curvature. The two columns ("1" and "4") with small constant axial load $P = 0.15f'_cA_g$ are calibrated in this study. Column "1" was subjected to a stepwise increasing cyclic loading protocol and column "4" to a mostly monotonic history, consisting of several small cycles followed by a big final excursion. For calibration purposes, the backbone parameters were based on the results of column 4 and the cyclic deterioration parameters on the results of column 1. Figure 3.13 presents the experimental and analytical hysteretic loops of columns 1 and 4 along with the input parameters. Both cases exemplify the difficulties in reproducing early inelastic cycles in reinforced concrete components when the analytical models do not include the cracking point. However, the pinching model simulates well the highly inelastic behavior.

Figure 3.14 depicts the NHE dissipation histories for the aforementioned cases. For column 4, the NHE is negligible up to the last cycle, in which most of the energy is dissipated. For column 1, the sum of positive and negative NHE is also very small compared to γ= 50. The reason is that the large slope of the post-capping branch is preventing the total NHE from reaching a value close to γ, even for systems that are very close to complete failure.

3.5 ILLUSTRATIONS OF CYCLIC DETERIORATION EFFECTS

As shown in previous sections, the deteriorating model is capable of reproducing the response of tests of components made of steel, reinforced concrete, and wood. Calibrations with component tests have provided typical values for the deteriorating system parameters. This section illustrates the effects various deterioration parameters have on the hysteretic response when a component is subjected to the CUREE loading protocol (Krawinkler et al., 2000) (Fig. 3.15). Three parameters are of primary interest: the ductility capacity δ_c/δ_y, the post-capping stiffness α_c, and the series of cyclic deterioration parameters γ_s, γ_c, γ_k, and γ_a. In these illustrations it is assumed that all four cyclic deterioration parameters are equal.

Figure 3.16 shows nine hysteretic responses that have the same post-capping stiffness, α_c = -0.10, in common. From left to right in the figure the ductility capacity decreases from δ_c/δ_y

= 6 to δ_c/δ_y = 4 and 2, whereas from top to bottom in the figure the cyclic deterioration parameter decreases from $\gamma_{s,c,k,a}$ = infinite to $\gamma_{s,c,k,a}$ = 100 and 25. Thus, the effect of a decrease in the ductility capacity can be studied by viewing the figure from left to right and the effect of a decrease in the cyclic deterioration parameter can be studied by viewing the figure from top to bottom. There are clear patterns both in the horizontal and vertical directions. It is noted, for instance, that for this specific loading history the ductility capacity becomes rather irrelevant if the cyclic deterioration parameter is small ($\gamma_{s,c,k,a}$ = 25), i.e., cyclic deterioration effects overpower the effect of monotonic ductility (see bottom row of the figure). This observation is consistent but not very relevant because the combination of a monotonically ductile component that experiences rapid cyclic deterioration is rather unlikely. For all other cases illustrated, the combination of ductility capacity and cyclic deterioration parameters control the response.

Figure 3.17 presents the same arrangement of systems, but using a steep post-capping slope corresponding to α_c = -0.50. There are clear differences between each graph of Figures 3.16–3.17, demonstrating the importance of the post-capping stiffness. For the steep post-capping slope corresponding to α_c = -0.50, the monotonic ductility capacity becomes much important because little "life" is left at deformations exceeding the monotonic ductility capacity.

The important observation to be made is that the effects of none of the deterioration parameters can be evaluated in isolation. It is the combination of all three deterioration parameters (δ_c/δ_y, α_c, $\gamma_{s,c,k,a}$) that governs the cyclic behavior.

3.6 ADDITIONAL OBSERVATIONS ON DETERIORATION MODEL

The power of the proposed deterioration model is in its versatility that makes it feasible to represent many deterioration modes in a transparent and physically justifiable manner. If the simplifications are acceptable that all cyclic deterioration modes can be represented by the same γ value, and that the exponent in Equation 3.6 can be taken as 1.0, then all cyclic deterioration modes are controlled by a single parameter, $\gamma_{s,c,k,a}$. There is no simpler way possible to describe cyclic deterioration. It is the combination of this single cyclic deterioration parameter with a backbone curve incorporating monotonic strength capping and a post-capping stiffness that makes this deterioration model simple but versatile. The following observations are believed to be of importance in the context of damage and deterioration modeling.

There are fundamental differences between this deterioration model and cumulative damage models. The latter merely count cumulative damage and use a counter to indicate degree of damage and complete "failure" (usually identified by the counter taking on a value of 1.0). They do not consider that cumulative damage causes a decrease in strength and stiffness and therefore leads to an increase in deformations. It is the loss of strength and the increase in deformation that ultimately will cause collapse of a structure. Moreover, cumulative damage models apply to components and not to structures. Many attempts are reported in the literature to extrapolate from component cumulative damage models to structural damage models, but none of these attempts are believed to have been successful in tracing damage close to collapse. Collapse is caused by deterioration in complex assemblies of components, and such deterioration must be modeled explicitly.

- The proposed deterioration model incorporates cyclic deterioration controlled by hysteretic energy dissipation as well as deterioration of the backbone curve (strength capping at δ_c/δ_y and a post-capping decrease in strength defined by α_c). This dual deterioration behavior is equivalent to the two-part damage concept contained in some cumulative damage models such as the Park-Ang model (Park and Ang, 1985). This model, which was developed specifically for reinforced concrete components, consists of a linear combination of displacement and energy demands, expressed as follows:

$$DM = \frac{\delta_{max}}{\delta_{ult}} + \frac{\beta}{F_y \delta_{ult}} \int dHE \tag{3.13}$$

where,

DM = damage measure

$\delta_{\max}$ = the maximum displacement of the system

δ_{ult} = the monotonic displacement capacity of the system

β = structural performance parameter

In concept, the parameters δ_{ult} and β of this cumulative damage model are equivalent to δ_c and γ of the proposed deterioration model.

- Inspection of Figures 3.9–3.10, 3.12, and 3.14 shows that the hysteretic energy-dissipation capacity $\gamma F_y \delta_y$ is rarely achieved in component tests. Components usually reach zero resistance long before this capacity is utilized. This happens because of

strength capping and post-capping strength decrease and is equivalent to the importance of the first term of the Park-Ang model given by Equation 3.13.

- In all studies reported in this report it is assumed that the exponent c in Equation 3.6 is 1.0. Based on cumulative damage concepts it can be argued that c should be greater than 1.0 (likely on the order of 1.5–2.0). This "simplification" is not believed to have a large effect on the response of deteriorating systems. An exponent greater than 1.0 will accelerate deterioration, but primarily for very large excursions. For such excursions, strength capping and post-capping strength decrease dominate over cyclic deterioration.

3.7 SUMMARY

This chapter describes the model developed for deteriorating structural components. The sources of deterioration considered are strength deterioration in the backbone curve and cyclic strength and stiffness deterioration. The models have been codified in an in-house SDOF program called SNAP and implemented in nonlinear analysis programs for MDOF structures that consider nonlinearities by means of concentrated plasticity (DRAIN-2DX and OpenSees).

The hysteretic models have been calibrated with experiments of components made of steel, wood, and reinforced concrete. Some of the experimental programs consist of several identical specimens subjected to different loading protocols. In the calibration process, the same system and deterioration parameters are used for all the loading protocols. The correlation for most of the cases is good, suggesting that the backbone characteristics and the parameter γ for cyclic deterioration are adequate to represent component behavior regardless of the loading protocol.

The effect of individual deterioration parameters on the hysteretic response depends largely on the relative values of all the other parameters. This can be observed from Figures 3.16–3.17, in which hysteretic responses for systems with variations of a particular parameter are compared.

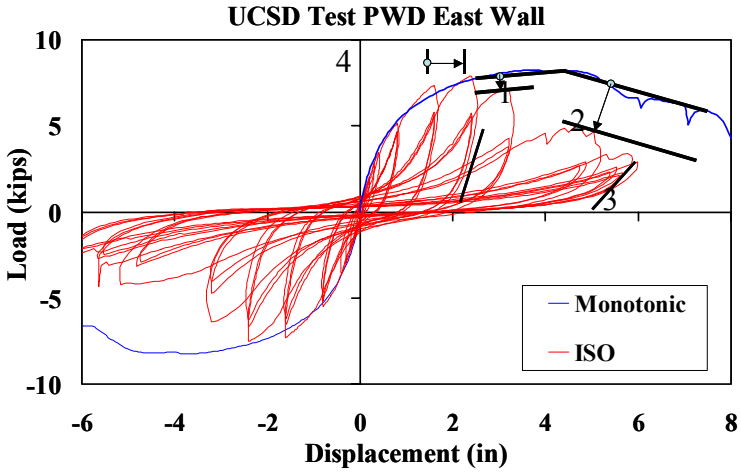

Fig. 3.1 Experimental hysteretic loops for a wood specimen subjected to monotonic and cyclic loading

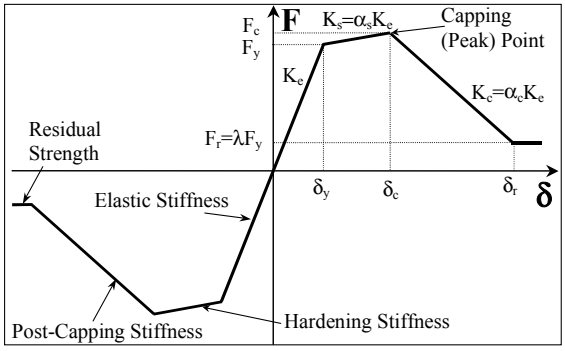

Fig. 3.2 Backbone curve for hysteretic models

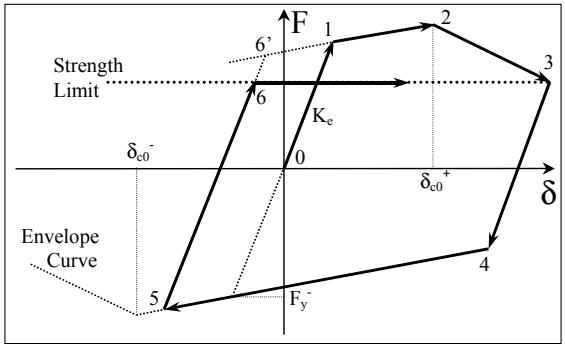

Fig. 3.3 Bilinear hysteretic model with strength limit

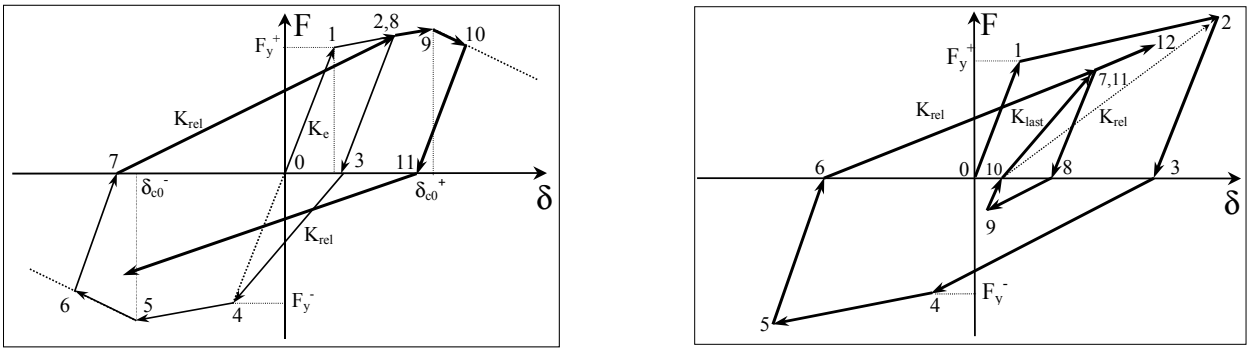

(a) (b)

Fig. 3.4 Peak-Oriented hysteretic model; (a) basic model rules, (b) Mahin and Bertero's modification (Mahin and Bertero, 1975)

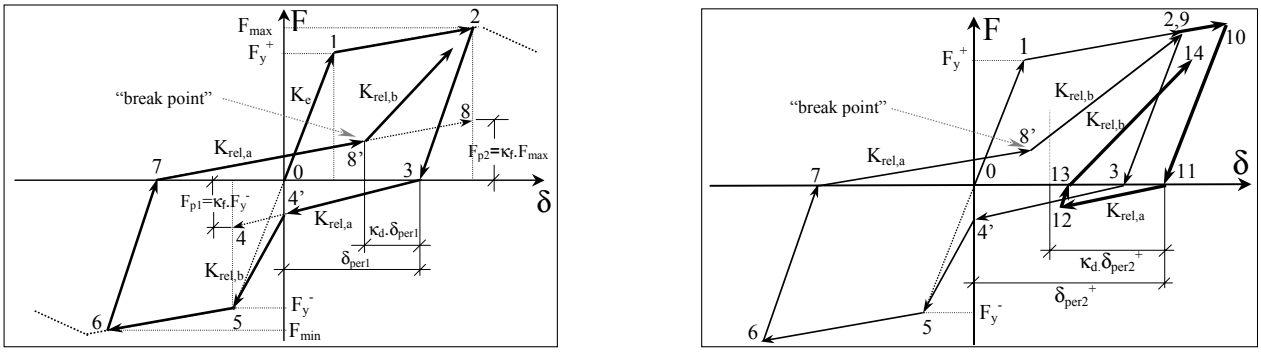

(a) (b)

Fig. 3.5 Pinching hysteretic model; (a) basic model rules, (b) reloading deformation at the right of break point

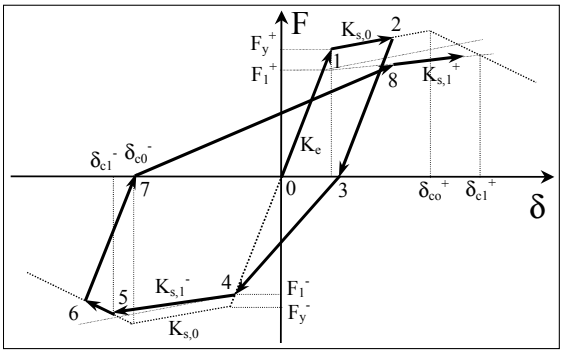

(a) Basic Strength Deterioration

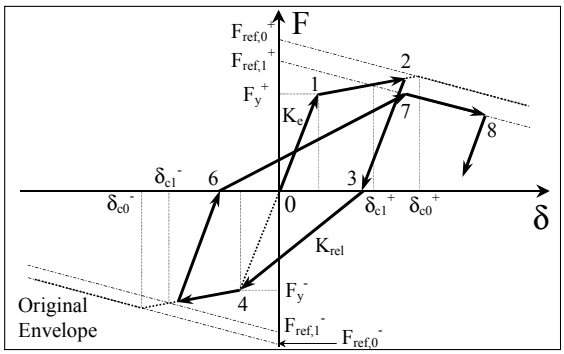

(b) Post-capping Strength Deterioration

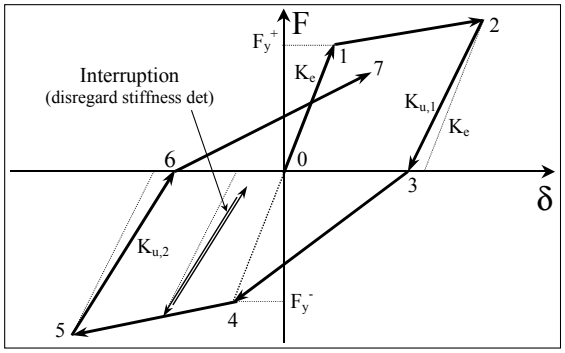

(c) Unloading Stiffness Deterioration

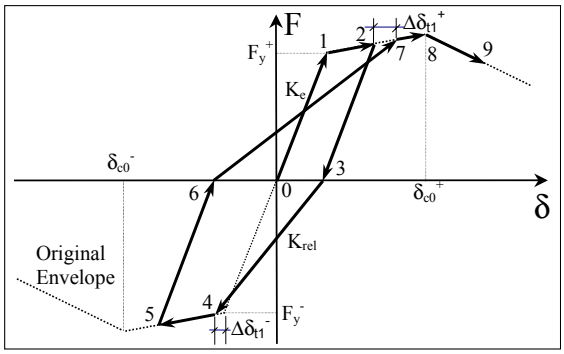

(d) Accelerated Reloading Stiffness Det.

Fig. 3.6 Peak-oriented model with individual deterioration modes

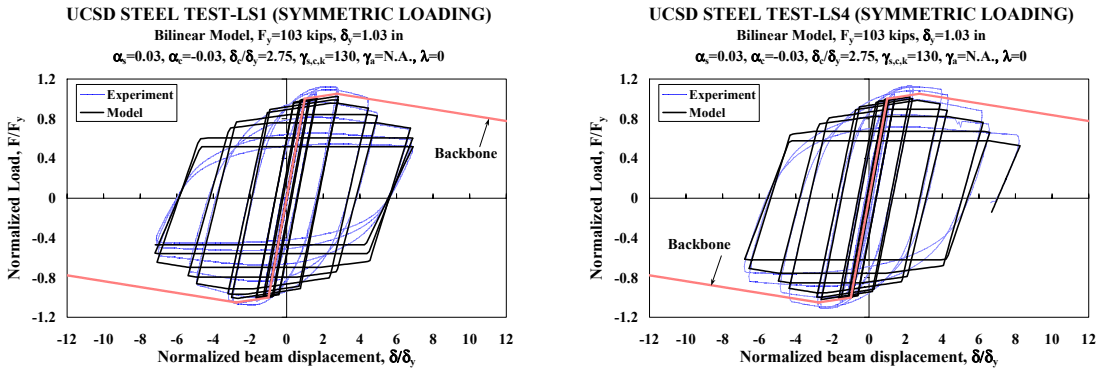

(a) Test LS-1 (b) Test LS-4

Fig. 3.7 Calibration of bilinear model on steel component tests using the SAC standard loading protocol (Uang et al., 2000)

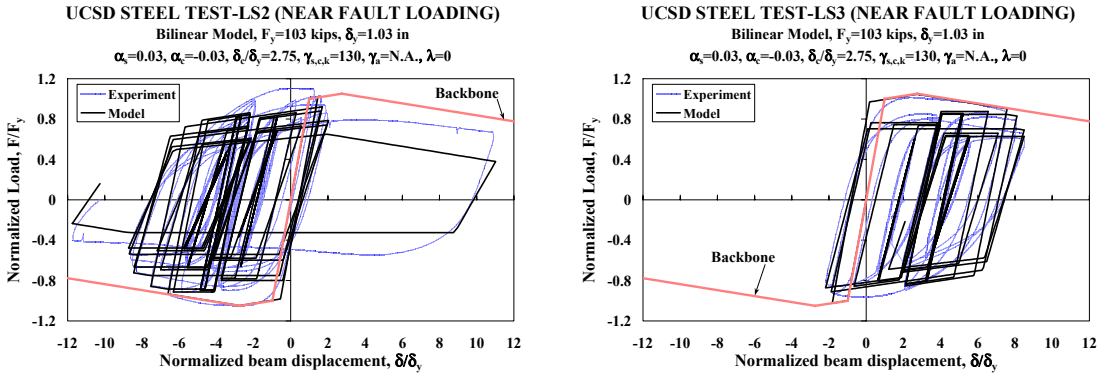

(a) Test LS-2 (b) Test LS-3

Fig. 3.8 Calibration of bilinear model on steel component tests using the SAC near-fault protocol (Uang et al., 2000)

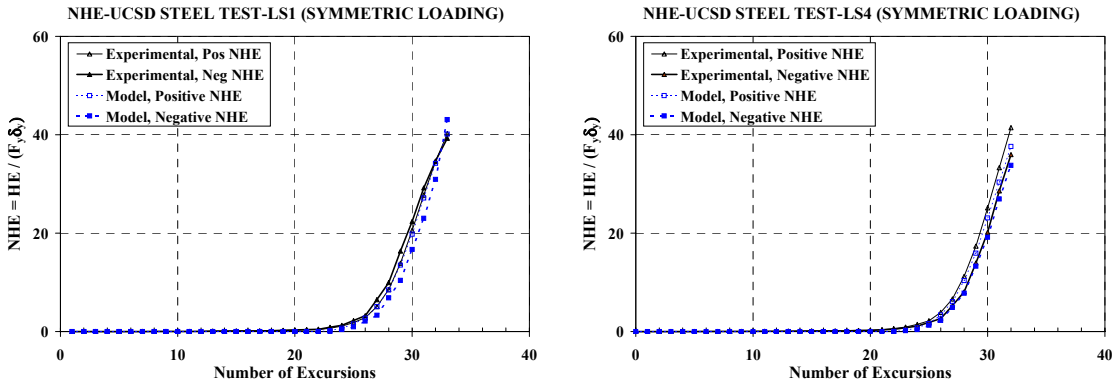

(a) Test LS-1 (b) Test LS-4

Fig. 3.9 History of NHE dissipation, SAC standard loading protocol test of Fig. 3.7, bilinear model

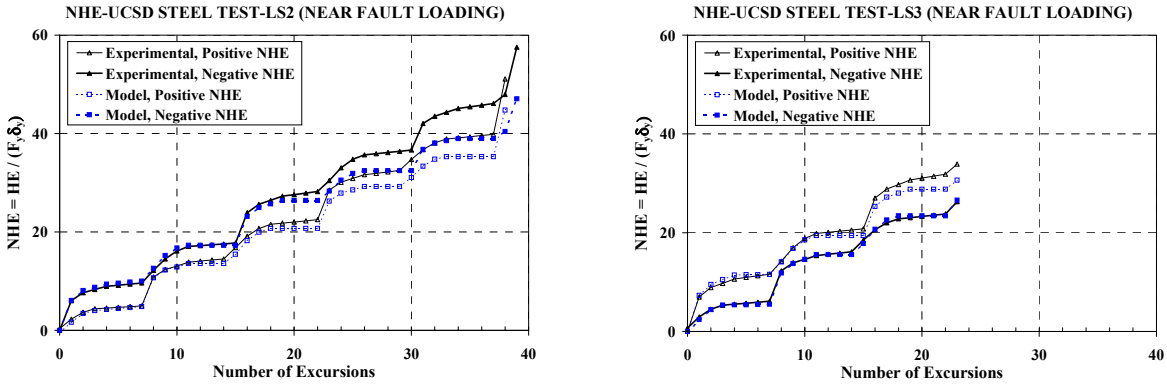

(a) Test LS-2 (b) Test LS-3

Fig. 3.10 History of NHE dissipation, SAC near-fault loading protocol tests of Fig. 3.8, bilinear model

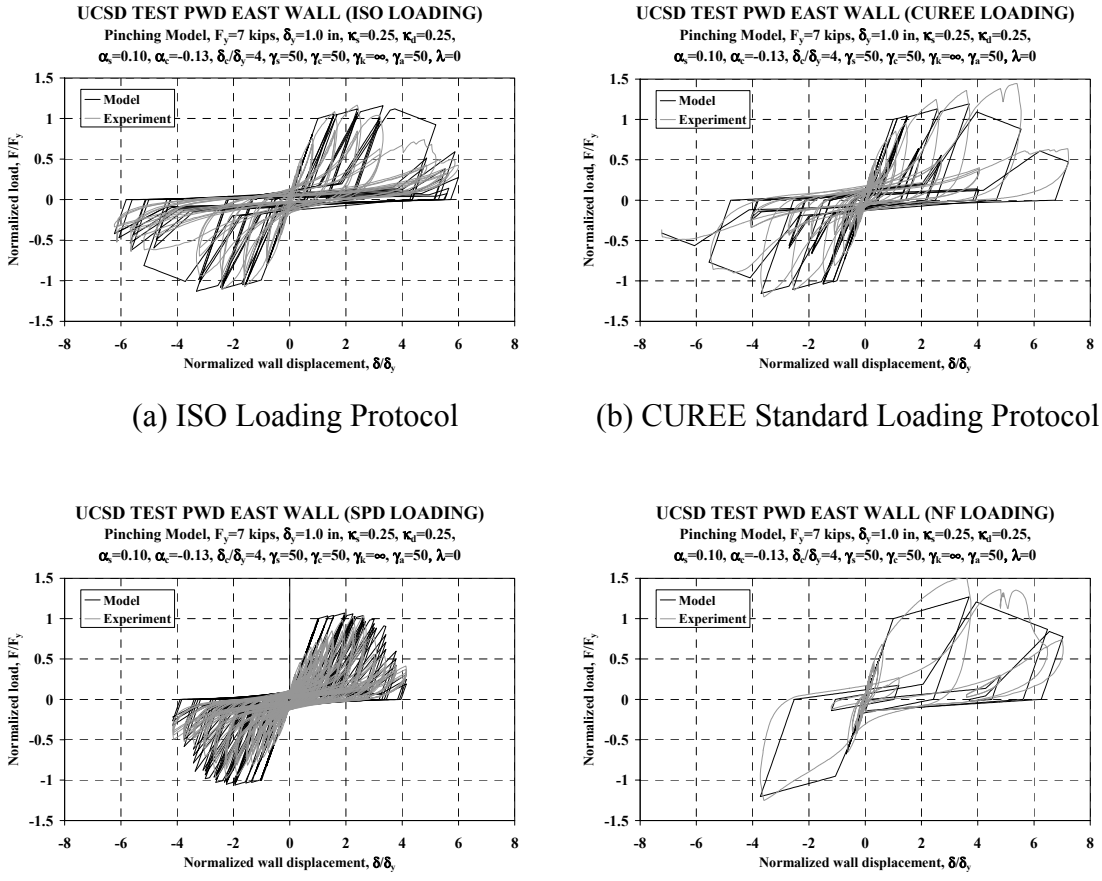

(a) ISO Loading Protocol (b) CUREE Standard Loading Protocol

(c) SPD Loading Protocol (d) CUREE Near-Fault Loading Protocol

Fig. 3.11 Calibration of pinching model on plywood shear-wall component tests (Gatto and Uang, 2002)

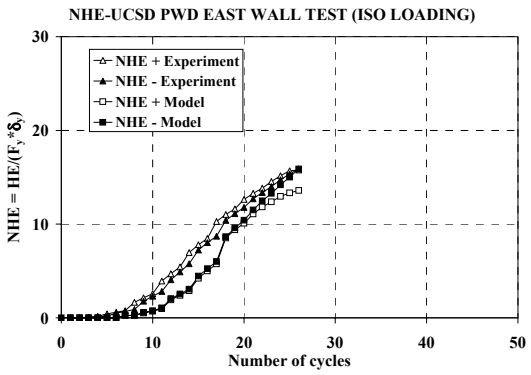

(a) ISO Loading Protocol

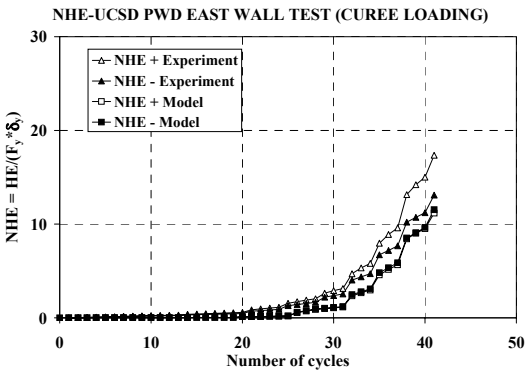

(b) CUREE Standard Loading Protocol

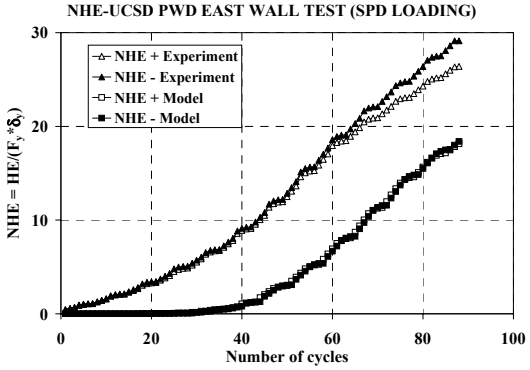

(c) SPD Loading Protocol

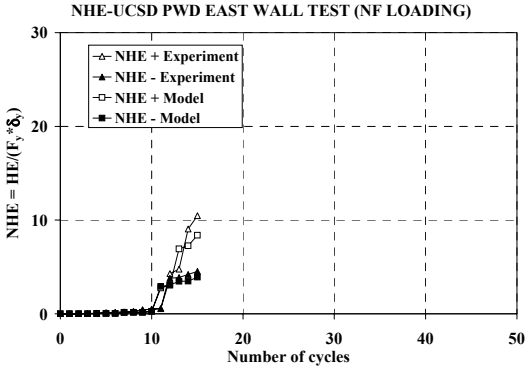

(d) CUREE Near-Fault Loading Protocol

Fig. 3.12 History of NHE dissipation, pinching model and loading protocols for tests of Fig. 3.11

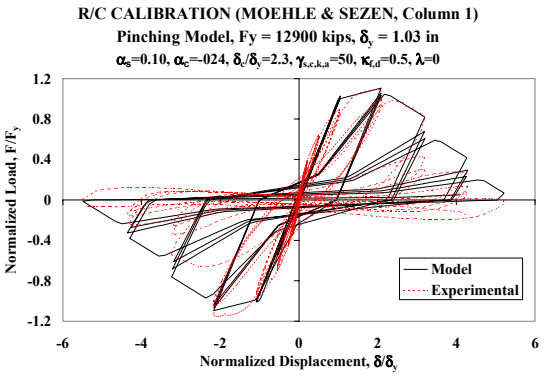

(a) Cyclic Loading Protocol

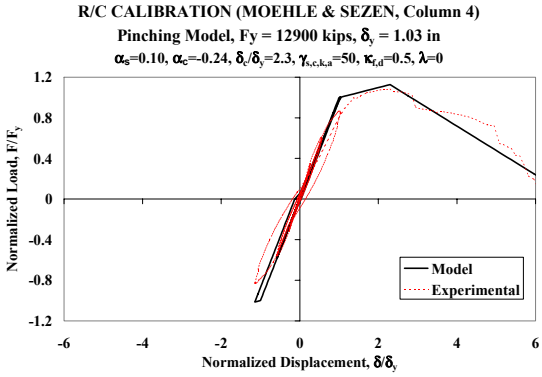

(b) Mostly Monotonic Loading Protocol

Fig. 3.13 Calibration of pinching model on reinforced concrete columns of Moehle and Sezen experiments (Sezen, 2000)

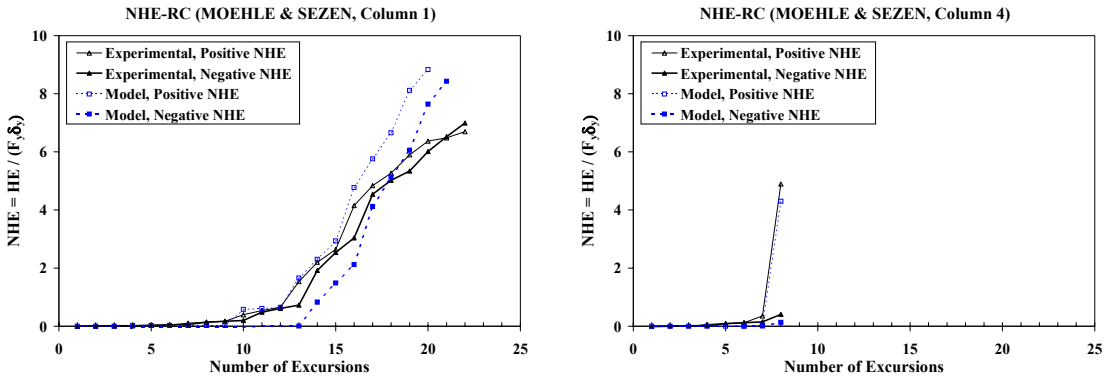

(a) Cyclic Loading Protocol (b) Mostly Monotonic Loading Protocol

Fig. 3.14 History of NHE dissipation, pinching model and tests of Fig. 3.13

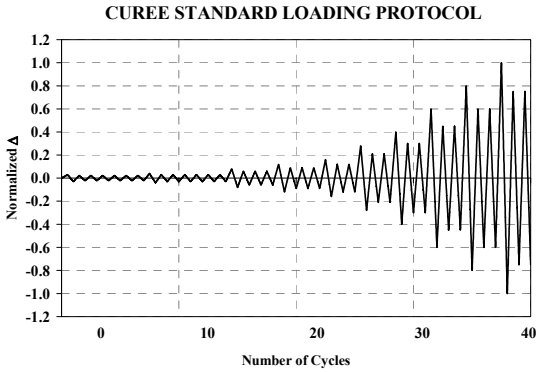

Fig. 3.15 CUREE standard loading protocol

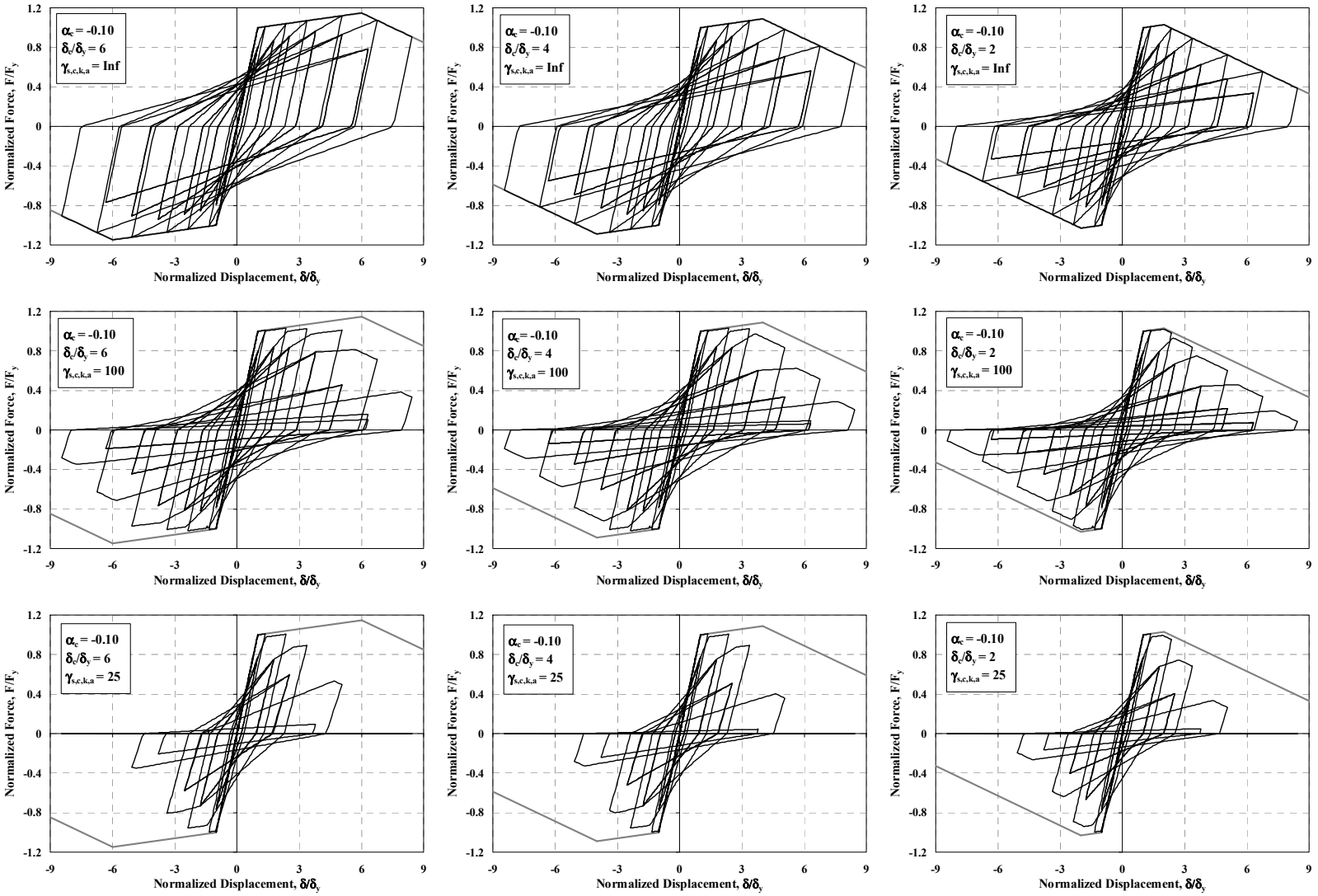

Fig. 3.16 Deterioration effect on hysteretic response; peak-oriented model, CUREE protocol, $\alpha_s = 0.03$, $\alpha_c = -0.10$

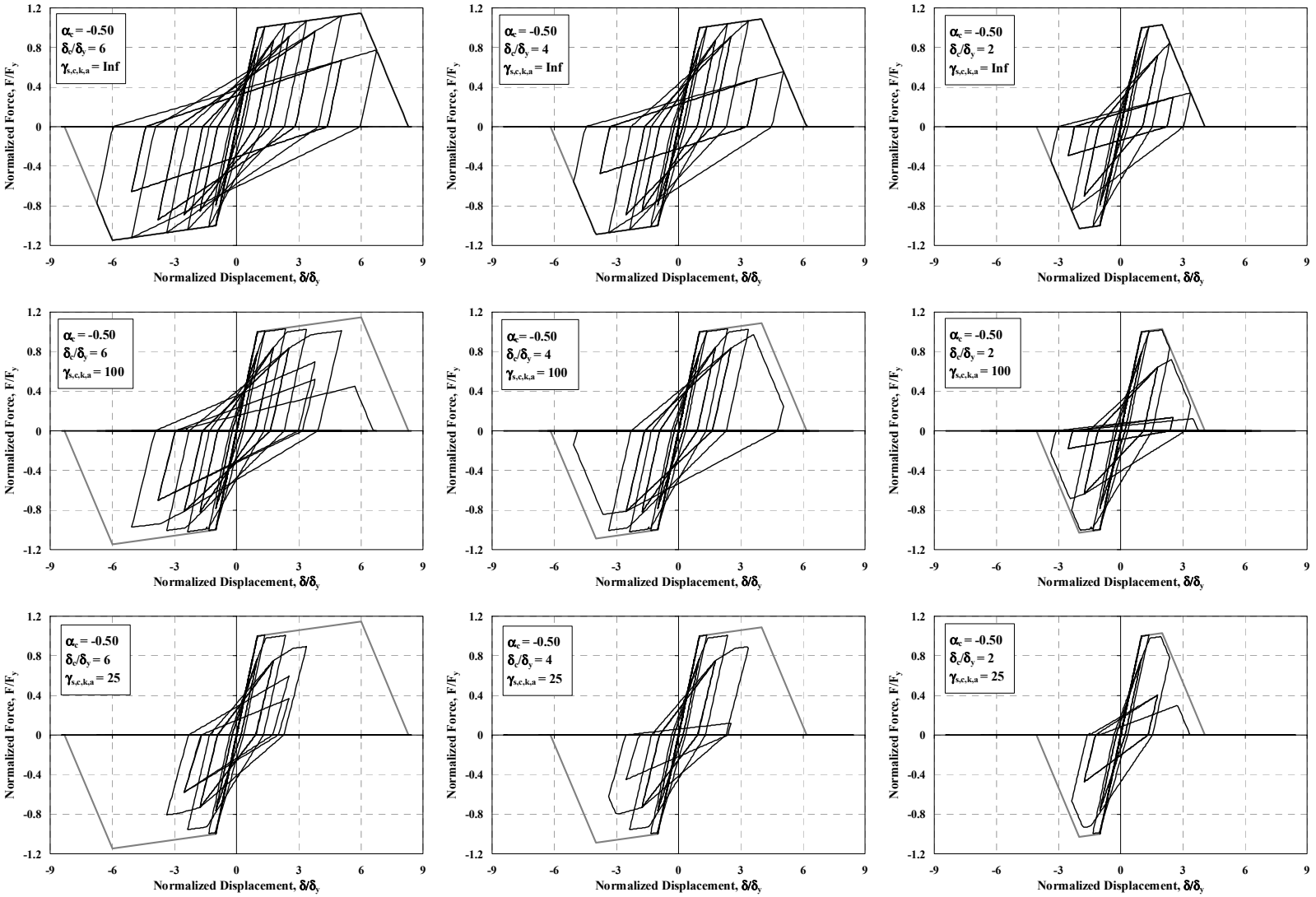

Fig. 3.17 Deterioration effect on hysteretic response; peak-oriented model, CUREE protocol, $\alpha_s = 0.03$, $\alpha_c = -0.50$

4 Collapse Assessment of SDOF Systems

4.1 INTRODUCTION

Even though the deterioration model described in Chapter 3 is a component model, in the SDOF study it is assumed that the system response follows the same hysteresis and deterioration rules as a representative component. Clearly this is a simplifying assumption, as it is idealistic to assume that all components of a structural system have the same deterioration properties and yield and deteriorate simultaneously. But such assumptions are often made when MDOF structures are represented with SDOF systems.

Parameter studies on SDOF systems are easily implemented and help to identify the system parameters that may have a negligible or dominant influence on MDOF structures. The small computational effort needed to analyze SDOF systems permits the evaluation of a large number of systems. In addition, the modification of a particular parameter generally has a larger influence on SDOF systems than on MDOF structures. The latter structures usually have elements yielding at different times and some of the elements never reach the inelastic range; thus, their global stiffness matrix has smaller modifications than the corresponding stiffness of SDOF systems.

In the past, a large number of studies have been carried out to evaluate the inelastic seismic demands of SDOF systems. Seismic demands have been studied by means of constant ductility inelastic displacement ratios (Miranda, 1993, 2000) or by means of strength reduction factors for constant ductility (Nassar and Krawinkler, 1991; Rahnama and Krawinkler, 1993). The latter study included the effect of strength and stiffness deterioration in hysteretic models with bilinear backbone curves. The results indicated that strength deterioration may greatly affect the response of SDOF systems, but the effects of unloading stiffness deterioration are relatively small. Gupta and Kunnath (1998) extended the investigation of Rahnama and Krawinkler, obtaining similar conclusions. However, these studies are based on systems without strength deterioration of the backbone curve and do not address the collapse limit state. More recently,

Song and Pincheira (2000) studied the effect of stiffness and strength deterioration on the maximum inelastic displacement of SDOF systems without including geometric nonlinearities. They found that the displacement ratio between a deteriorating and non-deteriorating system could be as large as two (especially in the short-period range) and that it varies significantly with the deterioration rate and type of ground motion. They assumed that an SDOF system collapses if its remaining strength is less than 10% of the yield strength. They reported that many systems collapsed for one or more ground motions under low strength coefficients but they did not trace this limit state for all the cases. Vamvatsikos (2002) carried out incremental dynamic analyses (IDAs) for pinched hysteretic SDOF systems that included a negative post-capping stiffness and residual strength but no cyclic deterioration. He detected that the cap displacement (δ_c, Fig. 4.1) and the slope of the post-capping stiffness are the two parameters that most affect the performance of medium-period-systems.

This chapter summarizes the results of a comprehensive parameter study on the collapse of SDOF systems with deteriorating hysteresis properties. In SDOF systems collapse occurs when the loading path is on the backbone curve (which may have deteriorated due to cyclic deterioration) and the restoring force approaches zero (Fig. 4.1). This behavior may occur because of the presence of a backbone curve branch with negative slope, a condition caused by P-Δ effects and/or a negative post-capping stiffness branch. Note that a backbone curve with only positive stiffness branches may also lead to collapse if cyclic strength deterioration is sufficiently large to exhaust the available energy-dissipation capacity.

In this part of the study, collapse is evaluated for a large number of SDOF systems subjected to a set of 40 ground motions. Statistics on the collapse capacity take into account the record to record variability. The effects of various system parameters are evaluated by comparing median collapse capacities of systems that have the same characteristics except for discrete variations in the studied parameter.

4.2 SYSTEMS AND GROUND MOTIONS CONSIDERED IN PARAMETER STUDY

The SDOF systems of the parameter study have common features, which include the same strain-hardening stiffness ratio (α_s = 0.03) and the same 20 elastic periods to be analyzed for each hysteretic case. Also, most of the systems are subjected to the same set of 40 GMs, although

a limited study is carried out for two additional sets that present different frequency content characteristics (Sections 4.4.6–4.4.7).

Collapse capacities are obtained in the fashion described in Section 2.3. The systems are analyzed under increasing relative intensity values to obtain $(S_a/g)/\eta$ - EDP relationships. The smallest relative intensity represents elastic behavior, i.e., $(S_a/g)/\eta = 1$. Thus, previous to carrying out the dynamic analyses, the spectral acceleration at the period of the system or the yielding strength is scaled to obtain this relative intensity. For subsequent analyses the relative intensity is increased until the response of the system becomes unstable, which means that the $(S_a/g)/\eta$ - EDP curve becomes flat (zero slope). The assessment of collapse is based not on EDPs but on the relative intensity of the system when collapse occurs. This relative intensity is referred as "collapse capacity," $(S_{a,c}/g)/\eta$. Statistics are carried out for collapse capacity at each period. The resulting median $(S_{a,c}/g)/\eta$ - T curves are called "median collapse capacity spectra," and are the main tool to evaluate collapse capacity and the influence of system parameters on collapse. In addition, the generated $(S_a/g)/\eta$ - EDP curves are utilized to investigate the effects of deterioration prior to collapse.

In order to reduce the number of combinations to be analyzed, the study is divided into two parts:

(1) Primary Parameter Study. Several discrete values are considered for the parameters of most interest and analyses are carried out for all possible combinations. The combinations are needed because the effect of a particular parameter on the response of the system may depend strongly on the relative value of the rest of the parameters.

(2) Secondary Parameter Study. This considers parameters that could have an influence on the response but are not included in the main parameter study; only representative systems are evaluated.

4.2.1 Parameters Evaluated in Primary Parameter Study

This part of the study focuses on the five system parameters described below, each of them with three or four discrete values. A large number of nonlinear analyses are generated because all these parameters are combined, and each combination includes 20 natural periods and 40 GMs, in which the relative intensity is increased until collapse is reached. To limit the number of

systems to be analyzed, the rest of the parameters remain fixed. Conditions that prevail for all systems are as follows:

(a) 20 natural periods of vibration ranging from $T = 0.1$ s to $T = 4$ s

(b) A set of 40 ordinary ground motions as described in 4.2.3

(c) The increment in the relative intensity is $[(S_a/g)/\eta]_{step} = 0.25$. The lowest value for $(S_a/g)/\eta$ used in the analysis is 1.0, which represents elastic behavior. If the system collapses under the effect of a particular ground motion, the algorithm iterates to locate the $(S_{a,c}/g)/\eta$ level with an accuracy of 0.1%.

(d) The hardening stiffness ratio is $\alpha_s = 0.03$. Previous studies have revealed that α_s has only a small effect on the response when the hardening stiffness ranges from about $0.02K_e$ to $0.08K_e$ (Krawinkler and Nassar, 1991).

(e) The initial percentage of critical damping is $\xi_o = 5\%$, and damping is proportional to mass.

(f) No residual strength is considered.

The system parameters investigated in the primary parameter study are described below (see Chapter 3 for the corresponding descriptions):

1. Post-capping stiffness ratio (α_c). The following α_c values cover the range of post-capping stiffness values obtained from experimental results (Sezen, 2000; Inoue et al., 2000; Elwood, 2002)
   (a) small, $\alpha_c = -0.1$
   (b) large, $\alpha_c = -0.3$
   (c) very large, $\alpha_c = -0.5$
2. Ductility capacity. The term "ductility" usually refers to the ability of a structure or its components to offer resistance in the inelastic domain of the response (Paulay and Priestley, 1992). In models with backbone curves with negative slope branches, the strength decreases for large deformations but the term ductility is used only to express the deformation associated with a certain drop in strength. This drop in strength ranges from 80 to 95% (Nakashima, 1994). In this research, ductility capacity is defined based on the displacement at which the peak strength is attained, i.e., no drop in strength is considered.
   (a) very ductile, $\delta_c/\delta_y = 6$
   (b) medium ductile, $\delta_c/\delta_y = 4$

(c) non-ductile, $\delta_c/\delta_y = 2$

3. Cyclic deterioration (CD) of basic strength, post-capping strength, unloading stiffness and reloading stiffness. The primary parameter study comprises deterioration of the four parameters with the same rate. Four levels of CD are considered based on the parameter γ, which defines the hysteretic energy capacity of the system.
   (a) no CD, $\gamma_{s,c,a,k}$ = infinite
   (b) slow CD, $\gamma_{s,c,a} = 100$ and $\gamma_k = 200$
   (c) medium CD, $\gamma_{s,c,a} = 50$ and $\gamma_k = 100$
   (d) rapid CD, $\gamma_{s,c,a} = 25$ and $\gamma_k = 50$
4. P-Δ effect
   (a) no P-Δ
   (b) small P-Δ, corresponding to $T_1 = 0.1N$ (see Section 4.3.6)
   (c) large P-Δ, corresponding to $T_1 = 0.2N$ (see Section 4.3.6)
5. Hysteretic models
   (a) peak-oriented
   (b) pinched (with $\kappa_{f,d} = 0.25$)
   (c) bilinear

Table 4.1 shows the studied combinations in the primary parameter study for peak-oriented models and no P-Δ. Identical analyses were carried out for pinching and bilinear models and for small and large P-Δ levels. The intermediate ductile system with parameters α_c = -0.10, $\delta_c/\delta_y = 4$, $\gamma_{s,c,k,a} = 100$, and P-Δ = 0 is often used as a reference case for presenting results. Because the evaluation is carried out for 20 periods, these characteristics represent a set of reference SDOF systems. However, the large number of combinations implies that some of the presented results cannot be compared with the reference systems.

4.2.2 Parameters Evaluated in Secondary Parameter Study

The parameters of the secondary parameter study are evaluated for representative systems. The discrete values for each parameter are given below.

1. Backbone curve with residual strength. The effect of this parameter is evaluated considering two residual strength levels. These levels are based on FEMA 356 (2000)

recommendations to specify deformation ranges in which the component responds with substantially reduced strength:

(a) $\lambda = 0.2\ F_y$

(b) $\lambda = 0.4\ F_y$

2. Effect of individual cyclic deterioration modes. In the primary parameter study, the same rate of deterioration is considered for all four modes of cyclic deterioration. In the secondary parameter study the effect of individual deterioration modes on collapse capacity is isolated.
3. Level of pinching in pinched hysteretic model: The effect on collapse capacity is evaluated for the following cases:

   (a) $\kappa_{f,d} = 0.25$ (from primary parameter analysis)

   (b) $\kappa_{f,d} = 0.5$

   (c) $\kappa_{f,d} = 0.75$
4. Damping of the system (ξ). The primary parameter study considers systems with mass proportional damping and initial (or elastic) percentage of critical damping $\xi_o = 5\%$. This percentage of critical damping is applied to the system without P-Δ effects. In this work, the effect on collapse capacity is studied for the following cases:

   (a) mass proportional damping for $\xi_o = 5\%$ and 10%

   (b) stiffness proportional damping for $\xi_o = 5\%$ and 10%

   (c) mixed formulation for $\xi_o = 5\%$ and 10%, preserving ξ_o value in the inelastic range.
5. Deteriorating systems subjected to near-fault ground motion (NFGM) records.
6. Deteriorating systems subjected to long-duration records.

4.2.3 Set of Ground Motion Records LMSR-N

In this study, most of the structural systems are subjected to a set of 40 "ordinary" ground motions recorded in California (LMSR-N, large magnitude small distance-new[7]). The records do not exhibit pulse-type near-fault characteristics and are recorded on stiff soil or soft rock, corresponding to soil type D according to NEHRP (FEMA-356, 2002). The source-to-site distance ranges from 13–40 km. and the moment magnitude from 6.5–6.9 (Table 4.2).

[7] The GM selection process for this bin is discussed in Medina (2002).

The selected intensity measure, IM, is the 5% linear elastic spectral acceleration at the period of the SDOF systems, $S_a(T)$. This IM has the advantage that seismic hazard data for S_a are readily available; however, there are drawbacks to the use of a single scalar IM, and alternatives are being investigated (Cordova et al., 2000; Luco, 2002). The use of S_a as IM implies that all the ground motions are scaled to a common S_a at the elastic period of the SDOF system. Thus, the frequency content of the ground motion cannot be considered explicitly. The large dispersion in spectral accelerations due to the different frequency content of the selected ground motions is illustrated in Figure 4.2, in which the records of set LSMR-N are scaled to have the same spectral acceleration at T = 0.9 s. Figure 4.2b shows the dispersion in terms of the standard deviation of the log of S_a for the scaled spectra, $\sigma_{\ln S_a}$, which is small only in the vicinity of T = 0.9 s. The dispersion increases with period, and response predictions may exhibit significant scatter depending on the extent of inelasticity, which leads to period elongation.

The use of a single set of GMs for most of this study is partly justified by previous studies showing that the inelastic response of SDOF and MDOF systems is not affected greatly by earthquake magnitude and distance to the source—except for near-fault regions (Shome, 1999; Miranda, 2000; Medina, 2002; Jalayer, 2003).

Regarding the size of the set of GMs, the uncertainty associated with the estimated EDPs and collapse capacities may be quantified as a function of the number of data points evaluated in the form of confidence levels. The use of a set of 40 GMs provides estimates of the median that are within a one-sigma confidence band of 10% as long as the standard deviation of the natural log of the collapse capacities or EDPs is less than $0.1\sqrt{N} = 0.63$, where N is the number of records (Medina, 2002).

4.3 RESULTS OF PRIMARY PARAMETER STUDY

Most of the results discussed and illustrated in this chapter represent statistical values, particularly medians. “Counted statistics” is used to obtain the first moments of EDPs given $(S_a/g)/\eta$, and “computed statistics” is utilized for collapse capacities (Appendix A). The EDPs used in the SDOF study are δ_{max}/S_d, δ_{max}/δ_y and occasionally normalized hysteretic energy dissipation, NHE. The presented results are for peak-oriented hysteresis models unless stated differently.

To identify the effect of each parameter on the response, the results are grouped in sets of similar systems that present a variation of specific parameters. Because none of the parameters can be evaluated independently of the others, the variation of parameters is carried out for systems with different characteristics. For instance, the effect of α_c on $(S_{a,c}/g)/\eta$ is quantified for different types of hysteretic models, δ_c/δ_y's, γ's and P-Δ levels (see Table 4.1). The following sections summarize the salient findings of this study.

4.3.1 Effect of Deterioration on EDPs Prior to Collapse

Although the main objective of this study is collapse capacity assessment, the evaluation of the response prior to collapse provides valuable information about the effect of various deteriorating models on EDPs. The main objectives of this section are (a) to quantify the increment in the response when deteriorating systems are used instead of non-deteriorating ones; and (b) to determine the intensity levels at which the response of deteriorating systems starts to deviate from that of non-deteriorating systems. In this investigation the term "non-deteriorating" is used for systems without any type of material deterioration, although they could include P-Δ effects. The results presented in this section are grouped according to variations of specific parameters and are for systems with T = 0.2, 0.9, and 3.6 s, corresponding to short-, medium-, and long-period systems, respectively.

Effect of Cyclic Deterioration (CD) on EDPs. Figure 4.3 shows $(S_a/g)/\eta$ - EDP curves for a system with T = 0.9 s, α_c = -0.10, δ_c/δ_y = 4, P-Δ = 0, and different $\gamma_{s,c,k,a}$ values for deteriorating systems. Curves for a non-deteriorating system with the same elastic and hardening stiffness and for the "equal displacement rule" are also included. For low relative intensities the equal displacement rule is approximately valid for all systems, i.e., for $R = (S_a / g) / \eta \le 4$, the ductility and relative intensity have approximately the same value, i.e., $R \approx \delta_{\max} / \delta_y$. Comparisons of the response between these systems indicate that the effect of CD is small (at most 10–15%) before the ductility capacity is reached ($\delta_{max}/\delta_y = \delta_c/\delta_y = 4$). The curves start to show large deviations from the non-deteriorating system once this threshold is surpassed. This can be observed best in Figure 4.3c by applying the equal displacement rule. All three figures clearly show the benefit being derived from an increase in the energy-dissipation capacity (increase in γ's) of the SDOF system—for a system with α_c = -0.10 and δ_c/δ_y = 4.

The results for very short and long-period systems with the same properties are presented in Figures 4.4 and 4.5, respectively. For systems with T = 0.2 s and rapid CD, a clear deviation from the non-deteriorating system is evident long before the ductility capacity is reached. On the other hand, for long-period systems the effect of CD is relatively small even for values of δ_{max}/δ_y much greater than the ductility capacity of 4. The above trends are similar for systems including P-Δ effects.

Effect of Post-Capping Stiffness on EDPs. In systems that are identical except for the post-capping stiffness branch, the EDPs are the same for displacements less than δ_c. For medium-period systems with a flat post-capping stiffness (α_c = -0.10), the relative intensity of the system may be increased significantly after this displacement threshold is surpassed (Fig. 4.6). However, for α_c = -0.30 and –0.50, the additional relative intensity that the system can sustain once $\delta_{max}/\delta_y > \delta_c/\delta_y$ is small.

The last observation holds true also for short- and long-period systems (Fig. 4.7), leading to the conclusion that only relatively small improvement in response can be obtained once the ductility capacity δ_c/δ_y is reached, unless the post-capping stiffness is relatively flat, i.e., it makes little difference whether α_c is –0.30 or –0.50. Only for α_c = -0.1 a clear improvement is observed for all systems. As Figure 4.7b shows, the improvement beyond $\delta_{max}/\delta_y = \delta_c/\delta_y = 4$, in terms of additional displacement capacity and additional "intensity capacity," is particularly large for long-period systems. P-Δ effects could modify this conclusion, especially for long-period systems where large instability coefficients usually have to be considered (see Section 4.3.6).

Effect of Ductility Capacity on EDPs. Figures 4.8–4.9 present median $(S_a/g)/\eta$ - EDP curves for identical systems except for the ductility capacity value. Because CD is not included, the curves for deteriorating and non-deteriorating systems are identical up to $\delta_{max}/\delta_y = \delta_c/\delta_y$. All the presented systems have a flat post-capping stiffness, and for this reason all systems exhibit a significant increase in displacement and intensity beyond that associated with the ductility capacity.

4.3.2 General Trends in Collapse Capacity Spectra, $(S_{a,c}/g)/\eta$ - T

Collapse capacity spectra are used in the following sections to evaluate the effects of the system parameters that greatly affect collapse. To obtain an idea of the possible collapse capacity values,

Figure 4.10 shows the range of median collapse capacity spectra for deteriorating peak-oriented models including all possible combinations of the primary parameter study (Table 4.1). Each median collapse capacity spectrum refers to the estimation of the geometric mean of the 40 individual collapse capacity spectra, which are obtained by subjecting a particular system to the records of the set LMSR-N (Section 2.3.4).

Figure 4.11 presents median collapse capacity spectra for representative systems, as well as the ratios of collapse capacities with respect to the most ductile system of the primary parameter study (α_c = -0.1, δ_c/δ_y = 6, $\gamma_{s,c,k,a}$ = Inf, P-Δ = 0). Note that collapse capacities of the reference case (α_c = -0.1, δ_c/δ_y = 4, $\gamma_{s,c,k,a}$ = 100, P-Δ = 0) are about 30% smaller that those of the most ductile system. Collapse capacities of the less ductile system are up to five times smaller than those of the most ductile one. However, from this figure alone it is difficult to identify the parameters that most influence the response of the system because several of them are modified at once. Thus, the effect of each individual parameter is isolated in the following sections. From here on, when ratios of collapse capacities are presented, they are always obtained by using the most ductile case of the specific parameter variation as the base case.

A basic conclusion from the primary parameter study is that the effect of any one parameter on the collapse capacity is dictated in part by the rest of the parameters. In this investigation, the interdependence is evaluated for the five parameters of the primary parameter study. For instance, the effect of α_c on collapse capacity is assessed for systems with different values of δ_c/δ_y, γ and P-Δ effect. The results are presented for systems with peak-oriented hysteretic models except when the effects of different hysteretic models are evaluated.

4.3.3 Effect of Post-Capping Stiffness on Collapse Capacity

The dependence of the median $(S_{a,c}/g)/\eta$ on α_c is shown in Figure 4.12 for periods between 0.1–1.0 s. The system corresponds to the reference case if α_c = -0.10. Except for very short-period systems, the collapse capacities are very sensitive to variations of α_c when this parameter is small. Collapse capacities increase exponentially when α_c approaches zero. For large α_c values, $(S_{a,c}/g)/\eta$ stabilizes at the relative intensity that the system can develop when the maximum displacement is equal to δ_c.

Figure 4.13 presents the effect of α_c on the median $(S_{a,c}/g)/\eta$ for a set of systems with δ_c/δ_y = 4, $\gamma_{s,c,k,a}$ = infinite, and no P-Δ effects. Median collapse capacity curves and ratios with

respect to the most ductile system of this set are presented. Except for very short-period systems, a large decrease in collapse capacity is observed for systems with α_c = -0.30 with respect to systems with α_c = –0.10. Any further increase in negative slope beyond α_c = -0.30 has a small effect because collapse occurs soon after δ_c has been reached. The effect of α_c on the collapse capacity increases for systems with longer periods when P-Δ = 0.

The effect of α_c is even larger for systems with smaller δ_c/δ_y. Figure 4.14 presents the effect of α_c for the same set of systems of Figure 4.13 except for δ_c/δ_y = 2. As can be seen, the collapse capacities are significantly reduced compared to δ_c/δ_y = 4; a reduction that is proportionally larger for systems with large α_c, leading to smaller collapse capacity ratios. That is to say, the effect of α_c on collapse capacity is magnified in systems with small ductility capacity because proportionally a larger fraction of the relative intensity is developed after δ_c is surpassed. If P-Δ effects are included, collapse capacities are greatly reduced for medium- and long-period systems where the stability coefficient is larger. Compare Figures 4.15–4.16 with Figures 4.13–4.14, respectively. As observed, the effect of α_c still is relevant and the ductility capacity parameter still has an important influence.

The influence of CD on the effect of α_c on collapse capacity is illustrated in Figure 4.17, which shows collapse capacities for the systems of Figure 4.13 but including medium CD (γ= 50). Larger collapse capacity ratios are observed because CD reduces in a larger proportion the collapse capacities of systems with small α_c. That is to say, the effect of α_c on collapse capacity is reduced for systems with large CD.

Collapse capacities of bilinear models are smaller than those of the peak-oriented models (compare Figs. 4.13–4.18). The main reason is that the negative post-capping stiffness affects the bilinear model more because of the "ratcheting" effect (Section 4.3.7). In bilinear models the effect of α_c on $(S_{a,c}/g)/\eta$ is smaller in the short-period range compared with the peak-oriented one. This occurs because of the large decrease in collapse capacity for systems with flat post-capping stiffness; compare Figures 4.13 and 4.18. Note that collapse capacities for bilinear models with α_c = -0.30 and α_c = -0.50 are practically the same.

The dispersion of collapse capacities is presented in Figure 4.19 for representative systems, using the standard deviation of the log of $(S_{a,c}/g)/\eta$. In general the dispersion is larger for more ductile systems, as the one with α_c = -0.10 and no P-Δ effects (4.19a). P-Δ effects slightly reduce the dispersion because they make the system less "ductile." The largest standard

deviation is at most about 0.60, which means that the estimates of the median are within a one-sigma confidence band of 10% because the number of records used is 40.

Summarizing, the effect of α_c may modify the collapse capacity by more than 100%, particularly for long-period systems with no P-Δ effects. The magnitude of this effect depends not only on the "ductility" of the system but also on the parameters that induce such behavior. For instance, systems are *less ductile* when δ_c/δ_y is smaller, but the effect of α_c becomes larger because a larger proportion of the nonlinear response occurs after δ_c has been reached. On the other hand, systems are *more ductile* when CD is slower, and in these systems the effect of α_c is more important.

4.3.4 Effect of Ductility Capacity on Collapse Capacity

The dependence of the median $(S_{a,c}/g)/\eta$ on δ_c/δ_y is illustrated in Figure 4.20. If δ_c/δ_y = 4, the SDOF system is equivalent to the reference system. The δ_c/δ_y -$(S_{a,c}/g)/\eta$ relationship is close to linear for all periods. For very short periods the corresponding curve is close to a horizontal line, indicating that the collapse capacity is not affected much by variations in δ_c/δ_y, as in the case of α_c.

Figure 4.21 shows the effect of δ_c/δ_y on systems with α_c = -0.10, γ= infinite, and P-Δ = 0. Median collapse capacity curves as well as the ratios with respect to the most ductile system are presented. Observe that except for very short periods, the median collapse capacity is essentially period independent (Fig. 4.21b). The effect of δ_c/δ_y on collapse capacities is significant, but much less than the ratio of ductility capacities. The main reason for the relatively small effect is the fact that because of the flat post-capping slope (α_c = 0.1) all systems exhibit a significant intensity increase beyond that associated with δ_c. Figure 4.22 shows the same information but using systems with α_c = -0.30. The steeper post-capping slope significantly reduces the collapse capacities, but also magnifies the effect of δ_c/δ_y. Collapse ratios close to 0.40 are observed. The effect of δ_c/δ_y increases for larger α_c values because collapse occurs relatively soon after δ_c is reached.

Collapse capacities are reduced if P-Δ effects are included, but collapse capacity ratios still tend to be period independent and with values similar to those obtained for systems with no P-Δ effects (compare Figs. 4.23 and 4.21). The effect of δ_c/δ_y on the collapse capacity for

systems with medium CD (γ = 50) is shown in Figure 4.24, which can be compared with the system with no CD (Fig. 4.21). The effect of δ_c/δ_y on the collapse capacity becomes relatively small for systems with significant CD.

Figure 4.25 shows similar information to that of Figure 4.21 but using systems with a bilinear model. Compared with peak-oriented models, the collapse capacities are smaller but the effect of δ_c/δ_y is larger. As will be explained in Section 4.3.7, bilinear models are more affected by the presence of a branch with negative stiffness. Therefore, the effect of reducing δ_c/δ_y has a larger effect on the collapse capacity because δ_c is surpassed at earlier stages of nonlinear behavior.

Figure 4.26 presents a measure of dispersion for systems having different δ_c/δ_y. There is no significant difference or clear trend among the dispersion curves for systems with large and small ductility capacity. This suggests that dispersion largely depends on the post-capping stiffness parameter rather than the ductility capacity. P-Δ effects reduce the standard deviation of the log of the data, especially for long-period systems.

4.3.5 Effect of Cyclic Deterioration on Collapse Capacity

Cyclic deterioration is assumed to be proportional to the energy-dissipation capacity of the system, defined by the parameter γ. The dependence of the median $(S_{a,c}/g)/\eta$ on γ is illustrated in Figure 4.27. If $\gamma_{s,c,k,a}$ = 100, the system corresponds to the reference system. The systems of Figure 4.27 have a negative post-capping branch (α_c = -0.10) that eventually leads to collapse even if CD is not present. As the figure shows, for these systems CD has an appreciable effect on the collapse capacity only if γ is on the order of 100 or smaller.

Figure 4.28 presents the effect of CD on collapse capacities for a set of systems with δ_c/δ_y = 4 and α_c = -0.10. Except for very short periods, the collapse capacity ratios are in essence period independent, with values as small as 0.5 (this large effect is observed only for α_c = -0.10). The expectation might be that CD has a larger effect for short-period systems because of the larger number of inelastic cycles. As Figure 4.28b shows, this is not true—for two reasons. First, for short-period systems the effects of all system parameters on the collapse capacity are small because of the dominant displacement amplification effect for inelastic systems. And second, for systems without CD the normalized hysteretic energy (NHE) demands are much

higher for short-period systems than for medium- and long-period systems, but the demands become less period sensitive for systems with cyclic deterioration (Fig. 4.29). Thus, the displacement amplification effect dominates over the effect of cyclic deterioration.

Figure 4.30 presents the same information as Figure 4.28, but for systems with small ductility capacity. The patterns are the same but the effect of CD on the collapse capacity is smaller for systems with small ductility capacity because these reach collapse faster and have less time to dissipate hysteretic energy. Figure 4.31 shows the effect of CD on the collapse capacity for systems with α_c = -0.30, which again can be compared with Figure 4.28. Once again, the presence of a parameter that reduces the collapse displacement in the system reduces the effect of CD on the collapse capacity because the number of inelastic cycles is decreased.

The effect of CD on the collapse capacity is much reduced in medium- and long-period systems that include P-Δ effects. Figure 4.32 presents the results for the set of systems of Figure 4.28 but including small P-Δ effects. Collapse capacity ratios for different CD values approach unity for long-period systems. This indicates that for such systems P-Δ effects dominate over the effect of CD on collapse capacity.

The effect of CD on the collapse capacity for bilinear models is illustrated in Figure 4.33, which can be compared with Figure 4.28. The collapse capacity ratios are about the same for bilinear and peak-oriented models, but the median collapse capacities are clearly smaller for the bilinear model for reasons that will be discussed in Section 4.3.7.

The dispersion for similar systems with different rates of CD (Fig. 4.34) indicates that the standard deviation of the log of the data decreases somewhat with an increase in CD.

It is concluded that the effect of CD on the collapse capacity always increases when any of the other system parameters cause a more ductile response. This is a clear pattern that was not detected in other parameters. However, the effect of CD on the collapse capacity is smaller than that caused by large variations in the backbone curve parameters and, for long-period systems, by P-Δ effects.

4.3.6 Effect of P-Δ on Collapse Capacity

Traditionally, P-Δ effects are quantified by means of the elastic stability coefficient (Sun et al., 1973; Bernal, 1986). This coefficient can be associated with a rotation of the original backbone curve (Fig. 4.1) and could have a very significant effect on the behavior of the system (Vian and

Bruneau, 2001). In fact, systems without material deterioration may collapse if P-Δ effects are sufficiently large. The stability coefficient is defined as:

$$\theta = \frac{P}{kh} = \frac{W\delta_y}{F_y h} \tag{4.1}$$

where P is the vertical acting load, which here is assumed to be equal to the weight of the SDOF system, $W = m/g$; k_e is the elastic stiffness, $k_e = F_y / \delta_y$; and h is the height of the system. For SDOF systems, the stability coefficient can be expressed in a simplified form by taking into account that:

$$T = 2\pi\sqrt{\frac{m}{k}} \tag{4.2}$$

After substituting Equation (4.2) into (4.1) and considering g = 981 cm/s^2, the elastic stability coefficient can be defined as a function of the period and the height (in centimeters) of the SDOF system:

$$\theta = \frac{25T^2}{h} \tag{4.3}$$

his equation helps to set practical limits for θ. For instance, if T = 1.0 s and the height of the system is 244 cm ($\approx 8'$); then $\theta \approx$ 0.10, which is a large coefficient for a system with T = 1.0 s. The reason for the large value is the small height of 244 cm, which is not representative for a medium-period system. Moreover, the number of parameters influencing P-Δ effect is increased if SDOF systems are used as simplifications of MDOF structures, i.e., the number of stories, assumed loading pattern, deflected shape of the MDOF structure, irregularities in height or plan, distribution of vertical load, etc. (Bernal, 1992). As discussed in Chapter 5, P-Δ effects for equivalent SDOF systems should be derived from both elastic and inelastic stability coefficients obtained from global pushover analysis of the MDOF structure.

Thus, stability coefficients for equivalent SDOF systems should be calculated for each specific structure. In order to establish general trends, in this section the effect of P-Δ on collapse capacity is evaluated by using the elastic stability coefficients corresponding to the first story of the generic frames used in Chapter 5. These frames have 3, 6, 9, 12, 15, and 18 stories, and for a given number of stories a stiff and a flexible model are designed by targeting a fundamental period of vibration of $T_1 = 0.1N$ and $T_1 = 0.2N$, respectively. For these frames, the elastic first-story stability coefficient can be estimated as $0.0178T_1$ and $0.0356T_1$ for the stiff and

flexible models, respectively. Consequently, the following three P-Δ levels are used here for each period:

(a) no P-Δ, $\theta = 0.0$

(b) small P-Δ, $\theta = 0.0178T_1$ (stiff system, $T_1 = 0.1N$)

(c) large P-Δ, $\theta = 0.0356T_1$ (flexible system, $T_1 = 0.2N$)

Figure 4.35 shows the stability coefficients for each P-Δ level as a function of the period of the system. The assigned levels are used only to identify general patterns.

The effect of P-Δ on collapse capacities is shown in Figure 4.36 for an intermediate ductile SDOF system. As observed, the P-Δ effect produces the largest modification of collapse capacities in the long-period range. The effect is largest in this range because of the large stability coefficients that overcome the 3% strain hardening of the second branch of the backbone curve and cause an effective negative tangent stiffness as soon as the yield displacement is reached. Note that in the long-period range the collapse capacities for systems with small and large P-Δ effects are similar. At this range, the strain-hardening slope has become negative for both P-Δ levels (Fig. 4.35). Therefore, merely the presence of a branch with negative stiffness greatly accelerates collapse, regardless of the value of the slope (Bernal, 1986; Gupta and Krawinkler, 2001).

Figure 4.37 shows the same information as Figure 4.36, but for systems with a small ductility capacity. The collapse capacity is reduced, but the collapse capacity ratios are similar for the two cases, indicating that ductility capacity does not greatly modify the effect of P-Δ on collapse capacity.

Figure 4.38 presents collapse capacities for the systems of Figure 4.36, but using a large α_c value. Comparing these two figures in the long-period range, it is seen that the effect of a large α_c value is large for systems without P-Δ effect but small for systems with P-Δ. The reason is that the backbone curve (without P-Δ effects) already has a steep negative α_c; thus, the increment in the negative stiffness due to the inclusion of P-Δ effects is small compared with systems with a small α_c.

The effect of P-Δ on the collapse capacity is marginally affected by the CD rate of the system, as revealed by a comparison of collapse capacities and corresponding ratios for systems with medium CD of Figure 4.39 with those of Figure 4.36.

Figure 4.40 displays collapse capacities for bilinear models. Comparing these results with those of Figure 4.36 (peak-oriented models), it is clear that the negative stiffness of the backbone curve has a larger effect on the deterioration of bilinear models. The following section provides more details in this respect.

4.3.7 Effect of Type of Hysteretic Model on Collapse Capacity

This section is aimed to test the effect of the type of hysteretic model on the collapse capacity, given that former sections have focused on results for peak-oriented models. To obtain a general idea of collapse capacities when using different hysteretic models, Figure 4.41a shows median $(S_{a,c}/g)/\eta$ ratios for pinching over peak-oriented models for all the systems that do not include P-Δ effects. The median collapse capacity of pinching models is larger than that of peak-oriented models, except in the short-period range. Figure 4.41b shows median collapse capacity ratios for bilinear over peak-oriented models without P-Δ effects. In this case the pattern reverses and the difference between collapse capacities is more pronounced.

Therefore, in the medium- and long-period ranges, collapse capacities are largest for pinching models, followed by those for peak-oriented and bilinear models (the same trends in the response of EDPs are obtained by Foutch, 1996). In the short-period range the behavior is reversed and the bilinear models have the largest collapse capacities. In the case of systems with P-Δ effects, the patterns for collapse capacities are preserved but the ratios are closer to 1.0, particularly for long-period systems (Fig. 4.42). The ratios are studied in more detail below to understand what system characteristics produce smaller or larger ratios in the former figures.

Figure 4.43 presents bilinear over peak-oriented collapse capacity ratios for two systems with extreme backbone curve features. One of the systems has a small ductility capacity and a flat post-capping stiffness (δ_c/δ_y = 2, α_c = -0.1), whereas the other has δ_c/δ_y = 6 and α_c = -0.3. The latter system[8] has large ductility capacity but collapse occurs soon after δ_c is surpassed because of the steep post-capping stiffness. That is to say, most of the collapse capacity is developed previous to the attainment of δ_c, i.e., in a range in which the hysteretic model behaves in the same way as that of a non-deteriorating system. For this system the ratios are closer to one, meaning that the collapse capacity is similar for both hysteretic models. This is in agreement

[8] These systems are useful to understand the patterns of Figure 4.43 but they are not usually expected in real components because of the combination of very ductile and non-ductile parameters in the same backbone curve.

with the results for EDPs obtained by Foutch (1998) and the results for *R*-factors for constant ductility obtained by Nassar and Krawinkler (1991).

In the systems with small ductility capacity (δ_c/δ_y = 2) the post-capping stiffness is reached relatively soon and because of the small post-capping stiffness (α_c = -0.1) a large part of the collapse capacity of the system is developed after δ_c is surpassed. In these systems, the bilinear over peak-oriented collapse capacity ratios are as low as 0.6, indicating that collapse capacity for bilinear models is substantially smaller than that of peak-oriented models. One reason, and probably the primary one, is the presence of a branch on the backbone curve with negative tangent stiffness, which produces a ratcheting effect for bilinear systems that tends to cause a faster collapse. However, a negative post-yielding slope may be originated by other factors. For instance, Rahnama and Krawinkler (1993) have concluded that peak-oriented models behave better than bilinear ones if large P-Δ effects are present that produce a negative post-yielding slope. The peak-oriented model spends most of its time in "inner" loops in which the loadings stiffness is always positive, rather than on the backbone curve where the negative tangent stiffness leads to drifting of the displacement response.

Figure 4.44 present the bilinear over peak-oriented collapse capacity ratios for several combinations of α_c and δ_c/δ_y. These graphs confirm that the steeper the post-capping slope, the closer the collapse capacities for both hysteretic models.

Figure 4.45 shows bilinear over peak-oriented collapse capacity ratios for systems with small α_c, medium or small δ_c/δ_y, and different rates of CD. The difference in collapse capacities is larger for systems with less cyclic deterioration. Therefore, the effect of cyclic deterioration is smaller in systems with bilinear models.

4.3.8 Increment in Collapse Capacity after Cap Displacement, δ_c, is Reached

Traditionally, guidelines including inelastic behavior, such as FEMA 356, consider that collapse of SDOF systems occurs almost immediately after the peak (cap) point in the backbone curve is reached or, at most, when the strength on the backbone curve has decreased 20% with respect to its peak value. This section aims to quantify the increase in collapse capacity after δ_c is reached.

In the first part, systems without P-Δ effects are studied. Figure 4.46 shows the median ratio of collapse capacity over the intensity level at which the ductility capacity of the systems is reached. As observed, the ratios increase for systems with longer period. The ratios of four

identical systems except for the CD rate are plotted in 4.46a. The ductility capacity of the systems is $\delta_c/\delta_y = 4$. The ratios are larger for systems with less CD, which indicates that the effect of CD on EDPs increases after δ_c is surpassed.

The ratios of 4.46b correspond to identical systems except for α_c. For systems with a steep post-capping slope, the increment in collapse capacity is small after δ_c is reached. But the increment is very large for systems with a flat post-capping slope. Figure 4.46c presents systems where the only parameter that is varied is the ductility capacity, and unlike former cases, the less ductile the system (smaller δ_c/δ_y), the larger is the increase in collapse capacity [9]. The reason is that the displacement until collapse after surpassing the peak displacement ($\delta_f - \delta_c$) is proportionally larger in systems with small δ_c/δ_y, particularly for flat post-capping slopes. This can be interpreted as having a larger δ_f/δ_c ratio. For instance, the systems of Figure 4.46 have ductility capacities of δ_c/δ_y = 2, 4, and 6, and δ_f/δ_c = 6.3, 3.8, and 3.0, respectively. Consequently, the system with small δ_c/δ_y and small α_c develops a large part of the collapse capacity once the negative slope is reached.

If P-Δ is included the above ratios are greatly reduced because the P-Δ effects lead faster to collapse when the slope of the backbone curve is negative, especially for long-period systems where the P-Δ effect dominates. This is observed in Figure 4.47, which repeats the results of Figure 4.46 but including small P-Δ effect. Figure 4.48 shows how the ratios decrease when the same system ($\delta_c/\delta_y = 4$ and $\alpha_c = -0.1$) is subjected to increasing P-Δ levels.

In summary, for models with small α_c collapse capacity may be underestimated by a great amount by neglecting the capacity of the system that is developed after δ_c is reached. For systems with large α_c, the collapse capacities may be approximated with the relative intensity developed when the peak displacement is reached.

4.4 RESULTS OF SECONDARY PARAMETER ANALYSIS

4.4.1 Effect of Residual Strength, λF_y, on Collapse Capacity

The effect of residual strength, which is not included in the primary parameter study, is evaluated in this section. Models with residual strength and no P-Δ effects do not collapse unless CD is

[9] The ratios for this set of systems have collapse capacities over relative intensities calculated at different δ_c/δ_y's, because this is the parameter that is being varied.

included and the hysteretic energy capacity is exhausted (Fig. 4.49a). When the system includes P-Δ effects, the backbone curve rotates and collapse occurs if $(S_a/g)/\eta$ is large enough to cause a zero restoring force when the loading path is on the backbone curve (Fig. 4.49b).

The displacement at which collapse occurs depends on the geometry of the backbone curve. Figure 4.50 presents displacements at collapse normalized by the yield displacement (δ_f / δ_y) for backbone curves with different residual strengths. The ratios correspond to ductile and non-ductile systems and include small P-Δ effects and no CD. As can be seen, the presence of residual strength increases the normalized collapse displacement in a larger proportion for non-ductile systems. Also, residual strength does not modify δ_f / δ_y ratios in long-period systems, where the large P-Δ effect leads to collapse before the loading path reaches the residual branch.

Recognizing that the effect of residual strength is sensitive to the geometry of the backbone curve, several analyses were performed for systems with small P-Δ effects and the following parameters: δ_c / δ_y = 2, 4, 6 and α_c = -0.10, -0.30. Residual strengths of $\lambda F_y = 0.2F_y$ and $0.4F_y$ are selected in accordance with FEMA 356, which recommends the former value for most of the beam-column elements in most structural materials. The residual strength of $0.4F_y$ is included because FEMA recommends residual strength values as large as 0.4, 0.6, and even $0.75F_y$ for some elements, e.g., shear walls and RC infilled columns. The results discussed below about the effect of residual strength on collapse capacity are for systems with small P-Δ effects and are grouped according to the CD rate.

Residual Strength Effect of Systems without CD. Figures 4.51–4.52 present collapse capacities for ductile and non-ductile systems with no CD. The addition of residual strength increases collapse capacities only for systems of short and medium periods. The increase is important only for non-ductile systems with λ = 0.4; for systems with λ = 0.2 the increment is negligible for all the systems.

Residual Strength Effect of Systems with CD. Collapse capacities for the same systems are presented in Figures 4.53–4.54, but considering a medium CD rate. In the very short-period range (T < 0.3 sec) the inclusion of CD greatly reduces the collapse capacity of systems with residual strength. Nonetheless, for short-period non-ductile systems including CD, the increment in collapse capacity when λ = 0.4 can be as much as twice that of models without residual strength (Fig. 4.54b). The reduction in collapse capacity is explained by observing that δ_{max} / δ_y ratios are greatly reduced in the short-period range when CD is included (Fig. 4.55).

Collapse Capacity Based on Pre-Established Collapse Displacement. As observed in Figure 4.55a, hysteretic models with residual strength and no CD may have unreasonably large displacements leading to unrealistic collapse capacities, especially in the short-period range. To avoid this situation, a judgment-based maximum displacement is imposed, in which the collapse displacement of the backbone curve with residual strength is at most 1.6 times the collapse displacement of the backbone curve without residual strength, $\delta_f\ (\lambda>0) \leq 1.6\ \delta_f\ (\lambda=0)$. This displacement constraint produces reasonable δ_{max}/δ_y ratios even when CD is not included (Fig. 4.56).

Figure 4.57 presents the effect of residual strength on collapse capacity for systems with the displacement restriction $\delta_f(\lambda>0) \leq 1.6\ \delta_f(\lambda=0)$. These results can be compared with those of Figures 4.51b and 4.52b. As observed, the maximum collapse capacity ratios are about 1.2 but only for non-ductile systems with $\lambda = 0.4$. For systems with $\lambda = 0.2$ the effect of residual strength on collapse capacity is negligible.

Hence, residual strength does not affect significantly the collapse capacity of most structural components when reasonable assumptions for λ and δ_f/δ_y ratios are made.

4.4.2 Effect of Individual Cyclic Deterioration Modes

The effect of CD on collapse capacity has been evaluated considering the same deterioration rate for basic strength, post-capping strength, unloading stiffness, and accelerated reloading stiffness deterioration. This section isolates the effect of each deterioration mode on collapse capacity, an assumption that may not be realistic but is useful for identifying the CD modes that are more relevant in the estimation of collapse capacity. For each analyzed deterioration mode the corresponding parameter γ is varied, whereas the rest of the modes remain without deterioration.

Cyclic Basic Strength Deterioration. This deterioration mode produces translation of the hardening branch toward the origin and deterioration of its slope (Section 3.3.2). The effect of this deterioration mode can be very different for systems with and without post-capping stiffness.

In systems without a post-capping branch collapse occurs when the hysteretic energy capacity of the system is exhausted, which means that restoring strength is zero. To illustrate this effect, Figure 4.58a presents the hysteretic response for a non-deteriorating system subjected to the CUREE standard loading protocol (Gatto and Uang, 2002), whereas Figure 4.58b shows the

hysteretic response for the same system but with γ_s = 50. As can be seen, the hysteretic response may be greatly modified when the only source of deterioration is cyclic basic strength deterioration. Regarding the effect of γ_s on collapse capacity, Figure 4.59 shows collapse capacities for similar systems without strength capping and different CD rates. The collapse capacity ratios for the less ductile systems (γ_s = 25) can be as low as 0.40 with respect to systems with slow CD[10] (γ_s = 100), corroborating that CD effects increase in systems without a negative branch in the backbone curve.

In systems with a post-capping branch the effect of cyclic basic strength deterioration is substantially smaller due to the presence of additional sources of deterioration. This is observed in Figure 4.60, which shows the hysteretic response for a system with δ_c/δ_y = 2 and α_c = -0.10 subjected to the CUREE standard loading protocol. For Figure 4.60a, the only source of deterioration is the negative post-capping stiffness, whereas Figure 4.60b also includes cyclic basic strength deterioration. Note that although the hardening branch moves inwards, the absolute value of cap displacement (δ_c) increases. The increase of δ_c implies that systems including strength CD may have a better response than systems not including CD, when subjected to ground motions. Figure 4.61 presents collapse capacity ratios for systems with a peak-oriented model, δ_c/δ_y = 2 and α_c = -0.10 and different rates of strength CD (the ratios are taken with respect to the system with no CD). As observed, some ratios are larger than one, indicating that when only strength CD is included, the effect of increasing the absolute value of δ_c may overcome the effect of strength capping. The box on the bottom left corner of Figure 4.61 shows the collapse capacity ratios when the four CD modes are included.

The conclusion is that cyclic basic strength deterioration must be combined with cyclic post-capping strength deterioration in order to accelerate collapse. Experimental results have demonstrated that indeed both cyclic deterioration modes occur simultaneously.

Cyclic Post-Capping Strength Deterioration. This individual CD mode translates the post-capping branch toward the origin (Section 3.3.3). To illustrate the magnitude of this effect, Figure 4.62a shows hysteretic responses for a system with δ_c/δ_y = 2 and α_c = -0.10, which can be compared with the response of the same system but without CD (Fig. 4.60a). As observed, the effect of cyclic post-capping strength deterioration is very large because the absolute cap

[10] The system with γ_s = infinite corresponds to the non-deteriorating one because strength capping is not included.

displacement is rapidly decreasing[11] and there is no cyclic basic strength deterioration to counteract this shifting. The rapid translation toward the origin of the cap displacement may overcome the effect of the other three CD modes. For instance, observe that the hysteretic response of Figure 4.62a is very similar to that of Figure 4.62b, which corresponds to the same system but including the four CD modes. This effect is also present in collapse capacity evaluation, as observed in Figure 4.63, which illustrates the large decrease in collapse capacities when only cyclic post-capping strength CD is present. The small window presents the ratios for similar systems in which the four modes of CD are included.

The large interdependence between basic strength and post-capping strength CD points out the futility of a study of these modes in an isolated way because the approach may lead to unreasonable results. Moreover, the isolation of these two modes is not justified by experimental information. The calibrations carried out in Section 3.4 indicate that the CD rates of these two modes are similar.

Cyclic Unloading Stiffness Deterioration. According to experimental results, the cyclic unloading stiffness deterioration rate may be different from the deterioration rate of the other CD modes. For instance, the rate of cyclic unloading stiffness deterioration for wood specimens may be very slow compared with that of the other CD modes (Krawinkler et al., 2000). The effect of cyclic unloading stiffness deterioration is illustrated in Figure 4.64, which presents the hysteretic response for a system including this CD mode. The effect on the response is not large, as can be seen from comparing Figures 4.64 and 4.60a.

The effect of the cyclic unloading stiffness deterioration mode on collapse capacity is practically negligible for models with strength capping (Fig. 4.65). The reason is that the effect of the strength deterioration due to the negative post-capping stiffness overcomes the effect of cyclic unloading stiffness deterioration. For peak-oriented and pinching models, this CD effect is even smaller than for bilinear models.

Cyclic Reloading (Accelerated) Stiffness Deterioration. This deterioration mode increases the absolute target displacement (Section 3.3.6) and occurs only in peak-oriented and pinching models. The hysteretic response for a system including this CD mode and subjected to the CUREE standard loading protocol is presented in Figure 4.66.

---

[11] The cap displacement, δ_c, is obtained as the intersection of the updated post-capping branch with the backbone curve. This is shown in Figure 4.62b for the second update of δ_c in the positive side.

Figure 4.67 shows the effect of cyclic reloading stiffness deterioration on the collapse capacity ratios for systems with strength capping. The small window shows a comparison with collapse capacity ratios when the effects of all the CD modes are present. The effect of cyclic reloading stiffness deterioration on collapse capacity increases with the deterioration rate, and for rapid CD rates may cause about the same deterioration as the four CD modes combined.

4.4.3 Effect of Level of Pinching in Pinched Hysteretic Model, $\kappa_{f,d}$

This section evaluates the influence of the level of pinching on the response of pinched models. Pinching of the hysteretic loop occurs when the loading path is directed first toward a "break" point instead of the maximum previous displacement (see Section 3.2.4). The level of pinching is controlled by the parameters κ_f and κ_d that define the "break" point. κ_f modifies the maximum load experienced in the direction of loading and κ_d is a percentage of the maximum permanent deformation (Fig. 3.6). Hysteretic models with small pinching have large kappa values ($\kappa_{f,d}$ close to 1.0) and are similar to hysteretic loops of peak-oriented models. The pinching models of the principal parameter study utilize $\kappa_{f,d} = 0.25$. The effect of pinching models with $\kappa_{f,d} = 0.50$ and 0.75 on the collapse capacity are discussed below.

Figure 4.68 shows the effect of the level of pinching on collapse capacities for a set of ductile systems. Three pinching models with $\kappa_{f,d}$ values of 0.25, 0.5, and 0.75 are considered, as well as the equivalent peak-oriented model. Collapse capacities for the latter model are very similar to those of the pinching model with $\kappa_{f,d} = 0.75$, the model with the smallest pinching effect. The collapse capacity ratios present differences of 15% for long-period systems, although for periods smaller than $T = 2$ s, the difference is within the 10% range. Figure 4.69 presents the same information for non-ductile systems. As can be seen, the effect of the level of pinching on the collapse capacity is even smaller for this set of systems.

4.4.4 Effect of Damping Formulation

This and the following section evaluate modifications in the response due to different damping formulations and percentage of initial critical damping, ξ_o.

Regarding the damping formulation, SDOF systems traditionally are analyzed using damping proportional to mass. Fajfar et al. (1993) studied the effect of different damping

formulations on the response of several EDPs and R factors. This section extends these results for deteriorating systems and is focused on the effect of different formulations on collapse capacity. The equation of motion for nonlinear SDOF systems illustrates the implications of this approach (Chopra, 1995):

$$m\ddot{u} + c\dot{u} + f_s(u,\dot{u}) = -m\ddot{u}_g(t) \tag{4.4}$$

where "f_s" is the restoring force for the linear and the nonlinear range and "c" is the critical damping coefficient. Damping formulation refers to whether "c" is proportional to mass, stiffness, or a combination of both.

If (4.4) is divided by the mass, m:

$$\ddot{u} + 2\xi\omega_n\dot{u} + \omega_n^2 \frac{u_y}{f_y} fs(u,\dot{u}) = -\ddot{u}_g(t) \tag{4.5}$$

where $\omega_n = \sqrt{k/m}$ is the natural frequency of the system, and u_y and f_y correspond to the displacement and force at yielding, respectively. The percentage of critical damping is given by:

$$\xi = \frac{c}{2m\omega_n} \tag{4.6}$$

At this point, it is convenient to introduce the usual approach for considering damping on MDOF structures. In these systems, damping may be expressed as linearly proportional to mass and stiffness, according to Rayleigh equation (Clough and Penzien, 1993):

$$C = \alpha M + \beta K \tag{4.7}$$

where M and K are the mass and stiffness of the MDOF structure, and α and β are the corresponding parameters of proportionality, which are obtained based on the frequencies of two modes of the structure. The damping for MDOF structures can be visualized as the "combined" curve of Figure 4.70. In the case of SDOF systems, the only frequency corresponds to the intersection of the "mass proportional" and "stiffness proportional" curves. Thus, in the elastic interval, ξ is constant and independent of the damping formulation ($\xi = \xi_0$), whereas in the inelastic range ξ varies according to one of the three formulations considered in this study:

(a) Damping proportional to mass. As observed in Figure 4.70, ξ increases in the inelastic interval if "c" is proportional to mass. The proportionality implies that:

$$c = \alpha\, m = 2\omega_{n,0}\xi_0 m \Rightarrow \qquad \alpha = 2\omega_{n,0}\xi_0 \tag{4.8}$$

where $\omega_{n,0}$ and ξ_0 are the initial natural frequency and initial percentage of critical damping, respectively. In the inelastic range α and "*c*" are not modified and by rearranging equations 4.6 and 4.8 the increment in ξ is obtained as:

$$\xi = \frac{\alpha\, m}{2m\omega_{n,t}} = \frac{2\omega_{n,0}\xi_0 m}{2m\omega_{n,t}} \Rightarrow \xi = \frac{\omega_{n,0}}{\omega_{n,t}}\xi_0 \tag{4.9}$$

The only variable in Equation (4.9) is $\omega_{n,t}$, which is the natural frequency based on the tangent stiffness. This frequency always decreases in the inelastic interval, causing an increment in ξ.

(b) Damping proportional to tangent stiffness. As can be seen in Figure 4.70, if *c* is proportional to stiffness, ξ decreases linearly with the natural frequency in the inelastic interval. Mathematically:

$$c = \beta\, k_t = \frac{2\xi_0}{\omega_{n,0}} k_t \Rightarrow \quad \beta = \frac{2\xi_0}{\omega_{n,0}} \tag{4.10}$$

In the inelastic range, the parameter of proportionality, β, is constant but *c* decreases because $k_t < k_e$. Substituting 4.10 in 4.6:

$$\xi = \frac{\beta\, k_t}{2m\omega_{n,t}} = \frac{\left(\frac{2\xi_0}{\omega_{n,0}}\right)k_t}{2m\omega_{n,t}} = \frac{\xi_0\omega_{n,t}^2 m}{2m\omega_{n,t}} \Rightarrow \xi = \frac{\omega_{n,t}}{\omega_{n,0}}\xi_0 \tag{4.11}$$

The last identity shows that ξ is reduced in the inelastic interval. Note from Equation 4.10 that if the system has damping proportional to initial stiffness, the obtained response is that of systems with damping proportional to mass.

(c) Mixed formulation. ξ can take any value located in the region delimited by the mass and stiffness proportional curves of Figure 4.70. The case that preserves ξ_o in the inelastic interval is analyzed below. For a system with constant damping, β must be adjusted according to the initial and inelastic frequencies:

$$c = \beta_t k_t \qquad\qquad \beta_t = \beta\frac{\omega_o}{\omega_t} \tag{4.12}$$

Then "*c*" is a function of two variables (β_t, k_t) that are adjusted each time the stiffness of the system is modified. The substitution of 4.12 in 4.6 shows that the percentage of critical damping in the inelastic interval is constant:

$$\xi = \frac{\beta_t k_t}{2m\omega_{n,t}} = \frac{\left(\frac{2\xi_0}{\omega_{n,0}}\right)\left(\frac{\omega_{n,0}}{\omega_{n,t}}\right)k_t}{2m\omega_{n,t}} = \frac{\xi_0 k_t}{m\omega_{n,t}^2} \Rightarrow \xi = \xi_0 \tag{4.13}$$

These three approaches are implemented in the program SNAP (Chapter 3) and are used to evaluate the modification in the response of deteriorating and non-deteriorating SDOF systems having ξ_o = 5 and 10%.

Effect of Damping Formulation (ξ_o = 5%). Figure 4.71 shows $(S_a/g)/\eta$ - EDP curves for a non-deteriorating system with T = 0.5 s under the three aforementioned damping formulations. Systems with damping proportional to mass have the smallest response because ξ is increased in the inelastic interval. Systems with damping proportional to tangent stiffness and systems with constant ξ have very similar response because the hardening ratio is small (α_s = 3%). As observed in the displacement ratios of Figure 4.71b, the effect of damping formulation is more important at large $(S_a/g)/\eta$ levels because the response is highly inelastic, which is the region where the formulations differ from each other. Figure 4.72 presents normalized displacement ratios for T = 0.2 and 0.9 s, showing that the effect of damping formulation is more relevant for systems with short periods. For deteriorating systems, $(S_a/g)/\eta$ - EDP curves present these trends up to close to collapse.

Regarding the collapse of deteriorating systems, models with stiffness proportional damping develop collapse capacities almost 20% smaller than those of systems with mass proportional damping. In the presence of P-Δ effects the differences are smaller, particularly for long-period systems (Figs. 4.73–4.74).

Effect of Damping Formulation (ξ_o = 10 %). The effect of damping formulation increases for systems with ξ_o = 10 %, where differences in collapse capacities may be on the order of 30% depending on the used damping formulation (Figs. 4.75–4.76).

4.4.5 Effect of Numerical Value of ξ_o

In this section, selected systems are analyzed utilizing ξ_o = 5 and 10%. Comparisons with different percentages of critical damping are carried out for systems with mass and stiffness proportional damping.

Effect of ξ_o for Systems with Mass Proportional Damping. Mass proportional damping is widely used for SDOF systems and is the formulation of the primary parameter analysis. Figure 4.77a presents median collapse capacities for ductile and non-ductile systems with ξ_o = 5 and 10%. Figure 4.77b shows collapse capacities ratios of systems with ξ_o = 10% over systems with ξ_o = 5% for both sets of systems. When using mass proportional damping, the effect of increasing ξ_o from 5% to 10% produces an increment in the collapse capacity of 15–20%. The properties of the hysteretic model do not greatly modify this percentage.

Effect of ξ_o for Systems with Stiffness Proportional Damping. The same systems are evaluated using damping proportional to stiffness. Figure 4.78 reveals that the use of systems with stiffness proportional damping produces smaller collapse capacities, but they are not greatly affected by the value of ξ_o. The reason is that when collapse takes place the response is highly inelastic, which reduces the importance of the damping force because it is proportional to the tangent stiffness.

4.4.6 Deteriorating SDOF Systems Subjected to Near-Fault Ground Motions

The following two sections deal with the response of SDOF systems subjected to near-fault ground motions (NFGMs) and long-duration (LD) records. Hysteretic energy dissipation is very different for these sets of records. In the case of systems subjected to NFGMs, a large part of the hysteretic energy is dissipated in one or two large pulses, whereas systems subjected to LD records dissipate energy throughout a large number of cycles. For this reason, special emphasis is given to the effect of CD on collapse capacity.

NFGMs are defined as GMs recorded less than 15 km from the fault rupture zone and exhibiting forward directivity. There is evidence that NFGMs have different frequency and duration characteristics than ordinary GM's because of forward directivity effects (Somerville et al., 1997), which take place if the rupture propagates toward the site. Since the propagation occurs at a velocity that is close to the shear wave velocity, most of the seismic energy from the rupture arrives at the site in a large pulse of motion at the beginning of the record. This large pulse is mostly oriented in the fault normal component and can be observed in the velocity time histories (Fig. 4.79).

Looking for a simplified approach, Alavi and Krawinkler (2001) demonstrated that pulses could be used to reproduce EDPs of non-deteriorating systems subjected to NFGMs. For this

reason, this parameter study includes a set of recorded NFGMs and a simple pulse model that attempts to reproduce with reasonable accuracy the collapse capacities obtained by using a set of NFGMs.

Pulse. The Pulse P2 (Alavi and Krawinkler, 2001) was utilized for representing the impulsive characteristics of NFGMs. The pulse is fully defined by a pulse shape and two parameters, i.e., the pulse period (T_p) and a pulse intensity parameter, which can be either the maximum pulse acceleration $a_{g,eff}$ or the maximum pulse velocity, $v_{g,eff}$. In this pulse the ground experiences a reversing displacement history that is generated through a double cycle of acceleration input. The acceleration input is represented by the square wave shown in Figure 4.80, which results in a triangular velocity cycle and a second-order reversing displacement history. The corresponding elastic strength demand spectrum is presented in Figure 4.81, where the period of the structure is normalized by the pulse period, and the spectral ordinates are normalized by the peak ground acceleration, $a_{g,eff}$.

Set of Records. The selected set of records, NF-11, includes 11 near-fault ground motions recorded mostly on stiff and very stiff soil, i.e., soils D and C, respectively, according to NEHRP (Table 4.3). The records have pulse periods ranging from about 1–4 s, which were calculated using the error minimization procedure proposed by Krawinkler and Seung-Jee. In the spectra for NFGMs, the periods are normalized by the pulse period, and the selected IM is $S_a(T/T_p)$ instead of $S_a(T)$. Figure 4.82 shows the spectra of individual ground motions and of the Pulse P2, scaled at $S_a(T/T_p) = 0.8$.

Collapse Capacities for NFGMs. Collapse capacities as a function of T/T_p, for systems with $\delta_c/\delta_y = 4$ and $\alpha_c = -0.10$, are presented in Figures 4.83–4.84 for models with no CD and rapid CD, respectively. The dispersion for both cases is presented in Figure 4.85, which is relatively small, especially when T/T_p is close to 1. Thus, the normalization of the system period reduces the dispersion.

Figure 4.83 shows an increase in collapse capacity of the NFGMs for larger T/T_p ratios, but the increase in collapse capacity for Pulse P2 is much larger than that for the median of the NFGMs. There is an abrupt increase in collapse capacity for Pulse P2 from $T/T_p = 0.6$ to 0.7. Most of the individual NFGM records also present this sudden increase, but each record has this increment at a different T/T_p ratio and the "jump" in collapse capacity is lost when the median is computed. Therefore, although collapse capacity patterns are similar for Pulse P2 and for most of individual NFGM records, Pulse P2 does not represent well the median of collapse capacities

obtained from the NF-11 records. It appears that a better approach to estimate the pulse period of these NFGMs is needed.

Figure 4.86 shows a comparison of median collapse capacities for NF-11 and for Pulse P2 for different CD rates. For systems with rapid CD rates, the collapse capacity for Pulse P2 and the median collapse capacity for NF-11 are similar because CD overcomes the differences in frequency content of NFGMs and pulses.

Effect of CD on Systems Subjected to NFGMs. Figure 4.87 presents collapse capacity spectra and spectral ratios for systems with $\delta_c/\delta_y = 4$ and $\alpha_c = -0.10$ when subjected to the set NF-11. The effect of CD on collapse capacities tends to increase with the T/T_p ratio. Because of the period normalization, the effect of CD for systems subjected to NFGMs and systems subjected to ordinary GMs cannot be directly compared. Nevertheless, the collapse ratios are consistently smaller when the set NF-11 is used (Figs. 4.87–4.28). The same trends for collapse ratios are preserved if α_c is changed to -0.30, as shown in Figure 4.88. Collapse capacities for the same systems subjected to ordinary GMs are presented in Figure 4.31.

4.4.7 Deteriorating SDOF Systems Subjected to Long-Duration Ground Motions

The set of records LSMR-N used in most of this study corresponds to California records. These GMs have relatively short strong motion duration and likely do not reflect the maximum influence that CD may have on collapse capacity because CD is based on the dissipated hysteretic energy during the THA. Therefore, the effect of CD on collapse capacity is expected to be more important if the GMs have longer duration because more hysteretic energy would be dissipated.

The strong motion duration is the time interval over which a significant amount of seismic energy is dissipated. Many of the available definitions are based on the Arias intensity (Bommer and Martinez Pereira, 1996), which is defined as (Arias, 1970):

$$I_A = \frac{\pi}{2g}\int_0^T a^2(t)dt \tag{4.14}$$

where $a(t)$ is the accelerogram of total duration T. The simplest measurements of strong motion duration are based on the interval over which a specified portion of I_A is achieved. Trifunac and Brady (1975) proposed an interval from 5%–95% that has been widely used. Therefore, strong motion duration is defined here as the time it takes for the cumulative energy of the GM record

to grow from 5%–95% of its value at the end of the history. It has been argued that this definition does not have a real physical significance because the duration is not correlated with seismic and geophysical parameters such as the rupture history (Bommer and Martinez Pereira, 1996). Although these shortcomings are recognized, this strong motion definition is accepted in order to make a parameter study manageable.

In this study, long-duration records are those having a strong motion duration longer than 30 s according to the Trifunac and Brady definition. Thirteen long-duration records (set LD-13) were selected with strong motion durations ranging from 30.4 to 49.9 s with a mean of 39.0 s (Table 4.4). In contrast, the set LMSR-N has strong motion durations ranging from 8–25 s, with a mean of 15.2 s.

Elastic Strength Demand Spectra. Figure 4.89 shows median elastic acceleration spectra scaled at $T = 0.5$ and 0.9 s. As can be seen, the shape of the median spectral acceleration for sets LD-13 and LMSR-N is similar, although the plateau of LD-13 is larger and starts the steep descending slope at about $T = 0.9$ s. This leads to some discrepancies between the two median spectra when the records are scaled. For spectra scaled at $T = 0.5$ s, the median spectral acceleration at the right of the scaled period is larger for LD-13, which suggests that at $T = 0.5$ s, the collapse capacity should be smaller when an SDOF system is subjected to the set LD-13. On the other hand, when scaling at $T = 0.9$ s the spectra are very similar to the right of the scaled period.

Normalized Hysteretic Energy. The dissipated hysteretic energy is expected to increase when SDOF systems are subjected to long-duration records. Figure 4.90 compares median NHE-at-collapse for peak-oriented models with slow CD subjected to the sets LD-13 and LMSR-N. Systems subjected to LD-13 dissipate more energy, especially in the short-period range. Figure 4.91 shows median NHE-at-collapse ratios of LD-13 over LMSR-N for several rates of CD. The effect of LD records is larger in the short- and medium-period ranges and for systems with low CD rate (large γvalues).

Collapse Capacity. Figure 4.92 shows the effect of CD on collapse capacity for peak-oriented systems subjected to the sets LD-13 and LMSR-N. Collapse capacities exhibit important differences in the short-period range, which are expected according to the elastic spectra of Figure 4.89. The collapse capacity ratios with respect to the case with infinite CD are shown in Figure 4.93, where it is observed that the effect of CD is larger for long-duration records, particularly for systems with $T < 1$ s and rapid CD rates. Although this is in agreement with the

results of NHE-at-collapse, the difference is within the 10% range for most of the periods and rates of CD. That is to say, the large effect of LD records on NHE-at-collapse is not reflected in collapse capacities. This suggests that a large part of the contribution to NHE in long-duration records comes from "trailing" excursions.

Figure 4.94 present the effect of LD records on similar systems with bilinear models. In the short- and medium-ranges, LD records produce differences in collapse capacity ratios of 15-20%, whereas for long periods the ratios are very similar. As explained in 4.3.7, bilinear systems deteriorate more under the presence of branches with negative slope. In peak-oriented models the inelastic deformation developed in a given direction is recovered as soon as reloading occurs, whereas in bilinear ones the recovery only occurs when the structure yields in the opposite direction. This behavior increases the effect of LD records on systems where the loading path is for more time on a branch with negative slope.

The small effect of LD records has been reported in the past by using simpler models. For instance, Rahnama and Krawinkler (1993) calculated the response of non-deteriorating SDOF systems and did not find a correlation between inelastic seismic demand parameters and the duration of strong motion. Bernal (1992) studied the correlation between long-duration records and collapse of non-deteriorating systems including P-Δ effects. He found that GM duration had a minor effect on the response of peak-oriented models, but some correlation with bilinear ones.

4.5 SUMMARY

4.5.1 Results of Primary Parameter Study

In this section the following five nonlinear parameters that affect the nonlinear response of SDOF systems are evaluated: the type of hysteretic model, post-capping stiffness, ductility capacity, cyclic deterioration, and P-Δ effects. All possible combinations among parameters were considered because the effect of a particular parameter on collapse capacity is dictated in great part by the relative value of the rest of the parameters. In addition, information prior to collapse was processed to identify differences between systems without and with deterioration before collapse takes place.

Effect of Deteriorating Models on EDPs. The cyclic deterioration effect modifies $(S_a/g)/\eta$ - EDP relationships, since the early stages of nonlinearity. However, this modification is small (within the 10% range) before the loading path reaches δ_c (Fig. 4.1). On the other hand,

post-capping stiffness and ductility capacity only modify the nonlinear response after surpassing δ_c but their effect on EDPs is larger. Thus, non-deteriorating models can estimate EDPs with reasonable accuracy as long as the maximum displacement does not exceed δ_c.

Effect of Post-capping Stiffness on Collapse Capacity, α_c. The collapse capacity is very sensitive to variations of α_c when this parameter is small. If α_c is very large the collapse capacities are not greatly modified by α_c variations. A change in post-capping stiffness from α_c = -0.1 to α_c = -0.3 may reduce the collapse capacity to 40% of its original value when no P-Δ effects are included. Any further increase in the slope has a small effect because collapse occurs soon after δ_c has been reached. The effect of α_c on collapse capacity is greatly reduced if important P-Δ effects are present, especially in ductile systems.

Effect of Ductility Capacity on Collapse Capacity, δ_c/δ_y. The relationship between collapse capacity and ductility capacity is almost linear for all values of $(S_{a,c}/g)/\eta$. Collapse capacities for systems with δ_c/δ_y = 2 can be up to 60% smaller than those for systems with δ_c/δ_y = 6. The actual percentage is mainly affected by post-capping stiffness and to a lesser degree by the CD rate. The effect of δ_c/δ_y on collapse capacity is essentially independent of the period of the system and, unlike the rest of the parameters, is not largely affected by the presence of P-Δ effects.

Effect of Cyclic Deterioration on Collapse Capacity. The collapse capacity increases for slower rates of CD, represented by larger γ values. The increment of collapse capacity is asymptotic because γ = infinite represents a deteriorating system with no CD, which has a finite collapse capacity. Collapse capacities vary by as much as a factor of 2 for similar systems with different CD rate. Collapse capacity ratios of systems with different CD are essentially period independent for systems without P-Δ effects. However, these ratios are greatly affected for systems including P-Δ effects, particularly in the medium- and long-period ranges.

P-Δ Effect on Collapse Capacity. The P-Δ effect is very important for ductile systems because these would be able to sustain large inelastic deformations if the P-Δ effect were not considered. P-Δ effects accelerate the collapse of deteriorating systems and may be the primary source of collapse for flexible but ductile structural systems. Their presence overpowers the effect of α_c and CD. But the results must be interpreted with caution because the relationship between P-Δ effects in SDOF and MDOF systems is complex. Rigorously, equivalent P-Δ effects in SDOF systems must be derived for each particular MDOF structure.

Effect of Hysteretic Model on Collapse Capacity. In the medium- and long-period ranges, the largest collapse capacities correspond to pinching models, closely followed by those of peak-oriented models. Collapse capacities of bilinear models are the smallest ones because the presence of a negative stiffness has a larger effect on this model.

Increment in Collapse after δ_c Is Reached. The collapse capacity of the system may increase by more than 100% with respect to the relative intensity at which the loading path reaches the peak strength, i.e., δ_c.

4.5.2 Results of Secondary Parameter Study

Residual Strength. The effect of residual strength is studied for systems with residual strength of 20% (small) and 40% (medium) of the yield strength of the system. The former is practically negligible for all the systems of interest. Medium residual strength may increase collapse capacity more than two times for non-ductile systems. However, when realistic collapse displacements are considered, the collapse capacity increases by 20% at most.

Effect of Individual Cyclic Deterioration Modes. The effect of individual cyclic deterioration modes must be viewed with caution because of the large interdependence among various deterioration modes. For instance, cyclic basic strength deterioration and cyclic post-capping strength deterioration modes should not be analyzed individually because the updated value of the cap displacement (δ_c) depends on both deteriorations modes.

Regarding the cyclic unloading stiffness deterioration mode, its effect is marginal when post-capping stiffness is included, especially on peak-oriented and pinching models because a large part of this CD effect is lost in the reloading. The effect is small mainly because it is overpowered by the deterioration in strength due to the negative slope of the backbone curve.

The effect of cyclic reloading stiffness deterioration on collapse capacity increases strongly with the deterioration rate and, for rapid CD rates, may cause about the same deterioration than the four CD modes combined.

Level of Pinching. The effect of the level of pinching on collapse capacities is small, usually within the 10% range. This is expected because differences between peak-oriented and highly pinched models ($\kappa_{f,d} = 0.25$) are not significant.

Damping. In the nonlinear range, ξ, increases for damping proportional to mass and decreases for damping proportional to stiffness. Consequently, analytical models with mass

proportional damping have a better response but they may lead to non-conservative results if ξ in the inelastic interval is expected to be similar to ξ in the elastic range.

If the backbone curve has small strain-hardening stiffness, the response of systems with damping proportional to tangent stiffness is very similar to that of systems with constant ξ in the linear and nonlinear ranges.

For systems with mass proportional damping, the effect of increasing ξ from 5–10%, may increase the collapse capacity of the system by more than 20%. This increase is roughly independent of the period of the system and the value of the system parameters. In systems with stiffness proportional damping, the modifications in collapse capacity due to modifications in ξ are negligible.

Systems Subjected to Near-Fault Ground Motions. The dispersion in collapse capacity is smaller when the period of the system is normalized by the pulse period of the NFGM records. The effect of CD on the collapse capacity is about 10–20% smaller when a system is subjected to a set of NFGMs instead of ordinary GMs.

Systems Subjected to Long-Duration Records. The effect of CD on collapse capacity increases when long-duration records are used instead of ordinary ground motions. This increment is larger in the short- and medium-period ranges, but the largest differences still do not exceed 10%–15%. On the other hand, NHE-at-collapse can be almost two times larger for systems subjected to long-duration records. Nevertheless, these large differences do not contribute to changes in the collapse capacity of the systems. It is likely that a large portion of the NHE at collapse corresponds to "trailing" excursions.

The effect of using a set of LD records is slightly larger for bilinear models because these models deteriorate more under the presence of branches with negative slope. This behavior increases the effect of LD records on systems in which the loading path is on a branch with negative slope for an increased amount of time.

SDOF systems have been subjected to three sets of GMs that dissipate energy in different ways. Under NFGMs, a large part of the HE is released in one or two large pulses; under long-duration GMs, the HE is dissipated in a large number of inelastic excursions. Energy dissipation for ordinary GMs is between these two cases. Nonetheless, the effect of CD on collapse capacity is not greatly modified by the set of GMs used in the analysis.

Table 4.1 SDOF systems of primary parameter study, peak-oriented models, P-Δ=0

DETERIORATING SDOF SYSTEMS Peak Oriented Models with P-Δ = 0			
Common Characteristics	**Post-Capping Stiffness**	**Ductility Capacity δ_c/δ_y**	**Cyclic Deterioration $\gamma_{s,c,k,a}$**
α_s = 0.03 T = 0.1 to 4.0 s λ = 0 (No residual strength) ξ_o = 5% $[(S_a/g)/\eta]_{initial}$ = 1.0 $[(S_a/g)/\eta]_{step}$ = 0.25	-	Infinite	Infinite
	-0.1	2	Infinite
			100
			50
			25
		4	Infinite
			100
			50
			25
		6	Infinite
			100
			50
			25
	-0.3	2	Infinite
			100
			50
			25
		4	Infinite
			100
			50
			25
		6	Infinite
			100
			50
			25
	-0.5	2	Infinite
			100
			50
			25
		4	Infinite
			100
			50
			25
		6	Infinite
			100
			50
			25

Table 4.2 Set of ordinary ground motion records, LMSR-N (after Medina, 2002)

Record ID	Event	Year	Mw	Station	R (km)	NEHRP Site	Mechanism	fHP (Hz)	fLP (Hz)	PGA (g)	PGV (cm/s)	PGD (cm)	D (s)	Rec. Length (s)
IV79cal	Imperial Valley	1979	6.5	Calipatria Fire Station	23.8	D	strike-slip	0.10	40	0.078	13.3	6.2	23.3	39.5
IV79chi	Imperial Valley	1979	6.5	Chihuahua	28.7	D	strike-slip	0.05		0.270	24.9	9.1	20.1	40.0
IV79cmp	Imperial Valley	1979	6.5	Compuertas	32.6	D	strike-slip	0.20		0.186	13.9	2.9	21.7	36.0
IV79e01	Imperial Valley	1979	6.5	El Centro Array #1	15.5	D	strike-slip	0.10	40.0	0.139	16.0	10.0	8.9	39.5
IV79e12	Imperial Valley	1979	6.5	El Centro Array #12	18.2	D	strike-slip	0.10	40.0	0.116	21.8	12.1	19.4	39.0
IV79e13	Imperial Valley	1979	6.5	El Centro Array #13	21.9	D	strike-slip	0.20	40.0	0.139	13.0	5.8	21.2	39.5
IV79nil	Imperial Valley	1979	6.5	Niland Fire Station	35.9	D	strike-slip	0.10	30.0	0.109	11.9	6.9	21.7	40.0
IV79pls	Imperial Valley	1979	6.5	Plaster City	31.7	D	strike-slip	0.10	40.0	0.057	5.4	1.9	10.7	18.7
IV79qkp	Imperial Valley	1979	6.5	Cucapah	23.6	D	strike-slip	0.05		0.309	36.3	10.4	15.7	40.0
IV79wsm	Imperial Valley	1979	6.5	Westmorland Fire Station	15.1	D	strike-slip	0.10	40.0	0.110	21.9	10.0	25.2	40.0
LP89agw	Loma Prieta	1989	6.9	Agnews State Hospital	28.2	D	reverse-oblique	0.20	30.0	0.172	26.0	12.6	18.4	40.0
LP89cap	Loma Prieta	1989	6.9	Capitola	14.5	D	reverse-oblique	0.20	40.0	0.443	29.3	5.5	13.2	40.0
LP89g03	Loma Prieta	1989	6.9	Gilroy Array #3	14.4	D	reverse-oblique	0.10	40.0	0.367	44.7	19.3	11.4	39.9
LP89g04	Loma Prieta	1989	6.9	Gilroy Array #4	16.1	D	reverse-oblique	0.20	30.0	0.212	37.9	10.1	14.8	39.9
LP89gmr	Loma Prieta	1989	6.9	Gilroy Array #7	24.2	D	reverse-oblique	0.20	40.0	0.226	16.4	2.5	11.5	39.9
LP89hch	Loma Prieta	1989	6.9	Hollister City Hall	28.2	D	reverse-oblique	0.10	29.0	0.247	38.5	17.8	17.4	39.1
LP89hda	Loma Prieta	1989	6.9	Hollister Differential Array	25.8	D	reverse-oblique	0.10	33.0	0.279	35.6	13.1	13.2	39.6
LP89hvr	Loma Prieta	1989	6.9	Halls Valley	31.6	D	reverse-oblique	0.20	22.0	0.134	15.4	3.3	16.2	39.9
LP89sjw	Loma Prieta	1989	6.9	Salinas - John & Work	32.6	D	reverse-oblique	0.10	28.0	0.112	15.7	7.9	20.3	39.9
LP89slc	Loma Prieta	1989	6.9	Palo Alto - SLAC Lab.	36.3	D	reverse-oblique	0.20	33.0	0.194	37.5	10.0	12.5	39.6
LP89svl	Loma Prieta	1989	6.9	Sunnyvale - Colton Ave.	28.8	D	reverse-oblique	0.10	40.0	0.207	37.3	19.1	21.2	39.2
NR94cen	Northridge	1994	6.7	LA - Centinela St.	30.9	D	reverse-slip	0.20	30.0	0.322	22.9	5.5	12.4	30.0
NR94cnp	Northridge	1994	6.7	Canoga Park - Topanga Can.	15.8	D	reverse-slip	0.05	30.0	0.420	60.8	20.2	10.4	25.0
NR94far	Northridge	1994	6.7	LA - N Faring Rd.	23.9	D	reverse-slip	0.13	30.0	0.273	15.8	3.3	8.8	30.0
NR94fle	Northridge	1994	6.7	LA - Fletcher Dr.	29.5	D	reverse-slip	0.15	30.0	0.240	26.2	3.6	11.8	30.0
NR94glp	Northridge	1994	6.7	Glendale - Las Palmas	25.4	D	reverse-slip	0.10	30.0	0.206	7.4	1.8	11.5	30.0
NR94hol	Northridge	1994	6.7	LA - Holywood Stor FF	25.5	D	reverse-slip	0.20	23.0	0.231	18.3	4.8	12.0	40.0
NR94lh1	Northridge	1994	6.7	Lake Hughes #1 #	36.3	D	reverse-slip	0.12	23.0	0.087	9.4	3.7	13.9	32.0
NR94lv2	Northridge	1994	6.7	Leona Valley #2 #	37.7	D	reverse-slip	0.20	23.0	0.063	7.2	1.6	12.5	32.0
NR94lv6	Northridge	1994	6.7	Leona Valley #6	38.5	D	reverse-slip	0.20	23.0	0.178	14.4	2.1	10.4	32.0
NR94nya	Northridge	1994	6.7	La Crescenta-New York	22.3	D	reverse-slip	0.10	0.3	0.159	11.3	3.0	11.0	30.0
NR94pic	Northridge	1994	6.7	LA - Pico & Sentous	32.7	D	reverse-slip	0.20	46.0	0.186	14.3	2.4	14.8	40.0
NR94stc	Northridge	1994	6.7	Northridge - 17645 Saticoy St.	13.3	D	reverse-slip	0.10	30.0	0.368	28.9	8.4	15.7	30.0
NR94stn	Northridge	1994	6.7	LA - Saturn St	30.0	D	reverse-slip	0.10	30.0	0.474	34.6	6.6	11.6	31.6
NR94ver	Northridge	1994	6.7	LA - E Vernon Ave	39.3	D	reverse-slip	0.10	30.0	0.153	10.1	1.8	15.9	30.0
SF71pel	San Fernando	1971	6.6	LA - Hollywood Stor Lot	21.2	D	reverse-slip	0.20	35.0	0.174	14.9	6.3	11.2	28.0
SH87bra	Superstition Hills	1987	6.7	Brawley	18.2	D	strike-slip	0.10	23.0	0.156	13.9	5.4	13.5	22.1
SH87icc	Superstition Hills	1987	6.7	El Centro Imp. Co. Cent	13.9	D	strike-slip	0.10	40.0	0.358	46.4	17.5	16.1	40.0
SH87pls	Superstition Hills	1987	6.7	Plaster City	21.0	D	strike-slip	0.20	18.0	0.186	20.6	5.4	11.3	22.2
SH87wsm	Superstition Hills	1987	6.7	Westmorland Fire Station	13.3	D	strike-slip	0.10	35.0	0.172	23.5	13.0	19.6	40.0

Table 4.3 Set of near-fault ground motions, NF-11

NFGM	Mw	R(km)	T_p (s) Approx	T_p (s) w/P_2	PGV	Soil USGS/ NEHRP	Corner Freq.	
							LF, Hz	HF, Hz
KB95obj	6.9	0.6	1.0	0.9	160	B/C	0.05	null
NR94newh	6.7	7.1		1.3	119	C/D	0.12	23
NR94rrs	6.7	7.5		1.2	174	C/D	null	null
EZ92erzi	6.7	2	2.0	2.1	119	C/D	0.1	null
NR94sylm	6.7	6.4		2.1	122	C/D	0.12	23
NR94wpi	6.7	7.2		2.2	109	B/C	0.1	30
IV79melo	6.5	0.0	3.0	2.6	117	C/D	0.1	40
IV79ar06	6.5	1.2		3.4	110	C/D	0.1	40
TW99tcu076	7.6	2.0		3.3	63	C/D	0.1	50
LN92luc	7.3	1.1	4.0	4.5	98	A/-	.08	60
TW99tcu075	7.6	1.5		4.1	87	C/D	0.03	50

Table 4.4 Set of long-duration records, LD-13

Long Duration Record	Mw	PGA gals	Accele-rogram Duration	Bracketed Duration (sec)
West. WA, Olympia 1949	6.5	71.4	80.0	41.3
Kern, Taft 021, 1952	7.7	153.0	54.2	30.3
Kern, Hol 090, 1952	7.7	43.0	78.5	31.3
Cerro Prieto, IV79, cp237	6.5	152.1	63.7	36.2
Llolleo, Chile 1985	8.0	551.9	100	36.2
Viña del Mar, Chile 1985	8.0	223.0	100	49.9
CHY015E, Taiwan 1999	7.6	142.4	150	37.5
CHY025W, Taiwan 1999	7.6	156.2	90.0	33.7
CHY046W, Taiwan 1999	7.6	139.6	90.0	33.0
CHY087W, Taiwan 1999	7.6	133.2	90.0	31.9
TCU120W, Taiwan 1999	7.6	220.8	90.0	32.6
TCU123W, Taiwan 1999	7.6	160.7	90.0	35.4
TCU138E, Taiwan 1999	7.6	191.1	150	34.1

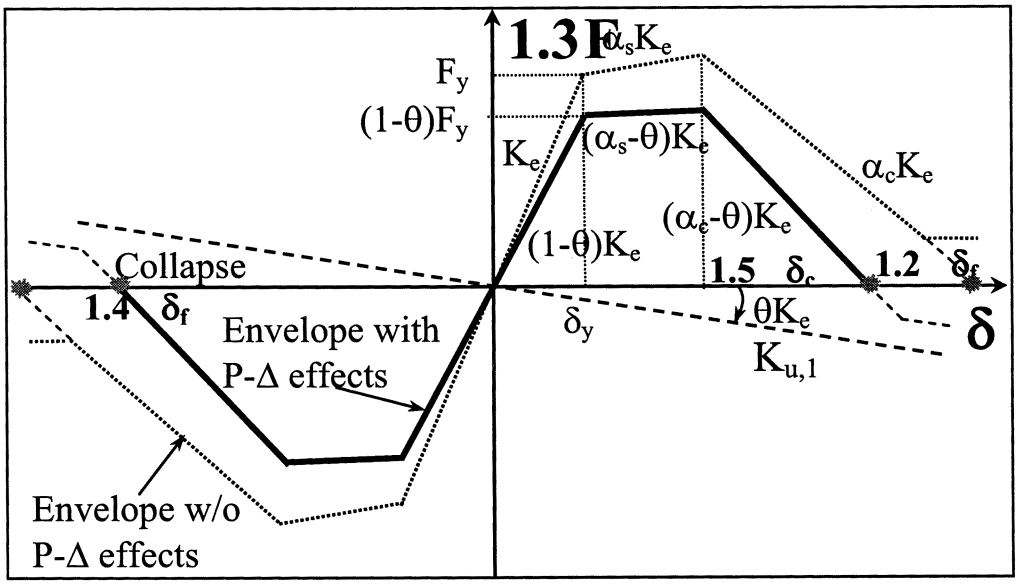

Fig. 4.1 Backbone curves for hysteretic models with and without P-Δ

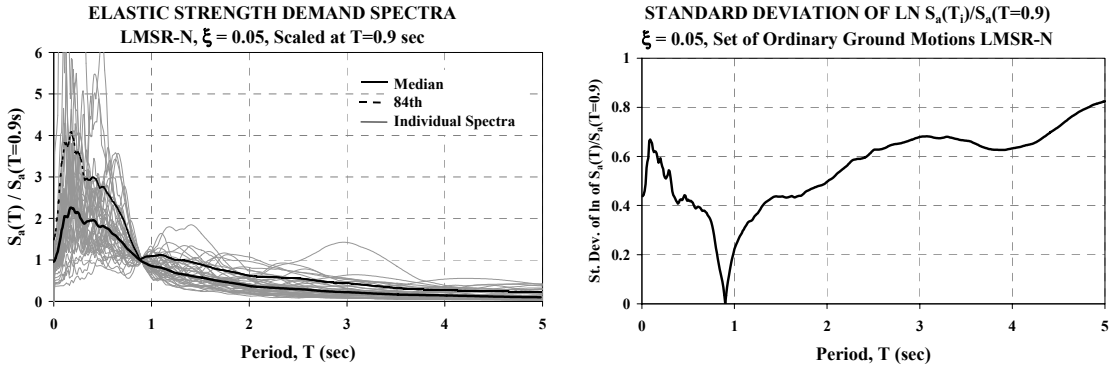

(a) Elastic Strength Demand Spectra (b) Dispersion of Spectra

Fig. 4.2 Spectra of ordinary GMs scaled to the same S_a at T = 0.9 s

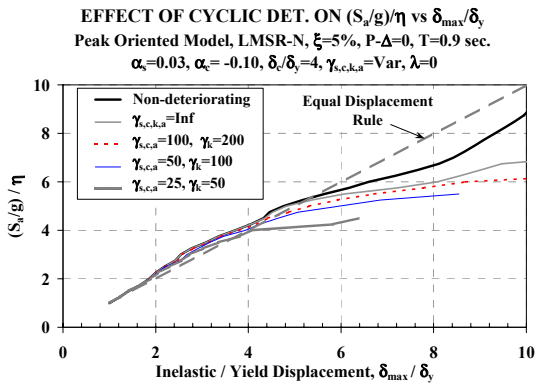

(a) $(S_a/g)/\eta$ - Median δ_{max}/δ_y Curves

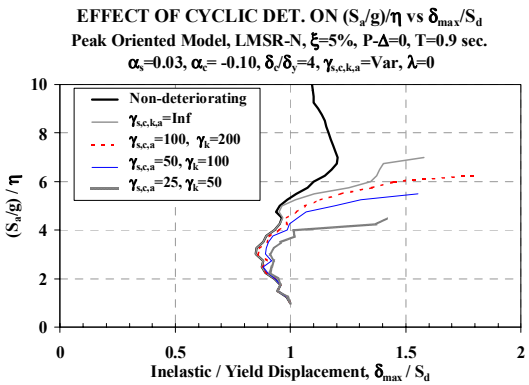

(b) $(S_a/g)/\eta$ - Median δ_{max}/S_d Curves

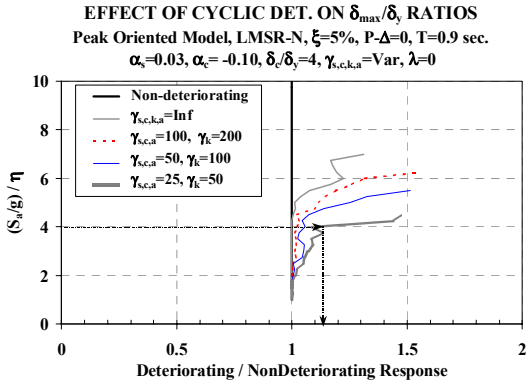

(c) $(S_a/g)/\eta$ - Median EDP ratios

Fig. 4.3 Effect of CD on EDPs, T = 0.9 s, α_c = -0.1, δ_c/δ_y = 4, P-Δ= 0

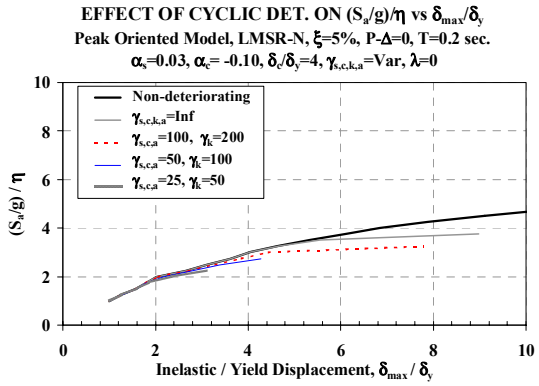

(a) $(S_a/g)/\eta$ - Median δ_{max}/δ_y Curves

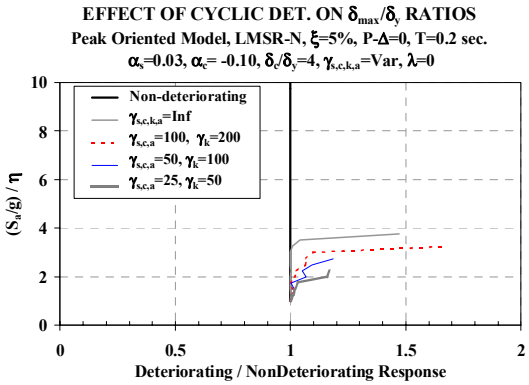

(b) $(S_a/g)/\eta$ - Median EDP ratios

Fig. 4.4 Effect of CD on δ_{max}/δ_y, T = 0.2 s, α_c = -0.1, δ_c/δ_y = 4, P-Δ= 0

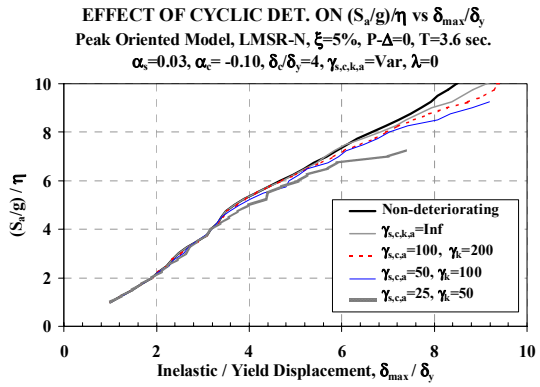

(a) $(S_a/g)/\eta$ - Median δ_{max}/δ_y Curves

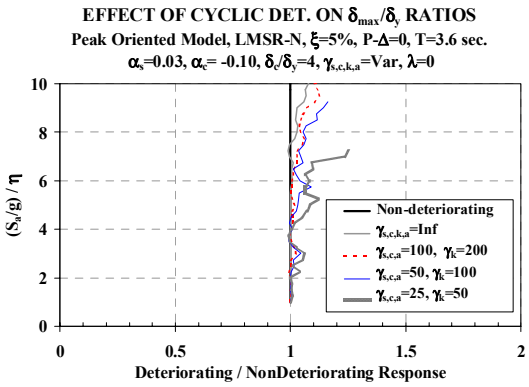

(b) $(S_a/g)/\eta$ - Median EDP ratios

Fig. 4.5 Effect of CD on δ_{max}/δ_y, T = 3.6 s, α_c = -0.1, δ_c/δ_y = 4, P-Δ= 0

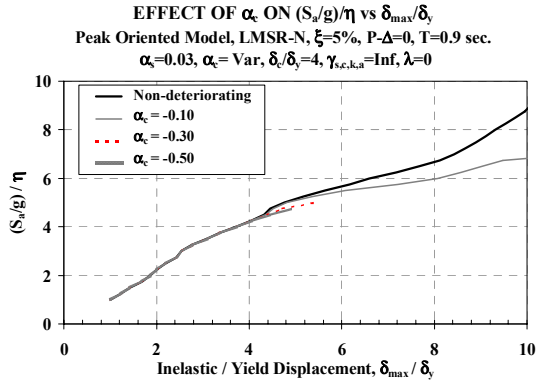

(a) $(S_a/g)/\eta$ - Median δ_{max}/δ_y Curves

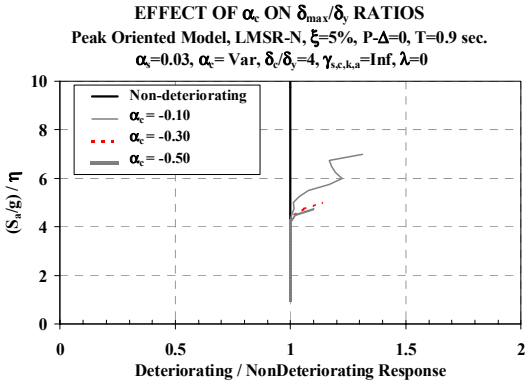

(b) $(S_a/g)/\eta$ - Median EDP ratios

Fig. 4.6 Effect of α_c on δ_{max}/δ_y, T = 0.9 s, δ_c/δ_y = 4, γ= inf., P-Δ= 0

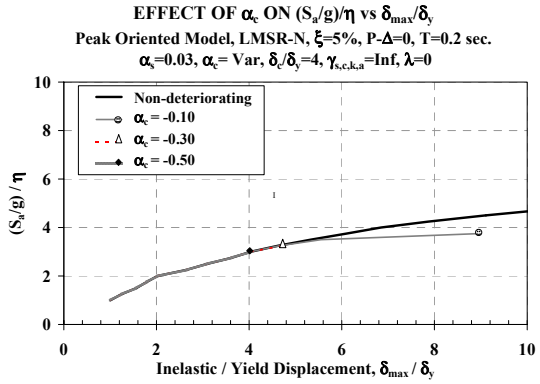

(a) T = 0.2 s.

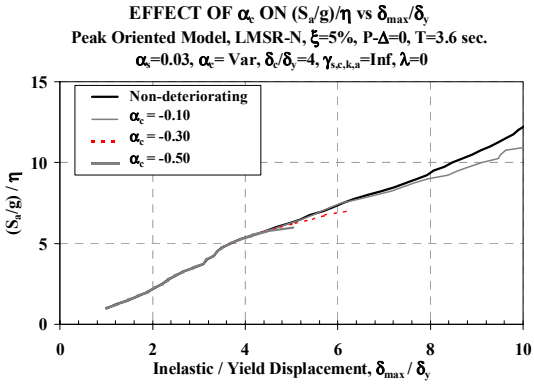

(b) T = 3.6 s.

Fig. 4.7 Effect of α_c on median δ_{max}/δ_y, T = 0.2 and 3.6 s, δ_c/δ_y = 4, γ= inf., P-Δ= 0

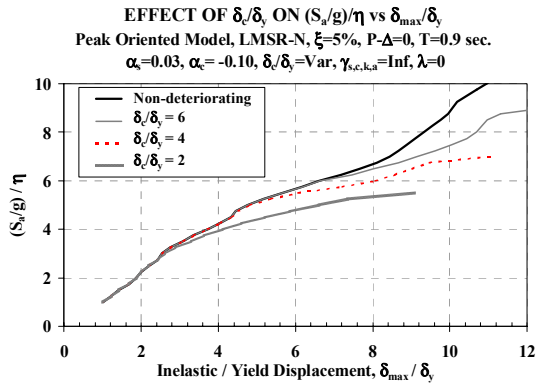

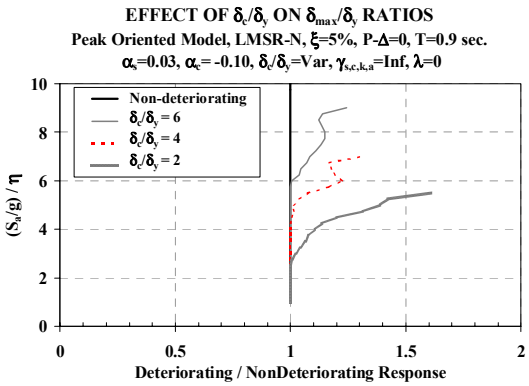

(a) $(S_a/g)/\eta$ - Median δ_{max}/δ_y Curves (b) $(S_a/g)/\eta$ - Median EDP ratios

Fig. 4.8 Effect of δ_c/δ_y on EDPs, T = 0.9 s, α_c = -0.1, γ= inf., P-Δ= 0

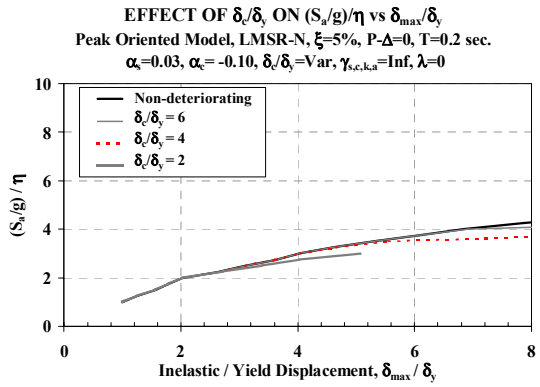

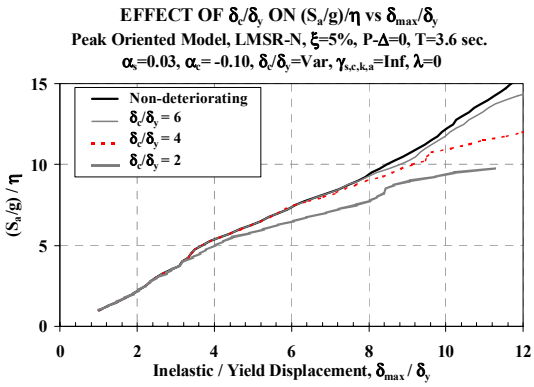

(a) T = 0.2 sec (b) T = 3.6 sec

Fig. 4.9 Effect of δ_c/δ_y on EDP ratios, T = 0.2 and 3.6 s, α_c = -0.1, γ= inf., P-Δ= 0

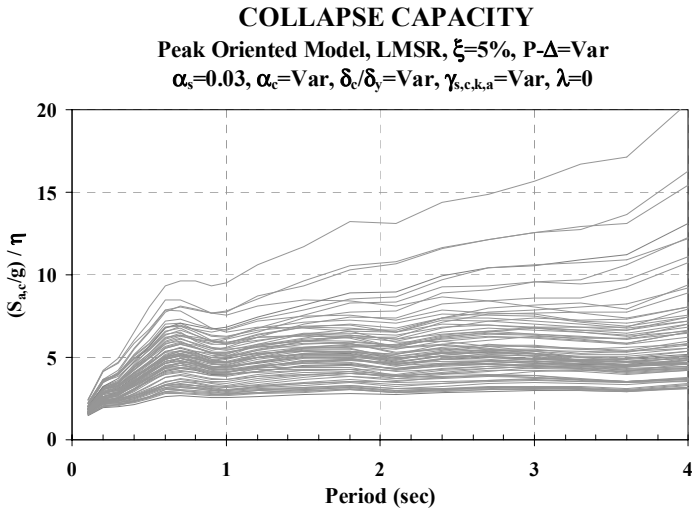

Fig. 4.10 Set of median collapse capacity spectra for peak-oriented models

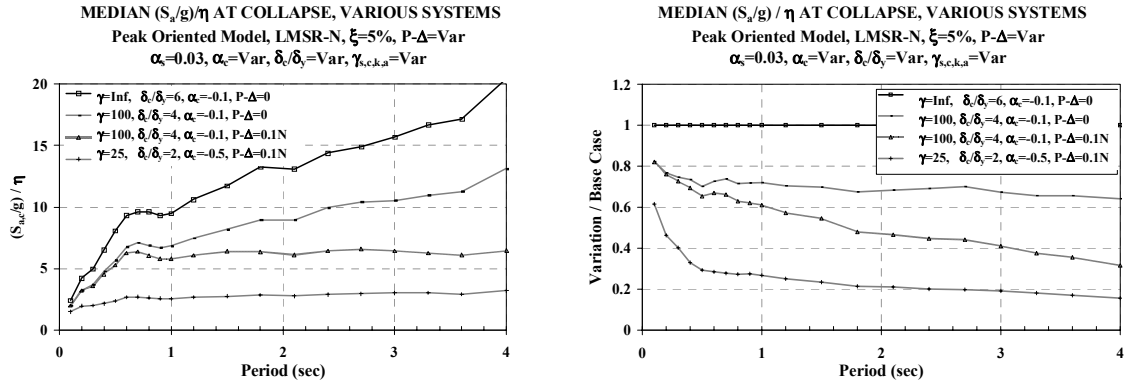

(a) Median Collapse Capacity Spectra (b) Median Collapse Capacity Ratios

Fig. 4.11 Collapse capacity spectra for selected peak-oriented models

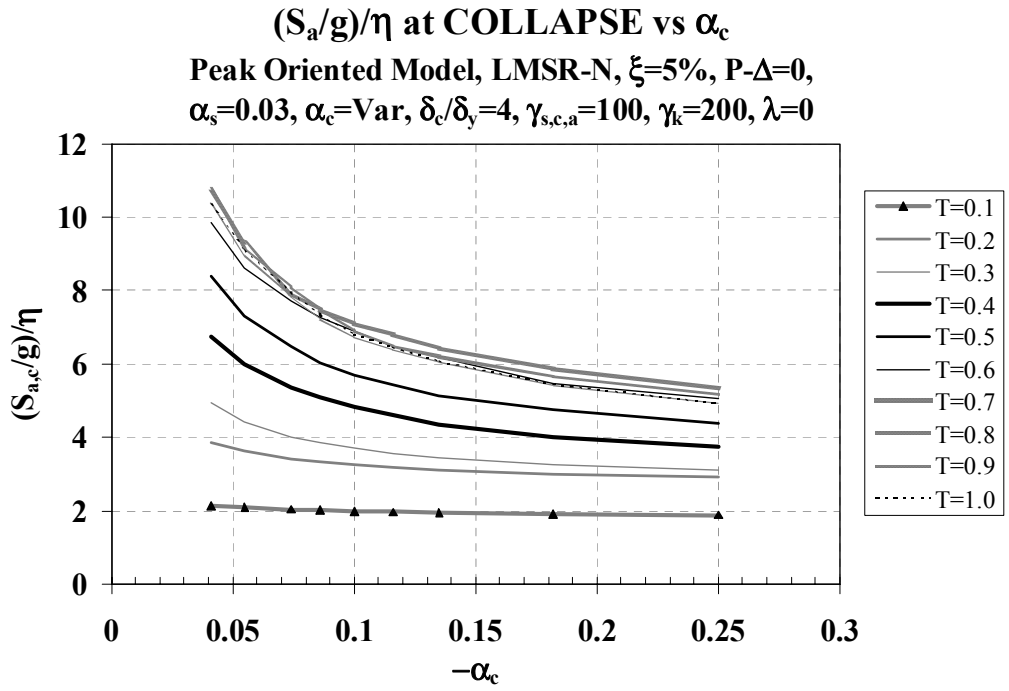

Fig. 4.12 Dependence of median $(S_{a,c}/g)/\eta$ on α_c; $\delta_c/\delta_y = 4$, slow CD, $T = 0.1$ s–1.0 s

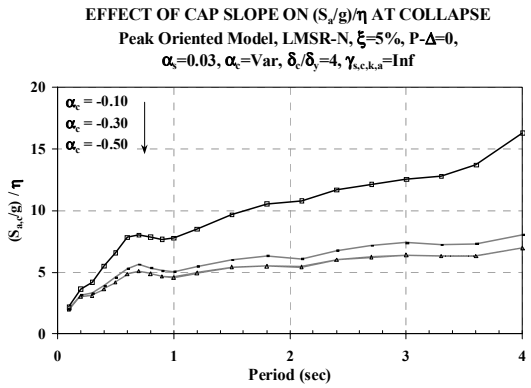

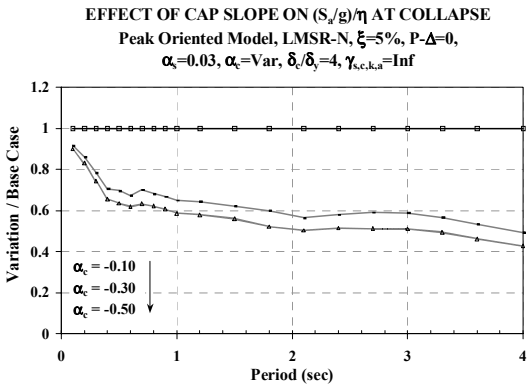

(a) Median Collapse Capacity Spectra (b) Median Collapse Capacity Ratios

Fig. 4.13 Effect of α_c on $(S_{a,c}/g)/\eta$; $\delta_c/\delta_y = 4$, no CD, no P-Δ

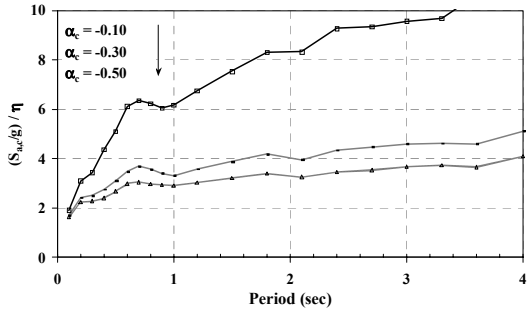

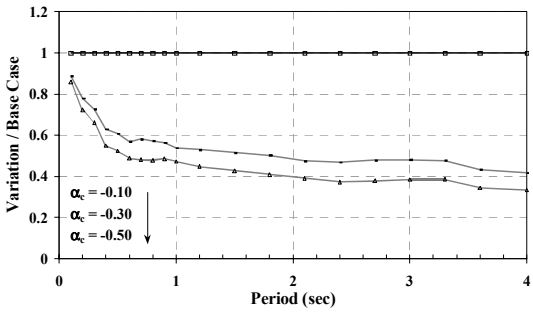

(a) Median Collapse Capacity Spectra (b) Median Collapse Capacity Ratios

Fig. 4.14 Effect of α_c on $(S_{a,c}/g)/\eta$; $\delta_c/\delta_y = 2$, no CD, no P-Δ

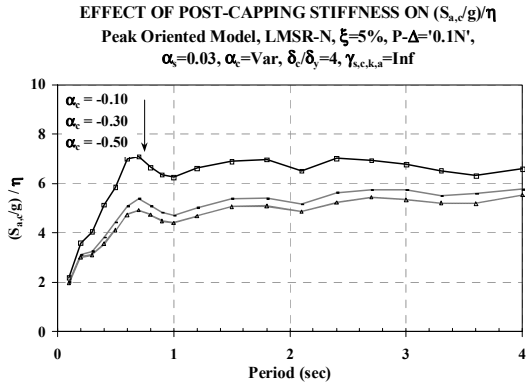

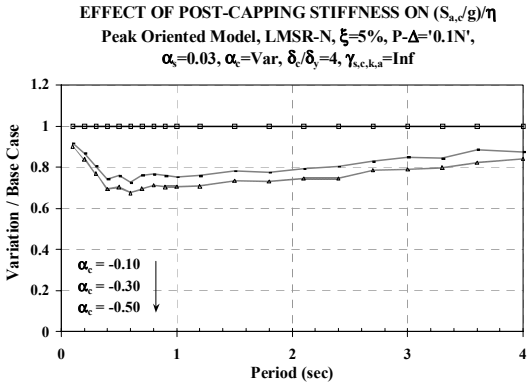

(a) Median Collapse Capacity Spectra (b) Median Collapse Capacity Ratios

Fig. 4.15 Effect of α_c on $(S_{a,c}/g)/\eta$; $\delta_c/\delta_y = 4$, no CD, small P-Δ

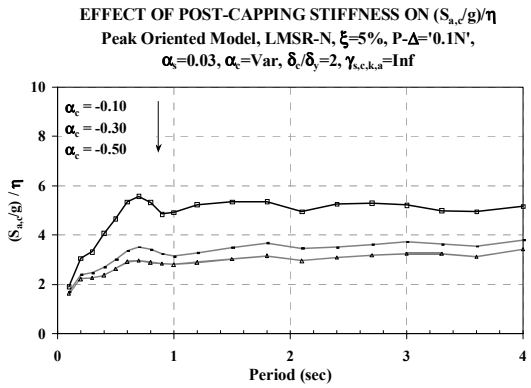

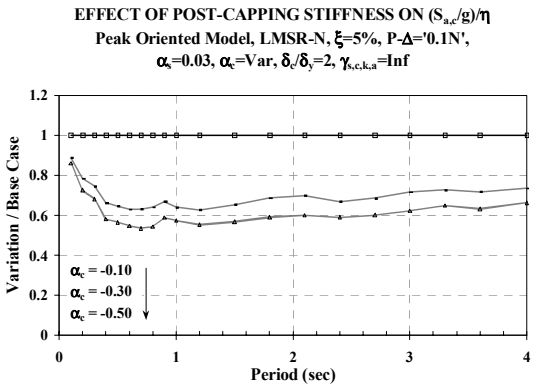

(a) Median Collapse Capacity Spectra (b) Median Collapse Capacity Ratios

Fig. 4.16 Effect of α_c on $(S_{a,c}/g)/\eta$; $\delta_c/\delta_y = 2$, no CD, small P-Δ

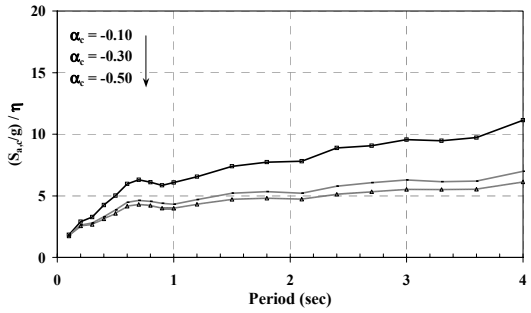

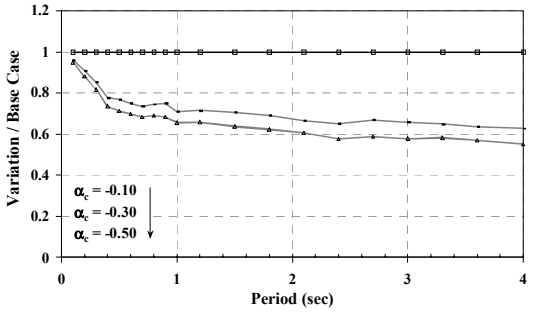

(a) Median Collapse Capacity Spectra (b) Median Collapse Capacity Ratios

Fig. 4.17 Effect of α_c on $(S_{a,c}/g)/\eta$; $\delta_c/\delta_y = 4$, medium CD, no P-Δ

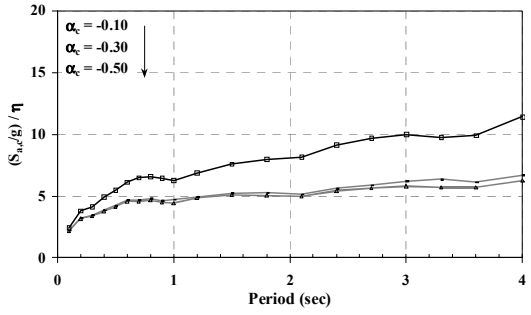

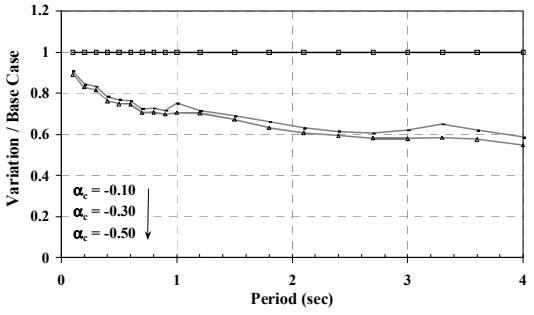

(a) Median Collapse Capacity Spectra (b) Median Collapse Capacity Ratios

Fig. 4.18 Effect of α_c on $(S_{a,c}/g)/\eta$; bilinear model, $\delta_c/\delta_y = 4$, no CD, no P-Δ

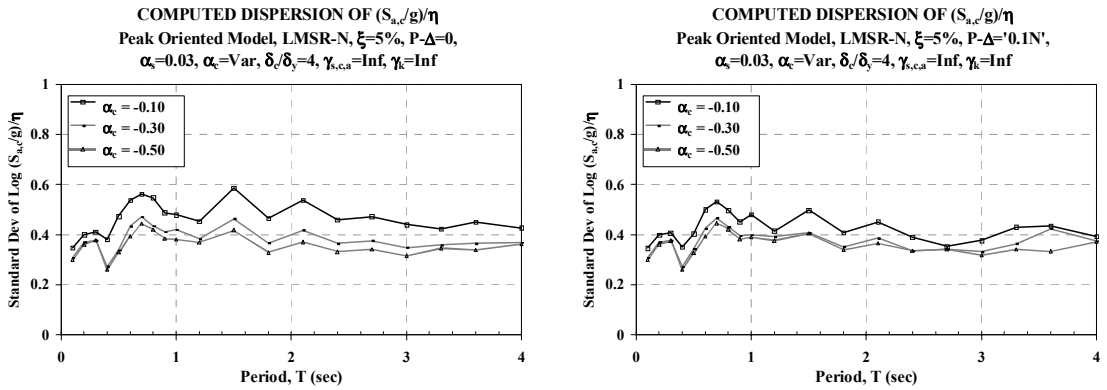

(a) P-Δ = 0 (b) P-Δ = 0.1*N*

Fig. 4.19 Effect of α_c on dispersion of $(S_{a,c}/g)/\eta$; δ_c/δ_y = 4, no CD

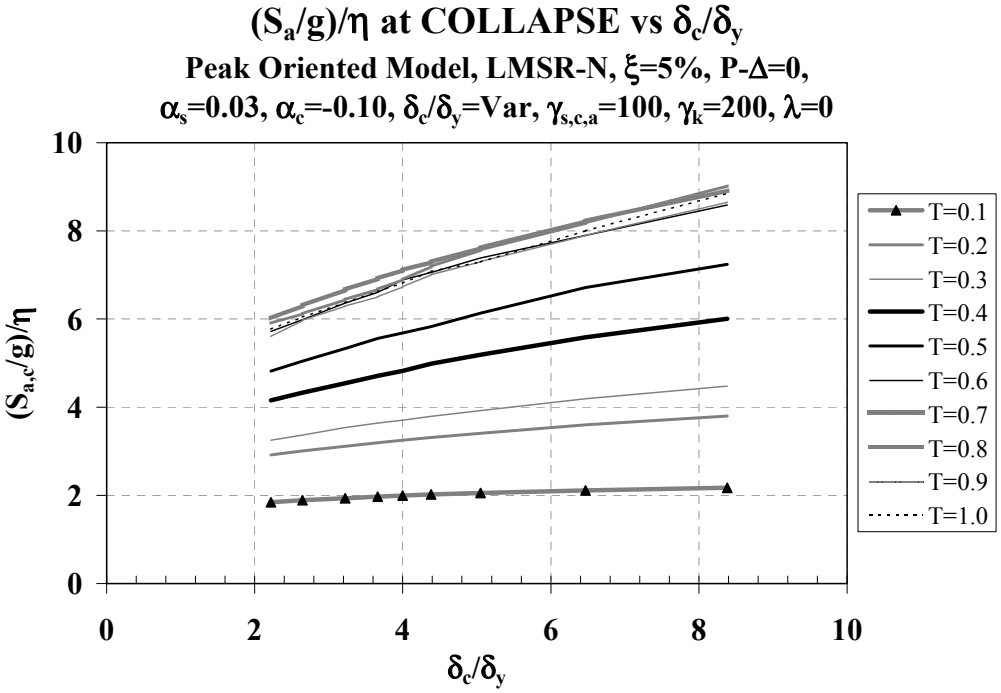

Fig. 4.20 Dependence of median $(S_{a,c}/g)/\eta$ on δ_c/δ_y; α_c = -0.1, slow CD, T = 0.1 s–1.0 s

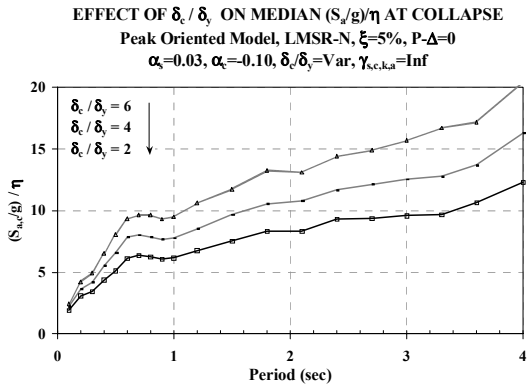

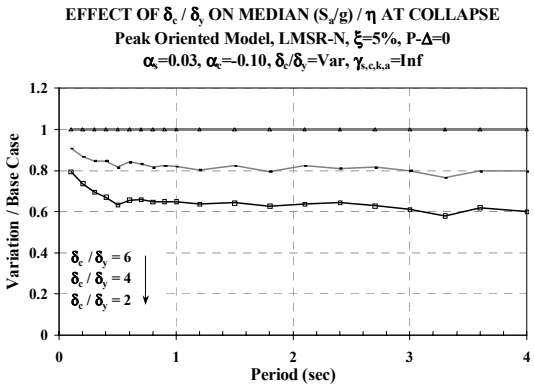

(a) Median Collapse Capacity Spectra (b) Median Collapse Capacity Ratios

Fig. 4.21 Effect of δ_c/δ_y on $(S_{a,c}/g)/\eta$; α_c = -0.1, no CD, no P-Δ

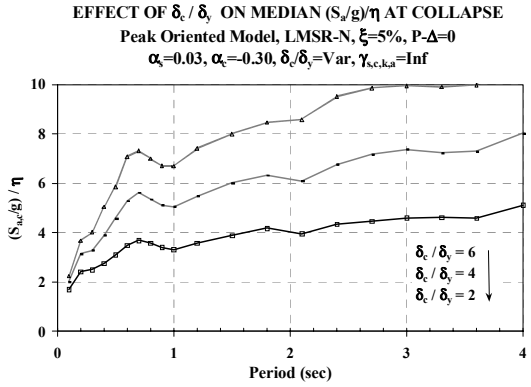

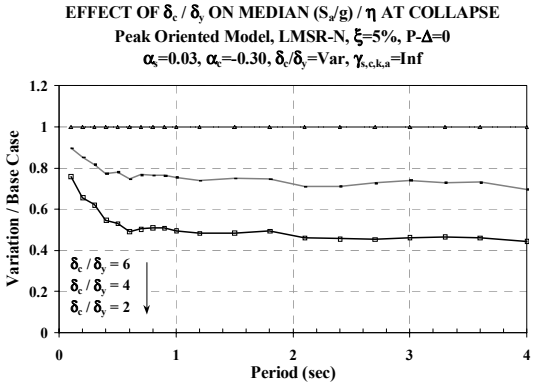

(a) Median Collapse Capacity Spectra (b) Median Collapse Capacity Ratios

Fig. 4.22 Effect of δ_c/δ_y on $(S_{a,c}/g)/\eta$; α_c = -0.3, no CD, no P-Δ

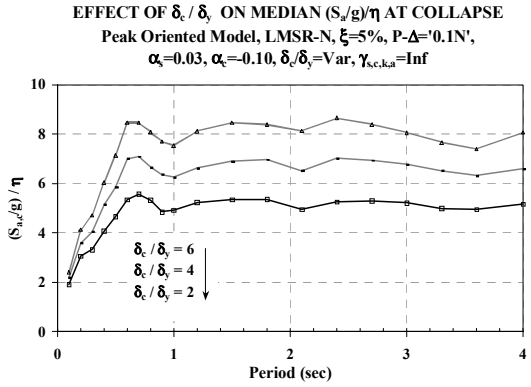

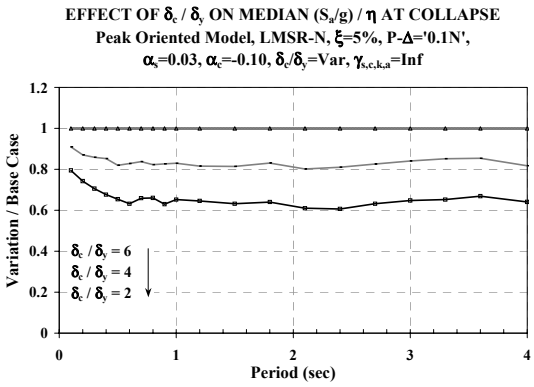

(a) Median Collapse Capacity Spectra (b) Median Collapse Capacity Ratios

Fig. 4.23 Effect of δ_c/δ_y on $(S_{a,c}/g)/\eta$; α_c = -0.1, no CD, small P-Δ

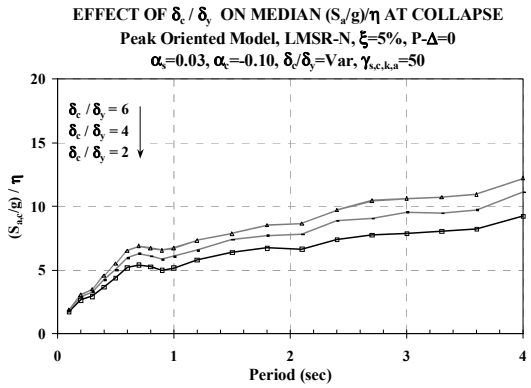

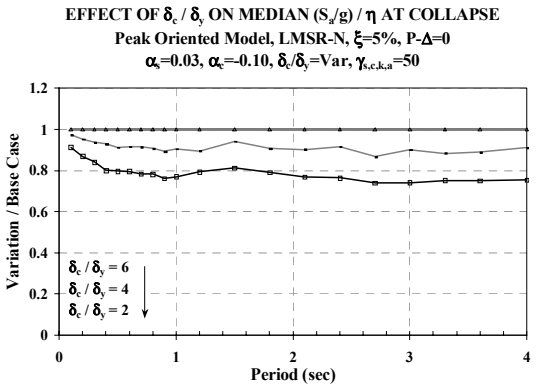

(a) Median Collapse Capacity Spectra (b) Median Collapse Capacity Ratios

Fig. 4.24 Effect of δ_c/δ_y on $(S_{a,c}/g)/\eta$; α_c = -0.1, medium CD, no P-Δ

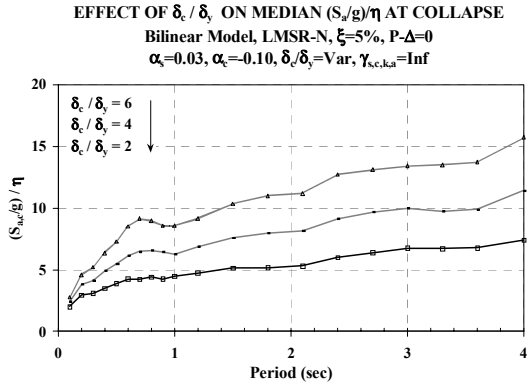

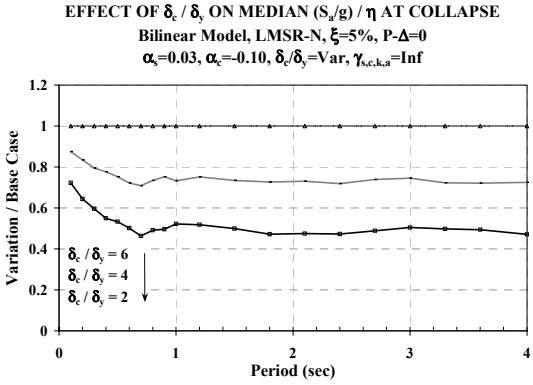

(a) Median Collapse Capacity Spectra (b) Median Collapse Capacity Ratios

Fig. 4.25 Effect of δ_c/δ_y on $(S_{a,c}/g)/\eta$; bilinear models, α_c = -0.1, no CD, no P-Δ

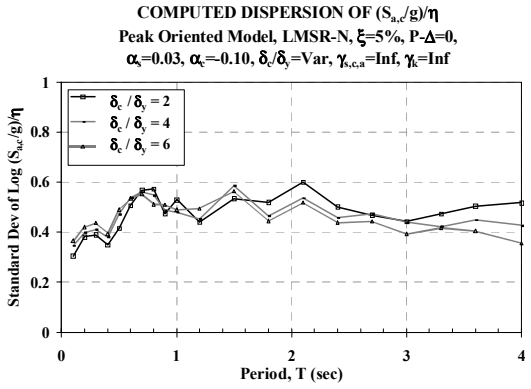

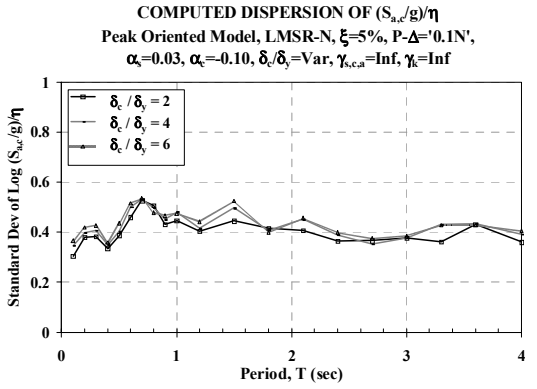

(a) P-Δ = 0 (b) P-Δ = 0.1*N*

Fig. 4.26 Effect of δ_c/δ_y on dispersion of $(S_{a,c}/g)/\eta$; α_c = -0.1, no CD

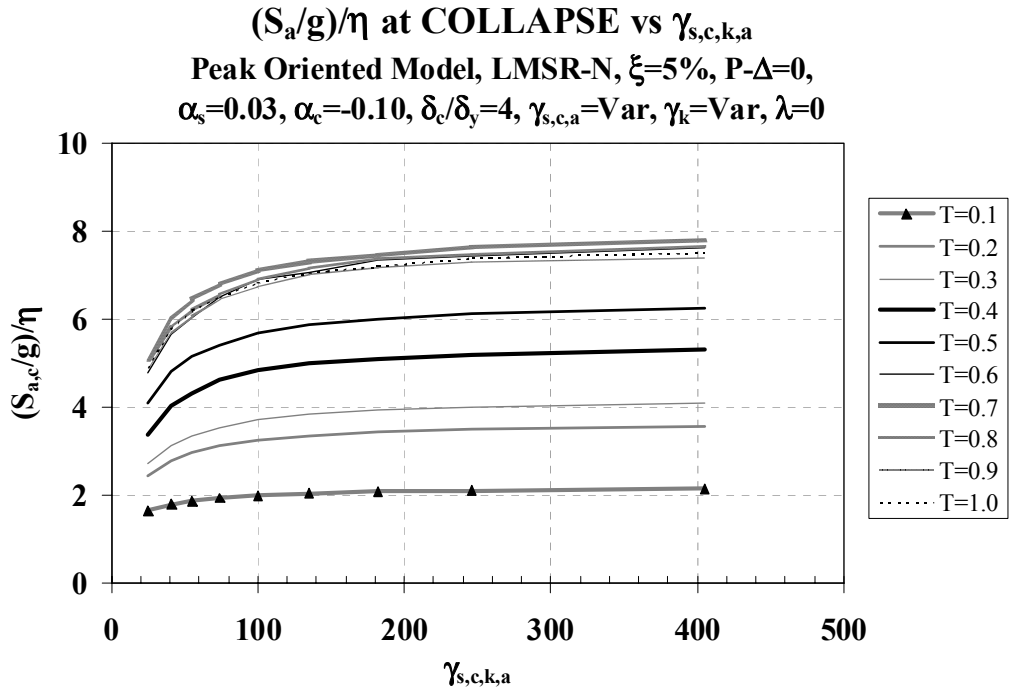

Fig. 4.27 Dependence of median $(S_{a,c}/g)/\eta$ on γ; α_c=-0.1, $\delta_c/\delta_y = 4$, T=0.1 s–1.0 s

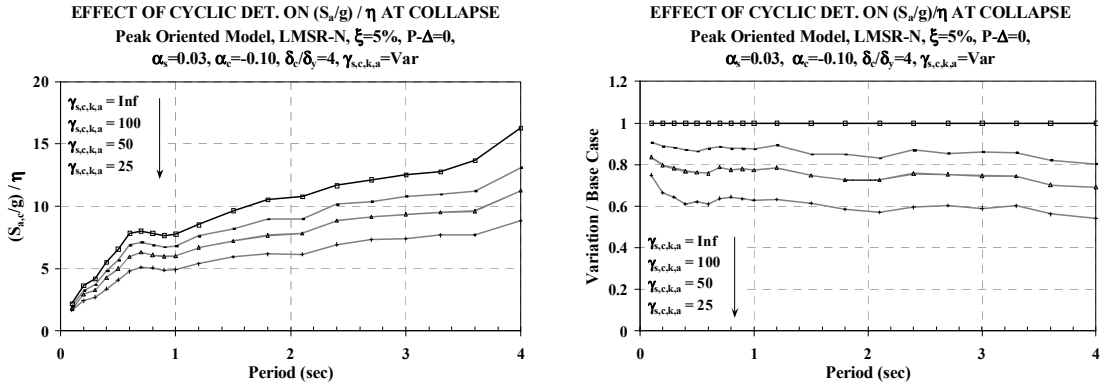

(a) Median Collapse Capacity Spectra (b) Median Collapse Capacity Ratios

Fig. 4.28 Effect of CD on $(S_{a,c}/g)/\eta$; $\delta_c/\delta_y = 4$, α_c = -0.1, no P-Δ

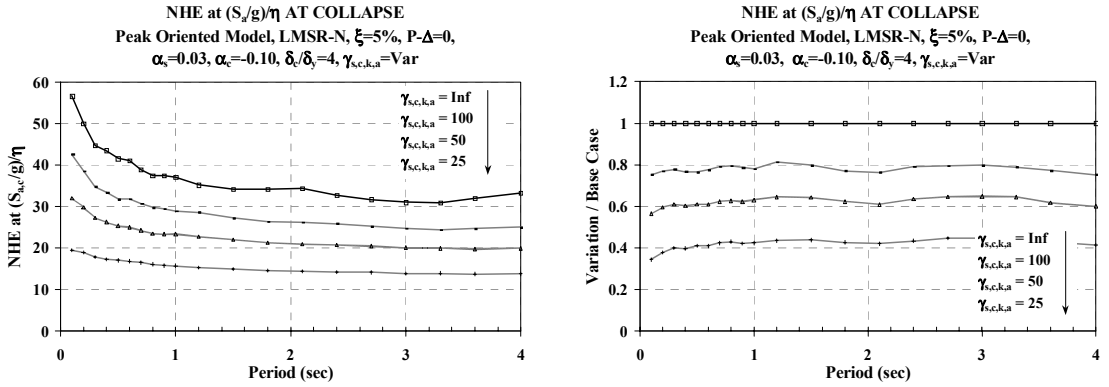

(a) Median NHE at $(S_{a,c}/g)/\eta$ (b) Ratios of Median NHE at $(S_{a,c}/g)/\eta$

Fig. 4.29 NHE associated with $(S_{a,c}/g)/\eta$ for different CD rates; $\delta_c/\delta_y = 4$, $\alpha_c = -0.1$, no P-Δ

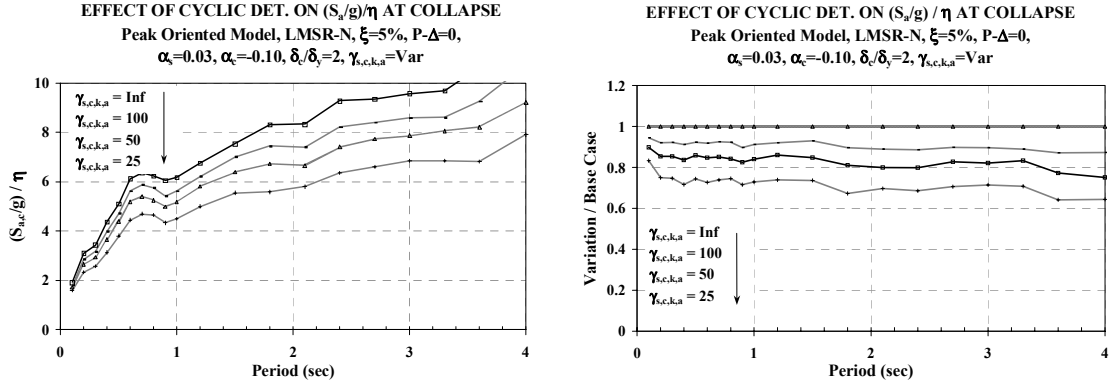

(a) Median Collapse Capacity Spectra (b) Median Collapse Capacity Ratios

Fig. 4.30 Effect of CD on $(S_{a,c}/g)/\eta$; $\delta_c/\delta_y = 2$, $\alpha_c = -0.1$, no P-Δ

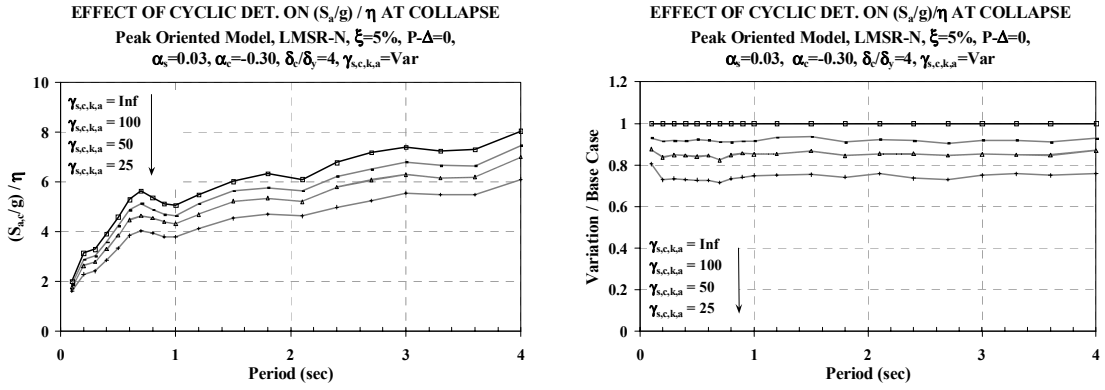

(a) Median Collapse Capacity Spectra (b) Median Collapse Capacity Ratios

Fig. 4.31 Effect of CD on $(S_{a,c}/g)/\eta$; $\delta_c/\delta_y = 4$, $\alpha_c = -0.3$ no P-Δ

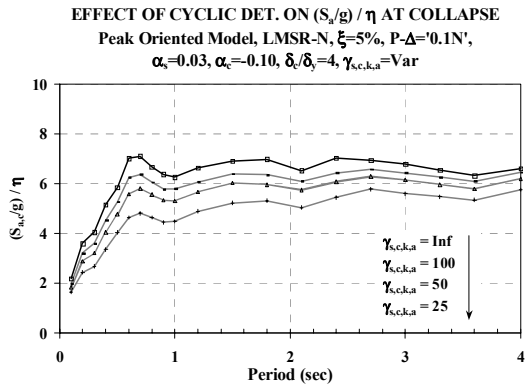

(a) Median Collapse Capacity Spectra

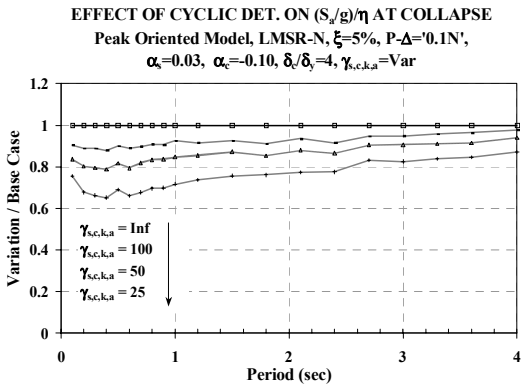

(b) Median Collapse Capacity Ratios

Fig. 4.32 Effect of CD on $(S_{a,c}/g)/\eta$; $\delta_c/\delta_y = 4$, $\alpha_c = -0.1$, small P-Δ

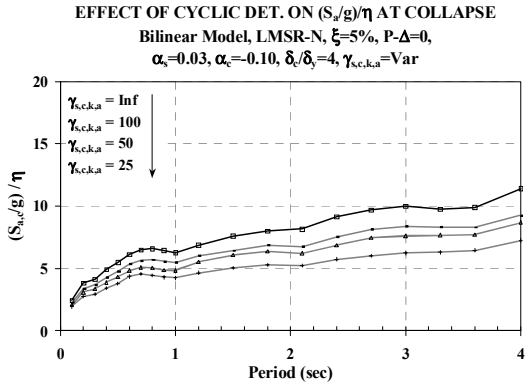

(a) Median Collapse Capacity Spectra

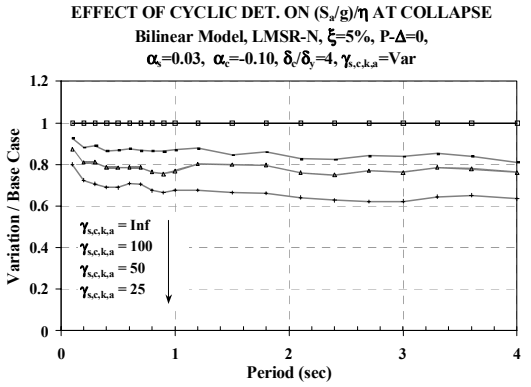

(b) Median Collapse Capacity Ratios

Fig. 4.33 Effect of CD on $(S_{a,c}/g)/\eta$; bilinear models, $\delta_c/\delta_y = 4$, $\alpha_c = -0.1$, no P-Δ

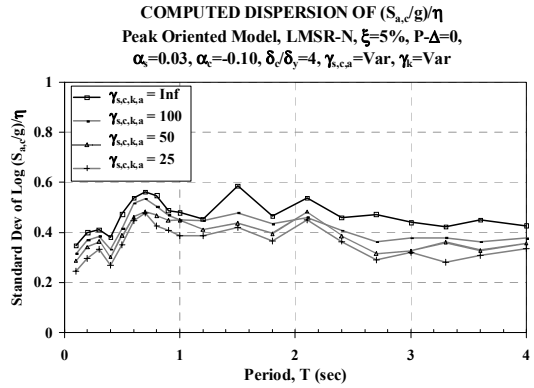

(a) P-Δ = 0

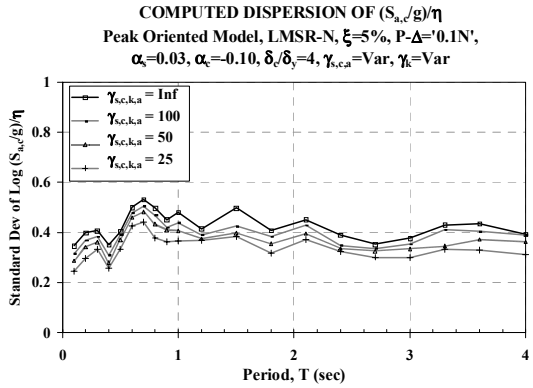

(b) P-Δ = 0.1*N*

Fig. 4.34 Effect of CD on dispersion of $(S_{a,c}/g)/\eta$; $\alpha_c = -0.1$, $\delta_c/\delta_y = 4$

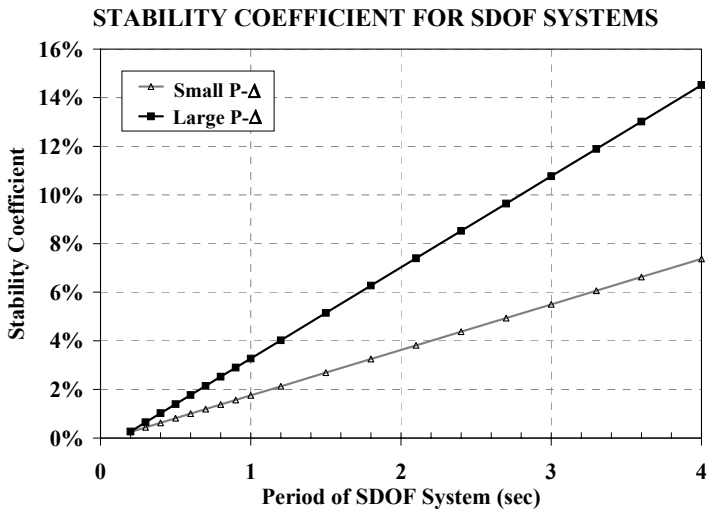

Fig. 4.35 Stability coefficients for SDOF parameter study

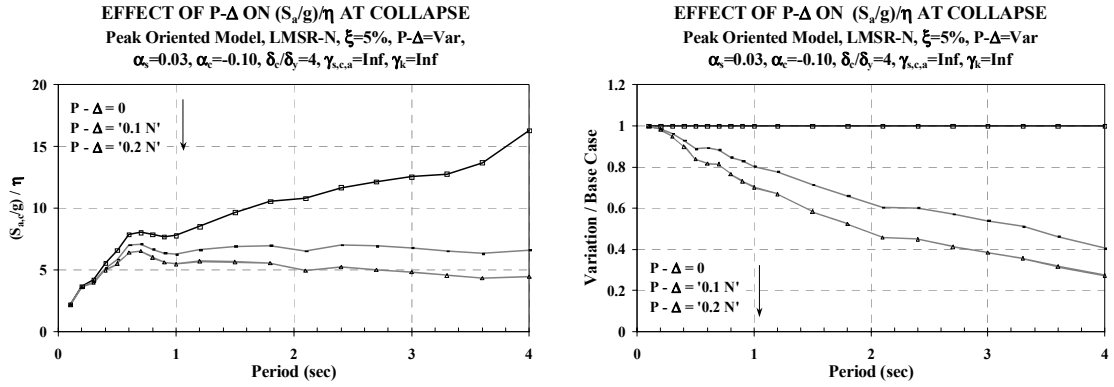

(a) Median Collapse Capacity Spectra (b) Median Collapse Capacity Ratios

Fig. 4.36 Effect of P-Δ on $(S_{a,c}/g)/\eta$; $\delta_c/\delta_y = 4$, $\alpha_c = -0.1$, no CD

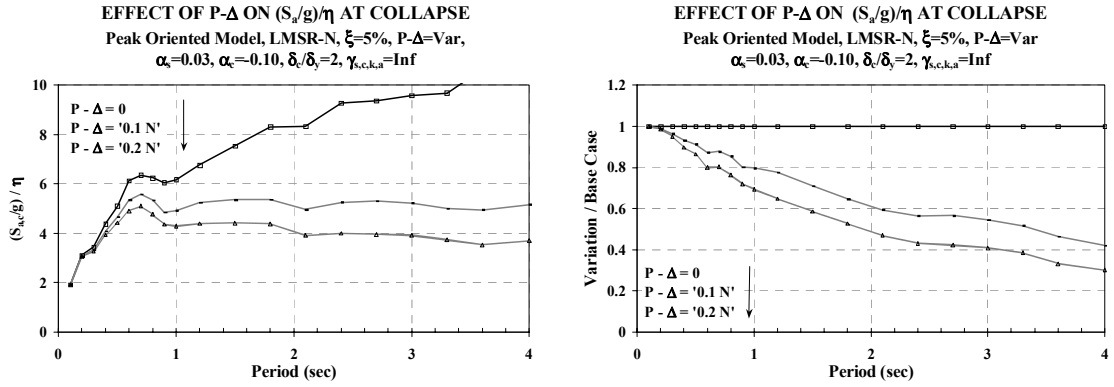

(a) Median Collapse Capacity Spectra (b) Median Collapse Capacity Ratios

Fig. 4.37 Effect of P-Δ on $(S_{a,c}/g)/\eta$; $\delta_c/\delta_y = 2$, $\alpha_c = -0.1$, no CD

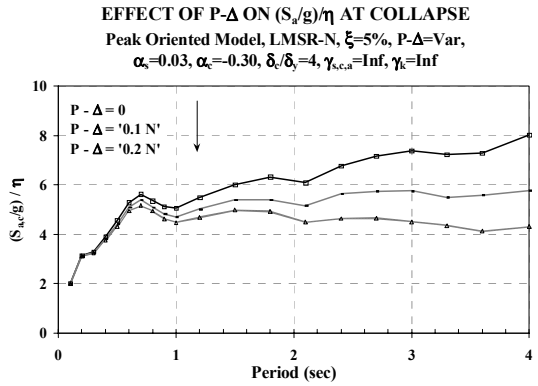

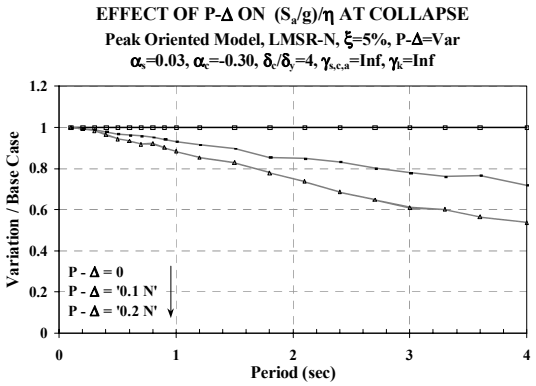

(a) Median Collapse Capacity Spectra (b) Median Collapse Capacity Ratios

Fig. 4.38 Effect of P-Δ on $(S_{a,c}/g)/\eta$; $\delta_c/\delta_y = 4$, $\alpha_c = -0.3$, no CD

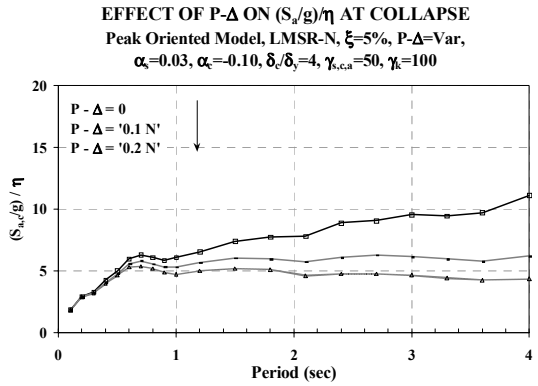

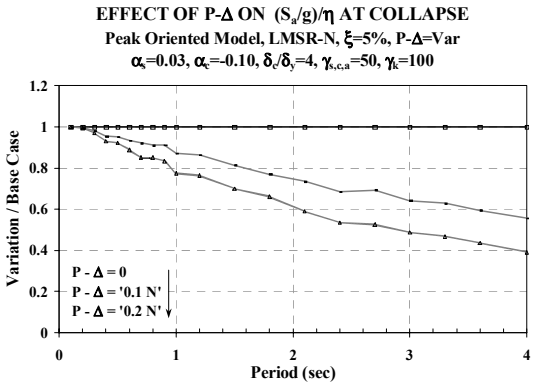

(a) Median Collapse Capacity Spectra (b) Median Collapse Capacity Ratios

Fig. 4.39 Effect of P-Δ on $(S_{a,c}/g)/\eta$; $\delta_c/\delta_y = 4$, $\alpha_c = -0.1$, medium CD

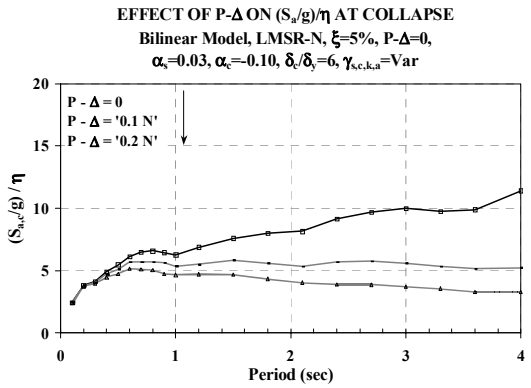

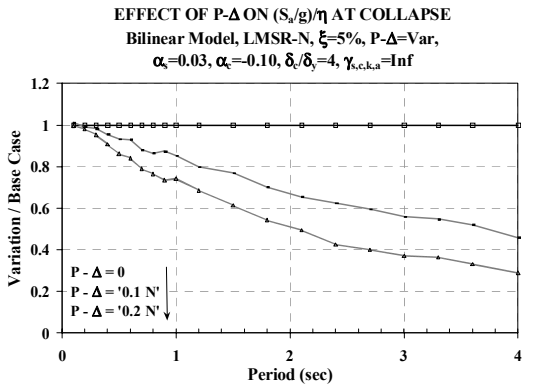

(a) Median Collapse Capacity Spectra (b) Median Collapse Capacity Ratios

Fig. 4.40 Effect of P-Δ effect on $(S_{a,c}/g)/\eta$; bilinear models, $\delta_c/\delta_y = 4$, $\alpha_c = -0.1$, no CD

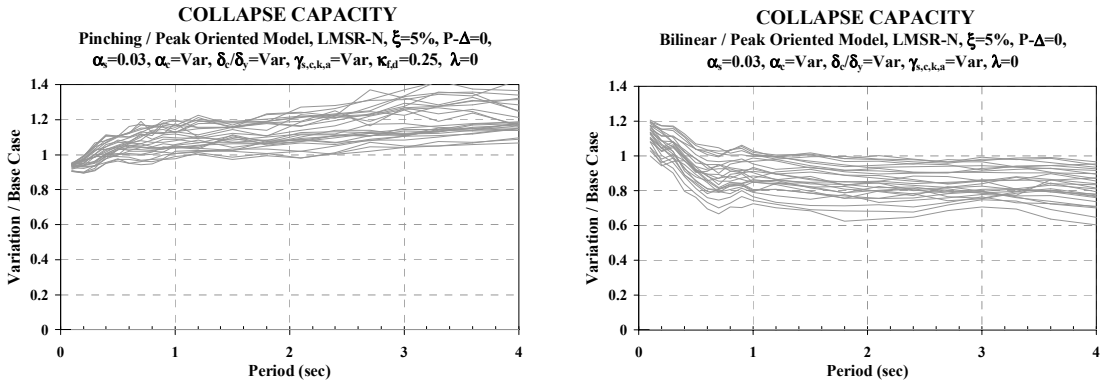

(a) Pinching / Peak-Oriented (b) Bilinear / Peak-Oriented

Fig. 4.41 Median collapse capacity ratios for different hysteretic models, P-Δ = 0

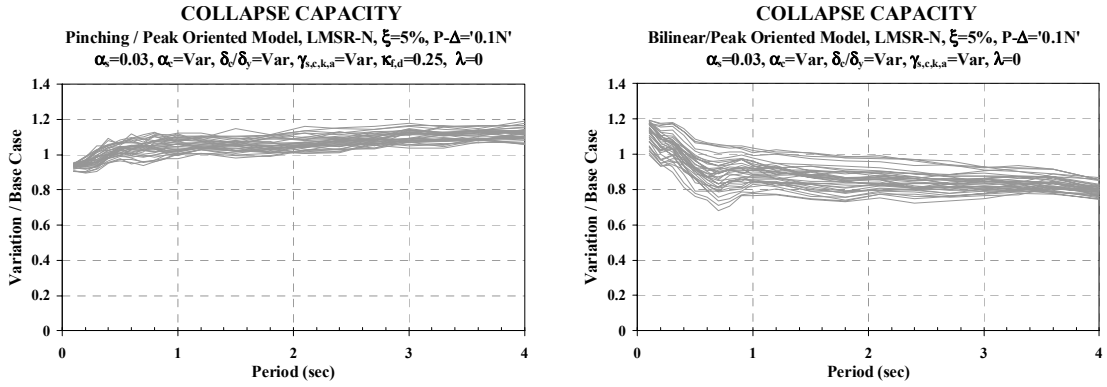

(a) Pinching / Peak-Oriented (b) Bilinear / Peak-Oriented

Fig. 4.42 Median collapse capacity ratios for different hysteretic models, P-Δ = 0.1*N*

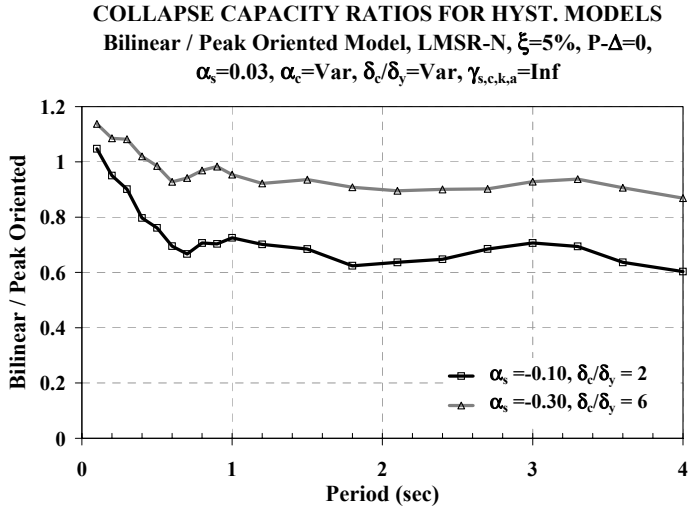

Fig. 4.43 Examples of collapse capacity ratios for bilinear / peak-oriented hysteretic models

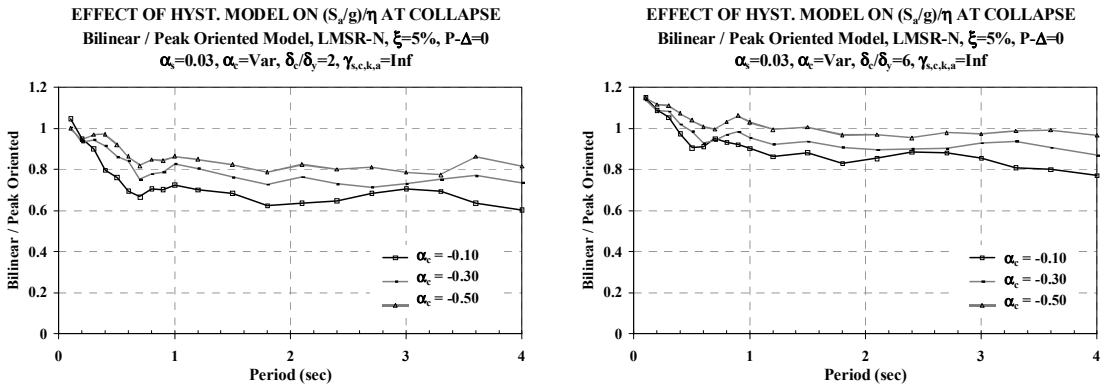

(a) $\delta_c/\delta_y = 2$ (b) $\delta_c/\delta_y = 6$

Fig. 4.44 Effect of hysteretic model on median collapse capacity; systems with different δ_c/δ_y and α_c values

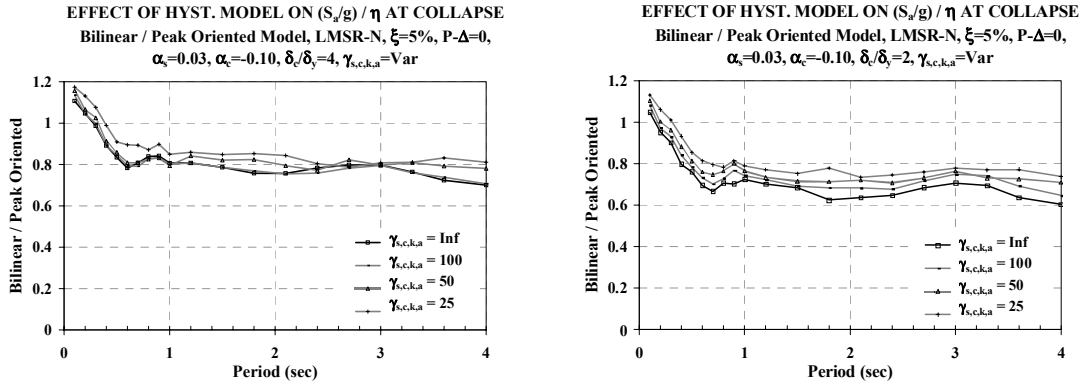

(a) α_c = -0.1, $\delta_c/\delta_y = 4$ (b) α_c = -0.1, $\delta_c/\delta_y = 2$

Fig. 4.45 Effect of hysteretic model on median collapse capacity; systems with different CD rates

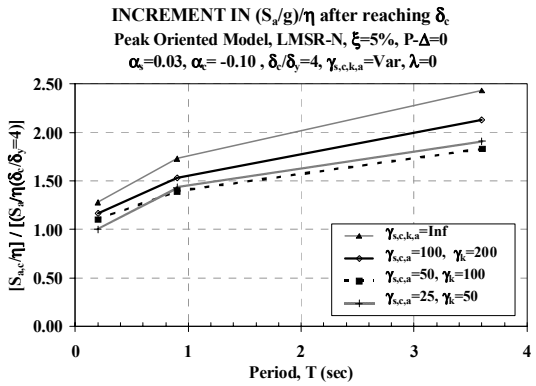

(a) Different CD Rates

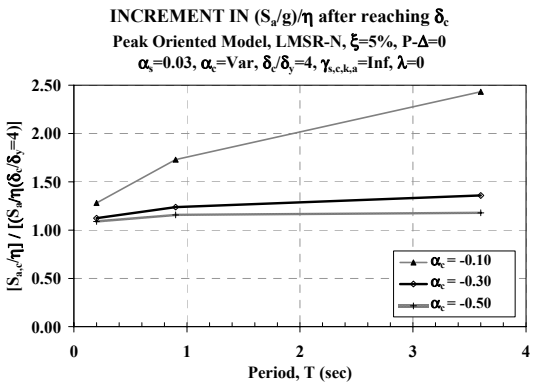

(b) Different α_c Slopes

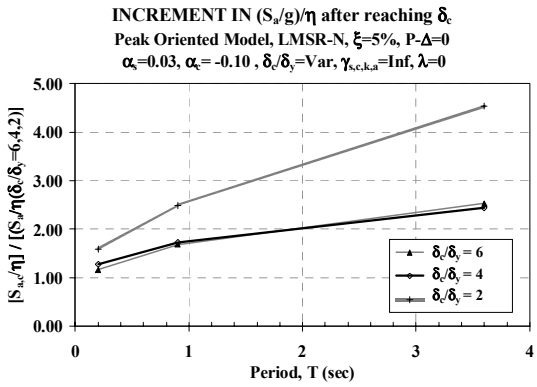

(c) Different δ_c/δ_y Ratios

Fig. 4.46 Median ratios of $(S_{a,c}/g)/\eta$ over $(S_a/g)/\eta$ when $\delta = \delta_c$; P-Δ =0

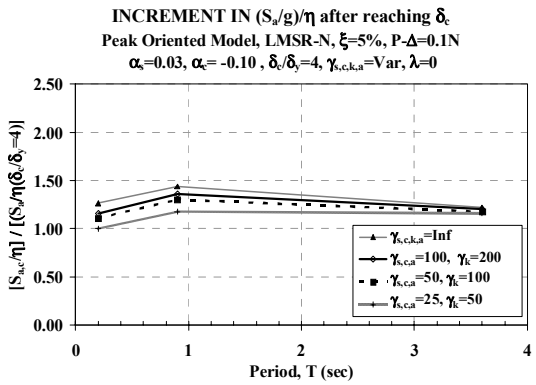

(a) Different CD Rates

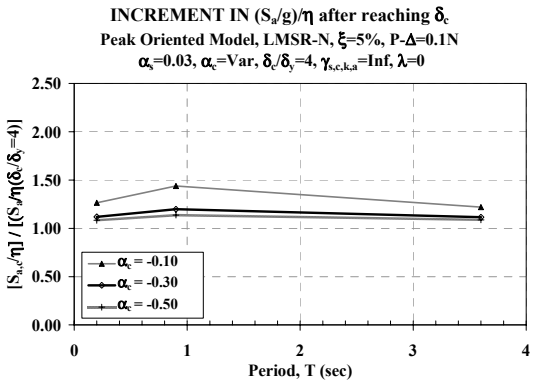

(b) Different α_c Slopes

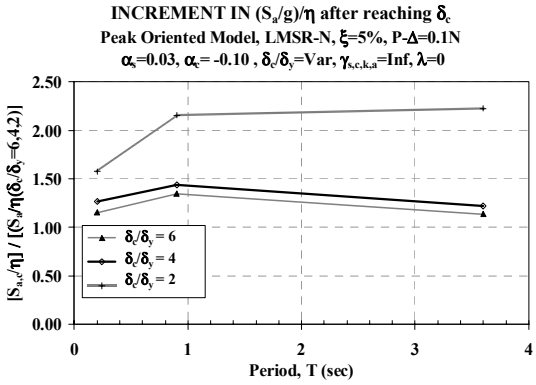

(c) Different δ_c/δ_y Ratios

Fig. 4.47 Median ratios of $(S_{a,c}/g)/\eta$ over $(S_a/g)/\eta$ when $\delta = \delta_c$; P-Δ =0.1*N*

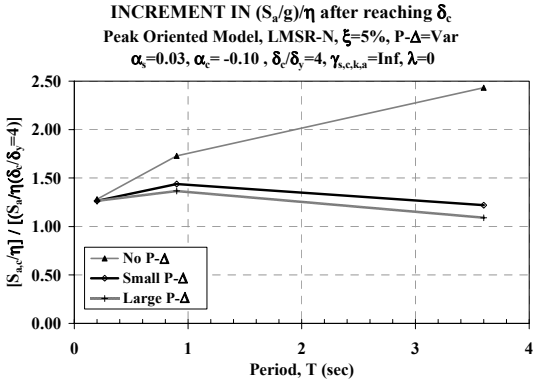

Fig. 4.48 Median ratios of $(S_{a,c}/g)/\eta$ over $(S_a/g)/\eta$ when $\delta = \delta_c$; different P-Δ levels

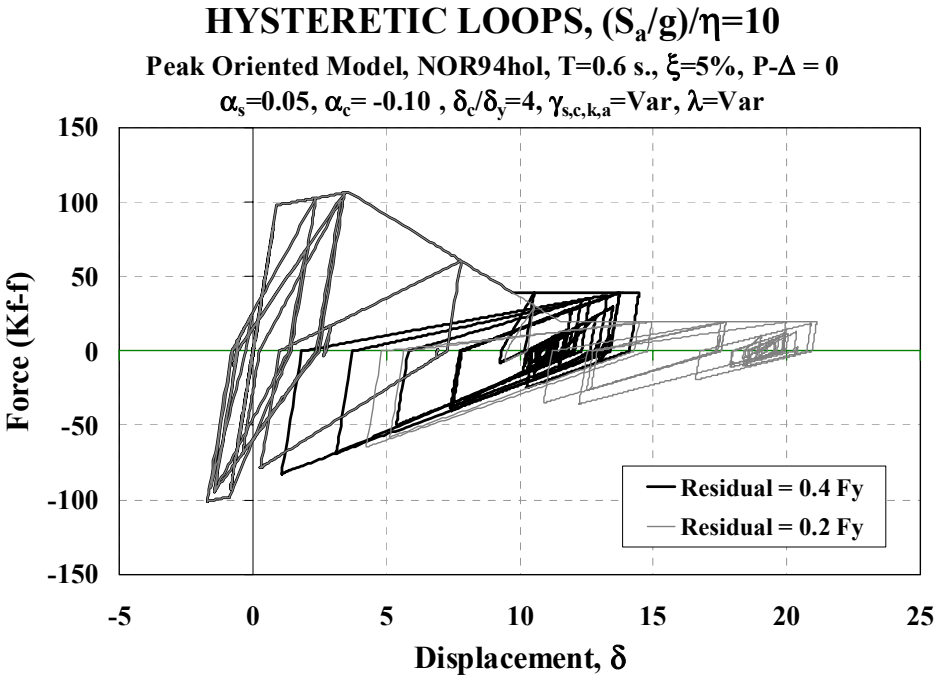

(a) P-Δ = 0

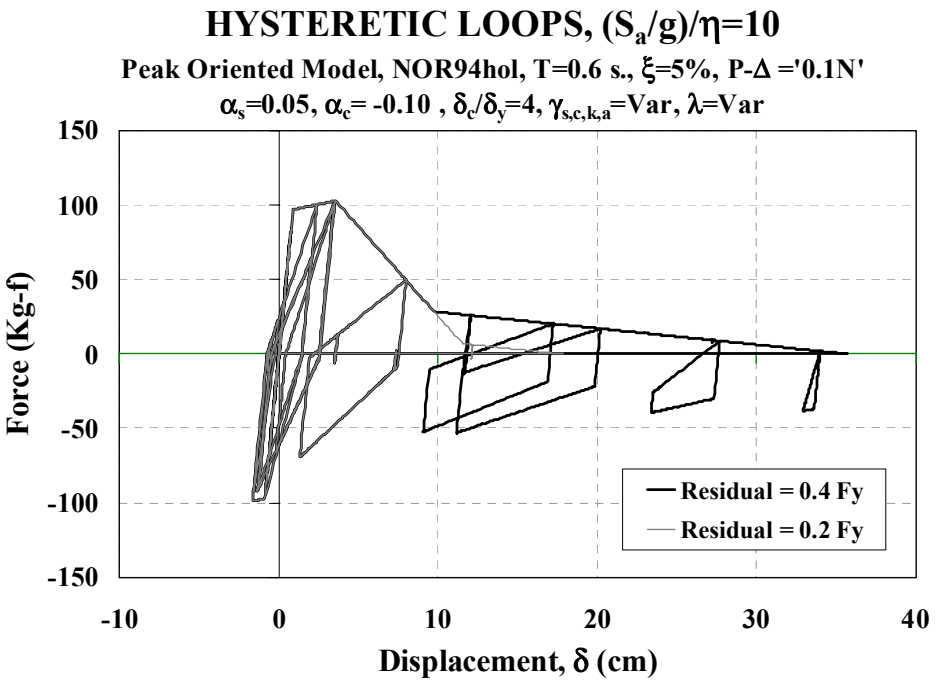

(b) P-Δ = 0.1N

Fig. 4.49 Hysteretic response for a system with residual strength

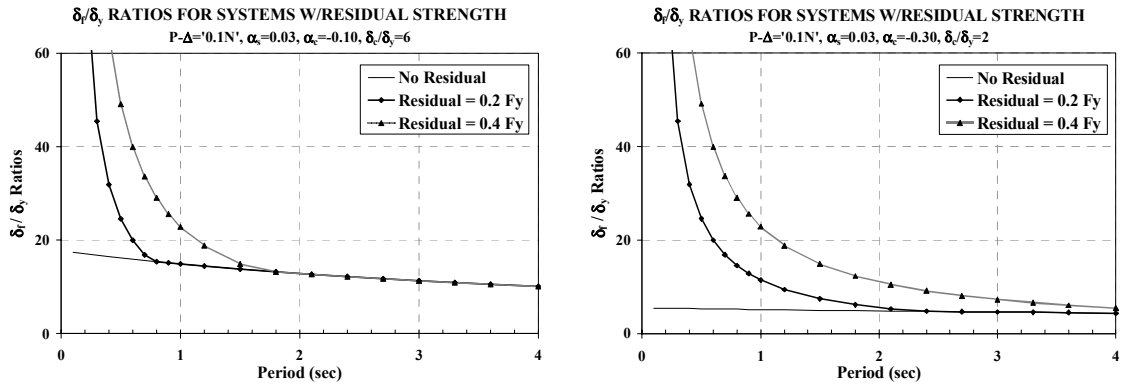

(a) Ductile Systems (b) Non-ductile Systems

Fig. 4.50 Normalized collapse displacements (δ_f/δ_y) for systems with residual strength

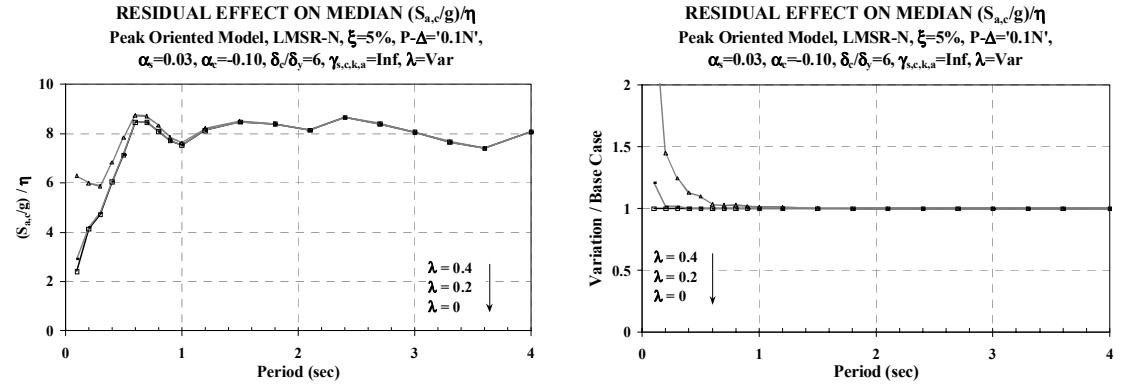

(a) Median Collapse Capacity Spectra (b) Median Collapse Capacity Ratios

Fig. 4.51 Effect of residual strength on ($S_{a,c}/g$)/η for ductile systems

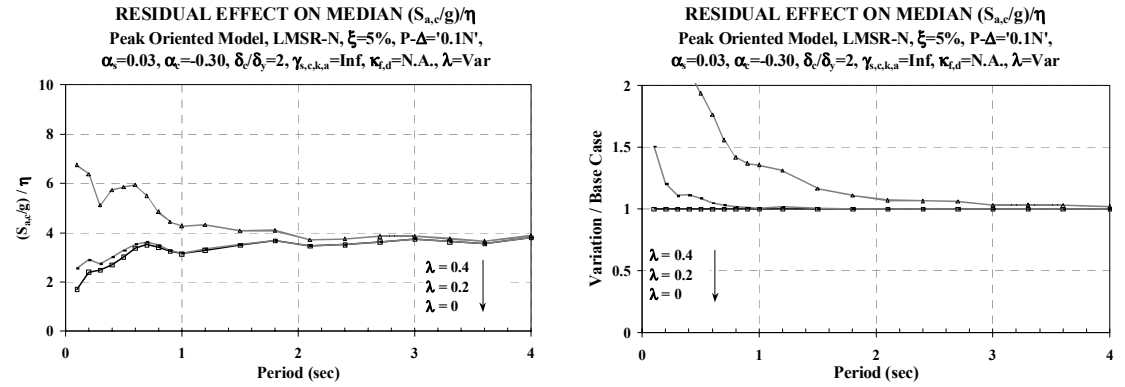

(a) Median Collapse Capacity Spectra (b) Median Collapse Capacity Ratios

Fig. 4.52 Effect of residual strength on ($S_{a,c}/g$)/η for non-ductile systems

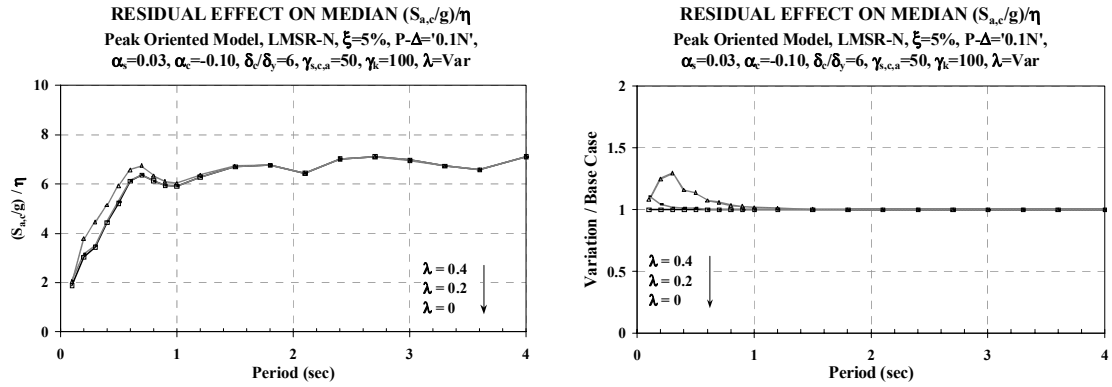

(a) Median Collapse Capacity Spectra (b) Median Collapse Capacity Ratios

Fig. 4.53 Effect of residual strength on $(S_{a,c}/g)/\eta$ for ductile systems with CD

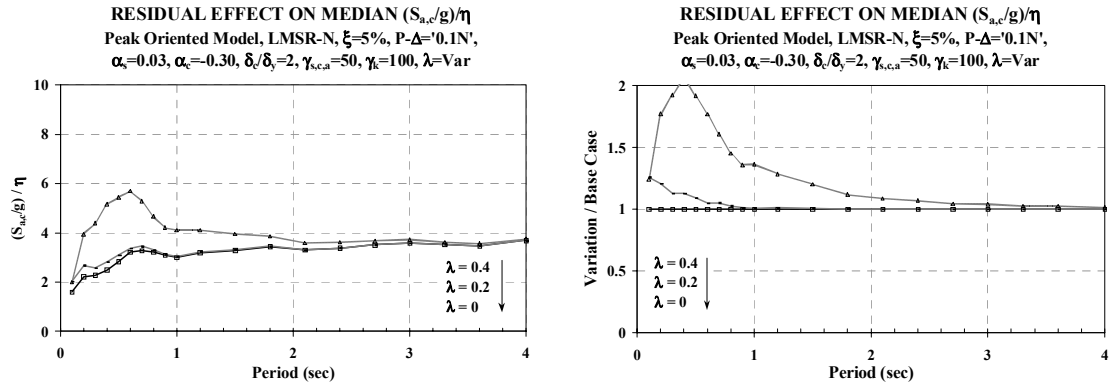

(a) Median Collapse Capacity Spectra (b) Median Collapse Capacity Ratios

Fig. 4.54 Effect of residual strength on $(S_{a,c}/g)/\eta$ for non-ductile systems with CD

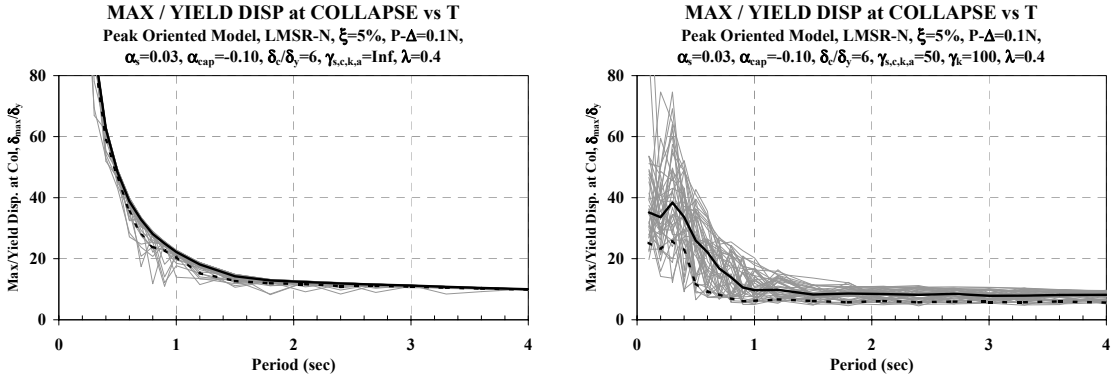

(a) No CD (b) Medium CD

Fig. 4.55 δ_{max}/δ_y at collapse for a ductile system

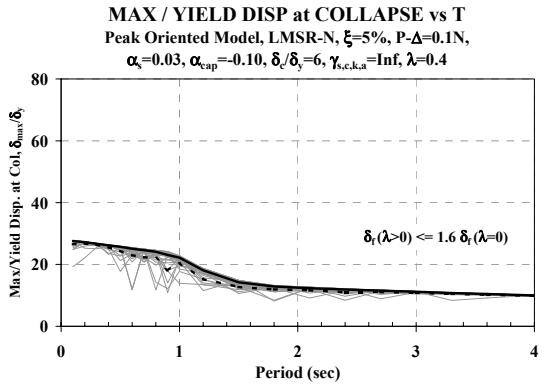

Fig. 4.56 δ_{max}/δ_y at collapse for a ductile system when $\delta_f(\lambda>0) \leq 1.6\ \delta_f(\lambda=0)$

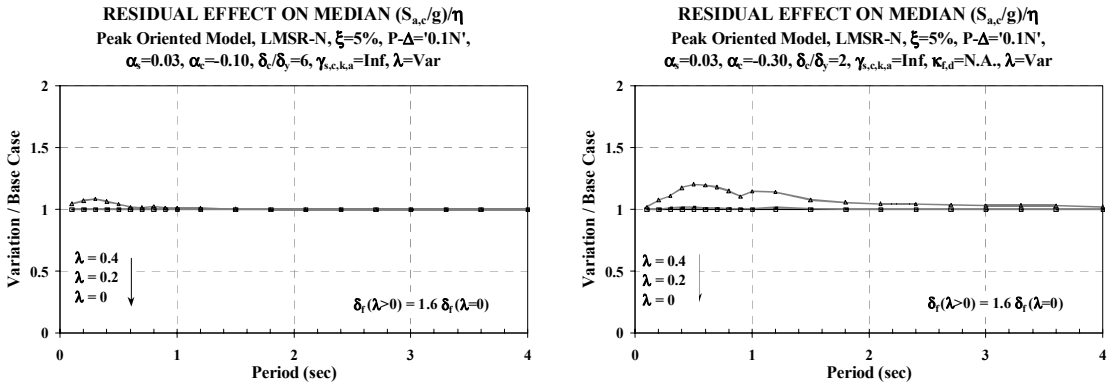

(a) Ductile Systems (b) Non-ductile Systems

Fig. 4.57 Effect of residual strength on collapse displacements considering $\delta_f(\lambda>0) \leq 1.6\ \delta_f(\lambda=0)$

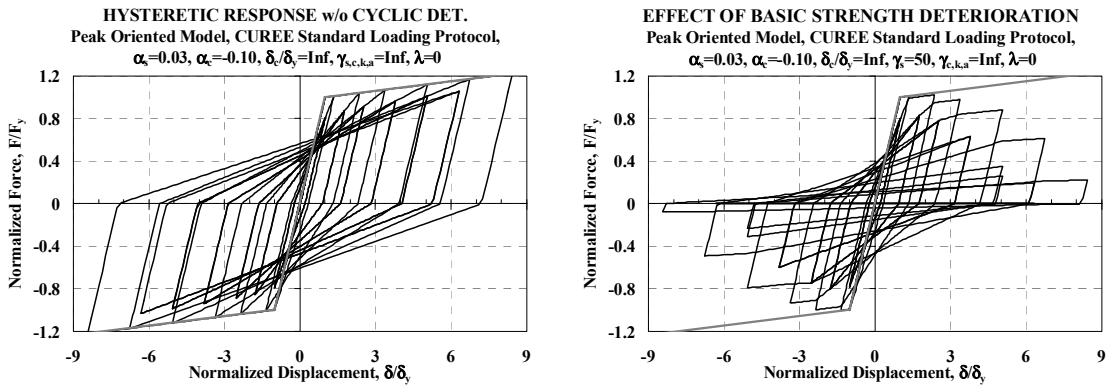

(a) No CD Included (b) Basic Strength CD

Fig. 4.58 Effect of cyclic basic strength deterioration on the hysteretic response of systems without strength capping

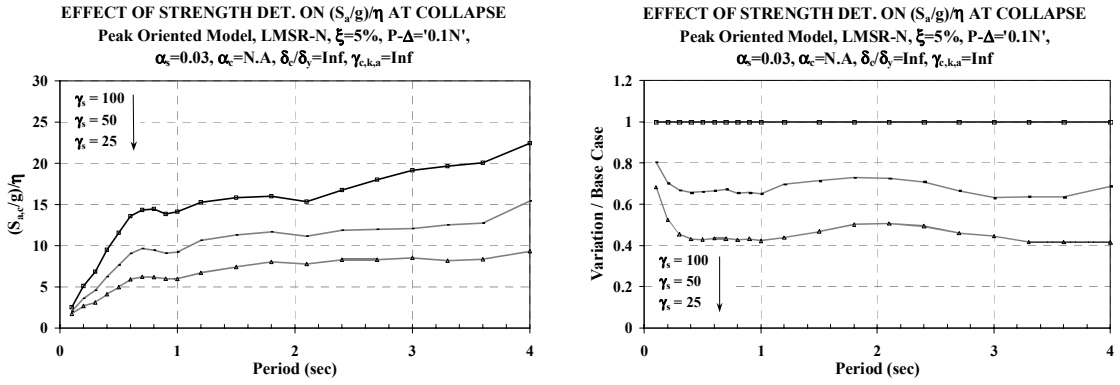

(a) Median Collapse Capacity Spectra (b) Median Collapse Capacity Ratios

Fig. 4.59 Effect of cyclic basic strength deterioration on $(S_{a,c}/g)/\eta$, systems without strength capping

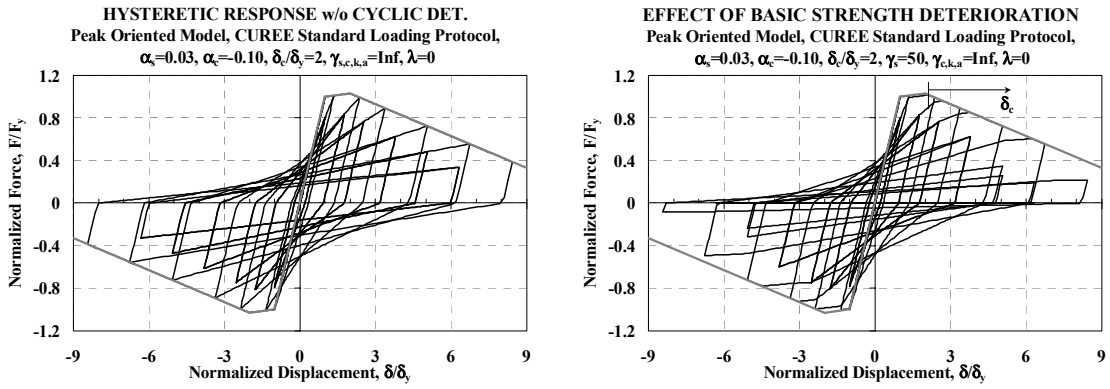

(a) No CD Included (b) Basic Strength CD

Fig. 4.60 Effect of cyclic basic strength deterioration on the hysteretic response of systems with strength capping

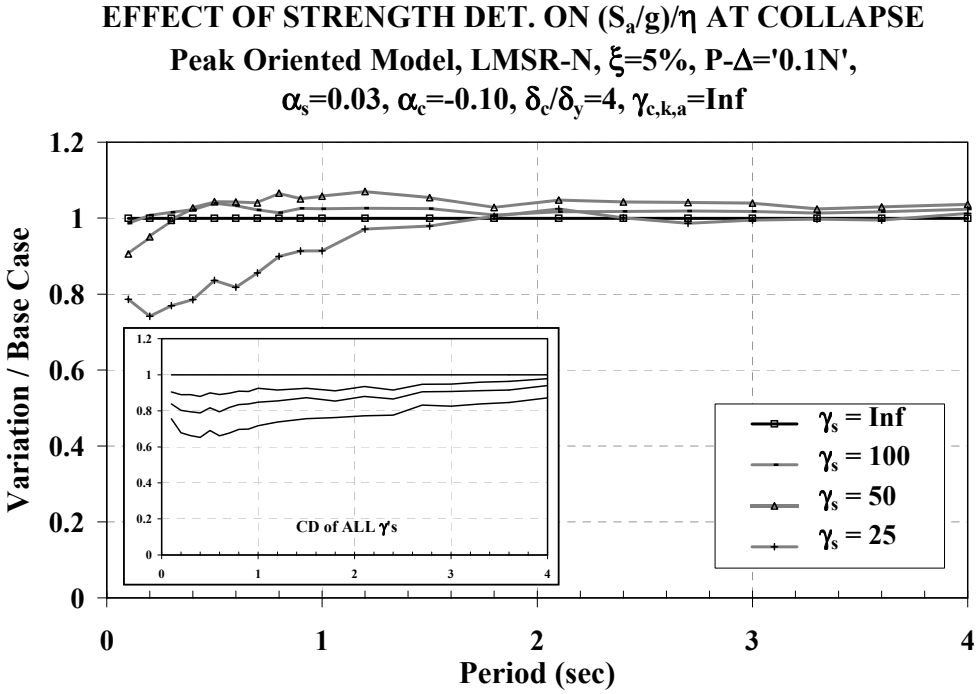

Fig. 4.61 Effect of cyclic basic strength deterioration on $(S_{a,c}/g)/\eta$

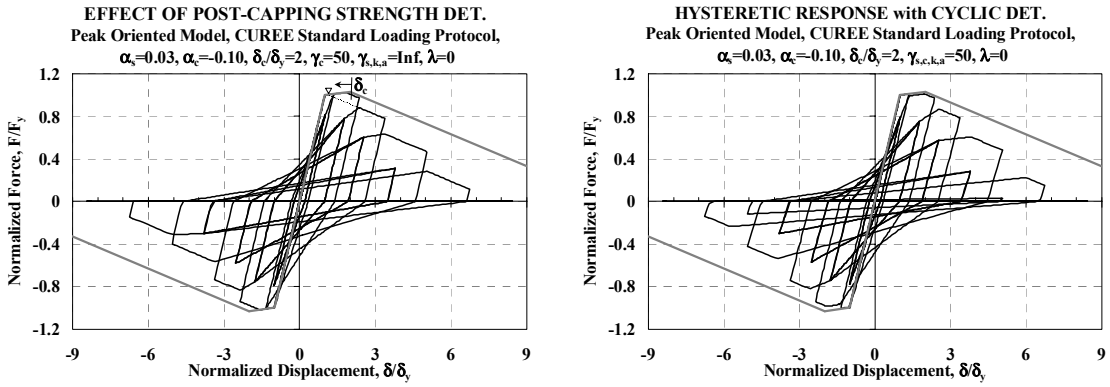

(a) Post-Capping Strength CD (b) CD for all Four Modes

Fig. 4.62 Effect of cyclic post-capping strength deterioration on the hysteretic response

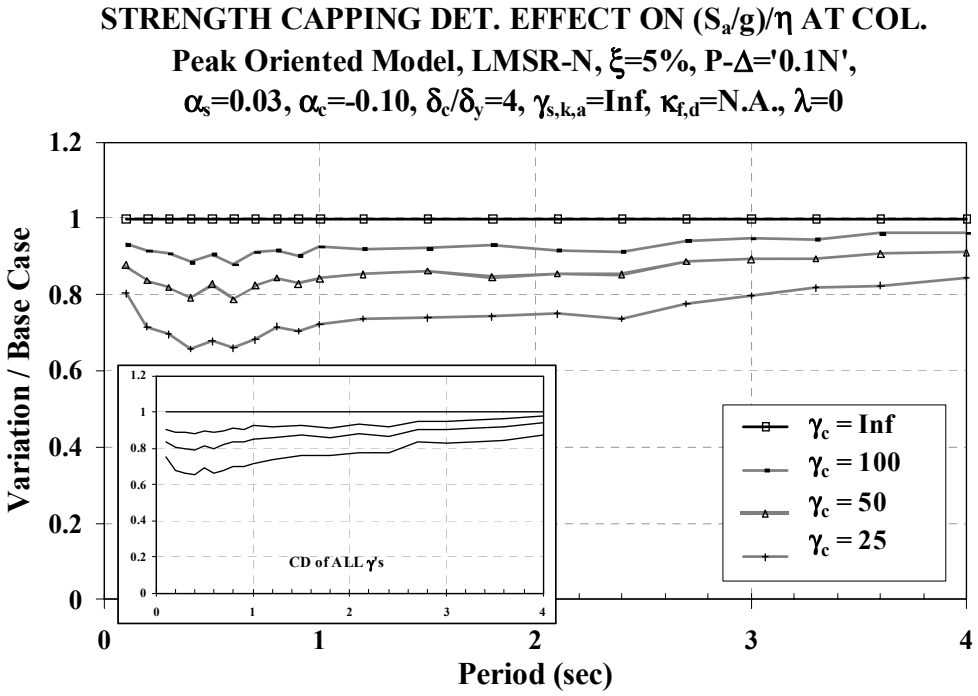

Fig. 4.63 Effect of cyclic post-capping strength deterioration on $(S_{a,c}/g)/\eta$

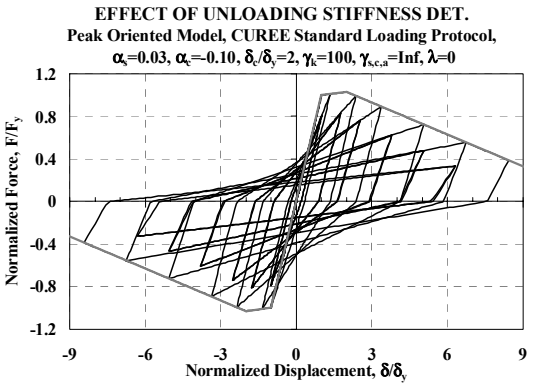

Fig. 4.64 Effect of cyclic unloading stiffness deterioration on the hysteretic response of a system with strength capping

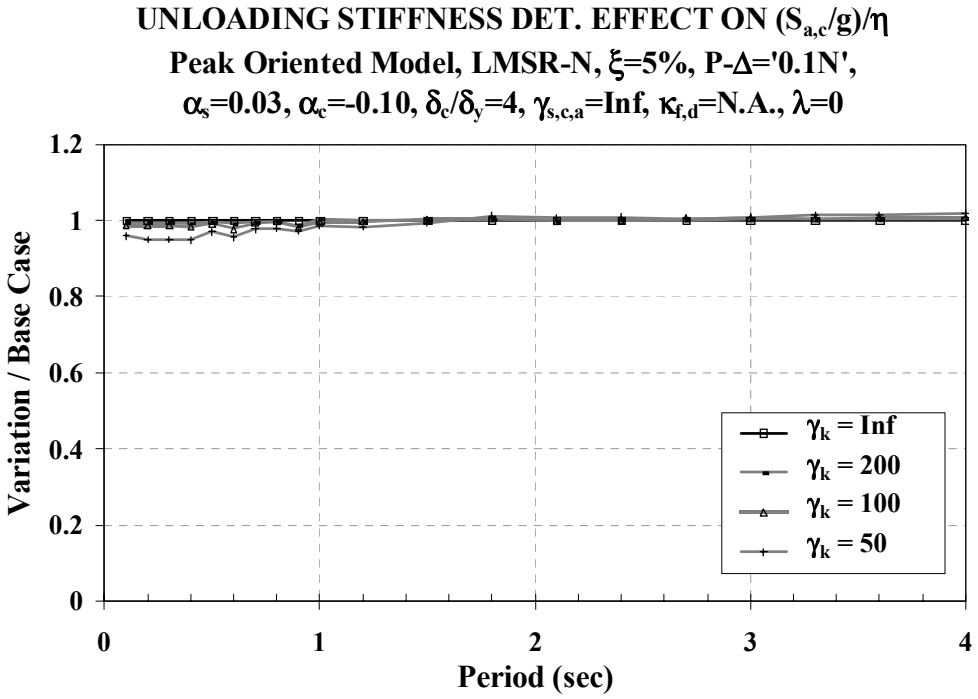

Fig. 4.65 Effect of cyclic unloading stiffness deterioration on $(S_{a,c}/g)/\eta$

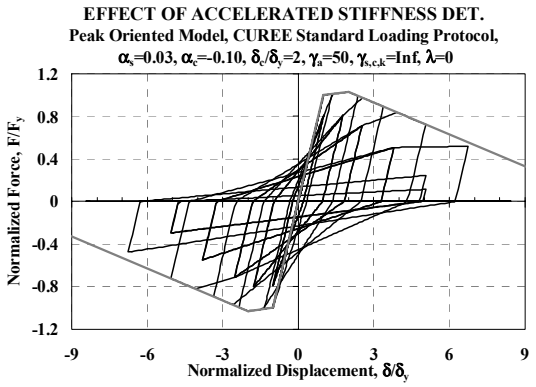

Fig. 4.66 Effect of cyclic reloading accelerated stiffness deterioration on the hysteretic response of a system with strength capping

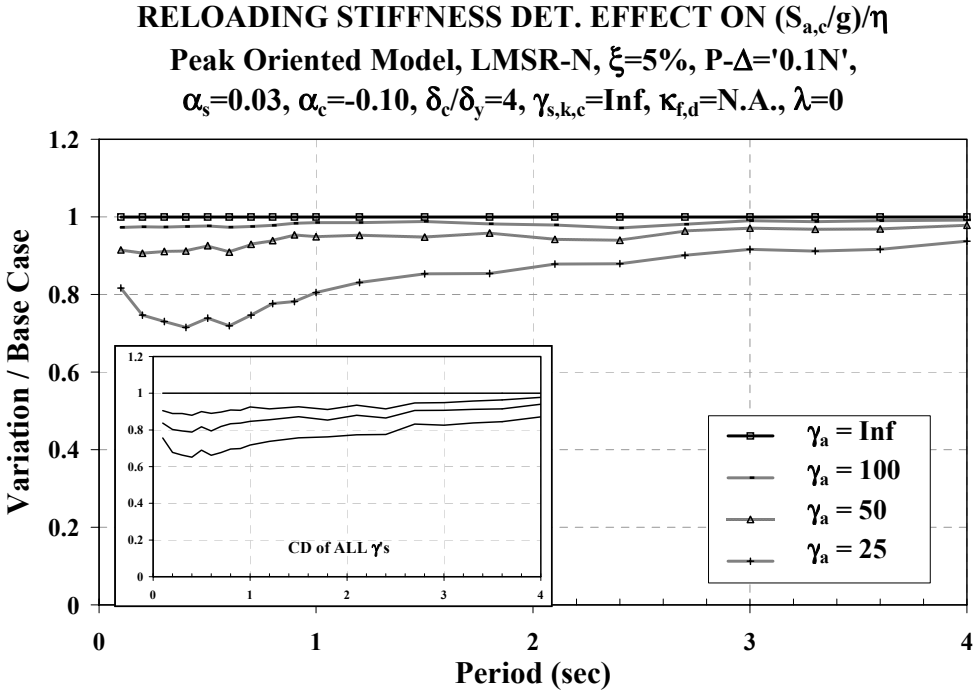

Fig. 4.67 Effect of cyclic accelerated stiffness deterioration on ($S_{a,c}/g$)/η

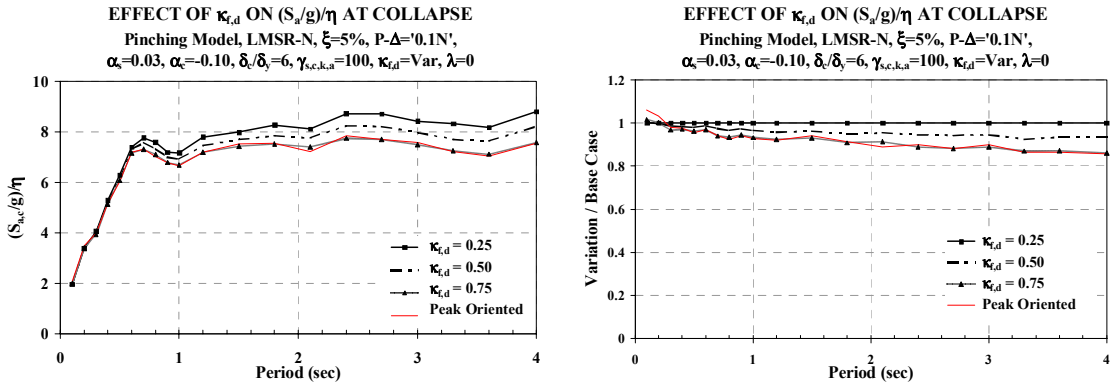

(a) Median Collapse Capacity Spectra (b) Median Collapse Capacity Ratios

Fig. 4.68 Effect of pinching level on $(S_{a,c}/g)/\eta$ for ductile systems

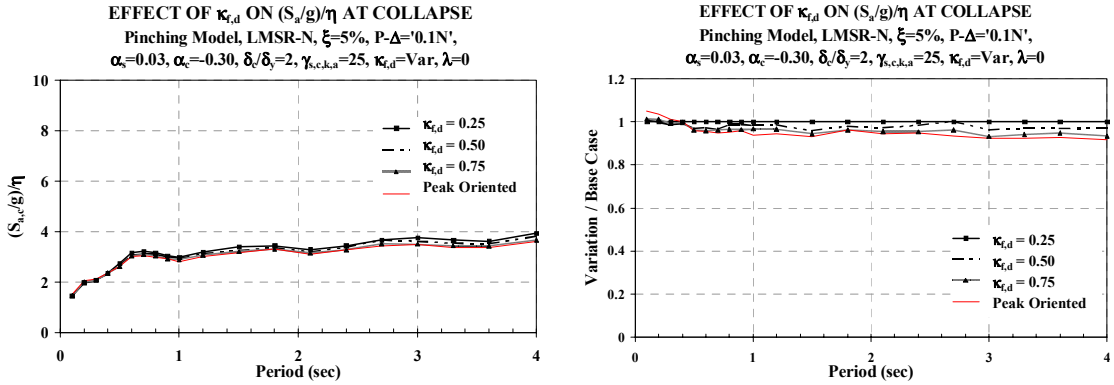

(a) Median Collapse Capacity Spectra (b) Median Collapse Capacity Ratios

Fig. 4.69 Effect of pinching level on $(S_{a,c}/g)/\eta$ for non-ductile systems

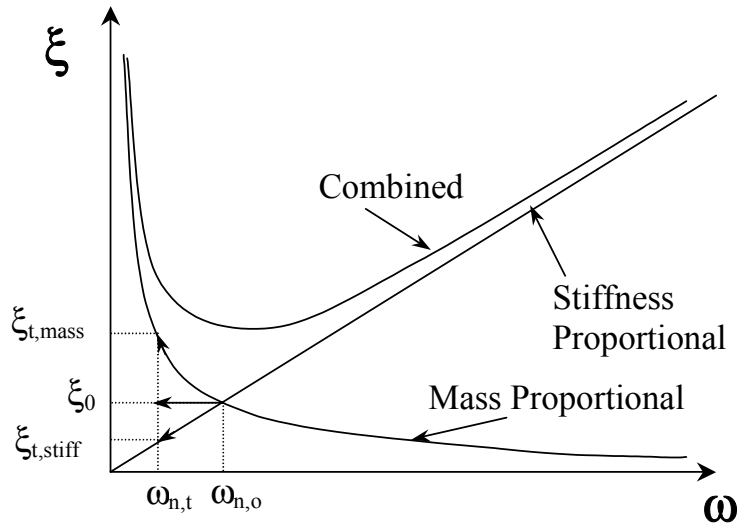

Fig. 4.70 Damping ratio–frequency relationship

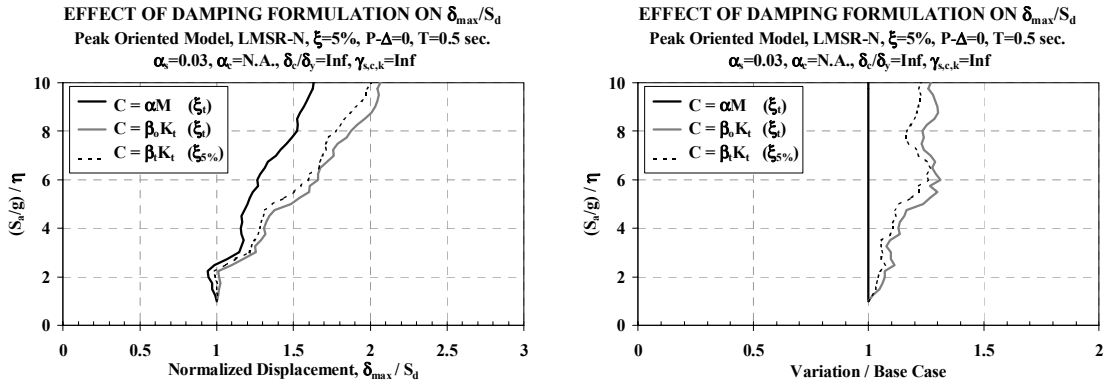

(a) Median $(S_a/g)/\eta$ - δ_{max}/S_d (b) Median δ_{max}/S_d Ratios

Fig. 4.71 Effect of damping formulation on δ_{max}/S_d for non-deteriorating systems, T = 0.5 s, ξ_o = 5%

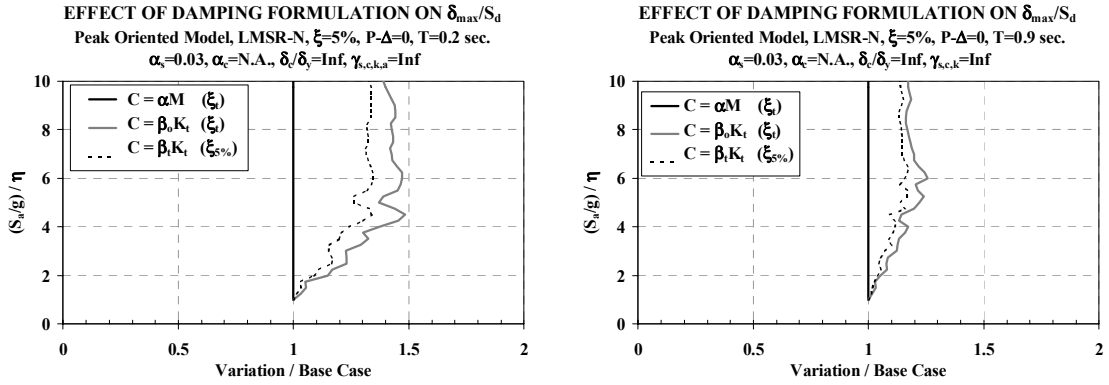

(a) T = 0.2 s (b) T = 0.9 s

Fig. 4.72 Effect of damping formulation on median δ_{max}/S_d ratios; non-deteriorating systems, ξ = 5%

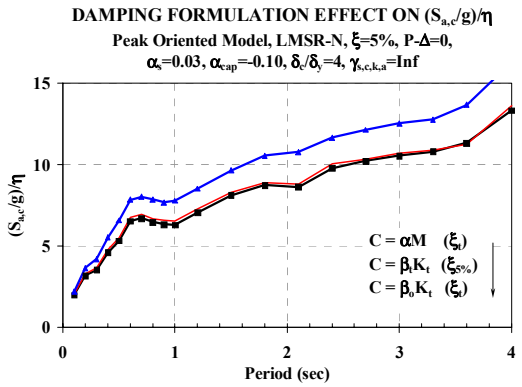

(a) Median Collapse Capacity Spectra

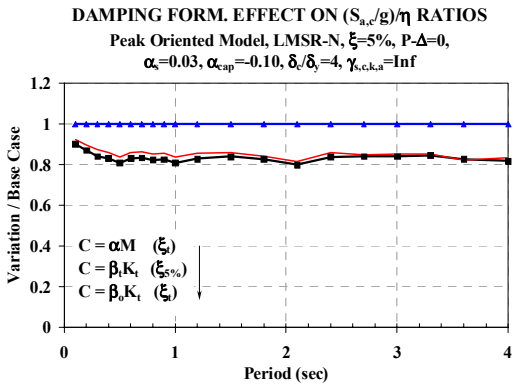

(b) Median Collapse Capacity Ratios

Fig. 4.73 Effect of damping formulation on $(S_{a,c}/g)/\eta$; P-Δ = 0, ξ_o = 5%

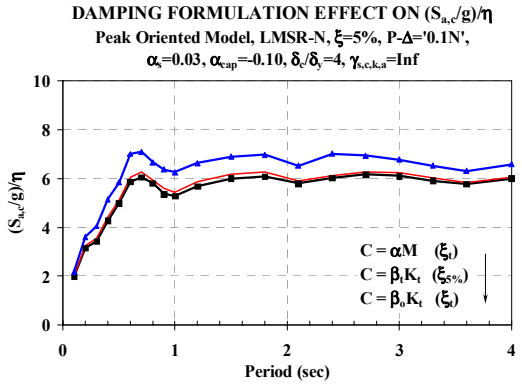

(a) Median Collapse Capacity Spectra

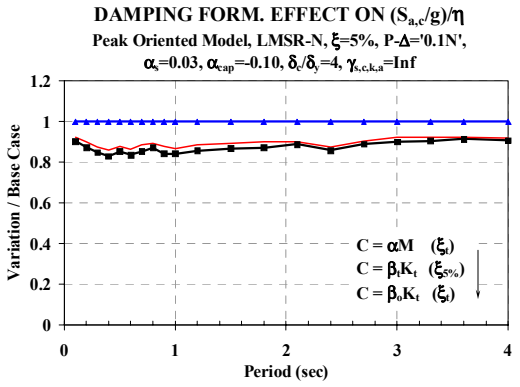

(b) Median Collapse Capacity Ratios

Fig. 4.74 Effect of damping formulation on $(S_{a,c}/g)/\eta$; small P-Δ, ξ_o = 5%

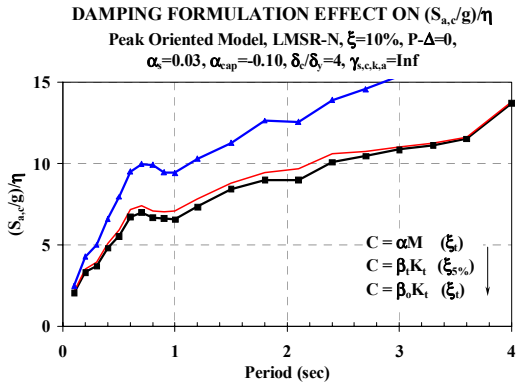

(a) Median Collapse Capacity Spectra

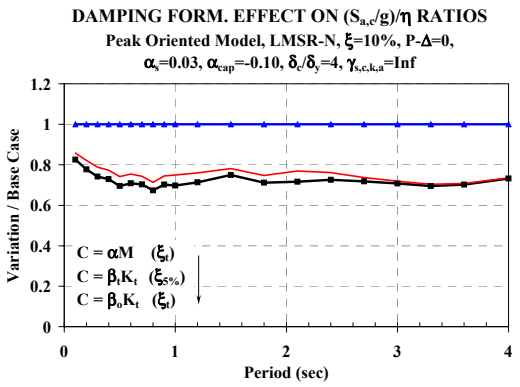

(b) Median Collapse Capacity Ratios

Fig. 4.75 Effect of damping formulation on $(S_{a,c}/g)/\eta$; P-Δ = 0, ξ_o = 10%

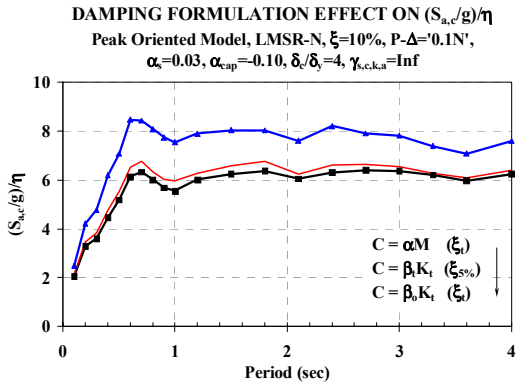

(a) Median Collapse Capacity Spectra

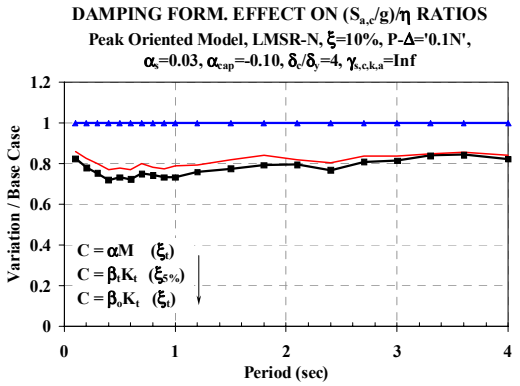

(b) Median Collapse Capacity Ratios

Fig. 4.76 Effect of damping formulation on $(S_{a,c}/g)/\eta$; small P-Δ, ξ_o = 10%

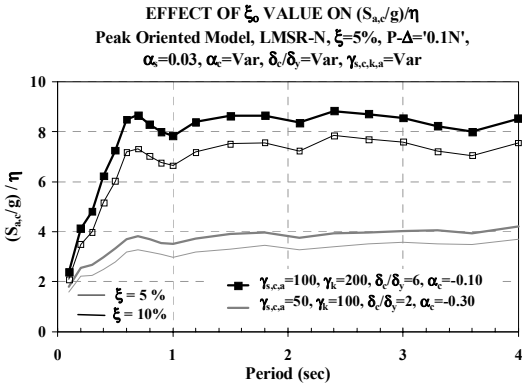

(a) Median Collapse Capacity Spectra

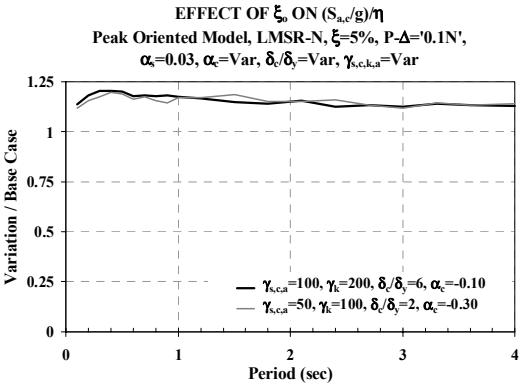

(b) Median Collapse Capacity Ratios

Fig. 4.77 Effect of ξ_o on $(S_{a,c}/g)/\eta$; mass proportional damping

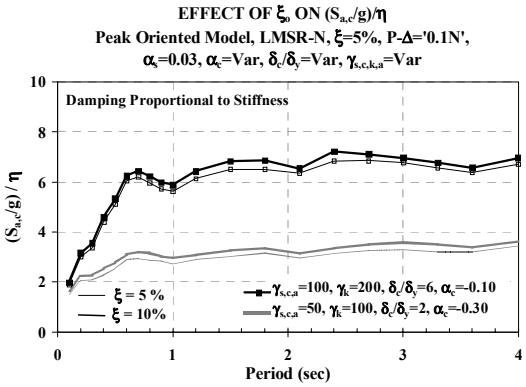

(a) Median Collapse Capacity Spectra

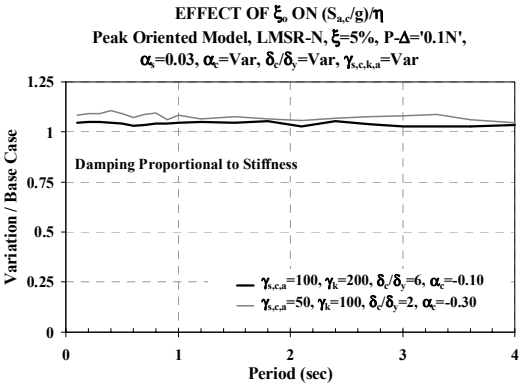

(b) Median Collapse Capacity Ratios

Fig. 4.78 Effect of ξ_o on $(S_{a,c}/g)/\eta$; stiffness proportional damping

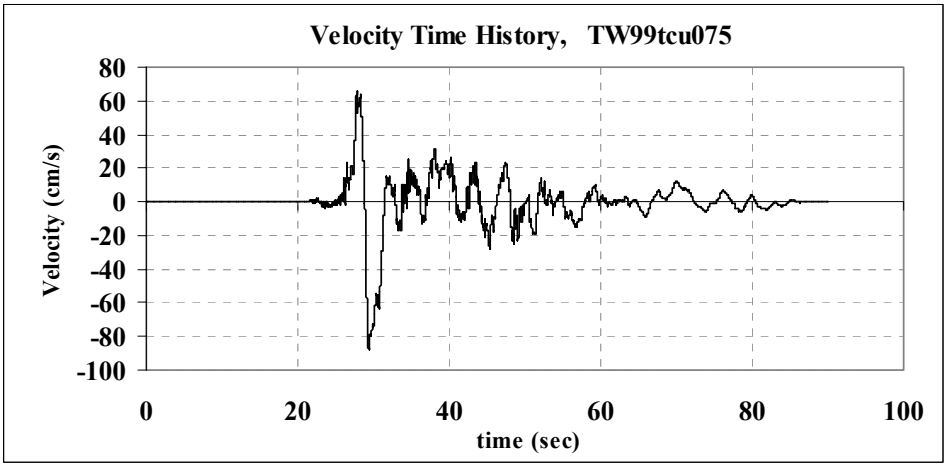

Fig. 4.79 Velocity time history of a typical NFGM

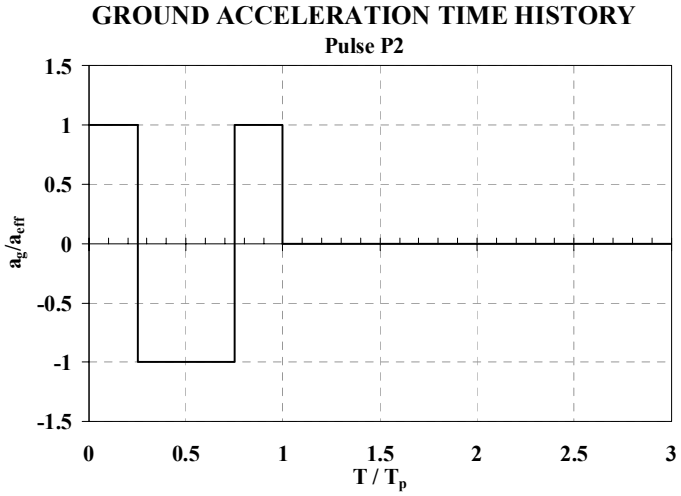

Fig. 4.80 Pulse P2 ground acceleration time history (Babak and Krawinkler, 2001)

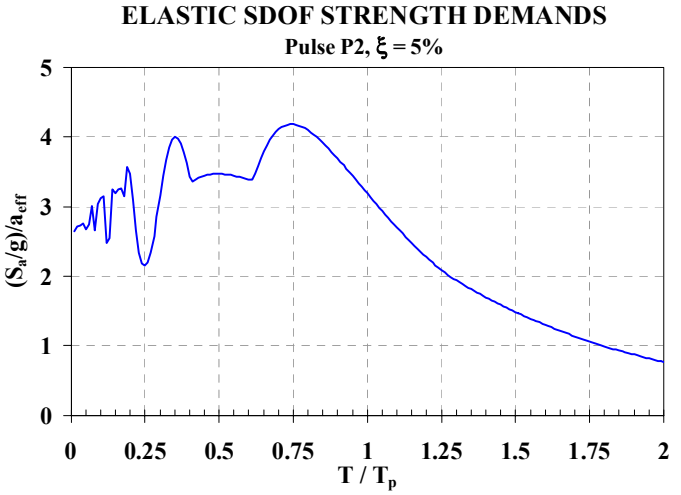

Fig. 4.81 Elastic strength (acceleration) demand spectrum for Pulse P2

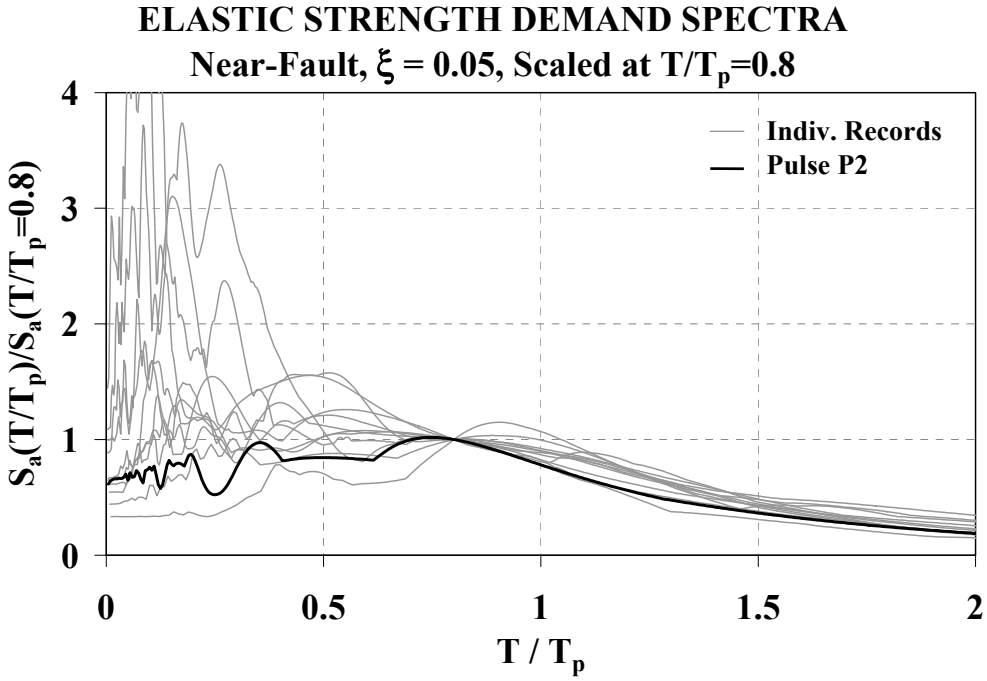

Fig. 4.82 Elastic strength demand spectra of NFGMs and Pulse P2, scaled at $S_a(T/T_p) = 0.8$

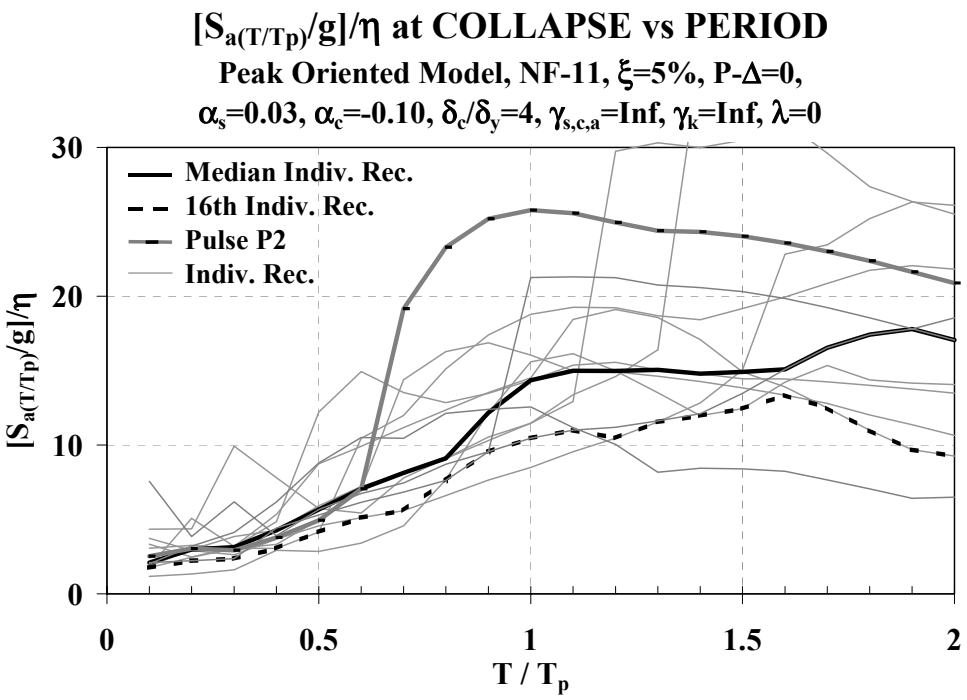

Fig. 4.83 Collapse capacities for systems w/o CD subjected to Set NF-11 and Pulse P2

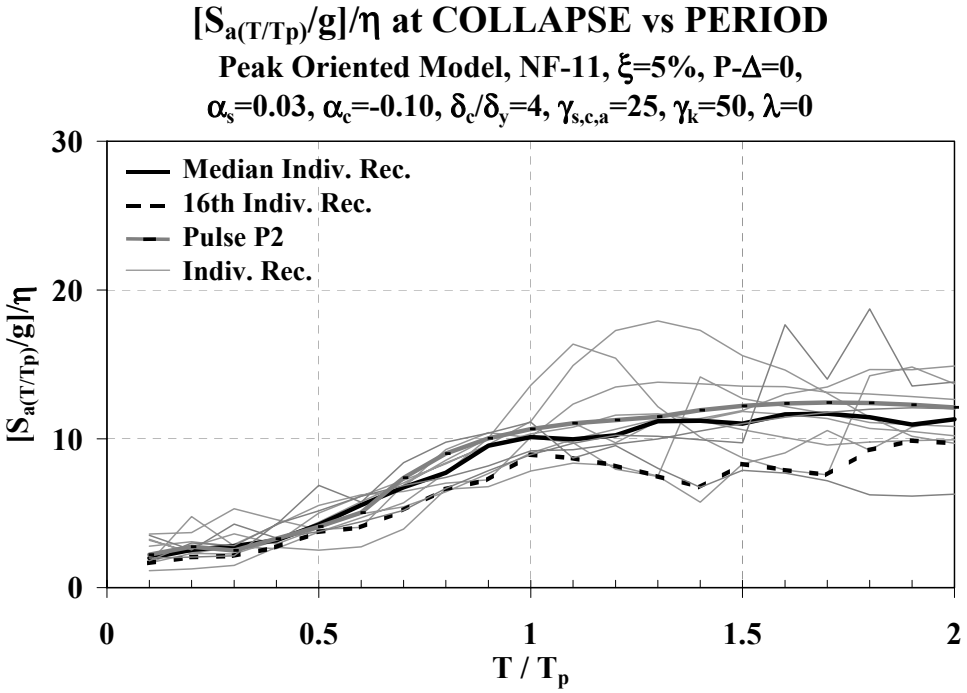

Fig. 4.84 Collapse capacities for systems with rapid CD subjected to Set NF-11 and Pulse P2

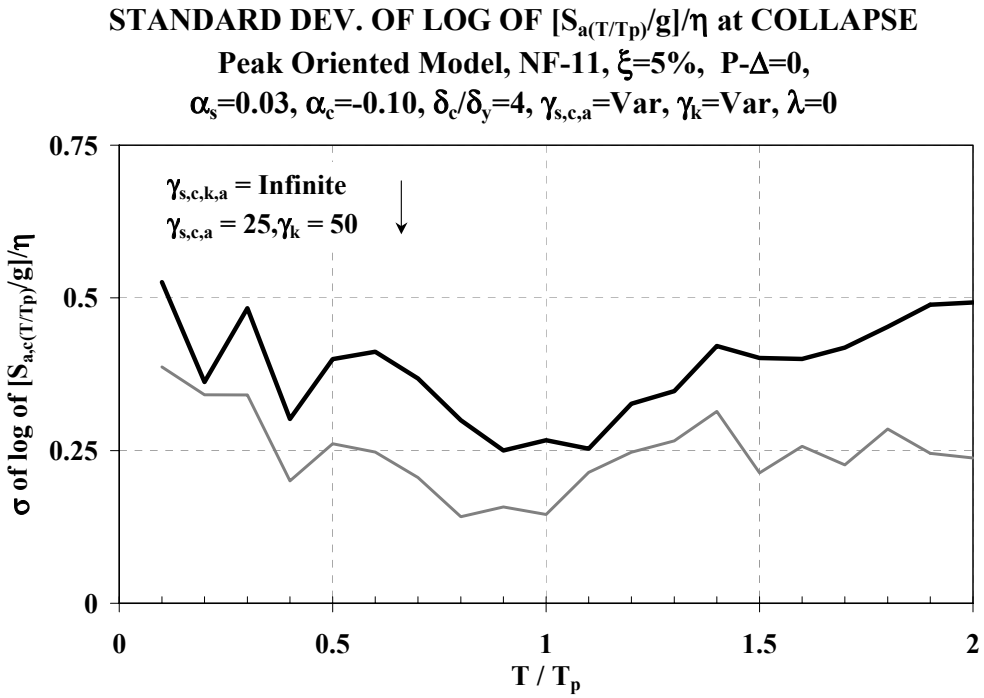

Fig. 4.85 Dispersion of collapse capacities for systems subjected to Set NF-11

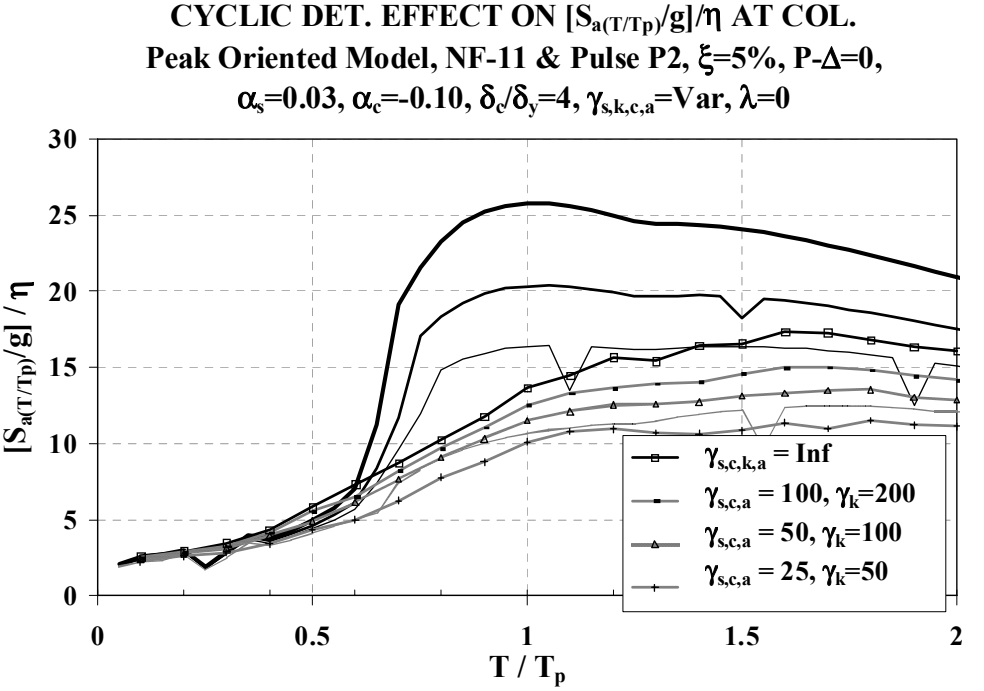

Fig. 4.86 Effect of CD on ($S_{a,c}/g$)/η for systems subjected to Set NF-11 and Pulse P2

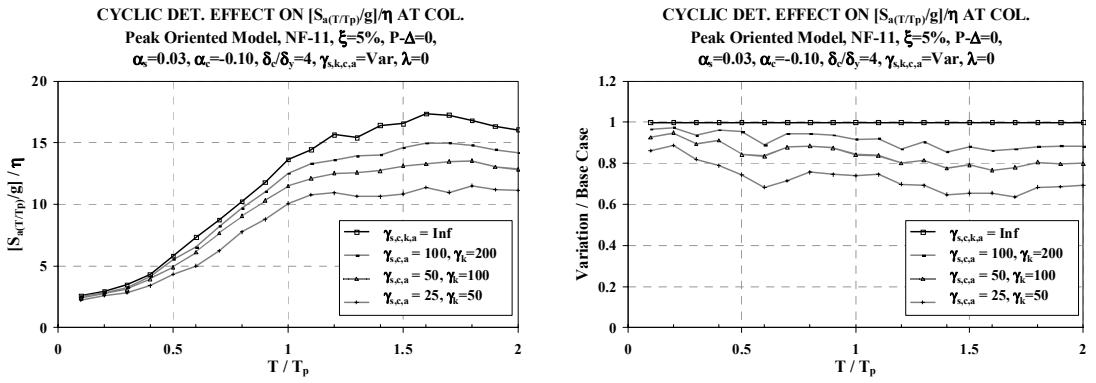

(a) Median Collapse Capacity Spectra (b) Median Collapse Capacity Ratios

Fig. 4.87 Effect of CD on $(S_{a,c}/g)/\eta$ for systems subjected to Set NF-11; $\delta_c/\delta_y = 4$, α_c = -0.10

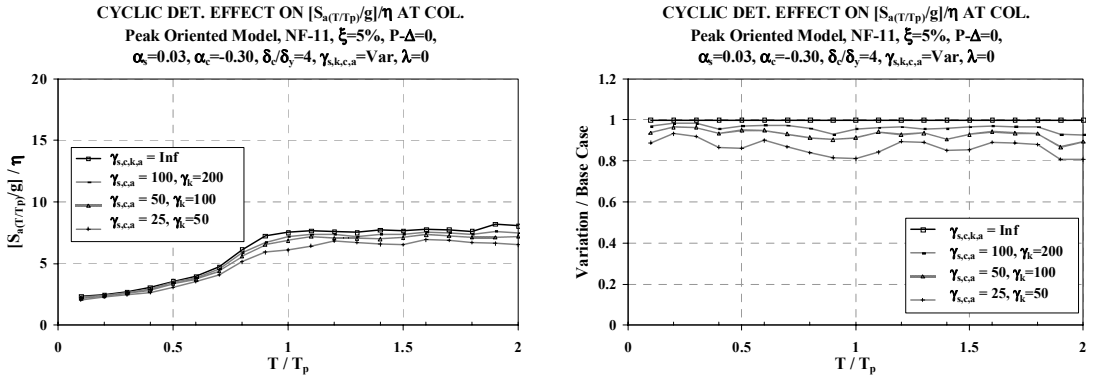

(a) Median Collapse Capacity Spectra (b) Median Collapse Capacity Ratios

Fig. 4.88 Effect of CD on $(S_{a,c}/g)/\eta$ for systems subjected to Set NF-11; $\delta_c/\delta_y = 4$, α_c = -0.30

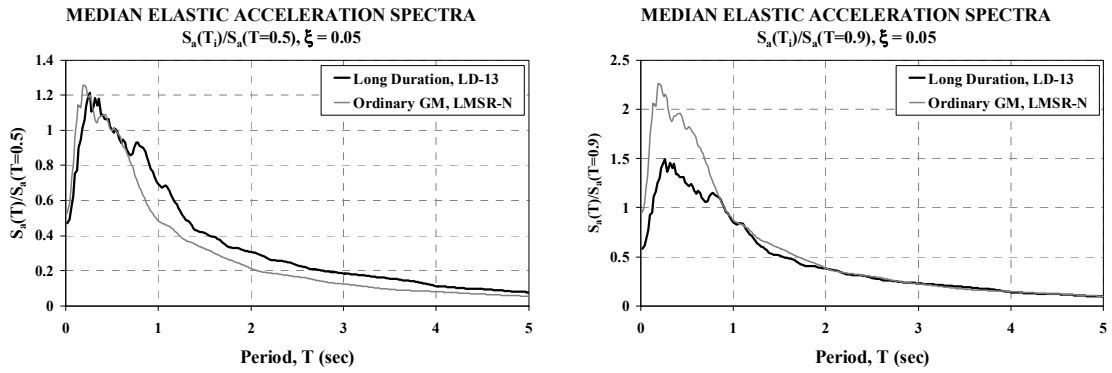

(a) Scaled at T = 0.5 s (b) Scaled at T = 0.9 s

Fig. 4.89 Median elastic acceleration spectra for Sets LD-13 and LMSR-N

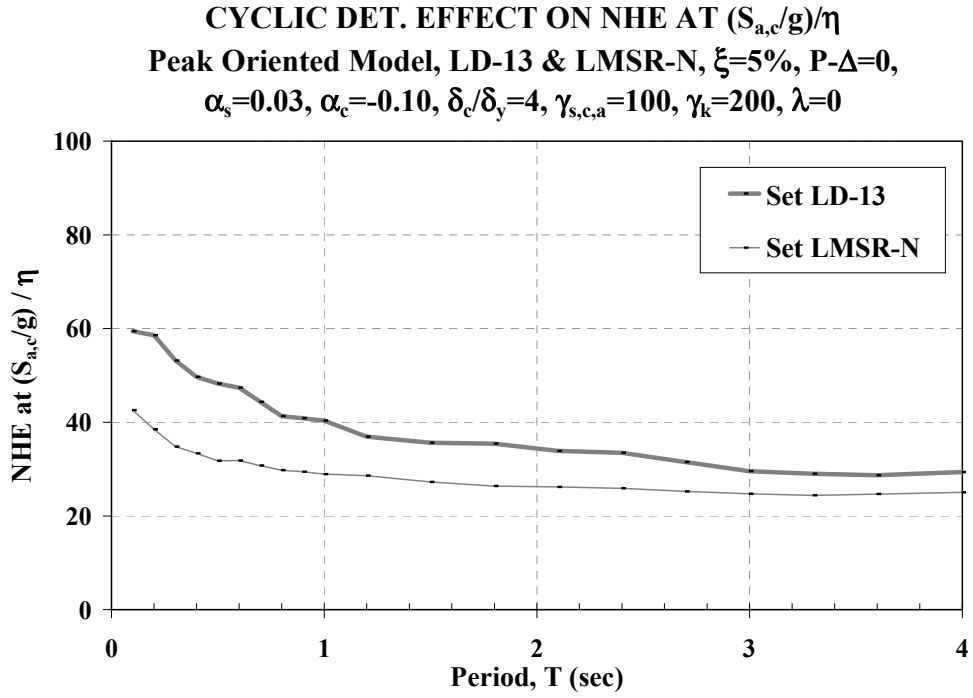

Fig. 4.90 NHE at collapse for reference SDOF system; slow CD for Sets LD-13 and LMSR-N

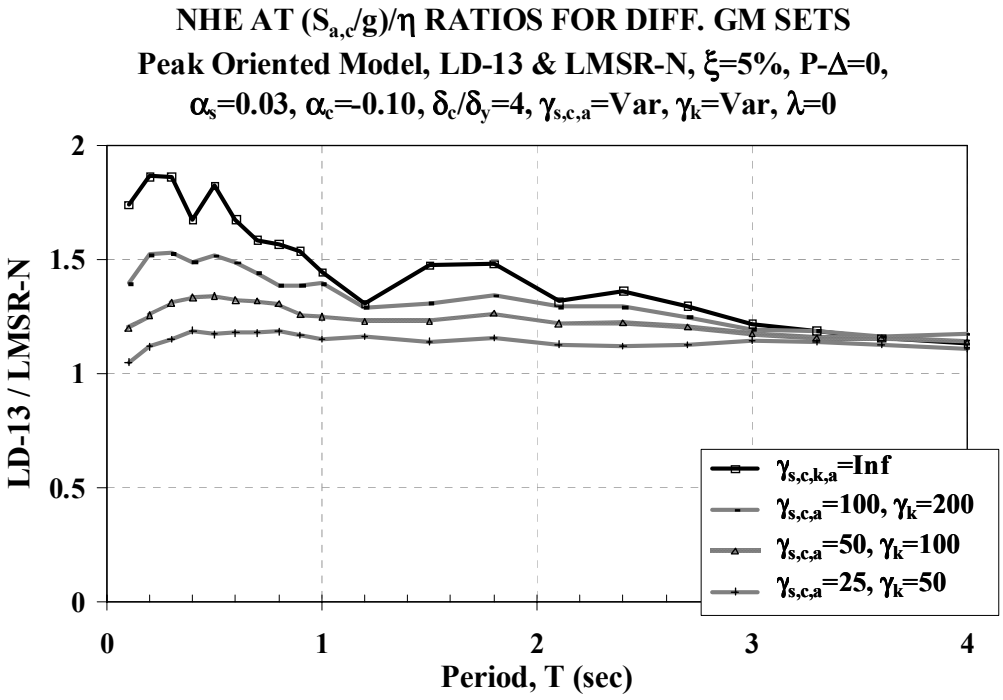

Fig. 4.91 Ratios of NHE at collapse for reference SDOF system with different CD rates, Sets LD-13 over LMSR-N

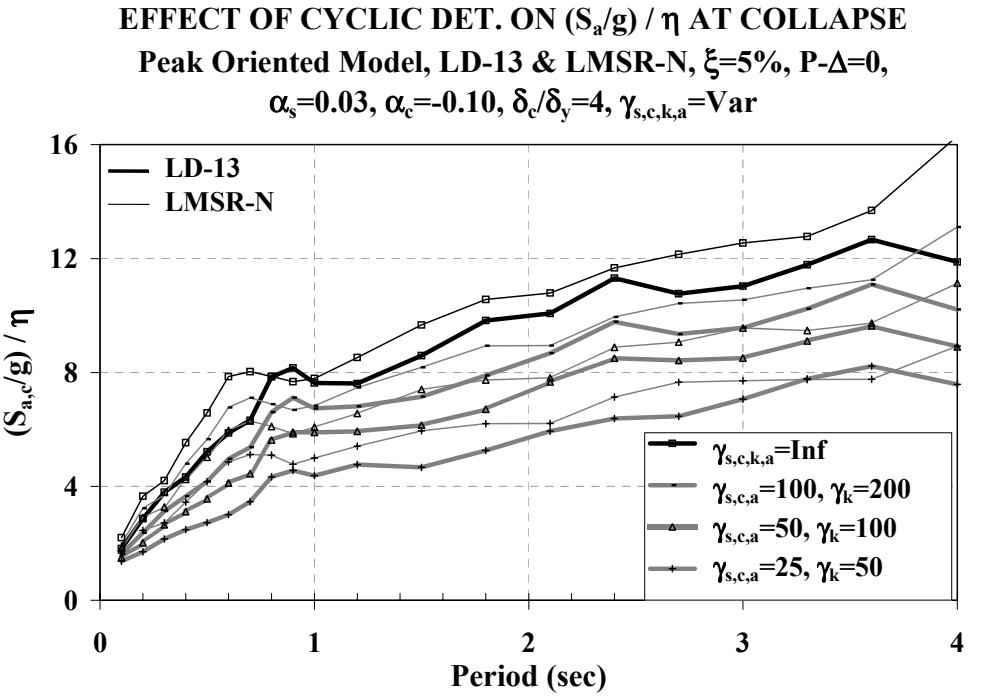

Fig. 4.92 Effect of CD on $(S_{a,c}/g)/\eta$ for systems subjected to sets of GM with different strong motion duration

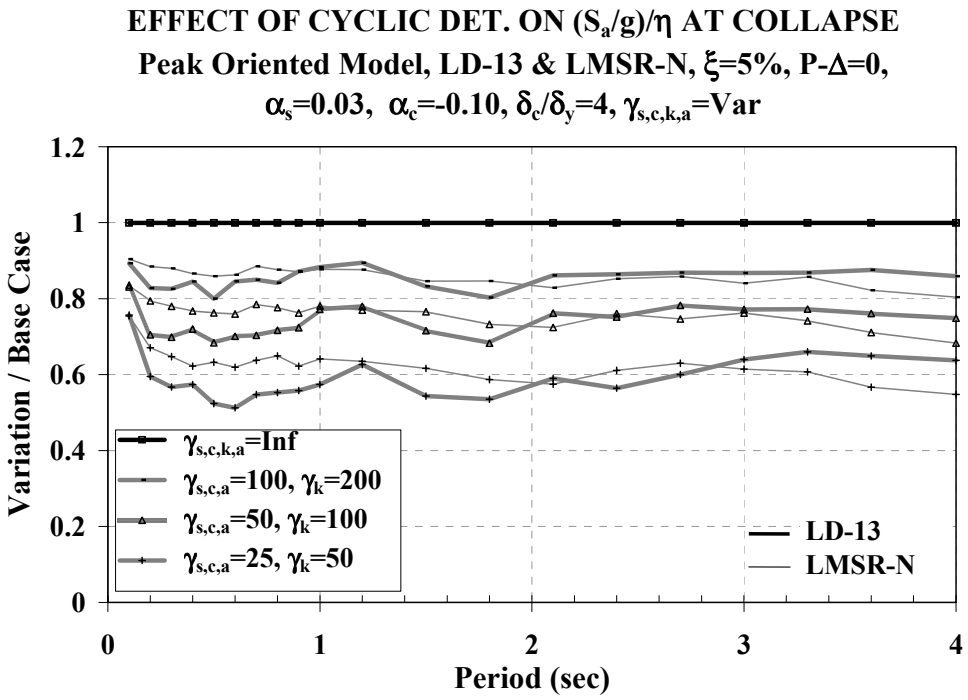

Fig. 4.93 Effect of CD on median collapse capacity ratios for systems subjected to sets of GM with different strong motion duration

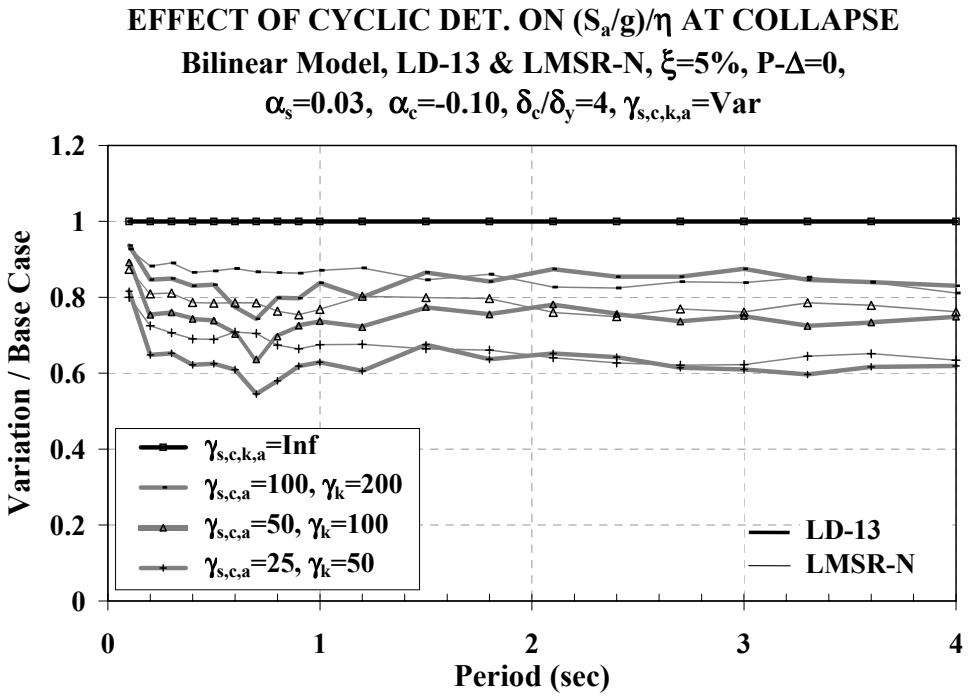

Fig. 4.94 Effect of CD on median collapse capacity ratios for systems subjected to Sets of GM with different strong motion duration, bilinear models

5 Global Collapse of MDOF Systems

5.1 INTRODUCTION

In MDOF structures collapse refers to the loss of ability to resist gravity loads. Collapse is local if one or several components carrying vertical load fail without compromising the stability of the whole system. Global collapse may occur by propagation of local collapses, often termed "progressive collapse" (Liu et al. 2003; Kaewkulchai and Willamson, 2003). In this study, global collapse implies dynamic instability in a side-sway mode, usually triggered by large story drifts that are amplified by P-Δ effects and deterioration in strength and stiffness.

Several investigations have focused on the topic of global collapse due to P-Δ effects. For instance, Bernal (1992) evaluated the safety against dynamic instability of two-dimensional non-deteriorating frames based on the reduction of a multi-story building to an equivalent SDOF system. The results indicated that the minimum base shear capacity needed to withstand a given ground motion without collapse is strongly dependent on the shape of the controlling mechanism. Gupta and Krawinkler (1999) evaluated the performance of steel moment-resisting frames (MRFs) in the SAC project. They concluded that P-Δ effects could lead to global collapse of the structures due to the development of a negative post-yielding stiffness in specific stories of the frame. Medina (2002) reached the same conclusions by evaluating non-deteriorating generic frames with different number of stories and different periods.

Most of the previous investigations of global collapse of MDOF systems focus on geometric nonlinearities (P-Δ effects), but few systematic studies have taken into account deterioration of strength and stiffness in the nonlinear range. Two exceptions are the works of Lee and Foutch (2001) and Jalayer (2003) (see Chapter 2). In this chapter, global collapse of generic frames is evaluated for systems including nonlinear behavior by means of concentrated plasticity. The building models utilize rotational springs that include deterioration of strength in the backbone curve and cyclic deterioration. The procedure for evaluating collapse capacity is

similar to that implemented for SDOF systems, i.e., the relative intensity is increased until the relative intensity–EDP curve becomes horizontal. The collapse capacity is expressed in terms of the maximum relative intensity the frame can withstand prior to collapse.

5.2 COLLAPSE CAPACITY OF MDOF SYSTEMS

The general procedure for computing collapse capacity has been described in Section 2.3. Global collapse is obtained by increasing the relative intensity, $[S_a(T_1)/g]/\gamma$, of the structure until the response of the system becomes unstable. $S_a(T_1)$ is a measure of the intensity of the ground motion and corresponds to the 5% damped spectral acceleration at the fundamental period of the structure, without P-Δ effects. γ is a measure of the strength of the structure and is equivalent to the base shear coefficient[12], $\gamma = V_y/W$, where V_y is the yield base shear without P-Δ effects and W is the weight of the structure.

$[S_a(T_1)/g]/\gamma$ represents the ductility dependent response modification factor, which in present codes is equal to the R-factor if no overstrength is present. $[S_a(T_1)/g]/\gamma$ may be interpreted in two ways; either keeping the ground motion intensity constant while decreasing the base shear strength of the structure (the R-factor perspective), or keeping the base shear strength constant while increasing the intensity of the ground motion, i.e., the IDA perspective[13] (Vamvatsikos and Cornell, 2002).

In MDOF structures, the threshold of inelastic behavior is not uniquely related to the intensity measure, $S_a(T_1)$, because the higher-mode effects are not included in the IM. Therefore, to assure elastic behavior for the lowest relative intensity, the selected initial relative intensity is chosen as $[S_{a,c}(T_1)/g]/\gamma = 0.25$. Since only bending elements are utilized in the generic frames (i.e., shear and axial failures are not modeled), collapse implies that the interstory drift in a specific story grows without bounds (incremental collapse), i.e., the $[S_a(T_1)/g]/\gamma$ - EDP curve becomes horizontal (Fig. 2.1). This large EDP increase with a minute increase in the relative intensity is associated with a state (not a mechanism in the classical sense) in which P-Δ effects become equal to the first-order story shear resistance provided by the structural elements.

[12] The nomenclature for the base shear coefficient (γ) should not be confused with that of the cyclic deterioration parameter $\gamma_{s,c,k,a}$.

[13] The dual interpretation is not correct if gravity moments are a major portion of the plastic moment capacity of the beams, and/or there are considerable changes in column axial forces due to overturning moments, as compared to the gravity induced axial forces in columns.

Collapse may occur in a single story or in a set of stories. An evaluation of the time history response data shows that for the generic frames used in this study, collapse usually occurs in the lower stories (mostly in the bottom story) of the structure.

Note that collapse is not associated with attaining zero strength in any of the structural elements. At some plastic hinge locations the bending resistance may have deteriorated to zero long before global collapse occurs. Zero bending resistance means that the "plastic hinge" responds like a natural hinge, since it is assumed that the element has sufficient shear capacity to prevent local gravity load collapse.

The relative intensity of the last point of the $[S_a(T_1)/g]/\gamma$ - EDP curve is the "collapse capacity" associated with the structural system and ground motion. Collapse capacity is expressed as $\{[S_a(T_1)/g]/\gamma\}_c$ or in a simpler form as $[S_{a,c}(T_1)/g]/\gamma$. For a system of given strength (γ), $S_{a,c}(T_1)/g$ represents the ground motion intensity leading to collapse, and for a given S_a value (hazard level), γ_c represents the strength threshold at incipient collapse. In the following discussion the emphasis is on median values of collapse capacity, which can be determined for different system parameters to assess the collapse sensitivity to deterioration properties of the structural system.

The dynamic nonlinear analyses for evaluating collapse capacity are performed with a modified version of DRAIN-2DX (1993) that includes the component deterioration models developed in this investigation (see Chapter 3). DRAIN-2DX does not update the geometric stiffness matrix in a THA and, consequently, it does not take into account large displacement effects. However, this limitation does not greatly affect the collapse capacity results. Adam and Krawinkler (2003) considered an updated Lagrangian element to include large displacements in the frames of this study by utilizing the OpenSees platform (OpensSees, 2002). They concluded that for standard frame configurations, large displacement considerations (including member P-δ) have no discernible effect on the seismic response up to incipient dynamic instability.

5.3 MDOF SYSTEMS USED FOR COLLAPSE EVALUATION

5.3.1 Basic Characteristics of Generic Frames

The MDOF systems of this study are two-dimensional regular generic frames of a single bay and several stories and are based on the models developed by Medina (2002). The frames include

rotational springs with deterioration in strength and stiffness. Their basic characteristics are the following:

- The frames have six different number of stories, $N = 3$, 6, 9, 12, 15, and 18 (Fig. 5.1).
- The fundamental period of the structure is associated with the number of stories. "Stiff frames" have a fundamental period $T_1 = 0.1N$, whereas "flexible frames" have $T_1 = 0.2N$. These values are considered to be reasonable lower and upper boundaries for moment-resisting frames. The overlap of the fundamental periods at $T_1 = 0.6$ s, 1.2 s, and 1.8 s allows assessing of the effects of N on the response.
- The same moment of inertia is assigned to the columns in a story and the beam above them.
- Relative element stiffnesses are tuned to obtain a straight line deflected shape for the first mode. Absolute stiffnesses are tuned to obtain the aforementioned periods.
- The strength design of the frames is such that simultaneous yielding is attained under a parabolic load pattern (NEHRP, $k = 2$).
- Centerline dimensions are used for all elements.
- The ratio of span to story height is 2.0.
- The same mass is used at all floor levels.
- The effect of gravity load moments on plastic hinge formation is not included.
- Global P-Δ is included, whereas member P-δ is disregarded. The mass used to consider P- Δ effects is 1.4 times larger than the seismically effective mass. That is to say, P is the dead load plus a live load equal to 40% of the dead load.
- Axial deformations and P-M-V interaction are not considered.
- Soil-structure interaction is neglected.
- For nonlinear dynamic analyses, 5% Rayleigh damping is assigned to the first mode and to the mode at which the cumulative mass participation exceeds 95%.
- Gravitational loads are applied at the beginning of the time history. The geometric stiffness matrix (K_g) is then calculated, added to the elastic stiffness matrix (K_e) and kept constant throughout the time history.
- Failure modes: In most cases, the strong column–weak beam philosophy is considered and the columns are modeled with infinite strength (BH frames) (Fig. 5.2). In Section 5.6 the columns are modeled with finite strength (BH-CH, i.e., beam hinge model with

possible yielding of columns). Springs are added to the ends of all the columns to permit plastic hinging in the columns. A weak first-story mechanism (WS) is also modeled.

Appendix B provides more information on the basic characteristics of the generic frames.

5.3.2 Deteriorating Characteristics of Plastic Hinge Springs of Generic Frames

To obtain a consistent evaluation of collapse capacity, the same deteriorating hysteretic model is assumed at every plastic hinge of the generic frames. A set of reference frames[14] with rotational springs of intermediate ductility is used as a starting point. In these frames, the parameters for the moment-rotation relationship at the ends of the members are as follows:

- Strain-hardening stiffness, $\alpha_{s,mem} = 0.03\ K_e$
- Small post-capping stiffness, $\alpha_{c,mem} = -0.1\ K_e$
- Medium ductility capacity, $(\delta_c/\delta_y)_{,mem} = 4$
- No cyclic deterioration (CD), $(\gamma_{s,c,k,a})_{mem}$ = infinite
- Peak-oriented hysteretic model

For reasons described in Appendix B, the elastic stiffness of members with concentrated plasticity is divided into the elastic stiffness of the rotational springs at the end of the member and the elastic stiffness of the beam-column element. Independently of these internal manipulations, the properties of the "springs" in the rest of this chapter refer to the moment-rotation relationship at the end of the member. The nomenclature is simplified and, for instance, $\alpha_{c,mem}$ becomes α_c.

For assessing the effect of different parameters, each parameter is varied individually while holding all others constant. The selection of parameters to be evaluated is primarily based on the results of the parametric study of SDOF systems. Parameters that do not have a large effect on the collapse capacity of SDOF systems are disregarded, i.e., residual strength and the level of pinching ($\kappa_{f,d}$). The emphasis is on those parameters that produce larger modifications to collapse capacity:

[14] A "set of frames" refers to the group of frames of 3, 6, 9, 12, 15, and 18 stories for $T_1 = 0.1N$ and $T_1 = 0.2N$ that share common characteristics in the springs of the members.

Post-capping stiffness ratio, α_c = -0.1, -0.3, and -0.5.

- Ductility capacity, δ_c/δ_y = 2, 4, and 6.
- Cyclic deterioration, $\gamma_{s,c,k,a}$ = 25, 50, 100 and infinite.
- Hysteretic models. Peak-oriented, pinching, and bilinear models.

Table 5.1 shows the sets of generic frames analyzed. Note that it includes a set of frames in which the variation is not related to the springs but to the P-Δ effects (cases 3 and 14).

5.3.3 Set of Ground Motions

The parametric study utilizes the set of 40 GMs used for SDOF systems, LMSR-N (Section 4.2.3). The intensity measure is the 5% damped spectral acceleration at the first mode period of the structure, $S_a(T_1)$. This choice implies that the frequency content of the ground motion cannot be considered explicitly and that the fundamental period of the structure is known. For this reason, the dispersion in the response depends on the importance of higher mode effects (scatter for $T < T_1$) and on the extent of inelasticity, which leads to period elongation (scatter for $T > T_1$).

Sections 5.4–5.7 summarize the salient findings for generic frames. The titles of the presented figures contain the following additional information as compared with the titles for SDOF systems: number of stories of the frame (*N)*, and failure mechanism (BH, BH-CH (see Section 5.3.1). A four-digit code is used for identifying the generic frames. The first two digits correspond to the number of stories and the other two to the first mode period. For instance, 0918 means a 9-story frame with T_1 = 1.8 s.

5.4 EDPS FOR GENERIC FRAMES WITH INFINITELY STRONG COLUMNS

5.4.1 Effect of Deterioration Parameters on EDPs

The assessment of several EDPs prior to collapse provides information on the effect of deterioration parameters on the response. The EDPs analyzed are:

- Normalized maximum roof drift angle, $\theta_{r,\max}/[S_d(T_1)/H]$, where H is the total height of the frame
- Normalized maximum story drift over the height, $\theta_{s,\max}/[S_d(T_1)/H]$
- Normalized maximum story drift profiles, $\theta_{si,\max}/[S_d(T_1)/H]$

- Maximum of story drift over story yield drift over the height, $(\theta_{si,\max}/\theta_{i,y})_{\max}$. The yield story drift ($\theta_{i,y}$) is obtained from a pushover analysis. Intentionally, this quantity is not referred to as "maximum story ductility." Traditionally, the term "ductility" refers to the ability of a component or a system to displace inelastically *without significant deterioration* in strength or stiffness. For non-deteriorating systems, this definition can be associated with the maximum story drift over the story yield drift. However, for deteriorating systems, the ratio $\theta_{si,\max}/\theta_{i,y}$ does not represent ductility because $\theta_{si,\max}$ may be associated with a large deterioration in strength.

Normalized maximum roof drift angles and normalized maximum story drift over height for the reference frame 0918 are presented in Figure 5.3, with the latter ones exhibiting much larger dispersions. The statistical curves for the same frames with non-deteriorating springs ("non-deteriorating frames") are also shown. As observed, the statistical results for deteriorating systems start to deviate from those of non-deteriorating systems at relative intensities clearly smaller than the collapse capacities.

Profiles of the normalized maximum story drift angle at several relative intensities are presented in Figure 5.4 for the reference and non-deteriorating frames 0918. The profiles describe the distribution of damage over the height of the structure. For elastic or close to elastic behavior, the maximum story drift angles occur in the upper portion of the frame. As the relative intensity level increases, the maximum story drift angle migrates from the top story to the bottom one. As observed, the profiles at low relative intensities are similar for both frames. However, the migration of the maximum story drift angle from top to bottom occurs earlier for the deteriorating model when collapse is close, e.g., compare the profile for the non-deteriorating frame at $[S_a(T_1)/g]/\gamma = 6.0$ with that of the reference frame at $[S_a(T_1)/g]/\gamma = 5.5$.

Effect of Post-capping Stiffness on EDPs. The effect of the post-capping stiffness of the beam springs on the ratio $(\theta_{si,\max}/\theta_{i,y})_{\max}$ is presented in Figure 5.5 for the 0918 frame. The frame with α_c = -0.10 corresponds to the reference frame. All the systems have the same response until the cap deformation (δ_c) of the springs is reached. The relative intensity at which this occurs is slightly less than $[S_a(T_1)/g]/\gamma = 2.0$, which is less than half of the collapse capacity, even for frames with steep post-capping stiffness (α_c = -0.30 and –0.50). Because of moment redistribution, there is an increase of at least 100% from the intensity at which the springs start to

deteriorate in strength to the intensity at which collapse occurs. This behavior is not observed in SDOF systems with steep α_c, where collapse occurs soon after the peak strength is reached. The ratios $(\theta_{si,\max}/\theta_{i,y})_{\max}$ for systems with α_c = -0.30 and –0.50 are very similar, a common phenomenon when comparing systems with steep negative slopes.

The ratios $(\theta_{si,\max}/\theta_{i,y})_{\max}$ at which the curves start to deviate from each other is about 2.5. As expected, this value is smaller than the ductility capacity of the rotational springs because not all of the springs yield at the same time.

Effect of Component Ductility Capacity on EDPs. Figure 5.6 shows $(\theta_{si,\max}/\theta_{i,y})_{\max}$ ratios for frames 0918 that have different ductility capacity in the rotational springs but the same α_c = -0.10. The frame with δ_c/δ_y = infinite corresponds to the non-deteriorating one, whereas the system with δ_c/δ_y = 4 is the reference case. Variations in the ductility capacity of the beam springs produce differences in the median response at $[S_a(T_1)/g]/\gamma < 2.0$.

Effect of Cyclic Deterioration on EDPs. Figure 5.7 presents the effect of CD on the ratios $(\theta_{si,\max}/\theta_{i,y})_{\max}$. The frames have springs with δ_c/δ_y = 4, α_c = -0.10 and different rates of CD. The story ductilities over the height for the non-deteriorating frame are also displayed. For frames with springs having finite $\gamma_{s,c,k,a}$ values, the curve $(\theta_{si,\max}/\theta_{i,y})_{\max} - [S_a(T_1)/g]/\gamma$ deviates from that of the non-deteriorating frame before the peak-strength of the springs is attained. However, the effect becomes significant only after the peak strength is surpassed.

5.4.2 Global Pushover Curves for Deteriorating Systems

The pushover method estimates force and deformation demands using a static incremental, inelastic analysis (Lawson et al., 1994; Krawinkler and Seneviratna, 1998). In this work, the method is used to study the behavior of deteriorating systems.

Figure 5.8 presents a comparison of global pushover curves for the non-deteriorating and the deteriorating reference frame 0909 when a parabolic lateral load pattern (NEHRP, k = 2) is applied to the system. For both systems the global strain-hardening stiffness is larger than in the beam springs (α_s = 0.04 vs. 0.03). For the deteriorating system the global "ductility capacity" (drift at onset of deterioration divided by yield drift) is smaller (3.0 vs. 4.0) and the global post-capping stiffness is steeper (α_c = -0.34 vs. –0.10) than in the beam springs. Also, for large

deformations there is a third post-yielding branch that indicates an apparent "recovery" in the stiffness of the global pushover curve. These observations deserve explanation.

One contributor to these differences is the fact that columns remain elastic throughout the pushover analysis. Thus, initial displacements, which define the elastic stiffness, come from elastic contributions of beams and columns. After the simultaneous yielding of the beam springs in the pushover analysis (because of the assumptions discussed previously), the incremental displacements in the global pushover curve contain deformations from beams (beam elastic deformations and plastic hinge spring deformations), and elastic deformations from columns. These elastic deformations in columns account for the increase in the effective α_s, part of the increase in α_c, and the decrease in δ_c/δ_y of the global pushover curve.

There is an additional phenomenon of inelastic redistribution that may affect the pushover curve (and dynamic time history results) at large inelastic deformations. If P-Δ effects are small and no strength deterioration occurs, the generic frames are expected to take on a deflected shape close to a straight line under a parabolic load pattern, regardless of the level of displacement. This is illustrated in Figure 5.9a for the non-deteriorating 1818 frame. This does not hold true when P-Δ effects are important (i.e., when they lead to a negative story tangent stiffness); see the deflection profiles of the 1836 frame in Figure 5.9b. In this frame the P-Δ effect amplifies the story drifts in the lower stories, which results in highly nonlinear deflected shapes with very large drifts in the lower stories and unloading (decrease in story drifts) in the upper stories.

Post-capping strength deterioration has a similar effect as P-Δ. Figure 5.10 shows deflected shapes associated with the roof drifts indicated with dotted vertical lines in Figure 5.8. Without post-capping strength deterioration, the deflected shapes remain essentially linear even though P-Δ (which is small for the 0909 frame) is included (Fig. 5.10a). When strength deterioration is included, the deflection profiles acquire a very different shape with great amplifications of drifts in the lower stories (Fig. 5.10b). This radical change in deflected shape occurs when the loading path is on the descending branch of the pushover curve. This change in deflected shape is the main reason for the difference between the α_c = -0.10 of the component model and the effective α_c = -0.34 seen in the global pushover.

The same phenomenon also accounts for the "recovery" portion of the pushover curve at very large drifts. This recovery portion comes from the fact that the lower portion of the frame

has undergone very large horizontal displacements and the global bending mode (i.e., the cantilever bending mode) of the infinitely strong columns starts to dominate over the effect of frame action. This is illustrated in Figures 5.11–5.12.

Figure 5.11 shows moment-rotation diagrams for beams at each floor level, from zero load to three load points, which are indicated in Figure 5.8 as "A," "B," and "C." At load point A (δ_r/δ_{yr} = 3.1, beginning of deterioration), all springs at the beam ends, bottom to top, as well as at the column base, are close to their capping points [$(\delta_c/\delta_y)_{elem}$ = 4] and the deflected shape is still close to linear. As the roof displacement increases further, the beams close to the bottom of the structure undergo large rotations and deteriorate rapidly in strength whereas the beams close to the top unload (since the lateral loads on the frame decrease). At point B (δ_r/δ_{yr} = 5.3) the column springs at the base and the second-story beam springs are at zero strength, and the global resistance of the structure has deteriorated to about $0.4V/V_y$. As the roof displacement is increased further, the springs at level 3 lose all their resistance and beam-moment deterioration propagates upward in the structure. This is also reflected in the deflection profiles of Figure 5.10.

Despite the complete loss of resistance in the bottom level springs, the structure still has some lateral resistance left because of the global bending strength of the columns. Only the strength at the column base is capped and subjected to deterioration, whereas the columns at all other locations have infinite strength. The moment–roof drift relationships of Figure 5.12 illustrate the transfer of resistance to the columns. In the first story, both the base of the columns and the beam reach their bending capacities and thereafter their strength deteriorates to zero, whereas the first-story column moment at level 2 (where the strength is infinite) increases even after the column base starts to deteriorate in strength. For lower-story columns, once the associated beam starts to deteriorate in strength, the column moment at the top of the story increases, whereas the column moment at the bottom of the same story decreases and reverses direction, taking large values opposite to the direction of frame action. Thus, for very large displacements the columns in the lower stories go into single curvature with large moments at both ends, i.e., the column acts more as a multi-story cantilever than a column in a moment-resisting frame. This observation has been reported elsewhere (Gupta and Krawinkler, 1999; Medina, 2002).

As can be seen from Figure 5.12, the column moments can become very large compared to the value when the beam reaches its bending strength. The implication is that the strong column–weak beam factor would have to be very large (larger than 3.0) in order to avoid column

plastic hinges at very large lateral displacements. The strong columns are responsible also for the stiffness recovery in the late stages of the global pushover curve shown in Figure 5.8. It is likely that such strong columns do not exist in actual frame structures, which makes the data presented here somewhat hypothetical. They are represented to evaluate and explain behavior from a mechanics perspective, but they have no significant bearing on the results presented for collapse capacities. The very large column moments occur at very large drifts, and an evaluation of the collapse capacities has disclosed that at these large drifts almost all IDAs have close to a horizontal slope, i.e., these phenomena dominate only close to collapse. The effect of limited column bending strength is discussed separately in Section 5.6.

5.4.3 De-Normalized EDPs

To illustrate "realistic" values for collapse capacities and associated drifts, the $[S_{a,c}(T_1)/g]/\gamma -$ EDP curves of the type shown in Figure 5.4 are de-normalized for several reference frames by assuming a base shear strength $\gamma = 0.6$, 0.6, 0.4, and 0.2 for periods of $T_1 = 0.3$, 0.6, 0.9, and 1.8 s, respectively.

Figures 5.13–5.14 present IDAs for maximum roof drift angle $[S_a(T_1)/g - \theta_{r,max}]$ for the reference frames 0303, 0306, 0909, and 0918. Note that most of the individual IDAs become almost horizontal at relatively small roof drifts, i.e., the large collapse roof drifts reported in the SAC studies (FEMA 350, 2000) are not observed here. One reason is that the elastic period of the SAC structures is even longer than that of the "flexible" structures used here, i.e., the yield drifts of the SAC structures are somewhat larger. However, most of the difference is attributed to the representation of component moment-rotation relationships using more realistic deterioration models in this study. Observe that the median EDP curves give the impression that the intensity increases at a rather high rate until the median curve terminates. This is not observed in the IDAs of individual records in which the rate of increase in intensity becomes small much earlier.

The figures also include the global pushover curves for each frame. The base shear strength of the global pushover curve is normalized by the inverse of the effective mass coefficient of the first mode to obtain an approximate correlation with $S_a(T_1)$. The correlation is not exact in the elastic range due to the effect of higher modes in the response. For the 9-story frames, the onset of the third post-yielding branch of the global pushover curves approximately

coincides with the EDP region in which most of the individual curves become flat, and could be considered as an indication of the roof drift at which collapse occurs.

Figure 5.15 presents the variation with relative intensity of the median $\theta_{s,max}/\theta_{r,max}$ ratio for several reference frames. This information can be used to estimate the maximum interstory drift based on the IDAs of Figures 5.13–5.14. For instance, for the 0918 frame of Figure 5.15, for which the individual IDAs become horizontal around a roof drift of 0.04, the associated maximum story drift is on the order of $2x0.04 = 0.08$.

5.5 COLLAPSE CAPACITY OF GENERIC FRAMES WITH INFINITELY STRONG COLUMNS

5.5.1 Collapse Capacity for the Set of Reference Frames

Figure 5.16 shows median and 16th percentile collapse capacity spectra for the set of reference frames. Collapse capacities are grouped in stiff ($T_1 = 0.1N$) and flexible ($T_1 = 0.2N$) frames. The collapse capacity strongly depends on the first mode period T_1. This is expected for the short-period structure with $T_1 = 0.3$ s, where the collapse capacity is much smaller than that for $T_1 = 0.6$ s. But the large decrease in collapse capacity for long-period structures is striking, indicating that the "period independent *R*-factor concept" may be way off for long-period structures, i.e., it would be non-conservative to assume that *R* is independent of *T*. The reason is the P-Δ effect, which is more important than might be expected.

The sensitivity to the number of stories is analyzed by comparing collapse capacity spectra for flexible and stiff frames with the same fundamental period (Fig. 5.16). In a vertical comparison, the frames have the same fundamental period and a different number of stories, e.g., 0306 and 0606. In the period range between $T = 0.6$ s and 1.5 s frames with more stories have larger collapse capacities for the same fundamental period. One of the reasons for this pattern is that frames with more stories have smaller P-Δ effects. However, the differences are 15% at most and for long fundamental periods the trend may be reversed (see frames 0918 and 1818), likely because of higher-mode effects or different influences of deterioration parameters on collapse capacities.

The effect of P-Δ is also appreciated in Figure 5.17, which shows collapse capacities versus the number of stories for flexible and stiff frames. Except for short-period frames, collapse capacities of stiff frames are larger (especially at long periods) because P-Δ effects are

smaller for these frames. The trend is reversed for the three-story frames because P-Δ effects are small and the displacements are more sensitive to the strength of the system, causing the structure with shorter fundamental period to have the smaller collapse capacity.

5.5.2 Effect of Post-Capping Stiffness on Collapse Capacity

The effect of the post-capping stiffness is isolated in Figure 5.18a, which shows median collapse capacities for frames similar to the reference frame but with different α_c values. There is a large difference between the collapse capacities for systems with α_c = -0.1 and -0.3. However, if α_c represents a steep slope, any further increase in slope has only a small effect because the component reaches zero strength soon after δ_c is reached. Figure 5.18b presents the collapse capacity ratios with respect to the most ductile system (the reference frame). The larger differences arise in the medium-period range, where ratios smaller than 0.7 are reported. This information may be compared with the ratios of Figure 4.12b, which presents collapse capacity ratios for SDOF systems with the same hysteretic properties as those of the springs at the beam ends of the frames. Although the P-Δ effects are not properly represented in the SDOF systems, the effect of post-capping stiffness on collapse capacity of SDOF and MDOF systems is comparable.

Figure 5.18c shows the dispersion in collapse capacity due to RTR variability in terms of the standard deviation of the log of $[S_{a,c}(T_1)/g]/\gamma$. The dispersion is not sensitive to the fundamental period of the frame and, although rather large, is smaller than that of the SDOF systems with the same hysteretic properties as the springs at the beam ends (Fig. 4.19a). The dispersion of collapse capacity is not greatly affected by changes of the α_c value of the springs of the reference frame. The same conclusion is obtained when the ductility capacity and the CD parameters are modified.

5.5.3 Effect of Ductility Capacity on Collapse Capacity

The effect of ductility capacity (δ_c/δ_y) on the median collapse capacity is illustrated in Figure 5.19a for systems with α_c = -0.10. The effect of δ_c/δ_y is significant and, as observed in the collapse capacity ratios of Figure 5.19b, essentially independent of the fundamental period of the structure or the number of stories of the frame. The collapse capacity ratios may be compared

with those of the SDOF system with the same hysteretic characteristics of the springs of the frames (Fig. 4.23b). The same trends are observed, although the ratios of the generic frames are slightly larger (closer to 1.0), indicating a smaller effect in the MDOF systems.

Figure 5.20 presents the effect of δ_c/δ_y for systems with α_c = -0.30. The steeper post-capping slope reduces the collapse capacities but increases the effect of δ_c/δ_y because collapse occurs relatively soon after δ_c is reached. That is to say, a larger proportion of the collapse capacity must be developed before the peak strength is surpassed.

5.5.4 Effect of Cyclic Deterioration on Collapse Capacity

Figure 5.21 illustrates the effect of CD on the collapse capacity of frames similar to the reference one but with different CD rates in the springs. The effect of CD is evident, although not overpowering, indicating that the combination of ductility capacity and post-capping stiffness is more important than the CD effect. The effect diminishes for long-period structures because of the dominant importance of P-Δ effects. Collapse capacity ratios of Figure 5.21b may be compared with those of Figure 4.28b for an SDOF system with the same hysteretic characteristics of the springs at the ends of the beams. It is observed that CD effects are larger for SDOF systems because these do not have redistribution capabilities.

The utilized set of GMs (LMSR-N) includes records with relatively short strong motion duration. However, according to the study of long-duration records for SDOF systems (Section 4.4.5), a large increase in the effect of CD on collapse capacity is not expected if a set of records with longer strong motion duration is used. Thus, CD appears to be an important but not dominant issue for collapse evaluation, unless the energy-dissipation capacity of the structural components is very small (γ= 25).

5.5.5 Effect of Hysteretic Models on Collapse Capacity

Figure 5.22 shows collapse capacity spectra for frames with peak-oriented, pinching, and bilinear models in the plastic hinge springs. The results indicate that frames with peak-oriented and pinching models have similar collapse capacities. On the other hand, the relative collapse capacities of frames with bilinear models present the same patterns as observed in SDOF systems. For MDOF systems with very small fundamental period the collapse capacity of frames

with bilinear springs is slightly larger than that of frames with peak-oriented or pinching springs. However, for frames with medium and long fundamental periods the trend reverses because the branch with negative slope in the plastic hinge springs has a larger "ratcheting" effect in bilinear models (Section 4.3.7).

5.5.6 Effect of P-Δ Effects on Collapse Capacity

Present engineering approaches have the potential to underestimate P-Δ effects, particularly for long-period structures where the elastic story stability coefficient (θ_e) severely undervalues the P-Δ effect in the inelastic range. In most practical cases the lower stories experience large drifts when the structure undergoes large inelastic deformations, and the story stability coefficient increases correspondingly.

P-Δ effects may produce collapse of the structures even without the inclusion of material deterioration. Figure 5.23 presents global pushover curves for the reference frame 1836 with and without including P-Δ effects. As observed, different stability coefficients exist for the elastic (θ_e) and inelastic ranges (θ_i). Figure 5.24a presents these coefficients for the generic frames. Both the elastic and the inelastic stability coefficients increase with the number of stories and depend on the strain hardening of the nonlinear elements, which for this study is 3% [15]. For stiff frames, θ_e and θ_i practically overlap, but for flexible frames with a large number of stories θ_i can be much larger than θ_e. As a result of the increase in both coefficients with the number of stories, the flexible frames of 9, 12, 15, and 18 stories exhibit a negative post-yield stiffness due to structure P-Δ effects (Fig. 5.24b). This negative post-yielding stiffness can be associated with eventual collapse of the frame under large relative intensities, even if non-deteriorating models are used. Note that the non-deteriorating frame 1818 does not exhibit a negative slope. As shown below, this frame does not collapse due to P-Δ, unlike non-deteriorating frames 0918 and 1836. This illustrates that the magnitude of P-Δ effects cannot be linked to some particular characteristic of the system such as the fundamental period or the number of stories.

Figure 5.25 presents median collapse capacities for the reference and for the non-deteriorating set of flexible frames. For non-deteriorating frames, collapse is caused solely by P-

[15] The strain-hardening coefficient of the global pushover curve ($\alpha_{s,0}$) is larger than 3% because the columns of the frame remain elastic.

Δ effects. As observed, for the 9-story frames (T_1 = 1.8 s) the collapse capacity of the non-deteriorating system is more than three times larger than that of the reference frame. However, for the 18-story frames (T_1 = 3.6 s.), P-Δ effects overpower the effect of material deterioration, and the collapse capacity of the non-deteriorating frame is only 40% larger than that of the reference frame. For non-deteriorating frames, the potential of collapse exists if the slope of the post-yielding slope in the global pushover curve is negative. Observe the strain-hardening slope of global pushover curves (Fig. 5.24b) and collapse capacities of non-deteriorating frames (Fig. 5.25).

To show the effect of P-Δ on collapse capacity, Figure 5.26 presents collapse capacities for the set of reference frames without and with P-Δ effects. As expected, the effects of P-Δ on collapse capacity are very large for long-period flexible structures. However, the important observation is that the effects of P-Δ on collapse capacity apparently are also very large for medium and even short period structures in which both the elastic and inelastic stability coefficients are small (Fig. 5.24a). The reason is that components of deteriorating structures have a range of post-capping negative tangent stiffness, which leads to a negative story and global tangent stiffness range, which in turn is amplified (steeper) by even small P-Δ effects. This is evident in the global pushover curves of Figure 5.27, which shows global pushover curves without and with consideration of P-Δ for the 1212 reference frame. If P-Δ is ignored in the analysis, the ratcheting effect in the negative stiffness range is greatly reduced and very large displacements can be achieved without collapse. The consequence is a very large overprediction of the collapse capacity. The conclusion is that any realistic prediction of collapse capacity must incorporate P-Δ effects.

5.6 RESULTS FOR GENERIC FRAMES WITH COLUMNS OF FINITE STRENGTH

The generic frames evaluated in previous sections include infinitely strong columns, an assumption that may lead to demands in the columns several times larger than those of the beams. This condition can be quantified by means of the maximum “strong column factor” (SCF), which for beam-hinge frames can be defined as the sum of the maximum moment demands of the columns framing into a joint divided by the sum of the plastic moment capacity of the beams framing into the joint. For single-bay generic frames, the SCF at any joint is equal

to $(2M_c/M_{p,b})_{max}$, where $M_{b,p}$ is the bending strength of the beam, and M_c is the largest column moment demand occurring during the THA). Figure 5.28 shows maximum SCF over the height for the stiff 9-story reference frame, revealing that close to collapse the median SCF is on the order of 3 or more. These values establish an upper bound because they are based on the maximum negative or positive moment of the columns that frame into the joint. The fact that the SCF increases with the intensity of the GM is in accordance with results reported by Nakashima and Sawaizumi (2000) and by Medina (2002).

In practical cases the column strength is limited, even if the strong column–weak beam philosophy is utilized. To evaluate the collapse capacity when the columns yield before reaching the large demands displayed in Figure 5.28, the column strengths of selected frames have been tuned, taking as reference Section 21.4.2.2 of ACI 318-02 (2002). This section establishes that for reinforced concrete members framing into a joint, $\sum M_c \geq 1.2\sum M_g$, where $\sum M_c$ is the sum of the moment capacity of the columns framing into the joint and $\sum M_g$ is the sum of the moment capacity of the beams. The frames that are designed with the strong column–weak beam philosophy with the possibility of yielding in the columns are denoted as BH-CH models, and are classified as follows:

(a) Frames with columns of "high strength": $\sum M_c = 2.4\sum M_g$, i.e., the strength of the columns is twice the minimum ACI guidelines ($M_c = 1.2M_g$ for the generic single-bay frames);

(b) Frames with columns of "intermediate strength": $\sum M_c = 1.2\sum M_g$, i.e., minimum strength ACI requirements ($M_c = 0.6M_g$ for the generic frames); and

(c) Frames with columns of "low strength": $\sum M_c = 1.0\sum M_g$, i.e., less than ACI requirements ($M_c = 0.5M_g$ for the generic frames).

A special case is derived from frames with first-story columns of low strength, in which all columns and beams are infinitely strong with the exception of the first-story columns. This arrangement leads to a weak first-story mechanism (WS).

Figure 5.29 presents the median collapse capacities for stiff and flexible reference frames of 3, 9, and 18 stories with columns of high strength, i.e., $M_c = 1.2M_{b,p}$. Because $M_c > M_{b,p}$, at any joint the beam yields first, even if the inflection point of the columns greatly shifts toward

one end. In spite of the large reserve strength in the columns, the collapse capacity of these frames may decrease up to 25% compared to that of frames with infinitely strong columns.

The same frames are analyzed using $\sum M_c = 1.2 \sum M_g$, i.e., $M_c = 0.6 M_{b,p}$. Figure 5.30 indicates that median collapse capacities for these BH-CH frames are drastically reduced with respect to those obtained for BH frames. Extensive plastic hinging in columns is observed long before the collapse capacity is attained and $[S_{a,c}(T_1)/g]/\gamma$ becomes small.

The set of frames BH-CH with the same moment capacity for beams and columns ($M_c = 0.5 M_{b,p}$) assures the development of story mechanisms. The median collapse capacities obtained for these frames (Fig. 5.31) are similar but even lower than those of BH-CH frames with $M_c = 0.6 M_{b,p}$. The median collapse capacity for frames with a weak first story is very close to that of the BH-CH model with $M_c = 0.5 M_{b,p}$, suggesting that the collapse mechanism of the analyzed generic frames for the latter two cases is usually in the first story.

The decrease in collapse capacity for frames with limited column strength is very large, but there is a caveat to consider. The generic structures used in this study have strength and stiffness properties that are tuned to a seismic load pattern and to a straight line first mode shape. This results in structures with flexible and weak upper stories, in which story mechanisms will form if plastic hinging is permitted in the columns. This may not be the case in most real structures in which the upper stories often are stronger and stiffer than needed for lateral load considerations alone. This caveat needs to be considered when interpreting the results presented here. Nevertheless, the results do demonstrate the need for a review of presently employed strong column–weak girder design criteria.

5.7 EQUIVALENT SDOF SYSTEMS INCLUDING P-Δ EFFECTS

Equivalent SDOF systems are used in current design practice to estimate the roof displacement of MDOF structures (ATC-40, 1996; Miranda, 1999; FEMA-356, 2000). Nevertheless, most of these approximations do not consider P-Δ effects in a proper manner. As observed in Figures 5.23 and 5.24a, the elastic and inelastic stability coefficients may be different when P-Δ effects become large. In these cases, a formulation based only on the elastic stability coefficient is unable to capture the inelastic response. This section presents a procedure to obtain the collapse capacity of MDOF structures based on nonlinear THA of equivalent SDOF systems including

large P-Δ effects. The basic difference with respect to current methodologies is the explicit consideration of the inelastic stability coefficient.

5.7.1 Equivalent SDOF Systems without Consideration of P-Δ Effects

The equivalent SDOF system without P-Δ effects is generated from the global pushover curve of the MDOF structure without P-Δ. Several approaches have been developed for obtaining an equivalent period and strength for the SDOF system. In this work, this equivalent system is obtained by simplified procedures because the emphasis is on equivalent SDOF systems with large P-Δ effects.

Regarding the period of the equivalent SDOF system, Seneviratna and Krawinkler (1997) observed that the first mode period T1 is a good approximation to the equivalent SDOF period T_{eq}, without considering P-Δ effects.

The ratio of the yield strength of the equivalent SDOF system to the base shear of the MDOF system can be approximated with the effective mass coefficient (ATC-40, 1996) of the first mode. This coefficient is defined as the effective modal mass over the total mass of the system, for the first mode:

$$a_{m,1} = \frac{\left(\vec{\Phi}_1^T \widetilde{M} \vec{r}\right)^2}{M\left(\vec{\Phi}_1^T \widetilde{M} \vec{\Phi}_1\right)} \tag{5.1}$$

where $\vec{\Phi}_1$ is the first mode shape of the MDOF system, $\widetilde{M}$ is the mass matrix, M is the total mass of the system, $\vec{r}$ is the influence vector representing the displacements of the masses resulting from static application of a unit ground displacement (Chopra, 1995). In the proposed procedure, the collapse capacity is obtained for the SDOF system and the results are multiplied by the inverse of the effective mass coefficient to translate them to the MDOF domain.

5.7.2 Auxiliary Backbone Curve and Stability Coefficient to Include P-Δ Effects

P-Δ Representation in SDOF Systems. In the SDOF domain, consideration of P-Δ effect implies *rotation* of the hysteresis diagram by an angle equal to the stability coefficient θ (Fig. 5.32a). For peak-oriented and pinching models, this geometric nonlinearity effect should not be replaced by an equivalent material nonlinearity effect in which the post-yield stiffness is reduced

by an angle equal to the stability coefficient (Fig. 5.32b). In the latter case the reloading stiffness branch begins at the intersection with the horizontal axis, whereas in the P-Δ case the reloading stiffness branch begins at the intersection with the rotated zero force axis. Pilot studies have shown that this early softening of stiffness of Figure 5.32b overestimates the collapse capacity of the system because the loading path tends to reduce the drifting of the displacement response ("ratcheting effect").

Also, as observed in Figure 5.32b, adjusting the post-yield stiffness does not modify the strength and stiffness in the elastic interval. As shown below, this difference is less relevant in the computation of collapse capacity than the early softening of the unloading stiffness.

Thus, P-Δ in SDOF systems should be represented by rotation of hysteresis diagrams. The question is what is the most appropriate stability coefficient (angle of rotation) to be employed. The P-Δ effect in MDOF systems depends on many aspects, including relative story strength and stiffnesses, distribution of gravity loads over the height, and extent of inelastic behavior. It can be argued that in the elastic range of response the maximum story stability coefficient is most appropriate. However, in the inelastic range the P-Δ effect grows, and its importance strongly depends on the deflected shape of the structure, which varies with the extent of inelastic behavior. Thus, the maximum elastic story stability coefficient loses much of its meaning in the inelastic range and it may underestimate the importance of P-Δ effects in MDOF systems. For instance, compare the median collapse capacity spectrum of the SDOF system (α_c = -0.10) of Figure 4.15a with that of Figure 5.16.

The search for appropriate stability coefficients in equivalent SDOF systems is a challenge partially addressed here. In this study, P-Δ effects are represented by the elastic and the inelastic stability coefficient obtained from the global pushover curve (Fig. 5.23).

Auxiliary SDOF System. As discussed in Section 5.5.6, the coefficients θ_i and θ_e are often different, but in an SDOF system the rotation applies to both the elastic and inelastic ranges. Thus, the need exists to create an auxiliary backbone curve whose rotation by an "auxiliary" stability coefficient results in the desired backbone curve including P-Δ effect, but with the constraint that the auxiliary stability coefficient should be close to θ_i. The relations between the auxiliary backbone curve and the backbone curves of the equivalent SDOF system with and without P-Δ are illustrated in Figure 5.33. The following three conditions are required to generate the auxiliary backbone and stability coefficient:

(a) The yield strength for the system with P-Δ must be the same when obtained from the original backbone without P-Δ and when obtained from the auxiliary backbone curve:

$$(1-\theta_{aux})F_{y,aux} = (1-\theta_e)F_{y,0} = F_{P\Delta} \tag{5.2}$$

The following subscripts refer to the backbone curves: "*0*" for the original backbone curve without P-Δ effects (from the global pushover curve), "PΔ" for the original backbone curve with P-Δ effects and "*aux*" for the auxiliary backbone curve.

(b) The post-yield stiffness including P-Δ effects is the same as when calculated with the auxiliary envelope or the original backbone curve:

$$(\alpha_{s,aux} - \theta_{aux})K_{aux} = (\alpha_{s,0} - \theta_i)K_0 \tag{5.3}$$

(c) The strain-hardening coefficient of the auxiliary backbone curve is the same as that of the original backbone curve, i.e.,

$$\alpha_{s,aux} = \alpha_{s,0} \tag{5.4}$$

The combination of Equations 5.2–5.4 results in the following stability coefficient, yield strength, and fundamental period for the auxiliary backbone curve:

$$\theta_{aux} = \frac{\theta_i - \theta_e\alpha_{s,0}}{1-\theta_e+\theta_i-\alpha_{s,0}}, \quad F_{y,aux} = \frac{1-\theta_e+\theta_i-\alpha_{s,0}}{1-\theta_e\alpha_{s,0}}F_{y,0}, \quad T_{aux} = T_0\sqrt{\frac{1-\alpha_{s,0}}{1-\theta_e+\theta_i-\alpha_{s,0}}} \tag{5.5}$$

For backbone curves with a small strain-hardening coefficient ($\alpha_s <$ 10%), the formulation can be condensed by assuming that the slope of the post-yield stiffness of the auxiliary backbone curve is equal to that of the original backbone curve (instead of using the same strain-hardening coefficient of Equation 5.4):

$$\alpha_{s,aux}K_{aux} = \alpha_{s,0}K_0 \tag{5.6}$$

This simplification does not lead to an appreciable loss of accuracy, and when Equation 5.6 is combined with Equations 5.2–5.3, the following expressions are produced:

$$\theta_{aux} = \frac{\theta_i}{1-\theta_e+\theta_i}, \quad F_{y,aux} = (1-\theta_e+\theta_i)F_{y,0}, \quad T_{aux} = T_0\sqrt{\frac{1}{1-\theta_e+\theta_i}} \tag{5.7}$$

This set of equations should be used with a coefficient $\alpha_{s,aux}$ obtained from Equation 5.6.

Simplified Auxiliary SDOF System. For systems with large P-Δ effects, the elastic stability coefficient is usually small compared with the inelastic one. In these cases, the formulation may admit an additional simplification in which the elastic stability coefficient is

assumed to be zero (Fig. 5.34). For the studied generic frames, this simplification may produce differences in collapse capacities in the order of 10% compared with the complete formulation. However, the approach provides flexibility to the procedure (see Section 5.7.4). Using this simplification, Equation 5.7 is adjusted as follows:

$$\theta_{aux} = \frac{\theta_i}{1+\theta_i}, \quad F_{y,aux} = (1+\theta_i)F_{y,0} \text{ and } T_{aux} = T_0\sqrt{\frac{1}{1+\theta_i}} \tag{5.8}$$

As a consequence of not including θ_e in the formulation, $F_{y,0} = F_{P\Delta}$ (Eq. 5.2), i.e., the yield strength of the backbone curve is not reduced due to P-Δ effects. Note that for peak-oriented and pinching models, neglecting the elastic stability coefficient *is not equivalent* to rotating the post-yielding branch, although the corresponding backbone curves are equal (see dotted backbone curve in Fig. 5.34).

The collapse capacities for equivalent SDOF systems, using different approaches for including P-Δ effects, are shown in Figure 5.35 for a peak-oriented non-deteriorating system. The period of the MDOF system without P-Δ effects is T_0 = 3.6 s. The curves represent collapse capacities for the following equivalent SDOF systems: (a) systems with auxiliary backbone curve based on θ_e and θ_i (θ_e is fixed at 0.09 and θ_i varies from 0.09 to 0.40; Equation 5.7 is employed to generate the auxiliary SDOF system), (b) systems with auxiliary backbone curve without considering θ_e, according to Equation 5.8, and (c) systems where only the post-yielding branch rotates based on θ_i, i.e., the incorrect P-Δ representation. If case (a) is taken as the reference one, it can be seen that case (c) greatly overestimates collapse capacities. This is evident from the comparison with collapse capacities of the auxiliary and simplified auxiliary SDOF systems [cases (a) and (b)]. The basic difference of these systems is the modification of the yield strength due to the consideration of θ_e. Observe that this modification does not significantly affect the corresponding collapse capacities.

5.7.3 Procedure to Obtain Collapse Capacity of MDOF Structures Based on Collapse Capacity of Equivalent SDOF Systems

The procedure proposed to compute the collapse capacity of non-deteriorating MDOF structures based on THA of auxiliary SDOF systems can be summarized as follows:

1. Global pushover analyses are performed for the MDOF structure with and without considering P-Δ effects to obtain the elastic and inelastic stability coefficients. It is recommended to select an inverted triangular or parabolic load pattern for this purpose.
2. The period of the SDOF system without P-Δ effects is set equal to the fundamental period of the frame without P-Δ effects. The auxiliary backbone curve and the auxiliary stability coefficient are obtained based on the elastic and inelastic stability coefficients.
3. The median collapse capacity is obtained based on the auxiliary SDOF system and the auxiliary stability coefficient. For this purpose, time history analyses are performed subjecting the auxiliary system to the selected set of GMs. The type of hysteretic model used in the nonlinear elements of the MDOF system is assigned to the equivalent SDOF system to represent the load-deformation response.
4. Collapse capacity of the MDOF structure is estimated based on the collapse capacity of the SDOF system, which is scaled up according to the inverse of the effective mass coefficient.

Alternatively, the THA of auxiliary SDOF systems (step 3) may be replaced by using $(S_{a,c}/g)/\eta - \theta_i$ curves for SDOF systems, which could be generated for several periods of interest. Once these curves are translated into the MDOF domain by means of the effective mass coefficient, the collapse capacity of the MDOF system is obtained based solely on θ_i.

5.7.4 Illustration of Procedure to Obtain Collapse Capacity of MDOF Structures Based on Collapse Capacity of Equivalent SDOF Systems

The peak-oriented non-deteriorating generic frame 1836 is used to illustrate the procedure because it is the frame with the largest P-Δ effect.

1. The global pushover curves with and without P-Δ effects are obtained by using a parabolic load pattern, which for this frame leads to a linear deflected shape in the elastic range. The reported stability coefficients are $\theta_e = 0.09$ and $\theta_i = 0.37$, and have been shown in Figure 5.23.
2. The period of the equivalent SDOF system without P-Δ effects is used as the fundamental period of the frame without P-Δ effects. Thus the data used for computing the auxiliary backbone curve are: $T_0 = 3.6s.$, $\alpha_{s,0} = 0.04$, $\theta_e = 0.09$ and $\theta_i = 0.37$. The parameters of

the auxiliary SDOF system are obtained from Equation 5.7: $\theta_{aux} = 0.29$, $T_{aux} = 3.18s.$, $F_{y,aux} = 1.28F_{y,0}$ and $\alpha_{s,aux} = 0.0313$.

3. Based on the auxiliary SDOF system and assuming a peak-oriented model, the median collapse capacity of the SDOF system is computed as $[(S_{a,c}/g)/\eta] = 2.39$.
4. The collapse capacity of the SDOF system is scaled up by the inverse of the effective mass coefficient of the first mode to obtain the MDOF collapse capacity. The effective mass coefficient for the 18-story frame is $\alpha_{m,1} = 0.77$, and the equivalent collapse capacity of the MDOF system is $[(S_{a,c}(T_1)/g)/\gamma] \cong 2.39/0.77 = 3.1$. The "exact" MDOF median collapse capacity, obtained by carrying out THA for the non-deteriorating frame 1836 is $[(S_{a,c}(T_1)/g)/\gamma] = 3.94$.

If the simplified auxiliary backbone curve is employed, Equation 5.8 is used for computing the parameters of the auxiliary SDOF system: $\theta_{aux} = 0.27$, $T_{aux} = 3.08s$, $F_{y,aux} = 1.37F_{y,0}$, and $\alpha_{s,aux} = 0.029$. The median collapse capacity of the simplified auxiliary SDOF system is $[(S_{a,c}(T_1)/g)/\gamma] = 2.59$ and the collapse capacity of the MDOF system is $[(S_{a,c}(T_1)/g)/\gamma] \cong 2.59/0.77 = 3.36$. Note that for this example the simplified auxiliary backbone curve provides a solution closer to the "exact" one.

If $(S_{a,c}/g)/\eta - \theta_i$ curves for the period of interest (T_0) were available, the collapse capacity of MDOF systems may be estimated without performing THAs. Figure 5.36 presents these curves for an SDOF system with $T_0 = 3.6$ s, which are obtained by varying θ_i and generating a simplified auxiliary SDOF system for each θ_i, according to Equation 5.8. The simplified auxiliary SDOF system provides more flexibility to the approach because the curves are not generated for a specific pair (θ_e, θ_i). As observed in Figure 5.36, the curve with collapse capacity for the SDOF system is scaled up based on the effective mass coefficient to obtain equivalent collapse capacities for the MDOF structure $[(S_{a,c}(T_1)/g)/\gamma - \theta_i]$. The coefficient θ_i obtained from the global pushover curves is used to obtain the equivalent MDOF collapse capacity. Observe that the use of θ_e would lead to a large overestimation of the collapse capacity of the MDOF system.

The procedure has been tested for several frames under different parameter variations. For instance, Figure 5.37 presents the median collapse capacity–stability coefficient curve and the "exact" collapse capacity for three non-deteriorating 18-story frames with different strain hardening in the springs. The squares indicate the collapse capacity based on the inelastic stability coefficient obtained from the global pushover analysis, whereas the stars indicate the "exact" collapse capacity of each system. These coefficients and the associated collapse capacities strongly depend on the strain-hardening coefficient of the nonlinear elements of the frame. The procedure results in a reasonable approximation, and it is likely that a more formal procedure for obtaining the equivalent system without P-Δ effects will result in a better approximation.

A similar example is developed by varying the ratio of the weight, P, used to consider P-Δ effects over the seismically effective weight, W. The stability coefficients of this study have been computed with a P/W ratio equal to 1.4, i.e., P is the dead load plus a live load equal to 40% of the dead load. Figure 5.38 shows stability coefficients as well as MDOF and equivalent MDOF collapse capacities for P/W ratios of 1.4, 1.2, and 1.0. Observe the large effect of the P/W ratio on the collapse capacity of the MDOF structure, which may lead to differences of almost 70% depending on the additional live load included in P.

5.8 SUMMARY

Effect of Deterioration on EDPs of Frames

- The relative intensity–EDP relationships for frame structures with deteriorating structural properties start to deviate from those of non-deteriorating frames long before collapse occurs.
- When the collapse level is approached, the migration of maximum story drift angles from top to bottom of the frames is more pronounced for deteriorating frames than for non-deteriorating ones.
- The rapid growth of the bottom story drifts with increasing relative intensity is evident from pushover deflection profiles, which change from a straight line profile at small relative intensities to a highly curved profile as more elements enter the range of post-capping strength deterioration. The deflection patterns are similar to those of non-deteriorating systems with large P-Δ effects.

- Unlike SDOF systems, entering the branch of negative slope in the plastic hinge springs does not produce immediate collapse even when this negative slope is steep. Neither is collapse produced when zero resistance is reached in some of the springs. This phenomenon is attributed to moment redistribution in MDOF systems.
- The effect of CD on EDPs is present at relatively low relative intensities, but is important only when the negative slope has been reached in the plastic hinge springs. For beam-hinge frames, the effect of CD is smaller in MDOF systems than in SDOF systems with the same hysteretic characteristics.

Effect of Deterioration on Collapse Capacity of Frames

- The collapse capacity strongly depends on the first mode period T_1. The large decrease in collapse capacity for long-period structures indicates that the period independent *R*-factor concept is not appropriate because of the large importance of P-Δ effects in the inelastic range.
- The dispersion of collapse capacity, defined as the standard deviation of the log of the data, is only mildly sensitive to the fundamental period of the frame and to deterioration parameters, and usually is on the order of 0.4.
- The slope of the post-capping branch of the plastic hinge springs has a significant effect on the collapse capacity. If this slope is small (e.g., α_c = -0.10), the strength of the component (and therefore the system) decreases slowly and component deformations much larger than δ_c can be attained before collapse occurs. If the slope is on the order of α_c = -0.30 or larger, the post-capping reserve deformations become small and collapse may occur much earlier. The median collapse capacity ratio due to a post-capping stiffness change from α_c = -0.10 to -0.30 may be as small as 0.70.
- The effect of component ductility capacity (δ_c/δ_y) on the collapse capacity of the frames is large and is essentially independent of the fundamental period of the frame, except for very short-period systems. However, collapse capacities for MDOF systems do not increase in the same proportion as with the component ductility capacities. For instance, an increase in component ductility capacity by a factor of 3 (from δ_c/δ_y = 2 to δ_c/δ_y = 6)

increases the median collapse capacity by a factor of about 1.6 if α_c = -0.1 and about 1.75 if α_c = -0.3.

- The effect of CD on collapse capacity is an important but not dominant issue for collapse evaluation.
- The collapse capacity of deteriorating frames is very similar when a pinching model is used for the plastic hinge springs at the beam ends instead of a peak-oriented one. When a bilinear model is used for the plastic hinge springs, the same patterns as for SDOF systems are observed. For MDOF systems with very short fundamental period, the collapse capacity of frames with bilinear springs is larger than that of frames with peak-oriented or pinching springs. However, for frames with medium and long fundamental periods the trend reverses because the branch with negative slope in the plastic hinge springs has a larger ratcheting effect in bilinear models (i.e., the story drifts increase more rapidly).
- Present code guidelines for strong column–weak beam designs do not prevent the development of plastic hinges in the columns. The maximum column moment demands will exceed the strength capacity given by this requirement at small relative intensities. In some cases, the strong column factor would have to be much larger than unity to prevent plastic hinging in columns in frame structures with highly inelastic response.
- Column hinging, which changes the mechanism leading to collapse, has a very detrimental effect on collapse capacity. The collapse capacity of generic frames with a strong column factor of 1.2 decreases drastically (in most cases by a factor smaller than 0.5) compared to that of generic frames with infinitely strong columns. If the strong column factor is 2.4, the collapse capacity decreases by about 25% or less.
- Weak first stories, defined here by plastic hinging in the first-story columns while keeping the structure above the first story elastic, have the most detrimental effect on collapse capacity. Collapse capacity for these systems is very similar to that of frames in which $\sum M_{p,c} = \sum M_{p,b}$.
- P-Δ effects can cause collapse of non-deteriorating flexible long-period structures, and greatly accelerate the collapse of deteriorating frames. Disregard of P-Δ effects may overestimate the collapse capacity of the generic frames by a factor of two or larger. This

overestimation is particularly large for flexible long-period frames in which the P-Δ effects overpower the effects of material deterioration.

- The importance of P-Δ effects can be judged by stability coefficients. For elastic response the elastic story stability coefficient is the appropriate measure. However, in the inelastic regime, in which P-Δ may cause a mechanism that spreads over one or several stories, the elastic story stability coefficient becomes a poor measure of the importance of P-Δ. In this case a global inelastic stability coefficient (defined by the difference in the post-yield slopes of the global pushover curves without and with P-Δ) should be employed.
- For tall and slender frames the global inelastic stability coefficient may be much larger than the elastic one. Thus, P-Δ effects may be much more important than estimated from an elastic stability coefficient.
- Attempts are made in this study to use equivalent SDOF systems for computing the collapse capacity of MDOF structures with large P-Δ effects. If the inelastic stability coefficient is incorporated in the equivalent SDOF system by means of an auxiliary backbone curve, the estimate of the MDOF collapse capacity obtained from the equivalent SDOF system is found to be reasonable, yet conservative (i.e., the actual collapse capacity is underestimated).

Table 5.1 Parameters of springs of sets of generic frames used for collapse evaluation

CASE	Model	α_c	δ_c/δ_y	$\gamma_{s,c,k,a}$	P-Δ	Observations
1	Peak-oriented	N.A.	Infinite	Infinite	Included	Non-Det. System
2		**-0.1**	2	Infinite	Included	Ductility Capacity effect
3			**4**	**Infinite**		**Reference Frame**
4				100		CD effect
5				50		CD effect
6				25		CD effect
7			6	Infinite		Ductility Capacity effect
8		-0.3	2	Infinite	Included	PostCap. Stiff & Duct. Effect
9			4	Infinite		PostCap. Stiff & Duct. Effect
10			6	Infinite		PostCap. Stiff & Duct. Effect
11		-0.5	4	Infinite	Included	Post-Capping Stiffness Effect
12	Pinching	-0.1	4	Infinite	Included	Hysteretic Model effect
13	Bilinear	-0.1	4	Infinite	Included	Hysteretic Model effect
14	Peak-oriented	-0.1	4	Infinite	Not Included	P-Δ effect

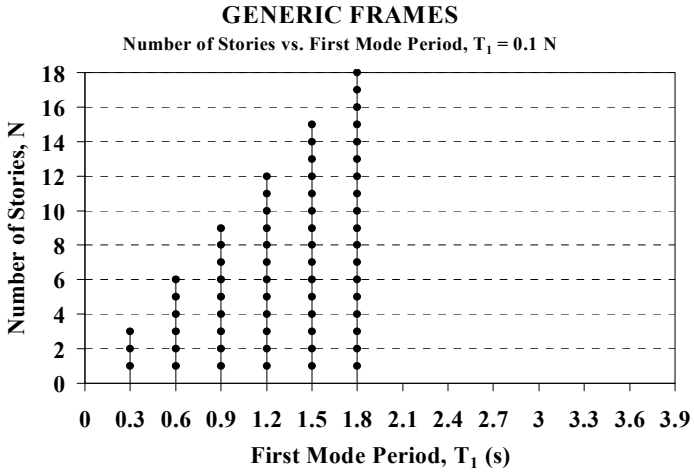

(a) Stiff Frames, $T_1 = 0.1N$

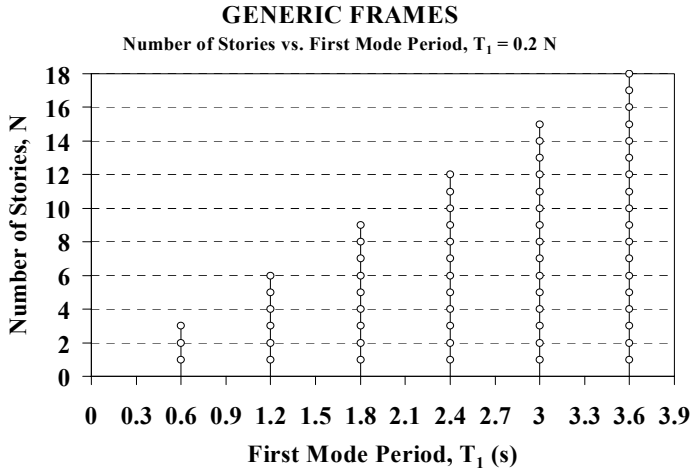

(b) Flexible Frames, $T_1 = 0.2N$

Fig. 5.1 Family of generic frames, stiff and flexible frames (after Medina, 2002)

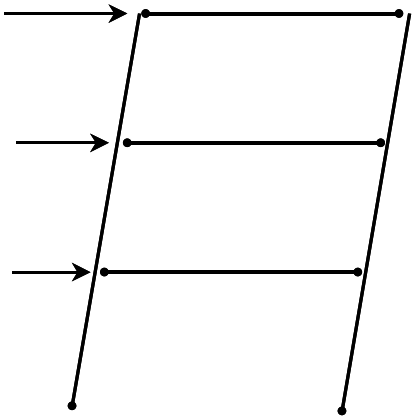

Fig. 5.2 Beam hinge (BH) mechanism

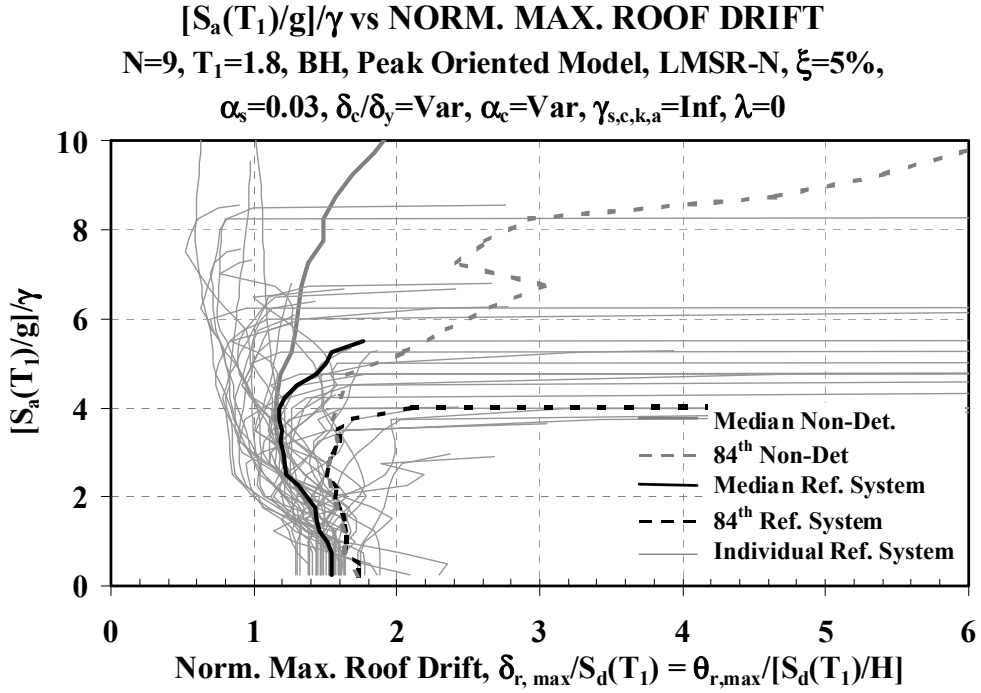

(a) Normalized Maximum Roof Drift

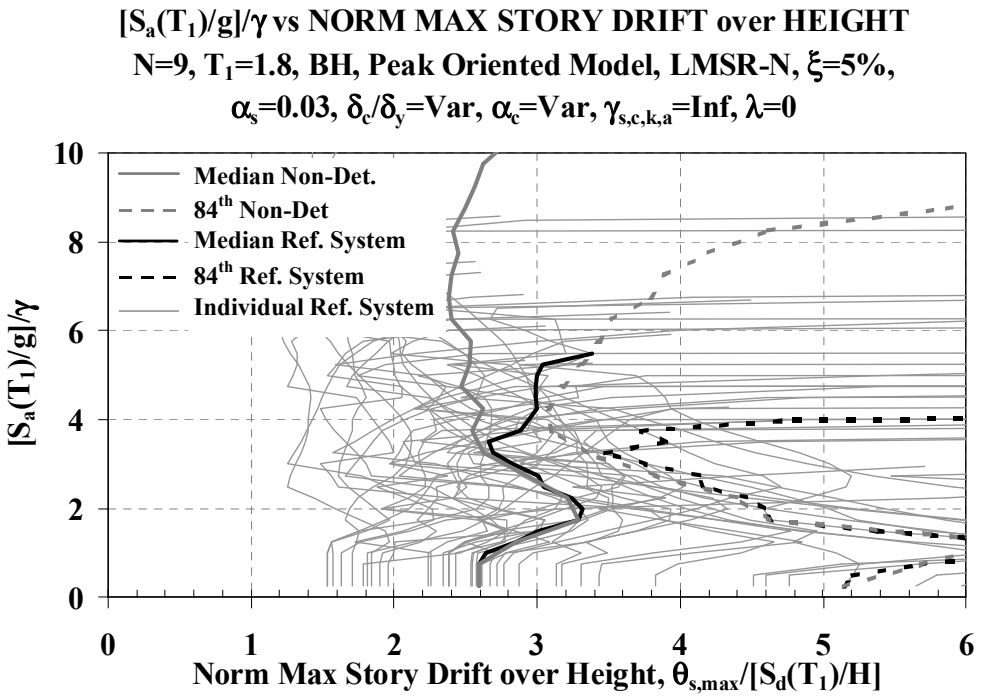

(b) Normalized Maximum Story Drift over Height

Fig. 5.3 Individual and statistical $[S_a(T_1)/g]/\gamma$– EDP relationships for set of reference frame 0918 and statistical relationships for set of non-deteriorating frames

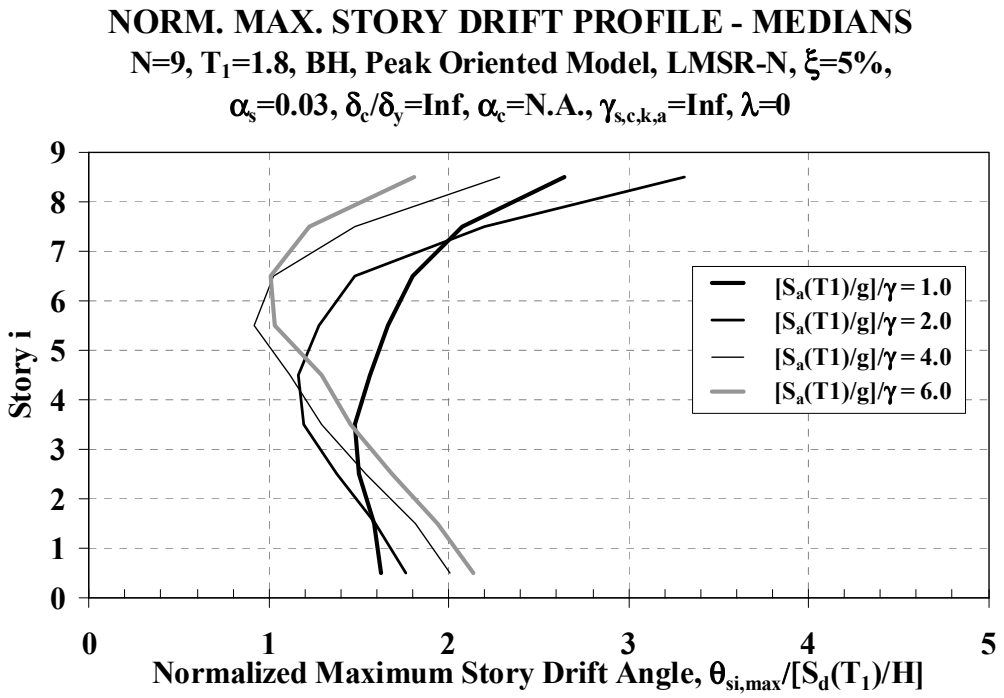

(a) Non-deteriorating Frame

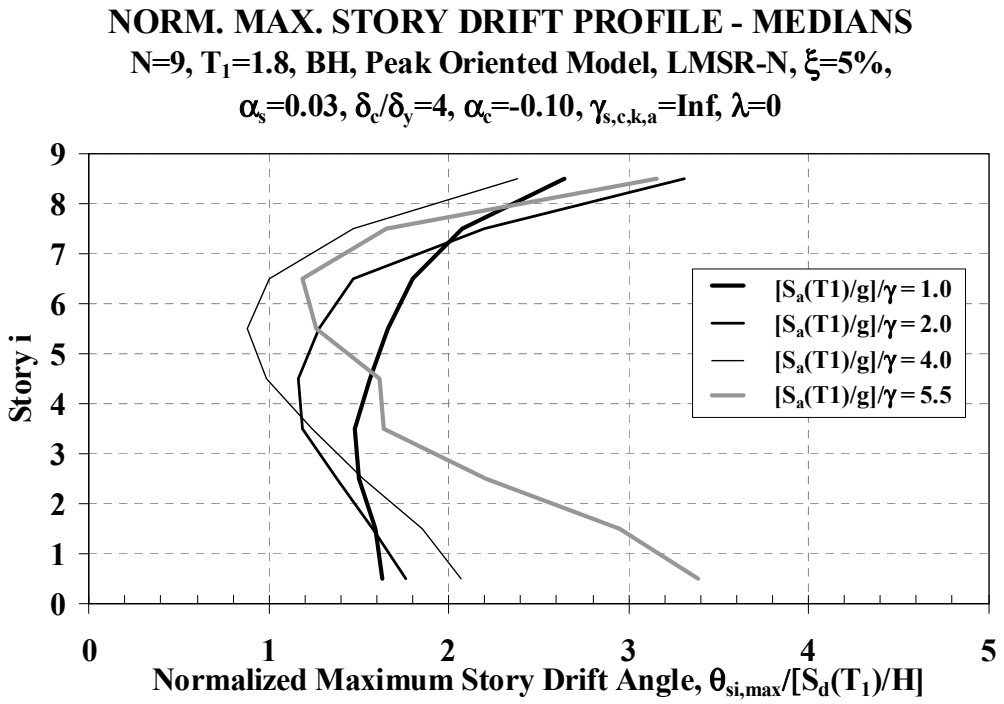

(b) Reference Frame

Fig. 5.4 Median normalized maximum story drift profiles for a 9-story frame with T_1 = 1.8 s

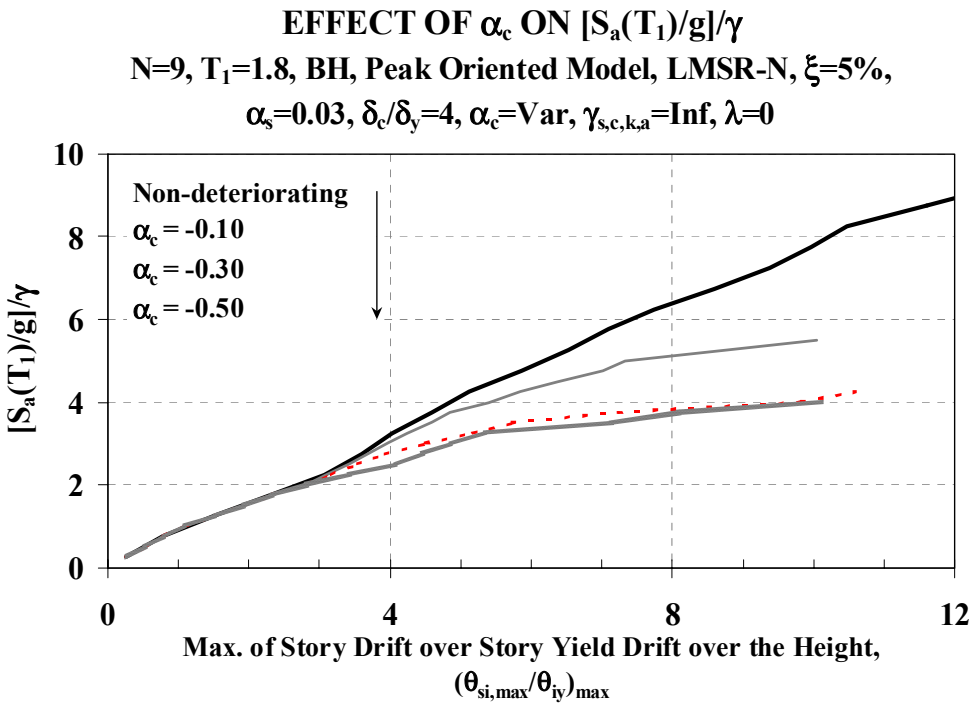

Fig. 5.5 Effect of α_c of rotational springs on maximum of story drift over story yield drift over the height, 9-story frames with T_1 = 1.8 s

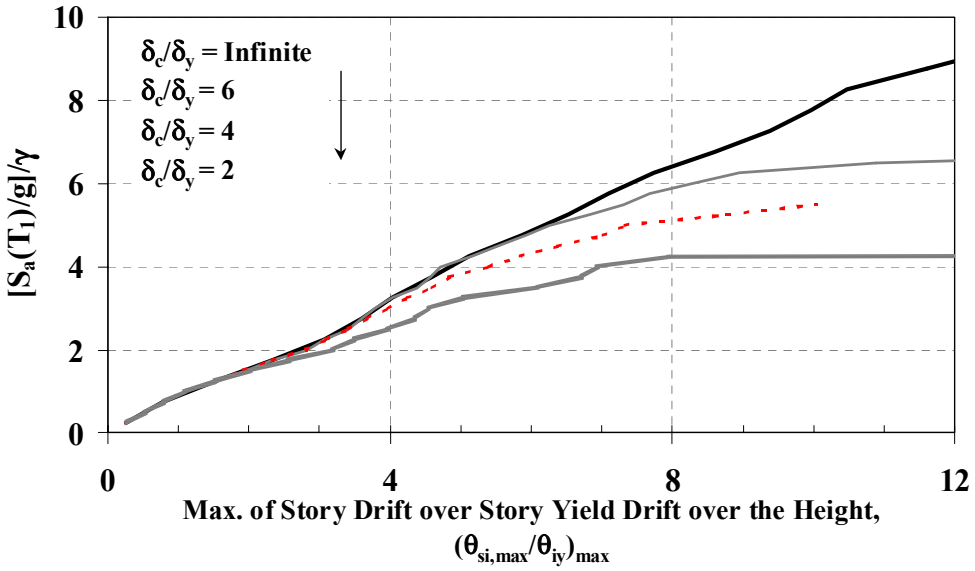

Fig. 5.6 Effect of δ_c/δ_y of rotational springs on maximum of story drift over story yield drift over the height, 9-story frames with T_1 = 1.8 s

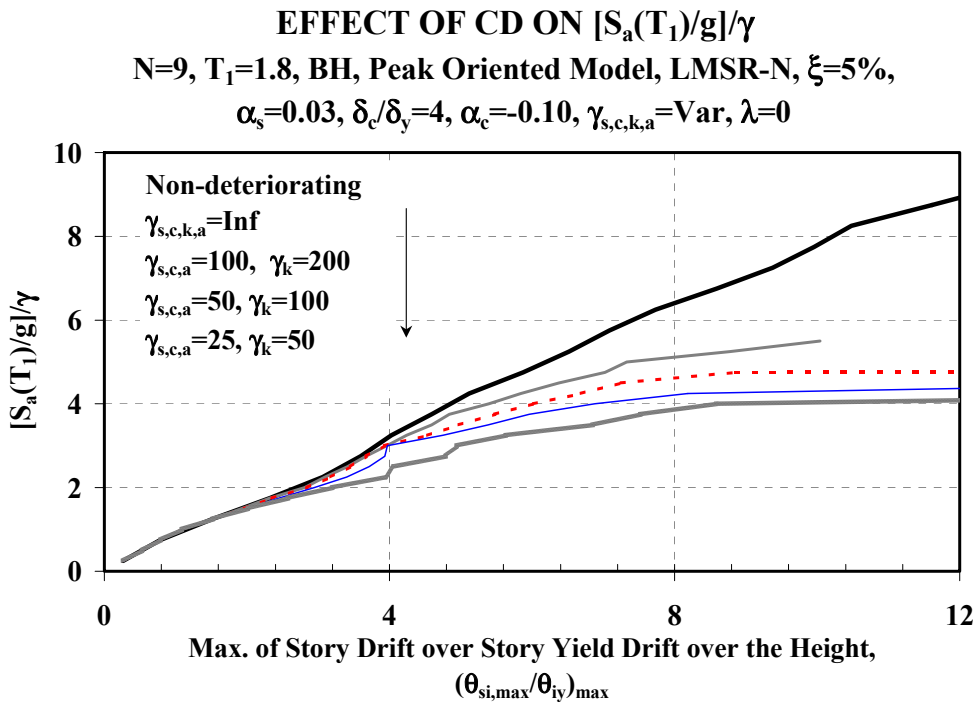

Fig. 5.7 Effect of CD rate of rotational springs on maximum of story drift over story yield drift over the height, 9-story frames with T_1 = 1.8 s

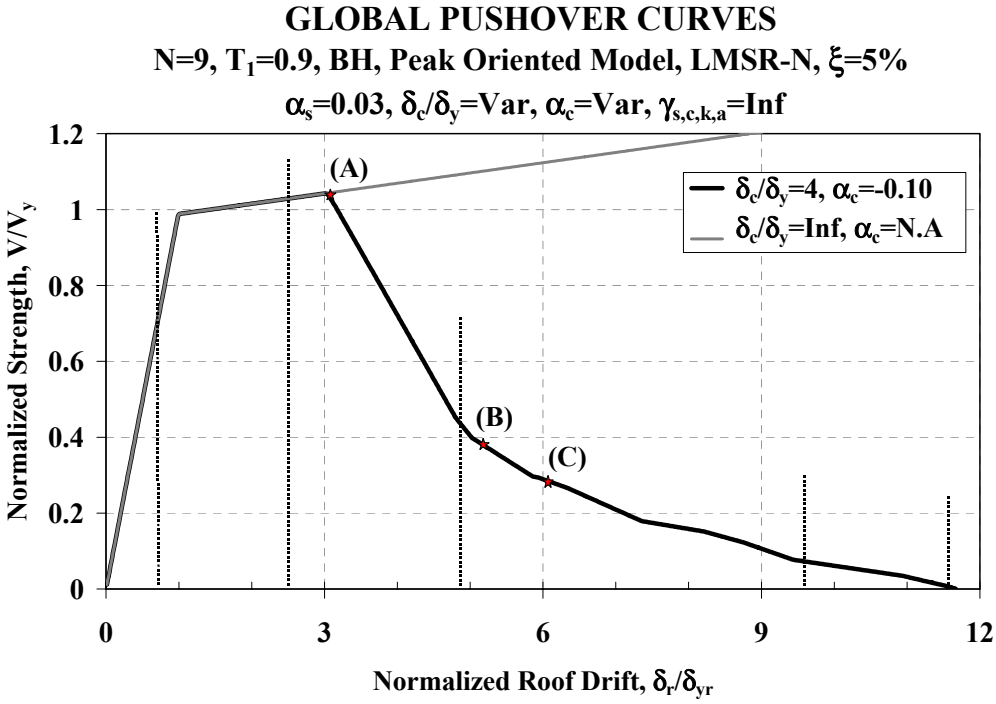

Fig. 5.8 Global pushover curves for the non-deteriorating and deteriorating (reference) frame 0909

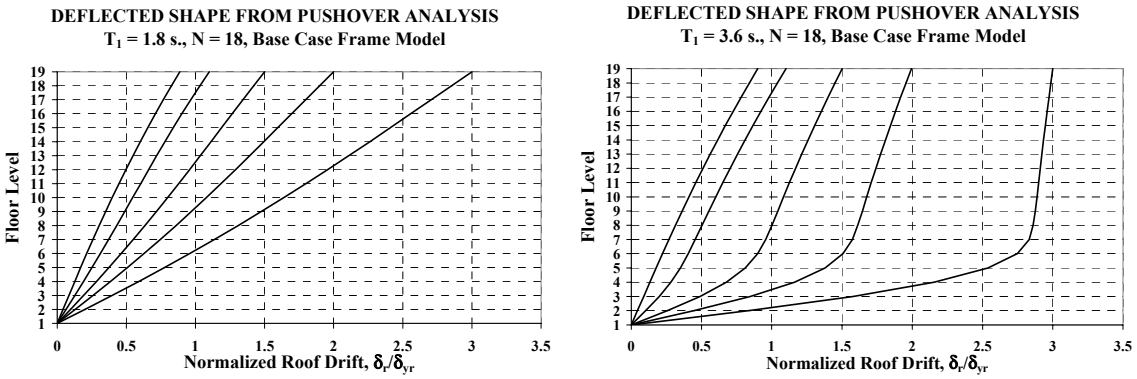

(a) T_1 = 1.8 s. (b) T_1 = 3.6 s.

Fig. 5.9 Deflected shapes from pushover analyses for non-deteriorating 18-story frames (after Medina, 2002)

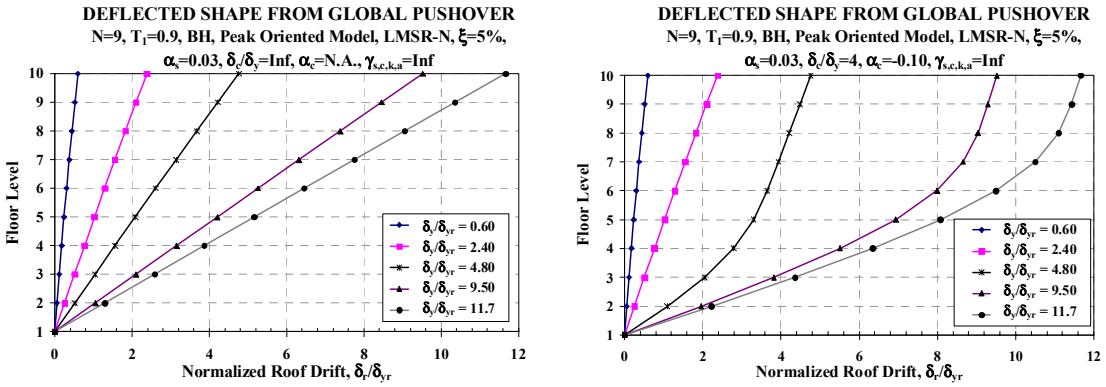

(a) Non- Deteriorating (b) Deteriorating Reference Frame

Fig. 5.10 Deflected shapes from pushover analyses for frame 0909

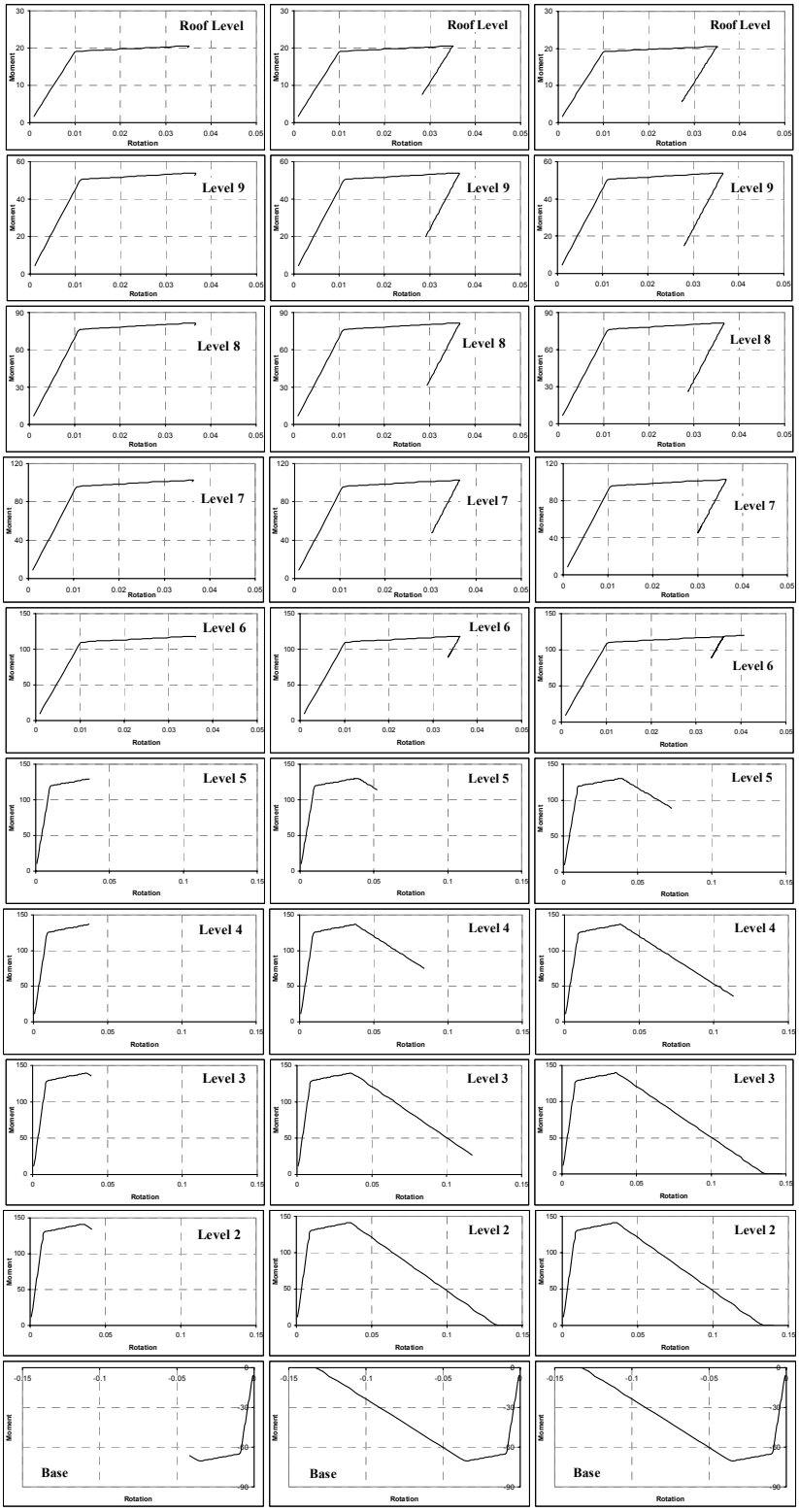

(a) δ_r/δ_{yr} = 0 to 3.1 (b) δ_r/δ_{yr} = 0 to 5.3 (c) δ_r/δ_{yr} = 0 to 6.4

Fig. 5.11 Moment–rotation relationships of rotational springs at beam ends and column base, reference frame 0909

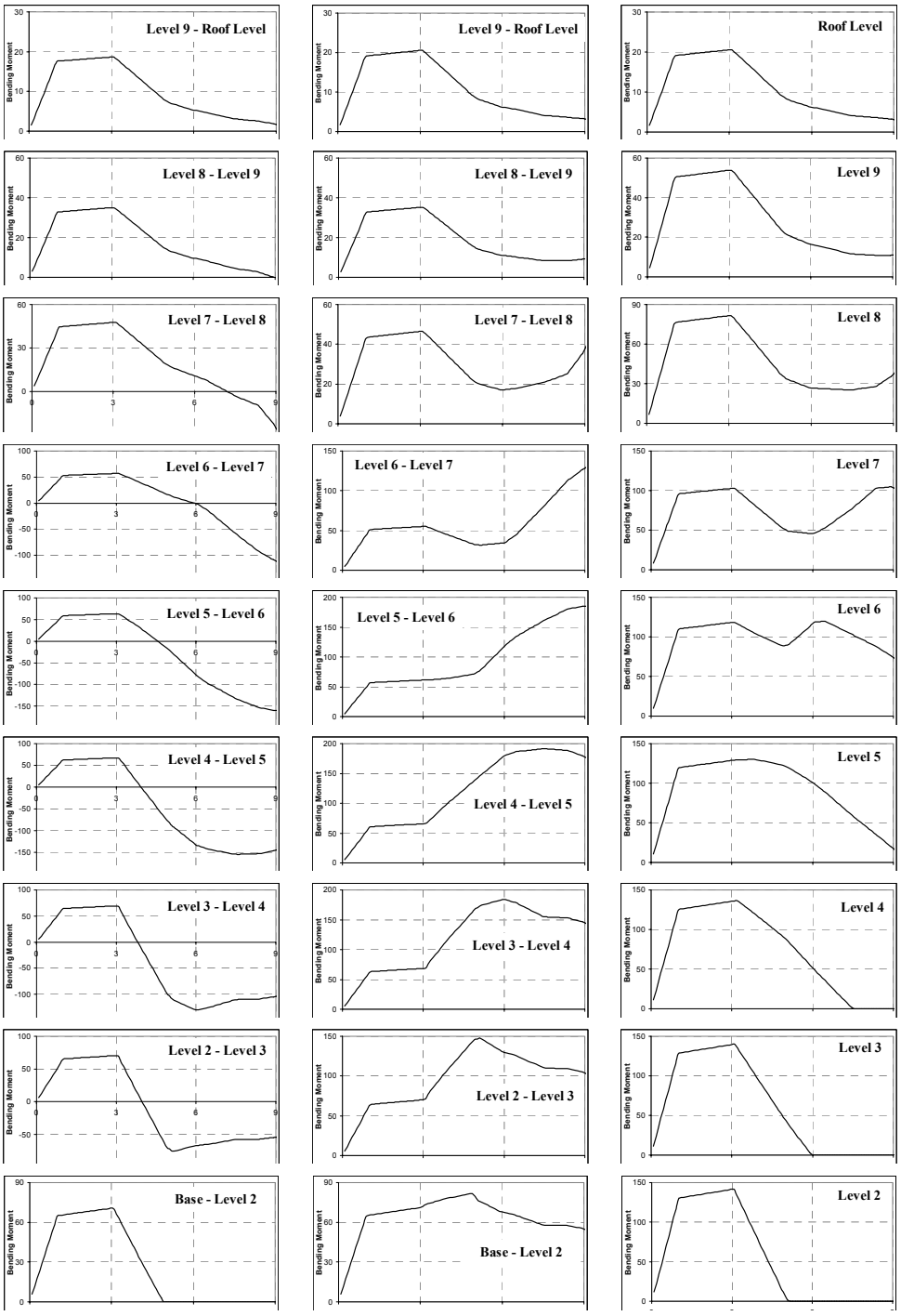

(a) Column, Lower Level (b) Column, Upper Level (c) Beam

Fig. 5.12 Moment (*1/1000) vs. normalized roof drift of columns and beams of reference frame 0909

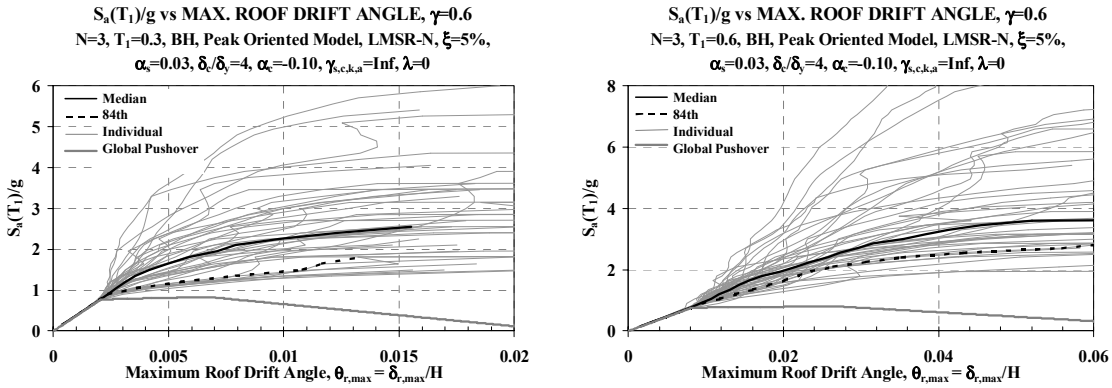

(a) Frame 0303, γ= 0.6 (b) Frame 0306, γ= 0.6

Fig. 5.13 Maximum roof drift angle from dynamic and static nonlinear analysis for the 3-story reference frames

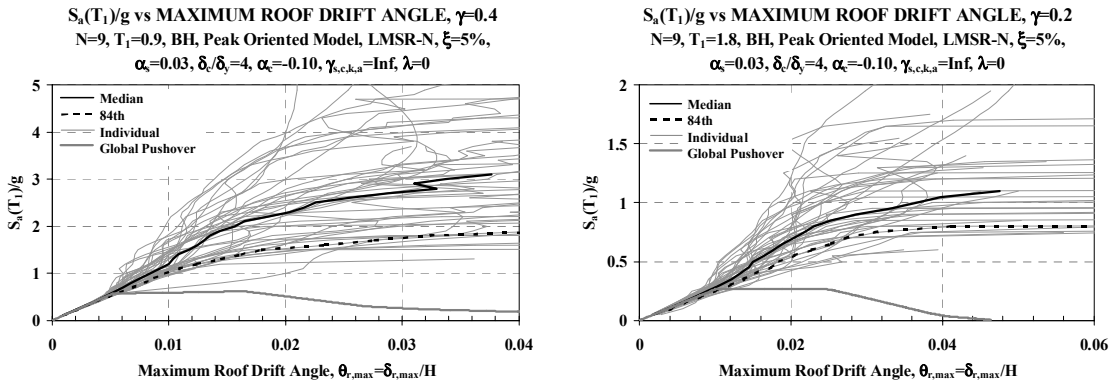

(a) Frame 0909, γ= 0.4 (b) Frame 0918, γ= 0.2

Fig. 5.14 Maximum roof drift angle from dynamic and static nonlinear analysis for the 9-story reference frames

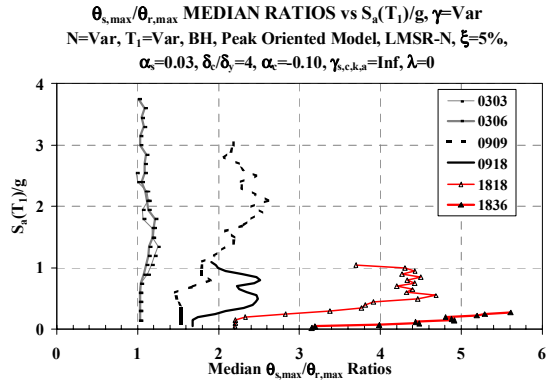

Fig. 5.15 Ratio of maximum interstory drift angle over maximum roof drift angle, 3 and 9-story-reference frames

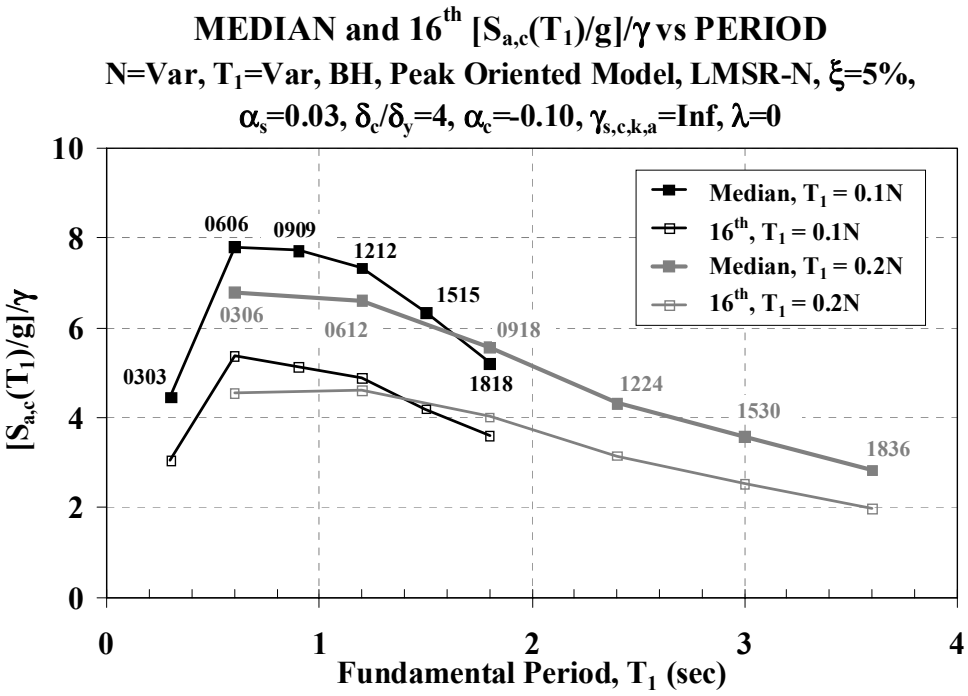

Fig. 5.16 Median and 16th percentile collapse capacity spectra, set of reference frames

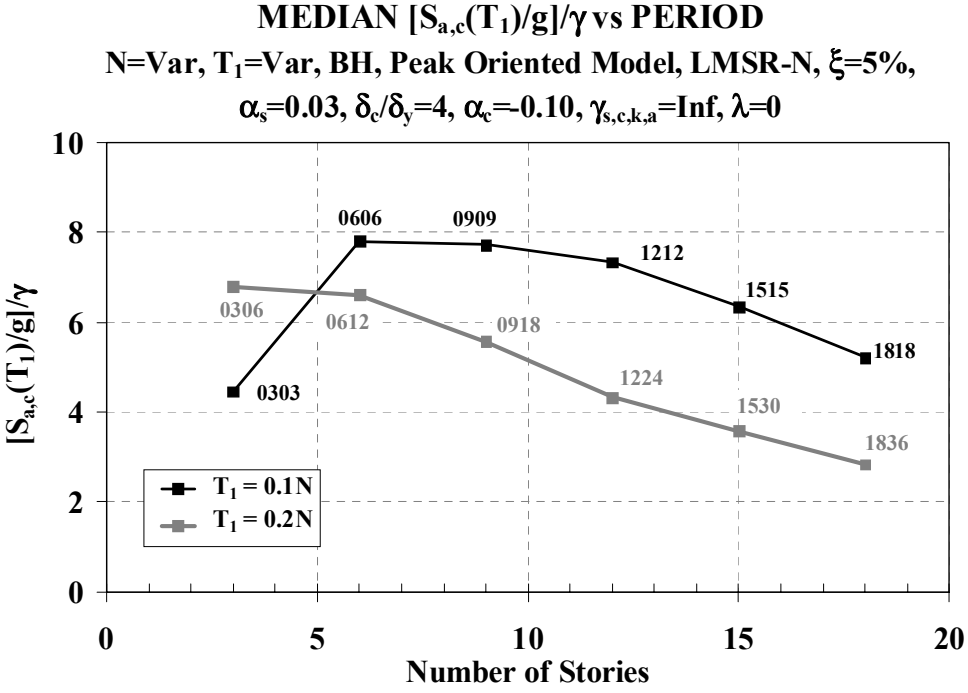

Fig. 5.17 Median collapse capacities — number of stories, set of reference frames

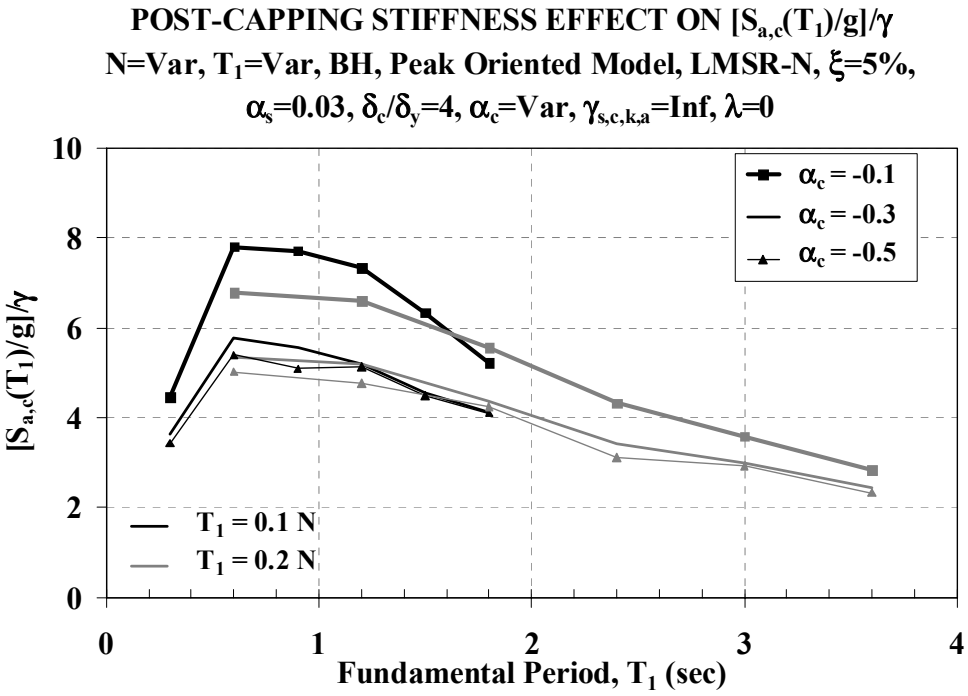

(a) Median Collapse Capacity Spectra

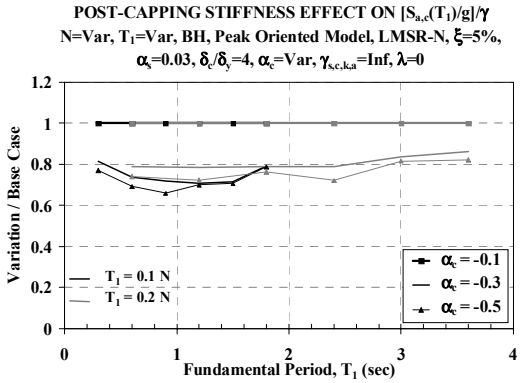

(b) Median Ratios of Col. Capacity Spectra

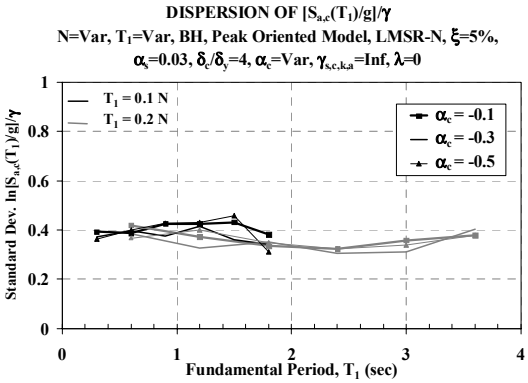

(c) Dispersion of Collapse Capacity Spectra

Fig. 5.18 Effect of α_c of springs on collapse capacity of generic frames, $\delta_c/\delta_y = 4$, $\gamma_{s,c,k,a}$ = inf.

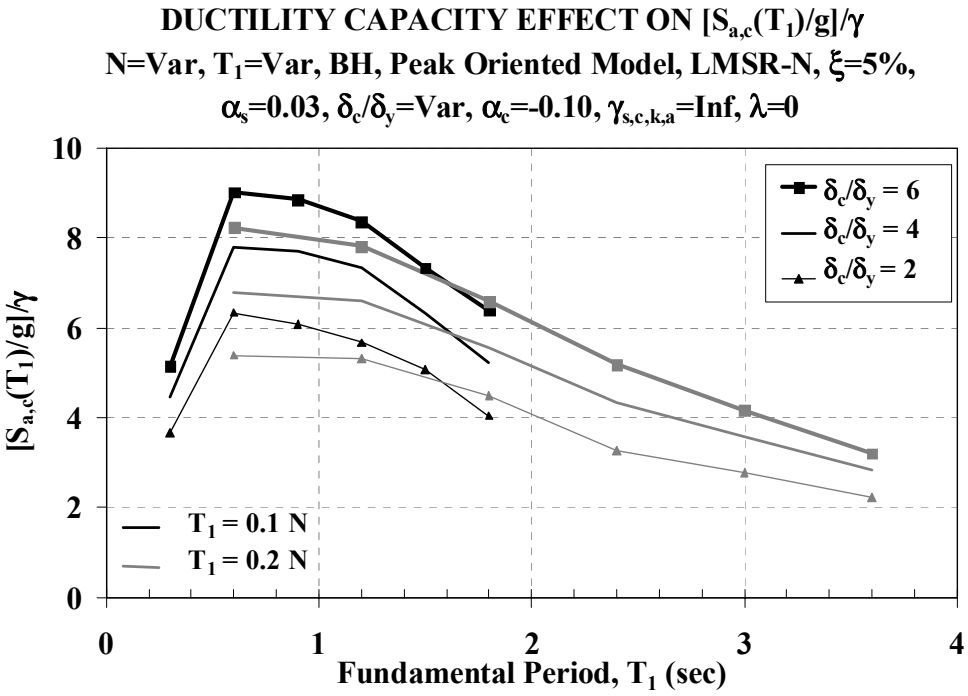

(a) Median Collapse Capacity Spectra

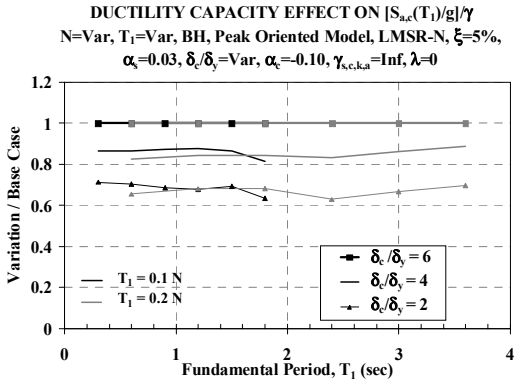

(b) Median Ratios of Col. Capacity Spectra

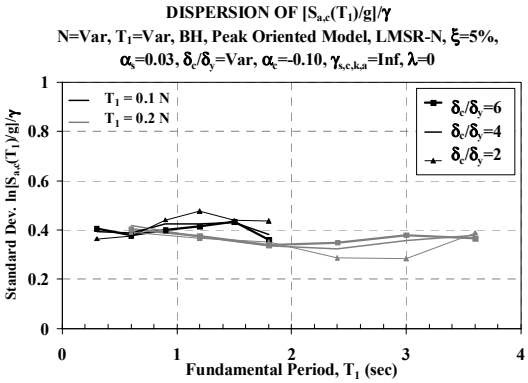

(c) Dispersion of Collapse Capacity Spectra

Fig. 5.19 Effect of δ_c/δ_y of springs on collapse capacity of generic frames, α_c = -0.1, $\gamma_{s,c,k,a}$ = inf.

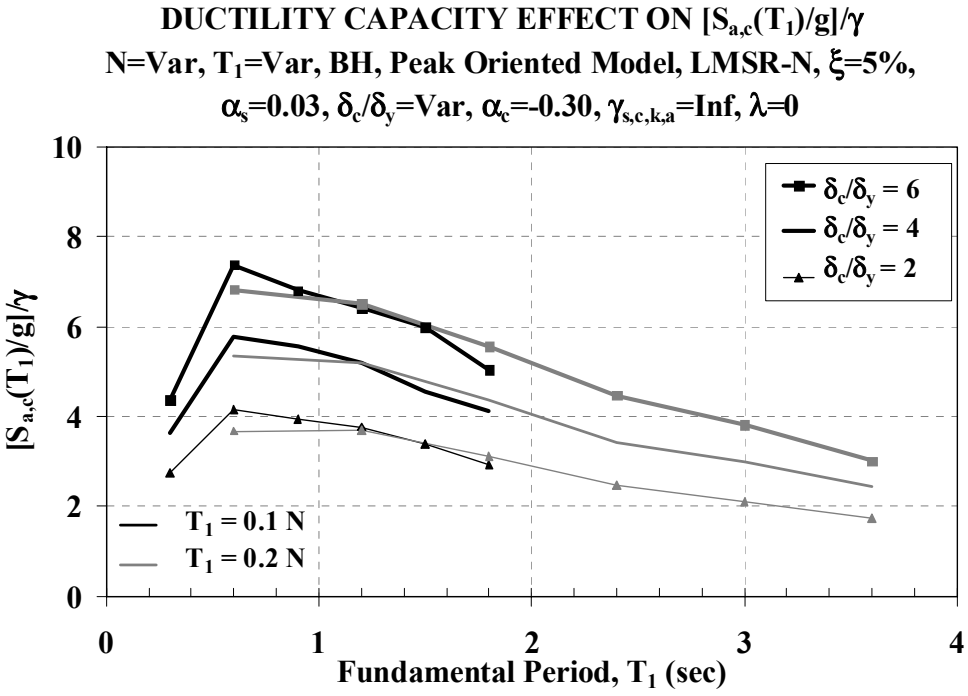

(a) Median Collapse Capacity Spectra

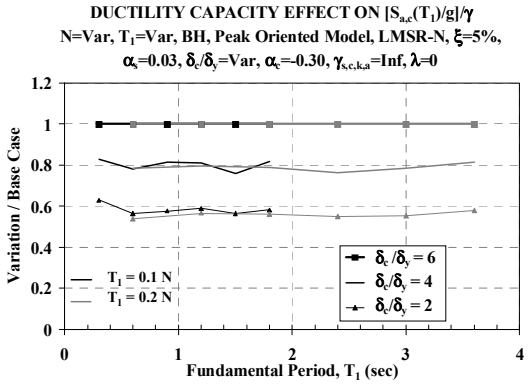

(b) Median Ratios of Col. Capacity Spectra

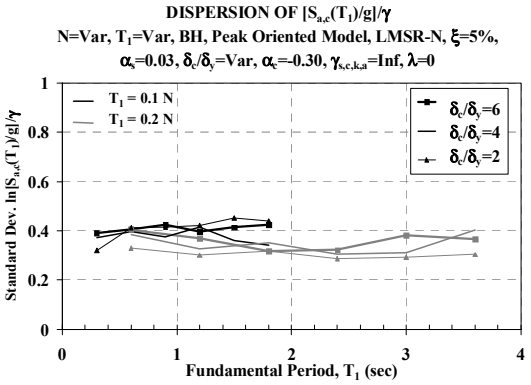

(c) Dispersion of Collapse Capacity Spectra

Fig. 5.20 Effect of δ_c/δ_y of springs on collapse capacity of generic frames, α_c = -0.3, $\gamma_{s,c,k,a}$ = inf.

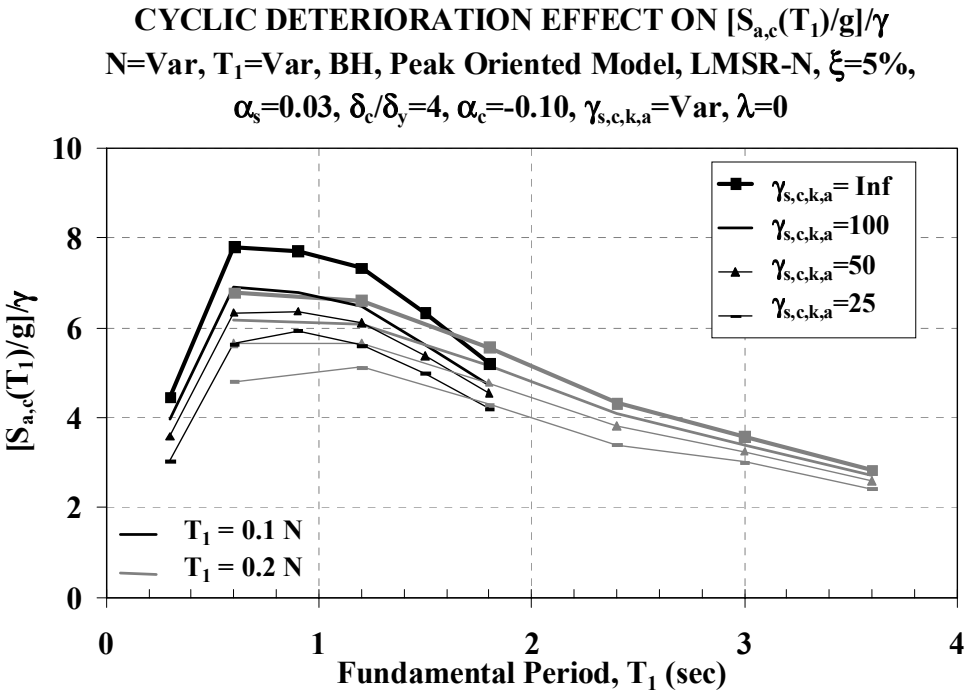

(a) Median Collapse Capacity Spectra

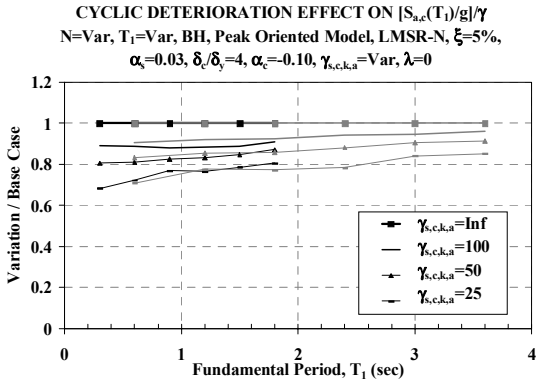

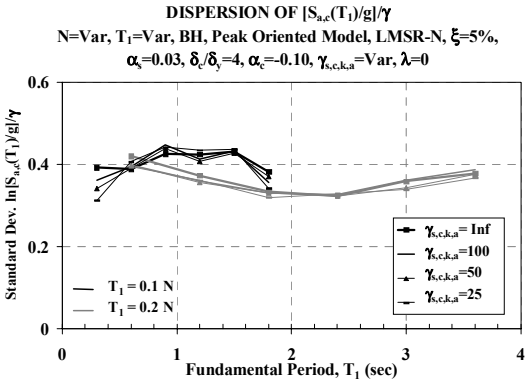

(b) Median Ratios of Col. Capacity Spectra (c) Dispersion of Collapse Capacity Spectra

Fig. 5.21 Effect of CD of springs on collapse capacity of generic frames, $\delta_c/\delta_y = 4$, $\alpha_c = -0.1$

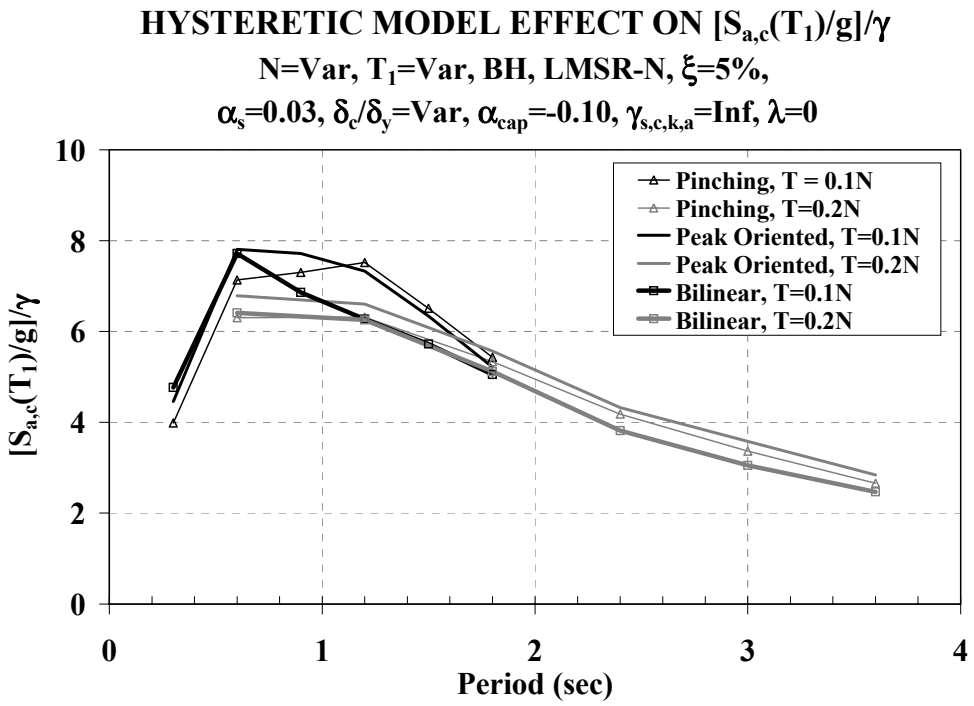

Fig. 5.22 Effect of hysteretic model on median collapse capacity of generic frames

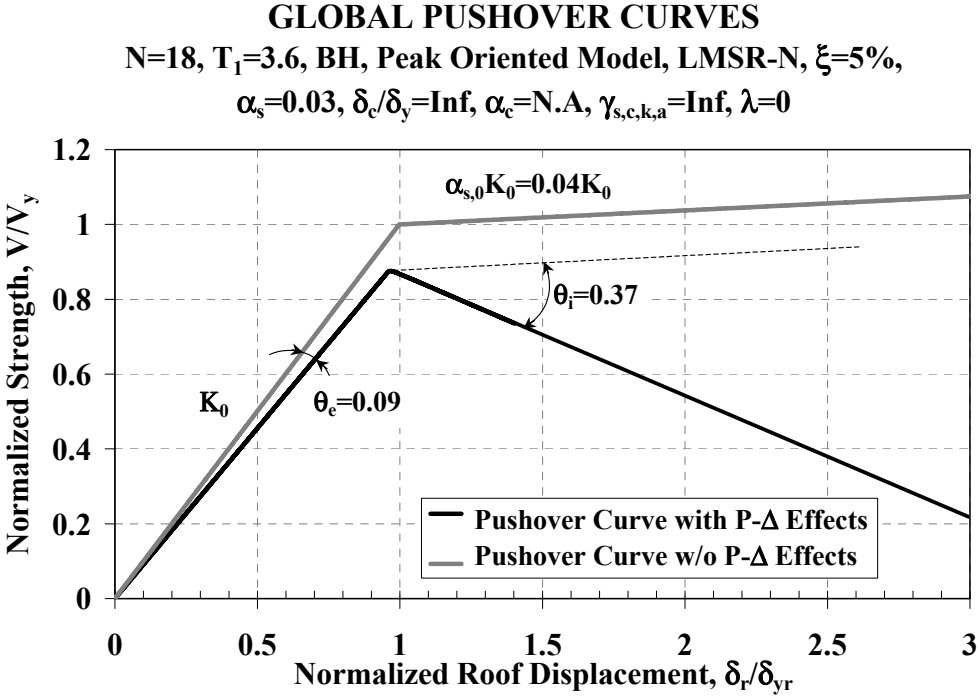

Fig. 5.23 Elastic and inelastic stability coefficients obtained from global pushover curves, peak oriented non-deteriorating frame 1836

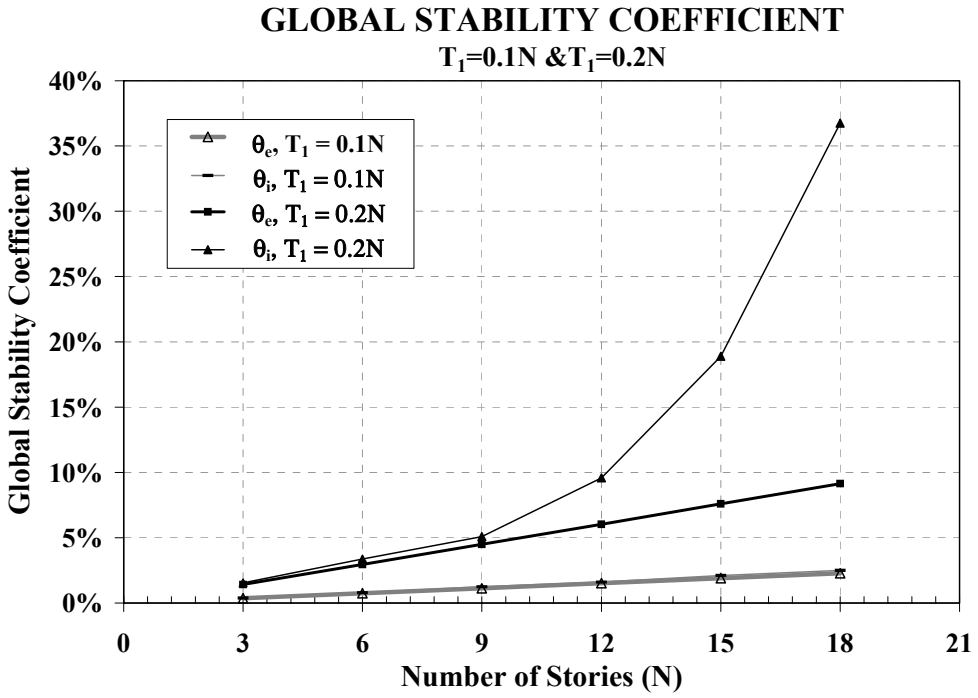

(a) Stability Coefficients from Global Pushover Curves

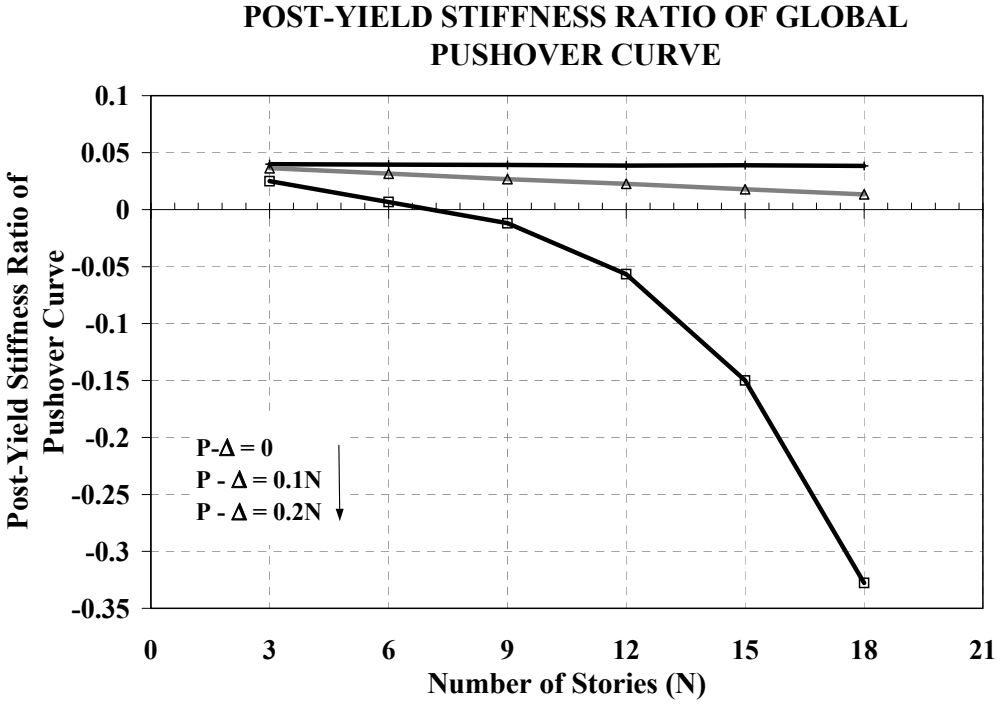

(c) Post-Yield Stiffness Ratio in Global Pushover Curve

Fig. 5.24 Post-yield stiffness ratio and stability coefficients from global pushover curves, generic frames with strain hardening in rotational springs of 3%

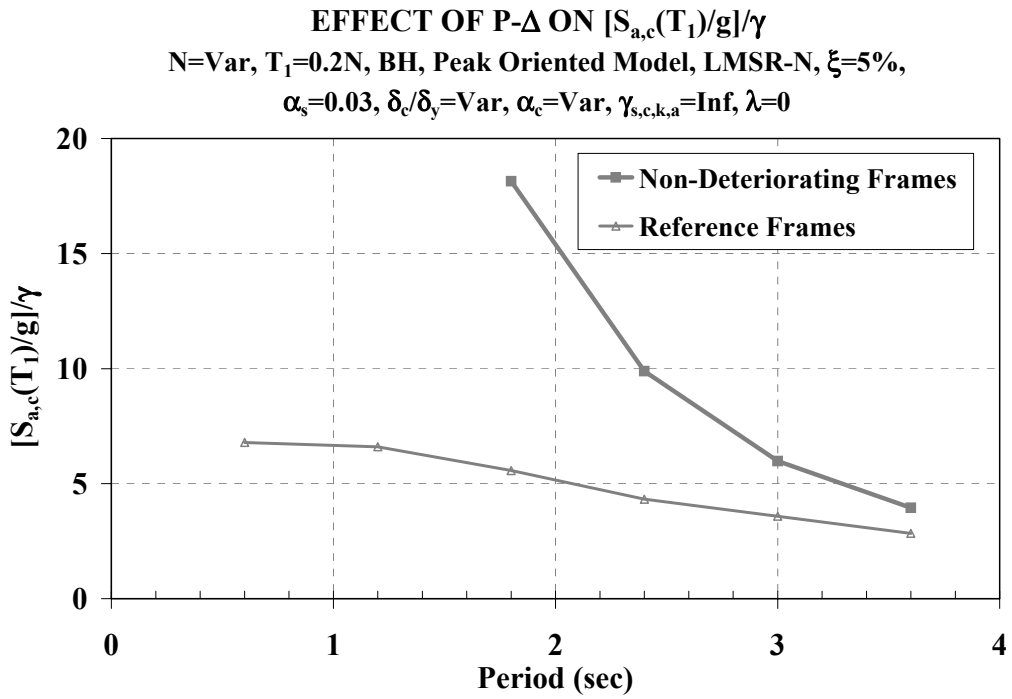

Fig. 5.25 Collapse capacity of flexible non-deteriorating and flexible reference frames with P-Δ effects

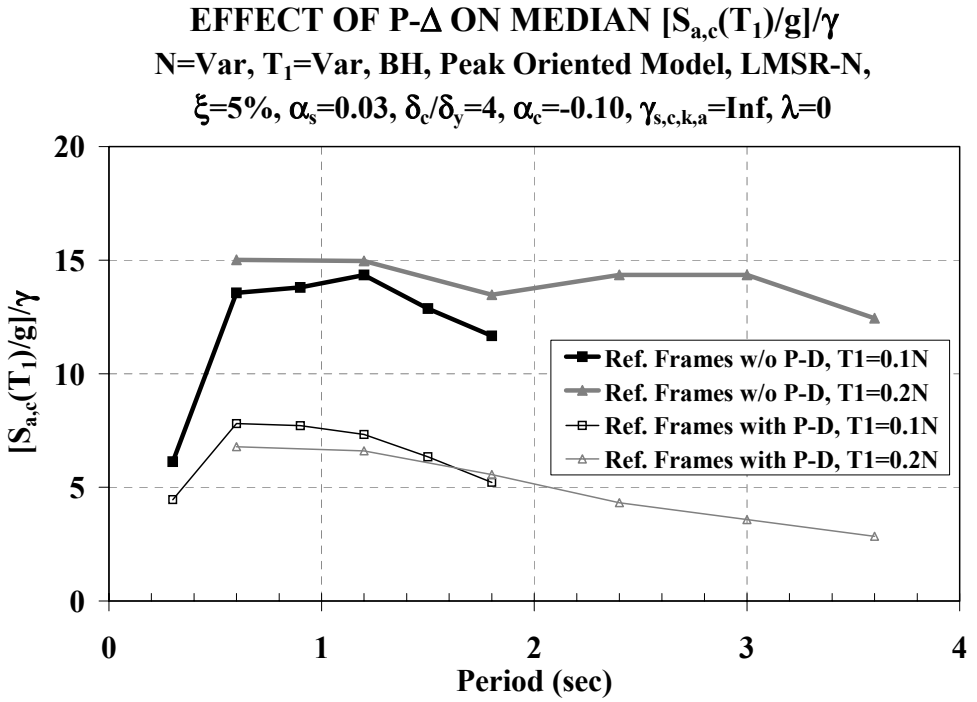

Fig. 5.26 Effect of P-Δ on collapse capacity of reference frames

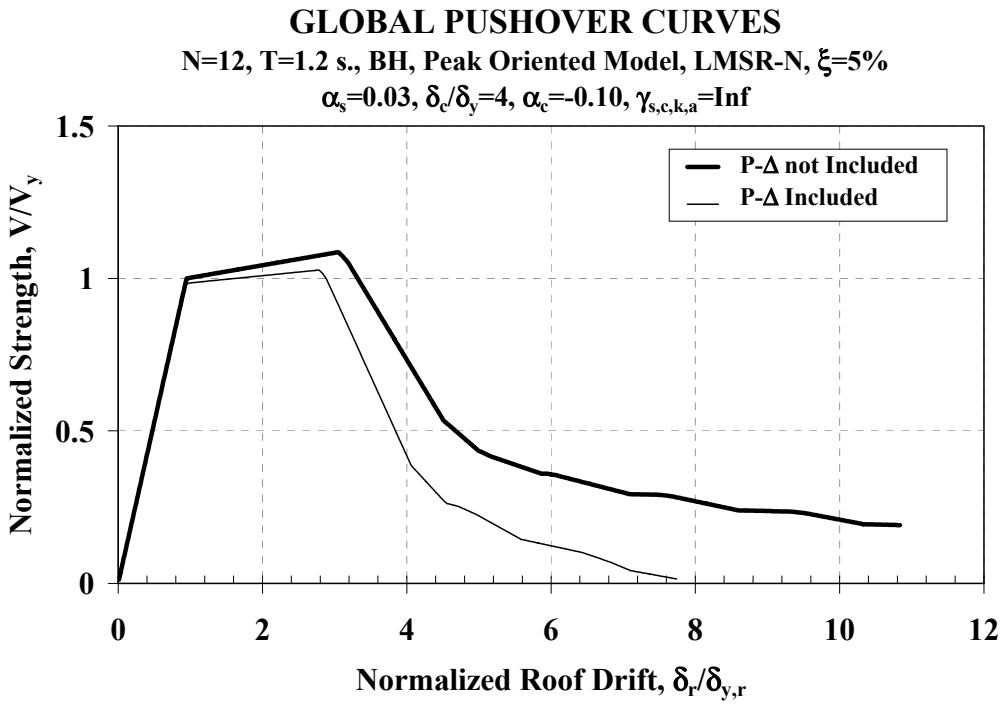

Fig. 5.27 Effect of P-Δ on global pushover curves for reference frame 1212

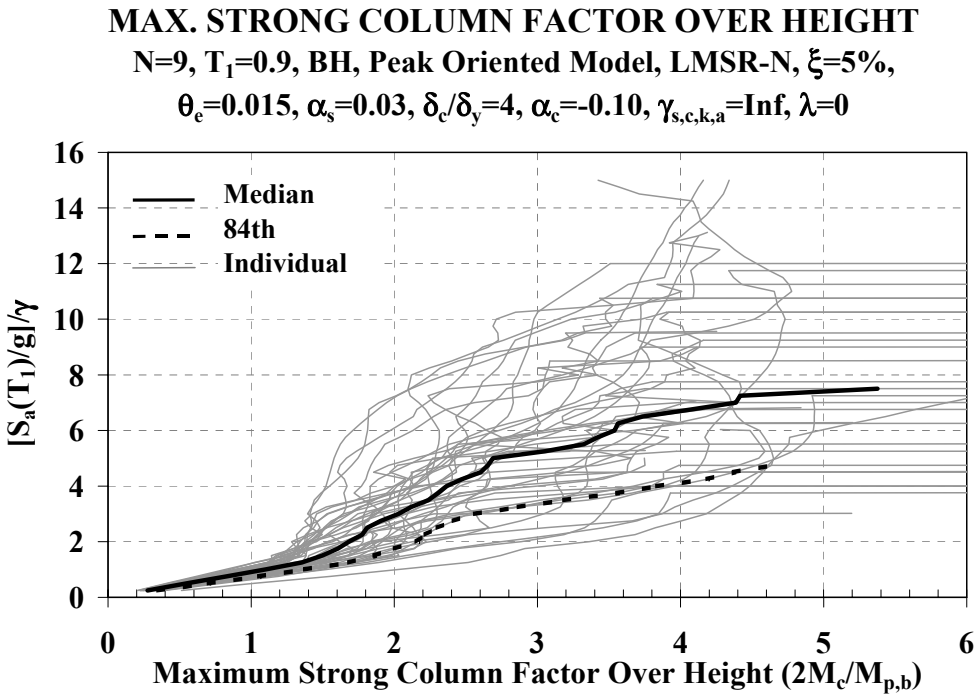

Fig. 5.28 Maximum strong-column factor over the height for reference frame 0909

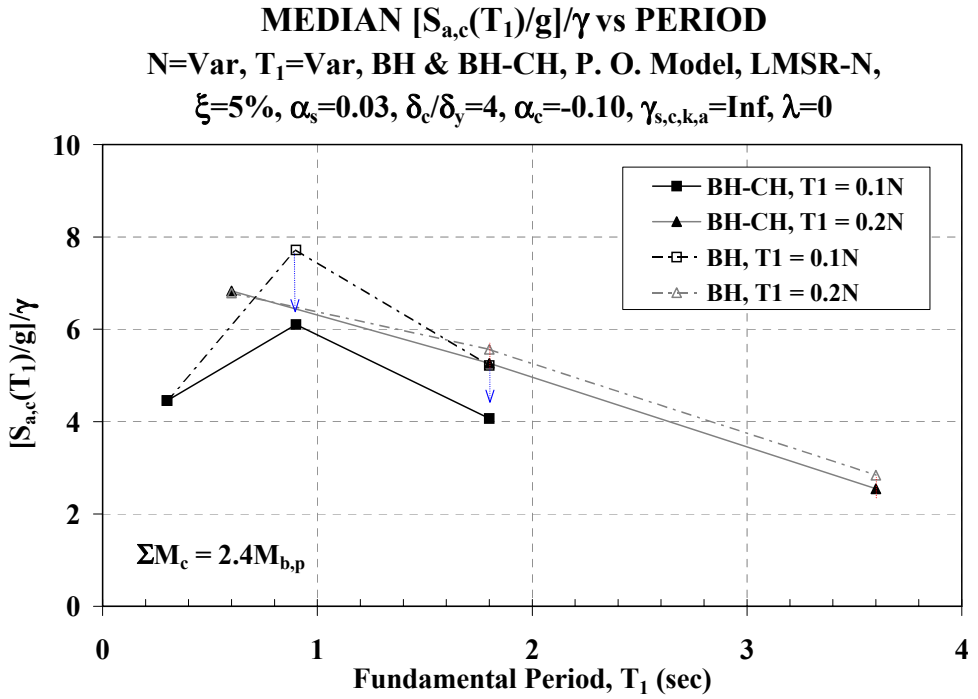

Fig. 5.29 Effect on median collapse capacity of including columns with high strength ($\sum M_c = 2.4 M_{b,p}$)

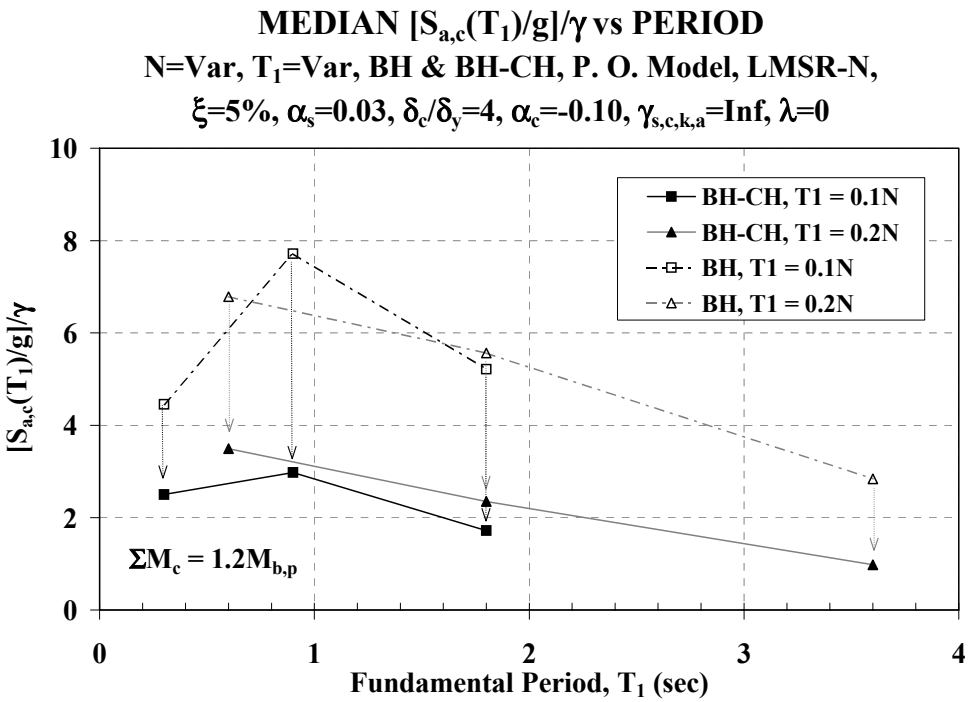

Fig. 5.30 Effect on median collapse capacity of including columns with intermediate strength ($\sum M_c = 1.2M_{b,p}$)

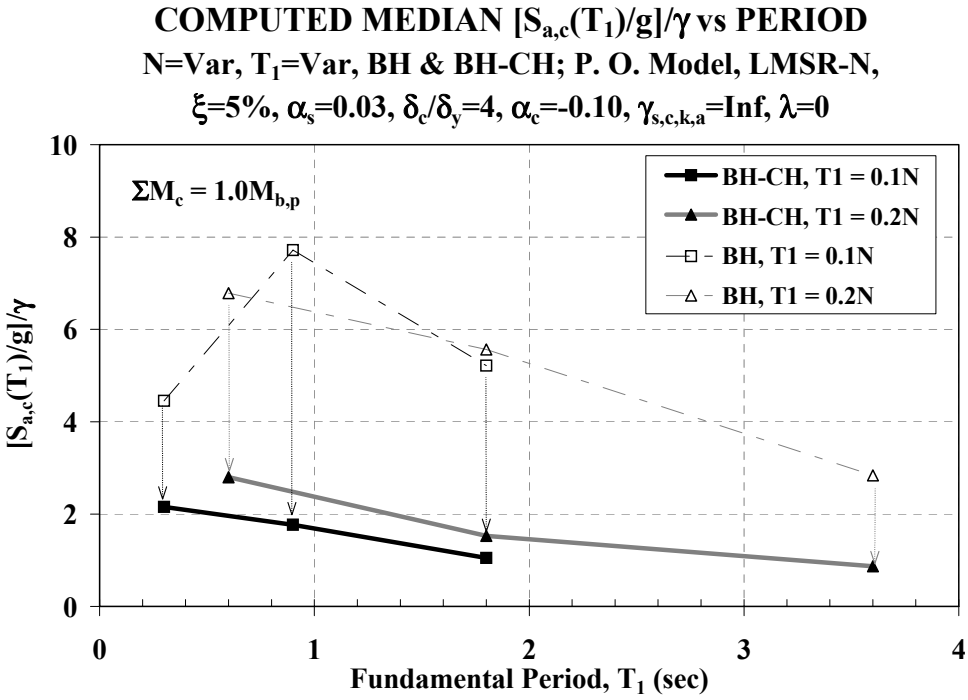

Fig. 5.31 Effect on median collapse capacity of including columns with low strength ($\sum M_c = 1.0M_{b,p}$)

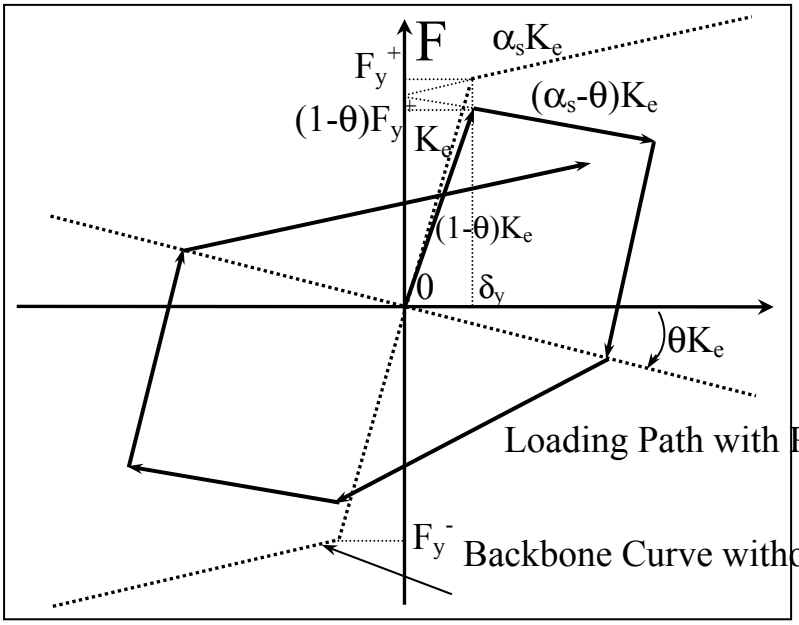

(a) P-Δ Representation by Rotation of Hysteresis Diagram

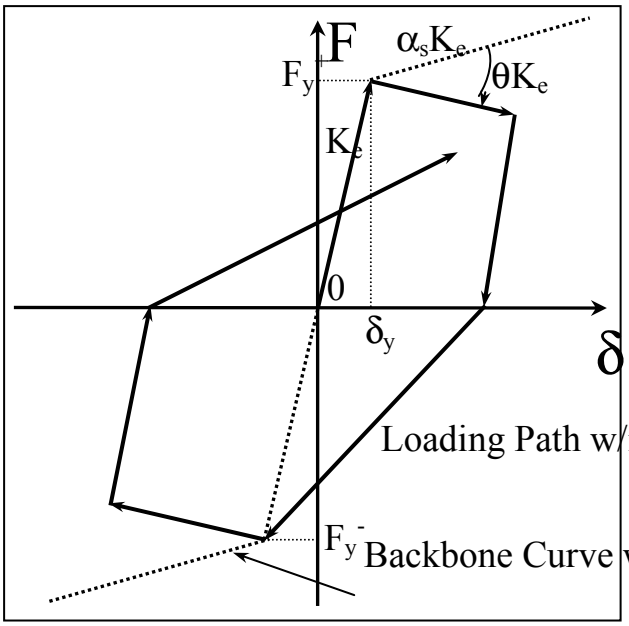

(b) Incorrect P-Δ Representation by Adjustment of Post-Yield Stiffness

Fig. 5.32 Representation of P-Δ effects in SDOF systems

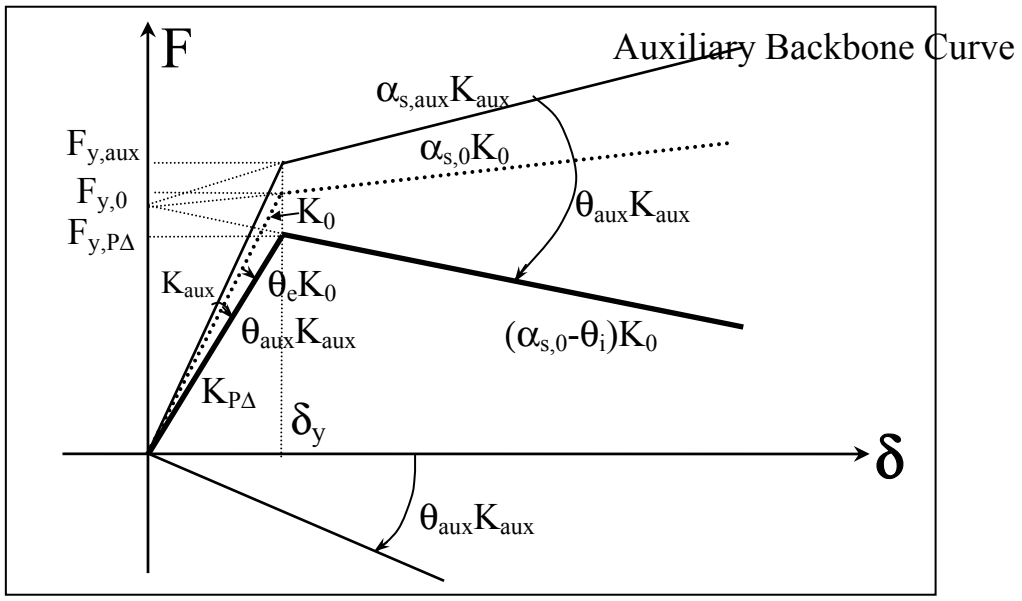

Fig. 5.33 P-Δ Effects obtained with an auxiliary backbone curve based on elastic and inelastic stability coefficients

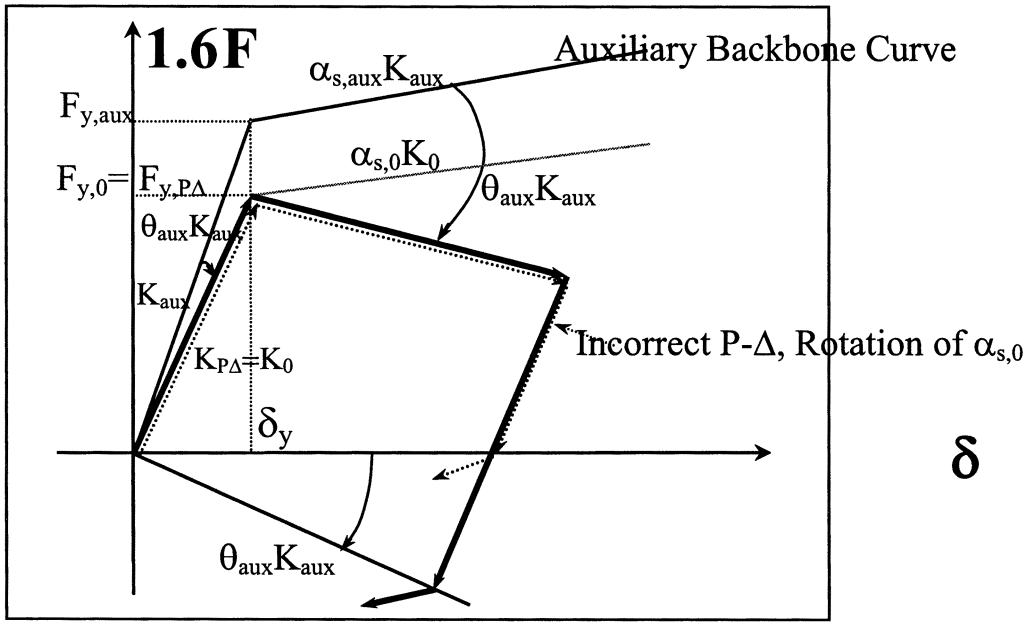

Fig. 5.34 P-Δ Effects obtained with a simplified auxiliary backbone curve and rotation of the strain hardening branch by the inelastic stability coefficient

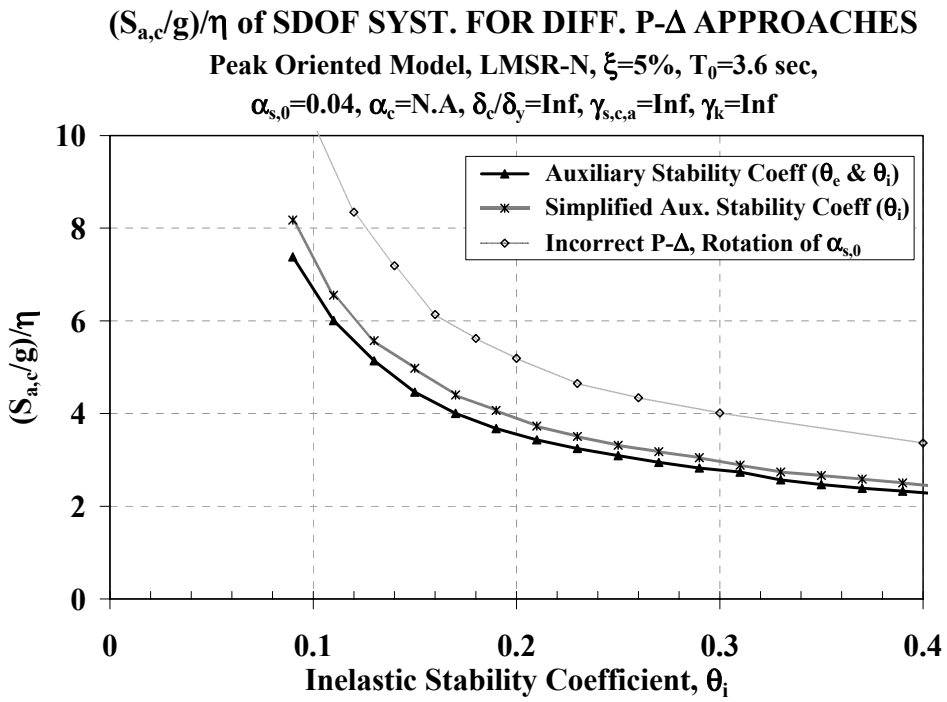

Fig. 5.35 Collapse capacities for equivalent SDOF systems using different P-Δ approaches

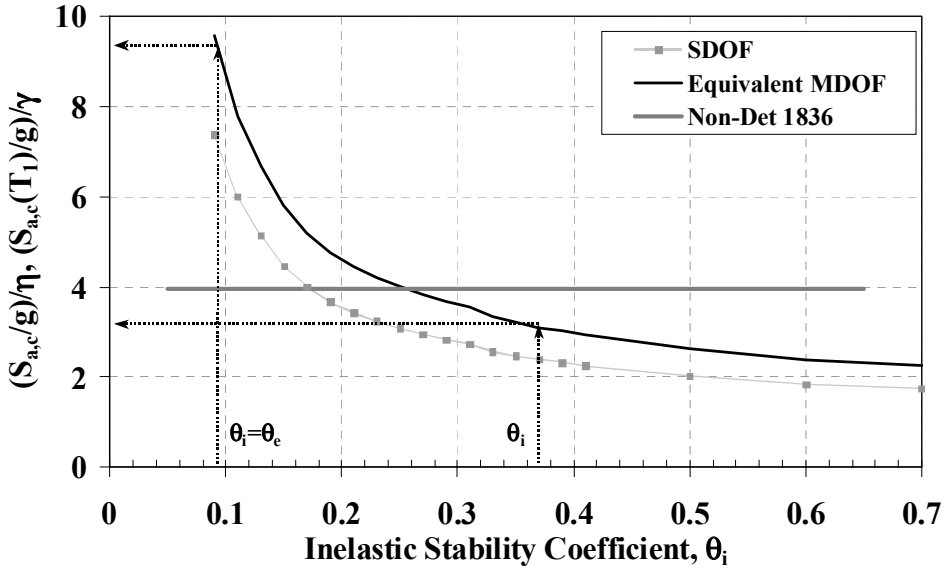

Fig. 5.36 Collapse capacity–inelastic stability coefficient curves obtained from SDOF systems with auxiliary backbone curves, T_0 = 3.6 s

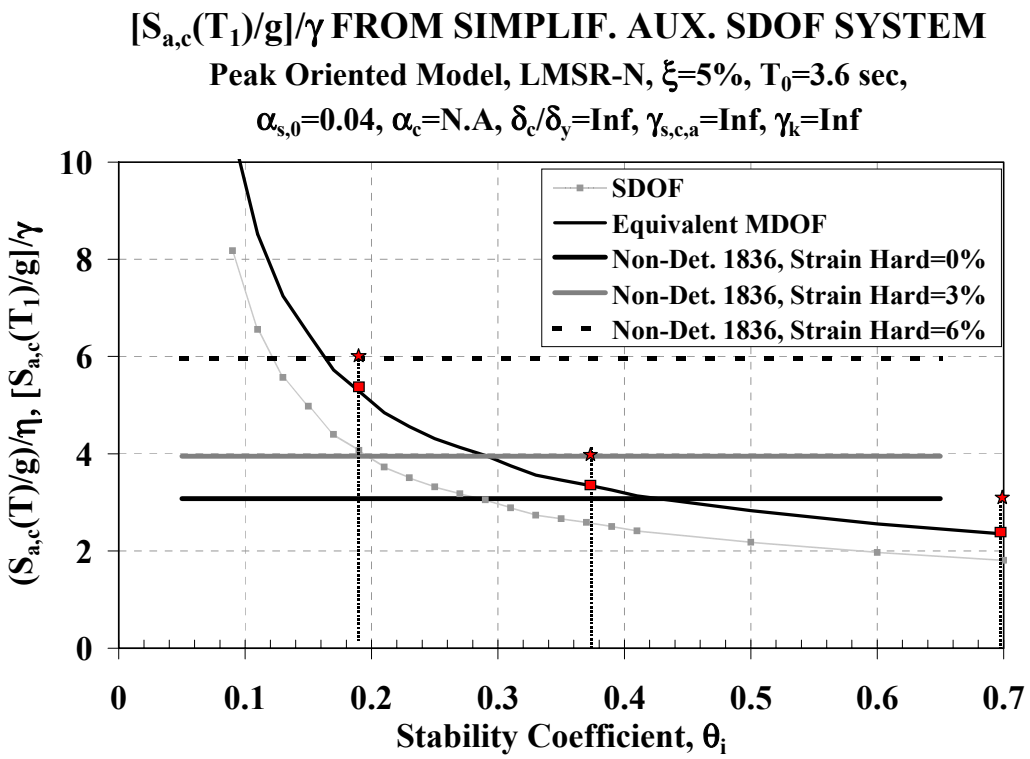

Fig. 5.37 Test of collapse capacity–inelastic stability coefficient curves for MDOF structures with T_0 = 3.6 s. and variations of α_s at the rotational springs

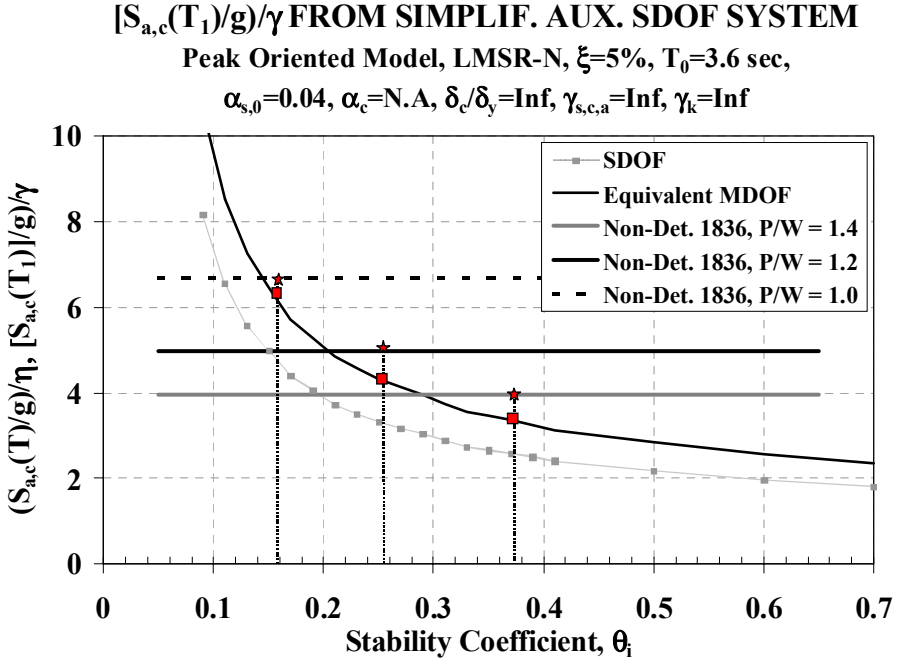

Fig. 5.38 Test of collapse capacity–inelastic stability coefficient curves for MDOF structures with T_0 = 3.6 s. and variations of P/W ratio

6 Effect of Uncertainty in System Parameters on the Variance of Collapse Capacity

6.1 INTRODUCTION

In previous chapters, collapse capacity has been evaluated considering deterministic system parameters, and record to record (RTR) variability has been the only source of uncertainty included in the dispersion of collapse capacity. Although the parameters of the structural system are also subjected to uncertainty, small attention has been paid to the study of probability distributions of system parameters. The main assumption has been that uncertainties related to the system parameters are expected to be small compared to those originated by RTR variability. For instance, Esteva and Ruiz (1989) studied the probability of failure of reinforced concrete (RC) MDOF structures when uncertainty is included in the system parameters. They utilized non-deteriorating systems and considered failure when the ductility demand at any given story reached some predetermined available capacity. Statistical information for parameters such as yielding strength of the bars, concrete strength, and dimensions was taken from investigations on distributions of the system parameters carried out by Mirza and McGregor (1979)[16]. The conclusion was that uncertainty of the aforementioned parameters did not produce large modifications on the probability of failure of the system.

The small effect of uncertainty in the system parameters on the response of non-deteriorating systems has led to the practice of replacing the distributions of the parameters with expected values. However, the uncertainty of system parameters in deteriorating systems has not been systematically evaluated. The results of chapters 4 and 5 suggest that the variance of collapse capacity could be significantly influenced by uncertainty in parameters that define the hysteresis model, such as ductility capacity, post-capping, stiffness or CD rate. The level of

[16] First moments and distributions of system parameters also can be found in Ellingwood (1983).

uncertainty of these parameters is large because of the intrinsic large aleatory variability in the nonlinear range and the inability to accurately evaluate these parameters, i.e., the epistemic uncertainty is also large.

In this chapter, the sensitivity of collapse capacity to uncertainty in the system parameters is investigated by using the first-order second-moment method (FOSM), whereas Monte Carlo simulations are employed to verify the accuracy of FOSM results. In the first part, different alternatives for applying the FOSM method to collapse capacity evaluation are explored for an SDOF system of intermediate ductile characteristics. Thereafter, the increment in the variance of collapse capacity is obtained for representative SDOF systems and for a set of generic frames with intermediate ductile features.

6.2 FOSM METHOD

6.2.1 General Formulation

Given a function $Y = f(Q_1, Q_2, ..., Q_n)$ and given that $\overline{Q}$ is a random vector, the mean and variance of Y can be approximated by a Taylor's series expansion of the performance function (f) about the expected values of the random variables (Wolff, 1994; Melchers, 1999; Baker and Cornell, 2003). The simplest approximation is termed a first-order second-moment (FOSM) method, as only first-order (linear) terms of the series are retained and only the first two moments (mean and variance) are considered. This means that the method is exact for linear performance functions, and that for a given degree of curvature, the method is more accurate for smaller values of the variances. The first two moments are calculated as follows:

$$\mu_Y \cong f(\mu_{Q_1}, \mu_{Q_2}, ..., \mu_{Q_n}) = f(\mu_{\overline{Q}}) \tag{6.1}$$

$$\sigma_Y^2 \cong \sum_{i=1}^{n}\sum_{j=1}^{n}\left(\frac{\partial f(\overline{Q})}{\partial q_i}\frac{\partial f(\overline{Q})}{\partial q_j}\right)_{\overline{Q}=\overline{\mu}_q} \rho_{q_i,q_j}\sigma_{q_i}\sigma_{q_j} \tag{6.2}$$

where $\overline{Q}$ is the vector of random system parameters, $\overline{\mu}_q$ is the vector of mean values of $\overline{Q}$, and the correlation coefficient is equal to:

$$\rho_{i,j} = \frac{Cov(Q_i Q_j)}{\sigma_{q_i}\sigma_{q_j}} \tag{6.3}$$

Note that the first moments of Y can be estimated without knowing the probability distribution of the function $Y = f(\overline{Q})$. The relative magnitudes of the terms in Equation 6.2 provide an explicit indication of the contribution to uncertainty of each variable. The disadvantages of the method are that it is necessary to approximate the value of the derivatives and that an error for nonlinear functions can be introduced by neglecting higher-order terms.

In the application of the method for computing the variance of collapse capacity, an additional term needs to be added to Equation 6.2 to account for the already calculated RTR variability (Section 6.2.2). Also, because FOSM is a simplified method that requires little information to be implemented, several alternatives for approximating the derivative of the function "*f*" in Equation 6.2 are presented in Section 6.2.3.

6.2.2 Computations in Log Domain of Data

In last section, the FOSM formulation is expressed in the *linear domain of the data,* i.e., the parameter values and collapse capacities utilized in Equations 6.1–6.3 are obtained directly from the time history analyses (THA). However, in this research it is preferred to compute the additional variance of collapse capacity in the *log domain of the data*, i.e., by using the natural logarithm of the parameter values and corresponding collapse capacities. The main reason is that high nonlinearities in the system parameters – collapse capacity relationships tend to be reduced in the log domain. Therefore, the results become less sensitive to numerical variations because the likelihood of evaluating collapse capacity in a highly nonlinear region is reduced. Appendix D provides more details of the reasons for preferring the computations in the log domain of the data.

The following formulation is derived from the methodology proposed by Baker and Cornell (2003) for estimating the role of supplementary variables in uncertainty. To compute the total variance in the *log domain*, collapse capacity [17] is initially expressed in the linear domain as:

---

[17] Collapse capacity was defined in Chapter 2 as $[(S_a/g)/\eta]_c$ for SDOF systems and as $\{[(S_a(T_1)/g)]/\gamma\}_c$ for MDOF systems. For the sake of simplicity, in this chapter this nomenclature is usually shortened to $S_{a,c}/\eta$ for SDOF systems and to $S_{a,c}(T_1)/\gamma$ for MDOF structures (although for developing the formulation, only $S_{a,c}/\eta$ is used). If collapse capacity is used as a subscript, the nomenclature is simplified to $S_{a,c}$.

$$S_{a,c}/\eta = f(Q_1, Q_2, ..., Q_n).\varepsilon_k(RTR) \tag{6.4}$$

where the random variable $\varepsilon_k(RTR)$ has a mean equal to one. This formulation is called the "multiplicative approach" because in the linear domain $\varepsilon_k(RTR)$ is a multiplier to the function $f(Q_1, Q_2, ..., Q_n)$. Taking the natural log on both sides of Equation 6.4:

$$\ln(S_{a,c}/\eta) = \ln(Q_1, Q_2, ..., Q_n)) + \ln(\varepsilon_k(RTR)) \tag{6.5}$$

Observe that in the log domain $\ln[\varepsilon_k(RTR)]$ is added to the new function "*g*." By using $X = \ln Q$, Equation 6.5 becomes:

$$\ln(S_{a,c}/\eta) = g(X_1, X_2, ..., X_n)) + \ln(\varepsilon_k(RTR)) \tag{6.6}$$

Since the expected value of $\ln[\varepsilon_k(RTR)]$ is equal to zero, the FOSM method estimates the mean as:

$$\mu_{\ln S_{a,c}} \cong \mu_{g(\overline{X})} \tag{6.7}$$

The variance of $\ln[\varepsilon_k(RTR)]$ is equal to $\sigma^2_{\ln S_{a,c}(RTR)}$, which is the variance of the collapse capacity when the system parameters are deterministic and the only source of uncertainty is RTR variability. Thus, the first-order approximation of the variance of collapse capacity is [18]:

$$\sigma^2_{\ln S_{a,c}(TOT)} \cong \sum_{i=1}^{n}\sum_{j=1}^{n}\left(\frac{\partial g(\overline{X})}{\partial x_i}\frac{\partial g(\overline{X})}{\partial x_j}\right)_{\overline{X}=\overline{\mu}_x} \rho_{x_i,x_j}\sigma_{x_i}\sigma_{x_j} + \sigma^2_{\ln S_{a,c}(RTR)} \tag{6.8}$$

The first term on the right-hand side of Equation 6.8 represents the contribution to the variance of collapse capacity due to uncertainty of all the system parameters. The correlation coefficient, ρ_{x_i,x_j}, is calculated in the same way as ρ_{q_i,q_j} (Equation 6.3).

If only one probabilistic system parameter is involved, Equation 6.8 simplifies to:

$$\sigma^2_{\ln S_{a,c}(TOT)} \cong \left(\frac{\partial g(\mu_x)}{\partial x}\right)^2 \sigma_x^2 + \sigma^2_{\ln S_{a,c}(RTR)} \tag{6.9}$$

Note that in the log domain of the data, the variance of collapse capacity due to RTR variability ($\sigma^2_{\ln S_{a,c}(RTR)}$) is added to the variance of collapse capacity due to uncertainty in the

---

[18] The term $\sigma^2_{S_{a,c}(TOT)}$ is denoted as $Var[S_{a,c}(TOT)]$ in the graphs of this chapter.

system parameters. This formulation assumes that, in the linear domain, the coefficient of variation of collapse capacity due to RTR variability is a constant for variations of the probabilistic parameter, i.e., $c.o.v._{S_{a,c}(RTR)}$ is constant under variations of x_i (see Appendix D).

6.2.3 Computation of Derivative

An approximation of the derivate, $\Delta g(\mu_{\bar{X}})/\Delta x_i$, needed to evaluate Equation 6.8 may be obtained in several ways. For instance, the performance function may be evaluated at two system parameter values and the derivative estimated as the slope of the straight line that connects the pairs [x_i, $g(x_i)$]. The simplest option is to consider the mean of the system parameter and its corresponding collapse capacity as one pair because these values are known. The second point can be any increment above or below the mean. It is recommended to take the increment as one standard deviation to capture some of the nonlinear behavior of the function over a range of likely values (Wolff, 1994; Baker and Cornell, 2003). In Figure 6.1, the straight line connecting these two points is dubbed "secant 1," and from now on, this approach will be referred as the "one-side" approach. The increment with respect to the mean value is represented as $\Delta = \pm n\sigma$, where n is a multiplier. For computations in the log domain of the data:

$$\frac{\partial g(\mu_x)}{\partial x} \cong \frac{\mu_{\ln S_{ac}(x_1)}(x_1 = \mu_x) - \mu_{\ln S_{ac}(x_2)}(x_2 = \mu_x \pm n\sigma_x)}{\pm n\sigma_x} \tag{6.10}$$

where $\mu_{\ln S_{ac}(x_i)}(x_i)$ is the log of the estimator of the geometric mean of collapse capacity (due to RTR variability) when the probabilistic system parameters are $\exp(x_1)$ and $\exp(x_2)$ [19]. This is an additional approximation because the estimator of the geometric mean is modified according to the GMs included in the bin. After this simplification the only source of uncertainty in the computation of the derivative is the uncertainty in the probabilistic parameter.

A second alternative to compute the derivative is to select the points located at one increment above and below the expected value of the random system parameter (Wolff, 1994). This option, which is referred as the "two-side" approach, is shown in Figure 6.1 with the straight line dubbed "secant 2." For smooth functions this method should result in a better

[19] Remember that $X = \ln Q$.

approximation because the slope of "secant 2" is closer to the derivative evaluated at μ_x. The computational effort increases because collapse capacity needs to be evaluated at two additional system parameter values. For computations in the log domain of the data, the derivative is approximated as:

$$\frac{\partial g(\mu_x)}{\partial x} \cong \frac{\mu_{\ln S_{ac}(x_1)}(x_1 = \mu_x + n\sigma_x) - \mu_{\ln S_{ac}(x_2)}(x_2 = \mu_x - n\sigma_x)}{\pm 2n\sigma_x} \tag{6.11}$$

There are other approaches for calculating the derivative such as the standard numerical differentiation method, which utilizes a central difference representation for the derivative (Hornbeck, 1975). These methods are not implemented because they involve a larger computational effort and a pilot study did not improve the accuracy of the results.

6.2.4 FOSM Equation for Parameter Study

In subsequent sections, δ_c/δ_y, α_c and $\gamma_{s,c,k,a}$ are considered the probabilistic system parameters of the structural system. For the sake of simplicity, the nomenclature of these parameters is shortened to δ, α, and γ, respectively, and Equation 6.8 can be particularized as follows:

$$\begin{aligned}
\sigma^2_{\ln S_{a,c}} = &\left(\frac{\partial g(\delta,\alpha,\gamma)}{\partial \delta}\right)^2\Bigg|_{\substack{\delta=\mu_{\ln\delta}\\ \alpha=\mu_{\ln\alpha}\\ \gamma=\mu_{\ln\gamma}}} \sigma^2_{\ln\delta} + \left(\frac{\partial g(\delta,\alpha,\gamma)}{\partial \alpha}\right)^2\Bigg|_{\substack{\delta=\mu_{\ln\delta}\\ \alpha=\mu_{\ln\alpha}\\ \gamma=\mu_{\ln\gamma}}} \sigma^2_{\ln\alpha} + \left(\frac{\partial g(\delta,\alpha,\gamma)}{\partial \gamma}\right)^2\Bigg|_{\substack{\delta=\mu_{\ln\delta}\\ \alpha=\mu_{\ln\alpha}\\ \gamma=\mu_{\ln\gamma}}} \sigma^2_{\ln\gamma} + \\
&2\left(\frac{\partial g(\delta,\alpha,\gamma)}{\partial \delta}\right)\left(\frac{\partial g(\delta,\alpha,\gamma)}{\partial \alpha}\right)\Bigg|_{\substack{\delta=\mu_{\ln\delta}\\ \alpha=\mu_{\ln\alpha}\\ \gamma=\mu_{\ln\gamma}}} \rho_{\alpha\delta}\sigma_{\ln\delta}\sigma_{\ln\alpha} + \\
&2\left(\frac{\partial g(\delta,\alpha,\gamma)}{\partial \delta}\right)\left(\frac{\partial g(\delta,\alpha,\gamma)}{\partial \gamma}\right)\Bigg|_{\substack{\delta=\mu_{\ln\delta}\\ \alpha=\mu_{\ln\alpha}\\ \gamma=\mu_{\ln\gamma}}} \rho_{\delta\gamma}\sigma_{\ln\delta}\sigma_{\ln\gamma} + \\
&2\left(\frac{\partial g(\delta,\alpha,\gamma)}{\partial \alpha}\right)\left(\frac{\partial g(\delta,\alpha,\gamma)}{\partial \gamma}\right)\Bigg|_{\substack{\delta=\mu_{\ln\delta}\\ \alpha=\mu_{\ln\alpha}\\ \gamma=\mu_{\ln\gamma}}} \rho_{\alpha\gamma}\sigma_{\ln\alpha}\sigma_{\ln\gamma} + \sigma^2_{\ln S_{a,c}(RTR)}
\end{aligned} \tag{6.12}$$

In this shortened nomenclature, for instance, the term $\left(\frac{\partial g(\delta,\alpha,\gamma)}{\partial \delta}\right)^2\Bigg|_{\substack{\delta=\mu_{\ln\delta}\\ \alpha=\mu_{\ln\alpha}\\ \gamma=\mu_{\ln\gamma}}}$ refers to the square of the derivative of the function "g" with respect to the system parameter δ_c/δ_y. The

function "g" depends on the parameters δ_c/δ_y, α_c, and $\gamma_{s,c,k,a}$. The derivative is obtained around the mean values of each one of the probabilistic parameters.

The first three terms of Equation 6.12 correspond to contributions to the variance of the natural logarithm of collapse capacity due to uncertainty in δ_c/δ_y, α_c, and $\gamma_{s,c,k,a}$. The following three terms involve correlations among these three parameters. For example, the fourth term is dubbed "$\delta\alpha$ correlation" and expresses the dependence of one parameter on the other one. In the following sections, the terms for the contributions to total variance of the log of collapse capacity are shortened as follows:

$$\begin{aligned}\sigma^2_{\ln S_{a,c}(TOT)} &= \sigma^2_{\ln S_{a,c}(\alpha)} + \sigma^2_{\ln S_{a,c}(\delta)} + \sigma^2_{\ln S_{a,c}(\gamma)} + \\ &\sigma^2_{\ln S_{a,c}(\rho_{\alpha.\delta})} + \sigma^2_{\ln S_{a,c}(\rho_{\delta.\gamma})} + \sigma^2_{\ln S_{a,c}(\rho_{\alpha.\gamma})} + \sigma^2_{\ln S_{a,c}(RTR)}\end{aligned} \tag{6.13}$$

$\sigma^2_{\ln S_{a,c}(\alpha)}$ is the contribution to variance of the log of collapse capacity due to uncertainty in post-capping stiffness. Similar interpretation is given to $\sigma^2_{\ln S_{a,c}(\delta)}$ and $\sigma^2_{\ln S_{a,c}(\gamma)}$.

$\sigma^2_{\ln S_{a,c}(\rho_{\delta.\alpha})}$ is the contribution to variance of the log of collapse capacity due to correlation between the parameters δ and α. Similar explanation is given to the terms $\sigma^2_{\ln S_{a,c}(\rho_{\delta.\gamma})}$ and $\sigma^2_{\ln S_{a,c}(\rho_{\alpha.\gamma})}$.

The three terms involving correlation among parameters can be condensed into a term called "combined correlation." Therefore, Equation 6.13 is condensed to:

$$\sigma^2_{\ln S_{a,c}(TOT)} = \sigma^2_{\ln S_{a,c}(\alpha)} + \sigma^2_{\ln S_{a,c}(\delta)} + \sigma^2_{\ln S_{a,c}(\gamma)} + \sigma^2_{\ln S_{a,c}(\rho_T)} + \sigma^2_{\ln S_{a,c}(RTR)} \tag{6.14}$$

where $\sigma^2_{\ln S_{a,c}(\rho_T)} = \sigma^2_{\ln S_{a,c}(\rho_{\alpha.\delta})} + \sigma^2_{\ln S_{a,c}(\rho_{\delta.\gamma})} + \sigma^2_{\ln S_{a,c}(\rho_{\alpha.\gamma})}$.

Sometimes all the contributions to variance of the log of collapse capacity due to the system parameters are grouped into a single term, $\sigma^2_{\ln S_{a,c}(\bar{X})}$, and Equation 6.14 is simplified as follows:

$$\sigma^2_{\ln S_{a,c}(TOT)} = \sigma^2_{\ln S_{a,c}(\bar{X})} + \sigma^2_{\ln S_{a,c}(RTR)} \tag{6.15}$$

6.3 EVALUATION OF FOSM METHOD FOR OBTAINING VARIANCE OF COLLAPSE CAPACITY

This section explores the most suitable alternatives for computing additional variance of collapse capacity using the FOSM method. Because the method is an approximation that simplifies the nature of the problem, the validity of obtained results depends on the assumptions made for each particular situation. For this reason, this section is divided into three parts. In the first part, only one system parameter at a time is considered in a probabilistic format. At this point, the most consistent alternatives for applying the FOSM method to a single probabilistic parameter are selected. In a second stage, uncertainty of several parameters is considered at the same time to evaluate the effect of correlation among them. In the third part, Monte Carlo simulation is used for verifying some of the results obtained by the FOSM method.

The SDOF system used for these evaluations is the reference system of Chapter 4, which is subjected to the set of records LMSR-N and has the following features:

- Peak-oriented hysteretic model
- No P-Δ effect
- Medium ductility capacity, $\delta_c/\delta_y = 4$
- Small post-capping stiffness, $\alpha_c = -0.1\ K_e$
- Slow cyclic deterioration rate, $\gamma_{s,c,k,a} = 100$

Variance of System Parameters. Statistical information about the parameters that define the hysteretic backbone and its corresponding cyclic deterioration are difficult to find in the literature. Possibly the best source for RC components is the database collected by Fardis and Biskinis (2003), in which statistical information for yield and ultimate rotation of components with different characteristics is presented. The ultimate rotation is defined as the rotation at which 15% of the peak strength is lost. The coefficients of variation (c.o.v.) of the yield and ultimate rotation is used for estimating the standard deviation of the log of ductility capacity in an approximated way because the rotation at peak strength is not computed in the database of Fardis and Biskinis. They report c.o.v. of about 0.55 for the ultimate rotation of rectangular RC members subjected mainly to cyclic loading.

Information about the variation of ductility capacity of steel beam-columns is taken from the database collected by Nakashima (1994). He compiled information from 224 tests carried out by Japanese researchers for steel beam-columns having an H-shaped cross section and bent about

the strong axis. In all the selected tests the lateral load was applied monotonically and the axial load remained constant during the experiment. Ductility capacities were measured considering that the strength on the backbone curve had dropped to 95% ($\delta_{c,95}$), 90% ($\delta_{c,90}$), and 80% ($\delta_{c,80}$) with respect to its peak value. According to the first definition of ductility capacity, the c.o.v. for components with very small axial load is *c.o.v.* ($\delta_{c,95}/\delta_y$) = 0.54. The c.o.v. increases for components subjected to significant axial load and is also expected to increase for tests including cyclic loads.

Based on these published data, a reasonable and likely conservative (high) value for the standard deviation of the log of ductility capacity is 0.60. Regarding the parameters α_c and $\gamma_{s,c,k,a}$, systematic information is not available in the literature. However, the limited information compiled from several component tests suggests that the dispersion is also high for these parameters. Thus, it has been decided to use the dispersion adopted for ductility capacity also for the parameters α_c and $\gamma_{s,c,k,a}$.

6.3.1 Sensitivity of Collapse Capacity due to a Single Probabilistic System Parameter

In this section the FOSM method is applied to a single probabilistic parameter for the purpose of evaluating the following parts of the process:

(a) Estimation of the derivative. The one-side and two-side approaches shown in Section 6.2.3 to approximate the derivative are tested. The sensitivity study also includes the effect of different increments for these approaches, i.e., the number of standard deviations at which the parameters are evaluated.

(b) Assumed dispersion. The implications of assuming a standard deviation of the log of the data of 0.60 for all the parameters are investigated by carrying out a sensitivity study that involves different dispersions for these parameters.

6.3.1.1 Post-Capping Stiffness

This parameter is relevant in collapse capacity evaluation because it greatly affects the displacement at which the backbone curve reaches zero restoring force or the residual strength. The boundaries for α_c are the horizontal and vertical slopes, i.e., $\alpha_c = 0$ and $\alpha_c = -\infty$,

respectively. Positive post-capping slopes are not consistent with the definition of a peak strength value at the displacement δ_c.

For the following calculations, the sign of α_c is changed from negative to positive to be able to compute logarithms, and the nomenclature is simplified as follows: $\mu_{\ln\alpha_c}=\mu_{\ln\alpha}=\ln(0.10)=-2.303$. Note that the mean in the log domain is the logarithm of the "deterministic" parameter value of the reference SDOF system.

Computation of the Derivative. The derivative of the function "*g*" due to variations in α_c is evaluated by considering that the rest of the parameters have mean values that remain constant under the aforementioned variations. The derivative is approximated as the straight line that connects two pairs of the form [$\ln\alpha_{c,i}$, $\ln S_{a,c}/\eta(\alpha_{c,i})$].

In the one-side approach, $S_{a,c}/\eta$ is evaluated at $-\alpha_{c,1}=\exp(m_{\ln\alpha})$ and $-\alpha_{c,2}=\exp(m_{\ln\alpha}\pm n\sigma_{\ln\alpha})$; see "secant 1" in Figure 6.1. The effect of different increments for the second pair is also studied, i.e., different "*n*" values. Eight increments are evaluated: $\Delta=\pm 0.25\sigma_{\ln\alpha}$, $\pm 0.5\sigma_{\ln\alpha}$, $\pm 1.0\sigma_{\ln\alpha}$, and $\pm 1.5\sigma_{\ln\alpha}$. In all cases, $\sigma_{\ln\alpha}=0.60$. For illustration, the two α_c values generated at $\Delta=\pm 1.0\sigma_{\ln\alpha}$ are:

$$16^{th}_{\ln\alpha}=\mu_{\ln\alpha}+\sigma_{\ln\alpha}=-2.903\Rightarrow-\alpha_c=\exp(-2.903)=0.055$$
$$84^{th}_{\ln\alpha}=\mu_{\ln\alpha}-\sigma_{\ln\alpha}=-1.703\Rightarrow-\alpha_c=\exp(-1.703)=0.182$$

SDOF analyses are performed at these eight increments in the period range from T = 0.1 to 4.0 s. Figure 6.2 shows collapse capacity spectra for different α_c values that correspond to the proposed increments. Figure 6.3 presents the dependence of median $(S_{a,c}/g)/\eta$ on α_c for all the evaluated periods. If these curves are plotted in a log-log space, they are smoother and closer to straight lines (Fig. 6.4), a feature that provides stability to the computation of the derivative.

To obtain an idea of the magnitude of the variances involved in the study, Figure 6.5 shows the variance of collapse capacity due to RTR variability and due to uncertainty in α_c ($\sigma^2_{S_{a,c}(RTR)}$ and $\sigma^2_{S_{a,c}(\alpha_c)}$, respectively). The derivative to compute $\sigma^2_{S_{a,c}(\alpha_c)}$ is obtained by evaluating α_c at $-\alpha_{c,1}=\exp(\mu_{\ln\alpha})$ and $-\alpha_{c,2}=\exp(\mu_{\ln\alpha}+\sigma_{\ln\alpha})$. As observed, $\sigma^2_{S_{a,c}(\alpha_c)}$ becomes relevant for the reference system in the long-period range.

The one-side approach for computing the variance of collapse capacity due to uncertainty in α_c ($\sigma^2_{\ln S_{a,c}(\alpha)}$) is presented in Figure 6.6 for all the considered increments. The additional

variance is presented as a fraction of the uncertainty due to RTR variability ($\sigma^2_{\ln S_{a,c}(\alpha)} / \sigma^2_{\ln S_{a,c}(RTR)}$). As can be seen, this ratio greatly varies according to the direction in which the increment is considered, and the differences are more pronounced for large increments i.e., compare $\sigma^2_{\ln S_{a,c}(\alpha)} / \sigma^2_{\ln S_{a,c}(RTR)}$ for $\Delta_{\ln\alpha} = +1.5\sigma_{\ln\alpha}$ and $\Delta_{\ln\alpha} = -1.5\sigma_{\ln\alpha}$ (Fig. 6.6b). On the other hand, the use of small increments ($\Delta_{\ln\alpha} = 0.25\sigma_{\ln\alpha}$) produces curves with erratic behavior because $\sigma^2_{\ln S_{a,c}(\alpha)}$ is more sensitive to numerical variations in the calculated collapse capacity.

For the two-side approach, the derivative is obtained by evaluating post-capping stiffness at $-\alpha_{c,1} = \exp(\mu_{\ln\alpha} - n\sigma_{\ln\alpha})$ and $-\alpha_{c,2} = (\mu_{\ln\alpha} + n\sigma_{\ln\alpha})$, which corresponds to "secant 2" in Figure 6.1. The $\sigma^2_{\ln S_{a,c}(\alpha)} / \sigma^2_{\ln S_{a,c}(RTR)}$ ratios under this alternative are shown in Figure 6.7. It is concluded that although this option requires a larger computational effort, it is more appropriate for this parameter because the additional uncertainty is less dependent on the increment ($\Delta_{\ln\alpha} = n\sigma_{\ln\alpha}$) and the curves are smoother.

Effect of Assumed Dispersion in α_c. The dispersion of the system parameters has been assumed as $\sigma_{\ln\alpha} = 0.60$. This section evaluates the effect of the selected dispersion of α_c by using four different standard deviation of the log of the parameter: $\sigma_{\ln\alpha} = 0.15$, 0.30, 0.60 and 0.90. The two-side approach is used for approximating the derivative and the considered increment is one standard deviation, i.e., α_c is evaluated at $-\alpha_{c,1} = \exp(\mu_{\ln\alpha} - \sigma_{\ln\alpha})$ and $-\alpha_{c,2} = \exp(\mu_{\ln\alpha} + \sigma_{\ln\alpha})$. As observed in Figure 6.8, the selected dispersion of α_c has a large influence on the $\sigma^2_{\ln S_{a,c}(\alpha)} / \sigma^2_{\ln S_{a,c}(RTR)}$ ratios.

6.3.1.2 Ductility Capacity

The evaluation carried out for α_c is repeated for δ_c/δ_y under similar assumptions, such as the same dispersion for the parameter, $\sigma_{\ln\delta} = 0.6$. Because the lower limit for this parameter is $\delta_c/\delta_y = 1$, a change of variable is performed, the new variable being $\delta_c/\delta_y - 1$ (when used as a subscript, it is simplified to δ). The change of variable is relevant when applying Monte Carlo simulation (Section 6.3.3) because a lognormal distribution is assigned for ductility capacity and this modification prevents the possibility of generating values for δ_c/δ_y smaller than unity.

Collapse capacity spectra generated with increments similar to those used for α_c are presented in Figure 6.9. For the reference system, the dispersion of collapse capacities is less affected by uncertainty in ductility capacity than by uncertainty in α_c. Figure 6.10 shows that $(\delta_c/\delta_y - 1)$–$S_{a,c}/\eta$ relationships can be approximated by straight lines in the linear and log space.

As in the case of α_c, the one-side approach for approximating the derivative leads to $\sigma^2_{\ln S_{a,c}(\delta)} / \sigma^2_{\ln S_{a,c}(RTR)}$ ratios that greatly depend on the selected increment. The problem is circumvented by approximating the derivative with the two-side approach (secant 2 in Fig. 6.1). The resulting $\sigma^2_{\ln S_{a,c}(\delta)} / \sigma^2_{\ln S_{a,c}(RTR)}$ ratios are shown in Figure 6.11.

For testing the selected value $\sigma_{\ln\delta} = 0.60$, $\sigma^2_{\ln S_{a,c}(\delta)}$ is evaluated for four ductility capacity dispersions: $\sigma_{\ln\delta} = 0.12$, 0.30, 0.60, and 0.90. In all cases, the two-side approach with an increment of one standard deviation is used for approximating the derivative. $\sigma^2_{\ln S_{a,c}(\delta)} / \sigma^2_{\ln S_{a,c}(RTR)}$ ratios for the selected dispersions are presented in Figure 6.12, which shows large differences in the results according to the selected $\sigma_{\ln\delta}$.

To put the results of Figure 6.12 into perspective with those shown in Figure 6.8, it is emphasized that the relatively small effect of ductility capacity on the variance, compared to the large effect of α_c is a consequence of choosing a central value of -0.10 for the latter parameter. In Section 4.3 it has been shown that for this flat post-capping stiffness the relative intensity at collapse (collapse capacity) is much larger than the relative intensity associated with reaching δ_c, and is not very sensitive to the ductility capacity. Different results would be obtained for a similar system but with a parameter α_c = -0.30.

6.3.1.3 Cyclic Deterioration

The hysteretic energy capacity is based on $\gamma_{s,c,k,a}$. A value $\gamma_{s,c,k,a} = \infty$ defines a system without cyclic deterioration effects. When used as a subscript, γ represents the four modes of cyclic deterioration.

The dispersion of the parameter $\gamma_{s,c,k,a}$ is also taken as $\sigma_{\ln\gamma} = 0.6$. Because collapse capacity is less sensitive to variations of CD rates, larger increments are used compared to previously discussed parameters: $\Delta = \pm 0.5\sigma_{\ln\gamma}$, $\pm 1.0\sigma_{\ln\gamma}$, $\pm 1.5\sigma_{\ln\gamma}$, and $\pm 2.33\sigma_{\ln\gamma}$. For a

central value of $\gamma_{s,c,k,a} = 100$, a variation of one standard deviation results in $\gamma_1 = 55$ and $\gamma_2 = 182$.

Figure 6.13 shows collapse capacity spectra for the reference SDOF system, $\gamma_{s,c,k,a}$ values corresponding to a central value of 100, and increments as listed in the previous paragraph. As observed, $S_{a,c}/\eta$ is less sensitive to different CD rates than to variations in previously discussed parameters. Figure 6.14 presents the dependence of median $S_{a,c}/\eta$ on $\gamma_{s,c,k,a}$ for different periods. For this parameter the curves do not resemble a linear function neither in the linear nor log space.

The two-side approach for approximating the derivative provides smooth $\sigma^2_{\ln S_{a,c}(\gamma)} / \sigma^2_{\ln S_{a,c}(RTR)}$ ratios that are not greatly affected by the size of the increment (Fig. 6.15). For estimating the effect of the selected dispersion of $\gamma_{s,c,k,a}$ on collapse capacity, $\sigma^2_{\ln S_{a,c}(\gamma)}$ is calculated for $\sigma_{\ln\gamma} = 0.30$, 0.60, 0.90, and 1.40. The results presented in Figure 6.16 indicate that the dispersion of $\gamma_{s,c,k,a}$ may be relevant for the $\sigma^2_{\ln S_{a,c}(\gamma)} / \sigma^2_{\ln S_{a,c}(RTR)}$ ratios, but not as much as the effect of the selected dispersion of α_c or δ_c/δ_y.

6.3.2 Sensitivity in Collapse Capacity due to Several Probabilistic Parameters

The contributions to $\sigma^2_{\ln S_{a,c}(TOT)}$ from ductility capacity, post-capping stiffness and CD, as well as possible correlation among them are evaluated for the reference SDOF system. The derivative is approximated with the two-side approach and the size of the increment with respect to the mean value is one standard deviation, i.e., the parameters are evaluated at $x_1 = \exp(\mu_{\ln x} - \sigma_{\ln x})$ and $x_2 = \exp(\mu_{\ln x} + \sigma_{\ln x})$.

6.3.3.2 Sensitivity due to Uncertainty in System Parameters, No Correlation

$\sigma^2_{\ln S_{a,c}(X_i)} / \sigma^2_{\ln S_{a,c}(RTR)}$ ratios for the three system parameters are shown in Figure 6.17 when considering the same dispersion for the three parameters, $\sigma_{\ln\alpha} = \sigma_{\ln\delta} = \sigma_{\ln\gamma} = 0.60$.

The contribution to total variance of collapse capacity ($\sigma^2_{\ln S_{a,c}(TOT)}$) of GMs and system parameters is shown in Figure 6.18. These graphs reveal the importance of uncertainty in the

post-capping stiffness for the reference SDOF system, which is due to the small value of this parameter. Note that the evaluation assumes the same dispersion for the three parameters, which does not necessarily occur in real components.

6.3.3.3 Sensitivity due to Uncertainty in System Parameters, Correlation Included

The estimation of coefficients of correlation usually is more complicated than estimating the first two moments for the individual parameters. The correlation among the deteriorating parameters is expected to be high because usually the system parameters of a given component tend to be less or more ductile to the same degree. For instance, it is likely to have a component with smaller ductility capacity if the post-capping slope is steeper. Correlation among the studied parameters is not documented, but the following low- and high-correlation factors are proposed based on judgmental criteria and values reported by Esteva and Ruiz (1989):

Low correlation: $\rho_{\alpha\delta} = \rho_{\alpha\gamma} = -0.5$ and $\rho_{\delta\gamma} = 0.5$

High correlation: $\rho_{\alpha\delta} = \rho_{\alpha\gamma} = -0.8$ and $\rho_{\delta\gamma} = 0.8$

$\rho_{\alpha\delta}$ is negative because usually a system with high ductile characteristics has a smaller post-capping stiffness coefficient and larger ductility capacity. The same reasoning is used for assigning the signs to the other two correlations.

Figure 6.19 presents individual contributions to $\sigma^2_{\ln S_{a,c}(TOT)}$ for the reference SDOF system, including "low" correlation. At some periods the variance of collapse capacity due to uncertainty in the system parameters, $\sigma^2_{\ln S_{a,c}(\bar{X})}$, is larger than that caused by RTR variability. Figure 6.20 shows the contributions of individual low correlations to the combined correlation. The correlation ratios are essentially period-independent except in the short-period range and the two larger ratios involve the post-capping stiffness parameter. This is expected because it is the parameter that most contributes to $\sigma^2_{\ln S_{a,c}(TOT)}$.

Figure 6.21 presents the same information as Figure 6.19 when high correlation is considered. $\sigma^2_{\ln S_{a,c}(\bar{X})}$ is not greatly modified when high correlation is used instead of low correlation.

6.3.3.4 FOSM Method without Explicit Contribution of Parameters

In former sections, the FOSM method has been used for computing the additional variance of collapse capacity due to individual parameters. The total contribution from system parameters has been computed by adding the explicit contribution to uncertainty of each parameter, as well as their corresponding correlations, which are calculated with Equation 6.8.

It is detected that combined correlation may be the most important contributor to variance of collapse capacity for some systems. However, the correlation contributions are derived in an indirect way in the FOSM method because correlation is not explicitly included in the THA or in the computation of the derivative. To verify the effect of the combined correlations obtained for the reference SDOF system, the properties of the three probabilistic parameters are modified at the same time and the FOSM method is applied. The parameters are varied in the same proportion for considering full correlation, i.e., $\rho_{x_i,x_j} = \pm 1$. The explicit contributions of each parameter are not recoverable in this approach but the correlation among parameters is implicit in the THA and does not need to be calculated by the FOSM method.

As a first step, $\sigma^2_{\ln S_{a,c}(TOT)}$ is computed considering explicit contributions of the parameters. The process is the same as in the previous section but considering full correlation among parameters. Then the effect of combined correlation is computed according to Equation 6.8. Figure 6.22 presents the variance of collapse capacity due to RTR variability and uncertainty in system parameters.

In a second step, the contribution of the parameters is not accounted for explicitly. Collapse capacity is evaluated for a system with low ductility, which considers the 16th percentile of δ_c/δ_y and $\gamma_{s,c,k,a}$ and the 84th of α_c. Collapse capacity is also evaluated for a system with high ductility, in which the former parameter percentiles are inverted. Thereafter, the derivative is computed with information of the systems with high and low ductility according to Equation 6.11. Because all the probabilistic parameters varied at once previous to performing the THA, Equation 6.8 is reduced to only one term that includes even the full correlation among the system parameters, i.e., FOSM is not required to compute the correlation. Figure 6.23 presents $\sigma^2_{\ln S_{a,c}(TOT)}$ under both approaches. The results computed with explicit and non-explicit contributions are very similar, validating the large combined correlations obtained with Equation 6.8.

Summarizing, alternatives for applying the FOSM method to collapse capacity sensitivity have been evaluated. The computations in the log domain are preferred, and parameter evaluation at $x_1 = \exp(\mu_{\ln x} - \sigma_{\ln x})$ and $x_2 = \exp(\mu_{\ln x} + \sigma_{\ln x})$ results in a good approximation to the derivative of Equation 6.8. Also, the sensitivity to low and high correlation has been explored without finding large differences in $\sigma^2_{\ln S_{a,c}(TOT)}$.

6.3.3 Monte Carlo Simulation

The distribution associated with the probabilistic description of system parameters is unknown but is not required in the FOSM method. It is likely that the real distribution of the system parameters may be approximated with a lognormal or a truncated Gaussian distribution. This is suggested from previous studies (Mirza and McGregor, 1979; Ellingwood, 1983) that have obtained distributions for some parameters of structural components. If the distribution of the system parameters were known, $\sigma^2_{\ln S_{a,c}(\bar{X})}$ could be calculated using Monte Carlo simulation, a technique that provides a more precise answer than the FOSM method but involves large computational effort. In this section, the distribution of the system parameters is assumed to be lognormal to test the ability of the FOSM method to deliver reasonable results on collapse capacity sensitivity.

Monte Carlo simulation involves sampling randomly to simulate artificially a large number of events. The technique requires the knowledge of the distribution of the system parameter and a performance function to correlate this distribution with collapse capacity. Then, the performance function is evaluated for many possible values of the random variables. Because the distributions of the system parameters must be known or assumed, the results for collapse capacity sensitivity are only accurate to the extent that these distributions are accurate.

Two approaches for applying Monte Carlo simulation to collapse capacity sensitivity are evaluated. They differ from each other in the method used to obtain the function that correlates the system parameter with collapse capacity.

6.3.3.1 Monte Carlo Simulation Using Time History Analysis (THA)

In this approach the system parameter is correlated with collapse capacity by performing a THA for each random number, which is computationally expensive. The simulation is applied to the reference SDOF system at T = 0.6 and 1.8 s. The following cases are addressed to verify several components of Equation 6.8 that are the basis of the FOSM method:

(a) Three simulations are carried out considering as a random variable only one system parameter. Simulations for α_c, δ_c/δ_y, and $\gamma_{s,c,k,a}$ are performed assuming lognormal distribution and a dispersion $\sigma_{\ln Xi} = 0.60$ for all the parameters.

(b) The three probabilistic parameters used in the FOSM method are taken as random variables at once. Lognormal distribution is assumed for all the parameters, and to account for full correlation, the same random number is used to compute the three system parameters[20]. The random number must be associated with each parameter in such a way that all the parameters represent about the same level of ductility. For instance, if the random number is 0.80, δ_c/δ_y and $\gamma_{s,c,k,a}$ values are associated to the 80th percentile in the corresponding CDF to produce a more ductile system. However, the cumulative distribution function (CDF) for α_c must correspond to 20th percentile because flatter α_c's make the system more ductile.

For each random number, the system parameters are modified and the THA is carried out for the 40 records of the set LMSR-N, but only the median value is recovered. This is an approximation that intends to obtain the dispersion on collapse capacity due entirely to the uncertainty in the system parameters and to eliminate RTR variability.

Figure 6.24 presents the dependence of median $S_{a,c}/\eta$ on α_c obtained for two different Monte Carlo simulations. In the first one, α_c is the only parameter considered in a probabilistic format (under the lognormality assumption), whereas the second relationship considers α_c, δ_c/δ_y and $\gamma_{s,c,k,a}$ as random variables (according to option b). The curves intersect at the median value of the parameter (α_c = 0.10), and the simulation in which the three parameters are varying together produces smaller collapse capacities to the right of the median α_c value. This is because not only α_c is causing less ductile behavior, but also δ_c/δ_y and $\gamma_{s,c,k,a}$. The reverse trend occurs for

[20] The same set of random numbers must be employed to evaluate the effect of modifying one or more variables when using Monte Carlo simulation (Melchers, 1999).

α_c < 0.10. Similar patterns for the dependence of collapse capacity on δ_c/δ_y and $\gamma_{s,c,k,a}$ are observed in Figures 6.25–6.26.

Figure 6.27 presents the fragility curve (CDF) that expresses the probability of collapse given the value of $(S_a/g)/\eta$ (see Chapter 7). The "counted" fragility curve (FC) is obtained by assigning to each individual collapse a probability of $1/N$ (N = total number of realizations) and adding the number of cases collapsing at each $(S_a/g)/\eta$ level. A good approximation to the counted FC is obtained by fitting a lognormal distribution. Thus, the collapse capacity distribution is very similar to a lognormal one when the system parameters also have a lognormal distribution.

Figure 6.28 compares the fitted collapse FC for uncertainty only in α_c with the corresponding FC when uncertainty is included in α_c, δ_c/δ_y, and $\gamma_{s,c,k,a}$. The dispersion in collapse capacity increases with the number of probabilistic parameters involved, which is indicated with a flatter FC.

The variances obtained with Monte Carlo simulation are very similar to those reported by the FOSM method. Figure 6.29 presents $\sigma^2_{\ln S_{a,c}(\bar{X})}$ obtained with the FOSM method and with Monte Carlo simulation at T = 0.6 and 1.8 s. The difference in the variance at T = 1.8 s. is 8%, whereas at T = 0.6 s, the variances are practically the same.

6.3.3.2 Monte Carlo Simulation Using Fitted Function instead of THA

The dependence of $S_{a,c}/\eta$ on the system parameters tends to be smooth (Figs. 6.3–6.4, 6.10, and 6.14). Therefore, instead of performing a THA for each realization, a function that correlates system parameters with collapse capacities is fitted through some discrete values. This procedure reduces the computational time but the fitted curve may miss irregularities captured by THA.

The method is applied to the reference SDOF system and is illustrated here using the post-capping stiffness parameter. A lognormal distribution is assumed for α_c, which in the log domain transforms into a Gaussian distribution of mean $\mu_{\ln\alpha} = \ln(0.10)$ and dispersion $\sigma_{\ln\alpha} = 0.60$. Expressions for $\ln(S_{a,c}/\eta)$ as a function of $\ln(\alpha_c)$ are obtained from fitting curves to the relationships of Figure 6.4. Figure 6.30a shows the exponential function fitted to the curve corresponding to T = 0.5 s. After Monte Carlo simulation is performed, the histogram of log of

collapse capacities is obtained (Fig. 6.31), which can be fitted with a normal distribution in the log domain of the data. The variance of collapse capacity obtained by this fitting is very similar to the one obtained by the FOSM method.

As an alternative, a straight line may be used to represent the $\ln(\alpha_c)$–$\ln(S_{a,c}/\eta)$ relationship with about the same coefficient of correlation (R = 0.98 instead of R = 0.99) (Fig. 6.30b). Moreover, if the straight line $\ln S_{ac} = a \ln \delta + b$ is a good representation of the $\ln(\alpha_c)$–$\ln(S_{a,c}/\eta)$ relationship, there is no need for Monte Carlo simulation because the variance of collapse capacity due to uncertainty in α_c is:

$$\sigma^2_{\ln S_{a,c}[\alpha]} = a^2 \sigma^2_{\ln \alpha} \tag{6.16}$$

Straight lines are fitted to the dependence of $S_{a,c}/\eta$ on α_c in the log space for all the evaluated periods (Figs. 6.3–6.4). Then, the slopes of the straight lines are used for obtaining the variance from a linear transformation. Figure 6.32 shows the $\sigma^2_{\ln S_{a,c}(\alpha)} / \sigma^2_{\ln S_{a,c}(RTR)}$ ratios obtained with the FOSM method and with the linear approximation. The curves are very similar because the FOSM method is exact for linear relationships.

The dependence of $\ln(S_{a,c}/\eta)$ on $\ln(\delta_c/\delta_y)$ also resembles straight lines and the same approach may be used. In the case of CD, the curves do not fit a straight line but the direct method still provides a large simplification to the simulation process.

In summary, Monte Carlo and FOSM methods deliver similar results for computing $\sigma^2_{\ln S_{a,c}(\bar{X})}$. The latter method is preferred because it requires much smaller computational effort and does not necessitate commitment to a distribution of the system parameters.

6.4 SENSITIVITY ANALYSIS FOR REPRESENTATIVE SDOF SYSTEMS

The contributions to the variance of collapse capacity depends on combinations of the system parameters α_c, δ_c/δ_y, and $\gamma_{s,c,k,a}$, which together represent the "ductility characteristics" of the system. This section evaluates five SDOF systems with different ductility characteristics and no P-Δ effects, and another five identical systems with "small" P-Δ effect. The probabilistic parameters are α_c, δ_c/δ_y, and $\gamma_{s,c,k,a}$ and the measure of dispersion is $\sigma_{\ln \alpha} = \sigma_{\ln \delta} = \sigma_{\ln \gamma} = 0.60$. The correlation factor is set as 0.8 for all cases, i.e., $\rho_{\alpha\gamma} = \rho_{\alpha\delta} = -0.8$ and $\rho_{\delta\gamma} = 0.8$.

Figure 6.33 presents sensitivity results on collapse capacity for a peak-oriented model with intermediate "ductility" characteristics and no P-Δ effect. The system is similar to the reference system but has $\gamma_{s,c,k,a}$ = 50 instead of 100. This modification intends to detect $\gamma_{s,c,k,a}$ ranges that produce larger contributions to the variance of $S_{a,c}/\eta$. According to Figure 6.14, the dependence of collapse capacity is higher when the mean of $\gamma_{s,c,k,a}$ is in the vicinity of 50 than when $\gamma_{s,c,k,a}$ is in the neighborhood of 100. This is reflected in a slight increment in the contribution of $\sigma^2_{\ln S_{a,c}(\gamma)}$ (Fig. 6.33a). However, $\sigma^2_{\ln S_{a,c}(\alpha)}$ still overpowers the contribution of the other two parameters, as it does the contributions to the combined correlation, which for long periods is even larger than that of RTR variability. Figure 6.33b presents the $\sigma^2_{\ln S_{a,c}(RTR)}$, $\sigma^2_{\ln S_{a,c}(\bar{X})}$, and $\sigma^2_{\ln S_{a,c}(TOT)}$ for the system with intermediate ductility characteristics. For systems with no P-Δ effects, the combined uncertainty in all the system parameters usually becomes the most important contributor to $\sigma^2_{\ln S_{a,c}(TOT)}$ for long-period systems. Also, for periods longer than about 0.6 s, the total variance of collapse capacity is essentially period independent and has a value close to $\sigma^2_{\ln S_{a,c}(TOT)} = 0.40$. Clearly these results strongly depend on the assumed measure of dispersion of the system parameters, which is taken here as $\sigma_{\ln\alpha} = \sigma_{\ln\delta} = \sigma_{\ln\gamma} = 0.60$. Figure 6.33c shows the contributions of the correlation among parameters to the combined correlation. The contributions are essentially period independent, and $\alpha\gamma$ and $\delta\alpha$ correlations have the largest contributions because α_c is the most important contributor of the three probabilistic parameters.

Figure 6.34 presents contributions to the variance of collapse capacity for a similar system but with α_c = -0.30. As observed, $\sigma^2_{\ln S_{a,c}(\alpha)}$ is no longer the most important contributor to $\sigma^2_{\ln S_{a,c}(TOT)}$ due to the presence of a steeper post-capping stiffness. The large value of α_c reduces $\sigma^2_{\ln S_{a,c}(\bar{X})}$ (Fig. 6.34b) and modifies the contributions from *i,j* correlations to the combined correlation (Fig. 6.34c).

Contributions to the variance of collapse capacity for a peak-oriented model with no P-Δ effects and low ductility characteristics are shown in Figure 6.35. As can be seen, the contribution of $\sigma^2_{\ln S_{a,c}(\alpha)}$ to $\sigma^2_{\ln S_{a,c}(TOT)}$ is again the most important for a single parameter, whereas $\sigma^2_{\ln S_{a,c}(\gamma)}$ is smaller compared with that of systems with intermediate ductility. Although this is the

most sensitive region for γ, the variation in post-capping stiffness overpowers the rest of the variations. Low ductility characteristics reduce the magnitude of $\sigma^2_{\ln S_{a,c}(TOT)}$, which oscillates between 0.20 and 0.30 for most of the periods, except in the short-period range.

The contributions to variance of $(S_{a,c}/g)/\eta$ for a system with high ductility are presented in Figure 6.36. $\sigma^2_{\ln S_{a,c}(\delta)}$ greatly increases for this system, although $\sigma^2_{\ln S_{a,c}(\alpha)}$ still is the largest one. CD contributions are reduced compared with the system with intermediate ductility because the dependence of collapse capacity on CD is smaller for higher γ's. For $T > 0.6$ s, $\sigma^2_{\ln S_{a,c}(TOT)}$ is essentially period independent with values slightly larger than 0.40. Note that the magnitude of $\sigma^2_{\ln S_{a,c}(TOT)}$ does not increase substantially compared with the system with intermediate "ductility" (Fig. 6.33). Regarding combined correlation, the results for systems with high ductility show that the ratio $\sigma^2_{\ln S_{a,c}(\rho_T)}/\sigma^2_{\ln S_{a,c}(\bar{X})}$ increases when $\sigma^2_{\ln S_{a,c}(\alpha)}$, $\sigma^2_{\ln S_{a,c}(\gamma)}$, and $\sigma^2_{\ln S_{a,c}(\delta)}$ are similar, in accordance with Equation 6.12.

Contributions to $\sigma^2_{\ln S_{a,c}(TOT)}$ for a bilinear model with intermediate ductility features and no P-Δ effects are shown in Figure 6.37a. In this case, δ_c/δ_y is the parameter with the largest contributions to variance of collapse capacity. Figure 6.37b shows that $\sigma^2_{\ln S_{a,c}(TOT)}$ decreases for bilinear models compared with equivalent results for peak-oriented models, particularly in the short- and medium-period range.

The results for similar systems that include P-Δ = "0.1*N*" (see Section 4.3.6) are presented in Figures 6.38–6.42. The contributions to variance of collapse capacity are considerably modified. There is a large reduction in $\sigma^2_{\ln S_{a,c}(\bar{X})}$, especially in the medium- and long-period ranges. The largest contributions to variance of collapse capacity come from uncertainties in ductility capacity and combined correlation, except for systems with low "ductility." $\sigma^2_{\ln S_{a,c}(\alpha)}$ is reduced because of the rotation of the entire backbone curve to include P-Δ effects. CD contribution is even smaller when P-Δ effects are present. Also, $\sigma^2_{\ln S_{a,c}(TOT)}$ is significantly reduced when P-Δ effects are included, especially in the long-period range. Most of this reduction comes from a decrease in $\sigma^2_{\ln S_{a,c}(\bar{X})}$, whereas $\sigma^2_{\ln S_{a,c}(RTR)}$ exhibits only small differences because of P-Δ effects.

In summary, combined correlation has the largest influence on $\sigma^2_{\ln S_{a,c}(TOT)}$ for most of the systems. The P-Δ level of the system greatly modifies the variance of collapse capacity due to uncertainty in the system parameters. The contributions of any probabilistic parameter to $\sigma^2_{\ln S_{a,c}(TOT)}$ depend on the location of the mean of the parameter in the $(S_{a,c}/g)/\eta$ - x_i relationship and on the ductility characteristics of all the other parameters.

6.5 SENSITIVITY COMPUTATION FOR MDOF SYSTEMS USING FOSM METHOD

$\sigma^2_{\ln S_{a,c}(\bar{X})}$ is computed for a set of generic frames designed with the strong column–weak beam philosophy, assuming that the columns are infinitely strong. The springs at the ends of the beams have a peak-oriented hysteretic model, $\delta_c/\delta_y = 4$, $\alpha_c = -0.10$, $\gamma_{s,c,k,a} = 50$ and no residual strength. The dispersion of system parameters is $\sigma_{\ln\alpha} = \sigma_{\ln\delta} = \sigma_{\ln\gamma} = 0.60$ and the correlation among parameters is $\rho_{ij} = 0.80$.

Contribution to variance of collapse capacity, correlations, and absolute variances are presented in Figures 6.43–6.45 for stiff frames ($T_1 = 0.1N$, periods from 0.3–1.8 s). For these frames, α_c is the system parameter with the largest influence on $\sigma^2_{\ln S_{a,c}(TOT)}$, whereas the combined correlation is the most important contributor to $\sigma^2_{\ln S_{a,c}(\bar{X})}$. The results for MDOF structures may be compared with those of the SDOF system that shares the same hysteretic properties of the springs at the beam ends of the frames[21] (see small window in Figs. 6.43 and 6.45). As observed, both SDOF and MDOF systems have $\sigma^2_{\ln S_{a,c}(\bar{X})}$ contributions that account for about 40% of $\sigma^2_{\ln S_{a,c}(TOT)}$. More than half of $\sigma^2_{\ln S_{a,c}(\bar{X})}$ comes from combined correlations.

The same results for flexible frames ($T_1 = 0.2N$, periods from 0.6–3.6 s) are presented in Figures 6.44–6.46. For these frames, the parameter δ_c/δ_y gains on influence for long-period frames, whereas the influence of uncertainty in post-capping stiffness diminishes.

---

[21] Rigorously, the equivalent SDOF system must be obtained from a global pushover analysis of the MDOF structure and taking into account the inelastic stability coefficient for computing the equivalent P-Δ effect.

Flexible frames may be compared with the region of the SDOF systems located between T = 0.6 and 3.6 s. The patterns for SDOF and MDOF systems are similar, but the contributions of uncertainty in the system parameters to the total variance are somewhat larger for MDOF systems.

6.6 SUMMARY

The first part of this chapter discusses the feasibility of applying the FOSM method for computing the variance of collapse capacity due to uncertainty in the system parameters. The most suitable alternatives for the implementation of the method are summarized below:

- The computations of variance of collapse capacity are carried out in the log domain of the data. This option is preferred over computations in the linear domain of the data because high nonlinearities in the dependence of collapse capacity on the system parameter are usually reduced. Also, the results become less sensitive in a domain that makes the curves smoother. In addition, there are physical lower limits for the system parameters that are better modeled with a lognormal distribution.
- The derivative of the function "g" used in the FOSM formulation is approximated with the slope of a straight line that connects two pairs of system parameters and corresponding collapse capacities. The two-side approach, in which the selected points are located at about the same distance from the mean [$x_1 = \exp(\mu_{\ln x} - n\sigma_{\ln x})$ and $x_2 = \exp(\mu_{\ln x} + n\sigma_{\ln x})$] is a better option than using the mean value and the mean plus some increment (one-side approach). In any case, if the one-side approach is employed, the increment should be taken in the "direction of interest."
- The preferred increment is about one standard deviation to capture some of the nonlinear behavior of the function over a range of likely values. Larger increments may produce biased results due to nonlinearities of the function, and smaller increments become sensitive to numerical variations of computed collapse capacities.
- Calculation of the contribution to variance of collapse capacity due to uncertainty in the system parameters ($\sigma^2_{\ln S_{a,c}(\bar{X})}$) is very sensitive to the assumed dispersion of the system parameters. Better knowledge of the behavior of components after the yielding point will reduce this dispersion significantly

- Monte Carlo simulation was used to verify some results obtained by using the FOSM method. If a lognormal distribution is assumed for the system parameters, the results for both techniques are very similar, since the dependence of collapse capacity on the system parameters is generally smooth. A function can be fitted to this relationship eliminating the necessity of carrying out a THA for each realization.

In the second part, a sensitivity study is carried out with representative SDOF systems and a set of MDOF generic frames.

- The variance of collapse capacity due to uncertainty in the system parameters ($\sigma^2_{\ln S_{a,c}(\bar{X})}$) may be larger than the variance due to RTR variability, $\sigma^2_{\ln S_{a,c}(RTR)}$. This occurs for long-period systems with no P-Δ effects and for $\sigma_{\ln\alpha} = \sigma_{\ln\delta} = \sigma_{\ln\gamma} = 0.60$ and $\rho_{i,j} = 0.8$. In the short-period range, $\sigma^2_{\ln S_{a,c}(\bar{X})}$ is small. Total variance of collapse capacity ($\sigma^2_{\ln(TOT)}$) ranges from about 0.20 for systems with low ductility to more than 0.40 for systems with high ductility.
- Variance of collapse capacity is very sensitive to variations of α_c for peak-oriented models with P-Δ = 0. The ratio of $\sigma^2_{\ln S_{a,c}(\alpha)}$ over $\sigma^2_{\ln S_{a,c}(RTR)}$ is similar for systems with low and high ductility. For bilinear models $\sigma^2_{\ln S_{a,c}(\alpha)}$ is less important because once the loading path is on the negative slope of the backbone curve, it is more difficult to avoid collapse and the value of the negative slope is less relevant.
- If high correlation is considered among parameters ($\rho_{i,j} = 0.8$), the contribution to variance of collapse capacity due to correlation among parameters ($\sigma^2_{\ln S_{a,c}(\rho_T)}$) is the largest component from uncertainty in the system parameters ($\sigma^2_{\ln S_{a,c}(\bar{X})}$), particularly for systems with no P-Δ effects.
- If P-Δ effect is included, $\sigma^2_{\ln S_{a,c}(\alpha)}$ is reduced, especially for long-period systems where larger stability coefficients produce larger negative slopes. Then the largest contribution to total variance of collapse capacity comes from δ_c/δ_y ($\sigma^2_{\ln S_{a,c}(\delta)}$).
- Ductility capacity (δ_c/δ_y) is the parameter with largest influence for systems with high ductility. This is particularly true for systems including P-Δ effects.

- The variance of collapse capacity due to uncertainty in CD ($\sigma^2_{\ln S_{a,c}(\gamma)}$) usually is small. For slow rates of CD (large $\gamma_{s,c,k,a}$'s) the dependence of collapse capacity on $\gamma_{s,c,k,a}$ is very small. Although the dependence increases for faster rates of CD (small $\gamma_{s,c,k,a}$'s, (Fig. 6.14), the influence of CD is overpowered by other factors such as the post-capping stiffness coefficient and P-Δ effects.
- The variance of collapse capacity is computed for a set of stiff and flexible generic MDOF frames. A comparison of $\sigma^2_{\ln S_{a,c}(\bar{X})}$ for stiff and flexible frames with the same fundamental period reveals that additional factors, such as the number of stories and P-Δ effects, have an important influence on the variance of collapse capacity.
- The results for variance of collapse capacity of MDOF structures were compared with those of SDOF systems that have the same hysteretic properties of the springs of the generic frames. Although these are not "precise" equivalent SDOF systems, the results suggest that sensitivity studies on SDOF systems are useful to detect most of the important trends in the computation of $\sigma^2_{\ln S_{a,c}(\bar{X})}$ for regular MDOF structures.

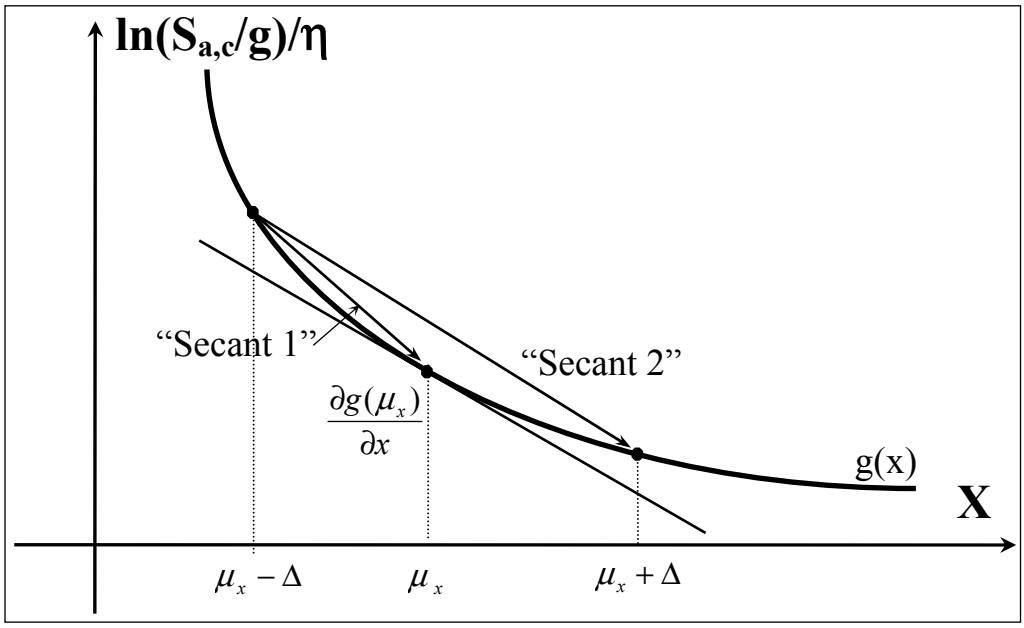

Fig. 6.1 Approximations of derivative $\partial g(\bar{x})/\partial x$ for computing $\sigma^2_{\ln S_{a,c}(X)}$ using the FOSM method

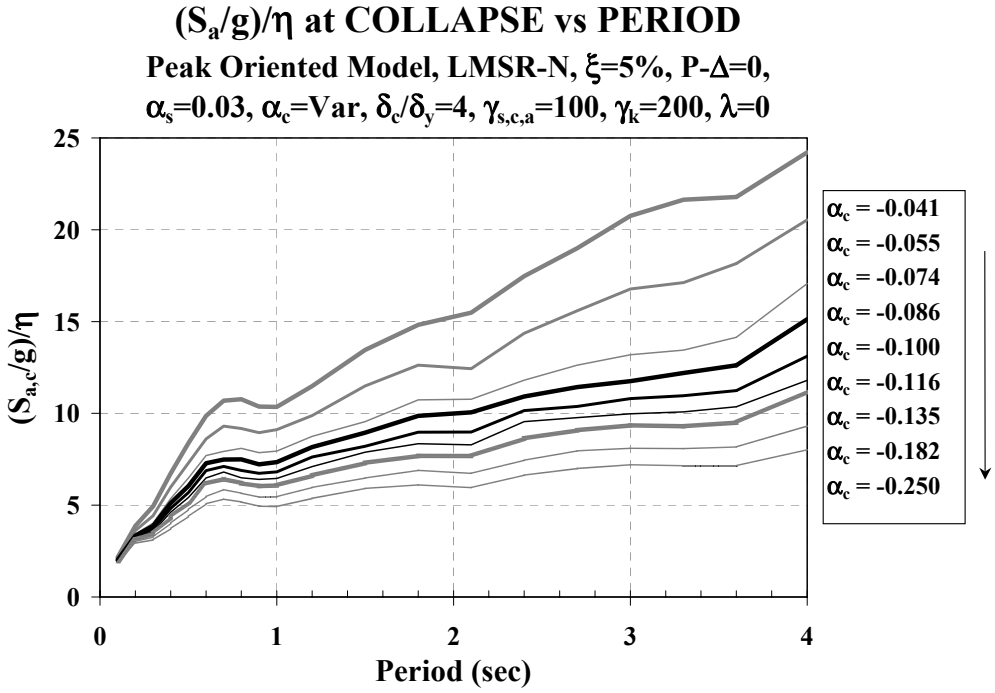

Fig. 6.2 Collapse capacity spectra for different α_c values; δ_c/δ_y = 4, slow CD

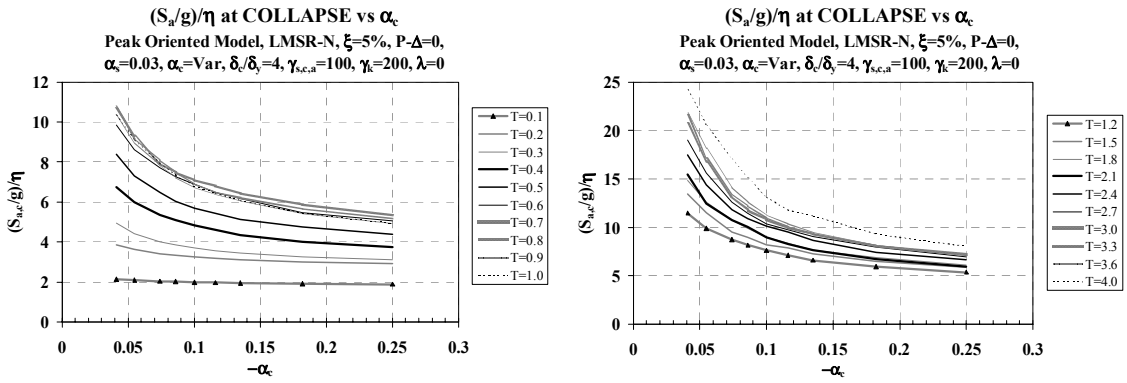

(a) Periods from T = 0.1 to 1.0 s (b) Periods from T = 1.2 to 4.0 s

Fig. 6.3 Dependence of median $(S_{a,c}/g)/\eta$ on α_c in the linear domain of the data; $\delta_c/\delta_y = 4$, slow CD

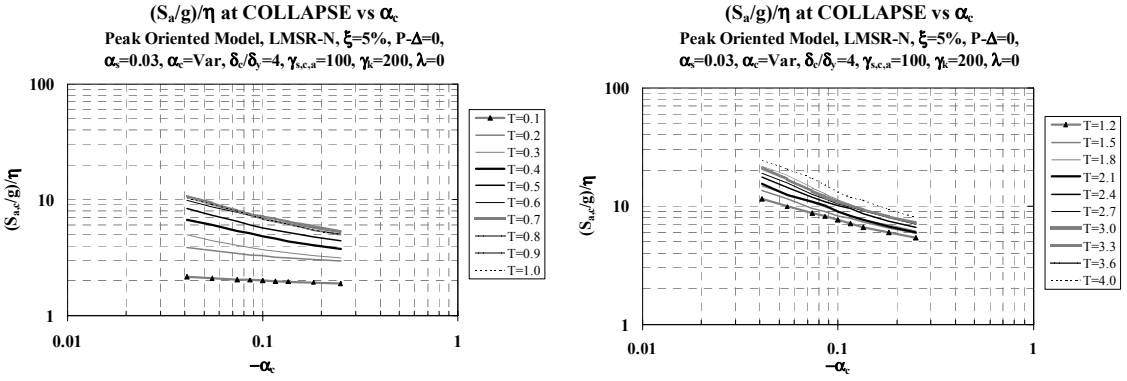

(a) Periods from T = 0.1 to 1.0 s (b) Periods from T = 1.2 to 4.0 s

Fig. 6.4 Dependence of median $(S_{a,c}/g)/\eta$ on α_c in the log domain of the data; $\delta_c/\delta_y = 4$, slow CD

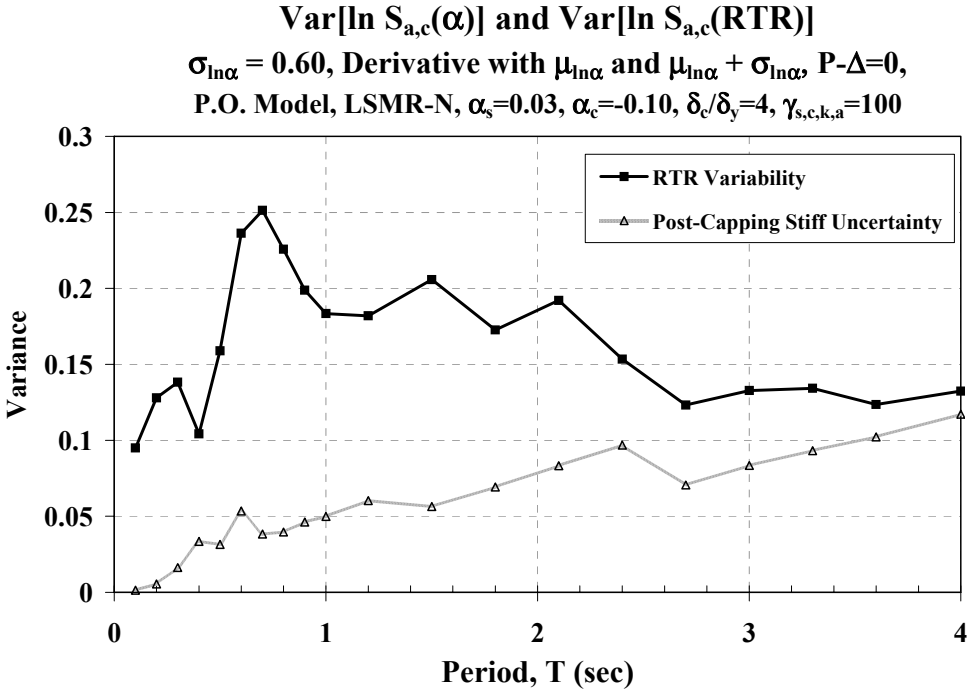

Fig. 6.5 $\sigma^2_{\ln S_{a,c}(\alpha)}$ **and** $\sigma^2_{\ln S_{a,c}(RTR)}$ **for reference SDOF system[22], derivative based on** $x_1 = \exp(\mu_{\ln\alpha})$ **and** $x_2 = \exp(\mu_{\ln\alpha} + \sigma_{\ln\alpha})$

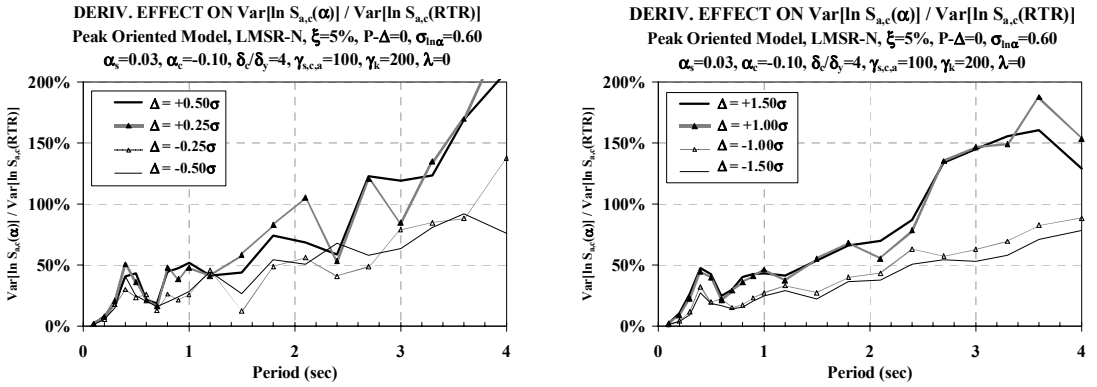

(a) $\Delta = n\sigma = \pm 0.25\,\sigma$ and $\pm 0.50\,\sigma$ (b) $\Delta = n\sigma = \pm 1.00\,\sigma$ and $\pm 1.50\,\sigma$

Fig. 6.6 Effect on $\sigma^2_{\ln S_{a,c}(\alpha)} / \sigma^2_{\ln S_{a,c}(RTR)}$ **of the increment used for computing the derivative; reference SDOF system,** $x_1 = \exp(\mu_{\ln\alpha})$ **and** $x_2 = \exp(\mu_{\ln\alpha} + n\sigma_{\ln\alpha})$

[22] Section 6.2.4 contains the definitions of contributions to variance of collapse capacity such as $\sigma^2_{\ln S_{a,c}(\alpha)}$.

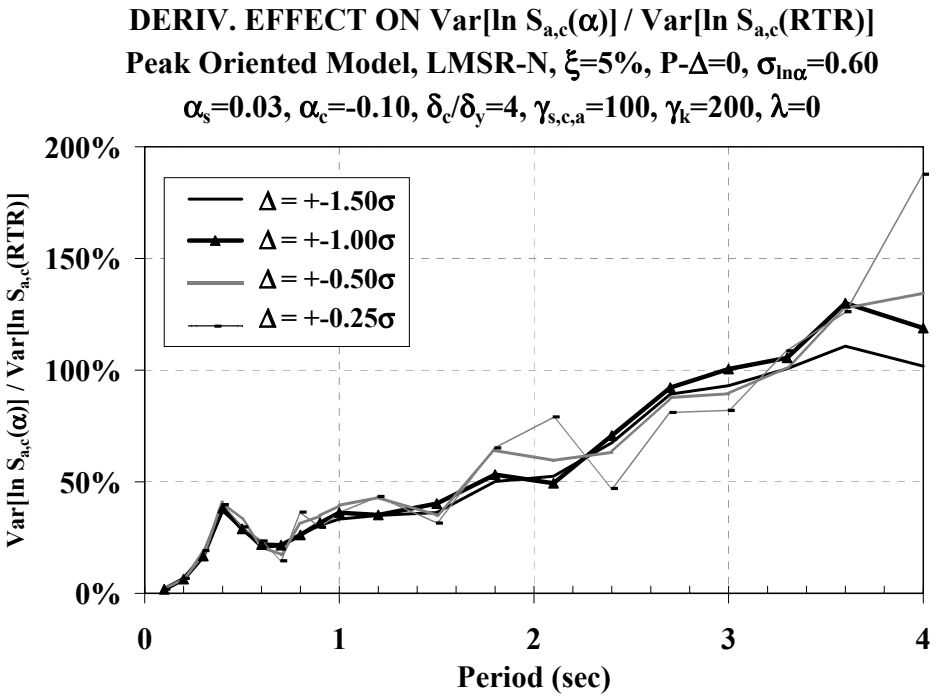

Fig. 6.7 Effect on $\sigma^2_{\ln S_{a,c}(\alpha)} / \sigma^2_{\ln S_{a,c}(RTR)}$ of the increment used for computing the derivative; reference system, $x_1 = \exp(\mu_{\ln\alpha} - n\sigma_{\ln\alpha})$ and $x_2 = \exp(\mu_{\ln\alpha} + n\sigma_{\ln\alpha})$

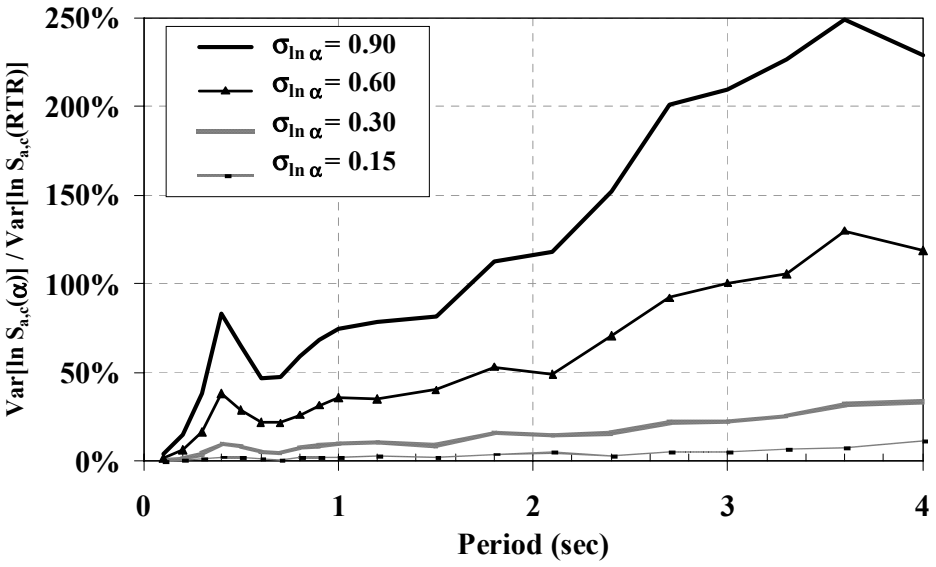

Fig. 6.8 Effect of the assumed $\sigma_{\ln\alpha}$ on $\sigma^2_{\ln S_{a,c}(\alpha)} / \sigma^2_{\ln S_{a,c}(RTR)}$ ratios; reference SDOF system, derivatives based on $x_1 = \exp(\mu_{\ln\alpha} - \sigma_{\ln\alpha})$ and $x_2 = \exp(\mu_{\ln\alpha} + \sigma_{\ln\alpha})$

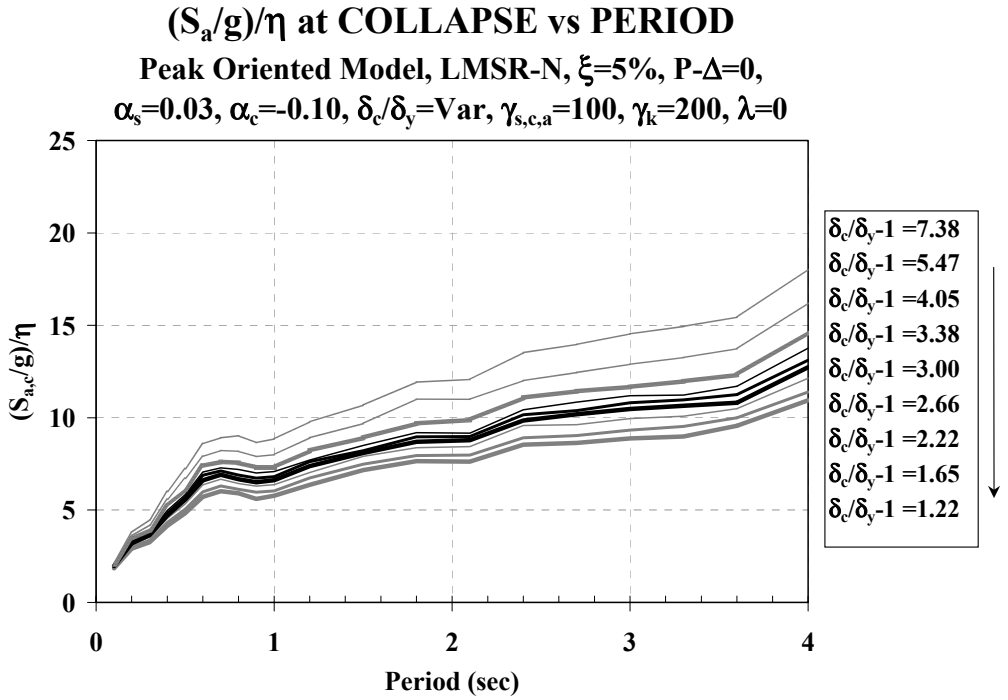

Fig. 6.9 Collapse capacity spectra for different (δ_c/δ_y –1); α_c = -0.10, slow CD

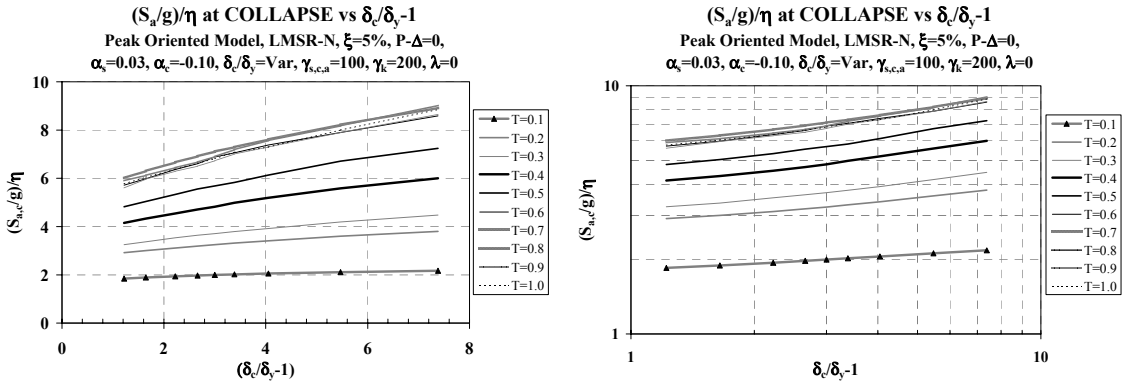

(a) Linear Domain of the Data (b) Log Domain of the Data

Fig. 6.10 Dependence of median ($S_{a,c}/g$)/η on δ_c/δ_y; α_c = -0.10, slow CD, periods from T = 0.1–1.0 s

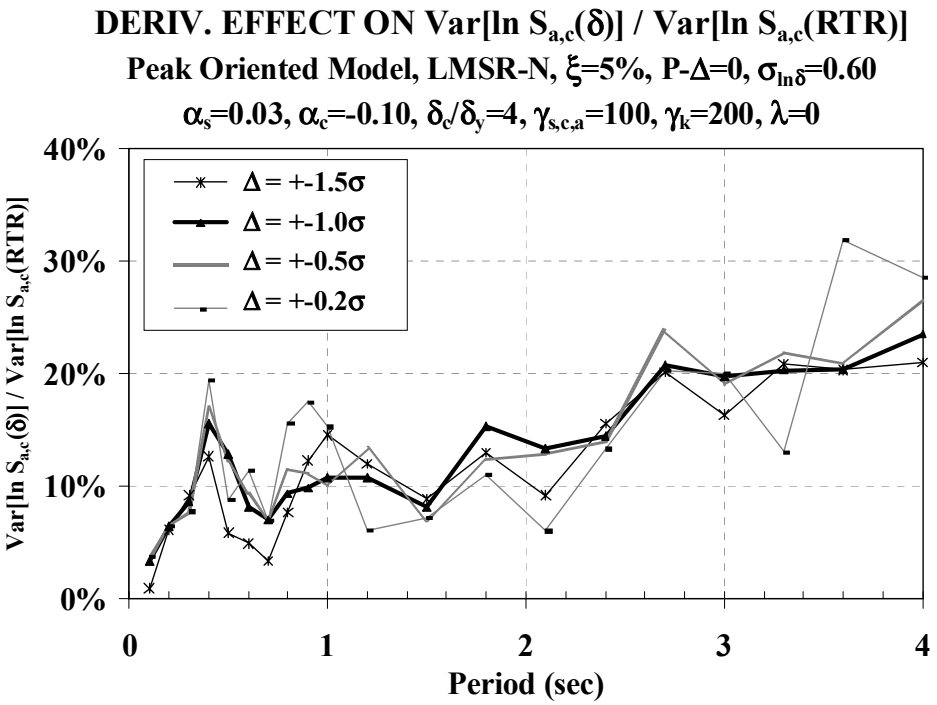

Fig. 6.11 Effect on $\sigma^2_{\ln S_{a,c}(\delta)} / \sigma^2_{\ln S_{a,c}(RTR)}$ of the increment used for computing the derivative; reference system, $x_1 = \exp(\mu_{\ln\delta} - n\sigma_{\ln\delta})$ and $x_2 = \exp(\mu_{\ln\delta} + n\sigma_{\ln\delta})$

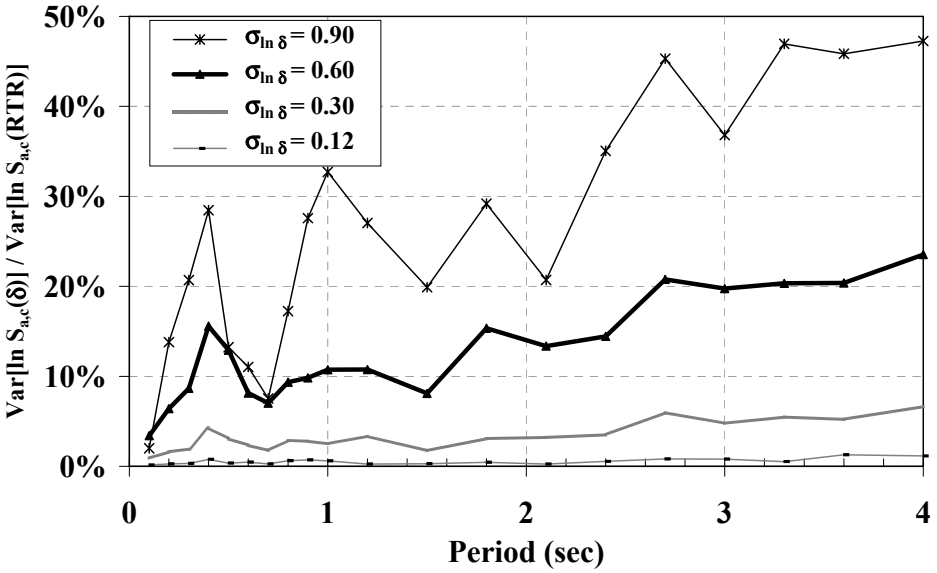

Fig. 6.12 Effect of the selected $\sigma_{\ln\delta}$ on $\sigma^2_{\ln S_{a,c}(\delta)} / \sigma^2_{\ln S_{a,c}(RTR)}$ ratios; reference SDOF system, derivatives based on $x_1 = \exp(\mu_{\ln\delta} - \sigma_{\ln\delta})$ and $x_2 = \exp(\mu_{\ln\delta} + \sigma_{\ln\delta})$

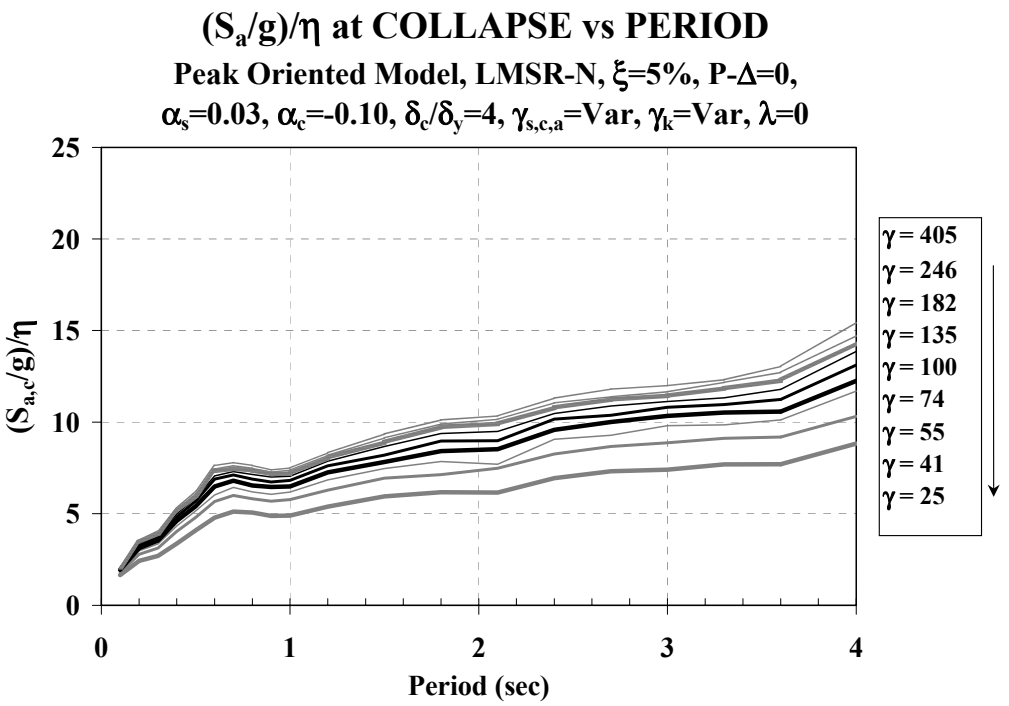

Fig. 6.13 Collapse capacity spectra for different CD rates; $\delta_c/\delta_y = 4$, $\alpha_c = -0.10$

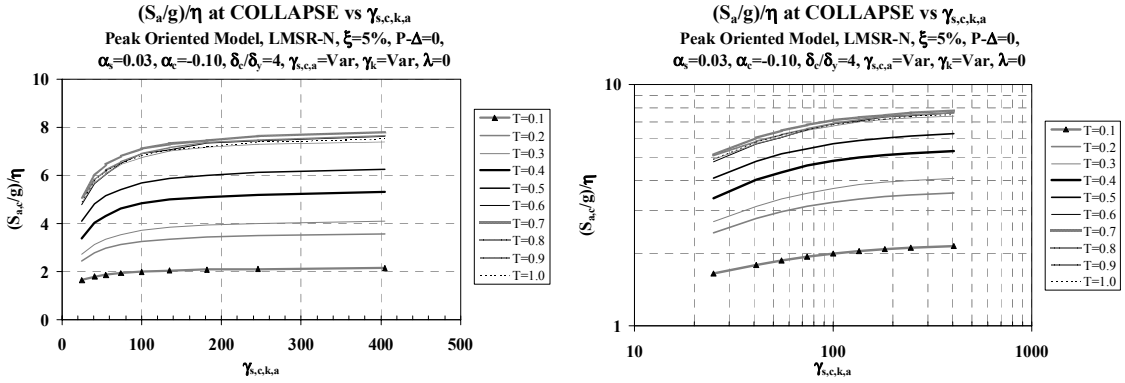

(a) Linear Domain of the Data (b) Log Domain of the Data

Fig. 6.14 Dependence of median $(S_{a,c}/g)/\eta$ on $\gamma_{s,c,k,a}$; $\alpha_c = -0.10$, $\delta_c/\delta_y = 4$, periods from T = 0.1–1.0 s

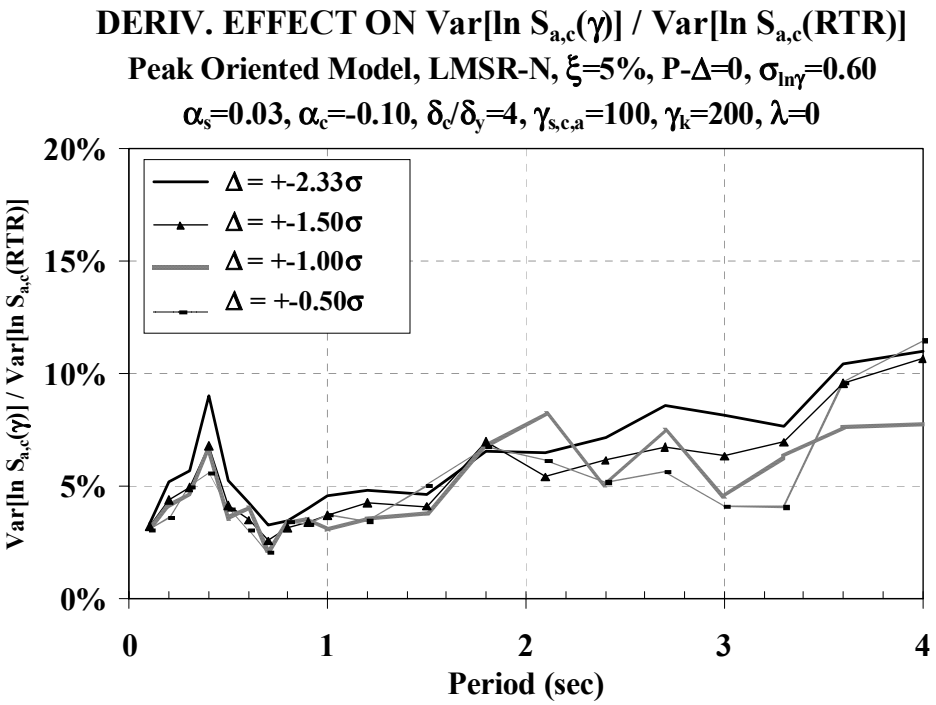

Fig. 6.15 Effect on $\sigma^2_{\ln S_{a,c}(\gamma)} / \sigma^2_{\ln S_{a,c}(RTR)}$ of the increment used for computing the derivative; reference system, $x_1 = \exp(\mu_{\ln\gamma} - n\sigma_{\ln\gamma})$ and $x_2 = \exp(\mu_{\ln\gamma} + n\sigma_{\ln\gamma})$

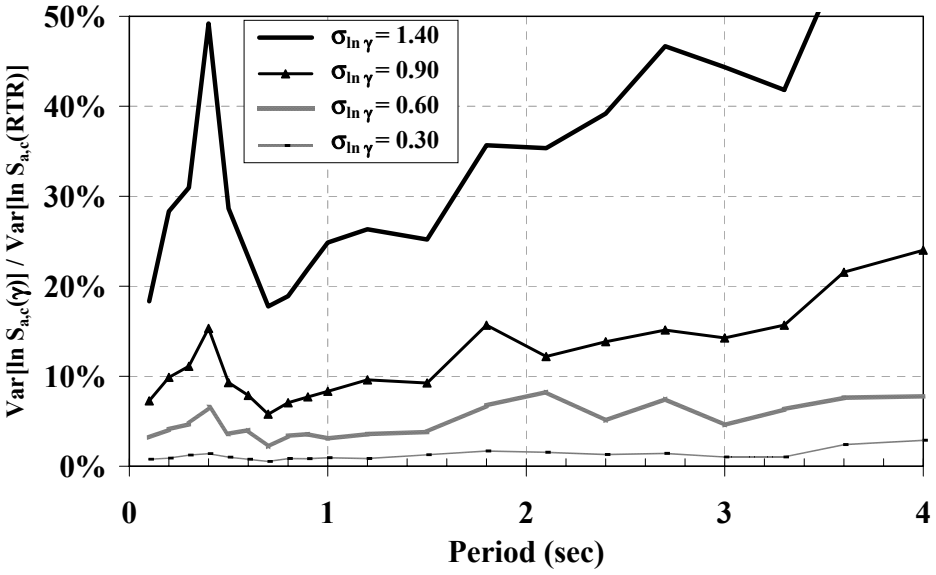

Fig. 6.16 Effect of the selected $\sigma_{\ln\gamma}$ on $\sigma^2_{\ln S_{a,c}(\gamma)} / \sigma^2_{\ln S_{a,c}(RTR)}$ ratios; reference SDOF system, derivatives based on $x_1 = \exp(\mu_{\ln\gamma} - \sigma_{\ln\gamma})$ and $x_2 = \exp(\mu_{\ln\gamma} + \sigma_{\ln\gamma})$

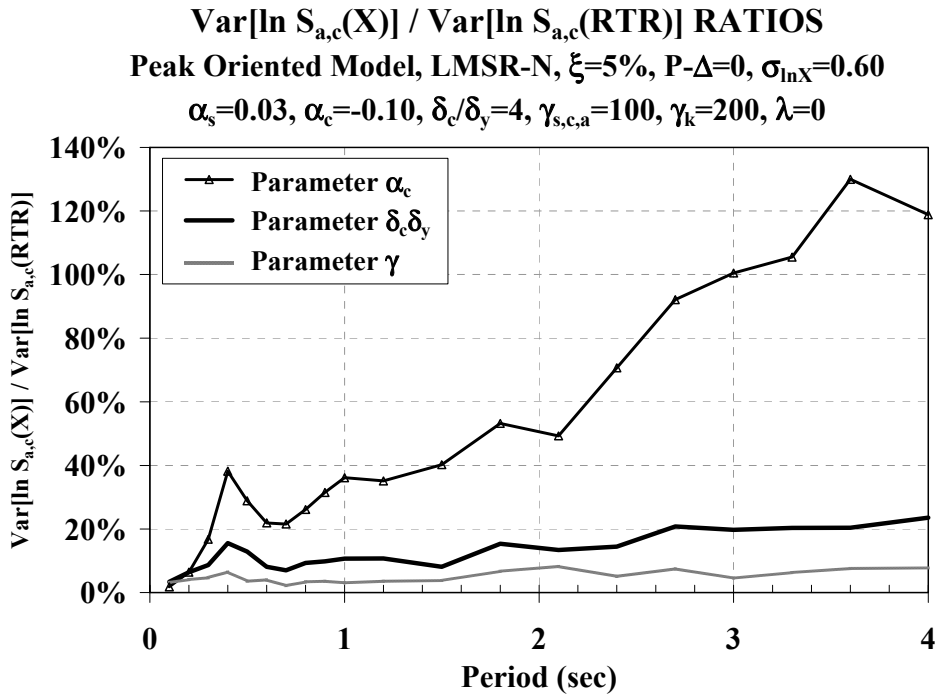

Fig. 6.17 $\sigma^2_{\ln S_{a,c}(X_i)} / \sigma^2_{\ln S_{a,c}(RTR)}$ **ratios for different system parameters; derivatives based on** $x_1 = \exp(\mu_{\ln x} - \sigma_{\ln x})$ **and** $x_2 = \exp(\mu_{\ln x} + \sigma_{\ln x})$**, reference system**

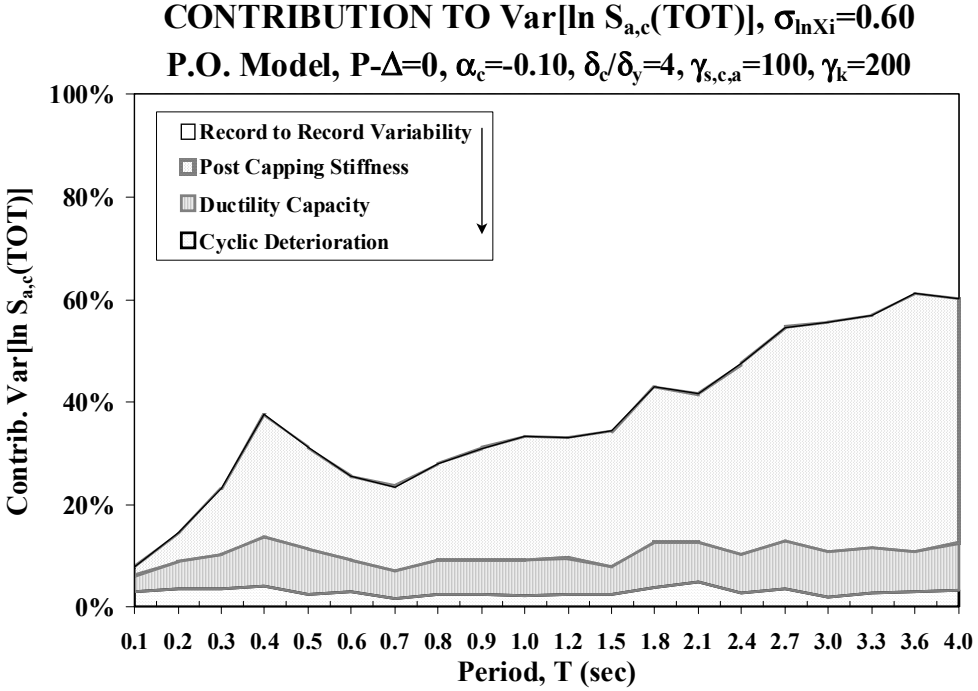

Fig. 6.18 Contribution of uncertainty in system parameters to $\sigma^2_{\ln S_{a,c}(TOT)}$**; reference system, no correlation included**

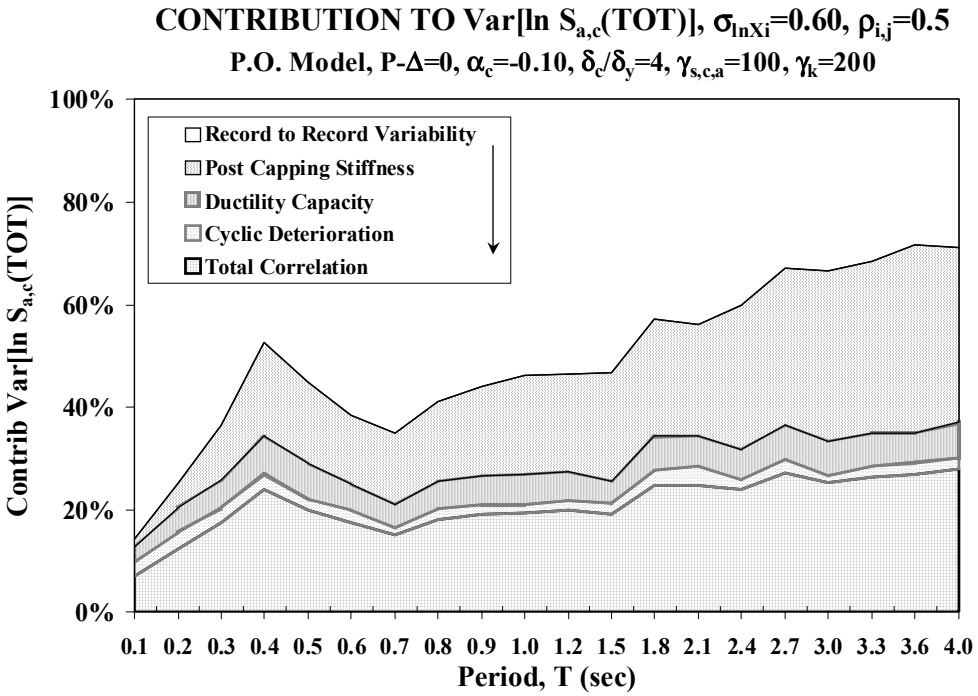

Fig. 6.19 Contribution of uncertainty in system parameters to $\sigma^2_{\ln S_{a,c}(TOT)}$; reference system, low correlation included

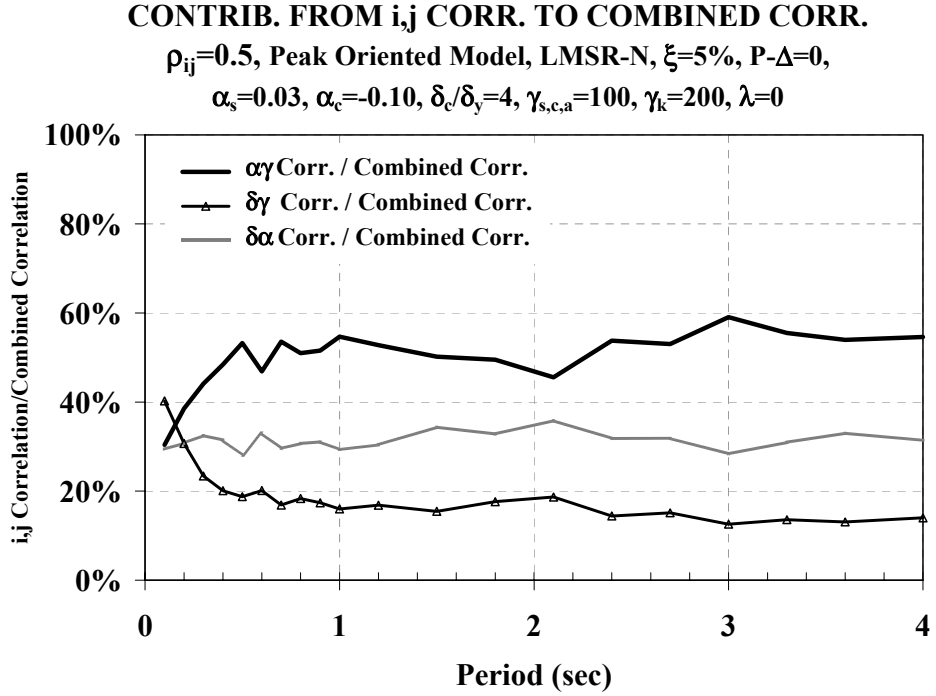

Fig. 6.20 Contribution of *ij* correlation to combined correlation, $\rho_{i,j} = 0.5$

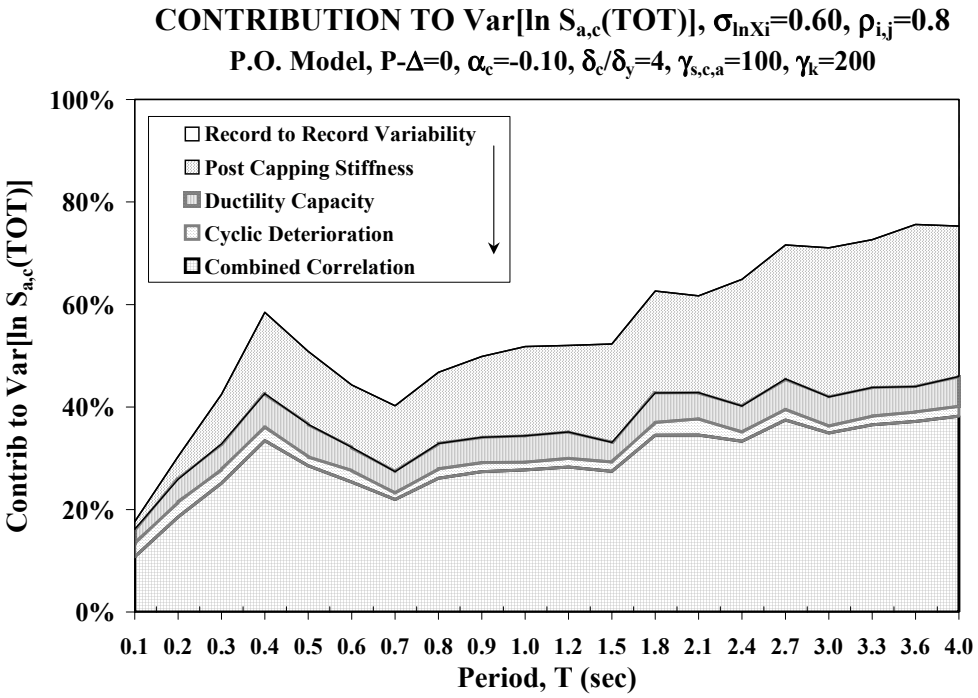

Fig. 6.21 Contribution of uncertainty in system parameters to $\sigma^2_{\ln S_{a,c}(TOT)}$; reference system, high correlation included

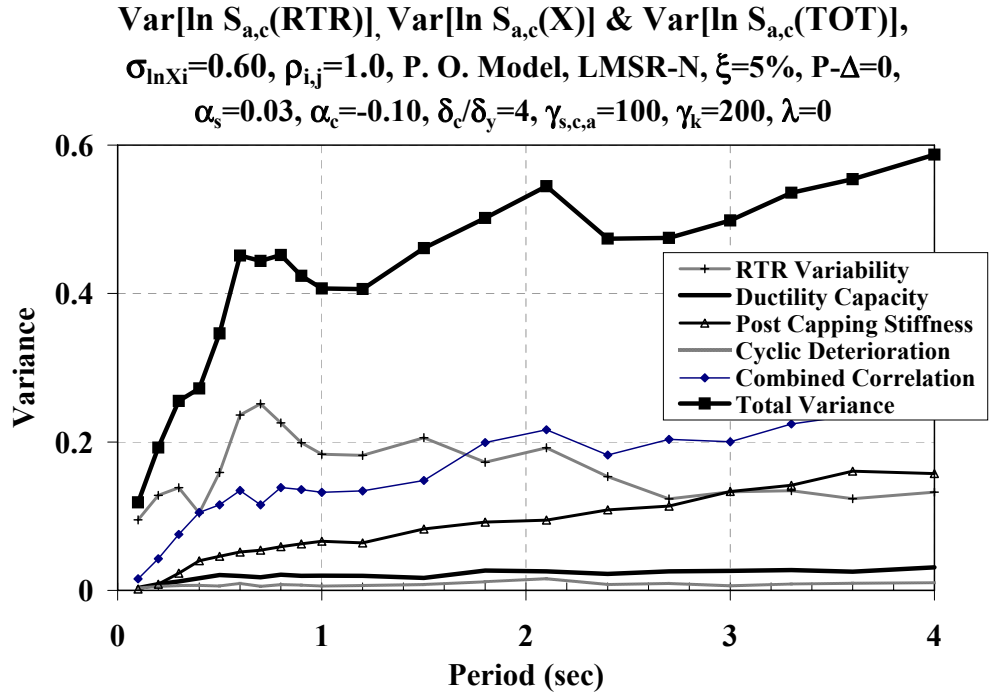

Fig. 6.22 $\sigma^2_{\ln S_{a,c}(RTR)}$, $\sigma^2_{\ln S_{a,c}(X)}$ and $\sigma^2_{\ln S_{a,c}(TOT)}$; reference system, full correlation

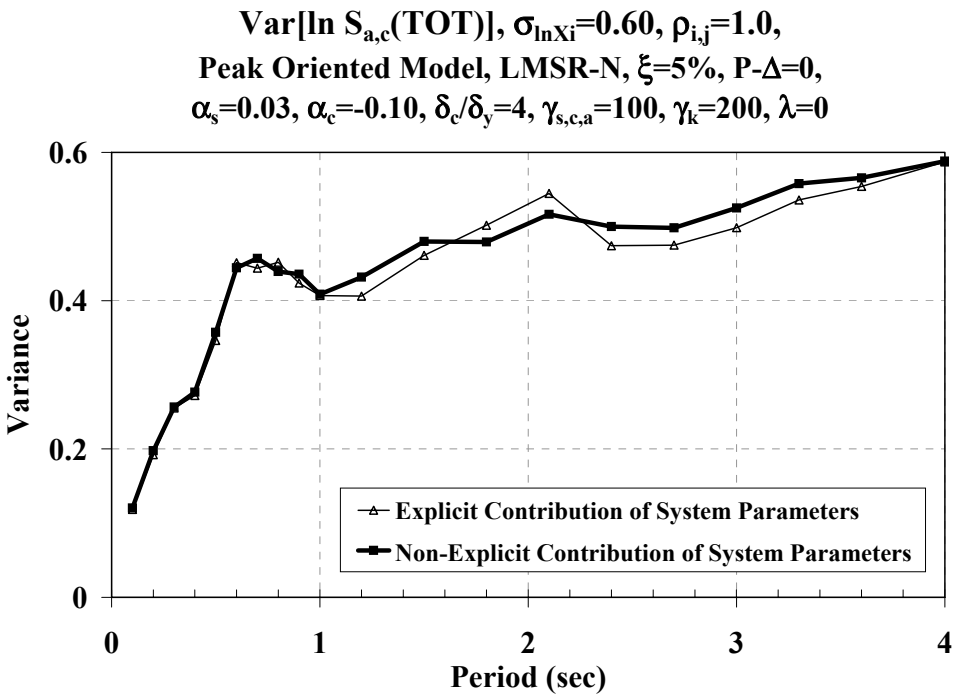

Fig. 6.23 Comparison of $\sigma^2_{\ln S_{a,c}(TOT)}$ obtained with FOSM method by considering explicit and non-explicit contribution of system parameters, full correlation

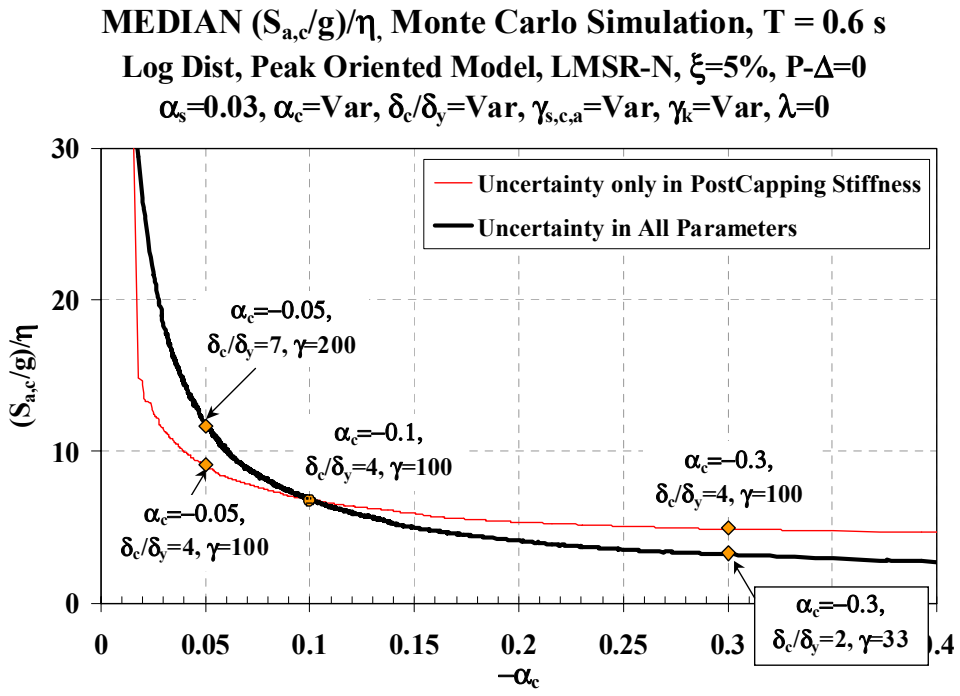

Fig. 6.24 Dependence of median $(S_{a,c}/g)/\eta$ on α_c. Monte Carlo simulation with uncertainty in α_c and in the three probabilistic system parameters, T = 0.6 s

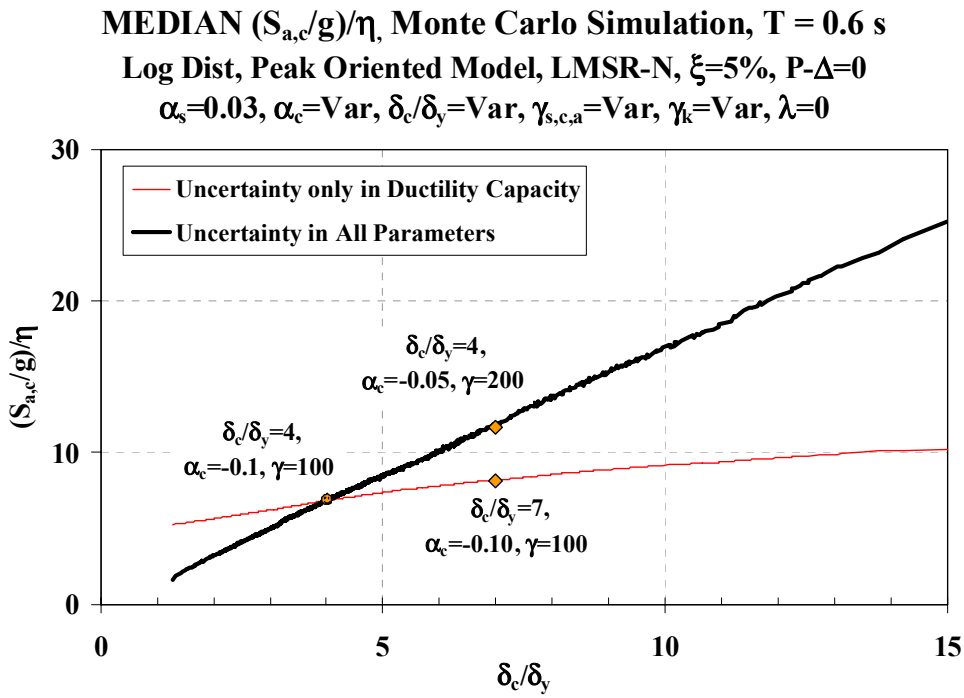

Fig. 6.25 Dependence of median $(S_{a,c}/g)/\eta$ on δ_c/δ_y; Monte Carlo simulation with uncertainty in δ_c/δ_y and in the three probabilistic system parameters, T = 0.6 s

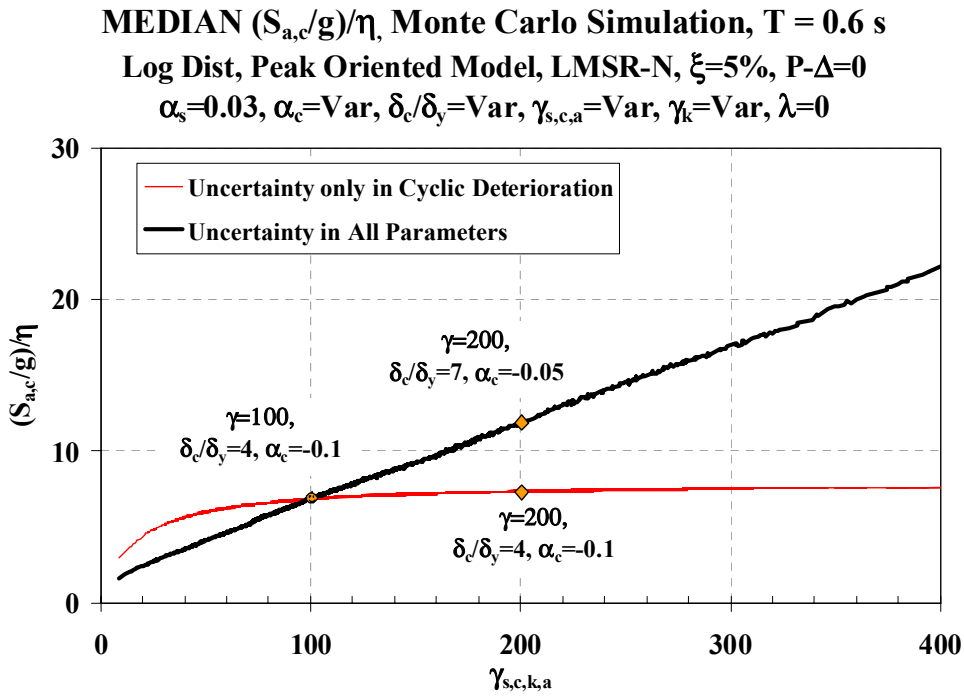

Fig. 6.26 Dependence of median $(S_{a,c}/g)/\eta$ on $\gamma_{s,c,k,a}$; Monte Carlo simulation with uncertainty in $\gamma_{s,c,k,a}$ and in the three probabilistic system parameters, T = 0.6 s

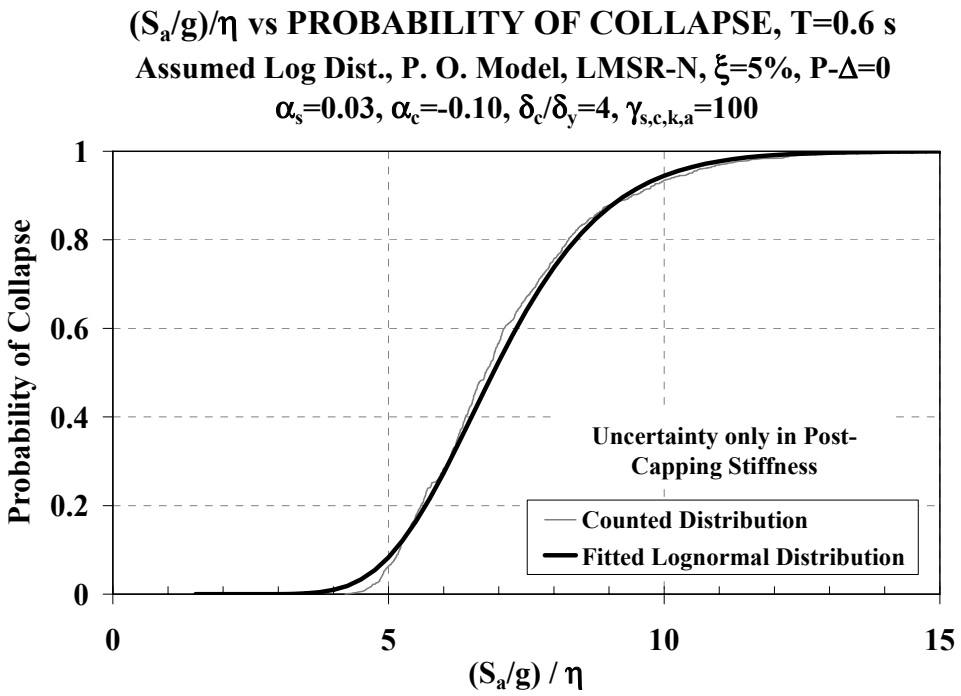

Fig. 6.27 Comparison of fragility curves obtained from counted and fitted lognormal distributions of $\sigma^2_{\ln S_{a,c}(\alpha)}$

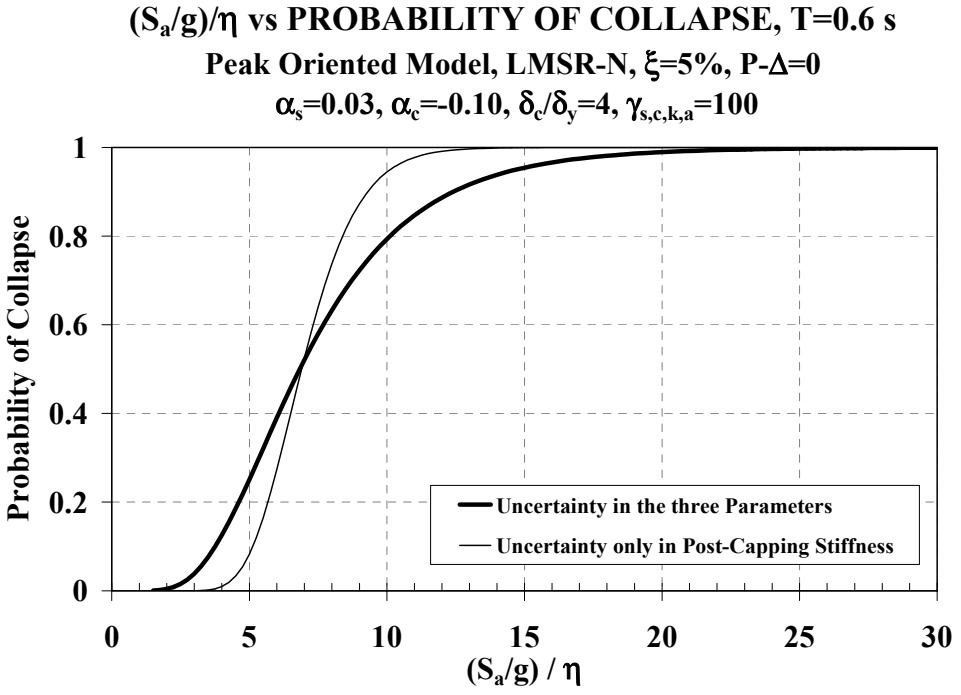

Fig. 6.28 Fragility curves from fitted lognormal distributions for $\sigma^2_{\ln S_{a,c}(\alpha)}$ and $\sigma^2_{\ln S_{a,c}(\bar{X})}$

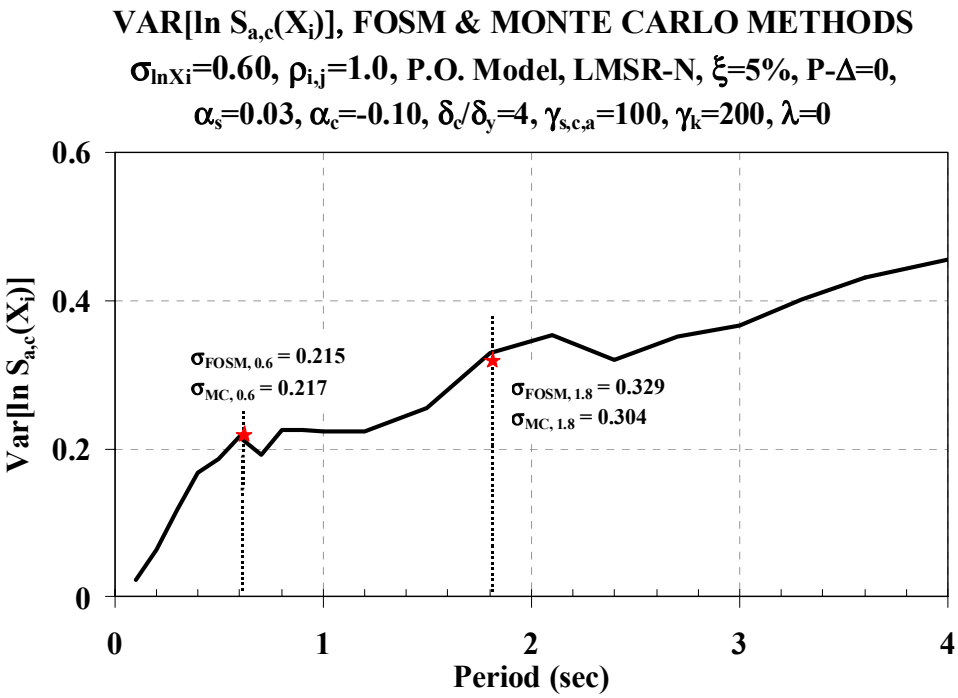

Fig. 6.29 Comparison of $\sigma^2_{\ln S_{a,c}(X_i)}$ obtained with FOSM (solid lines) and Monte Carlo simulation, reference system, full correlation

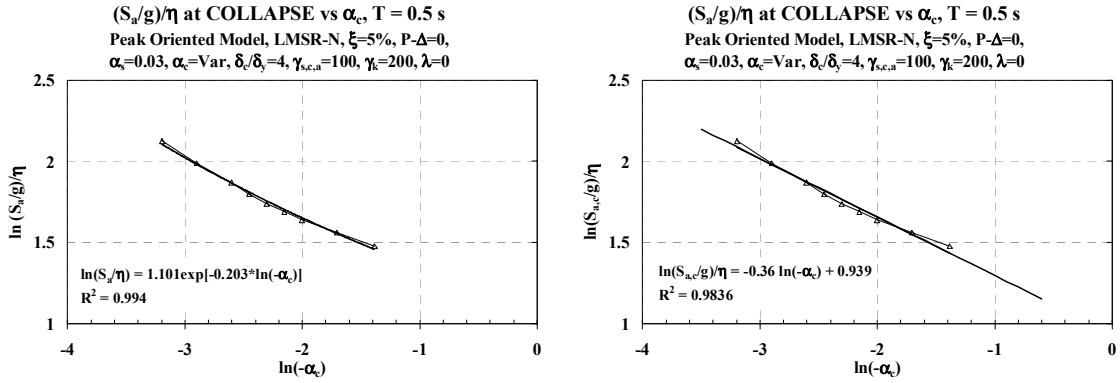

(a) Fitting with Exponential Curve (b) Linear Regression

Fig. 6.30 Regression for dependence of $(S_{a,c}/g)/\eta$ on α_c at T = 0.5 s, reference SDOF system

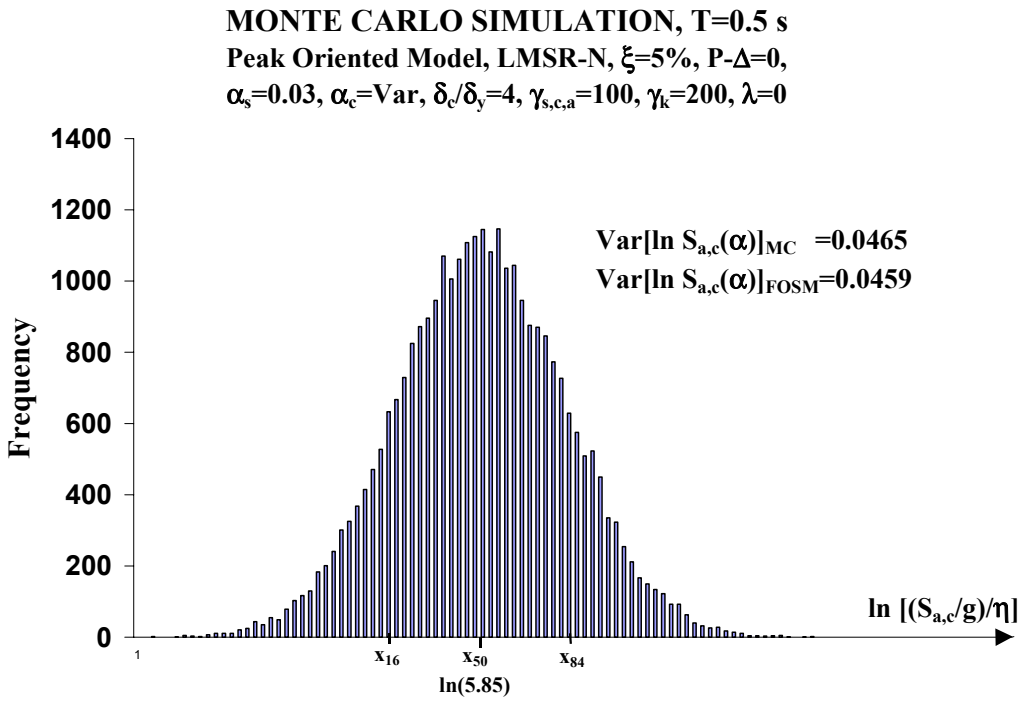

Fig. 6.31 Histogram of $\sigma^2_{\ln S_{a,c}(\alpha)}$ from Monte Carlo simulation; reference SDOF system, T = 0.5 s

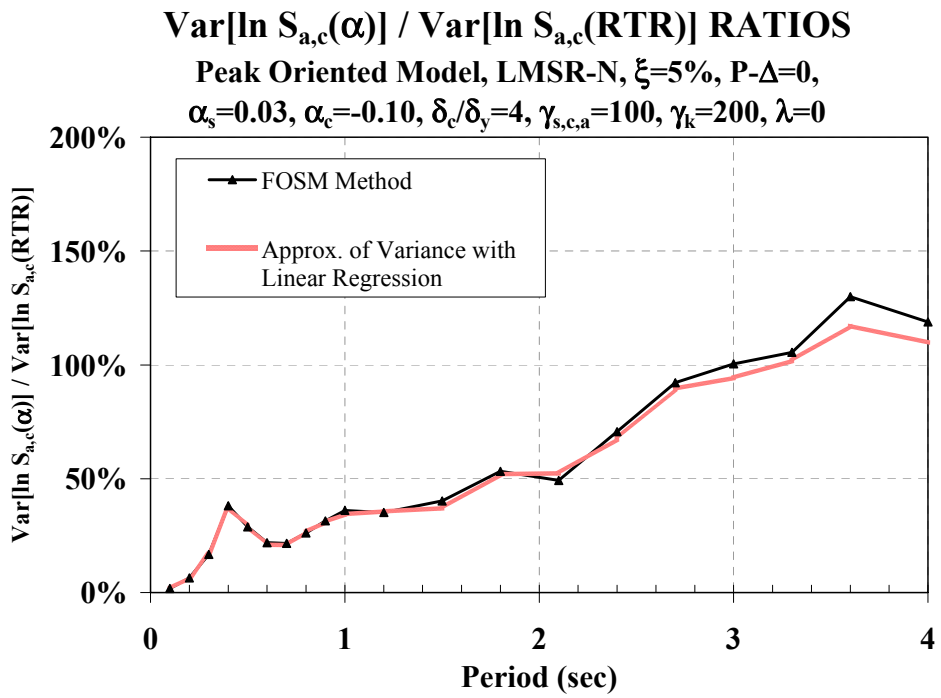

Fig. 6.32 Comparison of $\sigma^2_{\ln S_{a,c}(\alpha)} / \sigma^2_{\ln S_{a,c}(RTR)}$ ratios for FOSM method and approximation from linear regression, reference SDOF system

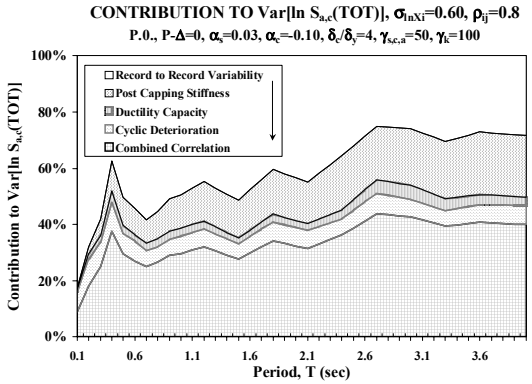

(a) Contributions to $\sigma^2_{\ln S_{a,c}(TOT)}$

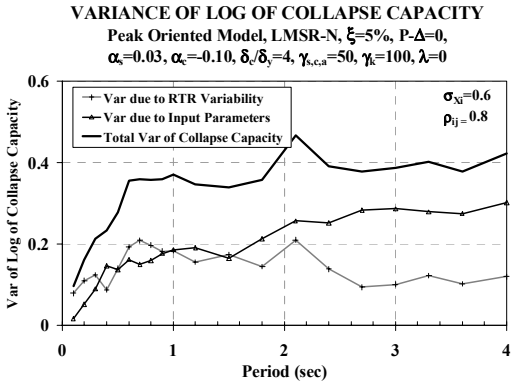

(b) $\sigma^2_{\ln S_{a,c}(RTR)}$, $\sigma^2_{\ln S_{a,c}(\bar{X})}$ and $\sigma^2_{\ln S_{a,c}(TOT)}$

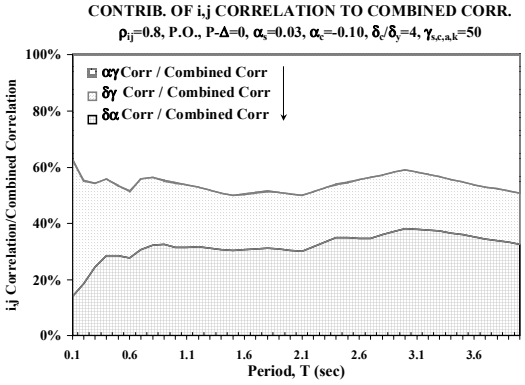

(c) *i,j* Correlation / Combined Correlation

Fig. 6.33 Contributions to variance of ($S_{a,c}/g$)/η for a peak-oriented system with intermediate ductility, no P-Δ

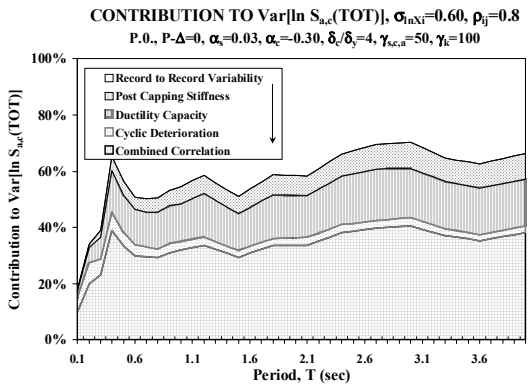

(a) Contributions to $\sigma^2_{\ln S_{a,c}(TOT)}$

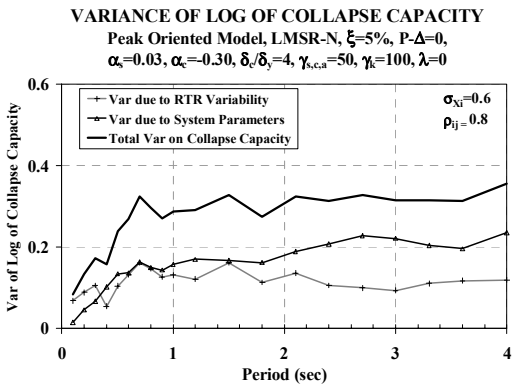

(b) $\sigma^2_{\ln S_{a,c}(RTR)}$, $\sigma^2_{\ln S_{a,c}(\bar{X})}$ and $\sigma^2_{\ln S_{a,c}(TOT)}$

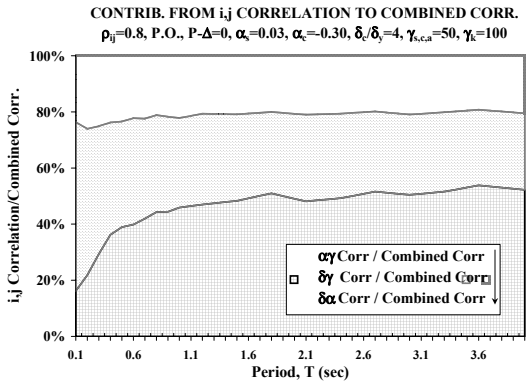

(c) *i,j* Correlation / Combined Correlation

Fig. 6.34 Contributions to variance of $(S_{a,c}/g)/\eta$ for a peak-oriented system with δ_c/δ_y = 4, α_c = -0.30, $\gamma_{s,c,k,a}$ = 50, no P-Δ effects

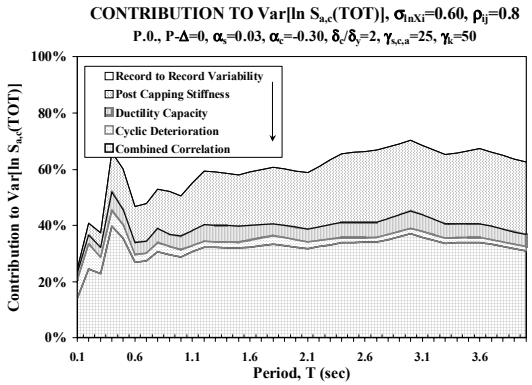

(a) Contributions to $\sigma^2_{\ln S_{a,c}(TOT)}$

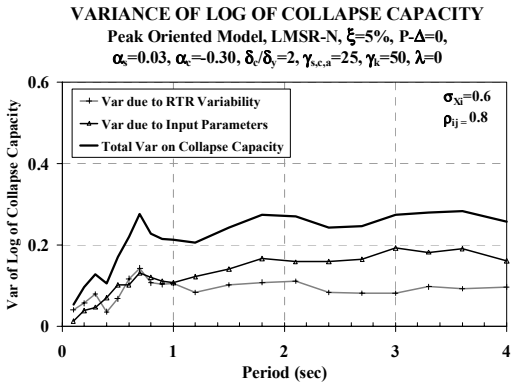

(b) $\sigma^2_{\ln S_{a,c}(RTR)}$, $\sigma^2_{\ln S_{a,c}(\bar{X})}$ and $\sigma^2_{\ln S_{a,c}(TOT)}$

Fig. 6.35 Contributions to variance of $(s_{a,c}/g)/\eta$ for a peak-oriented system with low ductility, no P-Δ

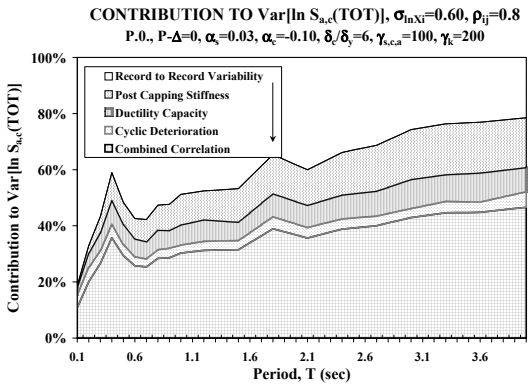

(a) Contributions to $\sigma^2_{\ln S_{a,c}(TOT)}$

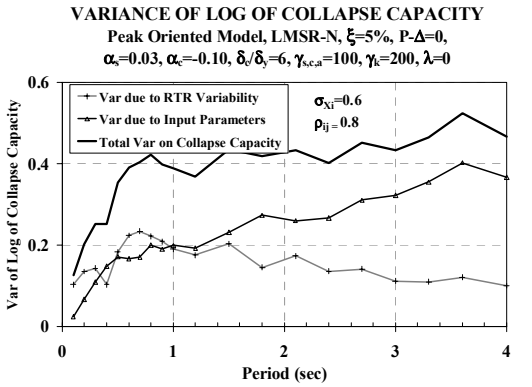

(b) $\sigma^2_{\ln S_{a,c}(RTR)}$, $\sigma^2_{\ln S_{a,c}(\bar{X})}$ and $\sigma^2_{\ln S_{a,c}(TOT)}$

Fig. 6.36 Contributions to variance of $(s_{a,c}/g)/\eta$ for a peak-oriented system with high ductility, no P-Δ

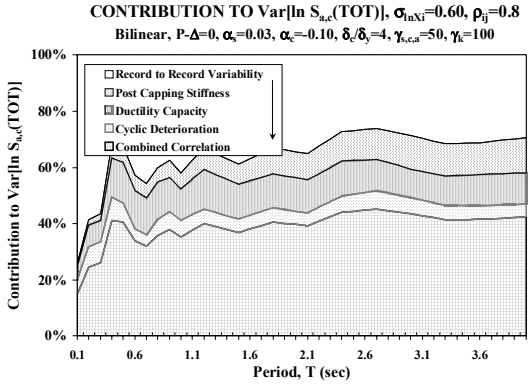

(a) Contributions to $\sigma^2_{\ln S_{a,c}(TOT)}$

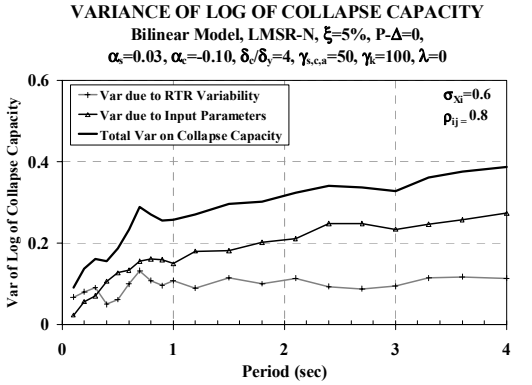

(b) $\sigma^2_{\ln S_{a,c}(RTR)}$, $\sigma^2_{\ln S_{a,c}(\bar{X})}$ and $\sigma^2_{\ln S_{a,c}(TOT)}$

Fig. 6.37 Contributions to variance of $(s_{a,c}/g)/\eta$ for a bilinear system with intermediate ductility, no P-Δ

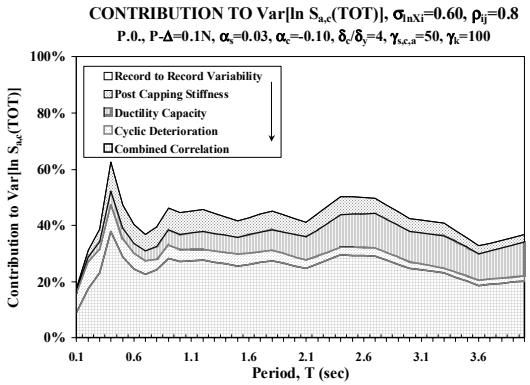

(a) Contributions to $\sigma^2_{\ln S_{a,c}(TOT)}$

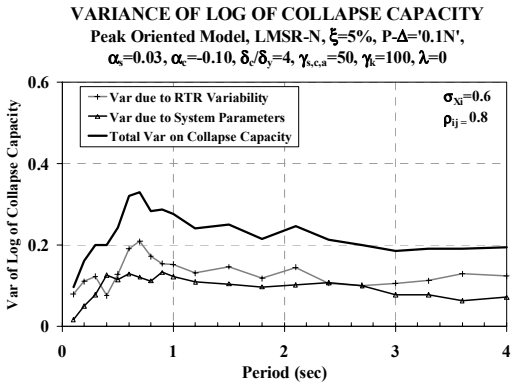

(b) $\sigma^2_{\ln S_{a,c}(RTR)}$, $\sigma^2_{\ln S_{a,c}(\bar{X})}$ and $\sigma^2_{\ln S_{a,c}(TOT)}$

Fig. 6.38 Contributions to variance of $(s_{a,c}/g)/\eta$ for a peak-oriented system with intermediate ductility, small P-Δ

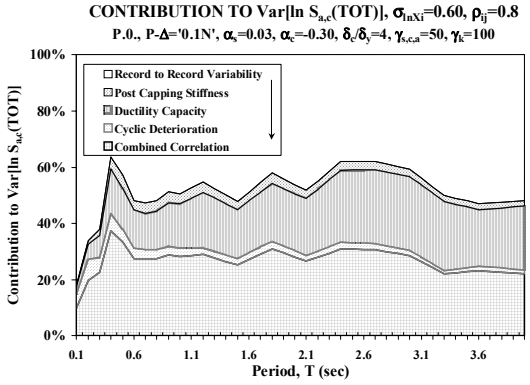

(a) Contributions to $\sigma^2_{\ln S_{a,c}(TOT)}$

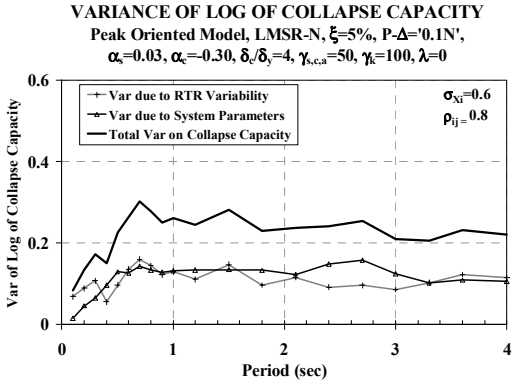

(b) $\sigma^2_{\ln S_{a,c}(RTR)}$, $\sigma^2_{\ln S_{a,c}(\bar{X})}$ and $\sigma^2_{\ln S_{a,c}(TOT)}$

Fig. 6.39 Contributions to variance of $(S_{a,c}/g)/\eta$ for a peak-oriented system with δ_c/δ_y = 4, α_c = -0.30, $\gamma_{s,c,k,a}$ = 50, small P-Δ

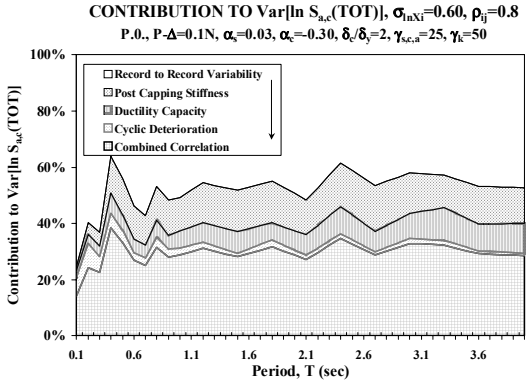

(a) Contributions to $\sigma^2_{\ln S_{a,c}(TOT)}$

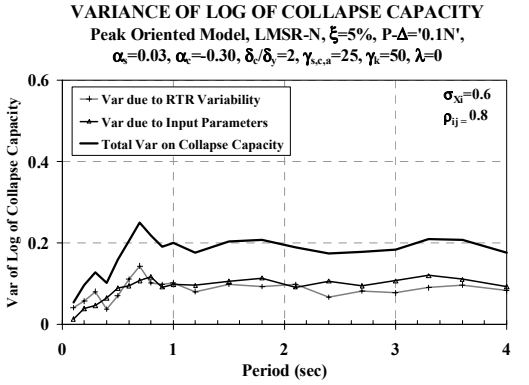

(b) $\sigma^2_{\ln S_{a,c}(RTR)}$, $\sigma^2_{\ln S_{a,c}(\bar{X})}$ and $\sigma^2_{\ln S_{a,c}(TOT)}$

Fig. 6.40 Contributions to variance of $(s_{a,c}/g)/\eta$ for a peak-oriented system with low ductility, small P-Δ

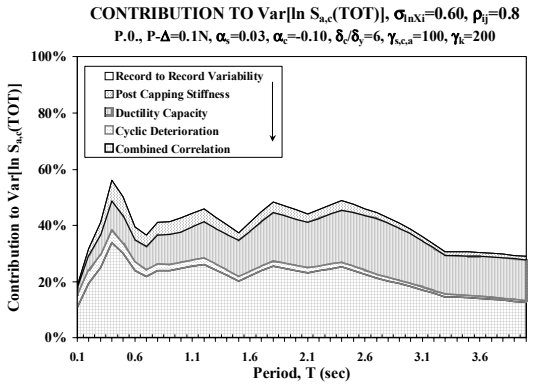

(a) Contributions to $\sigma^2_{\ln S_{a,c}(TOT)}$

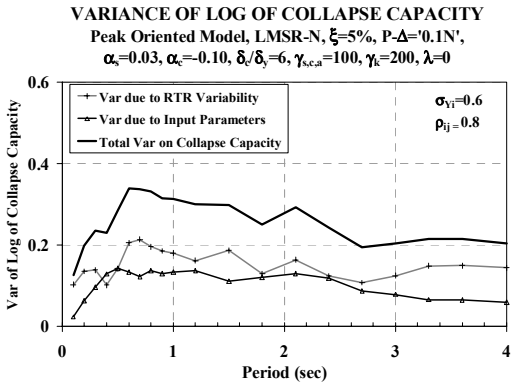

(b) $\sigma^2_{\ln S_{a,c}(RTR)}$, $\sigma^2_{\ln S_{a,c}(\overline{X})}$ and $\sigma^2_{\ln S_{a,c}(TOT)}$

Fig. 6.41 Contributions to variance of $(s_{a,c}/g)/\eta$ for a peak-oriented system with high ductility, small P-Δ

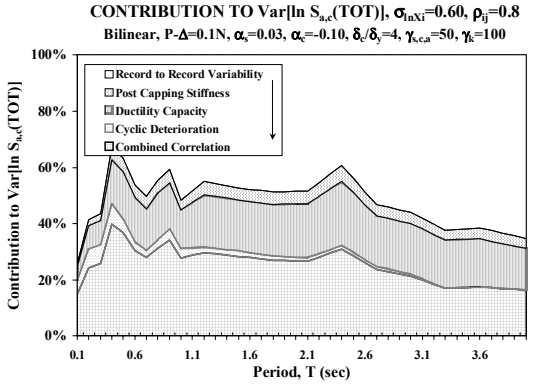

(a) Contributions to $\sigma^2_{\ln S_{a,c}(TOT)}$

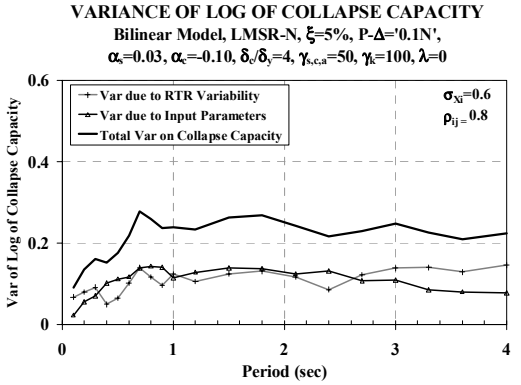

(b) $\sigma^2_{\ln S_{a,c}(RTR)}$, $\sigma^2_{\ln S_{a,c}(\overline{X})}$ and $\sigma^2_{\ln S_{a,c}(TOT)}$

Fig. 6.42 Contributions to variance of $(s_{a,c}/g)/\eta$ for a bilinear system with intermediate ductility, small P-Δ

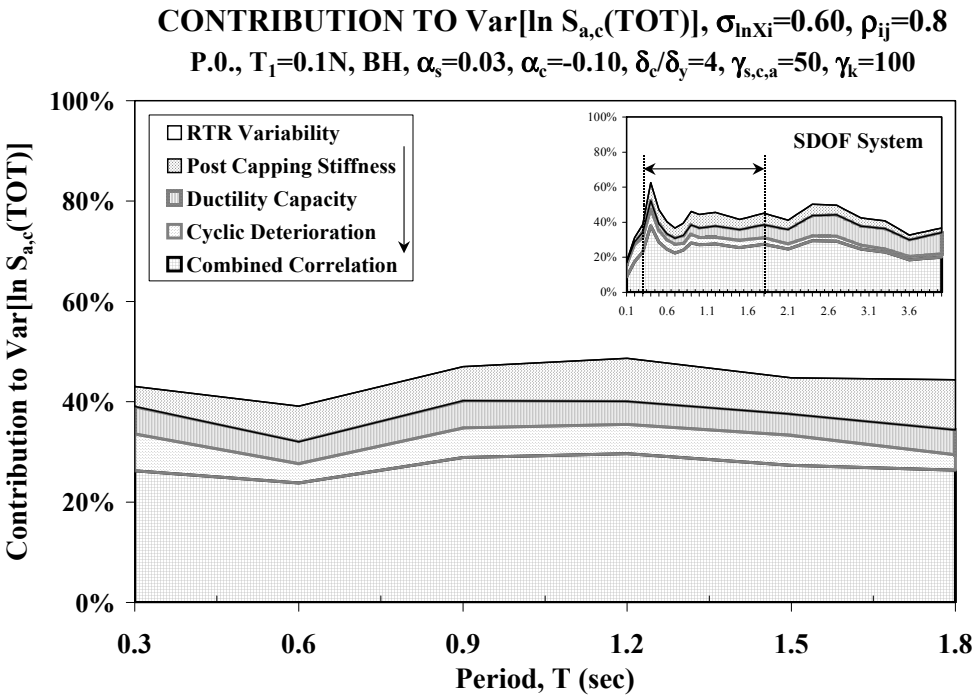

Fig. 6.43 Contributions to $\sigma^2_{\ln S_{a,c}(TOT)}$ for set of MDOF systems with $T = 0.1N$ and springs at ends of beams with intermediate ductile characteristics

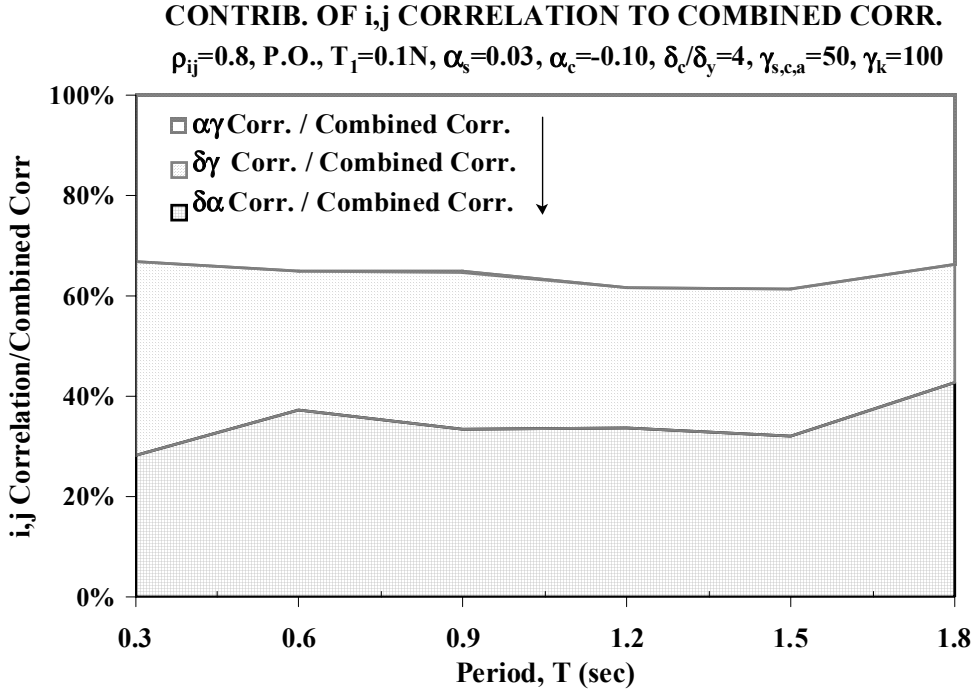

Fig. 6.44 *i,j* correlation / combined correlation for set of MDOF systems with $T = 0.1N$ and springs at ends of beams with intermediate ductile characteristics

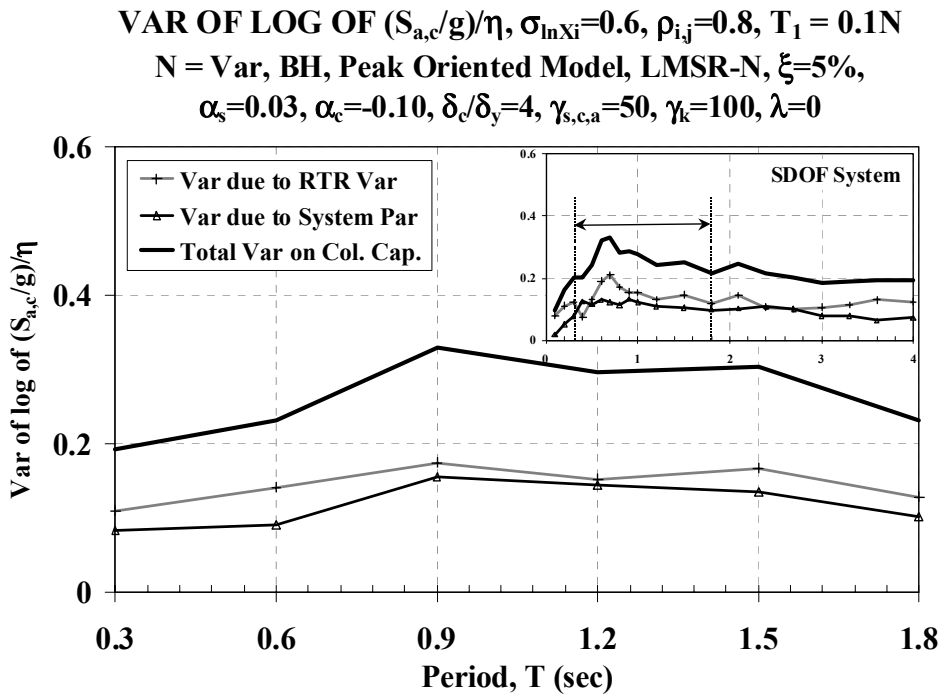

Fig. 6.45 $\sigma^2_{\ln S_{a,c}(RTR)}$, $\sigma^2_{\ln S_{a,c}(\bar{X})}$ and $\sigma^2_{\ln S_{a,c}(TOT)}$ **for set of MDOF systems with** $T = 0.1N$ **and springs at ends of beams with intermediate ductile characteristics**

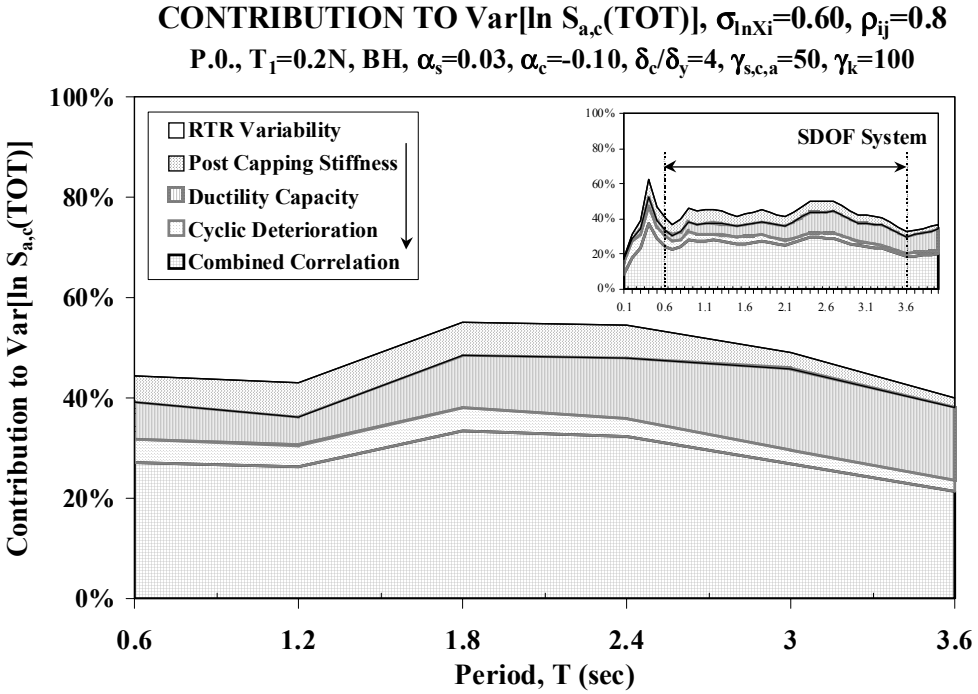

Fig. 6.46 Contributions to $\sigma^2_{\ln S_{a,c}(TOT)}$ **for set of MDOF systems with** $T = 0.2N$ **and springs at ends of beams with intermediate ductile characteristics**

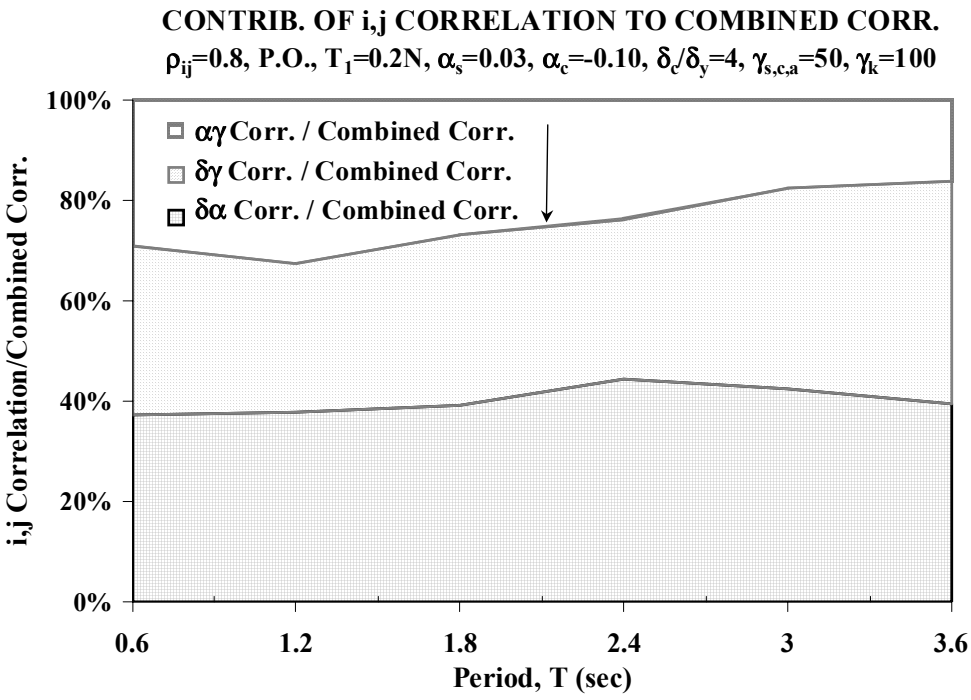

Fig. 6.47 ***i,j*** **correlation / combined correlation for set of MDOF systems with** $T = 0.2N$ **and springs at ends of beams with intermediate ductile characteristics**

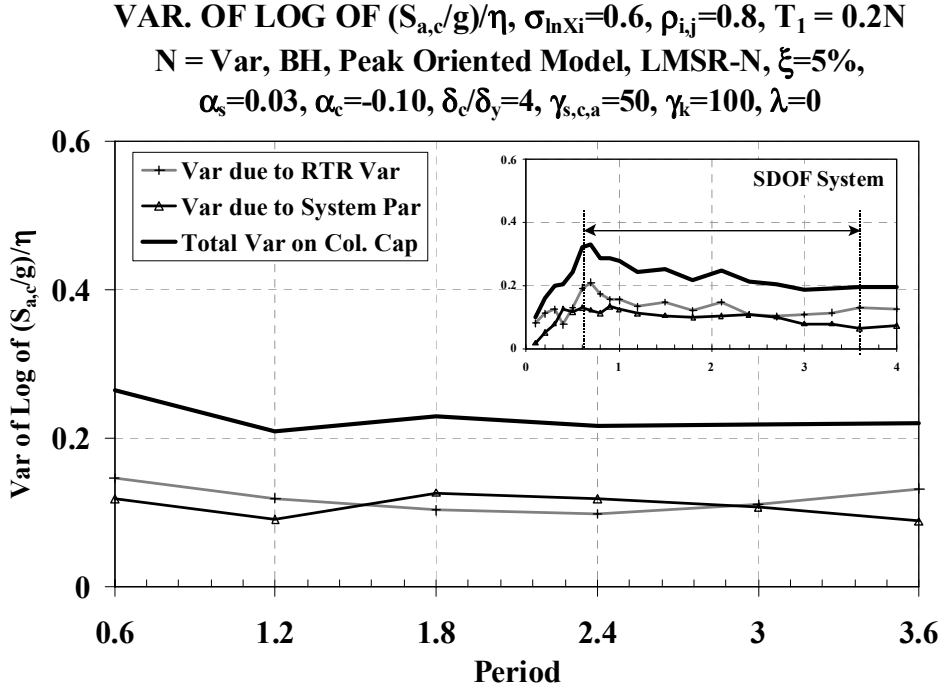

Fig. 6.48 $\sigma^2_{\ln S_{a,c}(RTR)}$, $\sigma^2_{\ln S_{a,c}(\bar{X})}$ **and** $\sigma^2_{\ln S_{a,c}(TOT)}$ **for set of MDOF systems with** $T = 0.2N$ **and springs at ends of beams with intermediate ductile characteristics**

7 Fragility Curves and Mean Annual Frequency of Collapse

7.1. INTRODUCTION

In seismic performance assessment, collapse constitutes one of several limit states of interest, such as a limit state that contributes to the cost of damage, if monetary losses or downtime are performance targets. In this context collapse could be viewed as a damage measure for which it is useful to develop fragility curves (FCs). In addition, collapse is the main source of casualties and loss of lives. In this context, collapse is an intermittent decision variable that could be described by the mean annual frequency (MAF).

This chapter explores alternatives for representing FCs based on computed collapse capacities and the effect that different system properties have on these curves. Previous to the presentation of the MAF of collapse, approximated hazard curves (HCs) for a specific site are introduced, which are derived from equal hazard spectra. Numerical integration is used for combining the FCs and HCs to obtain the MAF of collapse for a given site. The advantages of computing the MAF of collapse by using FCs derived directly from collapse capacities instead of EDPs associated with collapse are discussed.

7.2 COLLAPSE FRAGILITY CURVES (FCs)

A fragility function for a limit state expresses the conditional probability of exceeding the limit state capacity for a given level of ground motion intensity. The objective of this study is to evaluate the limit state of collapse by using the spectral acceleration at the fundamental period of the system as the ground motion intensity. Thus, the FC for these conditions is:

$$F_{C,S_{a,c}}(x) = P[S_a \geq S_{a,c} \big| S_a = x] = P[S_{a,c} \leq x] \tag{7.1}$$

$F_{C,S_{a,c}}(x)$ corresponds to the value of the fragility curve (FC) at spectral acceleration, *x,* for the limit state of collapse, i.e., the "collapse fragility curve." By considering that the demand ($S_a = x$) is statistically independent of the capacity of the system ($S_{a,c}$), the FC can be expressed as the probability that $S_{a,c}$ is less than or equal to *x*. The collapse FC can be viewed also as the cumulative distribution function (CDF) of a random variable, the collapse capacity, $S_{a,c}$.

In previous chapters, "collapse capacity" has been used as the parameter for collapse evaluation. This normalized parameter is defined as the ratio of the ground motion intensity to a structural strength parameter when collapse occurs ($[(S_a/\mathrm{g})/\eta]_c$ for SDOF systems and $\{[S_a(T_1)/g]/\gamma\}_c$ for MDOF systems[23]. Therefore, it is possible to generate "normalized collapse fragility curves" by using this normalized parameter instead of the ground motion intensity. For SDOF systems, normalized collapse FCs are obtained by modifying Equation 7.1 as follows:

$$F_{C,(S_{a,c}/g)/\eta}(x) = P[(S_{a,c}/g)/\eta \le x] \tag{7.2}$$

One of the advantages of assessing collapse based on the relative intensity (collapse capacity) is that the parameter can be easily de-normalized and plugged directly in Equation 7.1 (see Section 7.2.4.).

7.2.1 Normalized Counted Collapse Fragility Curves

Counted collapse fragility curves are obtained by treating the collapse capacity data as a random sample, i.e., equally likely outcomes. For instance, if the limit state of collapse is evaluated for a system subjected to 40 ground motions, the probability of collapse increases by 1/40 (0.025) after each individual collapse occurs.

Data of the type shown in Figure 2.4 are utilized to develop normalized collapse fragility curves, which describe the probability of collapse given the value of $(S_a/g)/\eta$ (or $[S_a(T_1)/g]/\gamma$ for MDOF systems). Typical results of counted fragility curves are presented in Figure 7.1a for SDOF systems of various periods but with the same baseline hysteretic properties:

- Peak-oriented model
- Medium ductility capacity, $\delta_c/\delta_y = 4$

[23] For the sake of simplicity, collapse capacity is also expressed as $(S_{a,c}/\mathrm{g})/\eta$ for SDOF systems and $[S_{a,c}(T_1)/g]/\gamma$ for MDOF systems.

- Small post-capping stiffness, α_c = -0.10
- No cyclic deterioration, $\gamma_{s,c,k,a}$ = infinite

As observed, normalized collapse fragility curves are very similar for SDOF systems with these hysteresis properties and periods longer than about T = 0.6 s. This is expected from observing that median collapse capacities for SDOF systems with P-Δ = 0.1N are essentially period independent for periods longer than about T = 0.6 s (Fig. 4.32a). Figure 7.1b presents fragility curves for systems with the same natural period T = 0.6 s, but different hysteretic properties. As can be seen, probability of collapse is very sensitive to hysteretic properties.

7.2.2 Normalized Collapse Fragility Curves Obtained by Fitting Lognormal Distribution to Data

Counted FCs are based on the real distribution of the sample data but are difficult to incorporate into analytical formulations. For this reason, a lognormal distribution is fitted to collapse capacity data and, although it is an approximation of the distribution of the sample data, it facilitates numerical and analytical calculations. The lognormal distribution is a logical selection for several reasons: (a) most of the individual collapse capacity data have a skewed distribution with a longer tail for upper values (Fig. 2.4 and 2.5 and Appendix C for a goodness-of-fit test), (b) collapse capacity values are always positive and, (c) previous studies have associated the distribution of spectral acceleration and the response of a nonlinear structure (in terms of EDPs) to lognormal distributions (Shome and Cornell, 1999).

Figure 7.2 presents FCs for different SDOF systems. The irregular curves are obtained from the ordered data points (counted FCs), whereas the smooth curves are the result of fitting a lognormal distribution to the data, which fits the data rather well. For this reason in the subsequent graphs for MDOF frames only the fitted distributions are shown.

The dependence of the fragility curves on the system period is presented in Figure 7.2a for SDOF systems with baseline hysteretic properties. As observed, for a given relative intensity the systems with short period have a higher probability of collapse. On the other hand, Figure 7.2b presents FCs for SDOF systems with the same elastic period (T = 0.6 s.) but different hysteretic properties. This figure shows the large sensitivity of the probability of collapse to the hysteretic properties, emphasizing the importance of "ductility" in the prevention of collapse.

The FCs of Figure 7.2b can be used for obtaining collapse capacity ratios for different probabilities of collapse, i.e., over the entire range of probabilities of collapse, the relative intensity of each FC is normalized by the relative intensity of the FC corresponding to the most ductile system (Fig. 7.3). The collapse capacity ratios obtained from the counted FCs are essentially independent of the probability of collapse in the range of 0.20–0.80. This indicates that the dispersion in the collapse capacity is approximately the same for each case. This observation may justify the extrapolation of the conclusions obtained from *median* collapse capacities ratios in Chapters 4 and 5 to other probabilities of collapse. In the case of the collapse capacity ratios obtained from fitted lognormal distributions, there is a clear pattern of a decrease in collapse capacity ratios for higher probabilities of collapse. In any case, the aforementioned extrapolation still would be feasible because the difference between the collapse capacity ratios at the probability of collapse of 0.50 and probabilities of collapse in the range from 0.20–0.80 is relatively small.

7.2.3 De-normalization of Collapse Fragility Curves

In most of this study, collapse capacities are based on the maximum relative intensity $(S_a/g)/\eta$ (or $[S_a(T_1)/g]/\gamma$ for MDOF systems) that the system may resist. However, to compute the MAF of collapse, these curves need to be de-normalized by a specific strength of the structural system. That is to say, the structural strength parameter (γ or η) should remain constant. As an illustration, Figure 7.4 presents de-normalized FCs for an SDOF system with baseline hysteretic properties under different base shear strengths. As can be seen, for a given probability of collapse the spectral acceleration at collapse decreases proportionally to the decrease in the strength of the system. Observe that for large shear strength values it is possible to anticipate small values of the MAF of collapse. For instance, for the system with $\eta = 1$, the probability of collapse is only of about 5% at the very large spectral acceleration $S_a/g = 3$. Therefore, the combination of this FC with any reasonable HC for a given site will result in a low MAF of collapse because the annual rate of exceedance of a ground motion with $S_a/g \geq 3$ will be very small.

7.2.4 Collapse Fragility Curves for MDOF Frames with Parameter Variations

Figure 7.5 presents FCs for MDOF systems that can be compared directly to the SDOF fragility curves of Figure 7.2a. These curves are obtained for generic frames with beam-hinge mechanism, in which the hysteretic properties of the springs at the end of the beams correspond to the baseline structural properties (see Chapter 5 for a description of the generic frames). The four-digit code identifies the number of stories and the first mode period of each frame, i.e., 0918 means a 9-story frame with T_1 = 1.8 s.

Figure 7.5 shows a pattern equivalent to that exhibited in the median collapse capacity spectra of MDOF systems (Chapter 5), of high fragility (small collapse capacity) for short period structures (T_1 = 0.3 s.), a large decrease in the fragility for medium period structures (T_1 = 0.6 and 0.9 s.), and then an increase in fragility for long-period structures (T_1 = 1.8 and 3.6 s.) because of the predominance of P-Δ effects.

The effects of ductility capacity and post-capping tangent stiffness are illustrated in Figures 7.6–7.7 for four frames with the first mode period varying from 0.3 s–3.6 s. An increase in the ductility capacity shifts the fragility curves to the right, but not by an amount proportional to the increase in ductility capacity. An increase in the slope of the post-capping tangent stiffness (from flat to steep) has a very detrimental effect on the fragility.

In concept, all observations that have been made previously for median collapse capacities hold true for the FCs. The value of these curves lies in their probabilistic nature that permits probabilistic expressions of performance and design decisions. For instance, if for a given long return period hazard (e.g., 2/50 hazard) a 10% probability of collapse could be tolerated, then the intersections of a horizontal line at a probability of 0.1 with the individual fragility curves provides targets for the *R*-factor that should be employed in design, in conjunction with the spectral acceleration associated with this hazard. If such horizontal lines are drawn in the graphs of Figures 7.6–7.7, it can be conjectured that the indicated *R*-values are low, even for rather ductile systems.

The second value of the fragility curves lies in the opportunity they provide for a rigorous computation of the MAF of collapse.

7.3 SPECTRAL ACCELERATION HAZARD

Information about the seismic hazard is necessary in order to obtain the MAF of collapse. Generally seismic hazard is reported in terms of 5%-damped spectral acceleration at the fundamental period of the system, $S_a(T_1)$, which becomes the ground motion intensity measure (IM). Hazard curves (HCs) report the mean annual frequency of exceeding a particular spectral acceleration for a given period and damping ratio.

Seismologists usually provide spectral acceleration hazard curves for a given site. This information may be approximated by a power-law relationship in the region of interest (FEMA 355C, 2000; Luco, 2002; Jalayer, 2003):

$$\lambda_{IM}(x) = P[IM \geq x] = k_o x^{-k} \tag{7.3}$$

or specifically:

$$\lambda_{S_a(T_1)}(S_a) = P[S_a(T_1) \geq S_a] = k_o S_a^{-k} \tag{7.4}$$

$\lambda_{S_a(T_1)}(S_a)$ is defined here as the MAF of the ground motion having a spectral response acceleration at the fundamental period of the system greater than S_a. For the small probabilities of interest here it is numerically equal to the annual probability of exceedance. The parameter k_o is a constant that depends on the seismicity of the site and k approximates the local slope of the hazard curve, in the log domain, around the return period of interest. The slope of the hazard curve is a function of the hazard level, location and response period.

To illustrate the computation of MAF of collapse, HCs for various periods are approximated from the equal hazard spectra employed in PEER studies for a Los Angeles building (Somerville and Collins, 2002) (Fig. 7.8). The equal hazard spectra for the site were derived from the USGS probabilistic ground motion maps for rock site conditions. Spectra for soil site conditions were generated from the rock site spectra by using the Abrahamson and Silva (1997) ground motion model. These curves represent an equal probability of exceeding the ground motion at any period for 50/50, 10/50, and 2/50 hazard levels. The hazard levels are based on a probability of exceedance in a 50-year period. For instance, 10/50 refers to the probability of exceedance of 10% in 50 years (1/475).

The values at each period are used to derive power-law relationships of the type of Equation 7.2. Several reasonable approaches could be proposed for this purpose. The simplest one is to approximate the hazard curve in the region of interest with a straight line in the log-log

domain of spectral acceleration and probability of exceedance. A linear regression analysis is used to fit the straight line (Fig. 7.9). The use of the three hazard levels "averages" the probability of exceedance over all the possible spectral acceleration values, which is convenient for the example of Section 7.4 because the region of interest for the MAF of collapse changes according to the period and the ductility characteristics of the system.

Figure 7.10 presents some of the hazard curves derived from the equal hazard spectra. As can be seen, the annual frequency of exceedance has reasonable limits even for small spectral accelerations, which usually does not occur when the approximation is made only with the 10/50 and 2/50 hazard levels. However, note that the probabilities of exceedance of the approximated HCs may be overestimated for large spectral accelerations because the linear regression flattens the HCs in this region. For this reason, in the computation of the MAF of collapse, the HCs are terminated at $S_a/g = 3$.

7.4 MEAN ANNUAL FREQUENCY OF GLOBAL COLLAPSE

7.4.1 Formulation

The MAF of collapse (λ_c) can be calculated once the de-normalized FCs of the system and HCs for the site of interest are known. The MAF of collapse is expressed as the mean annual frequency of the strong motion intensity (S_a) being larger than the collapse capacity (expressed as a function of $S_{a,c}$ given η) multiplied by the probability of having such a strong motion intensity:

$$\lambda_c = \int_0^\infty P[S_a > S_{a,c} \big| S_a = x].v.f_{S_a}(x).dx \tag{7.5}$$

where, $f_{S_a}(x)$ is the probability density function (PDF) at the spectral acceleration value x given an event of interest, and v represents the annual rate of the occurrence of such events (rate of seismicity). In Section 7.2 the first term of the integral was defined as the collapse fragility curve. Therefore:

$$\lambda_c = \int_0^\infty F_{C,S_{a,c}}(x).v.f_{S_a}(x).dx \tag{7.6}$$

The PDF of the spectral acceleration value can be expressed in terms of the complementary cumulative distribution (CCDF) function (Jalayer, 2003):

$$f_{S_a}(x) = \left| \frac{dG_{S_a}(x)}{dx} \right| \tag{7.7}$$

In this equality, the CCDF [$G_{S_a}(x)$] is the probability of exceeding a certain value, whereas the CDF [$F_{S_a}(x) = f_{S_a}(x)d(x)$] is the probability of being less than or equal to a certain threshold. Therefore, their corresponding derivatives are equal in absolute values but have opposite signs. By substituting Equation 7.7 in 7.6:

$$\lambda_c = \int_0^\infty F_{C,S_{a,c}}(x).\left|v.dG_{S_a}(x)\right| \tag{7.8}$$

In addition, the spectral acceleration hazard, $d\lambda_{Sa}(x)$, is equal to:

$$d\lambda_a(x) = v.dG_{S_a}(x) \tag{7.9}$$

by substituting Equation 7.9 in 7.8:

$$\lambda_c = \int_0^\infty F_{C,S_{a,c}}(x).\left|d\lambda_a(x)\right| \tag{7.10}$$

Equation 7.10 explicitly expresses the MAF of collapse in terms of the collapse fragility curve for a given median base shear strength over a S_a hazard curve pertaining to a specific site. The process of integrating Equation 7.10 has been illustrated graphically in Figure 2.10.

Note that this approach is more straightforward than the methodology for computing collapse based on displacement demands and capacities. The "EDP-based approach" decomposes the collapse limit state into two steps and requires an additional integration (Jalayer, 2003). First, the EDP hazard is obtained as the probability of exceeding a demand threshold given that the IM is equal to a certain value, *x*. In a second step, the probability of collapse is obtained as the likelihood of having an EDP demand hazard larger than the EDP capacity. Thus, it is concluded that the evaluation of global collapse based on the relative intensity of the system facilitates the computation of the mean annual frequency of collapse.

7.4.2 Computation of Mean Annual Frequency of Collapse for a Specific Site, SDOF Systems

The example presented in this section illustrates the methodology to compute the MAF of collapse for various periods and selected strength levels, η. It also permits a gross quantification of the effect of several parameters on the MAF of collapse.

Collapse FCs for SDOF systems with baseline hysteretic properties and P-Δ = 0.1N are shown in Figure 7.11 for different periods and for a yield strength coefficient $\eta = 0.2$. As can be seen, in the period range of T = 0.1 to 2.0 s, the longer the period the larger the spectral acceleration that leads to collapse for a given probability of collapse. This fact will be reflected in smaller MAF of collapse for SDOF systems with longer periods.

The FCs of Figure 7.11 and the HCs obtained from the equal hazard spectra (Section 7.3) are utilized for solving Equation 7.10 by numerical integration. The result of this integration is represented graphically in Figure 7.12, where a curve for MAF of collapse due to $S_a = x$ is obtained for T = 0.5 s. Figure 7.13 shows more of these curves for systems with different periods. The diamonds on the FCs of Figure 7.11 indicate the spectral acceleration at which the peaks of the curves for MAF of collapse due to $S_a = x$ occur. For this example, all the peaks are located at the spectral acceleration region at which the FC begins to build up, and where the probability of collapse is about 0.20.

The areas under the curves of Figure 7.13 corresponds to the MAFs of collapse, which are plotted in Figure 7.14 for several periods and different strengths for SDOF systems with the baseline hysteretic properties. The MAFs of collapse illustrate general trends and are the product of a rigorous computational process. Observe that the MAF of collapse may differ by several orders of magnitude for systems with the same properties but different yield strength.

A comparison of MAFs of collapse for systems of different hysteretic properties, given $\eta = 0.2$, is presented in Figure 7.15. The figure shows that the MAF of collapse can increase by more than one order of magnitude due to the ductile characteristics of the system. Figures 7.14–7.15 show a strong dependence of the MAF of collapse on the natural period of SDOF systems with otherwise identical properties.

Effect of Uncertainty in System Parameters. An SDOF system with baseline properties but $\gamma_{s,c,k,a} = 50$ is utilized for computing the MAF of collapse including uncertainty in system

parameters. Figure 6.33 presents the contribution of uncertainty in system parameters to variance of collapse capacity for the aforementioned system. This contribution can be larger than that due to RTR variability. The MAF of collapse for this system is presented for different periods and two different strengths in Figure 7.16. As can be seen, the additional variance increases the MAF of collapse by about 50–100% compared with the case where RTR variability is the only source of uncertainty.

The total variance in collapse capacity due to RTR variability and uncertainty in the input parameters may increase the MAF of collapse several times. Figure 7.17 presents MAFs of collapse for the former systems with $\eta = 0.2$, considering deterministic SDOF systems, systems with dispersion due to RTR variability, and systems with dispersion due to RTR variability plus uncertainty in the system parameters. If it were possible to calculate the collapse capacity of the system in a deterministic way, the MAF of collapse would decrease by more than a factor of four at some periods.

7.4.3 Computation of Mean Annual Frequency of Collapse for a Specific Site, MDOF Systems

The study of MAF of collapse for the generic frames of Chapter 5 is divided into MAFs for stiff and flexible frames. Figure 7.18 shows the FCs of the stiff frames ($T_1 = 0.1N$) for a base shear strength $\gamma = 0.2$ [24]. Unlike SDOF systems with P-Δ = $0.1N$ (small P-Δ), the collapse FCs are sensitive to variations of the fundamental period of the system over the full range of periods of interest. The main reason for this trend is the large P-Δ effect for systems with long fundamental period. This phenomenon is not observed in SDOF systems with small P-Δ effects because the elastic stability coefficient utilized in these systems does not capture the large P-Δ effects of the generic frames with long fundamental period.

The combination of FCs of Figure 7.18 with the corresponding HCs results in the MAFs of collapse shown in Figure 7.19 for several strength levels. The curves are for stiff MDOF systems with beam-hinge mechanism and baseline hysteretic properties in the springs of the beams. Figures 7.20–7.21 show equivalent FCs and MAFs of collapse but for flexible frames.

[24] The fundamental period for some generic frames does not coincide with the periods evaluated by Somerville and Collins. In these cases, the seismic hazard information has been obtained by interpolating the data of the existing periods.

Figure 7.22 presents the MAFs of collapse for stiff and flexible frames for two different strengths.

A comparison of Figures 7.19 and 7.21 for MDOF systems with the MAFs of Figure 7.14 (SDOF systems) leads to the following observations:

- For SDOF systems of equal strength (η value) the MAF of collapse decreases with period because S_a values decrease with period in uniform hazard spectra.
- For long-period MDOF systems the beneficial effect of smaller S_a values at a given hazard diminishes and essentially disappears. The cause is the P-Δ effect, which dominates the response of long-period structures, particularly in the presence of post-capping strength deterioration. For this reason the MAF of collapse curves in Figures 7.19 and 7.21 become essentially horizontal at longer periods (which is not observed in the SDOF curves).

7.5 SUMMARY

A rigorous approach is proposed for estimating the mean annual frequency (MAF) of collapse of SDOF and MDOF systems. The main observations are as follows:

- The collapse capacity data of Chapters 4 and 5 are used to develop fragility curves. It is observed that the probability of collapse is very sensitive to the hysteretic properties of the system, which corroborates the importance of using ductile components for preventing collapse.
- All the observations made in Chapters 4 and 5 for median collapse capacities hold true also for the fragility curves. This observation can be deduced from computing the collapse capacity ratios at different probabilities of collapse, which can be obtained directly from a set of different FCs (Fig. 7.3). These collapse capacity ratios do not change significantly for different probabilities of collapse in the range of the 20–80th percentile. Therefore, the median collapse capacity ratios of chapters 4 and 5, which reflect the difference in collapse capacity at the median value, may also be used for identifying behavioral trends for different probabilities of collapse.
- Non-ductile systems have fragility curves with steeper slope, indicating that failure may be brittle for these systems.

- If the spectral acceleration at the first mode period of the system is used as the intensity measure, then hazard curves can be developed using available seismic hazard information. The use of such hazard curves in the computation of the MAF of collapse, and of the collapse capacity information presented in chapters 4 and 5, should give good results provided the frequency content of the ground motions is insensitive to magnitude and distance (Medina, 2002; Jalayer, 2003), and provided the ground motions are representative for the hazard levels that control the MAF of collapse.
- To illustrate the computation of the MAF of collapse, equal hazard spectra are used for approximating hazard curves at several periods for a given site. A linear regression analysis is performed at each period with information at the 50/50, 10/50, and 2/50 hazard levels. The obtained hazard curves provide reasonable results for systems of different periods, strengths and ductility characteristics.
- The potential for global collapse of a frame structure can be expressed probabilistically in terms of a mean annual frequency of collapse using fragility curves derived from collapse capacities. The use of this type of FCs results in a straightforward calculation because a single integration is needed to relate the fragility curve with the seismic hazard of the site.
- The base shear strength of the system is a dominant factor in the magnitude of the MAF of collapse for a given system. Variations of the base shear strength from η (or γ for MDOF systems) = 0.5 to 0.1 may produce a difference in the MAF of collapse of more than two orders of magnitude.
- The MAF of collapse may increase by more than one order of magnitude for non-ductile systems compared with ductile ones.
- The MAF of collapse for MDOF systems shows the large effect of P-Δ for systems with longer periods.
- Uncertainty in the system parameters may increase the MAF of collapse by 50–100% (assuming the dispersions in the parameters of Chapter 6) compared with the cases in which RTR variability is the only source of uncertainty. For the studied systems, the MAF of collapse may decrease by more than a factor of four if it were possible to estimate collapse capacity in a deterministic way.

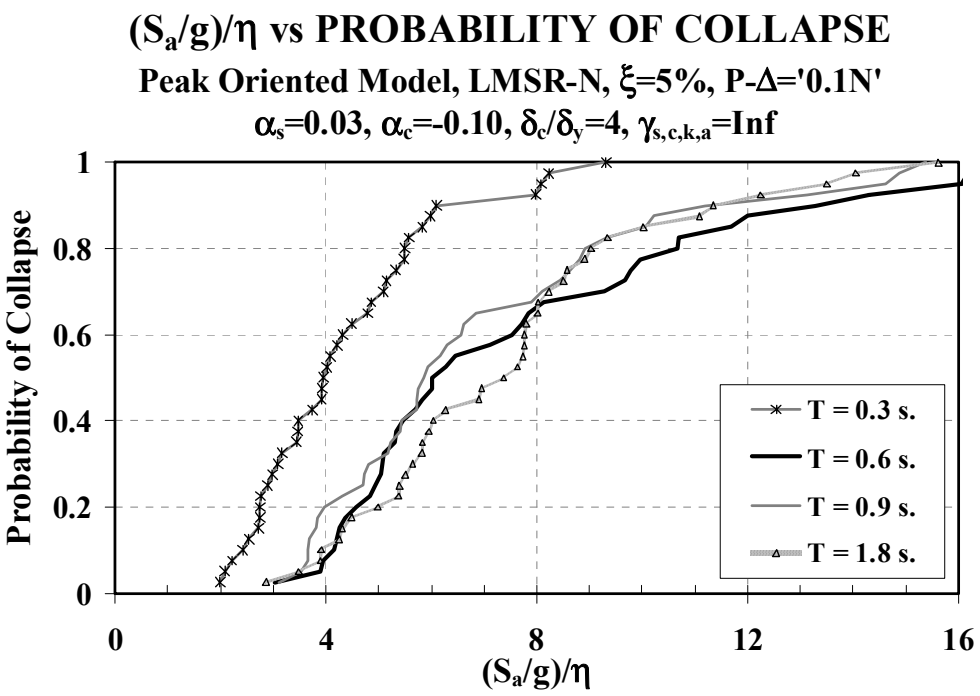

(a) Different Periods, Baseline Hysteretic Characteristics

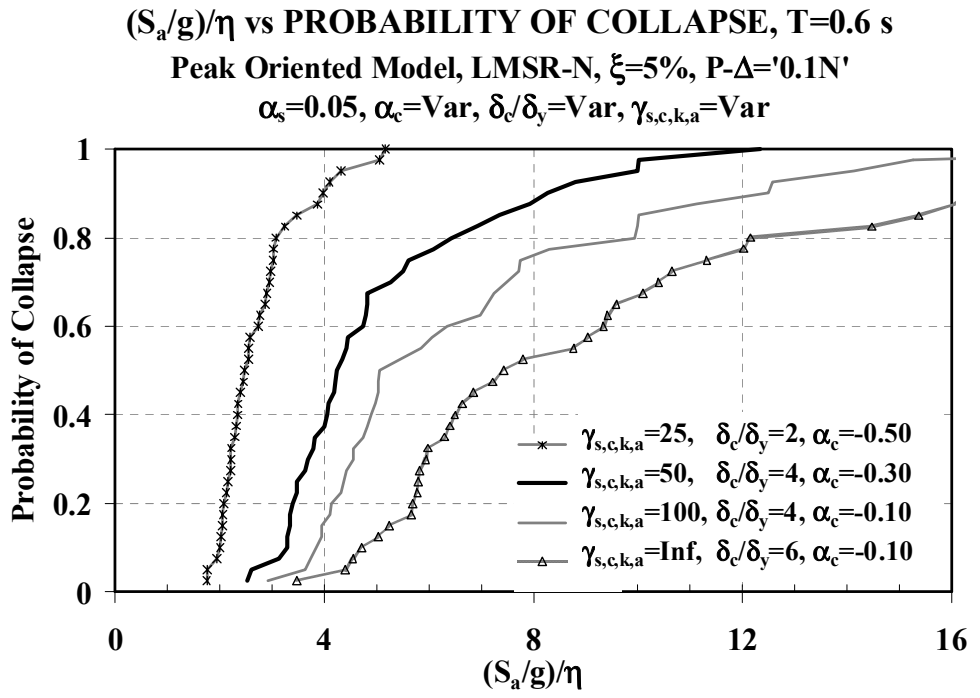

(b) Various Systems, $T = 0.6$ s

Fig. 7.1 Counted fragility curves for SDOF systems

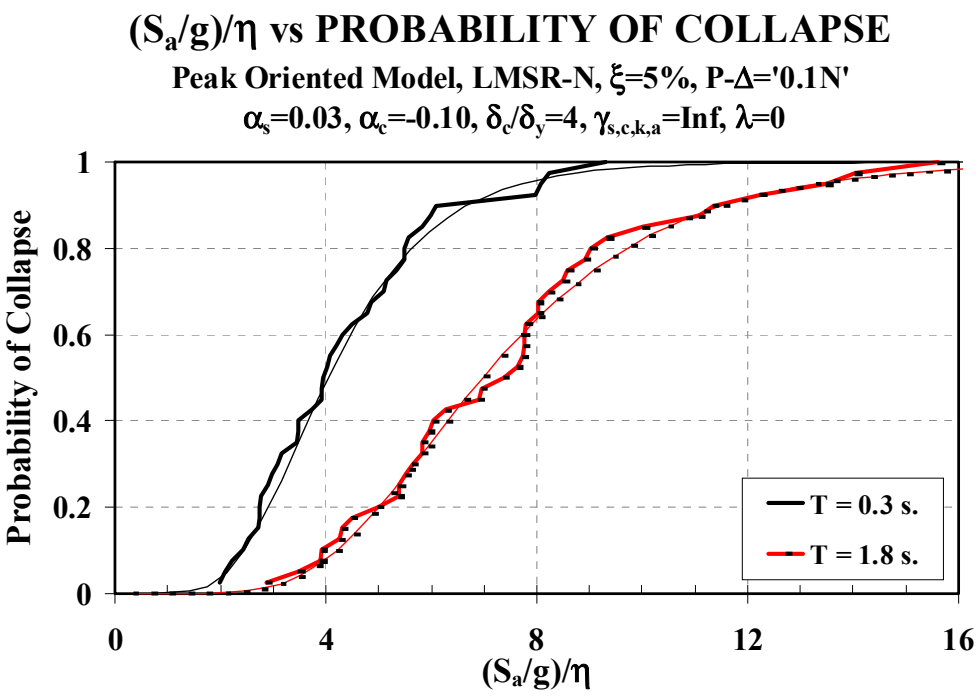

(a) $T = 0.3$ and 1.8 s, Baseline Hysteretic Properties

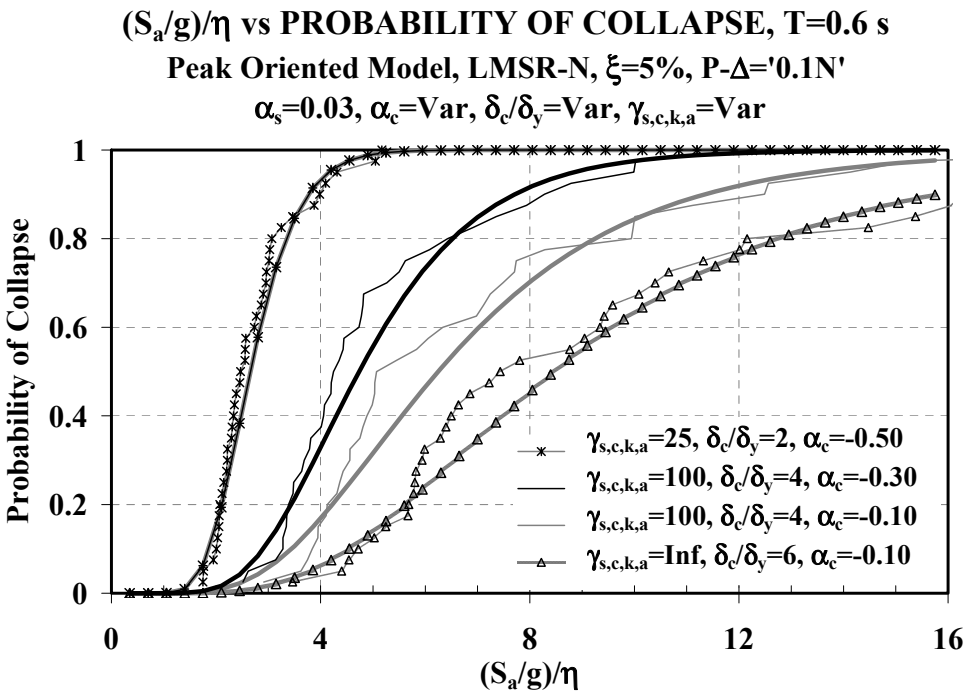

(b) Various Systems, $T = 0.6$ s

Fig. 7.2 Fragility curves for SDOF systems obtained by fitting a lognormal distribution

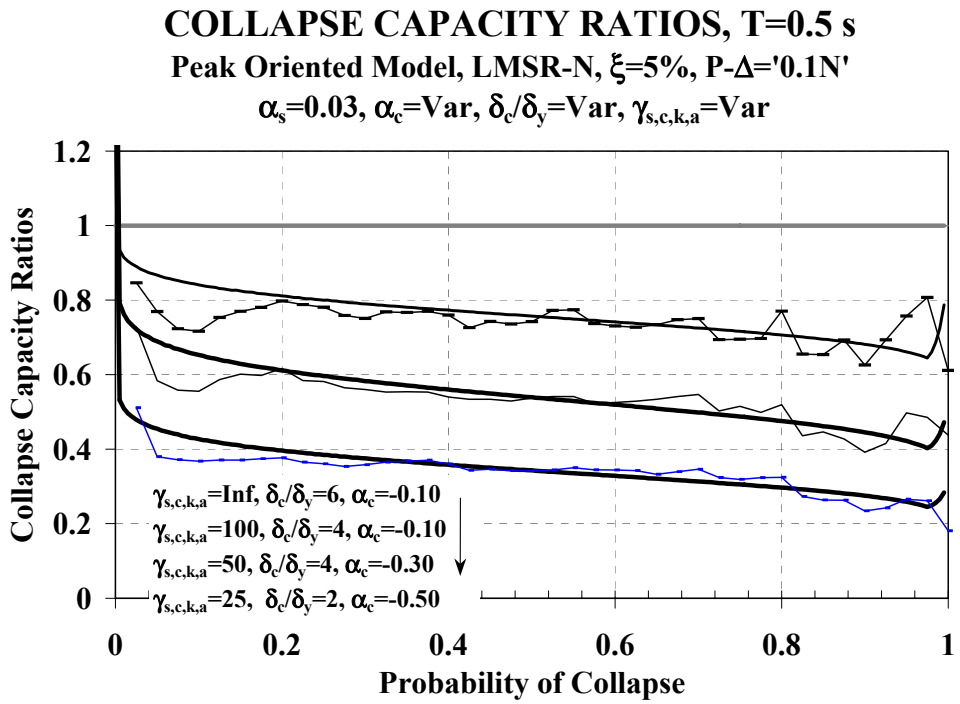

Fig. 7.3 Collapse capacity ratios for different probabilities of collapse, T = 0.5 s

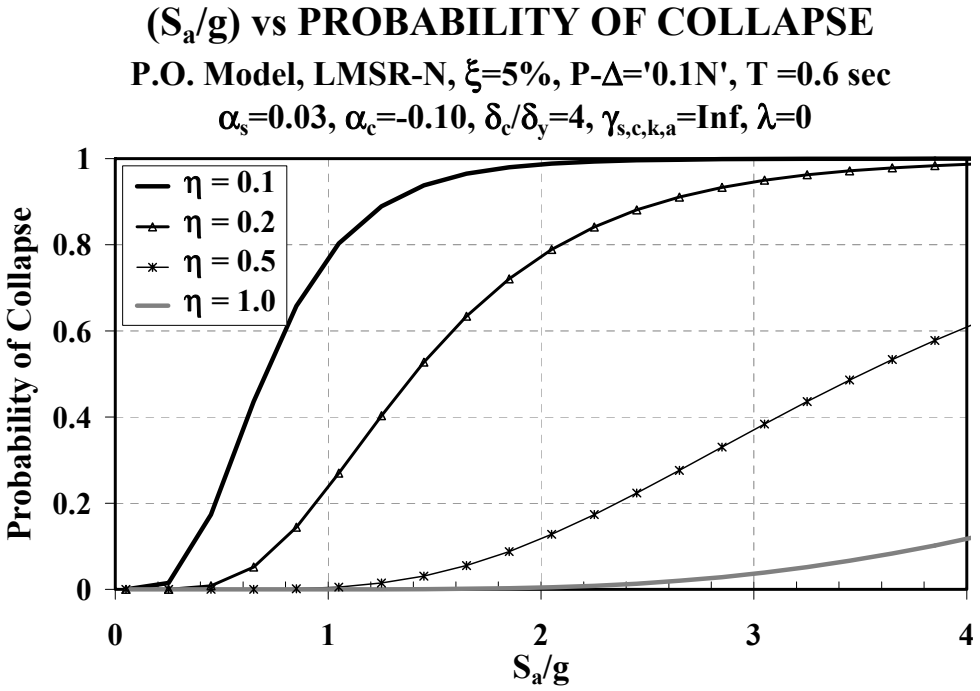

Fig. 7.4 De-normalization of fragility curves at different base shear strength for SDOF systems; baseline hysteretic properties, T = 0.6 s

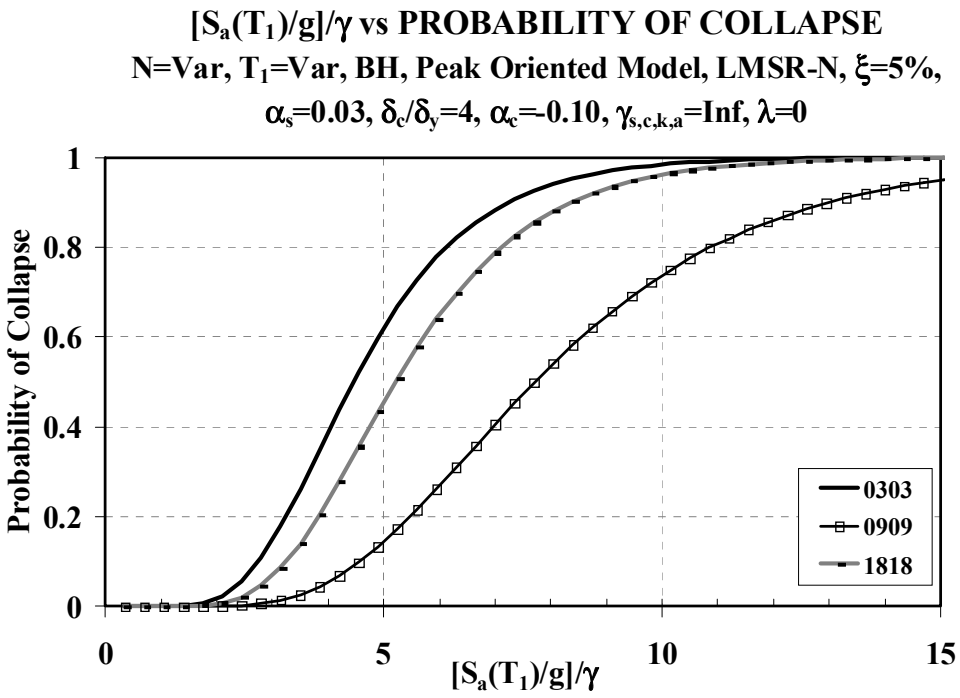

(a) $T_1 = 0.1N$

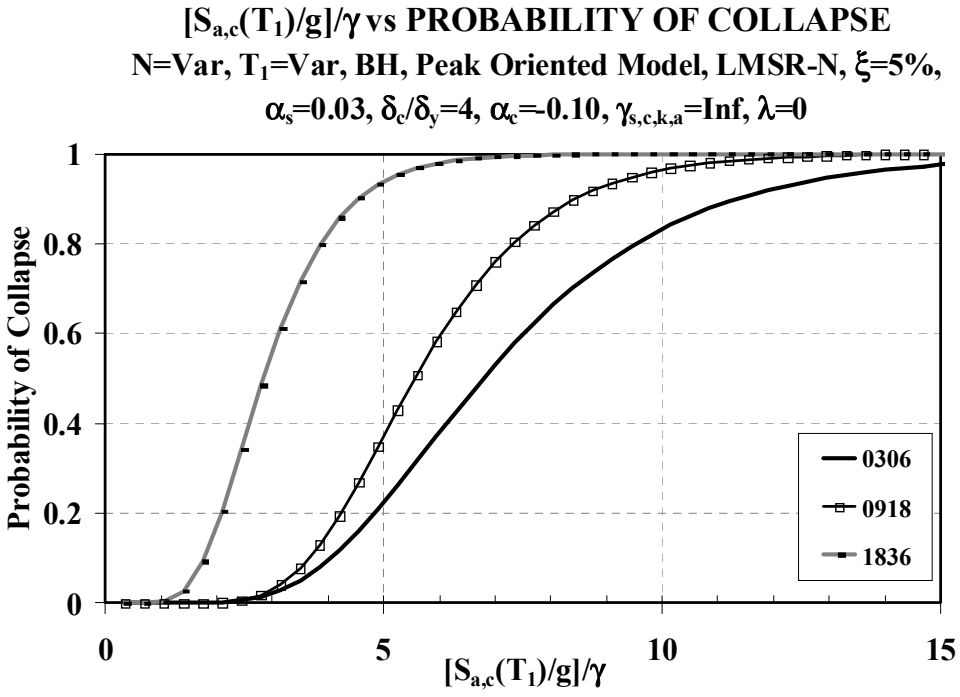

(b) $T_1 = 0.2N$

Fig. 7.5 Fragility curves for frame structures with springs at beams ends with baseline hysteretic properties

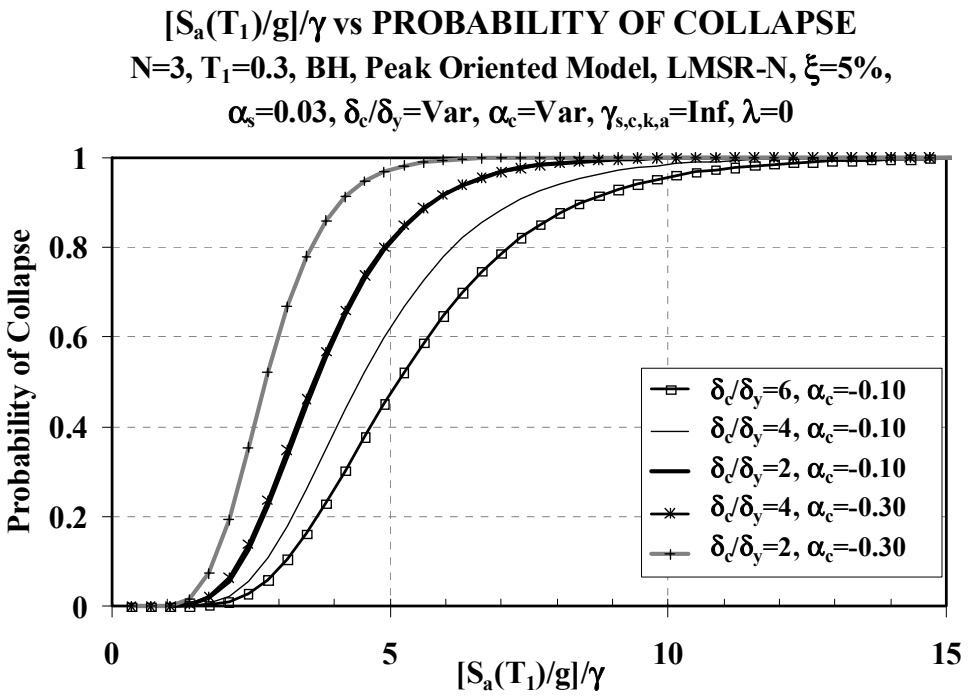

(a) 3-Story, T_1 = 0.3 s

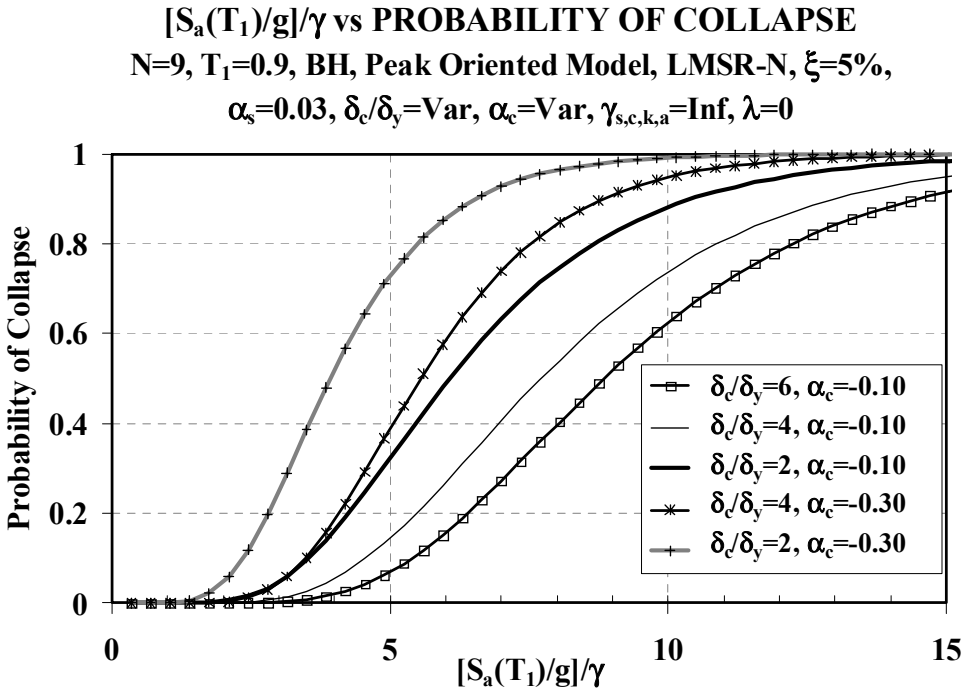

(b) 9-Story, T_1 = 0.9 s

Fig. 7.6 Fragility curves for stiff generic frames of 3 and 9 stories with parameter variations in springs of the beams

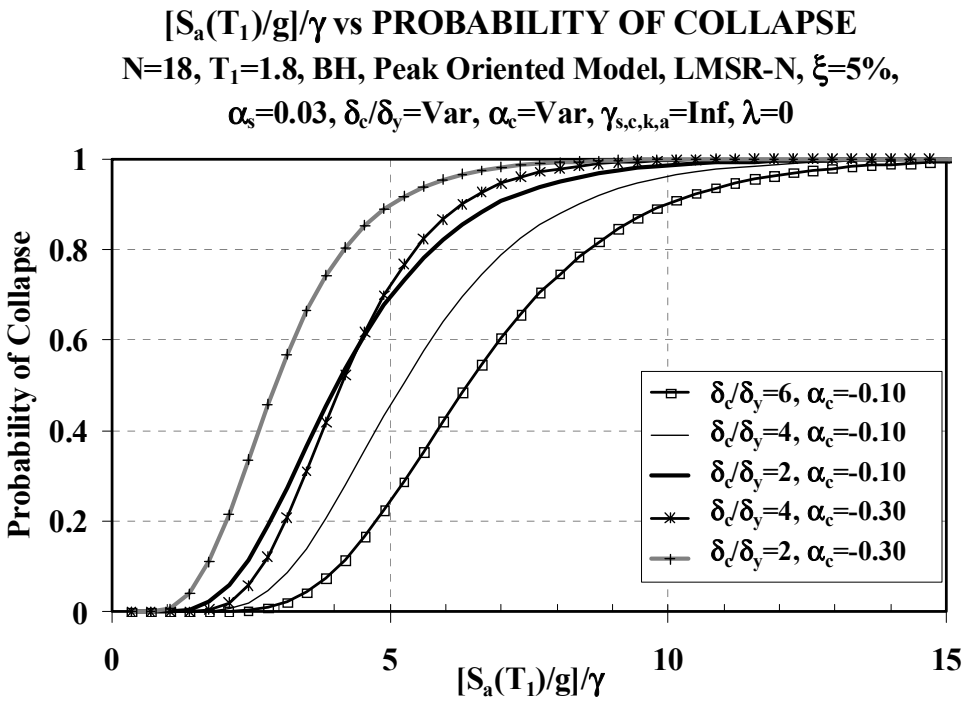

(a) 18-Story, T_1 = 1.8 s

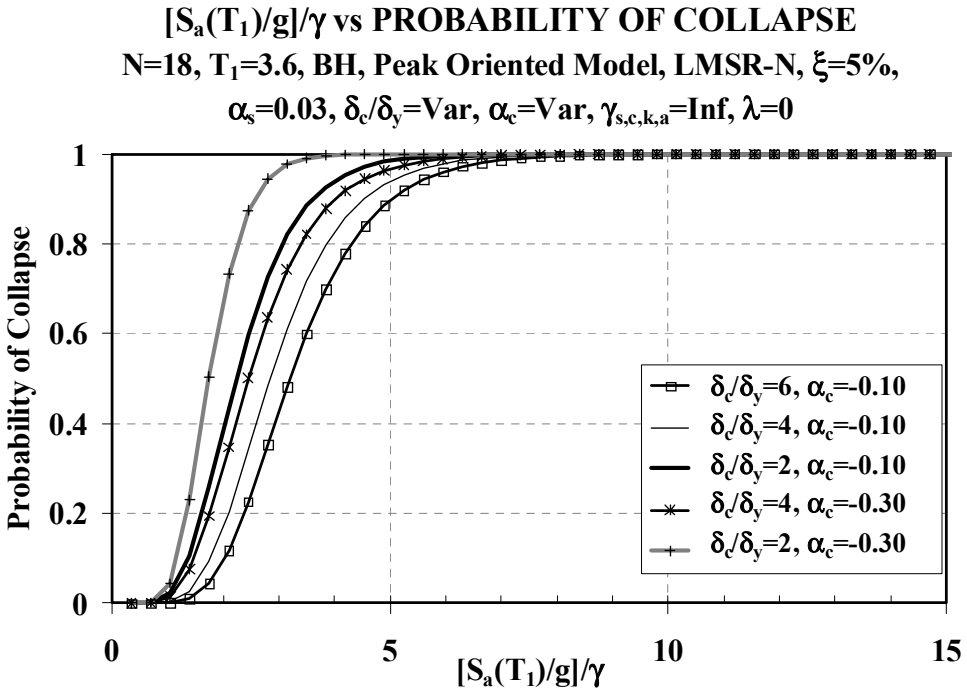

(b) 18-Story, T_1 = 3.6 s

Fig. 7.7 Fragility curves for 18-story generic frames with parameter variations in the springs of the beams

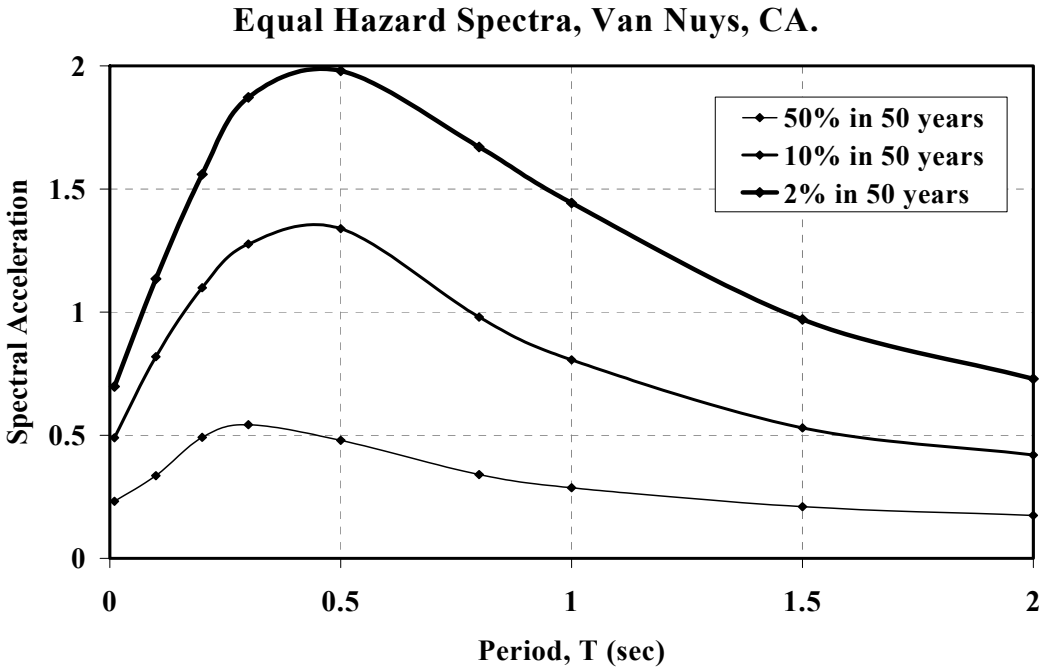

Fig. 7.8 Equal hazard spectra used to derive hazard curves for specific periods

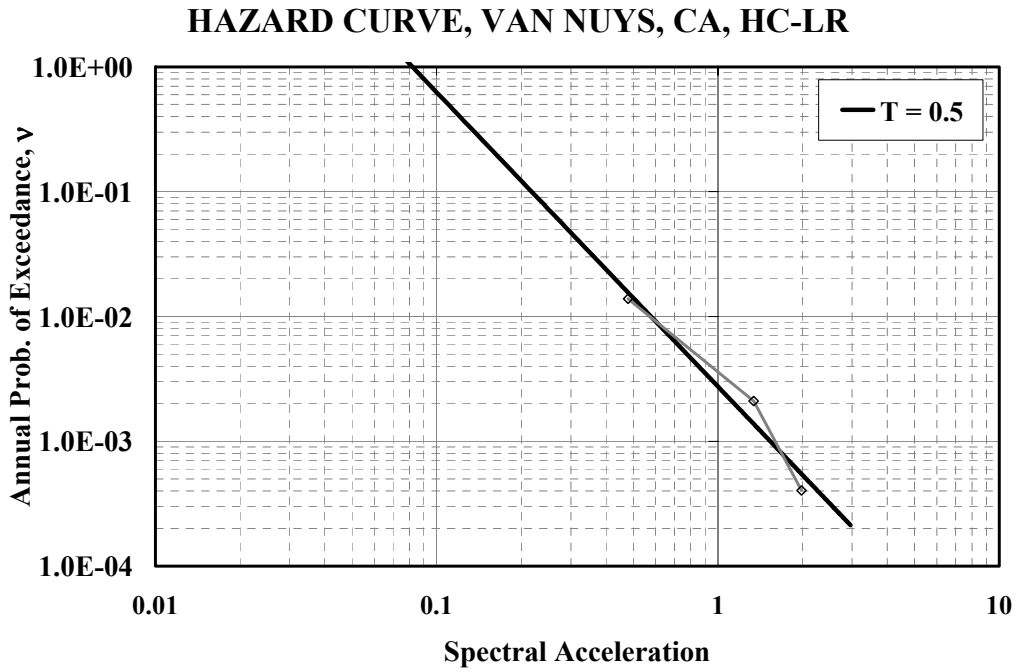

Fig. 7.9 Hazard curves obtained from linear regression analysis by using 50/50, 10/50, and 2/50 seismic hazard levels, T = 0.5 s

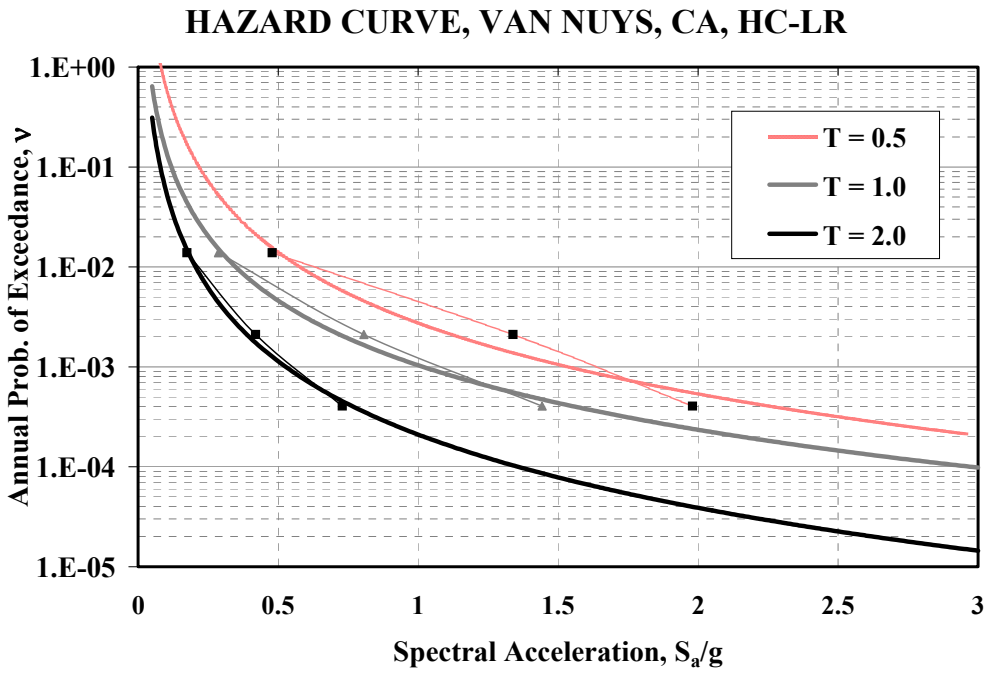

Fig. 7.10 Hazard curves obtained from linear regression analysis by using 50/50, 10/50, and 2/50 seismic hazard levels, T = 0.5, 1.0, and 2.0 s

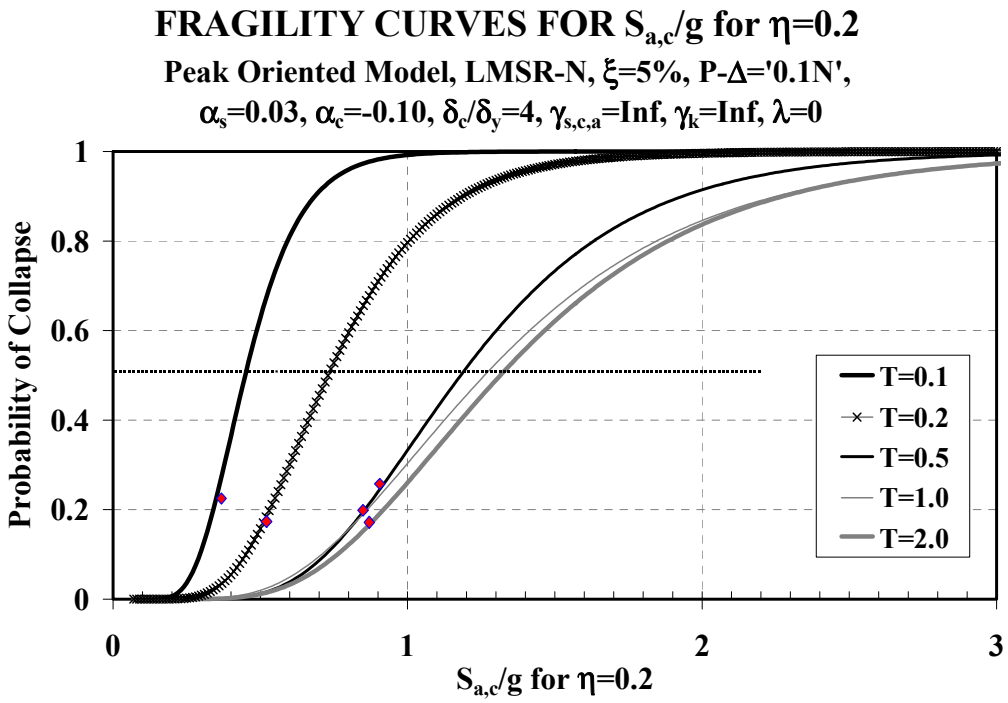

Fig. 7.11 Fragility curves of SDOF systems with baseline hysteretic properties for computing MAF of collapse, η = 0.2

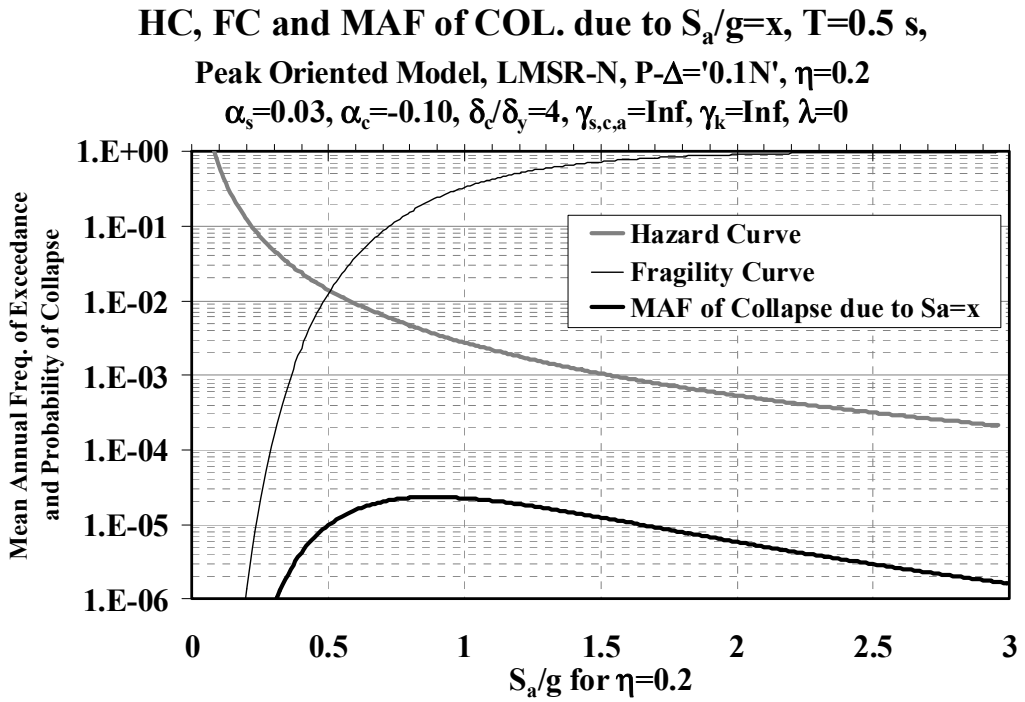

Fig. 7.12 HC, FC, and MAF of collapse due to $S_a = x$ at T = 0.5 s, SDOF system with baseline hysteretic properties, η = 0.2

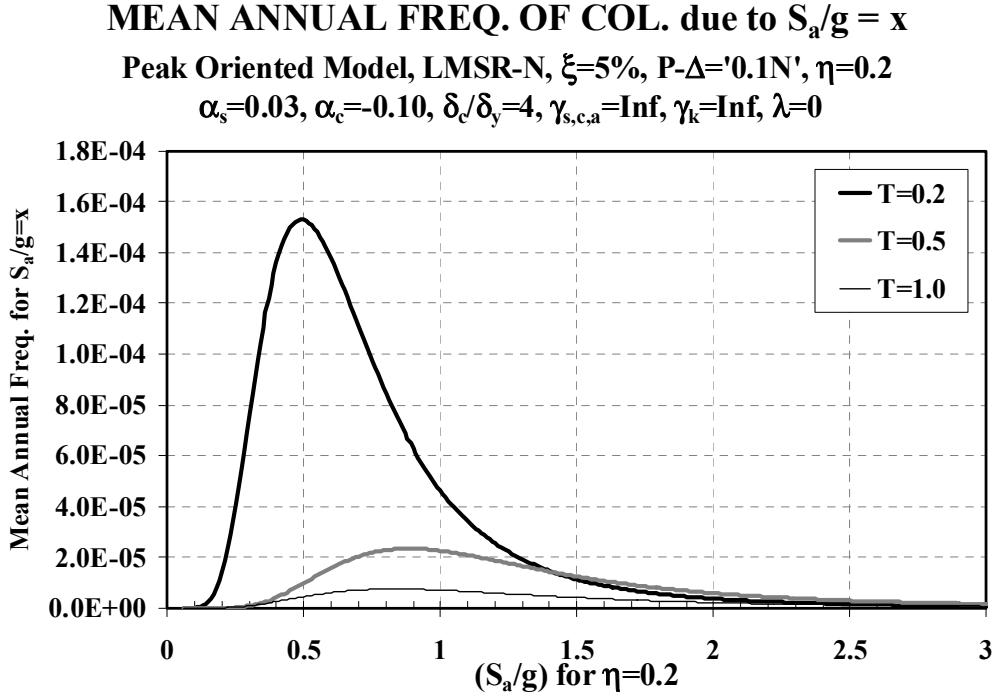

Fig. 7.13 Mean annual frequency of collapse due to $S_a = x$ for SDOF systems with baseline hysteretic properties, η = 0.2

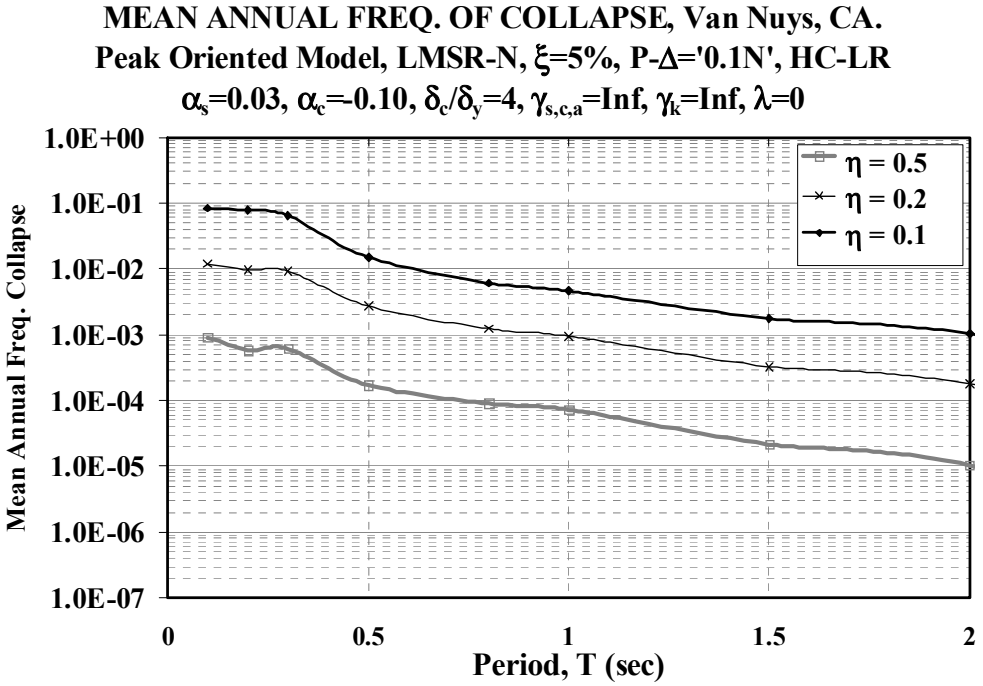

Fig. 7.14 Mean annual frequency of collapse for SDOF systems with baseline hysteretic properties for different η's and periods

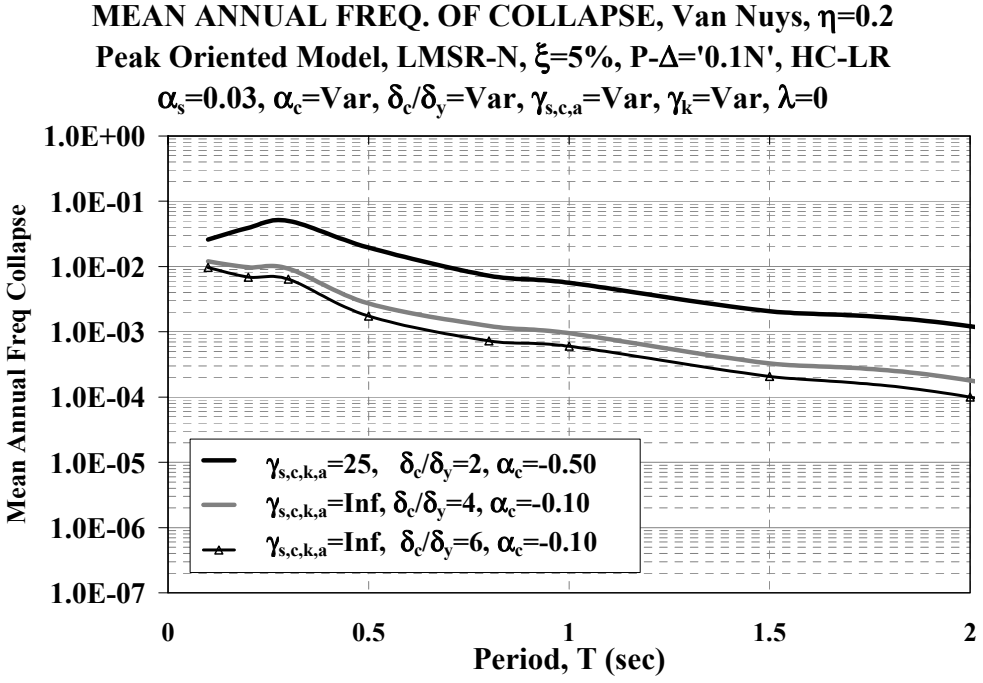

Fig. 7.15 Mean annual frequency of collapse for SDOF systems with different hysteretic properties, η = 0.2

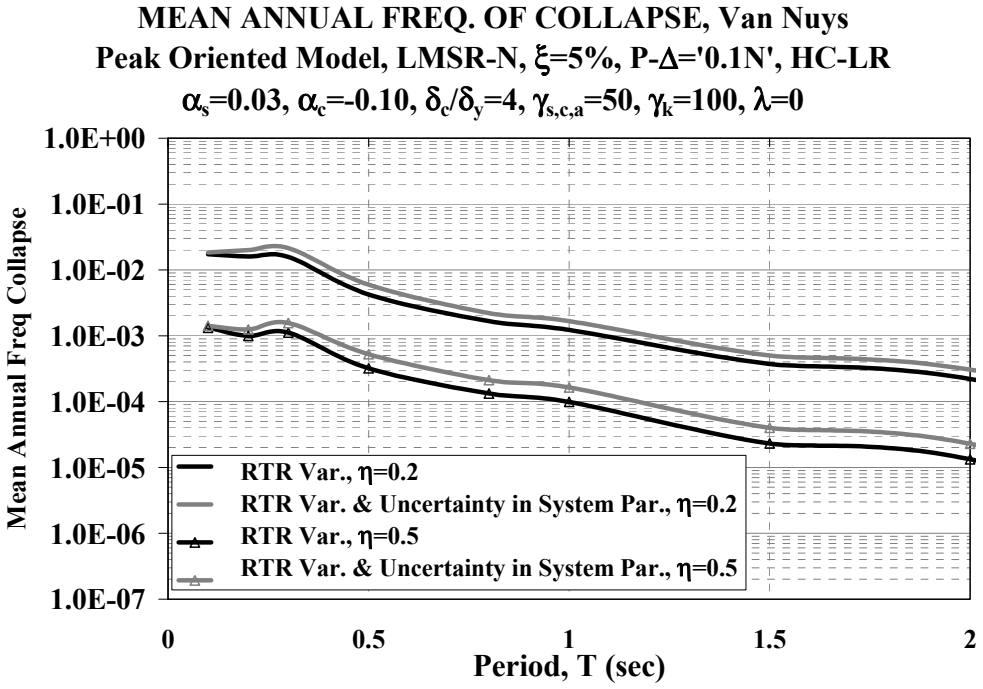

Fig. 7.16 MAF of collapse for SDOF systems with dispersion due to RTR variability plus uncertainty in the system par., α_c=-0.1, δ_c/δ_y=4, $\gamma_{s,c,k,a}$= 50

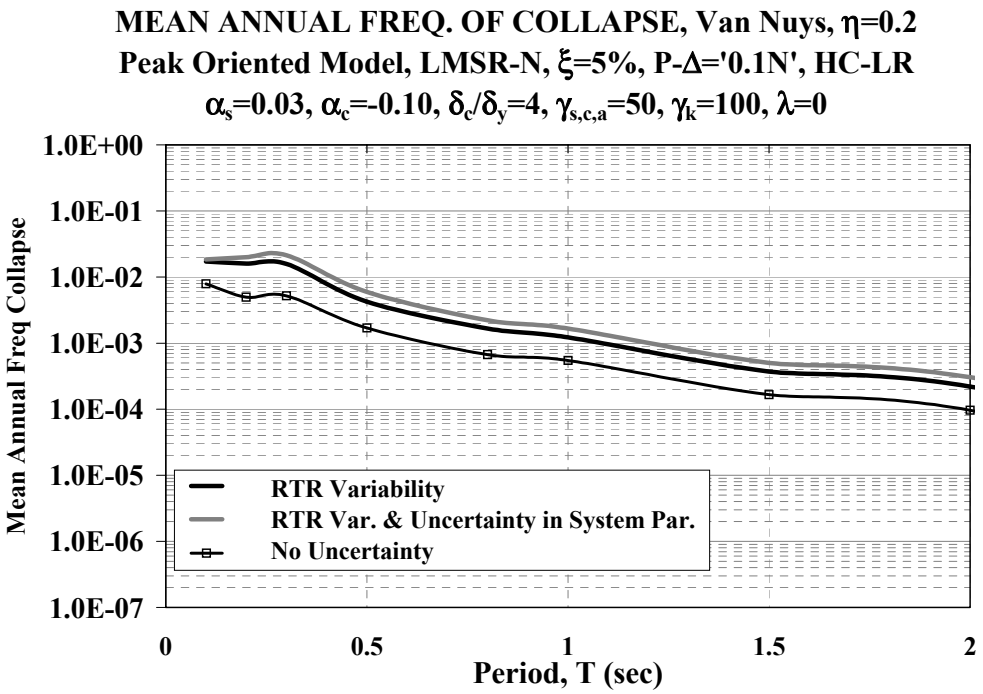

Fig. 7.17 MAF of collapse for deterministic SDOF systems, systems with dispersion due to RTR variability, and systems with dispersion due to RTR variability plus uncertainty in the system par., α_c=-0.1, δ_c/δ_y=4, $\gamma_{s,c,k,a}$= 50

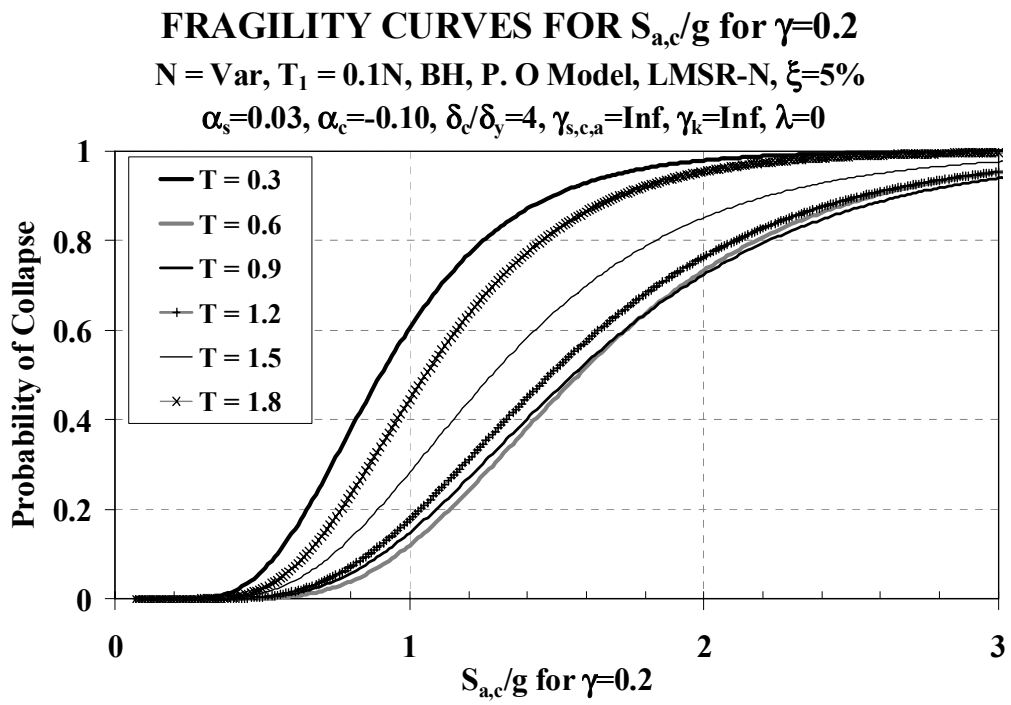

Fig. 7.18 Fragility curves of stiff generic frames with baseline hysteretic properties in the springs of the beams, γ= 0.2

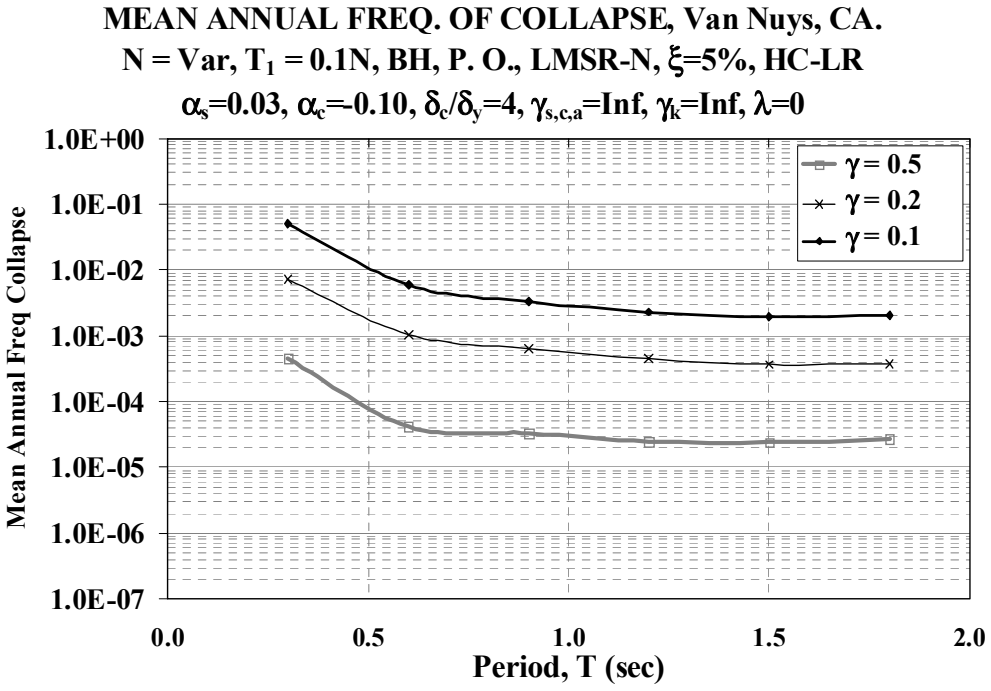

Fig. 7.19 Mean annual frequency of collapse for stiff generic frames, baseline hysteretic properties in the springs of the beams, different γs

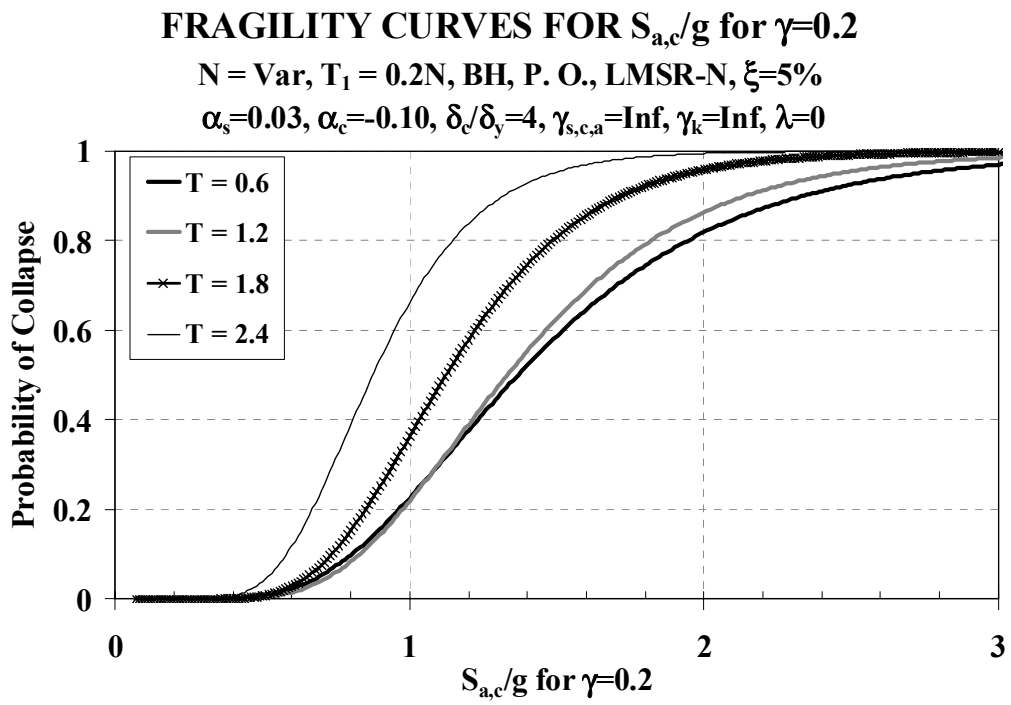

Fig. 7.20 Fragility curves of flexible generic frames with baseline hysteretic properties in the springs of the beams, γ = 0.2

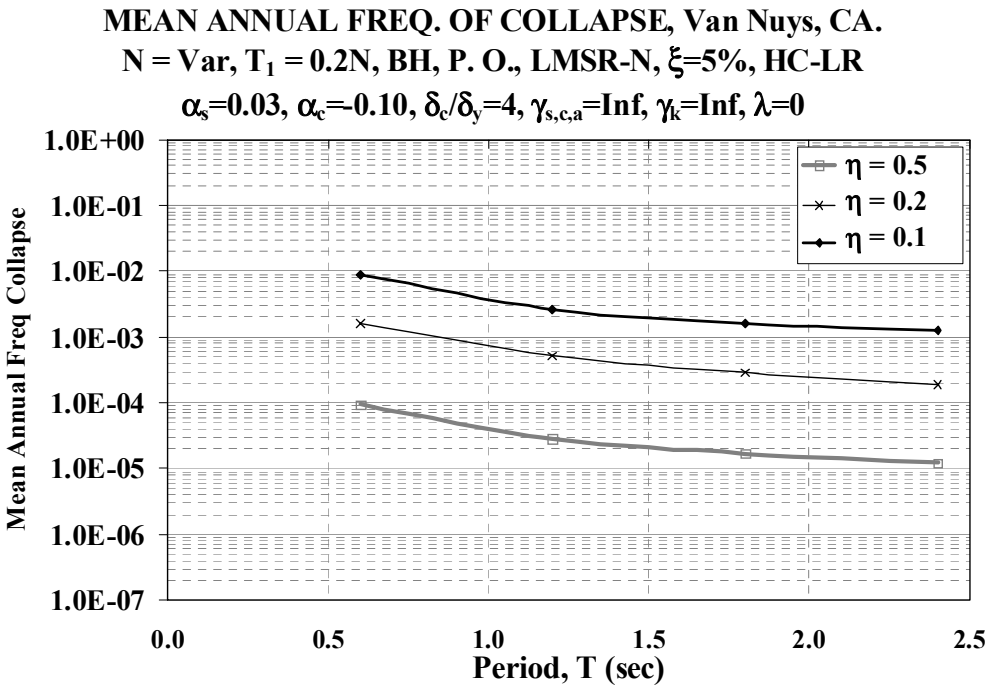

Fig. 7.21 Mean annual frequency of collapse for flexible generic frames, baseline hysteretic properties in the springs of the beams, different γ's

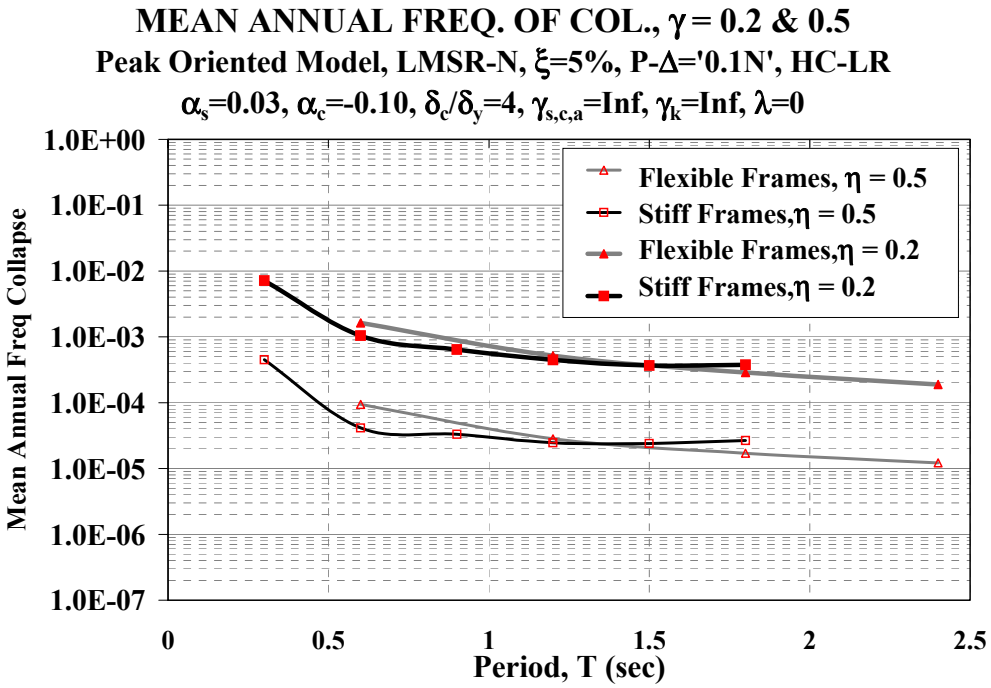

Fig. 7.22 Comparison of mean annual frequency of collapse for flexible and stiff frames, baseline hysteretic properties in the springs of the beams, different γ's

8 Summary and Conclusions

In earthquake engineering, "global collapse" refers to the inability of a structural system to sustain gravity loads under seismic excitation, and may have several causes. The propagation of an initial local failure (e.g., loss of axial force capacity in a column) may result in cascading or progressive collapse. Incremental collapse occurs if the displacement of an individual story, or a series of stories, is very large and P-Δ effects fully offset the deteriorated first-order story shear resistance. This report is concerned only with incremental or "side-sway" collapse, which is triggered by deterioration in strength or stiffness of the lateral load-resisting system and is accelerated by P-Δ effects.

Recently, deteriorating systems have been used to estimate collapse. For instance, Lee and Foutch (2001) and Jalayer (2003) employed the incremental dynamic analysis (IDA) concept (Vamvatsikos, 2002) for estimating the global dynamic stability capacity of steel and RC frames, respectively. Although they utilized deteriorating models, a "displacement-based" approach was used for evaluating collapse, i.e., failure was assessed based on engineering demand parameter (EDP) demands, which become very sensitive to small perturbations when the system is close to collapse. Other studies have focused on collapse predictions that either ignore material deterioration or use a cumulative damage index to simulate material deterioration while predicting response by using non-deteriorating systems.

This report proposes a methodology for evaluating global collapse based on deteriorating systems and a *relative intensity measure* instead of an EDP. The relative intensity is the ratio of ground motion intensity to a structural strength parameter. Usually, the ground motion intensity is defined as the 5%-damped spectral acceleration at the fundamental period of the system, whereas the structural strength parameter is the base shear strength of the system normalized by its seismic weight. The relative intensity is increased until the response of the system becomes

unstable, which means that the relative intensity – EDP curve becomes flat (zero slope). This relative intensity is referred to as "collapse capacity."

The main objectives of this study are to

- develop hysteretic models that incorporate all important phenomena contributing to global collapse,
- develop a consistent procedure for computation of the collapse capacity,
- obtain collapse capacities for representative SDOF systems and MDOF frame structures,
- identify the parameters that most influence collapse and to assess the sensitivity of collapse capacity to these parameters,
- quantify the dispersion of collapse capacity due not only to record to record variability but also to uncertainty in the structural parameters of the system,
- develop collapse fragility curves for SDOF and MDOF systems, and
- develop a methodology for computing the mean annual frequency of collapse.

Deteriorating Hysteretic Models

The results of this study depend strongly on the availability of hysteretic models to realistically represent the monotonic and cyclic behavior of structural components, including all important modes of strength and stiffness deterioration. A general but versatile hysteretic model is developed that can be adapted to bilinear, peak-oriented, and pinched hysteretic loops. The model considers capping and the associated deterioration of strength in the backbone curve and cyclic deterioration of strength and stiffness based on energy dissipation. The model has been calibrated with several experimental results of tests of structural steel, reinforced concrete, and wood components, obtaining good correlation in general. The backbone characteristics and the cyclic deterioration parameters are a function of the structural properties of the component. Thus, the calibrated parameters determined for a given specimen under a certain loading protocol can be used for different loading histories, provided that the salient features of the response are captured in the calibrated model.

Evaluation of Global Collapse

SDOF Parameter Study. In SDOF systems collapse occurs when the loading path is on the backbone curve (which may have deteriorated due to cyclic deterioration) and the restoring force approaches zero. Comprehensive parameter studies on SDOF systems are easily implemented and serve to identify the main collapse capacity trends for MDOF structures, as well as the system parameters that have dominant or negligible influence on the collapse capacity. It is observed that the variation of a particular parameter generally has a larger influence on SDOF systems than on MDOF structures, in which the elements yield at different times and some of them may never reach the inelastic range.

Assuming that the system response may be idealized by the hysteretic rules of representative component models, an extensive SDOF parameter study is carried out for assessing the effect of various system parameters on the collapse capacity. The study comprises systems for 20 periods of vibration ranging from T = 0.1–4 s. In most of the analyses, the systems are subjected to a set of 40 ordinary ground motions. In the primary parameter study, three or four values are considered for the parameters of most interest and analyses are performed for all possible combinations. The parameters to be evaluated are the post-capping stiffness ratio (α_c), the ductility capacity (δ_c/δ_y), cyclic deterioration (as a function of the parameter $\gamma_{s,c,k,a}$), P-Δ effect, and three different hysteretic models. In the secondary parameter study, representative systems are selected for investigating the effect on collapse capacity of the residual strength of the backbone curve, the individual cyclic deterioration modes, the level of pinching in pinched hysteretic models, the damping formulation of the system, and the effect of near-fault and long-duration ground motions records. The most relevant findings are the following:

- The effect of most of the aforementioned parameters on collapse capacity is dictated in great part by the relative value of all the other parameters.
- Prior to collapse, non-deteriorating models estimate EDPs with reasonable accuracy as long as the onset of strength deterioration in the backbone curve (cap displacement, δ_c) is not surpassed. Before this threshold is reached, cyclic deterioration is the only source of material deterioration and its effect on the EDPs is relatively small.

- Ductility capacity and post-capping stiffness are the two parameters that most influence the collapse capacity of a system. The effect of one of these two parameters is greatly affected by the relative value of the other parameter.
- Cyclic deterioration appears to be an important, but not dominant, issue for collapse evaluation.
- P-Δ effects must be included when SDOF systems are used as surrogates of MDOF structures. The elastic story stability coefficients of the MDOF systems may be a poor measure of the importance of P-Δ effects when equivalent SDOF systems are used to predict MDOF collapse capacities.
- In the medium- and long-period ranges (periods larger than about $T = 0.6$ s.), the largest collapse capacities correspond to pinching models, closely followed by those of peak-oriented models. Collapse capacities of bilinear models are the smallest because the presence of a negative stiffness has a larger effect on this model.
- The effect of a small residual strength (20% of maximum strength) on collapse capacity is practically negligible for all the studied systems. A residual strength of 40% may increase collapse capacity by a significant amount for non-ductile systems.
- When using pinching hysteretic models, the effect of the amount of pinching on collapse capacity is small, usually within the range of 10%.
- Collapse capacity for SDOF systems with mass proportional damping is larger (by about 20%) than that of systems with tangent stiffness proportional damping. This occurs because in the latter systems the damping force is reduced when the tangent stiffness is different from the elastic one.
- SDOF systems have been subjected to three sets of ground motions that dissipate hysteretic energy in different ways. Under near-fault ground motions, a large part of the hysteretic energy is released in one or two large pulses; under long-duration ground motions, the hysteretic energy is dissipated in a large number of inelastic excursions. For ordinary ground motions, the dissipated energy is in between these two cases. Nonetheless, the effect of cyclic deterioration on collapse capacity is not greatly affected by the set of ground motions used in the analysis.

MDOF Systems. In MDOF systems incremental collapse is associated with a mechanism in which P-Δ effects become equal to the deteriorated first-order story shear resistance provided by the structural elements. Collapse may occur in a single story or in a series of stories. An evaluation of the time history response data shows that for the generic frames used in this study, collapse usually occurs in the lower stories (mostly the first one) of the structure. The use of deteriorating models permits simulation of the response until collapse occurs. It also permits redistribution of moments to less damaged components and takes into account the ability of the system to sustain significantly larger deformations than those associated with reaching the ductility "capacity" of one component.

The MDOF systems used in this study are two-dimensional regular single-bay frames of 3, 6, 9, 12, 15, and 18 stories. The fundamental period of the frames is associated with the number of stories (N). "Stiff frames" have a fundamental period $T_1 = 0.1N$, whereas "flexible frames" have $T_1 = 0.2N$. The frames are designed in such a way that the first mode is a straight line and simultaneous yielding is attained in all stories when subjected to a parabolic load pattern. Unless otherwise specified, frames are designed according to the strong column – weak beam concept, i.e., columns are infinitely strong. Thus, a beam-hinge mechanism is developed, i.e., plastic hinges are confined to the beam ends and the base of the first-story columns. Global P-Δ effects are modeled in all cases. The frames are subjected to a set of 40 ordinary ground motions.

To obtain a consistent evaluation of collapse capacity, it is assumed that every plastic hinge of the generic frames has the same deteriorating hysteretic model. The effects of the following parameters on the collapse capacity are evaluated: post-capping stiffness ratio, ductility capacity, the rate of cyclic deterioration, and the type of hysteretic model. The main findings are summarized below:

- The collapse capacity, defined as the ratio of the spectral acceleration at the fundamental period of the structure [$S_a(T_1)$] divided by the base shear coefficient ($\gamma = V_y/W$) at collapse, strongly depends on the first-mode period (T_1). The large decrease in collapse capacity for long-period structures indicates that the period-independent R-factor concept is not appropriate because of the large importance of P-Δ effects in the inelastic range.
- As in SDOF systems, the post-capping stiffness and the ductility capacity of the rotational springs are the two deterioration parameters that most influence the collapse

capacity of MDOF systems. Due to moment redistribution in MDOF systems, entering the branch of negative slope in certain of the springs does not produce immediate collapse, even when this negative slope is very steep.

- The collapse capacity of deteriorating frames is very similar when a pinching model is used for the plastic hinge springs at the beam ends instead of a peak-oriented model. When a bilinear model is used for the plastic-hinge springs, similar patterns to those observed for collapse capacity of SDOF systems are detected. For MDOF systems with very short first period, the collapse capacity of frames with bilinear springs is larger than that of frames with peak-oriented or pinching springs. However, for frames with medium and long first periods the trend reverses because the branch with negative slope in the plastic hinge springs has a larger "ratcheting" effect in bilinear models, i.e., the story drifts increase more rapidly.
- Present code guidelines for strong column–weak beam designs do not prevent the development of plastic hinges in the columns. The column moment demands will exceed the strength capacity given by this requirement at small relative intensities.
- Column hinging, which changes the mechanism leading to collapse, has a very detrimental effect on collapse capacity. The collapse capacity of generic frames with a strong column factor of 1.2 decreases dramatically (in most cases by a factor smaller than 0.5) compared to that of generic frames with infinitely strong columns. If the strong-column factor is 2.4, the collapse capacity decreases by about 25% or less.
- P-Δ effects can cause collapse of non-deteriorating flexible long-period structures, and greatly accelerate the collapse of deteriorating structures. Disregard of P-Δ effects may overestimate the collapse capacity of the generic frames by a factor of two or larger. This overestimation is particularly large for flexible long-period frames in which the P-Δ effects are larger than the effects of material deterioration.
- For tall and slender frames, the global inelastic stability coefficient (defined by the difference in the post-yield slopes of the global pushover curves without and with P-Δ) may be much larger than the elastic coefficient. Thus, P-Δ effects may be more important that estimated from an elastic stability coefficient.
- Equivalent SDOF systems can be used for computing the collapse capacity of MDOF structures with large P-Δ effects, but they must take into account that the elastic and

inelastic stability coefficients may differ significantly. If this occurs, the global inelastic stability coefficient may be incorporated into the equivalent SDOF system by means of an auxiliary backbone curve. The estimate of the MDOF collapse capacity obtained from the equivalent SDOF system is found to be relatively accurate, yet conservative (i.e., the actual collapse capacity is underestimated).

Effect of Uncertainty in the System Parameters on Variance of Collapse Capacity

Dispersion in collapse capacity comes from record-to-record (RTR) variability and from uncertainty in the system parameters. The variance due to RTR variability is large and is explicitly considered in the time history results presented in chapters 4 and 5. The first-order second-moment (FOSM) method is employed to estimate the additional variance of collapse capacity due to uncertainty in the system parameters. The most salient findings are the following:

- Uncertainty in post-capping stiffness and ductility capacity produce the largest additional contributions to the variance of collapse capacity. The former one is more relevant for systems with small P-Δ effects and/or systems with peak-oriented or pinching models. Ductility capacity is more important when P-Δ effects are large and when a bilinear model is used.
- The presence of large P-Δ effects (i.e., in flexible long-period structures) drastically reduces the contribution of uncertainty in the system parameters to the variance of collapse capacity. In absolute terms, the variance of collapse capacity due to RTR variability experiences a small reduction due to the presence of P-Δ effects, whereas the variance of collapse capacity due to uncertainty in the systems parameters can have a large decrease when P-Δ effects are included.
- Sensitivity studies on SDOF systems are useful to detect important trends in the computation of the variance of collapse capacity due to uncertainty in the system parameters for regular MDOF structures.
- If high correlation is considered among parameters such as the ductility capacity and post-capping stiffness in each hinge (coefficient of correlation larger than about 0.8), the contribution to variance of collapse capacity due to correlation among parameters may be the most important contribution from uncertainty in the system parameters.

The use of the FOSM method for estimating the contributions of uncertainty in system parameters to the variance of the collapse capacity is an approximation. This approximation should be acceptable considering how little is known at this time about the uncertainty of the system parameters (type of distribution and the value of the measure of dispersion). Moreover, it is usually assumed that the main contributor to total uncertainty is the RTR variability, at least when the evaluation is based on EDPs. However, the contribution of system parameter variability to the variance of the collapse capacity may be comparable to that of the RTR variability if large, but not unrealistic, values for the measure of dispersion of the important system parameters are used. In this study, the standard deviation of the log of the probabilistic parameters is assumed as 0.60.

Mean Annual Frequency of Collapse

In the context of performance-based earthquake engineering, one performance objective is to provide "adequate" protection against collapse. A suitable measure for assessing collapse safety is the mean annual frequency (MAF) of collapse, which is obtained by combining a collapse fragility curve with the seismic hazard curve for a given site. In this context, the following observations and conclusions are made:

- Collapse fragility curves, which express the probability of collapse in terms of a relevant ground motion intensity measure ($S_a(T_1)$ is used for this purpose), are developed directly from the collapse capacity of the system computed from nonlinear time history analysis using an appropriate set of ground motions. They incorporate the effect of RTR variability but may also incorporate the effect of variability in the system parameters.
- The evaluation of global collapse based on the relative intensity of the system facilitates the computation of the MAF of collapse, which is obtained by integrating the collapse fragility curve for a given base shear strength over a spectral acceleration hazard curve pertaining to a specific site. On the other hand, the "EDP-based approach" decomposes the collapse limit state into two steps and requires an additional integration.
- For a structural system of given hysteretic properties, the base shear strength is a dominant factor in the magnitude of the MAF of collapse. Variations in the base shear strength from η = 0.5–0.1 (for SDOF systems) may produce a change in the MAF of collapse of more than two orders of magnitude. Variations in the ductility capacity of the

system from δ_c/δ_y = 2 to 6 may modify the MAF of collapse by more than one order of magnitude. It must be reminded that these conclusions are sensitive to the hazard curve slope (Jalayer, 2003). For California sites, as the one used in this work, the hazard curve slope usually is steep. Thus, the sensitivity would be less if the hazard curves corresponded to central and eastern U.S. sites.

- Uncertainty in the system parameters may increase the MAF of collapse by 50–100% (assuming the dispersions in the parameters as discussed in Chapter 6), as compared with the cases in which RTR variability is the only source of uncertainty.

Concluding Remarks

This study is a small step toward a comprehensive quantification of the limit states of global or partial collapse in earthquakes. There are various collapse modes, and only one is explicitly covered by the methodology explored in this study. Moreover, the conclusions drawn from this study are limited by the scope and assumptions made throughout this work.

An important contribution of this work is the development of a transparent methodology for the evaluation of incremental collapse, in which the assessment of collapse is closely related with the physical phenomena that lead to this limit state. That is to say, the methodology addresses the fact that collapse is caused by deterioration in complex assemblies of components that should be modeled explicitly.

In previous studies on collapse, damage indices or judgmental limits on engineering demand parameters are used as indirect ways for estimating attainment of this limit state. In the collapse methodology proposed in this work there are no indirect criteria. However, great uncertainty in collapse capacity still exists because of RTR variability and limited knowledge of the parameters of the deteriorating systems. More comprehensive experimental results will permit a better estimation of the uncertainty of the system parameters, and better intensity measures should reduce RTR variability. At that point, the proposed methodology should lead to a more precise evaluation of global collapse.

Suggestions for Future Work

Areas for future research on the evaluation of collapse potential of structures in earthquakes include the following:

- Improvement of the analytical tools to include all the deterioration effects and to model P-M-V interaction and local failure modes such as loss of gravity load resistance at beam-to-column and slab-to-column connections;
- Consistent experimental results for obtaining the distribution and first and second moments of the system parameters;
- More extensive calibration of the deteriorating hysteretic model with component test results
- Comparison of the MAF of collapse obtained with the proposed methodology with that obtained when computing collapse based on an "EDP-based approach";
- Application of the methodology to existing structures; and
- Assessment of other collapse modes, in particular propagation of local collapse, i.e., progressive collapse.

References

ACI Committee 318-02 (2002), "Building code requirements for structural concrete (ACI 318-02) and commentary (ACI 318R-02), "*American Concrete Institute*, Farmington Hills, MI.

Abrahamson, N. A. and Silva, W. J. (1997), "Empirical response spectral attenuation relations for shallow crustal earthquakes," *Seismological Research Letters*, 68, 1, pages 94-127.

Adam, C., and Krawinkler, H. (2003), "Large deflections of elastic-plastic frames exposed to pulse-type ground motion," *Proceedings of the Response of Structures to Extreme Loading*, Elsevier Science, Toronto, Canada, Aug. 3-6, 2003

Alavi, B. and Krawinkler, H. (2001), "Effects of near-fault ground motions on frame structures," *John A. Blume Earthquake Engineering Research Center*, Report No. 138, Department of Civil Engineering, Stanford University.

Arias, A. (1970), "A measure of earthquake intensity," *Seismic Design for Nuclear Power Plants*, R. J. Hansen Ed., MIT Press, pages 438-483

Aschheim, M. and Moehle, J. P. (1992), "Shear strength and deformability of RC bridge columns subjected to inelastic cyclic displacements," UCB/EERC-92/04, Berkeley: *Earthquake Engineering Research Center*, University of California

ATC-40, Applied Technology Council (1996), "Seismic evaluation and retrofit of concrete buildings," Report No. SSC 96-01, *Seismic Safety Commission*, Redwood City, California

Aydinoglu, M. N. (2001), "Inelastic seismic response analysis based on story pushover curves including P-Delta effects," Report No. 2001/1, *KOERI, Department of Earthquake Engineering*, Bogazici University, Istanbul, Turkey

Aydinoglu, M. N. and Fahjan, Y.M. (2002), "A unified formulation of the piecewise exact method for inelastic seismic demand analysis including P-Delta effect," Report No. 2002/3, *KOERI, Department of Earthquake Engineering*, Bogazici University, Istanbul, Turkey

Baker, J.W., and Cornell, C.A. (2003), "Uncertainty specification and propagation for loss estimation using FOSM methods," *PEER Technical Report* #2003-07.

Benjamin, J. R. and Cornell, C. A. (1970), *"Probability, statistics, and decision for civil engineers*," McGraw Hill, Inc. New York

Bernal, D. (1987), "Amplification factors for inelastic dynamic P-Delta effects in earthquake analysis," *Earthquake Engineering & Structural Dynamics*, 15, 5, July 1987, pages 635-651

Bernal, D. (1992), "Instability of buildings subjected to earthquakes," *Journal of Structural Engineering*, 118, 8, Aug. 1992, pages 2239-2260

Bernal, D. (1994), "Viscous damping in inelastic structural response," *Journal of Structural Engineering*, Vol. 120, No. 4, April 1994, pp. 1240-1254

Bernal, D. (1998), "Instability of buildings during seismic response," *Engineering Structures*, 20, 4-6, Apr.-June 1998, pages 496-502

Bommer, J. and Martinez-Pereira, A. (1996), "The prediction of strong-motion duration for engineering design," *Proceeding of the Eleventh WCEE*, Paper No. 84, Acapulco, Mexico

Chopra, A.K. (1995), *"Dynamics of structures: theory and applications to earthquake engineering*," Prentice Hall, Englewood Cliffs, NJ, 1995, 729 pages

Clough, R. W. and Penzien, J. (1993), *"Dynamics of structures*," McGraw Hill, Inc., New York, 1993, 738 pages, 2nd edition

Cordova, P., et. al.(2000), "Development of a two-parameter seismic intensity measure and probabilistic assessment procedure," PEER-2000/10, The Second U.S.-Japan Workshop on Performance-Based Earthquake Engineering Methodology for Reinforced Concrete Building Structures, 11-13 September, Japan, Berkeley: *Pacific Earthquake Engineering Research Center*, University of California, Mar. 2000, pages 195-214

Cornell, C. A. et. al. (2002), "Probabilistic basis for 2000 SAC Federal Emergency Management Agency Steel Moment Frame Guidelines," *Journal of Structural Engineering*, 128, 4, Apr. 2002, pages 526-534.

C.K. Sun, G. V. Berg and R.D. Hanson (1973), "Gravity effect on single-degree inelastic systems," *Journal of the Engineering Mechanics Division, ASCE,* 99, Feb. 1973, pages 183-200

D'Ambrisi, A and Filippou, F. (1999), "Modeling of cyclic shear behavior in RC members," *Journal of Structural Engineering,* 125, 10, Oct. 1999, pages 1143-1150

DRAIN-2DX (1993), "DRAIN-2DX: Basic program description and user guide," Report No. *UCB/SEMM-1993/17*, by Prakash, V., Powell, G. H., and Campbell, S., University of California, Berkeley, CA, Nov. 1993, 97 pages

Ellingwood, B. (1993), "Probabilistic codified design," Lecture notes presented at *Structural Reliability: Theory and Applications*, University of California at Berkeley, March 24, 1983

Elwood, K. J. (2002), "Shake table tests and analytical studies on the gravity load collapse of reinforced concrete frames," *Ph.D. Dissertation*, Department of Civil and Environmental Engineering, University of California, Berkeley.

Esteva, L. and Ruiz, S. (1989), "Seismic failure rates of multistory frames," *Journal of Structural Engineering,* 115, 2, Feb. 1989, pages 268-284

Fajfar, P., Vidic, T. and Fischinger, M. (1993), "Influence of damping model on the seismic response of nonlinear SDOF systems," *Structural Dynamics, EURODYN '93*, Balkema, Rotterdam

Fajfar, P. (2000), "A nonlinear analysis method for performance-based seismic design,"
Earthquake Spectra, 16, 3, Aug. 2000, pages 573-592

Fardis, M.N. and Biskinis, D.E. (2003), "Deformation capacity of RC members, as controlled by flexure or shear," *Proceeding of the Symposium in Honor of Professor Otani*, Japan, 2003.

FEMA 350 (2000), "Recommended seismic design criteria for new steel moment-frame buildings," *SAC Joint Venture*, September 2000

FEMA 355C (2000), "State of the art report on systems performance of steel moment frames subject to earthquake ground shaking," *SAC Joint Venture*, September 2000

FEMA 356 (2000), "Prestandard and commentary for the seismic rehabilitation of buildings," *Federal Emergency Management Agency*, Washington D.C.

FEMA 368 (2000), NEHRP recommended provisions for seismic regulations for new buildings and other structures, *Building Seismic Safety Council*, Washington D.C.

Foutch, D.A. and Shi, S. (1996), "Effect of hysteresis type on the seismic response of buildings," Proceedings of the *Sixth U.S. National Conference on Earthquake Engineering*, EERI, Oakland, California, 1998, 12 pages

Gatto, K. S. and Uang, C. M. (2002), "Effects of loading protocol and rate of loading on woodframe shearwall response," Seventh U.S. National Conference on Earthquake Engineering, EERI , Oakland, California, 2002, 10 pages

Gupta, A. and Krawinkler, H. (1999), "Seismic demands for performance evaluation of steel moment resisting frame structures," *John A. Blume Earthquake Engineering Research Center* Report No. 132, Department of Civil Engineering, Stanford University.

Gupta, B. and Kunnath, S. K. (1998), "Effect of hysteretic model parameters on inelastic seismic demands," Proceedings of the *Sixth U.S. National Conference on Earthquake Engineering*, EERI, Oakland, California, 1998, 12 pages

Hadidi, H. (1983), "Seismic response of SDOF systems including P-Delta effect and stiffness degradation," *Thesis for the Degree of Engineer*, August 1983.

Hornbeck, R. W. (1975), *"Numerical methods,"* Quantum Publishers, Inc., N.Y., pages 16-23.

Ibarra, L., Medina, R., Krawinkler, H. (2002), "Collapse assessment of deteriorating SDOF systems," *Proceedings of the 12th European Conference on Earthquake Engineering*, London, UK, Paper 665, Elsevier Science Ltd., September 9-13, 2002

Inoue, K., Asari, T. and Ishiyama, Y. (2000), "Lateral stiffness-strength distribution and damage concentration along the height of a building," *Proceedings of the 12th WCEE,* Upper Hutt, New Zealand, 2000, Paper No. 1764

Jalayer, F. (2003), "Direct probabilistic seismic analysis: implementing nonlinear dynamic assessments," *PhD. Dissertation* submitted to the Department of Civil Engineering, Stanford University

Jennings, P. and Husid, R. (1968), "Collapse of yielding structures during earthquakes," *Journal of the Engineering Mechanics Division, ASCE,* 94, EM5, pages 1045-1065,Oct. 1968

Kaewkulchai, G. and Willamson, E.B. (2003), "Progressive collapse behavior of planar frame structures," *Proceedings of the Response of Structures to Extreme Loading Conference*, Toronto, Canada, 2003

Kanvinde, A. M. (2003), "Methods to evaluate the dynamic stability of structures-shake table tests and nonlinear dynamic analyses," EERI Paper Competition 2003 Winner, *Proceedings of EERI Meeting*, Portland, Feb. 2003

Krawinkler, H., Parisi, F., Ibarra, L., Ayoub, A. and Medina, R. (2000), "Development of a testing protocol for woodframe structures," *CUREE Publication* No. W-02, 2000.

Krawinkler, H. and Seneviratna, G. D. P. K. (1998). "Pros and cons of a pushover analysis for seismic performance evaluation," *Journal of Engineering Structures*, 20, 4-6, Apr.-June 1998, pages 452-464.

Krawinkler, H., Zareian, F., Ibarra, L., Medina, R. and Lee, S. (2003), "Seismic demands for single– and multi-story wood buildings," *CUREE Publication* No. W-26, 2003.

Krawinkler, H., and Zohrei, M. (1983), "Cumulative damage in steel structures subjected to earthquake ground motions," *Journal on Computers and Structures,* 16, 1-4, 1983, pages 531-541

Kunnath, S. K., El-Bahy, A., Taylor, A. and Stone, W. (1997), "Cumulative Seismic Damage of Reinforced Concrete Bridge Piers," *Technical Report NCEER-97-006*, Sep. 1997

Kunnath, S. K., Reinhorn, A.M., Park, Y.J. (1990), "Analytical modeling of inelastic response of R/C structures," *Journal of Structural Engineering*, 116, 4, Apr. 1990, pages 996-1027

Kunnath, S. K., Reinhorn, A. M. and Abel, K. F. (1991), "A computational tool for evaluation of seismic performance of reinforced concrete buildings," *Computers and Structures*, 41, 1, 1991, pages 157-173

Kunnath, S. K., Mander, J.B. and Lee, F. (1997), "Parameter identification for degrading and pinched hysteretic structural concrete systems," *Engineering Structures*, 19, 3, pages 224-232.

Lawson, R. S., Vance, V. and Krawinkler, H. (1994), "Nonlinear static push-over analysis—why, when, and how?" *Proceedings of the 5th U.S. Conference in Earthquake Engineering*, Vol. 1, Chicago, IL.

Lee, K. and Foutch, D. A. (2001), "Performance evaluation of new steel frame buildings for seismic loads," *Earthquake Engineering and Structural Dynamics*, 31, pages 653-670

Liu, Y., Xu, L. and Grierson, D. E. (2003), "Performance of buildings under abnormal loading," *Proceedings of the Response of Structures to Extreme Loading Conference*, Toronto, Canada, 2003

Luco, N. (2002), "Probabilistic seismic demand analysis SMRF connection fractures and near-source effects," *PhD. Dissertation* submitted to the Department of Civil Engineering, Stanford University

Lynn, A., Moehle, J., Mahin, S. and Holmes, W. (1996), "Seismic evaluation of existing concrete building columns," *Earthquake Spectra*, Vol. 12, pages 715-739

MacRae, G. A., (1994), "P-Δ effects on single-degree-of-freedom structures in earthquakes," *Earthquake Spectra*, 10, 3, Aug. 1994, pages 539-568

Medina, R. (2002), "Seismic demands for nondeteriorating frame structures and their dependence on ground motions," *PhD. Dissertation* submitted to the Department of Civil Engineering, Stanford University

Mehanny, S.S.F. and Deierlein, G.G. (2000), "Modeling of assessment of seismic performance of composite frames with reinforced concrete columns and steel beams," *John A. Blume Earthquake Engineering Research Center* Report No. 135, Department of Civil Engineering, Stanford University

Melchers, R. E. (1999), *"Structural Reliability Analysis and Prediction*," John Wiley and Sons, Chichester

Miranda, E. (1993), "Evaluation for site-dependent inelastic seismic design spectra," Journal of Structural Engineering, 119, 5, pages 1319-1338

Miranda, E. and Bertero, V. (1994), "Evaluation of strength reduction factors for earthquake-resistant design," Earthquake Spectra, 10, 2, May 1994, pages 357-379

Miranda, E. (1998), "Simplified method to estimate maximum seismic interstory drift demands in multi-story buildings," *Proceedings, Sixth U.S. National Conference on Earthquake Engineering*, EERI, Oakland, California, 1998, 11 pages

Miranda, E. (1999), "Approximate seismic lateral deformation demands in multistory buildings," *Journal of Structural Engineering*, 125, 4, Apr. 1999, pages 417-425

Miranda, E. (2000), "Inelastic displacement ratios for structures on firm sites," *Journal of Structural Engineering*, 126, 10, pages 1150-1159

Miranda, E., Sinan, D.A. (2003), "Dynamic instability of simple structural systems," *Journal of Structural Engineering*, 129, 12, 2003

Mirza, S. and McGregor, J. (1979), "Variation in dimensions of reinforced concrete members," *Journal of Structural Engineering*, 105, ST4, Apr. 1979, pages 751-766

Nakamura, T., and Yoshimura, M. (2002), "Gravity load collapse of reinforced concrete columns with brittle failure modes," *Journal of Asian Architecture and Building Engineering*, 1, 1, pp. 21-27

Nakashima, M. (1994) "Variation of ductility capacity of steel beam-columns," *Journal of Structural Engineering*, 120, 7, July 1994, pages 1941-1960

Nakashima, M. and Sawaizumi, S. (2000), "Column-to-beam strength ratio required for ensuring beam-collapse mechanisms in earthquake responses of steel moment frames," *Proceedings of the 12 th WCEE,* Upper Hutt, New Zealand, 2000, Paper No. 1109

Nassar, A. and Krawinkler, H. (1991), "Seismic demands for SDOF and MDOF systems," *John A. Blume Earthquake Engineering Research Center Report* No. 90, Department of Civil Engineering, Stanford University.

OpenSees (2002), Open System For Earthquake Engineering Simulation, *Pacific Earthquake Engineering Research Center*, http://peer.berkeley.edu/

Otani, S. (1974), "Inelastic analysis of R/C frame structures," *Journal of Structural Division, ASCE*, 100, ST7, July 1974, pages 1433-1449

Panagiotakos, T. B. and Farids, M. N. (2001), "Deformations of reinforced concrete members at yielding and ultimate," *ACI Structural Journal*, 98, 2, March-April 2001

Park, Y. and Ang, A. (1985), "Mechanistic seismic damage model for reinforced concrete," *Journal of Structural Engineering*, 111, 4, Apr. 1985, pages 722-739

Paulay, T. and Priestly, M. J. N., (1992) *"Seismic design of reinforced concrete and masonry buildings*," John Wiley & Sons, Inc., 1992, 744 pages

Pincheira, J. A. and Dotiwala, F. S. (1996), "Modeling of nonductile RC columns subjected to earthquake loading," *Proceeding of the Eleventh WCEE*, Paper No. 315, Acapulco, Mexico

Pincheira, J. A., Dotiwala, F. S. and D'Souza, J. T. (1999), "Seismic analysis of older reinforced concrete columns," *Earthquake Spectra,* 15, 2, May 1999, pages 245-272

Rahnama, M. and Krawinkler, H. (1993), "Effect of soft soils and hysteresis models on seismic design spectra," *John A. Blume Earthquake Engineering Research Center* Report No. 108, Department of Civil Engineering, Stanford University.

SAC System Performance: Development of Earthquake Ground Motions, "Suites of earthquake ground motions for analysis of steel moment frame structures, Task 5.4.1." http://nisee.berkeley.edu/data/strong_motion/sacsteel/ground_motions.html

Santa-Ana, P. R. and Miranda, E. (2000), "Strength reduction factors for multi-degree-of-freedom systems," *Proceeding of the 12th WCEE*, Upper Hutt, New Zealand, 2000, Paper No. 1446

Seneviratna, G.D.P.K., and Krawinkler, H. (1997), "Evaluation of inelastic MDOF effects for seismic design," *John A. Blume Earthquake Engineering Center Report No. 120*, Department of Civil Engineering, Stanford University.

Sezen, H. (2000), "Evaluation and testing of existing reinforced concrete building columns," *CE299 Report*, University of California, Berkeley.

Shome, N. and Cornell A. (1999), "Probabilistic seismic demand analysis of nonlinear structures," *Report No. RMS-35*, Dept. of Civil Engineering, Stanford University.

Shi, S. (1997), "Connection element (type 10) for Drain-2DX," *PhD Thesis* submitted to the Department of Civil and Environmental Engineering, University of Illinois at Urbana-Champaign.

Sivaselvan, M.V., Reinhorn, A.M. (2000), "Hysteretic models for deteriorating inelastic structures." *Journal of Engineering Mechanics,* 126(6), pages 633-640

Somerville, P. and Collins, N. (2002), "Ground motion time histories for the Van Nuys building," *PEER Methodology Testbeds Project,* URS Corporation, Pasadena, CA. March 7, 2002.

Somerville, P., Smith, N., Punyamurthula, S., and Sun, J. (1997a), "Development of ground motion time histories for phase 2 of the FEMA/SAC steel project," *SAC Background Document, Report No. SAC/BD-97/04*.

Somerville, P., Smith, N., Graves, R. and Abrahamson, N. (1997b). "Modification of empirical strong ground motion attenuation relations to include the amplitude and duration effects of rupture directivity," *Seismological Research Letters,* 68, 1, pages 180-203.

Song, J. and Pincheira , J. (2000), "Spectral displacement demands of stiffness and strength degrading systems," *Earthquake Spectra,* 16, 4, Nov. 2000, pages 817-851.

Sun, C. K., Berg, G. V. and Hanson, R. D. (1973), "Gravity effect on single-degree inelastic systems," *Journal of Engineering Mechanics, ASCE,* 99, 1, pages 183-200

Takeda, T., Sozen, M., Nielsen, N. (1970), "Reinforced concrete response to simulated earthquakes," *Journal of the Structural Division,* 96, ST12, Dec.1970, pages 2557-2573

Takizawa, H. and Jennings, P. (1980), "Collapse of a model for ductile reinforced concrete frames under extreme earthquake motions," *Earthquake Engineering and Structural Dynamics,* 8, 1980, pages 117-144

Trifunac, M. D. and Brady, A. G. (1975), "A study of the duration of strong earthquake ground motion," *Bulletin of the Seismological Society of America*, Vol. 65, pages 581-626.

Uang, C. M., Yu, Q. S. and Gilton, C. S. (2000), "Effects of loading history on cyclic performance of steel RBS moment connections," Proceedings of the 12th WCEE, Upper Hutt, New Zealand, 2000, paper No. 1294,

UBC (1997), "Uniform Building Code," *International Conference on Building Officials*, Whittier, CA.

Vamvatsikos, D. and Cornell, C. A. (2002), "Incremental Dynamic Analysis," *Earthquake Engineering and Structural Dynamics*, 31, 3, Mar. 2002, pages 491-514.

Vamvatsikos, D. (2002), “Seismic performance, capacity and reliability of structures as seen through Incremental Dynamic Analysis,” *PhD. Dissertation* submitted to the Department of Civil Engineering, Stanford University

Vian, D. and Bruneau, M. (2001), “Experimental investigation of P-Delta effects to collapse during earthquakes,” *Technical Report MCEER-01-0001,* June 2001

Wen, Y. K. (1976), “Method for random vibration of hysteretic systems,” *Journal of Engineering Mechanics Division, ASCE,* 102, 2, pages 249-263

Williams, M. and Sexsmith, R. (1995), “Seismic damage indices for concrete structures: a state-of-the-art review,” *Earthquake Spectra,* 11, 2, May 1995, pages 319-348

Williamson, E.B. (2003), “Evaluation of damage and P-D effects for systems under earthquake excitation,” *Journal of Structural Engineering,* 129, 8, pages 1036-1046

Wolff, T. F. (1994), "Evaluating the reliability of existing levees," prepared for *U.S. Army Engineer Waterways Experiment Station,* Geotechnical Laboratory, Vicksburg, MS, Sep. 1994

Yoshimura, M. and Yamanaka, N. (2000), “Ultimate limit state of RC columns,” PEER-2000/10, The Second U.S.-Japan Workshop on Performance-Based Earthquake Engineering Methodology for Reinforced Concrete Building Structures, 11-13 September, Japan, Berkeley: *Pacific Earthquake Engineering Research Center*, University of California, Mar. 2000, pages 313-326

Yun, S-Y, Hamburger, R. O., Cornell, A. C., Foutch, D. A. (2002), “Seismic performance evaluation for steel moment frames,” *Journal of Structural Engineering,* 128, 4, Apr. 2002

Appendix A: "Counted" and "Computed" Statistical Values

In this investigation, central values and measures of dispersion are provided by "computed" or "counted" statistics according to the characteristics of the data. This appendix describes both procedures.

A.1 "COMPUTED" STATISTICAL VALUES

The median is considered the central value of interest and its best estimator is the "geometric mean," $\hat{x}$ [25]:

$$\hat{x} = \exp\left[\frac{\sum_{i=1}^{n} \ln x_i}{n}\right] \tag{A.1}$$

As a measure of dispersion, the standard deviation of the natural log of the data is computed by:

$$\sigma_{\ln x} = \sqrt{\sum_{i=1}^{n} \frac{(\ln x_i - \mu_{\ln x})^2}{n-1}} \tag{A.2}$$

where $\mu_{\ln x} = \frac{1}{n}\sum_{i=1}^{n} \ln x_i$.

$\sigma_{\ln x}$ is numerically approximately equal to the coefficient of variation ($c.o.v._x = \sigma_x / \mu_x$), at least for comparably small values, e.g., values smaller or equal than about 0.3.

[25] In Appendix C is shown that collapse capacity distribution may be approximated with a lognormal distribution. Under lognormality assumptions the geometric mean is a logical estimator of the median (Benjamin and Cornell, 1970).

An advantage of computed statistical values arises when the need exists to compare results from two sets of data. In this case, it is desirable to compute the median of the ratios of the data:

$$\hat{m}_{x/y} = \exp(m_{\ln x/y}) \tag{A.3}$$

where $m_{\ln x/y}$ is the mean of the log of the ratios of the data. The problem with this equation is that when the two sets of data are processed independently, the individual ratios, x/y, are not readily available. However, Equation A.3 can be manipulated in the following way to overcome this problem:

$$\hat{m}_{x/y} = \exp(m_{\ln x/y}) = \exp\left(\sum_{i=1}^{n} \frac{\ln(x/y)}{n}\right) = \exp\left(\sum_{i=1}^{n} \frac{\ln(x)}{n} - \sum_{i=1}^{n} \frac{\ln(y)}{n}\right) \tag{A.4}$$

$$\hat{m}_{x/y} = \exp(m_{\ln x} - m_{\ln y}) = \frac{\exp(m_{\ln x})}{\exp(m_{\ln y})} \Rightarrow \hat{m}_{x/y} = \frac{\hat{m}_x}{\hat{m}_y} \tag{A.5}$$

The last identity states that the estimator of the median of the ratios is equal to the ratio of the estimator of the medians. This adds flexibility to the procedure because statistics can be carried out independently for both systems and the computed medians can be compared a posteriori.

A.2 "COUNTED" STATISTICAL VALUES

In this alternative the median and different percentiles are directly obtained from the sorted data. For instance, for a set of 40 data points, the counted median is the average of the 20th and 21th sorted values; the 16th percentile is approximated with the 6th sorted value and the 84th percentile with the 34th sorted value.

The standard deviation of the natural log of the values may be estimated by using either the median and 16th; the median and 84th percentile, or the 16th and 84th percentiles:

$$\sigma_{\ln x} = \ln\left(\frac{x_{84}}{\hat{x}}\right) \ , \ \sigma_{\ln x} = \ln\left(\frac{\hat{x}}{x_{16}}\right) \text{ or } \sigma_{\ln x} = \ln\left(\frac{x_{84}}{x_{16}}\right)/2 \tag{A.6}$$

The value of $\sigma_{\ln x}$ varies according to the percentiles used for its computation. For calculating the dispersion of EDPs the median and 84th percentile are used. Counted statistics does not fit to any theoretical distribution, such as Gaussian or lognormal, but the obtained median and percentiles are associated with the real distribution of the data. Counted statistics is

very useful when data points are missing, i.e., when EDPs are undefined because collapse has taken place. If counted statistics is used, there is no need to stop a statistical evaluation when the first data are missing and the process can be continued until more than 50% of the individual data are lost.

Appendix B: Properties of Generic Frame Models

B.1 MODAL AND STRUCTURAL PROPERTIES OF THE GENERIC FRAMES

The main characteristics of the generic deteriorating frames used in this study are presented in Section 5.3. These frames are based on the non-deteriorating frames developed by Medina (2002) and have the same elastic modal and structural properties. As illustration, the modal properties for the 9-story frames are summarized in Table B.1. The table includes participation factors (PF_i), mass participation (MP_i), modal damping (ξ_i), and normalized mode shapes, ϕ_i.

Tables B.2 and B.3 present the following structural properties for the 9-story frames:

Stiffness properties (i denotes story or floor)

- Weight ratio, W_i/W (W = total weight)
- Moment of inertia ratio, I_i/I_1 (I is the same for columns and top beam in a story)
- Story stiffness ratio (load pattern independent), K_{ai}/K_{a1}. The story stiffness is defined as the story shear force required to produce a unit displacement of a subassembly consisting of a "story" (two columns and the beam above). The columns of the subassembly are fixed at the base and all three elements (two columns and beam) have the same moment of inertia.
- Floor stiffness ratio (load pattern independent), K_{fi}/K_{f2}. Floor stiffness is the story shear force required to produce a unit displacement of a subassembly consisting of a floor beam and half of the columns on top and below the floor level.
- Story stiffness ratio, K_{ki}/K_{k1}, based upon triangular load pattern and K_{si}/K_{s1}, based upon parabolic load pattern. Story stiffness is defined here as the load pattern dependent story shear force required to cause a unit story drift in that story.
- Beam stiffness ratio, K_{bi}/K_{b2}
- Spring stiffness at base, $K_c = 3EI / L$ of the second floor beam

Strength and deformation parameters for a structure designed with $\gamma = V_y / W = 1.0$ and a parabolic design load pattern without considering P-Δ effects.

- Story shear strength ratio, V_i/V_1
- Story overturning moment ratio, M_{OT}/M_{OT1} (overturning moment based on the axial loads and bending moments at the bottom of the columns in a story)
- Story strain-hardening ratio from pushover analysis, α_{si}
- Floor beam strength ratio, M_{ybi}/M_{yb2}
- Column strength at base, M_{yc}
- Beam end yield rotation ratio, θ_{yi}/θ_{y2}
- Column yield rotation at base, θ_{yc}
- Story drift ratio, δ_{si}/δ_r, where δ_{si} is the story drift in story i, and δ_r is the roof displacement
- Story drift angle ratio, θ_{si}/θ_r (θ_i is defined as δ_{si}/h_i and θ_r as δ_r/H, where h_i is the story height and H the total height)

Information on the rest of the frames can be found in Medina (2002).

B.2 STIFFNESS OF ROTATIONAL SPRINGS AT MEMBER ENDS

Each flexural member that has the potential to deform into the inelastic range is modeled by the following subelements connected in series: plastic hinge rotational springs at member ends and an elastic beam-column element. Therefore, the structural properties of the member are a combination of the properties of the subelements. The rotational stiffness of the member, K_{mem}, can be derived from the structural properties of the frame (Tables B.2–B.3), e.g., for beams subjected to double curvature bending $K_{mem} = 6EI_{beam}/L_{beam}$. The rotational stiffness, K_{mem}, can be related to the stiffness of the spring, K_s, and the stiffness of the beam-column element, K_{bc}, according to the following equation:

$$K_{mem} = \frac{1}{\frac{1}{K_s} + \frac{1}{K_{bc}}} = \frac{K_s K_{bc}}{K_s + K_{bc}} \tag{B.1}$$

Evident choices for subelement stiffnesses appear to be either

1. $K_{bc} = \infty$, in which case $K_s = K_{mem}$, or
2. $K_s = \infty$, in which case $K_{bc} = K_{mem}$

Both options are not desirable in the context of computer analysis with the program DRAIN-2DX, which utilizes an event-by-event solution strategy.

An infinite beam stiffness would force all deformations into the plastic hinge springs, which would lead to the following two problems:

- The elastic spring stiffness, which has to be defined a priori, would be the same regardless of the moment gradient in the beam or column (e.g., $6EI_{beam}/L_{beam}$, if it is assumed that the beam deforms in double curvature). In reality, the moment gradient may change during the time history analysis (THA), which would not be accounted for in this model
- All damping would have to be assigned to the rotational springs at the beam ends, which causes spurious damping moments at frame joints that are not in static equilibrium because DRAIN-2DX's damping formulation is based on initial member stiffnesses (see Section B.4).

Thus, the first option is discarded.

The second option, considering an infinite spring stiffness would cause numerical instability problems and would also make it impossible to express strain-hardening and post-capping stiffnesses as fractions of the elastic spring stiffness. Thus, this option also had to be discarded.

In order to avoid the problems of the second option and to minimize the problems associated with the first option, it was decided to use an elastic spring stiffness that is "n" times larger than the rotational stiffness of the beam-column element, K_{bc}, i.e.,:

$$K_s = nK_{bc} \tag{B.2}$$

where n is a number >> 1; a value of $n = 10$ was used throughout this study. The stiffness of the subelements can now be expressed as a function of the total stiffness of the member and the multiplier n,:

$$K_{bc} = \frac{n+1}{n} K_{mem} \qquad K_s = (n+1)K_{mem} \tag{B.3}$$

A large value on *n* accomplishes the following: (a) it minimizes the problems identified in the first option because now all damping can be assigned to the elastic beam-column element and changes in moment gradients in this subelement can be accounted for, and (b) it permits incorporation of all backbone and cyclic deterioration characteristics in the plastic hinge rotational spring. But the properties of these springs need to be modified because the deterioration properties belong to the full element and not to the springs alone.

B.3 PARAMETERS FOR DETERIORATING SPRINGS

In Section B.2 the elastic stiffness of the member is related to the elastic stiffness of the rotational springs and the beam-column element. Additional parameters must be adjusted in the nonlinear range to reproduce the moment-rotation relationship at the end of the elements. Figure B.1 presents the hysteretic response of a beam member, which is the combination of the individual moment-rotations of the springs and the beam-column element. The moment-rotation of the beam-column element remains elastic during all the THA and the nonlinear response is entirely due to the springs. The parameters of the plastic hinge spring must be adjusted to be able to reproduce the nonlinear moment-rotation behavior of the member.

Strain-Hardening Coefficient. The strain-hardening coefficient of the plastic hinge of the spring ($\alpha_{s,s}$) must be adjusted to obtain the strain-hardening coefficient for the moment-rotation of the member, $\alpha_{s,mem}$. Because the subelements are connected in series, the increment in rotation of the total element in *the post-yielding range* is the sum of the increments in rotation of the two subelements in this interval:

$$\Delta\theta_{mem} = \Delta\theta_s + \Delta\theta_{bc} = \frac{\Delta M_{in}}{K_{s,s}} + \frac{\Delta M_{in}}{K_{bc}} \tag{B.4}$$

where ΔM_{in} is the increment in strength developed in the inelastic range and $K_{s,s}$ is the stiffness of the spring for the strain-hardening branch. The strain-hardening coefficient of the springs as a function of $\alpha_{s,mem}$ is obtained by substituting Equation B.3 into Equation B.4 and by considering that $\Delta\theta_{mem} = \dfrac{\Delta M_{in}}{\alpha_{mem} K_{mem}}$:

$$\alpha_{s,s} = \frac{(n+1)\alpha_{s,mem}}{n+1-n\alpha_{s,mem}} \tag{B.5}$$

Note that the strain-hardening coefficient of the spring depends only on $\alpha_{s,mem}$ and n. For instance, to obtain 3% strain hardening in the moment-rotation relationship at the end of the element, the springs require a post-yield rotational spring coefficient $\alpha_{s,s} = 0.0028$ (when $n = 10$).

In the extreme case that n = 0, the beam-column element is rigid and $\alpha_{s,s} = \alpha_{s,mem}$.

Post-Capping Stiffness Coefficient. The stiffness coefficient for the post-capping branch is calculated in the same way as that of the strain-hardening branch because it also is expressed as a fraction of the elastic stiffness of the member. For the reference frame (Section 5.3.2), the post-capping stiffness coefficient for the moment-rotation relationship at the end of the beam is $\alpha_{c,mem} = -0.10$. If $n = 10$, the post-capping stiffness coefficient to be used for the springs is $\alpha_{c,s} = -0.0083$.

Ductility Capacity of the Spring. The ductility capacity of the spring must be adjusted to obtain the correct ductility capacity of the moment-rotation relationship at the end of the member. By adding the deformation of the subelements in the elastic and inelastic ranges it is possible to derive the following equation that provides the ductility capacity of the spring:

$$(\delta_c / \delta_y)_s = \left[(\delta_c / \delta_y)_{mem} - 1\right](1-\alpha_{s,mem})n + (\delta_c / \delta_y)_{mem} \tag{B.6}$$

For the reference frames, the ductility capacity of the moment-rotation at the end of the beam is $(\delta_c / \delta_y)_{mem} = 4$. The ductility capacity of the spring when $n = 10$ is $(\delta_c / \delta_y)_s = 33.1$.

Parameter γ for Cyclic Deterioration. The parameter γ to be used in the springs needs to be adjusted to simulate the correct rate of deterioration of the moment-rotation relationship of the member. The following expression computes $\gamma_{s,c,k,a}$ for the spring:

$$(\gamma_{s,c,k,a})_s = (n+1)(\gamma_{s,c,k,a})_{mem} \tag{B.7}$$

This relationship is exact only for elastic-plastic models but the error is very small (less than 1%) for the range of strain-hardening coefficients used in this work.

B.4 MODELING OF PLASTIC HINGES TO AVOID SPURIOUS DAMPING MOMENTS

The damping for the generic frames is based on the Rayleigh damping formulation:

$$\underline{C} = \alpha \underline{M} + \beta_o \underline{K_o} \tag{B.8}$$

where $\underline{C}$ is the viscous damping matrix, $\underline{M}$ is the mass matrix, $\underline{K_o}$ is the initial stiffness matrix, and α and β_o are mass and stiffness proportional factors. This formulation is implemented in the DRAIN-2DX computer program.

An alternative viscous damping matrix is given by:

$$\underline{C_t} = \alpha \underline{M} + \beta_t \underline{K_t} \tag{B.9}$$

where $\underline{C_t}$ is the current damping matrix, $\underline{K_t}$ is the tangent (current) stiffness matrix, and β_t is the stiffness proportional factor.

To avoid unbalance of forces during the analysis, which is based on an event-to-event strategy, DRAIN-2DX only utilizes the constant damping matrix formulation of Equation B.8 (DRAIN-2DX, 1993). However, a constant damping matrix causes spurious damping moments at the joints once a change of stiffness occurs in nonlinear elements that have stiffness proportional damping based on their initial stiffness (Bernal, 1994). That is to say, although dynamic equilibrium is satisfied, spurious damping moments cause static equilibrium to be violated at joints.

The use of a current damping matrix was discarded because K_t in the solution of the equation of motion may lead to a potential unbalance of forces when an event-to-event strategy is implemented. Moreover, it is not clear how to use a tangent stiffness formulation when nonlinear elements have a negative slope. Thus, to obtain an approximate solution that satisfies static and dynamic equilibrium, a constant damping matrix formulation (Equation B.8) was selected with the following conditions: (a) plastic hinging is modeled by using nonlinear rotational springs with an initial stiffness several times larger than that of the beam-column element and (b) zero stiffness proportional damping is assigned to the springs.

Adjustment of Damping in Subelements

Because no stiffness proportional damping is assigned to the nonlinear rotational springs, the β (stiffness proportional) factor for the beam-column element needs to be adjusted. For $n = 10$, the

β factor must be multiplied by 1.1 to compensate for the lack of stiffness proportional damping provided by the rotational springs.

Table B.1 Modal properties, N = 9, T_1 = 0.9 and 1.8 s

Modal Properties					*Story/Floor*	*Mode Shapes*				
Mode	T_i / T_1	PF_i	MP_i	ξ_i		ϕ_1	ϕ_2	ϕ_3	ϕ_4	ϕ_5
1	1.000	1.421	0.789	0.050	0/1	0.000	0.000	0.000	0.000	0.000
2	0.394	0.626	0.117	0.040	1/2	0.111	0.229	-0.491	-0.624	-0.773
3	0.230	-0.298	0.045	0.050	2/3	0.222	0.431	-0.809	-0.806	-0.631
4	0.152	-0.226	0.022	0.068	3/4	0.333	0.579	-0.828	-0.386	0.295
5	0.107	-0.165	0.012	0.094	4/5	0.444	0.645	-0.506	0.362	0.875
					5/6	0.556	0.606	0.072	0.851	0.262
					6/7	0.667	0.437	0.686	0.558	-0.808
					7/8	0.778	0.119	0.982	-0.424	-0.544
					8/9	0.889	-0.361	0.533	-1.000	1.000
					9/10	1.000	-1.000	-1.000	0.590	-0.334

Table B.2 Structural properties, N = 9, T_1 = 0.9 s

Story/Floor	*Stiffness Properties*								*$\gamma = V_y / W = 1.0$, Parabolic Design Load Pattern*								
	W_i / W	I_i / I_1	K_{ai} / K_{a1}	K_{fi} / K_{f2}	K_{ki} / K_{k1}	K_{si} / K_{s1}	K_{bi} / K_{b2}	K_c	V_i / V_1	M_{OTi} / M_{OT1}	α_{si}	M_{ybi} / M_{yb2}	M_{yc}	$\theta_{ybi} / \theta_{yb2}$	θ_{cy}	δ_{si} / δ_r	θ_{si} / θ_r
0/1								7316974					64920		0.009		
1/2	0.111	1.000	1.000	1.000	1.000	1.000	1.000		1.000	1.000	0.036	1.000		1.000		0.096	0.861
2/3	0.111	0.965	0.965	0.963	0.996	0.980	0.965		0.996	0.859	0.036	0.988		1.024		0.097	0.875
3/4	0.111	0.913	0.913	0.908	0.982	0.937	0.913		0.982	0.719	0.037	0.964		1.056		0.100	0.902
4/5	0.111	0.836	0.836	0.829	0.951	0.872	0.836		0.951	0.581	0.038	0.919		1.098		0.104	0.938
5/6	0.111	0.739	0.739	0.727	0.895	0.785	0.739		0.895	0.447	0.039	0.846		1.145		0.109	0.981
6/7	0.111	0.618	0.618	0.602	0.807	0.674	0.618		0.807	0.321	0.040	0.737		1.193		0.115	1.031
7/8	0.111	0.475	0.475	0.453	0.681	0.541	0.475		0.681	0.207	0.042	0.587		1.234		0.120	1.084
8/9	0.111	0.311	0.311	0.275	0.509	0.385	0.311		0.509	0.112	0.043	0.388		1.247		0.126	1.138
9/10	0.111	0.131	0.131	0.500	0.284	0.206	0.131		0.284	0.040	0.045	0.147		1.120		0.132	1.189
	W	I_1	K_{a1}	K_{f2}	K_{k1}	K_{s1}	K_{b2}		V_1	M_{OT1}		M_{yb2}		θ_{yb2}		δ_r	θ_r
	(k)	(in^4)	(k/in)	(k/in)	(k/in)	(k/in)	(k-in)	(k-in)	(k)	(k-in)		(k-in)	(k-in)	(rad)	(rad)	(in)	(rad)
	1800	24222	3226	562	1141	1120	14633949		1800	1841684		130200		0.009		16.800	0.013

Table B.3 Structural properties, N = 9, T_1 = 1.8 s

Story/Floor	*Stiffness Properties*								*$\gamma = V_y / W = 1.0$, Parabolic Design Load Pattern*								
	W_i / W	I_i / I_1	K_{ai} / K_{a1}	K_{fi} / K_{f2}	K_{ki} / K_{k1}	K_{si} / K_{s1}	K_{bi} / K_{b2}	K_c	V_i / V_1	M_{OTi} / M_{OT1}	α_{si}	M_{ybi} / M_{yb2}	M_{yc}	$\theta_{ybi} / \theta_{yb2}$	θ_{cy}	δ_{si} / δ_r	θ_{si} / θ_r
0/1								1829244					64920		0.035		
1/2	0.111	1.000	1.000	1.000	1.000	1.000	1.000		1.000	1.000	0.036	1.000		1.000		0.096	0.861
2/3	0.111	0.965	0.965	0.963	0.996	0.980	0.965		0.996	0.859	0.036	0.988		1.024		0.097	0.876
3/4	0.111	0.913	0.913	0.908	0.982	0.938	0.913		0.982	0.719	0.037	0.964		1.056		0.100	0.902
4/5	0.111	0.836	0.836	0.829	0.951	0.873	0.836		0.951	0.581	0.038	0.919		1.098		0.104	0.938
5/6	0.111	0.739	0.739	0.727	0.895	0.785	0.739		0.895	0.447	0.039	0.846		1.145		0.109	0.981
6/7	0.111	0.618	0.618	0.602	0.807	0.674	0.618		0.807	0.321	0.040	0.737		1.193		0.115	1.031
7/8	0.111	0.475	0.475	0.453	0.681	0.541	0.475		0.681	0.207	0.042	0.587		1.234		0.120	1.084
8/9	0.111	0.311	0.311	0.275	0.509	0.385	0.311		0.509	0.112	0.043	0.388		1.247		0.126	1.138
9/10	0.111	0.131	0.131	0.220	0.284	0.206	0.131		0.284	0.040	0.045	0.147		1.120		0.132	1.190
	W	I_1	K_{a1}	K_{f2}	K_{k1}	K_{s1}	K_{b2}		V_1	M_{OT1}		M_{yb2}		θ_{yb2}		δ_r	θ_r
	(k)	(in^4)	(k/in)	(k/in)	(k/in)	(k/in)	(k-in)	(k-in)	(k)	(k-in)		(k-in)	(k-in)	(rad)	(rad)	(in)	(rad)
	1800	6055	807	141	284	281	3658487		1800	1841684		130200		0.036		66.900	0.052

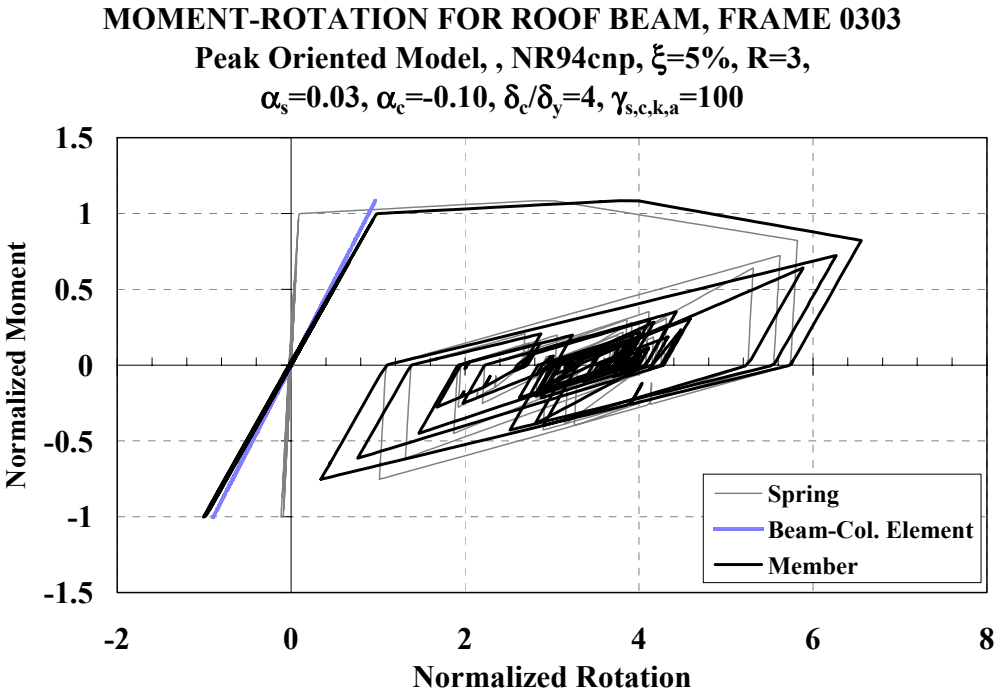

Fig. B.1 Moment-rotation relationship for a member based on the moment-rotation of the plastic hinge springs and elastic beam-column element

Appendix C: Probability Distribution of Collapse Capacity

In much of this report, estimators for the geometric mean and dispersion of collapse capacity are computed without fitting a distribution to the data. However, sometimes it is more convenient to evaluate global collapse and mean annual frequency of collapse by fitting a continuous distribution. Information about the distribution of collapse capacities is not reported in the literature, although it is known that the response of nonlinear structures may fit a lognormal distribution (Shome and Cornell, 1999). Furthermore, the distribution of collapse capacity due to RTR variability presents a long upper tail (Figs. 2.4–2.5), which suggests that a lognormal distribution may fit well. This appendix intends to verify that a lognormal distribution can be a good fitting of collapse capacity distribution.

C.1 LOGNORMAL DISTRIBUTION PAPER AND KOLMOGOROV-SMIRNOV GOODNESS-OF-FIT TEST

A widespread method for verifying the distribution assumption is to plot the results in a probability paper to obtain a straight line for the assumed distribution. If the assumption is reasonable, the cumulative frequency curve of the data is close to the straight line, and shows no systematic curvature.

A Kolmogorov-Smirnov goodness of-fit-test is used to quantify how well the data fit the distribution models. The tests concentrates on the deviation between the hypothesized cumulative distribution function, $F_X(x)$, and the observed cumulative histogram (Benjamin and Cornell, 1970):

$$F^*(X^{(i)}) = \frac{i}{n} \tag{C.1}$$

in which $X^{(i)}$ is the i^{th} largest observed value in the random sample of size n. The maximum of the aforementioned deviations is calculated as follows,

$$D = \max_{i=1}^{n}\left[\left|F^*(X^{(i)}) - F_X(X^{(i)})\right|\right] \quad \text{(C.2)}$$

That is to say, D is the largest of the absolute values of the n differences between the hypothesized CDF and the observed empirical CDF (counted) evaluated at the observed values in the sample. Theoretically, the value of D depends on n. For a specified significance level α, the test compares the observed maximum difference D with the critical value c, as follows:

$$P[D \le c] = 1 - \alpha \quad \text{(C.3)}$$

Critical values c at various significance levels α are tabulated in Benjamin and Cornell (1970). If the observed D is less than the critical value c, the proposed distribution is accepted at the specified significance level α; otherwise, the assumed distribution would be rejected.

C.2 COLLAPSE CAPACITY DISTRIBUTION DUE TO RTR VARIABILITY

In this section goodness-of-fit tests are illustrated for a lognormal distribution that is fitted to collapse capacity data in which the dispersion is entirely due to RTR variability. Collapse capacities for three different peak-oriented SDOF systems, with T = 0.6 s, are plotted on lognormal probability paper along with the fitted lognormal distribution (Fig. C.1). The left vertical axis corresponds to the inverse function for the standard normal distribution of the CDF of collapse capacity, $\Phi^{-1}\{F[(S_{a,c}/g)/\eta]\}$ or in a simplified way $\Phi^{-1}\{F_{C,S_{a,c}}\}$. The right vertical axis indicates the corresponding cumulative probabilities. The graphs are for systems with "low," "intermediate," and "high" ductility and the data fit well to a straight line, even at small and large fractiles.

For this evaluation, the 5% significance level is selected, which is of common use. The number of collapse capacities is 40, which is the number of ground motions in the LMSR-N set to which the system is subjected. For a set of 40 data points and a 5% significant level (α = 0.05), the critical value is c = 0.21 [26](Benjamin and Cornell, 1970). The test statistic (D) is included in Figures C.1–C.3 for the three aforementioned SDOF systems. Because the test

[26] For a sample size with a number of data, n, larger than 40, the critical statistic at 5% confidence level can be computed as $c = 1.36/\sqrt{n}$

statistic values are less than the critical value, the assumption of lognormal distribution for collapse capacity cannot be rejected at the 5% significance level.

Figure C.2 shows lognormal distribution fittings for collapse capacities generated for 3 and 6-story generic frames that have a fundamental period T_1 = 0.6 s. The dispersion of the data is also entirely due to RTR variability. Once again, the visual fit is satisfactory and the computed "D" are smaller than c = 0.21. Thus, the assumption of lognormal distribution for collapse capacities of these generic frames cannot be rejected at the 5% significance level.

C.3 SUMMARY

The collapse capacities of several systems were plotted on lognormal probability paper along with the fitted lognormal distribution, obtaining a good fit even at small and large fractiles. To quantify how well the collapse capacity data fit the lognormal distribution, Kolmogorow-Smirnov goodness-of-fit tests have been carried out. SDOF systems with low, intermediate and high ductile characteristics, as well as stiff and flexible generic frames have been tested. In all cases the critical value "c" for a 5% significance level is almost twice as large as the computed parameter D. These tests provide good arguments for representing collapse capacity data by a lognormal distribution.

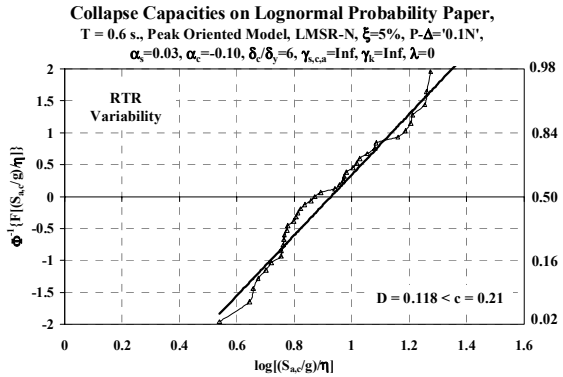

(a) High Ductility

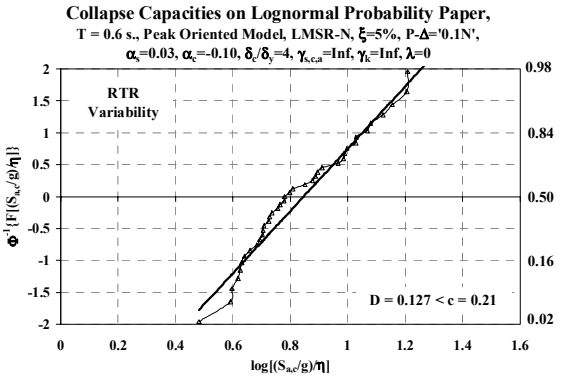

(b) Intermediate Ductility

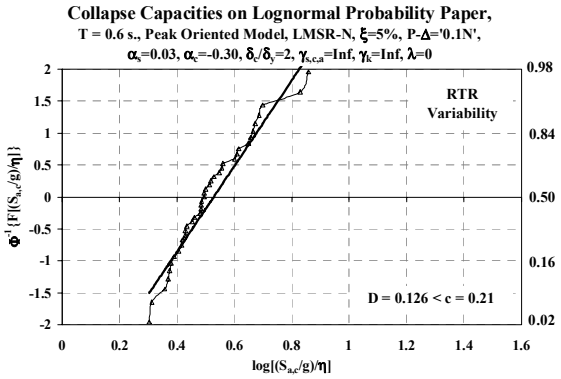

(c) Low Ductility

Fig. C.1 Fitting of lognormal distribution to collapse capacity data; peak-oriented SDOF systems; dispersion due to RTR variability

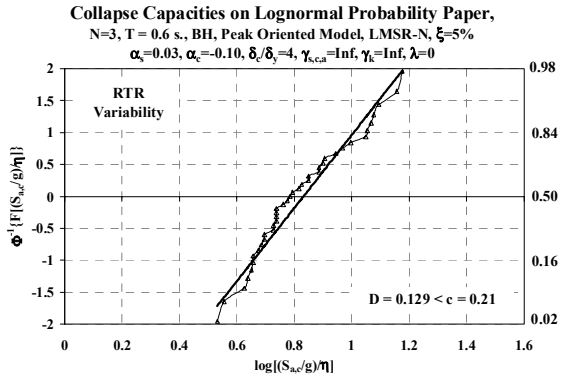

(a) 3-Story Frame (Flexible)

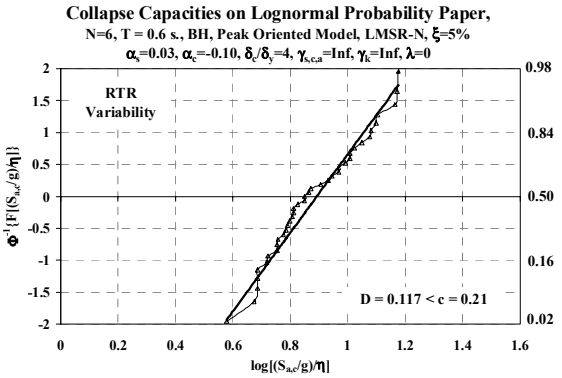

(b) 6-Story Frame (Stiff)

Fig. C.2 Fitting of lognormal distribution to collapse capacity data; generic frames with T_1 = 0.6 s; springs with intermediate ductility

Appendix D: Computations of Variance of Collapse Capacity in the Linear Domain of the Data

In Chapter 6 additional variance of collapse capacity due to uncertainty in the system parameters is computed by applying the FOSM method in the log domain of the data. As an alternative, this appendix presents an overview of the FOSM method with computations in the linear domain of the data. Arguments are presented for why computations in the log domain of the data are preferable.

D.1 FORMULATION FOR COMPUTATIONS OF COLLAPSE CAPACITY IN LINEAR DOMAIN

An "additive" approach is used for computing the total variance in the linear domain of the data, i.e., collapse capacity is expressed as a function "*f*" *plus* a random variable that depends on RTR variability:

$$S_{a,c} / \eta = f(\overline{Q}) + \varepsilon_z(RTR) \tag{D.1}$$

where $\overline{Q}$ is the vector of random system parameters and $\varepsilon_z(RTR)$ is a random variable with zero mean. Then, the total variance of collapse capacity, $\sigma^2_{S_{a,c}(TOT)}$, is given by:

$$\sigma^2_{S_{a,c}(TOT)} \cong \sum_{i=1}^{n}\sum_{j=1}^{n}\left(\frac{\partial f(\overline{Q})}{\partial q_i}\frac{\partial f(\overline{Q})}{\partial q_j}\right)_{\overline{Q}=\overline{\mu}_q} \rho_{q_i,q_j}\sigma_{q_i}\sigma_{q_j} + \sigma^2_{S_{a,c}(RTR)} \tag{D.2}$$

To compare results obtained in the log and linear domain of the data, the geometric mean and dispersion of the probabilistic parameter(s) must be equivalent. Because the distribution of the system parameters is unknown, a first-order approximation is used:

$$\mu_x \cong \exp(\mu_{\ln x}), \qquad \sigma_x \cong \mu_x \sigma_{\ln x} \tag{D.3}$$

D.2 LINEAR DOMAIN AND LOG DOMAIN OF DATA

Some arguments in favor of the use of computations in the log domain of the data are presented based on the reference SDOF system of Chapter 4, considering uncertainty in the post-capping stiffness coefficient, α_c. The first argument is related with the differences in the formulation, i.e., the multiplicative versus additive approach. The second one is about the stability in the computations of the variance of collapse capacity.

D.2.1 Multiplicative versus Additive Approach

Computations in the log domain of the data are based on a multiplicative approach, i.e., the random variable $\varepsilon_k(RTR)$ multiplies the function $f(Q_1,Q_2,...,Q_n)$ (Eq. 6.4). Thus, in the log domain of the data $\sigma^2_{\ln S_{a,c}(RTR)}$ is added to the variance of collapse capacity due to uncertainty in the input parameters (Equation 6.8). This implies that the standard deviation of the log of collapse capacity due to RTR variability is the same for variations of a given probabilistic parameter ($\sigma_{\ln S_{a,c}(RTR)}$ is constant under variations of x_i). In the linear domain, this means that $c.o.v._{S_{a,c}(RTR)}$ is constant under variations of x_i

On the other hand, the computations in the linear domain of the data consider an additive approach, i.e., the random variable $\varepsilon_z(RTR)$ is added to the function $f(Q_1,Q_2,...,Q_n)$. This implies that the standard deviation of collapse capacity due to RTR variability is assumed as a constant for variations of the probabilistic parameter ($\sigma_{S_{a,c}(RTR)}$ is constant under variations of x_i).

Figures D.1–D.2 show the behavioral trends of $\sigma_{S_{a,c}(RTR)}$ and $c.o.v._{S_{a,c}(RTR)}$ under variations of α_c, for reference SDOF systems at different periods. The patterns indicate that the $c.o.v._{S_{a,c}(RTR)}$ tends to be more constant under variations of α_c. This trend is more consistent with the multiplicative approach. Therefore, the computations in the log domain of the data are the most reasonable alternative from this point of view. Similar patterns were obtained for variations of ductility capacity and cyclic deterioration.

D.2.2 Computations in Linear and Log Domain of Data

The additional variance of collapse capacity for the reference SDOF system due to uncertainty in the post-capping stiffness coefficient ($\sigma^2_{S_{a,c}(\alpha)}$) is obtained by applying the FOSM method with computations in the linear domain of the data, (see Section 6.3.1.1). The mean and standard deviation of α_c are derived from Equation D.3: $\mu_\alpha \cong 0.10$ and $\sigma_\alpha \cong 0.10(0.6) = 0.06$. Once the sign is inverted[27], the 16th and 84th percentiles for computations in the linear domain of the data are obtained:

$$16^{th}_{\alpha} \cong \mu_\alpha + \sigma_\alpha = -0.10 + 0.06 = -0.04$$

$$84^{th}_{\alpha} \cong \mu_\alpha + \sigma_\alpha = -0.10 - 0.06 = -0.16$$

Note that these percentiles differ from those computed in the log domain of the data for the 16th and 84th percentiles (α_c = -0.055 and -0.182, respectively). The discrepancy adds another source of uncertainty to the comparison.

Once the collapse capacities for the 16th and 84th percentiles of α_c in the linear domain of the data are computed, $\sigma^2_{S_{a,c}(\alpha)}$ is calculated according to Equation D.2 and is presented in Figure D.3 as a percentage of variance of collapse capacity due to RTR variability ($\sigma^2_{S_{a,c}(\alpha)} / \sigma^2_{S_{a,c}(RTR)}$). As observed, these ratios are more than two times larger than the $\sigma^2_{\ln S_{a,c}(\alpha)} / \sigma^2_{\ln S_{a,c}(RTR)}$ ratios for computations in the log domain of the data.

The large difference in the results of Figure D.3 may be caused by the domain of the calculations itself or by the fact that the 16th and 84th percentiles are different for each domain. A closer look at the region where α_c is evaluated reveals that $\alpha_{16^{th}}$ is on the border of a highly nonlinear region (Fig. D.4). To eliminate the uncertainty due to collapse capacities evaluated at different percentiles, the 16th and 84th percentiles used for the computations in the log domain of the data are also used for the computations in the linear domain, i.e., $\alpha_{c,1} = -0.055$ and $\alpha_{c,2} = -0.182$. Note that in the linear domain these values do not correspond to the 16th and 84th and are not at the same distance from the mean value. Figure D.5 presents the ratios of variance of collapse capacity due to uncertainty in α_c over the variance of collapse capacity due to RTR

[27] The sign is inverted to be able to obtain natural logarithms (Section 6.3.1.1)

variability for computations on both domains. This time the ratios of additional uncertainty are very similar. This suggests that the different formulation utilized in each domain (multiplicative versus additive approach) is less important than the values at which the probabilistic parameter is evaluated for obtaining the derivative.

To verify the importance of the selected percentiles of α_c, the collapse capacity in the log domain of the data is computed using the α_c values that were obtained for the 16th and 84th percentiles in the linear domain. The $\sigma^2_{\ln S_{a,c}(\alpha)} / \sigma^2_{\ln S_{a,c}(RTR)}$ ratios for different percentiles in the log domain of the data are very similar (Fig. D.6). This indicates that the dependence of collapse capacity on the selected percentiles of α_c is less sensitive in the log domain of the data (Fig. 6.4).

D.3 SUMMARY

The above observations for uncertainty in the post-capping stiffness coefficient were also made for uncertainty in ductility capacity and cyclic deterioration. Thus, computations in the log domain of the data should be preferred for several reasons. In the first place, the multiplicative approach is more consistent with the identified behavioral trends of collapse capacity under variations of the probabilistic parameter. Also, the relationships between probabilistic parameters and collapse capacities are smoother in the log domain of the data, which tends to reduce variations in the results due to local irregularities. However, the main reason for this preference is that computations in the log domain of the data reduce the likelihood of evaluating collapse capacity in a highly nonlinear region.

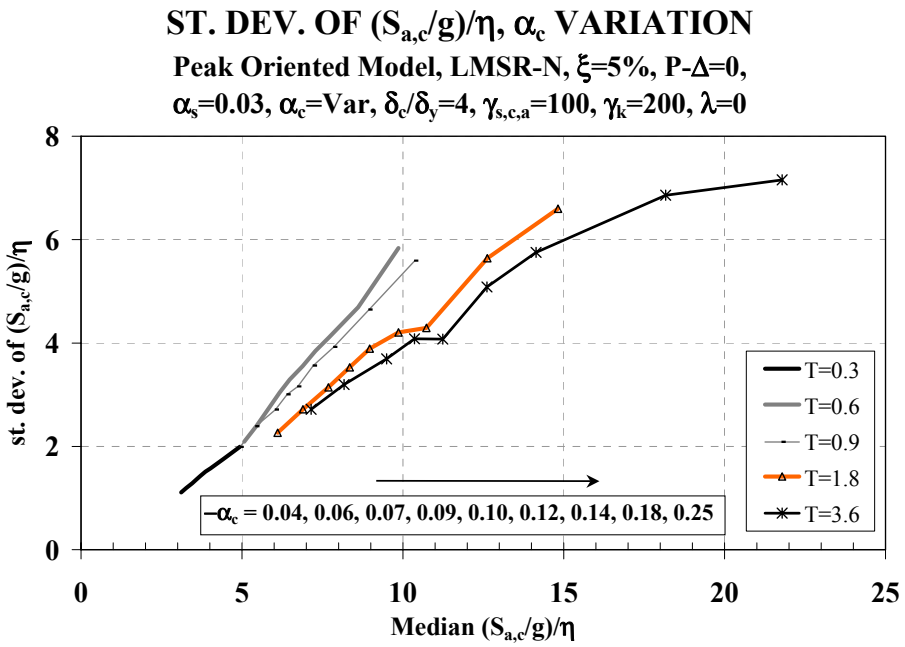

Fig. D.1 Standard deviation of collapse capacity under variations of α_c

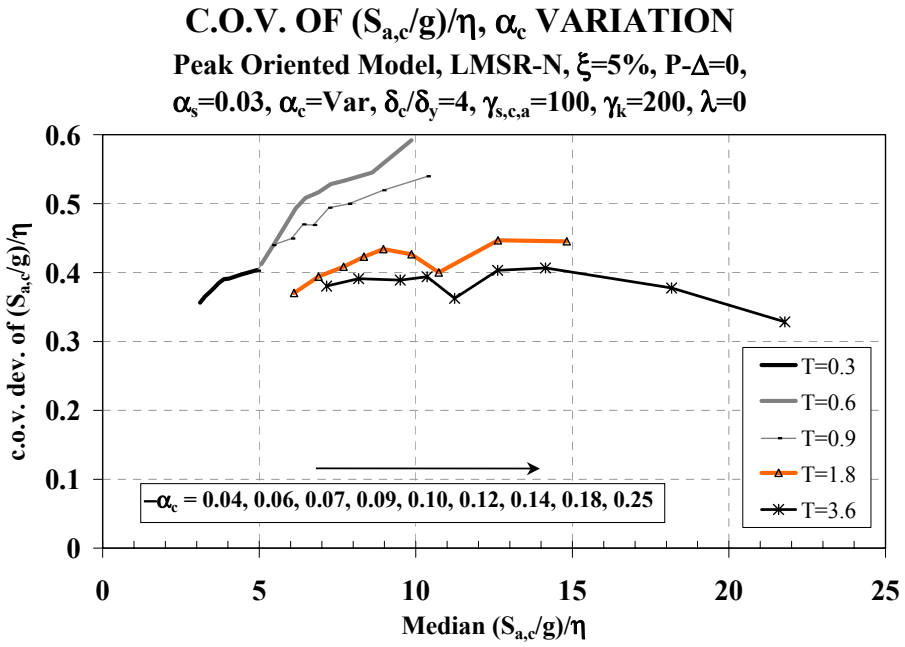

Fig. D.2 Coefficient of variation of collapse capacity under variations of α_c

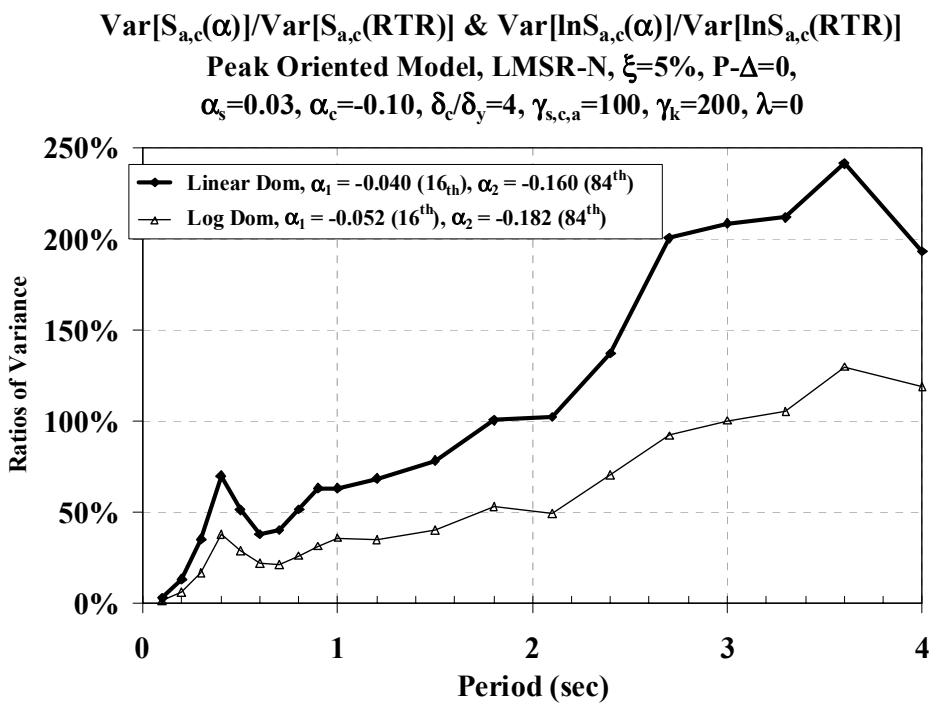

Fig. D.3 Effect of the domain of the computations on $\sigma^2_{S_{a,c}(\alpha)} / \sigma^2_{S_{a,c}(RTR)}$ and $\sigma^2_{\ln S_{a,c}(\alpha)} / \sigma^2_{\ln S_{a,c}(RTR)}$ ratios. Derivatives with α_c at 16th and 84th of each domain

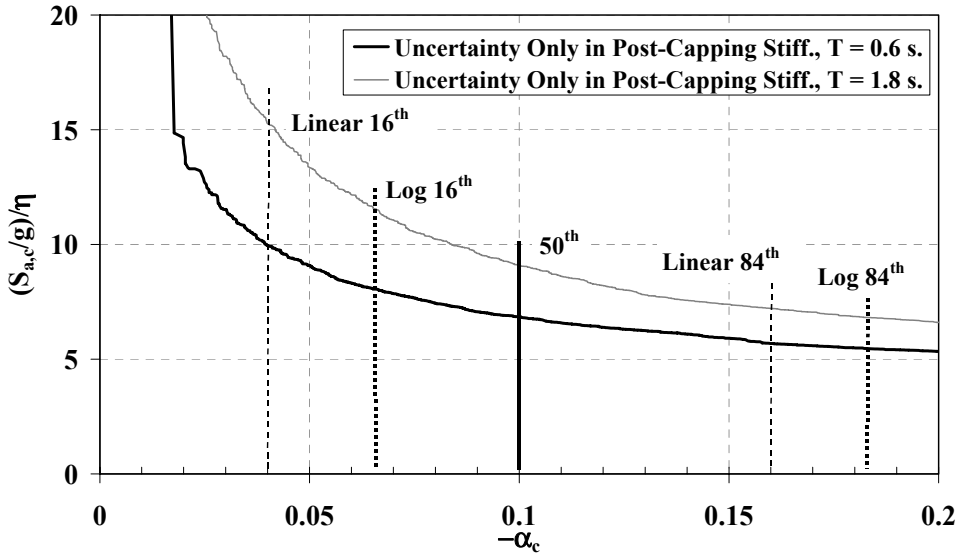

Fig. D.4 16th and 84th percentiles for computing the derivative on the linear and log domain of the data

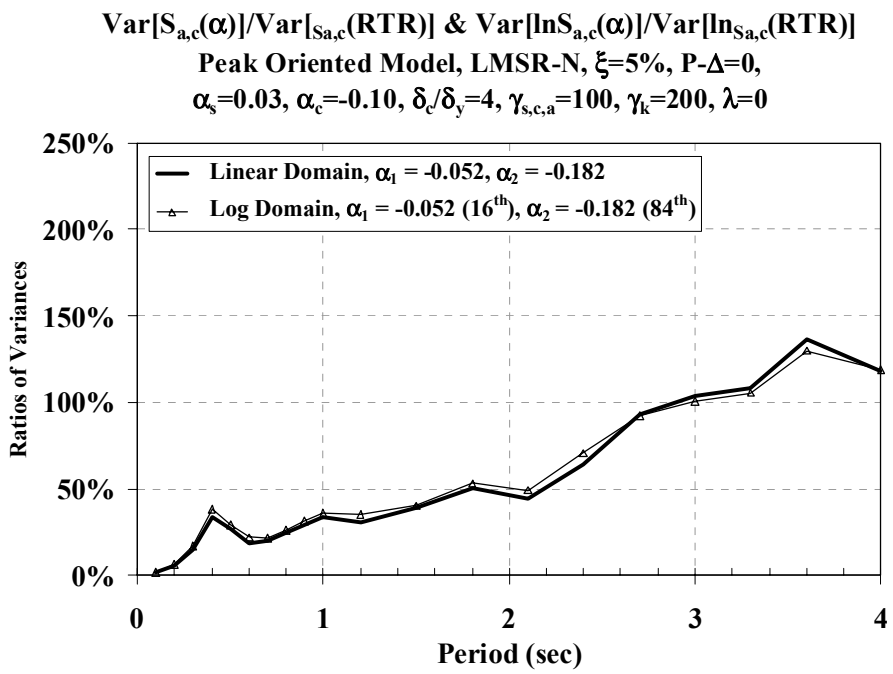

Fig. D.5 Effect of the domain of the computations on $\sigma^2_{S_{a,c}(\alpha)} / \sigma^2_{S_{a,c}(RTR)}$ and $\sigma^2_{\ln S_{a,c}(\alpha)} / \sigma^2_{\ln S_{a,c}(RTR)}$ ratios. Derivatives with $16^{th}_{\ln\alpha}$ and $84^{th}_{\ln\alpha}$ for both domains

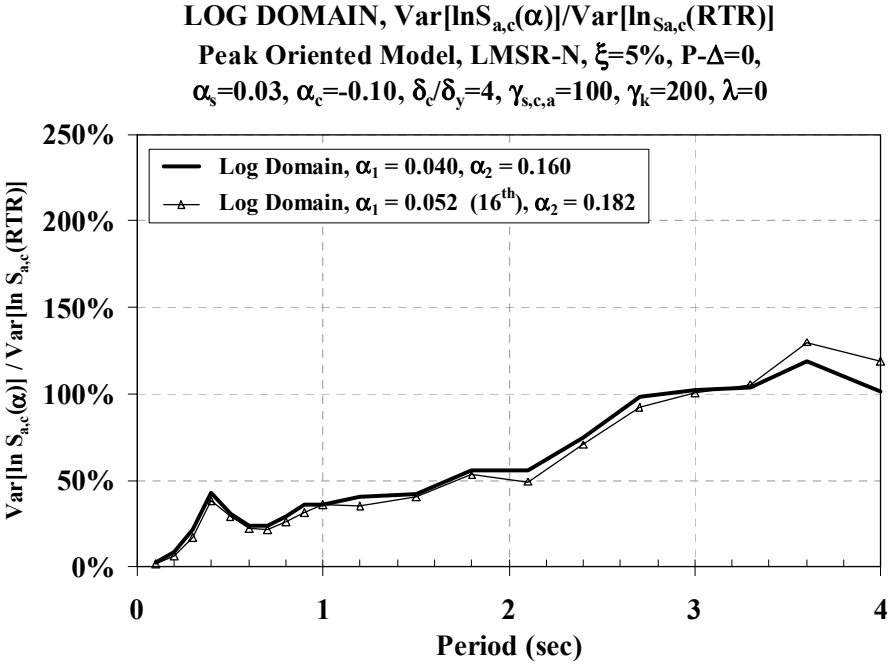

Fig. D.6 $\sigma^2_{\ln S_{a,c}(\alpha)} / \sigma^2_{\ln S_{a,c}(RTR)}$ Ratios for computations in the log domain of the data. Derivatives with α_c at $16^{th}_{\ln\alpha}$ and $84^{th}_{\ln\alpha}$ and at 16^{th}_{α} and 84^{th}_{α}

PEER REPORTS

PEER reports are available from the National Information Service for Earthquake Engineering (NISEE). To order PEER reports, please contact the Pacific Earthquake Engineering Research Center, 1301 South 46th Street, Richmond, California 94804-4698. Tel.: (510) 231-9468; Fax: (510) 231-9 461.

PEER 2005/06 *Global Collapse of Frame Structures under Seismic Excitations*. Luis F. Ibarra and Helmut Krawinkler. September 2005.

PEER 2005/01 *Empirical Characterization of Site Conditions on Strong Ground Motion.* Jonathan P. Stewart, Yoojoong Choi, and Robert W. Graves. June 2005.

PEER 2004/09 *Electrical Substation Equipment Interaction: Experimental Rigid Conductor Studies.* Christopher Stearns and André Filiatrault. February 2005.

PEER 2004/08 *Seismic Qualification and Fragility Testing of Line Break 550-kV Disconnect Switches.* Shakhzod M. Takhirov, Gregory L. Fenves, and Eric Fujisaki. January 2005.

PEER 2004/07 *Ground Motions for Earthquake Simulator Qualification of Electrical Substation Equipment.* Shakhzod M. Takhirov, Gregory L. Fenves, Eric Fujisaki, and Don Clyde. January 2005.

PEER 2004/06 *Performance-Based Regulation and Regulatory Regimes.* Peter J. May and Chris Koski. September 2004.

PEER 2004/05 *Performance-Based Seismic Design Concepts and Implementation: Proceedings of an International Workshop.* Peter Fajfar and Helmut Krawinkler, editors. September 2004.

PEER 2004/04 *Seismic Performance of an Instrumented Tilt-up Wall Building.* James C. Anderson and Vitelmo V. Bertero. July 2004.

PEER 2004/03 *Evaluation and Application of Concrete Tilt-up Assessment Methodologies.* Timothy Graf and James O. Malley. October 2004.

PEER 2004/02 *Analytical Investigations of New Methods for Reducing Residual Displacements of Reinforced Concrete Bridge Columns.* Junichi Sakai and Stephen A. Mahin. August 2004.

PEER 2004/01 *Seismic Performance of Masonry Buildings and Design Implications.* Kerri Anne Taeko Tokoro, James C. Anderson, and Vitelmo V. Bertero. February 2004.

PEER 2003/18 *Performance Models for Flexural Damage in Reinforced Concrete Columns.* Michael Berry and Marc Eberhard. August 2003.

PEER 2003/17 *Predicting Earthquake Damage in Older Reinforced Concrete Beam-Column Joints.* Catherine Pagni and Laura Lowes. October 2004.

PEER 2003/16 *Seismic Demands for Performance-Based Design of Bridges.* Kevin Mackie and Božidar Stojadinovi . August 2003.

PEER 2003/15 *Seismic Demands for Nondeteriorating Frame Structures and Their Dependence on Ground Motions.* Ricardo Antonio Medina and Helmut Krawinkler. May 2004.

PEER 2003/14 *Finite Element Reliability and Sensitivity Methods for Performance-Based Earthquake Engineering.* Terje Haukaas and Armen Der Kiureghian. April 2004.

PEER 2003/13 *Effects of Connection Hysteretic Degradation on the Seismic Behavior of Steel Moment-Resisting Frames.* Janise E. Rodgers and Stephen A. Mahin. March 2004.

PEER 2003/12 *Implementation Manual for the Seismic Protection of Laboratory Contents: Format and Case Studies.* William T. Holmes and Mary C. Comerio. October 2003.

PEER 2003/11 *Fifth U.S.-Japan Workshop on Performance-Based Earthquake Engineering Methodology for Reinforced Concrete Building Structures.* February 2004.

PEER 2003/10 *A Beam-Column Joint Model for Simulating the Earthquake Response of Reinforced Concrete Frames.* Laura N. Lowes, Nilanjan Mitra, and Arash Altoontash. February 2004.

PEER 2003/09 *Sequencing Repairs after an Earthquake: An Economic Approach.* Marco Casari and Simon J. Wilkie. April 2004.

PEER 2003/08 *A Technical Framework for Probability-Based Demand and Capacity Factor Design (DCFD) Seismic Formats*. Fatemeh Jalayer and C. Allin Cornell. November 2003.

PEER 2003/07 *Uncertainty Specification and Propagation for Loss Estimation Using FOSM Methods.* Jack W. Baker and C. Allin Cornell. September 2003.

PEER 2003/06 *Performance of Circular Reinforced Concrete Bridge Columns under Bidirectional Earthquake Loading*. Mahmoud M. Hachem, Stephen A. Mahin, and Jack P. Moehle. February 2003.

PEER 2003/05 *Response Assessment for Building-Specific Loss Estimation.* Eduardo Miranda and Shahram Taghavi. September 2003.

PEER 2003/04 *Experimental Assessment of Columns with Short Lap Splices Subjected to Cyclic Loads*. Murat Melek, John W. Wallace, and Joel Conte. April 2003.

PEER 2003/03 *Probabilistic Response Assessment for Building-Specific Loss Estimation.* Eduardo Miranda and Hesameddin Aslani. September 2003.

PEER 2003/02 *Software Framework for Collaborative Development of Nonlinear Dynamic Analysis Program.* Jun Peng and Kincho H. Law. September 2003.

PEER 2003/01 *Shake Table Tests and Analytical Studies on the Gravity Load Collapse of Reinforced Concrete Frames.* Kenneth John Elwood and Jack P. Moehle. November 2003.

PEER 2002/24 *Performance of Beam to Column Bridge Joints Subjected to a Large Velocity Pulse.* Natalie Gibson, André Filiatrault, and Scott A. Ashford. April 2002.

PEER 2002/23 *Effects of Large Velocity Pulses on Reinforced Concrete Bridge Columns.* Greg L. Orozco and Scott A. Ashford. April 2002.

PEER 2002/22 *Characterization of Large Velocity Pulses for Laboratory Testing.* Kenneth E. Cox and Scott A. Ashford. April 2002.

PEER 2002/21 *Fourth U.S.-Japan Workshop on Performance-Based Earthquake Engineering Methodology for Reinforced Concrete Building Structures*. December 2002.

PEER 2002/20 *Barriers to Adoption and Implementation of PBEE Innovations.* Peter J. May. August 2002.

PEER 2002/19 *Economic-Engineered Integrated Models for Earthquakes: Socioeconomic Impacts.* Peter Gordon, James E. Moore II, and Harry W. Richardson. July 2002.

PEER 2002/18 *Assessment of Reinforced Concrete Building Exterior Joints with Substandard Details.* Chris P. Pantelides, Jon Hansen, Justin Nadauld, and Lawrence D. Reaveley. May 2002.

PEER 2002/17 *Structural Characterization and Seismic Response Analysis of a Highway Overcrossing Equipped with Elastomeric Bearings and Fluid Dampers: A Case Study*. Nicos Makris and Jian Zhang. November 2002.

PEER 2002/16 *Estimation of Uncertainty in Geotechnical Properties for Performance-Based Earthquake Engineering.* Allen L. Jones, Steven L. Kramer, and Pedro Arduino. December 2002.

PEER 2002/15 *Seismic Behavior of Bridge Columns Subjected to Various Loading Patterns.* Asadollah Esmaeily-Gh. and Yan Xiao. December 2002.

PEER 2002/14 *Inelastic Seismic Response of Extended Pile Shaft Supported Bridge Structures.* T.C. Hutchinson, R.W. Boulanger, Y.H. Chai, and I.M. Idriss. December 2002.

PEER 2002/13 *Probabilistic Models and Fragility Estimates for Bridge Components and Systems.* Paolo Gardoni, Armen Der Kiureghian, and Khalid M. Mosalam. June 2002.

PEER 2002/12 *Effects of Fault Dip and Slip Rake on Near-Source Ground Motions: Why Chi-Chi Was a Relatively Mild M7.6 Earthquake*. Brad T. Aagaard, John F. Hall, and Thomas H. Heaton. December 2002.

PEER 2002/11 *Analytical and Experimental Study of Fiber-Reinforced Strip Isolators*. James M. Kelly and Shakhzod M. Takhirov. September 2002.

PEER 2002/10 *Centrifuge Modeling of Settlement and Lateral Spreading with Comparisons to Numerical Analyses***.** Sivapalan Gajan and Bruce L. Kutter. January 2003.

PEER 2002/09 *Documentation and Analysis of Field Case Histories of Seismic Compression during the 1994 Northridge, California, Earthquake.* Jonathan P. Stewart, Patrick M. Smith, Daniel H. Whang, and Jonathan D. Bray. October 2002.

PEER 2002/08 *Component Testing, Stability Analysis and Characterization of Buckling-Restrained Unbonded Braces™.* Cameron Black, Nicos Makris, and Ian Aiken. September 2002.

PEER 2002/07 *Seismic Performance of Pile-Wharf Connections.* Charles W. Roeder, Robert Graff, Jennifer Soderstrom, and Jun Han Yoo. December 2001.

PEER 2002/06 *The Use of Benefit-Cost Analysis for Evaluation of Performance-Based Earthquake Engineering Decisions*. Richard O. Zerbe and Anthony Falit-Baiamonte. September 2001.

PEER 2002/05 *Guidelines, Specifications, and Seismic Performance Characterization of Nonstructural Building Components and Equipment*. André Filiatrault, Constantin Christopoulos, and Christopher Stearns. September 2001.

PEER 2002/04 *Consortium of Organizations for Strong-Motion Observation Systems and the Pacific Earthquake Engineering Research Center Lifelines Program: Invited Workshop on Archiving and Web Dissemination of Geotechnical Data, 4–5 October 2001*. September 2002.

PEER 2002/03 *Investigation of Sensitivity of Building Loss Estimates to Major Uncertain Variables for the Van Nuys Testbed.* Keith A. Porter, James L. Beck, and Rustem V. Shaikhutdinov. August 2002.

PEER 2002/02 *The Third U.S.-Japan Workshop on Performance-Based Earthquake Engineering Methodology for Reinforced Concrete Building Structures*. July 2002.

PEER 2002/01 *Nonstructural Loss Estimation: The UC Berkeley Case Study.* Mary C. Comerio and John C. Stallmeyer. December 2001.

PEER 2001/16 *Statistics of SDF-System Estimate of Roof Displacement for Pushover Analysis of Buildings.* Anil K. Chopra, Rakesh K. Goel, and Chatpan Chintanapakdee. December 2001.

PEER 2001/15 *Damage to Bridges during the 2001 Nisqually Earthquake.* R. Tyler Ranf, Marc O. Eberhard, and Michael P. Berry. November 2001.

PEER 2001/14 *Rocking Response of Equipment Anchored to a Base Foundation.* Nicos Makris and Cameron J. Black. September 2001.

PEER 2001/13 *Modeling Soil Liquefaction Hazards for Performance-Based Earthquake Engineering.* Steven L. Kramer and Ahmed-W. Elgamal. February 2001.

PEER 2001/12 *Development of Geotechnical Capabilities in OpenSees.* Boris Jeremi . September 2001.

PEER 2001/11 *Analytical and Experimental Study of Fiber-Reinforced Elastomeric Isolators*. James M. Kelly and Shakhzod M. Takhirov. September 2001.

PEER 2001/10 *Amplification Factors for Spectral Acceleration in Active Regions.* Jonathan P. Stewart, Andrew H. Liu, Yoojoong Choi, and Mehmet B. Baturay. December 2001.

PEER 2001/09 *Ground Motion Evaluation Procedures for Performance-Based Design.* Jonathan P. Stewart, Shyh-Jeng Chiou, Jonathan D. Bray, Robert W. Graves, Paul G. Somerville, and Norman A. Abrahamson. September 2001.

PEER 2001/08 *Experimental and Computational Evaluation of Reinforced Concrete Bridge Beam-Column Connections for Seismic Performance*. Clay J. Naito, Jack P. Moehle, and Khalid M. Mosalam. November 2001.

PEER 2001/07 *The Rocking Spectrum and the Shortcomings of Design Guidelines.* Nicos Makris and Dimitrios Konstantinidis. August 2001.

PEER 2001/06 *Development of an Electrical Substation Equipment Performance Database for Evaluation of Equipment Fragilities*. Thalia Agnanos. April 1999.

PEER 2001/05 *Stiffness Analysis of Fiber-Reinforced Elastomeric Isolators.* Hsiang-Chuan Tsai and James M. Kelly. May 2001.

PEER 2001/04 *Organizational and Societal Considerations for Performance-Based Earthquake Engineering.* Peter J. May. April 2001.

PEER 2001/03 *A Modal Pushover Analysis Procedure to Estimate Seismic Demands for Buildings: Theory and Preliminary Evaluation.* Anil K. Chopra and Rakesh K. Goel. January 2001.

PEER 2001/02 *Seismic Response Analysis of Highway Overcrossings Including Soil-Structure Interaction.* Jian Zhang and Nicos Makris. March 2001.

PEER 2001/01 *Experimental Study of Large Seismic Steel Beam-to-Column Connections.* Egor P. Popov and Shakhzod M. Takhirov. November 2000.

PEER 2000/10 *The Second U.S.-Japan Workshop on Performance-Based Earthquake Engineering Methodology for Reinforced Concrete Building Structures.* March 2000.

PEER 2000/09 *Structural Engineering Reconnaissance of the August 17, 1999 Earthquake: Kocaeli (Izmit), Turkey.* Halil Sezen, Kenneth J. Elwood, Andrew S. Whittaker, Khalid Mosalam, John J. Wallace, and John F. Stanton. December 2000.

PEER 2000/08 *Behavior of Reinforced Concrete Bridge Columns Having Varying Aspect Ratios and Varying Lengths of Confinement.* Anthony J. Calderone, Dawn E. Lehman, and Jack P. Moehle. January 2001.

PEER 2000/07 *Cover-Plate and Flange-Plate Reinforced Steel Moment-Resisting Connections.* Taejin Kim, Andrew S. Whittaker, Amir S. Gilani, Vitelmo V. Bertero, and Shakhzod M. Takhirov. September 2000.

PEER 2000/06 *Seismic Evaluation and Analysis of 230-kV Disconnect Switches.* Amir S. J. Gilani, Andrew S. Whittaker, Gregory L. Fenves, Chun-Hao Chen, Henry Ho, and Eric Fujisaki. July 2000.

PEER 2000/05 *Performance-Based Evaluation of Exterior Reinforced Concrete Building Joints for Seismic Excitation.* Chandra Clyde, Chris P. Pantelides, and Lawrence D. Reaveley. July 2000.

PEER 2000/04 *An Evaluation of Seismic Energy Demand: An Attenuation Approach.* Chung-Che Chou and Chia-Ming Uang. July 1999.

PEER 2000/03 *Framing Earthquake Retrofitting Decisions: The Case of Hillside Homes in Los Angeles.* Detlof von Winterfeldt, Nels Roselund, and Alicia Kitsuse. March 2000.

PEER 2000/02 *U.S.-Japan Workshop on the Effects of Near-Field Earthquake Shaking.* Andrew Whittaker, ed. July 2000.

PEER 2000/01 *Further Studies on Seismic Interaction in Interconnected Electrical Substation Equipment.* Armen Der Kiureghian, Kee-Jeung Hong, and Jerome L. Sackman. November 1999.

PEER 1999/14 *Seismic Evaluation and Retrofit of 230-kV Porcelain Transformer Bushings*. Amir S. Gilani, Andrew S. Whittaker, Gregory L. Fenves, and Eric Fujisaki. December 1999.

PEER 1999/13 *Building Vulnerability Studies: Modeling and Evaluation of Tilt-up and Steel Reinforced Concrete Buildings.* John W. Wallace, Jonathan P. Stewart, and Andrew S. Whittaker, editors. December 1999.

PEER 1999/12 *Rehabilitation of Nonductile RC Frame Building Using Encasement Plates and Energy-Dissipating Devices.* Mehrdad Sasani, Vitelmo V. Bertero, James C. Anderson. December 1999.

PEER 1999/11 *Performance Evaluation Database for Concrete Bridge Components and Systems under Simulated Seismic Loads.* Yael D. Hose and Frieder Seible. November 1999.

PEER 1999/10 *U.S.-Japan Workshop on Performance-Based Earthquake Engineering Methodology for Reinforced Concrete Building Structures.* December 1999.

PEER 1999/09 *Performance Improvement of Long Period Building Structures Subjected to Severe Pulse-Type Ground Motions*. James C. Anderson, Vitelmo V. Bertero, and Raul Bertero. October 1999.

PEER 1999/08 *Envelopes for Seismic Response Vectors.* Charles Menun and Armen Der Kiureghian. July 1999.

PEER 1999/07 *Documentation of Strengths and Weaknesses of Current Computer Analysis Methods for Seismic Performance of Reinforced Concrete Members.* William F. Cofer. November 1999.

PEER 1999/06 *Rocking Response and Overturning of Anchored Equipment under Seismic Excitations.* Nicos Makris and Jian Zhang. November 1999.

PEER 1999/05 *Seismic Evaluation of 550 kV Porcelain Transformer Bushings.* Amir S. Gilani, Andrew S. Whittaker, Gregory L. Fenves, and Eric Fujisaki. October 1999.

PEER 1999/04 *Adoption and Enforcement of Earthquake Risk-Reduction Measures.* Peter J. May, Raymond J. Burby, T. Jens Feeley, and Robert Wood.

PEER 1999/03 *Task 3 Characterization of Site Response General Site Categories*. Adrian Rodriguez-Marek, Jonathan D. Bray, and Norman Abrahamson. February 1999.

PEER 1999/02 *Capacity-Demand-Diagram Methods for Estimating Seismic Deformation of Inelastic Structures: SDF Systems*. Anil K. Chopra and Rakesh Goel. April 1999.

PEER 1999/01 *Interaction in Interconnected Electrical Substation Equipment Subjected to Earthquake Ground Motions.* Armen Der Kiureghian, Jerome L. Sackman, and Kee-Jeung Hong. February 1999.

PEER 1998/08 *Behavior and Failure Analysis of a Multiple-Frame Highway Bridge in the 1994 Northridge Earthquake.* Gregory L. Fenves and Michael Ellery. December 1998.

PEER 1998/07 *Empirical Evaluation of Inertial Soil-Structure Interaction Effects.* Jonathan P. Stewart, Raymond B. Seed, and Gregory L. Fenves. November 1998.

PEER 1998/06 *Effect of Damping Mechanisms on the Response of Seismic Isolated Structures.* Nicos Makris and Shih-Po Chang. November 1998.

PEER 1998/05 *Rocking Response and Overturning of Equipment under Horizontal Pulse-Type Motions.* Nicos Makris and Yiannis Roussos. October 1998.

PEER 1998/04 *Pacific Earthquake Engineering Research Invitational Workshop Proceedings, May 14–15, 1998: Defining the Links between Planning, Policy Analysis, Economics and Earthquake Engineering.* Mary Comerio and Peter Gordon. September 1998.

PEER 1998/03 *Repair/Upgrade Procedures for Welded Beam to Column Connections.* James C. Anderson and Xiaojing Duan. May 1998.

PEER 1998/02 *Seismic Evaluation of 196 kV Porcelain Transformer Bushings.* Amir S. Gilani, Juan W. Chavez, Gregory L. Fenves, and Andrew S. Whittaker. May 1998.

PEER 1998/01 *Seismic Performance of Well-Confined Concrete Bridge Columns.* Dawn E. Lehman and Jack P. Moehle. December 2000.